UNIVERSITE D'AIX-MARSEILLE

Physique et Sciences de la Matière

MADIREL/UMR N°7246

Thèse présentée pour obtenir le grade universitaire de docteur

Discipline : Physique et sciences de la matière
Spécialité : Matière condensée et nanosciences

Virginie BENOIT

Relation entre structure et texture de matériaux poreux et l'évaluation de leurs propriétés de piégeage du CO_2

Soutenue le 19/12/2017 devant le jury :

MCF. Frédéric PLANTIER	Université de Pau	Rapporteur
Prof. Christophe VOLKRINGER	ENS de chimie de Lille	Rapporteur
Prof. Guillaume MAURIN	Institut Charles Gerhardt	Examinateur
Prof. Pascale ROUBIN	Aix-Marseille Université	Présidente
MCF. Isabelle BEURROIES	Aix-Marseille Université	Co-directrice
Dr. Philip LLEWELLYN	Directeur de Recherche avec CNRS	Directeur de thèse

UNIVERSITE D'AIX-MARSEILLE

Physique et Sciences de la Matière

MADIREL/UMR N°7246

Thèse présentée pour obtenir le grade universitaire de docteur

Discipline : Physique et sciences de la matière
Spécialité : Matière condensée et nanosciences

Virginie BENOIT

Relation entre structure et texture de matériaux poreux et l'évaluation de leurs propriétés de piégeage du CO_2

Soutenue le 19/12/2017 devant le jury :

MCF. Frédéric PLANTIER	Université de Pau	Rapporteur
Prof. Christophe VOLKRINGER	ENS de chimie de Lille	Rapporteur
Prof. Guillaume MAURIN	Institut Charles Gerhardt	Examinateur
Prof. Pascale ROUBIN	Aix-Marseille Université	Présidente
MCF. Isabelle BEURROIES	Aix-Marseille Université	Co-directrice
Dr. Philip LLEWELLYN	Directeur de Recherche avec CNRS	Directeur de thèse

Remerciements

Ces travaux de thèse ont été réalisés au sein du Laboratoire Madirel (MAtériaux Divisés, Interfaces, Réactivité, Electrochimie) à l'Université Aix-Marseille, campus de l'Etoile. Ce doctorat a été soutenu financièrement par le projet européen M^4CO_2.

Je tiens tout d'abord à remercier vivement Messieurs Christophe Volkringer, Professeur à l'Ecole Nationale Supérieur de Chimie de Lille et Frédéric Plantier, Maitre de Conférences à l'Université de Pau pour avoir évalué ce travail de thèse en tant que rapporteurs. Je souhaite également exprimer ma gratitude aux autres membres du jury Madame Pascale Roubin, Professeur à l'Université Aix-Marseille et Monsieur Guillaume Maurin, Professeur à l'Institut Charles Gerhardt pour avoir lu attentivement ce travail de recherche.

Je souhaite remercier Monsieur Philip. L.Llewellyn et Madame Isabelle Beurroies, mon directeur et ma co-directrice de thèse pour m'avoir permis de réaliser ce projet de thèse durant ces trois années dans de très bonnes conditions. Je souhaite leur exprimer ma gratitude pour m'avoir encadré, conseillé et soutenu. En effet, Monsieur Philip L.Llewellyn et Madame Isabelle Beurroies ont toujours pris le temps nécessaire pour répondre à mes questions scientifiques et d'ordre expérimental. Je tiens également à les remercier pour m'avoir permis de valoriser ce travail de thèse en me donnant l'opportunité de prendre la parole lors de congrès scientifiques (présentations orales et posters).

Ce travail de thèse a été mené dans le cadre du projet européen M^4CO_2, cela a conduit à des réunions de projet biannuel ainsi qu'à des collaborations. De plus, je souhaite remercier Monsieur Freek Kaptjein, coordinateur du projet, pour les questions qu'il m'a posé lors des réunions et ses remarques qui ont été à chaque fois constructives. Je voudrai remercier l'équipe de Christan Serre (Madame Nathalie Stenou, Monsieur Marvin Benzaqui) de l'Université de Versailles pour les nombreux échanges que l'on a eus notamment à propos de l'étude sur le MOF MIL-96(Al). Je souhaite remercier les équipes de Guy De Weireld de l'Université de Mons et de Guillaume Maurin qui ont également participé à l'étude sur le MIL-96(Al) et pour les autres discussions que l'on a pu avoir. Enfin, je souhaite remercier l'équipe de Paul Wright et sa doctorante Angelica Orsi (Université de S^t Andrews, Ecosse) avec qui les échanges scientifiques ont toujours été très intéressants.

Je tiens à remercier Messieurs Yvan Cécere et Dominique Vincent pour leur travail technique mais aussi leur investissement lors de problèmes d'appareillages.

Je souhaite remercier Madame Maud Mercury qui m'a encadré lors de mon stage de Master 2 et m'a permis de rencontrer Monsieur Philip L.Llewellyn et Madame Isabelle Beurroies qui m'ont ensuite proposé ce travail de recherche au sein de l'équipe EnAP.

Je remercie justement toute l'équipe EnAP pour m'avoir si bien accueillie, tant sur le plan scientifique qu'humain. Pour les congrès et les réunions partagés avec une très bonne ambiance merci à Sandrine Bourrelly et Emily Bloch. Je voudrai remercier Marie-Vanessa Coulet pour les nombreuses discussions scientifiques et personnelles que j'ai toujours énormément appréciées. Je tiens à remercier l'ensemble du laboratoire, les personnes ont toujours été très sympathiques avec moi (Maryline Barbaroux, Joëlle Forestier, etc…)

Bien évidemment je souhaite remercier mes collègues de bureaux : Pierre-Henry, Damien, Ege, Nico, Rifan et Paul pour les nombreuses discussions, pauses café, les pépés du vendredi ou encore les fous rire. Un grand merci à toi Pierre-Henry pour avoir su organisé des sorties entre doctorants et avoir amené de l'ambiance dans le groupe ! On a partagé une très bonne atmosphère dans ce bureau,

mais je tiens aussi à remercier tous les autres doctorants. Tu n'étais pas dans notre bureau mais merci à toi Christophe pour tous ces bons moments et la découverte du Drama Club avec Laurence !

D'un point de vue personnel, je tiens à remercier de tout cœur mes parents, mon frère et Cassandra, qui ont toujours été là pour moi avec un soutien sans failles durant toutes ces années.

Julien, je souhaite te remercier pour avoir été à mes côtés pendant ces derniers mois d'écriture, pour ta compréhension, ton soutien, ton aide précieuse sans toi la fin aurait été beaucoup plus difficile ! Merci d'être là. Je voudrai remercier tes parents, Michèle et Marc, qui m'ont également soutenu (en aménageant à chaque fois le bureau !), conseillé et encouragé, ton frère Antony et Mickaël également, cela m'a énormément touché.

Merci à toutes les personnes qui étaient présente le jour de la soutenance, ma famille dont mes grands-parents qui ont fait le déplacement tout comme Michèle et Marc, Franck et merci aux amis.

Enfin merci à toutes les personnes que j'aurais pu oublier involontairement. Pour les doctorants et futurs thésards je vous souhaite une bonne continuation et bonne chance !

« Sachez vous éloigner car, lorsque vous reviendrez à votre travail, votre jugement sera plus sûr… »

Léonard de Vinci,
(1452 - 1519)

SOMMAIRE

INTRODUCTION

Introduction

Actuellement, l'émission de gaz à effet de serre dans l'atmosphère, principalement le dioxyde de carbone (CO_2), est une préoccupation tant sur le plan environnemental qu'économique. Les émissions de CO_2 proviennent majoritairement de sources anthropogéniques, c'est-à-dire liées à l'activité humaine et contribuent au réchauffement climatique. Les centrales électriques, les industries chimiques et pétrochimiques, les cimenteries, etc. constituent les sources émettrices de CO_2 qui représentaient environ 56.6% des émissions totales de gaz à effet de serre en 2004 [1]. Des organisations et conventions telles que : 'The International Panel on Climate Change (IPCC)' créée en 1988 et la Convention-cadre des Nations Unies sur les changements climatiques de 1992, dont est issu le Protocole de Kyoto (1997) et plus récemment la COP21 en 2015 ont pour objectif d'établir des solutions visant à réduire les rejets de gaz à effet de serre [2]

Si la première solution est de diminuer la consommation énergétique, de nombreuses mesures visent à capturer et stocker le CO_2. Ainsi, des technologies de capture et de séquestration du CO_2 sont proposées et regroupées sous l'appellation 'Carbon Capture and Storage' (CCS). Dans le but de capturer efficacement le CO_2 émis à partir de combustible fossile, trois approches sont envisagées : la post-combustion, la pré-combustion et l'oxy-combustion. Il existe différentes techniques de séparation de CO_2 pouvant être appliquées en fonction des conditions de pression et de température du flux gazeux: l'absorption, l'adsorption, la distillation cryogénique et les membranes [3]. Parmi ces techniques, l'absorption par solution aqueuse d'amine (monoéthanolamine, MEA) est largement répandue à l'échelle industrielle. Cependant, ce type de technologie présente certains inconvénients tels que : une faible capacité d'absorption de CO_2 du solvant, des problèmes de corrosion des installations, une dégradation du solvant par la présence d'impuretés dans le gaz (SO_2, NO_2, HCl, etc.) et une consommation élevée d'énergie lors de la régénération du solvant [4].

Actuellement, les membranes représentent une alternative prometteuse par rapport aux méthodes conventionnelles de séparation de gaz telle que l'absorption à base de solutions aqueuses d'amines. Une membrane étant une barrière perméable et sélective séparant deux milieux, elle permet le passage préférentiel de certains composés en mélange gazeux et/ou liquide. Les membranes présentent les avantages suivants : elles ne nécessitent pas de changement de phase liquide-gaz, elles sont faciles à mettre en œuvre et présentent une faible empreinte carbone. Il existe différents types de membrane : polymérique, inorganique et à matrice mixte.
La première membrane polymérique a été synthétisée dans les années 80 pour la capture du CO_2 issu du gaz naturel [5]. Cependant, les membranes polymériques présentent certains inconvénients: une faible résistance aux contaminants, une faible stabilité chimique et thermique ainsi qu'une perméabilité et une sélectivité limitées. Dans le but d'améliorer les propriétés de séparation de gaz, des membranes de nature inorganique à base de céramique [6], de carbone [7], de zéolithes [8], d'oxydes [9], de Metal-Organic Frameworks (MOFs) [10] etc ont été développées. Bien que ces membranes inorganiques présentent d'excellentes propriétés de séparation de gaz, elles offrent une faible résistance mécanique.

Ainsi, les membranes à matrice mixte ont été élaborées afin d'allier à la fois la résistance mécanique des membranes polymériques et les bonnes propriétés de séparation de gaz des membranes inorganiques. Une membrane à matrice mixte est composée d'une phase polymérique au sein de laquelle sont dispersées des particules de matériaux poreux du type : zéolithes, charbons actifs, silice etc.

Cette thèse s'est effectuée dans le cadre du projet européen M^4CO_2 'Mixed Matrix Membranes based on highly engineered Metal-organic frameworks and polymer (M4) for energy efficient CO_2 capture'

(FP7/2007-2013) qui s'inscrit dans cette problématique de conception de membranes à matrice mixte pour la séparation du CO_2.

Dans ce projet, les particules de matériaux poreux sont à base de MOFs. Les MOFs sont des matériaux poreux cristallins construits à base d'ions métalliques et de ligands organiques pour former des structures tridimensionnelles (3D). Ils possèdent une grande diversité de propriétés physiques et chimiques grâce aux différents métaux et ligands organiques disponibles. De plus, ils possèdent des surfaces spécifiques et des volumes poreux élevés, ce qui en fait des matériaux prometteurs pour les applications de séparation de gaz [11], [12].

L'objectif de ce travail était d'étudier différents facteurs que l'on peut distinguer dans deux groupes (i) la nature du MOFs: influence des conditions de synthèse, de la fonctionnalisation ou du changement de ligand organique dont les effets sont d'engendrer des textures et structures différentes.

(ii) les propriétés du procédé d'adsorption: influence de la présence d'eau, énergie mise en jeu, qui permettent de mieux comprendre les mécanismes mis en œuvre.

Globalement tous ces paramètres ont une influence sur les propriétés d'adsorption de CO_2 (capacité d'adsorption, enthalpie d'adsorption, sélectivité) par les MOFs et il est intéressant de dégager des tendances afin d'identifier les paramètres ayant le plus fort impact afin de prévoir et d'optimiser des synthèses de nouveaux matériaux et des conditions opératoires.

Le premier chapitre est consacré : à la description des techniques de séparation de CO_2 dont l'adsorption et à la présentation des différents types d'adsorbants pouvant être utilisés. Le deuxième chapitre, rappelle le principe du phénomène d'adsorption, les techniques expérimentales employées ainsi que les outils permettant l'exploitation des données d'adsorption.

Le chapitre trois recense les capacités d'adsorption de CO_2, les enthalpies d'adsorption et les sélectivités obtenues pour différentes familles de MOFs.

Enfin le dernier chapitre, aborde une approche « relation de structure-propriété » (QSPR) avec des matériaux de structure bien définie : les 'Zeolitic Imidazolate Frameworks' (ZIFs), dans le but de dégager des tendances par rapport à l'adsorption de CO_2.

References

[1] A. Samanta, A. Zhao, G. K. H. Shimizu, P. Sarkar, et R. Gupta, « Post-Combustion CO2 Capture Using Solid Sorbents: A Review », *Ind. Eng. Chem. Res.*, vol. 51, n° 4, p. 1438-1463, févr. 2012.

[2] « IPCC Fourth Assessment Report: Climate Change 2007 (AR4) ». [En ligne]. Disponible sur: http://www.ipcc.ch/publications_and_data/ar4/wg2/en/contents.html. [Consulté le: 06-nov-2017].

[3] J. C. M. Pires, F. G. Martins, M. C. M. Alvim-Ferraz, et M. Simões, « Recent developments on carbon capture and storage: An overview », *Chem. Eng. Res. Des.*, vol. 89, n° 9, p. 1446-1460, sept. 2011.

[4] A. A. Olajire, « CO2 capture and separation technologies for end-of-pipe applications – A review », *Energy*, vol. 35, n° 6, p. 2610-2628, juin 2010.

[5] R. W. Baker et K. Lokhandwala, « Natural Gas Processing with Membranes: An Overview », *Ind. Eng. Chem. Res.*, vol. 47, n° 7, p. 2109-2121, avr. 2008.

[6] S. Smart, C. X. C. Lin, L. Ding, K. Thambimuthu, et J. C. D. da Costa, « Ceramic membranes for gas processing in coal gasification », *Energy Environ. Sci.*, vol. 3, n° 3, p. 268-278, mars 2010.

[7] A. F. Ismail et L. I. B. David, « A review on the latest development of carbon membranes for gas separation », *J. Membr. Sci.*, vol. 193, n° 1, p. 1-18, oct. 2001.

[8] J. Caro et M. Noack, « Zeolite membranes – Recent developments and progress », *Microporous Mesoporous Mater.*, vol. 115, n° 3, p. 215-233, nov. 2008.

[9] S. Basu, A. L. Khan, A. Cano-Odena, C. Liu, et I. F. J. Vankelecom, « Membrane-based technologies for biogas separations », *Chem. Soc. Rev.*, vol. 39, n° 2, p. 750-768, janv. 2010.

[10] J. Gascon, F. Kapteijn, B. Zornoza, V. Sebastián, C. Casado, et J. Coronas, « Practical Approach to Zeolitic Membranes and Coatings: State of the Art, Opportunities, Barriers, and Future Perspectives », *Chem. Mater.*, vol. 24, n° 15, p. 2829-2844, août 2012.

[11] D. M. D'Alessandro, B. Smit, et J. R. Long, « Carbon Dioxide Capture: Prospects for New Materials », *Angew. Chem. Int. Ed.*, vol. 49, n° 35, p. 6058-6082, août 2010.

[12] K. Sumida *et al.*, « Carbon Dioxide Capture in Metal–Organic Frameworks », *Chem. Rev.*, vol. 112, n° 2, p. 724-781, févr. 2012.

Chapitre 1 – Procédés de capture, techniques de séparation et matériaux poreux pour la capture du dioxyde de carbone

Table des matières

Chapitre 1 - Procédés de capture, techniques de séparation et matériaux poreux pour la capture du dioxyde de carbone

Ce premier chapitre expose les enjeux sociétaux et environnementaux liés aux émissions de dioxyde de carbone (CO_2) et les procédés actuels de capture de CO_2 : pré-combustion, post-combustion et oxy-combustion. Dans ce chapitre, sont abordées les techniques de séparation gazeuse de CO_2 (avantages, inconvénients et domaines d'applicabilité). Un certain nombre de ces techniques utilisent des matériaux poreux. Ainsi une comparaison entre les principaux matériaux poreux utilisés habituellement est faite avec les Metal-Organic Frameworks (MOFs) : matériaux poreux hybrides organiques-inorganiques récemment envisagés pour ces applications.

A. Contexte environnemental

Depuis ces dernières décennies, il y a une augmentation des émissions de gaz à effet de serre (GES) dans l'atmosphère, principalement le dioxyde carbone (CO_2) contribuant au réchauffement climatique. D'autres gaz sont émis en plus du CO_2 comme le méthane (CH_4), les protoxydes d'azote (N_2O), les hydrofluorocarbures (HFCs), les perfluorocarbures (PFCs) et les hexafluorocarbures de sulfure (F6C) [1]. Le CO_2 émis provient de diverses sources anthropogéniques (Figure 1.1) et représentait en 2004 environ 77% de la totalité des gaz à effet de serre rejetés à l'échelle mondiale, dont 50% provenait de la combustion de matière fossile [2]. De plus, entre les années 1970 et 2004, les rejets de CO_2 sont passés de 21 à 38 Gt/année soit une augmentation d'environ 80%. Les émissions mondiales de CO_2 sont amenées à augmenter au cours des prochaines décennies à cause de la croissance économique et du développement industriel même si en France la tendance est à la décroissance depuis 2006.

Des organisations et conventions telles que : 'The International Panel on Climate Change (IPCC)' formé en 1988 et la Convention-cadre des Nations Unies sur les changements climatiques en 1992 dont est issu le Protocole de Kyoto de 1997 et plus récemment la COP21 en 2015 ont pour objectif d'établir des solutions visant à réduire les rejets de gaz à effet de serre. L'utilisation d'énergies renouvelables (biomasse, solaire, etc.) à la place de sources carbonées pour la production d'énergie est une alternative envisageable. Néanmoins, les technologies proposées ne sont pas encore assez développées pour permettre des applications industrielles.

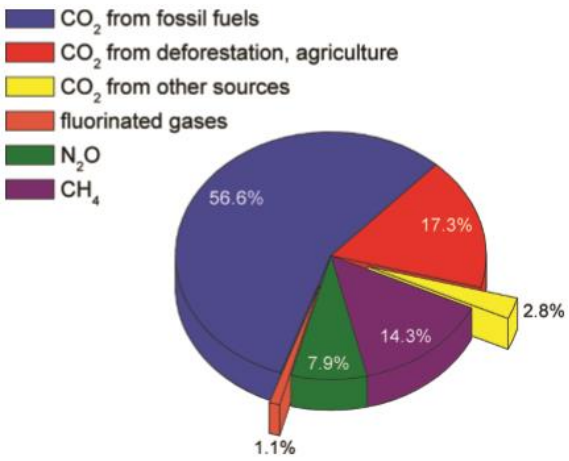

Figure 1.1 - Contribution (%) des différents gaz à effet de serre à la globalité des émissions incluant les diverses sources anthropogéniques émettrices de CO_2, en 2004 dans le monde [1]

Pour contrôler et stabiliser les émissions de CO_2, des solutions de capture et de stockage du CO_2 sont proposées et regroupées sous l'appellation 'Carbon Capture and Storage (CCS)' et comprenant trois étapes :

- La capture :

Actuellement, trois processus sont envisagés pour la capture du CO_2: correspondant aux procédés de post et de pré- et d'oxy-combustion. Ces procédés utilisent différentes techniques pour séparer le CO_2 des gaz de combustion : l'absorption, l'adsorption, la distillation et la séparation membranaire. Ces procédés et techniques sont détaillés dans la section C.

- Le transport :

L'acheminement du CO_2 se fait via des pipelines, des bateaux ou des camions citernes. Le choix du mode de transport dépend de la distance à parcourir entre le point de capture du CO_2 et son lieu de stockage. Préalablement au transport, le CO_2 est séparé des impuretés (eau, méthane, sulfure d'hydrogène, etc.) ayant pu être captées avec la capture du CO_2. Le CO_2 gazeux est ensuite compressé dans un état de fluide supercritique dans une gamme de pression de 80 à 150 bar et une densité de 900 $kg.m^3$. Le coût du transport dépend de la composition et de la pression du courant de CO_2 et du mode de transport choisi. Généralement, cela varie entre 90 et 120 kWh/ tonne de CO_2 [3].

- Le stockage :

Il existe trois options possibles pour le stockage du CO_2 : géologique, océanique ou sa minéralisation. La minéralisation du CO_2 consiste en sa transformation en carbonates par réaction chimique [4]. Cela permet le stockage du CO_2 sur une longue période, cependant c'est un procédé coûteux. Le stockage océanique se fait par injection du CO_2 en profondeur dans l'océan. L'acidification des océans par le CO_2 peut affecter négativement l'écosystème marin. Une option adéquate est le stockage géologique dans des réservoirs.

B. Procédés de capture du CO_2

Le dioxyde de carbone (CO_2), gaz à effet de serre, formé lors de la combustion de matière fossile (pétrole, charbon, gaz naturel) est majoritairement rejeté dans l'atmosphère. Actuellement, trois types d'approches de CCS sont envisagées (Figure 1.2) :

- Pré-combustion
- Post-combustion
- Oxy-combustion

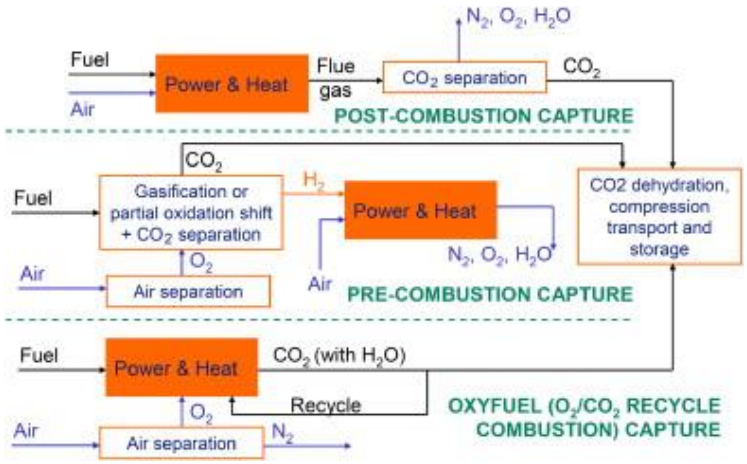

Figure 1.2 - Représentation des trois types de technologies de capture du CO_2 : post- pré- et oxy-combustion [2]

1. Post-combustion

La capture du CO_2 s'effectue suite à la calcination sous air de combustible fossile comme le charbon ou le gaz naturel (Figure 1.2). En sortie, les gaz de combustion produits sont à la pression atmosphérique (1 bar). Ils sont composés de CO_2, N_2 et d'impuretés (H_2O, NO_x, SO_x, etc.). La teneur en CO_2 et en impuretés des gaz de combustion est fonction de la nature du combustible utilisé. Cependant la concentration en CO_2 n'excède pas 15% (vol). Le tableau 1.1 fournit un exemple de composition pour la combustion de charbon.

Molécule	Concentration (en volume)
N_2	73-75%
CO_2	15-16%
H_2O	5-7%
O_2	3-4%
SO_2	800 ppm
SO_3	10 ppm
NO_x	500 ppm
HCl	100 ppm
CO	20 ppm
Hydrocarbures	10 ppm
Hg	1 ppb

Tableau 1.1 – Exemple type de composition d'un flux gazeux provenant de la combustion du charbon [1]

La technique de séparation de CO_2 la plus répandue pour la post-combustion est l'absorption par solvant aminé (voir C.1.a). Le procédé de post-combustion peut s'appliquer à des installations industrielles existantes, ce qui est un avantage majeur sur les autres techniques de capture de CO_2. La faible concentration de CO_2 par rapport au N_2 dans les gaz de combustion entraine de grands volumes gazeux à traiter au sein des unités de séparation. Cela impacte directement les coûts de dimensionnement et en fait le principal désavantage de la post-combustion.

2. Oxy-combustion

De manière similaire à la post-combustion, la séparation du CO_2 des gaz de combustion s'effectue en aval de l'étape de calcination.

L'oxy- et la post-combustion diffèrent par la nature des comburants employés qui sont respectivement l'oxygène et l'air. La présence d'une unité de séparation d'air fournit l'oxygène. L'oxygène pur en tant que comburant produit des gaz de combustion de composition suivante : CO_2, SO_2, H_2O et des particules. Le SO_2 est éliminé par des méthodes de désulfurisation et l'eau par condensation. La concentration en CO_2 des gaz de combustion avoisine 80-98%, suivant la nature de la matière fossile [3].

Comparativement à la post-combustion, les techniques de séparation du CO_2 par oxy-combustion sont plus efficaces car la concentration en CO_2 est élevée. De plus, le N_2 est éliminé avant la calcination ce qui ne génère pas de NO_x. L'oxy-combustion s'avère donc être un procédé de capture très avantageux. Toutefois, la présence de SO_x est un inconvénient car cela peut créer des problèmes de corrosion. Le désavantage principal de l'oxy-combustion est le coût de l'installation engendré par l'unité de séparation d'air.

3. Pré-combustion

Le CO_2 est séparé du combustible fossile (charbon, gaz naturel) en amont de la combustion contrairement à la post- ou l'oxy-combustion. Le procédé de pré-combustion s'applique majoritairement aux centrales électriques à cycle combiné à gazéification intégrée (CCGI). Lorsque la matière fossile est le charbon, celui-ci subit une première étape dite de 'gazéification' en présence d'oxygène qui produit un gaz de synthèse 'syngas' composé principalement d'un mélange de H_2 et CO (1.1). Une seconde réaction appelée 'Water Gas Shift Reaction' convertit le CO en présence de vapeur d'eau en un mélange CO_2 et H_2 (1.2). Dans le cas où le combustible fossile est le gaz naturel, le syngas est produit à partir du 'reformage' du CH_4 en présence de vapeur d'eau (1.3) [3]:

$$Charbon \rightarrow CO_{(g)} + H_{2(g)} \quad (1.1)$$

$$CO_{(g)} + H_2O \rightarrow H_{2(g)} + CO_{2(g)} \quad (1.2)$$

$$CH_4 + H_2O \rightarrow CO + H_{2(g)} \quad (1.3)$$

Le procédé de pré-combustion génère un mélange gazeux avec une concentration en CO_2 élevée (> 20%). En raison de la forte concentration en CO_2, l'efficacité des techniques de séparation de CO_2 sont améliorées comme pour l'oxy-combustion, rendant la technique de pré-combustion avantageuse. L'inconvénient majeur de la pré-combustion est le coût élevé de l'installation.

4. Bilan

Le tableau 1.2 fourni les domaines d'applications, les avantages et les inconvénients de chaque procédé de capture de CO_2.

	Avantages	Inconvénients
Post-combustion : Faible pression partielle du CO_2 ; Pression atmosphérique (1 bar) du flux de gaz	Applicable à une majeure partie des installations industrielles implantées	- Nécessité de traiter de grands volumes gazeux pour augmenter la concentration en CO_2
Oxy-combustion : Pression partielle du CO_2 élevée ; Pression du flux de gaz élevée	Applicable à des installations existantes	Production de O_2 Maintenir le système à faible température réduit l'efficacité du procédé
Pré-combustion : Pression partielle du CO_2 élevée ; Pression du flux de gaz élevée	Augmentation de l'efficacité de séparation Réduction potentiel des coûts de compression	Applicable à de nouvelles installations industrielles Coût des équipements

Tableau 1.2 – Avantages, inconvénients et domaine d'applicabilité des procédés de capture de CO_2

C. Techniques de séparation

Cette section aborde les diverses techniques de séparation applicables aux procédés de post-, de pré- et d'oxy-combustion pour la capture de CO_2 à partir de mélanges gazeux. Ces techniques comprennent l'absorption, l'adsorption, la distillation cryogénique et la perméation gazeuse (séparation membranaire) [4].

1. Absorption

L'absorption est un phénomène chimique ou physique qui repose sur la dissolution d'une espèce (atome, ion ou molécule) au sein d'une phase gazeuse, liquide ou solide. Lorsque l'absorption est d'origine chimique la dissolution s'effectue par réaction chimique contrairement à l'absorption physique qui est dépendante de la pression et de la température du flux de gaz à traiter (loi de Henry).

A l'échelle industrielle, le procédé d'absorption est largement utilisé pour le traitement de gaz acide : H_2S, NO_x et CO_2 [5].

a) Absorption chimique : solution aqueuse d'amines

L'absorption chimique par solution aqueuse d'amines est une technique de séparation commercialisée et très répandue pour la capture de CO_2. Typiquement, les solutions aqueuses d'amines les plus fréquemment utilisées sont : la monoéthanolamine (MEA), la diéthanolamine (DEA), la méthyldiéthanolamine (MDEA), la diglycolamine (DGA), la diisopropylamine (DIPA). Une étude a été menée par Veawab *et al*. [6] visant à comparer les performances d'absorption de CO_2 de ces différentes solutions aqueuses d'amines : MEA, DEA, MDEA, DGA et DIPA. Cette étude a révélé une efficacité d'absorption de CO_2 de plus de 90% en faveur de la MEA surpassant celles des autres solutions aqueuses d'amines car la MEA à une cinétique d'absorption de CO_2 plus rapide.

Au sein de la colonne d'absorption, la MEA et le CO_2 réagissent pour former des espèces carbamates (1.4). Dans le but de relâcher le CO_2 contenu dans la solution de MEA, celle-ci est envoyée dans une colonne de désorption ou elle est chauffée (100-200°C). La solution de MEA appauvrie en CO_2 est ensuite refroidie (40-65°C) pour être recyclée dans la colonne d'absorption.

$$C_2H_4OHNH_2(MEA) + H_2O + CO_2 \leftrightarrow C_2H_4OHNH_3^+ + HCO_3^- \quad (1.4)$$

L'avantage majeur de cette technique de séparation est la pureté du flux de CO_2 obtenu (> 99%). Néanmoins, l'absorption par MEA présente des inconvénients :

- La faible capacité d'absorption en CO_2 du solvant
- La détérioration du solvant par certains composés tels que SO_2, NO_2, HCl, HF. Cela provoque une perte de solvant, des problèmes de corrosion et l'émission de nitrosamines, nitramines potentiellement dangereuses pour la santé humaine et l'environnement
- La régénération du solvant nécessite des températures élevées entrainant une forte consommation énergétique

Une alternative à l'absorption par MEA est l'utilisation de solutions aqueuses de sels d'ammonium (ex : carbonate d'ammonium). Cette technique de séparation s'appelle 'Chilled Ammonia Process' (CAP) : l'absorption de CO_2 s'effectue à basse température (0-20°C) tandis que la régénération du solvant se fait à des températures et pression élevées [7]. L'absorption par sels d'ammonium entraîne moins de problèmes de dégradation par rapport à l'utilisation de MEA, ce qui en fait une technique de séparation prometteuse.

b) Absorption physique

Les procédés d'absorption physique reposent sur la dissolution des composés présents dans le gaz sans réaction chimique et sont principalement utilisés pour le traitement de gaz acides : CO_2, H_2S, COS, SO_2 [3]. Typiquement, les solvants employés sont organiques ex : le méthanol. L'absorption des gaz acides s'effectue à basse température (20 à -60°C) pour des pressions élevées de 10 à 80 bar. La régénération s'effectue par désorption des gaz acides par détente (abaissement de la pression) du solvant usé ou par stripage (extraction des composés par l'air ou un gaz inerte, le diazote). Les performances d'absorption des procédés physiques dépendent de: la température de mise en contact entre le gaz et le solvant ainsi que de la pression partielle dans le gaz du composé à séparer, dans notre cas le CO_2. L'efficacité d'absorption est optimale à basse température et pour une pression partielle élevée en CO_2.

Les procédés physiques les plus connus et les plus utilisés sont [8]:

- Selexol : ce procédé a été mis en œuvre par la firme américaine 'Allied Chemical Corporation' et s'applique au traitement de gaz naturel principalement pour la capture de dioxyde de carbone (CO_2) et de composés soufrés (H_2S). Le solvant organique employé est le diméthyle éther polyéthylène glycol de formule chimique $[CH_3(CH_2CH_2O)_nCH_3]$ avec n variant entre trois et neuf. En amont de l'unité d'absorption, une étape de séchage du gaz d'entrée est nécessaire en raison de l'affinité élevée entre le solvant et l'eau. Le procédé Selexol peut s'effectuer à basse pression, néanmoins son efficacité est optimale à haute pression.

- Rectisol : ce procédé s'applique principalement à la purification de gaz de synthèse pour l'élimination des gaz acides (H_2S, COS) [9]. Cependant, cette technique de séparation peut également s'appliquer au traitement de gaz naturel pour l'élimination du CO_2. Le procédé Rectisol utilise le méthanol comme solvant organique. Dans les conditions normales de température et de pression, le méthanol a une pression de vapeur saturante élevée, c'est pourquoi l'absorption s'effectue à basse température (entre -40 et -62°C) afin de limiter son évaporation. La régénération du solvant s'effectue par la mise en contact avec un courant d'eau grâce à la miscibilité complète méthanol/ eau. L'énergie et le coût de l'opération engendré par la réfrigération du solvant peuvent être considérés comme un désavantage du procédé Rectisol.

- Fluor : le procédé Fluor a été élaboré par la compagnie américaine 'Fluor Corporation' et s'applique à la décarbonatation de flux gazeux ayant une forte teneur en CO_2. Ce procédé utilise le carbonate de propylène comme solvant organique. L'absorption s'effectue pour une plage de température comprise entre -20 et 0°C.

L'intérêt majeur des procédés d'absorption physique réside dans l'étape de régénération ne nécessitant pas de traitement thermique et qui contribue à diminuer les coûts de l'installation. Néanmoins, les procédés d'absorption physique présentent des inconvénients liés à l'affinité des solvants : co-absorption d'hydrocarbure lourd, sélectivité élevée vis-à-vis du H_2S. Cela peut impacter de manière négative la séparation du CO_2. Les procédés d'absorption physique sont plutôt envisagés pour la pré-combustion.

2. Distillation cryogénique

La distillation cryogénique s'emploie pour la séparation gazeuse, en particulier pour l'élimination de gaz acides : le CO_2 et l'H_2S contenus respectivement dans les gaz de combustion et le gaz naturel (5). Contrairement à une distillation 'classique' pour laquelle la séparation des constituants du mélange se base sur leur température d'ébullition, celle-ci repose sur leur température de condensation. Afin de récupérer le CO_2 des gaz de combustion, le mélange est refroidi dans une gamme de températures de -100 à -135°C soit en dessous du point triple du CO_2 -56°C [10]. Le CO_2 solidifié est ensuite compressé dans une gamme de pression de 100 à 200 bar afin d'être séparé des gaz légers. Le CO_2 compressé est intéressant pour le transport par pipeline. La distillation cryogénique s'applique à des mélanges gazeux ayant une forte teneur en CO_2. Cette technique a l'avantage de séparer le CO_2 du mélange gazeux avec un taux de pureté élevé aux alentours de 90-95% [10]. Cependant, la distillation cryogénique reste très énergivore et coûteuse en raison des conditions opératoires (basse température et haute pression). De plus, si l'effluent gazeux contient de l'eau, il est nécessaire de l'éliminer au préalable au risque de former de la glace.

3. Adsorption

Le terme 'adsorption' désigne le phénomène d'enrichissement d'un ou plusieurs constituants au voisinage d'une interface fluide (liquide ou gaz)/ solide. Sous l'appellation adsorption sont regroupés deux phénomènes appelés 'physisorption' et 'chimisorption' qui se distinguent par la force des interactions mises en jeu.

La physisorption fait référence à un processus exothermique gouverné par des interactions de faible énergie de type Van der Waals entre les molécules adsorbées et la surface du solide. La chimisorption désigne le phénomène pour lequel les molécules adsorbées sont liées à la surface du solide par

réaction chimique. Dans le cas de la physisorption, l'étape de désorption permet de restituer l'adsorbant et les molécules adsorbées dans leur état initial sans altération des propriétés chimiques et physiques. Les interactions de faible énergie permettent donc une régénération totale de l'adsorbant à la fois faiblement énergétique et coûteuse. C'est un avantage majeur pour les procédés industriels de type post- ou pré-combustion.

La partie qui suit comprend une description d'adsorbants potentiellement attractifs pour la séparation de CO_2 dont les 'Metal-Organic Frameworks' qui font intervenir la physisorption et qui sont les matériaux de base de l'étude. La description du phénomène d'adsorption et les interactions mises en jeu sont discutées au chapitre 2.

a) Adsorbant chimique

(1) Oxydes métalliques

Les oxydes métalliques sont des espèces composées de l'association d'atomes d'oxygène et de métaux. Les sites basiques des oxydes métalliques et le caractère acide du CO_2 favorisent son adsorption, notamment pour ceux ayant un faible rapport charge/ rayon les rendant plus ioniques en augmentant le caractère basique des sites [11], [12]. Ils comprennent les oxydes métalliques alcalins (Na_2O, K_2O) et alcalino-terreux (CaO, MgO) mais les oxydes métalliques couramment étudiés sont à base de calcium, magnésium ou encore des zirconates de lithium. Néanmoins, d'autres oxydes métalliques peuvent être utilisés tel que les oxydes de sodium, de césium, de barium, de fer, etc [13]–[16].

La capture du CO_2 par un oxyde métallique se base sur la réaction chimique exothermique suivante [13] :

$$MO(s) + CO_2\ (g) \rightarrow MCO_3\ (s) \qquad (1.5)$$

L'oxyde métallique réagit avec le CO_2 dans des proportions stœchiométriques équivalentes pour former un carbonate de métal alcalino-terreux.

Les minéraux à base de calcium sont largement répandus dans la nature sous forme de calcaire ou de dolomite faisant des oxydes de calcium, des adsorbants facilement disponibles. Les oxydes de calcium sont employés pour des procédés à haute température tels que la production d'hydrogène ; la séparation de CO_2 des gaz de combustion.

Basée sur la stœchiométrie de la réaction de carbonatation, la quantité maximale théorique de CO_2 adsorbée par un oxyde de calcium est de 17.8 mmol.g^{-1}. Certaines études ont montré que l'adsorption de CO_2 par des oxydes de calcium est influencée par divers facteurs :

- La nature du précurseur : une étude menée par Han *et al.* [17] sur trois oxydes de calcium différents et ayant comme précurseurs la dolomite a montré des capacités d'adsorption de CO_2 dépendantes de la teneur en oxyde de calcium. Les capacités d'adsorption de CO_2 obtenues varient entre 2 et 8 mmol.g^{-1} et sont plus faibles que celles obtenues pour un oxyde de calcium dérivant d'un précurseur pur de $CaCO_3$ (12 mmol.g^{-1}).

- La cinétique d'adsorption : l'adsorption de CO_2 par des oxydes de calcium se fait en deux étapes [13]. Une première étape assez rapide, dédiée à la formation d'une couche de carbonate où le taux de carbonatation est influencé par deux paramètres : la température et la pression. Une seconde étape plus lente, ou le taux de carbonatation est affecté par le remplissage des pores

et très peu par la pression de CO_2. Comparativement à d'autres adsorbants tels que les zéolithes (section b) 1)) ou les charbons actifs (section b 2) (i)), plusieurs heures sont nécessaires pour atteindre 70% de la capacité totale d'adsorption de CO_2.

Les oxydes de calcium possèdent les avantages d'être à faible coût et facilement disponibles en raison de l'abondance des précurseurs.

Les oxydes métalliques peuvent être employés pour la 'Chemical-Looping Combustion (CLC)'. La 'Chemical-Looping Combustion' initialement proposée par Richter et Knoche en 1983 est un procédé prometteur pour la capture de CO_2 [18]. De manière analogue aux procédés conventionnels de combustion, cette technique repose sur une réaction d'oxydo-réduction à la différence que le contact entre le combustible et le comburant est indirect. Ce procédé nécessite l'utilisation de deux réacteurs distincts, respectivement dédiés aux flux d'air et de combustible fossile (Figure 1.3).

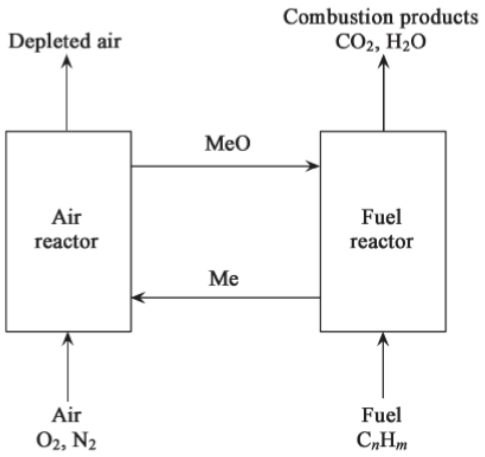

Figure 1.3 – Schéma fonctionnel de la 'Chemical-Looping Combustion (CLC)' ou MeO et Me représentent les courants de gaz vecteurs respectivement d'oxyde métallique et de métal [3]

La connexion entre ces deux réacteurs est assurée par un lit de particules fluidisé circulant du réacteur d'air au réacteur de combustible fossile. Typiquement, des lits de particules d'oxydes métalliques tels que Fe_2O_3, NiO, CuO ou Mn_2O_3 sont employés [3]. Au sein du réacteur de flux d'air, l'oxydation du dioxygène, réaction exothermique, entraine la formation d'oxyde métallique de type MeO. La réduction du combustible fossile, réaction endothermique, conduit à la formation de gaz de combustion : CO_2 et H_2O ainsi qu'une espèce métallique de type Me. Le dioxyde de carbone est ensuite séparé de l'eau par condensation.

(2) Composés hydrotalcites

Les composés hydrotalcites (HTlcs) appartiennent à la classe des argiles de type anionique et sont étudiés pour divers domaines d'applications : la catalyse, l'échange anionique et l'adsorption. Ces composés sont constitués d'un ensemble de couches d'hydroxyde métallique de formule générale $[(M^{2+}_{1-x}M^{3+}_{x}(OH)_2]^{x+}(A^{m-}_{x}/m\ .\ nH_2O)^{x-}$ ou : M^{2+} = Mg^{2+}, Ni^{2+}, Zn^{2+} etc.; M^{3+} = Al^{3+}, Fe^{3+}, Cr^{3+} etc.; A^{m-} = CO_3^{2-} ; SO_4^{2-}, NO^{3-} etc ; et x compris entre 0.17 et 0.33 [19]. L'excès de charges positives (divalentes et trivalentes) localisées au sein des sites octaédriques des couches d'hydroxyde est contrebalancé par les charges anioniques et les molécules d'eau situées entre les couches d'hydroxyde.

Les hydrotalcites adsorbent de faibles quantités de CO_2 (< 1 mmol.g^{-1}) par rapport à d'autres adsorbants chimiques. L'adsorption de CO_2 par des hydrotalcites est influencée par plusieurs paramètres :

- Le ratio de cations divalents/ trivalents : une étude menée par Rodrigue *et al.* [19], [20] sur trois hydrotalcites commerciales a mis en évidence une quantité de CO_2 adsorbée optimale (± 0.4 mmol.g^{-1}) pour un ratio de cations Mg^{2+}/ Al^{3+} de 1 :1 à 1 bar et 573K.

- La nature de la charge anionique : Rodrigue *et al.* [19], [20] ont montré un effet de la nature de l'anion sur la capacité d'adsorption de CO_2. A 1 bar et 573K, ils ont observé une augmentation de la quantité de CO_2 adsorbée de 0.2 à 0.5 mmol.g^{-1}, respectivement pour les anions OH^- et CO_3^{2-}.

b) Physisorbants

(1) Zéolithes

Les zéolithes sont des structures cristallines poreuses naturelles ou synthétiques applicables aux domaines de la séparation gazeuse et de la purification ; de l'échange ionique ou encore de la catalyse [21]. Ce sont des matériaux inorganiques à base d'atomes de silicium et dont quelques éléments sont généralement substitués par des atomes d'aluminium (aluminosilicates).

Les zéolites d'aluminosilicate sont des structures rigides en 3D qui reposent sur un motif tétraédrique TO_4 (T = atomes de silicium et d'aluminium), de formule générale $M_{x/n}[(AlO_2)_x(SiO_2)_y].MH_2O$ (M = contre ion). L'électronégativité existant au sein des structures zéolitiques est compensée par le contre ion (métaux alcalins ou alcalino-terreux) localisé dans les cavités [22].

Les zéolithes sont connues pour leurs propriétés de tamis moléculaire grâce à des réseaux poreux bien définis et des tailles de pores allant de 0.5 à 1.2 nm. Il existe plus de 170 topologies zéolitiques (LTA ; FAU etc.) recensées par 'The International Zeolithe Association (IZA)'[23].

A titre d'exemple, les structures de zéolithe de type A et faujasite (FAU) X et Y à base d'unités sodalites (SOD) sont représentées en Figure 1.4. Les zéolithes X et Y possèdent des structures et des topologies identiques mais diffèrent par leurs rapports Si/Al qui sont respectivement de 1-1.5 et 1.5-3 [22].

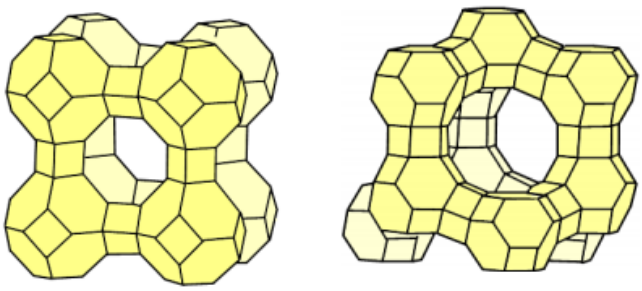

Figure 1.4 – Structures à base de cage sodalite (SOD) avec un arrangement de zéolithe de type A (gauche) et de faujasite (FAU) : zéolithes X et Y (droite) [24]

L'adsorption de CO_2 au sein des zéolithes est gouvernée par le phénomène de physisorption. Ce type de matériau adsorbe des quantités plus élevées de CO_2 que d'autres adsorbants comme les composés hydrotalcites. Cependant, divers facteurs peuvent avoir un impact sur les capacités d'adsorption de CO_2 tels que :

- La nature du contre ion : De Brieve *et al.* [25] ont effectué l'adsorption de CO_2 à 273K sur une zéolithe NaY et un lot de zéolithes avec différentes teneurs en Ca^{2+}. Les auteurs ont observé une quantité de CO_2 adsorbée pour la zéolithe NaY d'environ 5 $mmol.g^{-1}$ à 0.1 bar, supérieure aux quantités adsorbées par les zéolithes contenant le contre ion Ca^{2+}.

- Le rapport Si/Al : l'adsorption de CO_2 a été réalisée à 295K par Tezel *et al.* [26] sur un lot de zéolithes commerciales dont : 13X, HZSM-5-30, HiSiv 3000 (de type ZSM-5), HY-5 avec différents rapports SiO_2/ Al_2O_3 respectivement 2.2, 30, > 1000 et 5.1. Les capacités d'adsorption de CO_2 obtenues sont : 4.5, 2, 1.5 et 1.2 $mmol.g^{-1}$ pour les zéolithes 13X, HZSM-5-30, HiSiv 3000 (de type ZSM-5), HY-5. Les auteurs suggèrent une variation des capacités d'adsorption de CO_2 liée aux différents rapports SiO_2/ Al_2O_3 ainsi qu'à la nature et la charge des contre-ions.

- Le type de zéolithe : Aguilar-Armenta *et al.* [27], ont effectué l'adsorption de CO_2 à 290K sur trois types de zéolithes naturelles erionite (ERI), mordenite (MOR), clinoptilolite (HEU) qui ont des rapports Si/Al différents. En effet, ce rapport est compris entre 3 et 3.5 pour une zéolithe de type erionite, entre 4.17 et 5.0 et entre 4.25 et 5.25 pour celles du types modernite et clinoptililite. Les capacités d'adsorption de CO_2 obtenues sont respectivement: 2.7 ; 1.6 et 1.5 $mmol.g^{-1}$. Selon les auteurs, une plus grande capacité d'adsorption de CO_2 pour la zéolithe de type erionite est attribué à une plus grande quantité d'aluminium tandis que pour les zéolithes de type modernite et clinoptilolite les rapports Si/Al sont proches.

(2) A base de carbone

(i) Charbons actifs

Les charbons actifs sont des matériaux poreux amorphes méso ou microporeux à base de carbone dont le domaine d'application s'étend du traitement des eaux à la récupération de solvant ; la séparation gazeuse pour H_2S, C_2S ou encore le CO_2 [28].

Les charbons actifs sont obtenus à partir de la carbonisation et l'activation de précurseurs carbonés tels que le charbon (ex : charbon bitumineux, lignite), les sous-produits industriels (ex : pétrole, coke de brai), ou encore la biomasse (ex : bois).

- La carbonisation : elle s'effectue à haute température dans une atmosphère inerte au cours de laquelle les atomes d'hydrogène, d'oxygène et d'azote sont éliminés pour produire une matière carbonée appelée 'char'.

- L'activation : elle peut être chimique ou physique et vise à améliorer les propriétés de surface (porosité ; sites actifs ; surface spécifique). L'activation physique consiste en la gazéification partielle de la matière carbonée par de la vapeur, de l'air ou du CO_2 à température élevée aux alentours de 1100-1250 K [29]. L'activation chimique s'effectue à basse température avec l'utilisation d'agents chimiques tel que l'hydroxyde de potassium (KOH) ; l'acide phosphorique (H_3PO_4) ou le chlorure de zinc ($ZnCl_2$) [1], [22], [29].

Les propriétés texturales (distribution de taille de pores, surface, etc.) ainsi que les propriétés d'adsorption des charbons actifs sont fonction de la nature du précurseur utilisé. La diversité des précurseurs carbonés disponibles implique un faible coût pour la production de charbons actifs à échelle industrielle, ce qui en fait un avantage considérable sur les autres types d'adsorbants. Parmi les charbons actifs, de nouvelles classes d'adsorbant sont émergentes telles que les tamis moléculaires carbonés ou les nanotubes de carbone.

Plusieurs travaux ont montré que la capacité d'adsorption de CO_2 des charbons actifs est fonction de la pression et de la température.

- La pression : Siriwardane *et al.* [30] ont réalisé l'adsorption de CO_2 à 298K jusqu'à 20 bar pour trois adsorbants : un charbon actif (G-32H) et deux tamis moléculaires les zéolithes 13X et 4A. Leurs résultats montrent à basse pression (1,7 bar) une capacité d'adsorption de CO_2 plus faible pour le G-32H que pour les zéolithes 13X et 4A : respectivement de 2.0; 2.5 et 3.0 $mmol.g^{-1}$. A plus haute pression (13,7 bar), la capacité d'adsorption de CO_2 est plus élevée pour le G-32H que pour les zéolithes 4A et 13X soit 4, 3,3 ; 3,5 $mmol.g^{-1}$ [5]. Selon les auteurs, la plus grande capacité d'adsorption de CO_2 du G-32H à haute pression en comparaison avec la zéolithe 13X s'explique par une surface spécifique plus élevée respectivement de 506 et 897 m^2/g.
- La température : Do *et al.*[31] ont mesuré les quantités de CO_2 adsorbées sur un charbon actif (Ajax) à 0.2 bar pour une gamme de températures allant de 298 à 373K. Cette étude a mis en évidence la diminution des capacités d'adsorption de CO_2 avec l'augmentation de la température.

L'amélioration des propriétés d'adsorption des charbons actifs fait l'objet de certaines études. Maroto-Valer *et al* [32] ont modifié la surface de charbon actif obtenu à partir d'anthracite par des groupements nitrés alcalins soit par traitement à haute température d'ammoniaque ou par imprégnation de polyethylenamine (PEI). Leurs résultats montrent une augmentation de la capacité d'adsorption de CO_2 pour les charbons actifs modifiés. Dans le cas de l'imprégnation par PEI, la capacité d'adsorption de CO_2 augmente avec la température (de 30 à 75°C).

(ii) Nanotubes de carbone

Les nanotubes de carbone sont des structures définies et ordonnées composées de macromolécules à une dimension (Figure 1.5). Ils sont divisés en deux catégories : les mono parois 'Single-Walled Carbon Nanotubes (SWCNT)' et les multi parois 'Multi-Walled Carbon Nanotubes (MWCNT)' [33].Les SWCNTs sont constitués d'une seule couche de feuille de graphène tandis que les MWCNTs en sont composés de plusieurs couches concentriques (cylindres). La longueur des nanotubes de carbone est de l'ordre de plusieurs nanomètre ou micromètres. Cependant, le diamètre varie et est compris entre 0.4 et 2 nm pour les SWCNTs et 2 et 100 nm pour les MWCNTs [34].

Figure 1.5 – Structure d'une unité de base constituant les nanotubes de carbone [35]

Les nanotubes de carbone sont des matériaux stables chimiquement, thermiquement et qui possèdent de bonnes propriétés mécaniques et des surfaces élevées [34]. Ces matériaux sont applicables dans divers domaines : biocapteurs ; catalyse ; stockage de gaz et notamment la séparation de CO_2. Les nanotubes de carbone sont étudiés pour l'adsorption de CO_2, N_2 et le mélange CO_2/ N_2.

Cinke *et al.* [36] ont caractérisé des nanotubes de carbones purifiés à mono paroi (SWCNTs) par adsorption de diazote à 77K. La surface spécifique, le volume microporeux, le volume poreux total obtenus sont élevés et sont respectivement de 1587 $m^2.g^{-1}$; 0,28 $cm^3.g^{-1}$; 1,55 $cm^3.g^{-1}$.

L'adsorption de CO_2 a été effectuée à différentes températures (0, 35, 125, 200°C) et pour une gamme de pression de 0-1 bar. Les isothermes d'adsorption montrent une diminution de la quantité adsorbée de CO_2 lorsque la température augmente. A 35°C, l'adsorption de CO_2 a été réalisée sur un nanotube de carbone non purifié et un charbon actif. Le nanotube de carbone purifié adsorbe environ deux fois plus de CO_2 que le charbon actif, pour lequel les sites d'adsorption favorable au CO_2 ont été identifiés de chaque côté du nanotube. Les auteurs expliquent ce résultat par une répartition non uniforme des sites d'adsorption du charbon actif et un faible nombre ayant de l'affinité pour le CO_2. En revanche, le nanotube de carbone non purifié adsorbe une quantité moindre de CO_2 que le charbon actif. Ce résultat est confirmé par une étude réalisée par Lu *et al.* [37]. Dans cette même étude, ils ont mis en évidence une augmentation des quantités de CO_2 adsorbées pour les nanotubes de carbone greffés par des groupements 3-aminopropyltriethoxysilane ($H_2NCH_2CH_2CH_2$-$Si(OCH_2CH_3)_3$. D'après les auteurs, la présence de groupements amines augmentent la basicité de la surface de l'adsorbant et l'affinité pour les molécules de CO_2. De plus, les nanotubes de carbone greffés présentent des quantités de CO_2 adsorbées plus élevées en comparaison avec une zéolithe et un charbon actif.

Les isothermes d'adsorption de nanotubes de carbone pour les mélanges CO_2/ N_2 et CO_2/ CH_4 ont été prédites par modélisation (Grand Canonical Monte-Carlo) respectivement par Razavi *et al.* [38] et Huang *et al.* [39]. Leurs résultats respectifs ont montré une adsorption préférentielle des nanotubes de carbone pour le CO_2 par rapport au N_2 et CH_4 donc une bonne sélectivité.

(iii) Graphène

Le graphène, forme allotropique du carbone, est à l'origine de matériaux carbonés : fullerène (0 D) ; nanotubes de carbone (2D). Le graphène est un matériau cristallin dont le motif de base est un arrangement cyclique de six atomes de carbone pour former une structure bidimensionnelle d'une,

deux ou plusieurs couches carbonées [40]. Le graphène est utilisé pour des applications dans les domaines des batteries lithium, super condensateurs, séparation de gaz [41].

Les matériaux en graphène ont des surfaces spécifiques élevées. Gosh *et al.* [42] ont réalisé l'adsorption de diazote à 77K pour des échantillons composés de plusieurs feuilles de graphène (entre trois et quatre). Les surfaces spécifiques BET obtenues varient de 639 à 1500 m^2/g. Dans cette même étude, l'adsorption de CO_2 à 1 bar et 195K montre une capacité d'adsorption élevée de 35 wt %. Le graphène constitué d'une feuille, possède la plus grande capacité d'adsorption de CO_2: 37,93 wt %.

(3) Silice mésoporeuse

Les silices mésoporeuses sont des matériaux poreux ordonnés à base de silicate/ aluminosilicate qui ont été découverts par la société 'Mobil Research' dans les années 90 et ont été regroupés sous le nom de 'M41S'[43]. Cette famille comprend les phases d'oxydes mésoporeuses suivantes: la MCM-41, la MCM-48 et la MCM-50 qui se différencient par leur réseaux respectifs hexagonal, cubique et lamellaire[43], [44].

La synthèse de silices mésoporeuses repose sur l'hydrolyse et la condensation de précurseurs en présence de tensio-actifs (auto-assemblage de molécules de surfactants). L'élimination du tensio-actif par extraction ou calcination conduit au matériau final. Il existe une grande diversité de voies de synthèse des silices mésoporeuses conduisant à des matériaux avec des propriétés d'adsorption et des tailles de pores variables de 20 à 100 Å [45]

Les silices mésoporeuses les plus connues sont la MCM-41 (MCM= 'Mobile Crystalline Material') et la SBA-15 (SBA = 'Santa Barbara Amorphous'). Ces deux types de matériau ont une structure hexagonale possédant des pores en forme de canaux à une dimension dont la taille est contrôlable. La surface spécifique BET ainsi que les volumes poreux sont également contrôlables et peuvent atteindre respectivement 1000 $m^2.g^{-1}$ et 1 $cm^3.g^{-1}$ [22]. La MCM-41 et la SBA-15 ont été étudiées pour le stockage et la séparation de gaz grâce à l'amélioration des interactions entre la surface et le gaz notamment le CO_2 via la fonctionnalisation de la surface de l'adsorbant.

(4) Metal-Organic Frameworks (MOFs)

Les Metal-Organic Frameworks (MOFs) sont des matériaux micro/ mesoporeux cristallins potentiellement applicables aux domaines du stockage de gaz ; de la séparation gazeuse et purification; de la catalyse ou encore de la délivrance médicamenteuse [46].

Les MOFs sont des matériaux hybrides organique-inorganique à base de centres métalliques (métaux simple ou 'clusters métalliques') liés les uns aux autres par des ligands organiques permettant de construire un réseau de coordination en une-, deux, ou trois-dimension(s) (Figure 1.6).

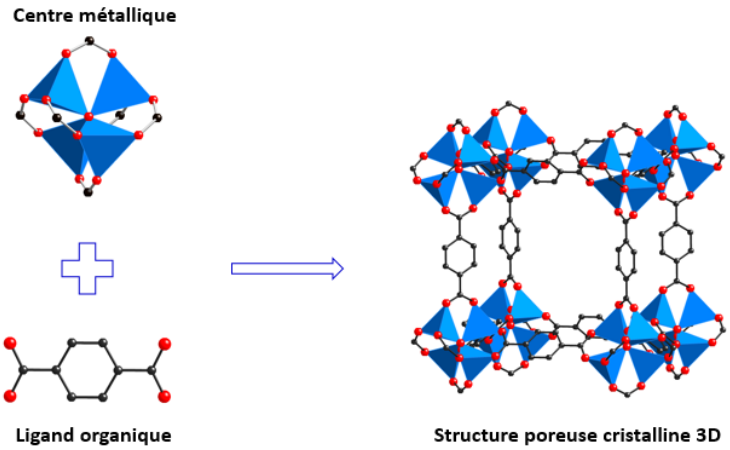

Figure 1.6 – Représentation schématique de la structure d'un MOF composé de centres métalliques liés aux molécules de ligands organiques pour former une structure tridimensionnelle

Les métaux utilisés peuvent être divalents (Cu, Zn, etc.) ; trivalents (Al, Cr, etc.) ou tétravalents (V, Zr, etc.) et les ligands organiques peuvent être des groupements carboxylate, imidazolate, phosphonate ou pyrazolate. De par la diversité des métaux, des ligands et leur fonctionnalisation, il existe une large gamme de MOFs pouvant être synthétisés avec des propriétés de surface (taille des pores, volume poreux, acidité/ basicité, etc.) ajustables aux applications désirées. Les MOFs sont connus pour posséder des structures poreuses bien définies avec des surfaces spécifiques BET et volume poreux élevés.

Plusieurs facteurs peuvent impacter les propriétés d'adsorption (capacité d'adsorption ; sélectivité) des MOFs tels que :

- Effet de 'la taille ' du ligand organique : K.S. Walton et R.Q. Snurr [47], [48] ont réalisé une étude portant sur la détermination des surfaces spécifiques BET par méthode de simulation numérique (Grand Canonical Monte Carlo) sur une série de MOFs : IRMOF-1, -10, -16, possédant des tailles de ligand croissantes. Leurs résultats montrent une augmentation de la surface spécifique BET lorsque la taille du ligand est croissante: respectivement de 3000, 5000 et 6200 $m^2.g^{-1}$. Des résultats similaires ont été observés dans le cas de la série des MIL-140-A, -B, -C et –D pour la taille des pores, les surfaces spécifiques BET et les volumes poreux [49].

- Effet de 'la fonctionnalisation' du ligand organique : cela permet de moduler les propriétés physico-chimiques de surface des MOFs dans le but d'améliorer certaines propriétés telles que la capacité d'adsorption et la sélectivité vis-à-vis du CO_2. Yang *et al.* [50], ont étudié l'impact de la fonctionnalisation du ligand organique par différents groupements polaires et apolaires (-Br, $-NH_2$, $-(OH)_2$, $-NO_2$, $-SO_3H$, $-(CF_3)_2$, $-CO_2H$) sur une série de UiO-66(Zr) pour la séparation CO_2/CH_4. D'une manière générale, une amélioration de l'affinité pour le CO_2, de la capacité ainsi que de la sélectivité en présence de groupements polaires est observée. Pour cette série de matériaux, les meilleures capacités et sélectivités ont été obtenues pour les UiO-66(Zr) fonctionnalisés par les groupements $–SO_3H$ et $–CO_2H$.

- Effet du 'métal ou cluster métallique' : pour la plupart des MOFs, la coordination des centres métalliques aux ligands crée un effet d'écrantage impliquant une faible contribution de leur part lors de l'adsorption [22]. Cependant, certains MOFs possèdent des sites de coordination insaturés (Coordinative Unsaturated Sites, 'CUS') qui sont des acides de Lewis et agissent comme des sites d'adsorption spécifiques susceptibles d'avoir une plus grande interaction

avec les molécules d'adsorbat. A titre d'exemple Dietzel *et al.* [51] ont montré que les CUS présent dans le CPO-27-Ni agissent comme de forts sites d'adsorption pour le CO_2.

- Effet de la 'flexibilité' : La flexibilité des MOFs peut être induite par divers stimuli : pression mécanique, changement de température ou encore la nature de l'adsorbant. Dans le cas du MIL-53(Cr) et MIL-53(Al) la flexibilité et notamment le 'breathing effect' a été mis en évidence lors de l'adsorption de molécules polaires telles que le CO_2 à température ambiante. Bourrelly *et al.* [46]ont montré que les MIL-53(Cr, Al) passent d'une forme 'Large Pore' (LP) (état de déshydratation) à une forme 'Narrow Pore' (NP) pour des pressions inférieures à 6 bar tandis qu'au-delà de 6 bar une forme LP est retrouvée. Cet effet de respiration n'est pas observé dans le cas d'adsorption de molécules apolaires telles que le CH_4. La flexibilité des MOFs peut être inhibée par le changement du centre métallique, c'est le cas du MIL-47(V) en comparaison au MIL-53 (Cr, Al).

Dans le cadre de ce travail, les MOFs microporeux (diamètre de pore inférieur à 20 Å) ont été étudiés car ils sont amenés à présenter des effets de confinements et de tamis moléculaire importants pouvant favoriser la sélectivité vis-à-vis du CO_2. Au cours de ce travail, les MOFs seront comparés à la zéolithe NaX [53] et le tamis moléculaire carboné Takeda 5A [52] largement étudiés pour leurs propriétés d'adsorption de CO_2 pris comme matériaux de référence. Quelques exemples de familles de MOFs microporeux sont donnés ci-dessous.

La dénomination 'MIL-n' fait référence aux Metal-Organic Frameworks découverts et synthétisés par l'équipe de G. Férey et C. Serre au sein l'institut Lavoisier à Versailles (MIL = Matériau de l'Institut Lavoisier). Les matériaux MIL-100, MIL-101 et MIL-53 sont les plus connus et font l'objet de nombreuses études pour la séparation de gaz.

(a) MIL-53

Les matériaux MIL-53 de formule chimique $M(OH)(O_2C\text{-}C_6H_4\text{-}CO_2)$ sont formés d'une infinité de chaines d'octaèdres métalliques $MO_4(OH)_2$ reliées les unes aux autres par des molécules de ligand organique, le benzène dicarboxylate (BDC). Cet arrangement conduit à des structures en trois dimensions composées de tunnels à une dimension en forme de losange. Les matériaux MIL-53 ont été synthétisés avec différents métaux tel que le chrome, l'aluminium, le fer, le gallium, l'indium[53]–[58].

La famille des matériaux MIL-53 est principalement connue pour la flexibilité de leur structure. Bien que la structure des MIL-53 reste inchangée, la nature du métal a un impact sur la flexibilité. L'effet de l'interaction de molécules avec les 'murs' de la structure provoque une transition de structure avec une variation du volume de cellule. Par exemple, l'hydratation-déshydratation des matériaux MIL-53 (Cr^{3+}, Al^{3+}) conduit à une variation de la structure d'une amplitude de plus de 5Å (Figure 1.7).

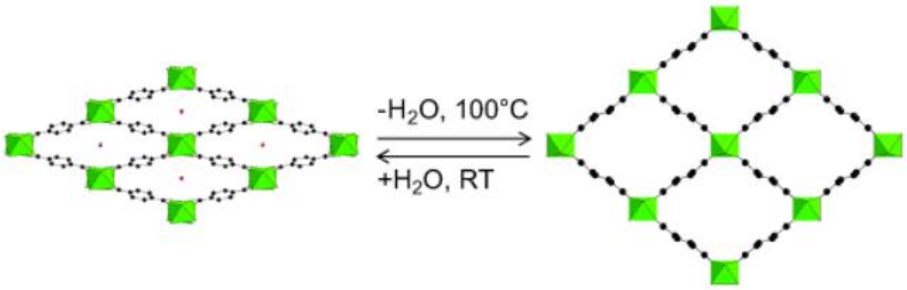

Figure 1.7 – Effet de respiration induit par la déshydratation du MIL-53(Cr^{3+}, Al^{3+}) : forme hydratée petits pores (gauche) et forme déshydratée grands pores (droite) [59]

L'activation sous vide du MIL-53(Cr^{3+}, Al^{3+}) mène à une forme déshydratée appelée 'large pore' ou 'forme ouverte'. La porosité est plus élevée et le diamètre de pore est proche de 8.5Å. Le groupe de G. Férey a mesuré une surface spécifique BET équivalente avoisinant 1200 m²/g pour le MIL-53(Cr^{3+}, Al^{3+})[54]. Lors de l'adsorption de CO_2, la structure du MIL-53(Cr^{3+}, Al^{3+}) repasse sous forme de 'petit pore' ou 'forme fermée' pour s'ouvrir et devenir à nouveau 'large pore' sous l'effet de l'augmentation de la pression. Cela se traduit par une inflexion sur l'isotherme d'adsorption. Ce phénomène est appelé 'effet de respiration'.

(b) CuBTC

Le metal-organic framework CuBTC ou HKUST-1 de formule chimique $[Cu_3(btc)_2(H_2O)_3]$ a été synthétisé à l'Université de Science et Technologie de Hong Kong en 1999 [60]. Le CuBTC est construit à partir de l'association de deux atomes de cuivre (Cu^{2+}) avec quatre atomes d'oxygène provenant de deux molécules de ligands organiques, le benzène 1,3,5-tricarboxylate, pour former une structure en trois dimensions. Le Cu-BTC est composé de deux sortes de pores. Un premier pore central d'une taille de 9Å entouré de seconds pores plus petits de 5Å formant des sortes de poches ('pockets'). Ces deux types de pores sont interconnectés par des fenêtres triangulaires d'une taille de 3,5 Å (Figure 1.8)

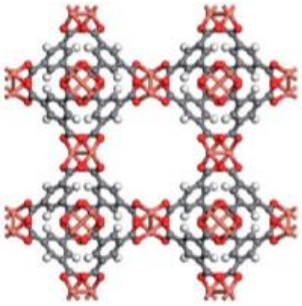

Figure 1.8 – Structure du metal-organic framework Cu-BTC ou HKUST-1 [60]

En fonction des conditions de synthèse et d'activation, la surface spécifique BET équivalente du CuBTC varie de 690 [60] à 1700 m²/g [61]. De plus, la structure du CuBTC est instable en présence d'eau. L'activation sous vide du CuBTC provoque des sites de coordination insaturés (CUS) de Cu^{2+} (acide de Lewis) qui peuvent avoir une forte interaction pour certaines molécules telles que CO_2. Le CuBTC est un matériau qui a été étudié pour diverses applications : séparation et stockage de gaz, catalyse.

(c) UiO-66

Le matériau UiO-66 (Université d'Oslo) de formule chimique $[Zr_6O_4(OH)_4(CO_2)_{12}]$ est un MOF largement synthétisé car il présente d'excellentes propriétés d'adsorption de CO_2 [62]. De plus, il est stable thermiquement et en présence d'eau.

La structure de l'UiO-66 consiste en un noyau interne $Zr_6O_4(OH)_4$ dans lequel les faces triangulaires d'octaèdres ZrO_6 sont alternativement délimité par des groupements μ_3-O et μ_3-OH. Les polyèdres des arrêtes sont coordonnés aux carboxylates (μ_2-(CO_2)) provenant des ligands organiques (acide 1,4 benzène dicarboxylate) pour former un cluster d'oxyde de zirconium de formule $Zr_6O_4(OH)_4(CO_2)_{12}$. Chaque cluster d'oxyde de zirconium est lié à 12 molécules de ligand organique pour former une structure cubique tridimensionnelle. Cela conduit à une cage centrale octaédrique de diamètre interne de 11 Å entourée par huit cages tétraédriques de diamètre interne de 8Å. La connexion entre ces deux types de cages se fait par des fenêtres triangulaires d'environ 6Å (Figure 1.9).

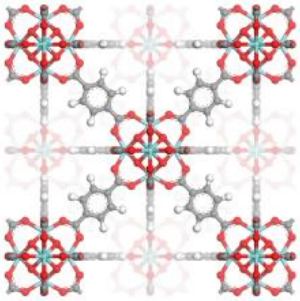

Figure 1.9 – Structure du MOF UiO-66 composée de cages centrales octaédriques (gauche) entourées par huit autres cages tétraédriques (droite) [63]

La caractérisation du MOF UiO-66 a montré qu'il est stable thermiquement jusqu'à 300°C et possède une surface spécifique BET équivalente aux alentours de 1000m²/g. La fonctionnalisation du ligand benzene dicarboxylate par des groupements $–NH_2$, $-NO_2$, -Br, -1,4-naphtyl, -1,5-OMe peut conduire à la diminution de la surface spécifique et du volume poreux de l'UiO-66. L'introduction de ces groupes d'atomes a pour objectif d'améliorer à la fois l'interaction entre la structure et les différents adsorbables et la sélectivité de ces matériaux.

(d) Zeolitic Imidazolate Frameworks (ZIF's)

Les 'Zeolitic Imidazolate Framewors (ZIFs)' sont des matériaux poreux cristallins qui appartiennent à la classe des MOFs. Ils sont construits à partir d'ions métalliques (M= Zn, Co) connectés aux atomes d'azotes des ligands organiques imidazole ($C_3N_2H_3^-$ = Im) pour former des structures tridimensionnelles (3D) [64]. De nombreux ZIFs sont synthétisés grâce à la diversité des ions métalliques et du ligand organique fonctionnalisé ou non. Ce sont des structures proches de celles des zéolithes avec un angle M-Im-M de 145° équivalent à Si-O-Si de 145°. De plus, certains ZIFs possèdent des topologies similaires à celles des zéolithes telles que : ANA, BCT, DFT, GIS, GME, LTA, MER, RHO and SOD [64].

Les ZIFs ont à la fois une bonne stabilité chimique et thermique ainsi qu'une porosité bien définie les rendant attractifs pour des applications de séparation de gaz. Un des ZIFs les plus connus pour la séparation gazeuse est le ZIF-8 qui possède : une topologie sodalite (SOD) et une surface spécifique BET de 1400 $m^2.g^{-1}$ [65].

Dans cette section quelques MOFs de la littérature ont été détaillés, il est à noter que parmi les MOFs à base d'aluminium le MIL-120 est intéressant pour la séparation de gaz avec des pores de dimensions 5.4*4.7 Å [66]. Cependant il existe d'autre type de MOFs utilisant différents métaux dont le magnésium Mg^{2+}, le MIL-123 [67]. Ce MOF est construit à partir de deux types de cavités assez larges qui sont de super octaèdres indépendamment connectés les unes aux autres générant un double réseau qui s'interpénètre pour former un réseau 3D. Il existe également des MOFs à base de lithium, le Li_2(2,6-NDC) ULMOF-1, constitué de couches d'anti-fluorite à deux dimensions connectées aux sommets aux octaèdres de LiO pour former une structure tridimensionnelle [68].

c) Effet de l'eau

La présence d'eau dans les gaz de combustion est un facteur pouvant avoir un impact négatif sur les capacités d'adsorption de CO_2 des adsorbants. [66]. En effet, Ruthven *et al.* [67] ont mené une étude sur l'adsorption de CO_2 à 298K sur deux zéolithes de type faujasite : NaLSX et LiLSX en présence de différentes quantités d'eau. Les résultats obtenus montrent une forte diminution des capacités d'adsorption de CO_2 lorsque la quantité d'eau augmente.

A titre d'exemple, lorsque les zéolithes NaLSX et LiLSX ne contiennent pas d'eau elles adsorbent respectivement 1.7 et 3.2 $mmol.g^{-1}$ de CO_2 à 0.04 bar. Pour une charge en eau d'environ 8 wt%, les capacités d'adsorption de CO_2 sont 0.8 et 1 $mmol.g^{-1}$.

Dans le cas des charbons actifs, les capacités d'adsorption de CO_2 sont très peu affectées par la présence d'eau car leurs surfaces sont généralement hydrophobes. Néanmoins, un stockage prolongé de charbon actif en conditions humides contribue à réduire leur capacités d'adsorption de CO_2[68].

Dans le cas des MOFs, la capacité d'adsorption de CO_2 peut être affectée par la présence d'eau [69]. C'est par exemple le cas du HKUST-1 où sa capacité d'adsorption de CO_2 diminue fortement en présence d'eau [70]. En effet à 1 bar et 298K, les capacités d'adsorption de CO_2 sont environ 300 $mg.g^{-1}$ et 25 $mg.g^{-1}$ respectivement lorsque l'échantillon est sec où entièrement humidifié. Néanmoins, pour une charge d'eau de 4 wt%, Yazaydin *et al.* [70] ont noté une amélioration de la capacité d'adsorption de CO_2. Les capacités d'adsorption de CO_2 d'autres matériaux, tels que le CPO-27-Ni, qui semble être prometteur pour de la post-combustion sont affectées par la présence d'eau. Liu *et al.* [71] ont observé une diminution des capacités d'adsorption de CO_2 et des sélectivités CO_2/N_2 pour un taux d'humidité relative de 3%. Néanmoins pour les ZIF-68 et -69 et un taux d'humidité de 5%, les sélectivités CO_2/N_2 sont maintenues à faible pression et augmentent à plus haute pression (> 10 bar) malgré une diminution de la capacité d'adsorption de CO_2.[72].

Cela montre qu'en présence d'eau, les capacités d'adsorption ainsi que les sélectivités vis-à-vis du CO_2 peuvent être affectées négativement mais aussi améliorées dans certains cas.

4. Techniques de régénération des adsorbants

Après saturation de l'adsorbant, une étape importante et nécessaire est sa régénération pour permettre sa réutilisation au cours des prochains cycles d'adsorption/ désorption [1]. A l'échelle industrielle, il est préférable que la régénération s'effectue avec une faible consommation énergétique afin d'en réduire les coûts. Plusieurs techniques de régénération ont été développées basées sur la diminution de pression (Pressure ou Vacuum Swing Adsorption, PSA ou VSA) ou l'augmentation de la température (Temperature ou Electric Swing Adsorption, TSA ou ESA) :

- 'Pressure Swing Adsorption (PSA)' : l'adsorption s'effectue à haute pression (supérieure à la pression atmosphérique) à cause de la compression des gaz de combustion en amont de la colonne d'adsorption. La désorption de molécules cibles telles que le CO_2 s'effectue à la pression atmosphérique par réduction de la pression totale.
- 'Vacuum Swing Adsorption (VSA)': l'adsorption s'effectue pour des conditions de pression et température proches de l'ambiante. La pression de désorption est inférieure à la pression atmosphérique car elle s'effectue sous vide.

- 'Temperature Swing Adsorption (TSA)': la désorption est réalisée par un courant d'air chaud.

- 'Electric Swing Adsorption (ESA)' : la désorption s'effectue par effet Joule

A titre d'exemple, la régénération des zéolithes s'effectue généralement par PSA ou TSA [13]. En comparaison avec les zéolithes, la désorption ou régénération des charbons actifs nécessite moins d'énergie ce qui est un avantage à l'échelle industrielle [73].

5. Membranes

La séparation gazeuse membranaire s'effectue par le transfert d'une force motrice : la pression. Depuis la commercialisation des premières membranes polymériques dans les années 80, le domaine des membranes connait un fort développement. Perma (actuellement une division d'Air Product) a synthétisé la première membrane polymérique à base de polysulfone pour la séparation d'hydrogène [74].

En comparaison avec les techniques conventionnelles de séparation décrites précédemment, les membranes possèdent plusieurs avantages :

- Diminution des coûts d'exploitation et des besoins énergétiques, taille des équipements et déchets générés
- Réduction de l'empreinte carbone
- Pas de nécessité de changement de phase comme pour l'absorption par solvant chimique

Deux paramètres permettent d'évaluer l'efficacité d'une membrane : la perméabilité et la sélectivité. Ces deux grandeurs sont spécifiques à chaque membrane et chaque type de séparation gazeuse : CO_2/N_2, O_2/N_2, CO_2/CH_4, etc [75]. Les performances des membranes sont évaluées en reportant les valeurs de perméabilité et de sélectivité sur le diagramme de Robeson, un exemple est fourni ci-dessous pour la séparation CO_2/N_2 (Figure 1.10).

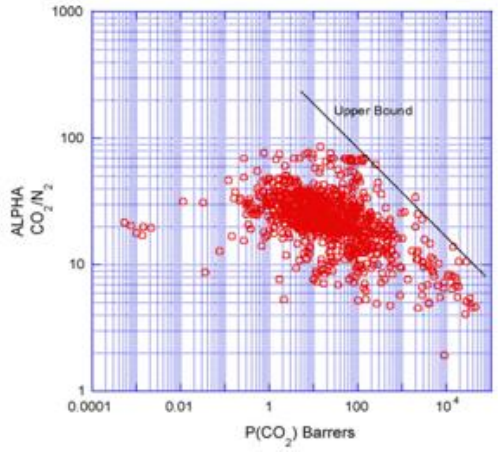

Figure 1.10 – 'Robeson Upper Bound 2008 [75]' exprimant la sélectivité (α) CO_2/N_2 en fonction de la perméabilité de CO_2

La perméabilité ou coefficient de perméabilité, P_i, représente la capacité d'une molécule à passer à travers une membrane. Ce coefficient est défini de la manière suivante :

$$P = \frac{J_i.l}{\Delta p_i} \tag{1.6}$$

Autrement dit, la perméabilité s'exprime comme le flux molaire de gaz (J_i) diffusant au travers d'une membrane, normalisé par la différence de pression de gaz (Δp_i) de chaque côté de la membrane et également en fonction de son épaisseur l. La perméabilité d'une molécule est généralement donné en barrer soit 1 barrer = 1.10^{-10} cm^3 (STP) cm/cm^2 s cmHg ou encore 1 barrer = $3.344.10^{-16}$ mol.m.m^{-2}.Pa^{-1}.s^{-1}.

La sélectivité décrit la capacité d'une membrane à séparer deux molécules i et j qui sont transportées au travers de la membrane, cela correspond au ratio de leur perméabilité (1.7) [76] :

$$\alpha_{ij} = P_i/P_j \tag{1.7}$$

a) Membranes polymériques

Le transport de molécules à travers des membranes polymériques est gouverné par des mécanismes de 'solution-diffusion'. Concernant leurs propriétés de séparation, elles possèdent de plus grandes sélectivités que les membranes inorganiques en raison d'un plus faible volume libre. Néanmoins, les propriétés de séparation de ces membranes sont limitées car lorsque la perméabilité augmente la sélectivité diminue et inversement. L'amélioration des sélectivités et des perméabilités de ces membranes est un challenge qui fait l'objet de nombreuses études.

Les membranes polymériques sont facilement manufacturables et possèdent de bonnes propriétés mécaniques. Les désavantages sont [76]:

- Faible résistance aux contaminants de type H_2S
- Faible stabilité thermique et chimique
- Limite sélectivité/ perméabilité

Les membranes polymériques commercialisées sont applicables aux séparations suivantes : CO_2/ CH_4 (gaz naturel) ; O_2/ N_2 (air) ; H_2/ N_2.

Parallèlement à l'optimisation des membranes polymériques, les membranes inorganiques ont été développées.

b) Membranes inorganiques

Les membranes inorganiques sont constituées majoritairement d'oxydes métalliques, de zéolithes, de silice, de tamis moléculaires ou de nanotubes à base de carbone. Quatre types de mécanismes peuvent gouverner la séparation de gaz au sein de membranes inorganiques : la diffusion de Knudsen, la diffusion de surface, la condensation capillaire et le tamisage moléculaire [77]. Ces membranes possèdent les avantages d'être à la fois résistantes à de hautes températures et à certains agents chimiques. Néanmoins, elles présentent certains inconvénients :

- Un coût élevé
- Une reproductibilité moyenne
- Une faible résistance mécanique

Par rapport aux membranes polymériques, les membranes inorganiques montrent de meilleures sélectivités en raison de leur plus grande porosité, améliorant les propriétés de séparation de gaz.

c) Membranes à matrices mixtes (MMM's)

Les membranes à matrices mixtes sont des matériaux composites constitués de micro- ou nanoparticules inorganiques (phase discontinue) incorporées dans une matrice polymérique (phase continue) (Figure 1.11). L'objectif des MMM's est de combiner les meilleures propriétés de séparation de gaz des matériaux inorganiques avec les propriétés mécaniques intéressantes des polymères et leur fabrication assez simple.

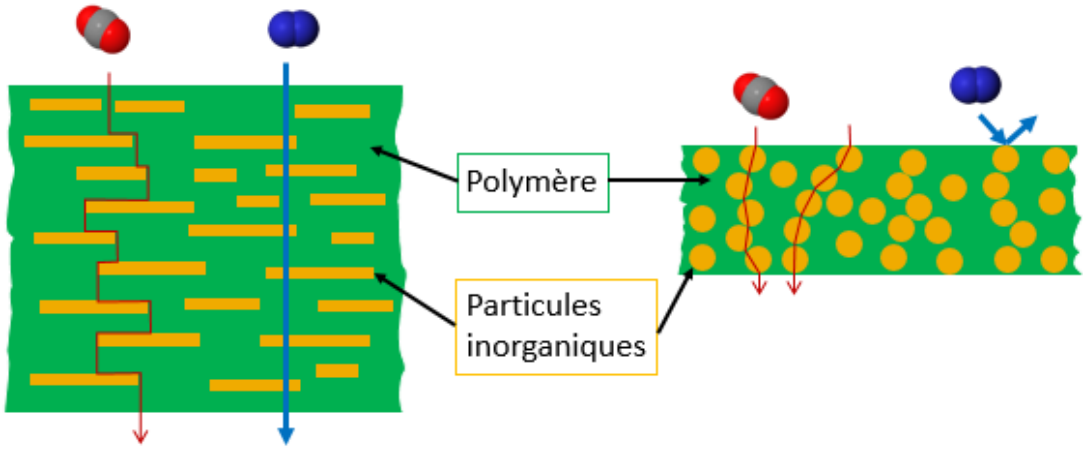

Figure 1.11 – Schéma d'une membrane à matrice mixte composée d'une phase polymérique (vert) au sein de laquelle sont dispersées des particules inorganiques (jaune) et exemple de transport de molécules

Dans le cadre du projet européen M^4CO_2, le choix des matériaux poreux à intégrer aux polymères s'est orienté sur les MOFs car ils possèdent des aires spécifiques élevées, de grands volumes poreux et offrent une large diversité de structure due à leur chimie adaptable (nature du métal, fonctionnalisation du ligand) par rapport aux zéolites et charbons actifs.

La Figure 1.11 illustre un exemple de mécanisme de transport au travers d'une membrane à matrice mixte pour une séparation gazeuse CO_2/N_2. La Figure 1.11 à gauche montre que la molécule de CO_2 diffuse au travers de la phase polymérique sans passer par les particules inorganiques tandis que la molécule de N_2 traverse la membrane. Ce type de mécanisme ou la diffusion prédomine induit une

diminution de la sélectivité de la membrane. Cependant, l'objectif général du projet M^4CO_2 est une amélioration des performances de séparation des membranes à matrice mixtes à la fois en termes de perméabilité et de sélectivité. La Figure 1.11 à droite met en évidence le type de transport souhaité : un effet de tamis moléculaire. Dans cette configuration, la molécule de N_2 ne passe pas au travers de la membrane à cause de son diamètre cinétique supérieure à celui de la taille des pores des matériaux poreux tandis que la molécule de CO_2 diffuse et est adsorbée par ces particules inorganiques.

Néanmoins dans l'élaboration de membrane à matrice mixte, l'intégration de MOFs ou tout autre type de particules inorganiques à une phase polymérique entraîne une modification des performances de la membrane et trois cas de structure à l'interface sont possibles :

- Lorsque le MOF et le polymère ne sont pas compatible cela crée un 'vide interfacial' ou 'trou'. Cela engendre une augmentation de la perméabilité par la présence de ce 'vide interfacial' et une diminution de la sélectivité.
- Lorsqu'il y a une bonne adhésion MOF/ polymère, un blocage partiel ou complet des pores peut survenir à cause de solvants ou contaminants lors de la synthèse ou après. En cas de blocage partiel, il y a généralement une diminution de la perméabilité tandis que la sélectivité dépend du degré de blocage. En cas de blocage total, les MOFs se comportent comme des matériaux non poreux.
- Lorsque l'adhésion MOF/polymère est parfaite cela diminue le 'vide interfacial' et donc la perméabilité mais cela permet d'augmenter la sélectivité.

Les bonnes performances d'une membrane à matrice mixte dépendent de l'optimisation de l'interaction particules inorganiques/ polymère.

Il existe diverses configurations de mise en œuvre de membrane à matrice mixte [76] :

- A couche dense 'Flat dense MMM's'
- Asymétrique à feuille plane 'Flat sheet asymmetric MMM's' ou à fibre creuse 'Hollow fiber asymmetric MMM's'

Dans le cadre du projet M^4CO_2, les membranes à matrices mixtes à fibre creuse sont développées. Celles-ci sont constituées d'une fine couche n'excédant pas 200 nm, sélective pour la séparation de gaz et supportée par un substrat poreux assurant les propriétés mécaniques.

6. Bilan

La Figure 1.12 ci-dessous illustre les différents procédés et techniques de séparation de CO_2 pouvant être utilisés.

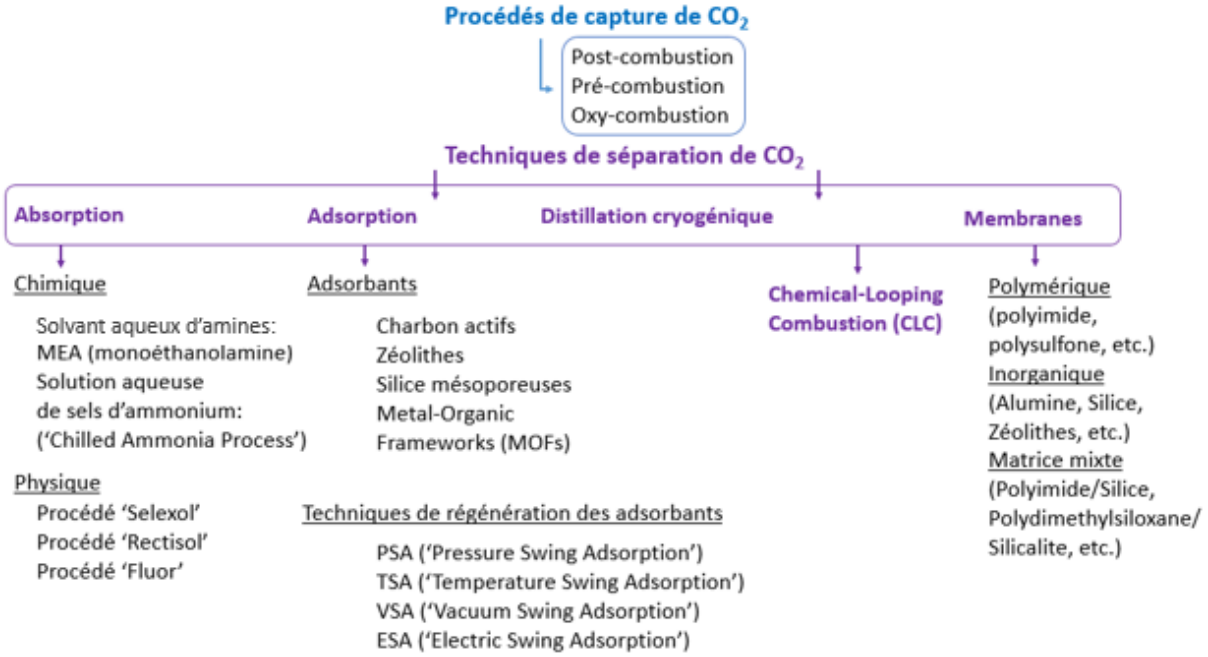

Figure 1.12 – Récapitulatif des procédés de capture et des techniques de séparation de CO_2

D. Projet de thèse

Ce travail de thèse s'inscrit au sein du projet européen M^4CO_2, 'Mixed Matrix Membranes à base de Metal-Organic Frameworks and polymères (M4)' en vue de la capture de CO_2.
Le projet M^4CO_2 concerne la conception de membranes à matrice mixte (MMM's) composées de matériaux poreux (les MOFs) et de polymères pour la séparation gazeuse de CO_2 en vue des applications de post et de pré-combustion. Pour cela, des institutions de recherche et des industriels ont été impliqués dont le CNRS, Total, Polymem etc.

La séparation gazeuse par membrane ne nécessite pas de changement de phase gaz/ liquide en comparaison avec les technologies usuelles (absorption par solvants aminés, distillation cryogénique), ce qui donne lieu à une réduction de l'empreinte carbone et des coûts de la séparation du mélange gazeux. En effet, le « prix du carbone » a été évalué environ à 24-35 €/ tonne de CO_2 pour une installation de capture de CO_2, il est donc nécessaire de se tourner vers des techniques de séparation moins énergivores. De plus, le dimensionnement des unités de séparation membranaires est peu complexe et permet d'opérer en conditions continues.

Les membranes à matrices mixtes allient à la fois la résistance mécanique des membranes polymériques et les propriétés de séparation des membranes inorganiques.
Ainsi, le projet M^4CO_2 a pour objectif de concevoir des prototypes de membranes à matrice mixte visant à améliorer et/ou surpasser les performances de séparation de CO_2 des MMM's ou celles obtenues par les autres technologies.

Le choix des matériaux poreux à intégrer aux polymères s'est orienté sur les Metal-Organic Frameworks (MOFs) et trois générations de MOFs ont été synthétisés :

- 1ère génération : MOFs possédant une seule taille de pore pour lesquelles la synthèse de nanoparticules est facilement réalisable (NH_2-MIL-53(Al), ZIF-8, $(CO_2H)_2$-UiO-66(Zr))
- 2nd génération : MOFs stables comprenant des tailles de pores et des fonctionnalisations différentes (UiO-66(Zr) ; MIL-53 ; MIL-91 ; $Sc_2(BDC\text{-}NH_2)_3$; $Sc_2(BDC\text{-}NO_2)_3$)
- 3ème génération : synthèse de particules de 'core-shell' contenant des mésopores pour la pénétration du polymère et des micropores pour améliorer la séparation de gaz.

Dans le cadre du projet M^4CO_2, les membranes sont conçues en module asymétrique de fibre creuse ('asymmetric hollow fiber') et sont constituées de l'association d'une fine couche sélective de MOFs n'excédant pas une épaisseur de 150-300 nm et d'un support poreux. Les performances et la stabilité de ces membranes dépendent à la fois de l'épaisseur de la couche sélective de MOFs ainsi que de l'affinité MOFs/ polymère. Le succès des MMM's réside dans l'optimisation de l'interaction MOFs/ polymère passant par la fonctionnalisation de surface. Ainsi, des nanoparticules de MOFs possédant des morphologies et des structures variables et une fonctionnalisation adaptée ont été synthétisées.

Contribution

Dans le cadre du projet européen M^4CO_2, nous avons été impliqués dans la caractérisation texturale et thermodynamique des Metal-Organic Frameworks (MOFs) pour la capture de CO_2. Les caractérisations texturales et thermodynamiques concernent respectivement la détermination des aires spécifiques, des volumes poreux ainsi que des enthalpies d'adsorption du CO_2 des MOFs. Ajouté à cela, les capacités d'adsorption du CO_2 et les sélectivités ont été obtenues à partir des isothermes d'adsorption. L'ensemble de ces paramètres sera défini au chapitre 2. La Figure 1.13 met en évidence notre contribution et nos interactions avec les différents partenaires. En effet, les MOFs que nous avons caractérisés ont été fournis par différentes institutions de recherche (Université de Versailles, Université de Saint Andrews et Johnson Matthey). Les données expérimentales d'adsorption ont été confrontées à la fois avec celles obtenues par simulation et avec les expériences de co-adsorption ce qui permet l'identification des mécanismes d'adsorption.

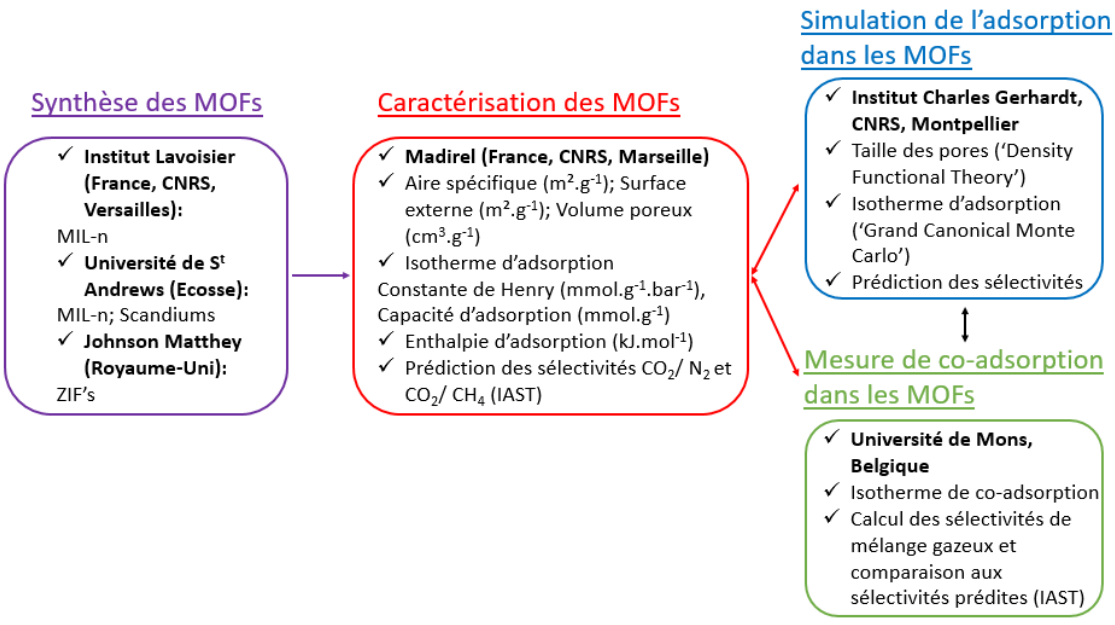

Figure 1.13 – Représentation schématique de notre contribution au projet M^4CO_2 et des interactions avec les différents partenaires

MOFs étudiés

Le choix des MOFs étudiés au cours de ce projet de thèse ainsi qu'une description de leur structure est fourni ci-dessous.

MIL-96(Al)

Le MOF MIL-96(Al), à base d'aluminium, a été synthétisé par l'Institut Lavoisier de Versailles. Cette phase est issue de la réaction entre un aluminium et un groupement aromatique carboxylique, il a pour formule brute : $Al_{12}O(OH)_{18}(H_2O)_3(Al_2(OH)_4)[btc]_6.24H_2O$. La phase du MOF MIL-96(Al) décrite dans ce travail a été revisitée par Marvin *et al.* [78] durant le projet M^4CO_2 car un désordre cristallographique de la structure initialement synthétisée par Loiseau *et al.* [79] a été suspecté.

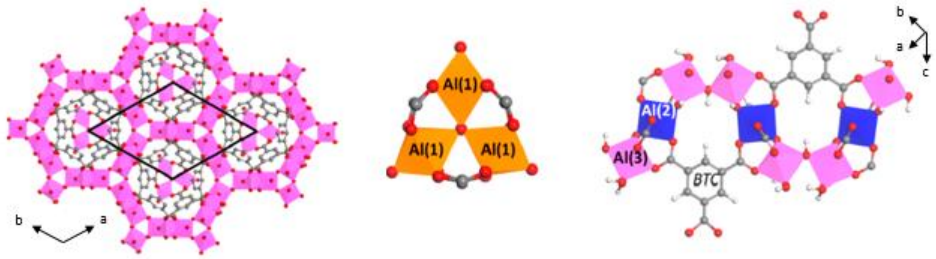

Figure 1.14 – Charpente du MIL-96(Al) selon l'axe c (gauche) ainsi que les deux blocs inorganiques qui le constitue: un trimère d'aluminium (milieu) et une chaîne sinusoidale à 18 membres (droite) composée de deux autres types de trimères [78]

La Figure 1.14 présente la phase MIL-96(Al) qui est une structure tridimensionnelle composée d'octaèdres d'aluminium coordonnés entre eux par des ligands trimésiques $[btc]^{3-}$. La structure du MIL-96(Al) résulte de l'assemblement de deux blocs inorganiques distincts. Le premier bloc est constitué d'atomes d'aluminium entourés de cinq atomes d'oxygènes provenant des acides carboxyliques et d'une molécule d'eau pour former des trimères $AlO_5(H_2O)$ (Figure 1.14, milieu). Tandis que le second bloc est un réseau 2D constitué par des chaines sinusoïdales d'octaèdres d'aluminium $Al_2O(OH)_4$ et $AlO_4(OH)_2$ interconnectées pour former un cycle hexagonal à 18 membres. La cohésion de la structure du MIL-96(Al) est assurée par la connexion de ces deux blocs inorganiques grâce aux molécules de ligands. Il en résulte un réseau en 3D constitué de trois types de cavités. La première cavité est délimitée par deux trimères selon l'axe c qui sont connectés à la chaîne sinusoïdale à 18 membres par six ligands btc. Cette cavité de forme ellipsoïdale a les dimensions suivantes : 9.5*12*11.3 Å et un volume poreux de 700 $Å^3$. La seconde cavité est définie par trois trimères interconnectés par des ligands de façon plane et qui sont reliés à deux unités de la chaîne sinusoïdale par six ligands btc. Cette cavité en forme de bipyramide a pour dimension 3.6*4.46 Å. La dimension de la fenêtre entre ces deux cavités est de 3.6*4.5 Å. La troisième cavité se trouve entre trois trimères (plan a,b) et deux unités trimériques selon l'axe c, elle a une forme sphérique de dimensions 11 Å. La dimension de la fenêtre entre la seconde et la troisième cavité est de 1.2*1.9 Å.

Sc_2BDC_3 et $Sc_2(BDC\text{-}NO_2)_3$

Les MOFs à base de scandium : Sc_2BDC_3 et $Sc_2(BDC\text{-}NO_2)_3$ ont été synthétisés par l'Université de S^t Andrews. Le MOF scandium téréphtalate, Sc_2BDC_3, est obtenu à partir d'ion trivalent Sc^{3+} et d'un groupement aromatique carboxylique (BDC = 1,4-benzène di-carboxylate), il a pour formule brute $Sc_2(O_2CC_6H_4CO_2)_3$. La Figure 1.15 présente la structure de la phase scandium.

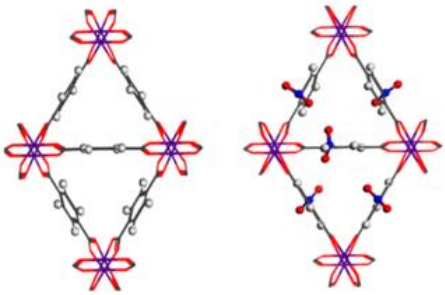

Figure 1.15 – Structures du Sc_2BDC_3 (gauche) et $Sc_2(BDC\text{-}NO_2)_3$ (droite) optimisées par la méthode de modélisation 'Density Functional Theory (DFT)' [80]

La structure du Sc_2BDC_3 résulte de l'association d'octaèdres de scandium, ScO_6, qui sont interconnectés par des molécules de ligands organiques pour former un réseau en 3D constituéde canaux triangulaires. Il en résulte un diamètre de pore de 3.6 Å. La phase $Sc_2(BDC\text{-}NO_2)_3$ est obtenue à partir de la fonctionnalisation des molécules de ligands par des groupements nitro ($-NO_2$) formant un réseau 3D composé de canaux triangulaires. Les atomes d'oxygènes des groupements $–NO_2$ sont dirigés vers le centre des canaux impliquant une diminution de la taille des pores. En effet, le diamètre de pore a été évalué à 2.9 Å.

MIL-69(Al)

Le MOF MIL-69(Al) à base d'aluminium a été synthétisé par l'Institut Lavoisier de Versailles. La phase MIL-69(Al) s'obtient à partir d'ions trivalents Al^{3+} et de 2,6-naphtalènedicarboxylique, il a pour formule brute : $Al(OH)(O_2C\text{-}C_{10}H_6\text{-}CO_2).H_2O$. La structure de la phase MIL-69(Al) est présentée dans la Figure 1.16.

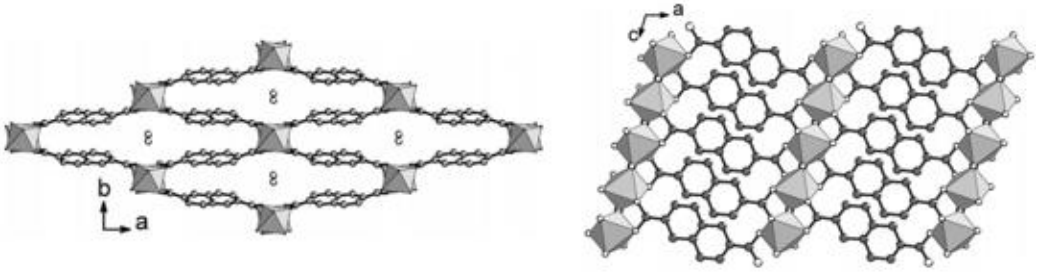

Figure 1.16 – Structure du MIL-69(Al) (gauche) et représentation des chaînes infinies d'octaèdres d'aluminium $AlO_4(OH)_2$ connectés aux ligands selon l'axe c [81]

Comme le montre la Figure 1.16, le MIL-69(Al) résulte de la connexion de chaînes infinies d'octaèdres d'aluminium, $AlO_4(OH)_2$, liés entre elles aux sommets par des groupements hydroxyles μ_2-OH et coordonnés par des molécules de ligands 2,6-naphtalènedicarboxylique (ndc). Il en résulte un réseau en 3D contenant des tunnels aplatis suivant la direction parallèle aux chaînes d'octaèdres d'aluminium (axe c). Le MIL-69(Al) est composé de canaux à une dimension avec une ouverture de pore de 2.7 Å dans lesquels une molécule d'eau est piégée. Celle-ci interagit à la fois avec les groupements hydroxyles et les atomes d'oxygène des carboxylates par des liaisons hydrogènes. Lors de l'élimination de molécules d'eau, la phase MIL-69(Al) n'est pas dégradée, elle est stable jusqu'à 450°C. De plus, les tunnels sont maintenus dans un état contracté grâce aux interactions π-π entre les groupements naphtalène.

NH_2-MIL-53(Al)

Parmi les MOFs de la famille des matériaux MIL-53, le MIL-53(Al) est obtenu à partir de cation trivalent Al^{3+} et d'acide 1,4-benzènedicarboxylique (H_2BDC). Le MIL-53(Al) est constitué d'octaèdres $AlO_4(OH)_2$ liés aux sommets par des groupements hydroxyles afin de former des chaines infinies liées entre elles par des ligands organiques. Il en résulte une charpente tridimensionnelle composée de pores en forme de losange avec une taille de pore de 8.5 Å.

Le MIL-53(Al) est principalement connu pour la flexibilité de sa structure sous l'effet de stimuli comme l'adsorption de gaz. Dans le contexte de l'élaboration de membrane à matrice mixte, il est préférable d'utiliser des MOFs microporeux non flexibles pour éviter des problèmes de compatibilité et de stabilité entre le MOF et le polymère dans le domaine de pression fixé. C'est pourquoi les propriétés d'adsorption de CO_2 du MIL-53 fonctionnalisé par des groupements amino, NH_2-MIL-53(Al) de structure rigide, ont été étudiées dont la structure est présentée dans la Figure 1.17.

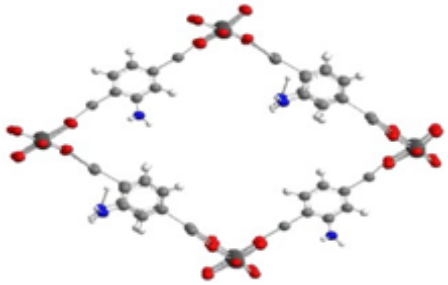

Figure 1.17 – Structure du MIL-53(Al) fonctionnalisé par des groupements amino (-NH_2) [83]

Stavitski *et al.* [84] ont montré que les groupements –NH_2 contribuent au maintien de la structure dans une forme *'narrow pore*' via la création de liaisons hydrogène avec les unités AlO_6 et joue un rôle indirect sur l'adsorption de CO_2. Cela conduit également à une diminution de la taille de pore évaluée à 6.0 Å pour le NH_2-MIL-53(Al).

MIL-91(Ti)

Le MOF MIL-91(Ti), diphosphonate de titane, a été synthétisé par l'université S^t Andrews sous conditions de reflux. Initialement, la phase MIL-91(Ti) a été synthétisée par Serre *et al.* en 2006 [85] sous conditions hydrothermales. Durant le projet M^4CO_2, des conditions de reflux ont été choisies pour démontrer que les MOFs microporeux peuvent être produits avec des conditions de 'synthèse verte' sans altérer leurs propriétés d'adsorption de CO_2.

La phase MIL-91(Ti) est issue de la réaction entre un ion tétravalent, Ti^{4+}, et un ligand organique l'acide N,N'-pipérazine bis-méthylène phosphonique (O_3P-CH_2-NC_4H_8N-CH_2-PO_3). Le MIL-91(Ti) a pour formule brute : $TiO(H_2L)\cdot nH_2O$ (n ~ 4.5) ou L est le ligand organique.

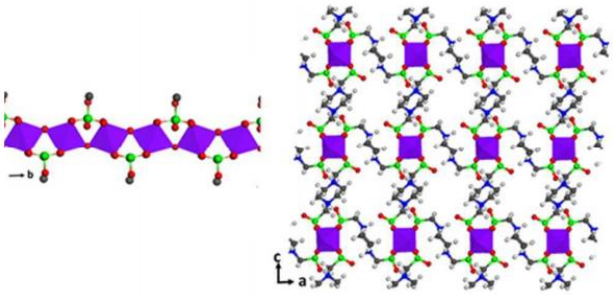

Figure 1.18 – Structure des octaèdres de titane, TiO_6, coordonnés aux sommets par deux groupements PO_3C (gauche) et charpente du MIL-91(Ti) (droite) selon l'axe b [86]

Comme le montre la Figure 1.18, la structure du MIL-91(Ti) consiste en un réseau 3D composé d'octaèdres de titane TiO_6 pour lesquels chacun d'entre eux est lié aux sommets par deux groupements PO_3C coordonnés aux chaînes voisines de ligand. Cela délimite une taille de pore accessible qui a été estimée à 3.5*4.0 Å.

Les matériaux poreux 'Zeolitic Imidazolate Frameworks (ZIFs)'

Pour rappel, les ZIFs sont des matériaux poreux cristallins appartenant à la classe des MOFs et qui ont des topologies analogues à celles des zéolithes. De par la variété de métaux, des ligands organiques et leur fonctionnalisation, il en ressort une grande diversité de structures de ZIFs avec des réseaux poreux en 3D.

Au cours de ce projet de thèse quatre ZIFs ont été caractérisés, fournis par l'entreprise Jonson Matthey et qui possèdent deux topologies distinctes : sodalite (SOD) et rhomboédral (RHO). Les ZIFs de topologie sodalite sont constitués de larges cages sodalite qui sont interconnectées entre elles par des fenêtres. Tandis que les ZIFs de topologie rhomboédrale sont obtenus à partir de la fonctionnalisation en position quatre et cinq de groupement imidazole.

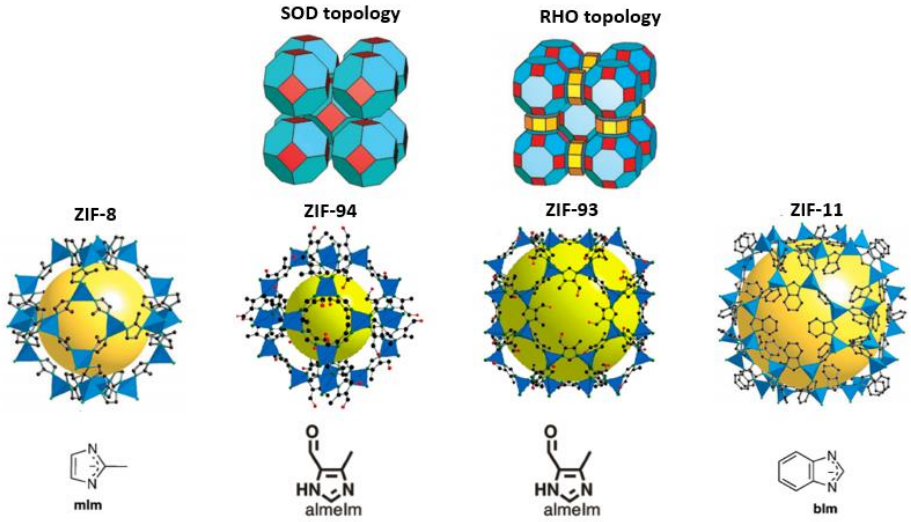

Figure 1.19 – Topologie sodalite (SOD) et rhomboédrale (RHO) (en haut) ainsi que les structures des ZIF-8, ZIF-94, ZIF-93 et ZIF-11 et leur ligand organiques (en bas)

Les ZIF-8 et ZIF-94 ont une topologie sodalite tandis que les ZIF-93 et ZIF-11 possèdent une topologie rhomboédrale. En plus de topologie distinctes, ces ZIFs sont constitués de différents ligands organiques bien que leur centre métallique soit identique, Zn^{2+}. En effet, les ZIF-94 et ZIF-93 ont le même ligand

organique : 4-aldémethylimidazole (aImeIm) tandis que les ligands pour les ZIF-8 et ZIF-11 sont respectivement : 2-méthylimidazole (mIm) et benzimidazole (bIm). La taille des cages sodalite dans le cas du ZIF-94 est de 9.1 Å interconnectées par des fenêtres d'une ouverture de 3.4 Å alors que dans le cas du ZIF-8 la taille des cages et des fenêtres sont de 11.6 et 3.4 Å. Pour les ZIF-93 et ZIF-11, les tailles de cage et de fenêtres sont respectivement : 17.9 et 3.0 Å et 14.6 et 3.7 Å. Il est à noter que ces ZIFs sont stables thermiquement pour des températures allant jusqu'à 300°C.

Pour conclure sur le choix de ces matériaux poreux, ils ont été sélectionnés par rapport à leur petite taille de pore afin de favoriser un effet de tamis moléculaire pour la séparation de CO_2 mais également parce qu'ils présentent une bonne stabilité thermique. De plus, parmi ces MOFs le MIL-96(Al) est stable à l'eau ce qui peut être un avantage pour des conditions de post-combustion ou le flux de gaz contient des traces ou des petites quantités d'eau. Afin d'annuler la flexibilité du MOF MIL-53(Al) pour une incorporation dans une membrane à matrice mixte, deux stratégies ont été étudiées : bloquer la flexibilité via des interactions π-π, le MIL-69(Al) ou par la fonctionnalisation du ligand par des groupements amino (-NH_2), le NH_2-MIL-53(Al). Au cours de ce projet de thèse, les adsorbants 'Zeolitic Imidazolate Frameworks (ZIFs)' ont également été caractérisés car ils présentent de grandes surfaces spécifiques, une porosité bien définie et ils sont stables thermiquement et chimiquement. De plus il a été montré que comme pour les MOFs à base de carboxylate, les ZIFs ont une grande capacité d'adsorption de CO_2.

Le tableau 1.3 résume les données de structures de ces différents matériaux poreux.

Nom	Centre métallique	Ligand organique	Topologie	Taille des fenêtres (Å)	Taille des cages (Å)
MIL-96(Al)	Al^{3+}	Benzène tri-carboxylate (BTC)	Structure en 'nid d'abeille'	3.6*4.5 et 1.2*1.9	9.5*12*11.3/ 3.6*4.5/ 11
$Sc_2(BDC\text{-}NO_2)_3$	Sc^{3+}	Benzène di-carboxylate (BDC)	Canaux triangulaire	-	2.9
MIL-69(Al)	Al^{3+}	2,6-naphtalenedicarboxylique (NDC)	Canaux en losange (1D)	-	2.7*19.4
NH_2-MIL-53(Al)	Al^{3+}	Benzène di-carboxylate (BDC)	Canaux en losange (1D)	-	6.0
MIL-91(Ti)	Ti^{4+}	Acide N,N'-pipérazine bis-méthylène phosphonique	-	-	3.5*4.0
ZIF-8	Zn^{2+}	2-méthylimidazole (mIm)	SOD	3.4	11.6
ZIF-94	Zn^{2+}	4-aldeméthylimidazole (aImeIm)	SOD	3.4	9.1
ZIF-93	Zn^{2+}	4-aldeméthylimidazole (aImeIm)	RHO	3.0	17.9
ZIF-11	Zn^{2+}	Benzimidazole (bIm)	RHO	3.7	14.6

Tableau 1.3 – Résumé des centres métalliques, ligands organiques, topologies et tailles des pores des matériaux poreux caractérisés au cours de ce projet de thèse

Résumé

L'objectif de ce premier chapitre est d'exposer les différents procédés et techniques de séparation de CO_2 disponibles afin de limiter l'émission de gaz à effet de serre. La technique d'adsorption et les différents matériaux poreux pouvant être utilisés pour cette technique: zéolithes, charbons actifs, nanotubes de carbone et Metal-Organic Frameworks (MOFs) ont été abordés.

Les MOFs, matériaux hybrides organique-inorganique possèdent des surfaces spécifiques et des volumes poreux généralement élevés pouvant être supérieurs à ceux des zéolithes. De plus, leurs propriétés physiques et chimiques adaptables les rendent potentiellement attractifs pour la séparation de gaz. Ainsi, les MOFs sont des matériaux de choix pour être intégrés au sein de la phase polymérique des membranes à matrice mixte pour l'application visée : la séparation du CO_2.

References

[1] K. Sumida *et al.*, « Carbon Dioxide Capture in Metal–Organic Frameworks », *Chem. Rev.*, vol. 112, n° 2, p. 724-781, févr. 2012.

[2] J. Gibbins et H. Chalmers, « Carbon capture and storage », *Energy Policy*, vol. 36, n° 12, p. 4317-4322, déc. 2008.

[3] A. A. Olajire, « CO2 capture and separation technologies for end-of-pipe applications – A review », *Energy*, vol. 35, n° 6, p. 2610-2628, juin 2010.

[4] J. D. Figueroa, T. Fout, S. Plasynski, H. McIlvried, et R. D. Srivastava, « Advances in CO2 capture technology—The U.S. Department of Energy's Carbon Sequestration Program », *Int. J. Greenh. Gas Control*, vol. 2, n° 1, p. 9-20, janv. 2008.

[5] J. C. M. Pires, F. G. Martins, M. C. M. Alvim-Ferraz, et M. Simões, « Recent developments on carbon capture and storage: An overview », *Chem. Eng. Res. Des.*, vol. 89, n° 9, p. 1446-1460, sept. 2011.

[6] « CO2 absorption performance of aqueousalkanolaminesinpacke... - Google Scholar ». [En ligne]. Disponible sur: https://scholar.google.com/scholar?hl=fr&as_sdt=0%2C5&inst=2952611022847718469&q=CO2+absorption+performance+of+aqueousalkanolaminesinpackedcolumns.&btnG=. [Consulté le: 31-oct-2017].

[7] V. Darde, K. Thomsen, W. J. M. van Well, et E. H. Stenby, « Chilled ammonia process for CO2 capture », *Int. J. Greenh. Gas Control*, vol. 4, n° 2, p. 131-136, mars 2010.

[8] « Production des gaz de synthèse ». [En ligne]. Disponible sur: https://www-techniques-ingenieur-fr.lama.univ-amu.fr/base-documentaire/archives-th12/archives-operations-unitaires-genie-de-la-reaction-chimique-tiajb/archive-1/production-des-gaz-de-synthese-j5480/. [Consulté le: 06-nov-2017].

[9] H. Weiss, « Rectisol wash for purification of partial oxidation gases », *Gas Sep. Purif.*, vol. 2, n° 4, p. 171-176, déc. 1988.

[10] J. C. M. Pires, F. G. Martins, M. C. M. Alvim-Ferraz, et M. Simões, « Recent developments on carbon capture and storage: An overview », *Chem. Eng. Res. Des.*, vol. 89, n° 9, p. 1446-1460, sept. 2011.

[11] Z. Yong, V. Mata, et A. E. Rodrigues, « Adsorption of carbon dioxide at high temperature—a review », *Sep. Purif. Technol.*, vol. 26, n° 2, p. 195-205, mars 2002.

[12] A. Auroux et A. Gervasini, « Microcalorimetric study of the acidity and basicity of metal oxide surfaces », *J. Phys. Chem.*, vol. 94, n° 16, p. 6371-6379, août 1990.

[13] S. Choi, J. H. Drese, et C. W. Jones, « Adsorbent Materials for Carbon Dioxide Capture from Large Anthropogenic Point Sources », *ChemSusChem*, vol. 2, n° 9, p. 796-854, sept. 2009.

[14] T. Zhao, E. Ochoa-Fernández, M. Rønning, et D. Chen, « Preparation and High-Temperature CO2 Capture Properties of Nanocrystalline Na2ZrO3 », *Chem. Mater.*, vol. 19, n° 13, p. 3294-3301, juin 2007.

[15] J. Tai, Q. Ge, R. J. Davis, et M. Neurock, « Adsorption of CO2 on Model Surfaces of Cesium Oxides Determined from First Principles », *J. Phys. Chem. B*, vol. 108, n° 43, p. 16798-16805, oct. 2004.

[16] M. Tutuianu, O. R. Inderwildi, W. G. Bessler, et J. Warnatz, « Competitive Adsorption of NO, NO2, CO2, and H2O on BaO(100): A Quantum Chemical Study », *J. Phys. Chem. B*, vol. 110, n° 35, p. 17484-17492, sept. 2006.

[17] Z. Li, N. Cai, Y. Huang, et H. Han, « Synthesis, Experimental Studies, and Analysis of a New Calcium-Based Carbon Dioxide Absorbent », *Energy Fuels*, vol. 19, n° 4, p. 1447-1452, juill. 2005.

[18] H. J. RICHTER et K. F. KNOCHE, « Reversibility of Combustion Processes », in *Efficiency and Costing*, vol. 235, 0 vol., AMERICAN CHEMICAL SOCIETY, 1983, p. 71-85.

[19] Z. Yong et A. E. Rodrigues, « Hydrotalcite-like compounds as adsorbents for carbon dioxide », *Energy Convers. Manag.*, vol. 43, n° 14, p. 1865-1876, sept. 2002.
[20] Z. Yong, Mata, et A. E. Rodrigues, « Adsorption of Carbon Dioxide onto Hydrotalcite-like Compounds (HTlcs) at High Temperatures », *Ind. Eng. Chem. Res.*, vol. 40, n° 1, p. 204-209, janv. 2001.
[21] K. S. Walton, M. B. Abney, et M. Douglas LeVan, « CO2 adsorption in Y and X zeolites modified by alkali metal cation exchange », *Microporous Mesoporous Mater.*, vol. 91, n° 1, p. 78-84, avr. 2006.
[22] J. Rouquerol, F. Rouquerol, P. Llewellyn, G. Maurin, et K. S. W. Sing, *Adsorption by Powders and Porous Solids: Principles, Methodology and Applications*. Academic Press, 2013.
[23] « Database of Zeolite Structures ». [En ligne]. Disponible sur: http://www.iza-structure.org/databases/. [Consulté le: 06-nov-2017].
[24] D. Bonenfant, M. Kharoune, P. Niquette, M. Mimeault, et R. Hausler, « Advances in principal factors influencing carbon dioxide adsorption on zeolites », *Sci. Technol. Adv. Mater.*, vol. 9, n° 1, p. 013007, 2008.
[25] J. A. Michelena, G. Peeters, E. F. Vansant, et P. de Bièvre, « Recueil des Travaux Chimiques des Pays-Bas Journal of the Royal Netherlands Chemical Society: The adsorption of carbon monoxide and carbon dioxide in calcium-exchanged zeolite Y », *Recl. Trav. Chim. Pays-Bas*, vol. 96, n° 5, p. 121-124, janv. 1977.
[26] P. J. E. Harlick et F. H. Tezel, « An experimental adsorbent screening study for CO2 removal from N2 », *Microporous Mesoporous Mater.*, vol. 76, n° 1, p. 71-79, déc. 2004.
[27] R. Hernández-Huesca, L. Díaz, et G. Aguilar-Armenta, « Adsorption equilibria and kinetics of CO2, CH4 and N2 in natural zeolites », *Sep. Purif. Technol.*, vol. 15, n° 2, p. 163-173, mars 1999.
[28] F. Rodríguez-Reinoso et M. Molina-Sabio, « Activated carbons from lignocellulosic materials by chemical and/or physical activation: an overview », *Carbon*, vol. 30, n° 7, p. 1111-1118, janv. 1992.
[29] S. Sircar, T. C. Golden, et M. B. Rao, « Activated carbon for gas separation and storage », *Carbon*, vol. 34, n° 1, p. 1-12, janv. 1996.
[30] R. V. Siriwardane, M.-S. Shen, E. P. Fisher, et J. A. Poston, « Adsorption of CO2 on Molecular Sieves and Activated Carbon », *Energy Fuels*, vol. 15, n° 2, p. 279-284, mars 2001.
[31] D. D. Do et K. Wang, « A new model for the description of adsorption kinetics in heterogeneous activated carbon », *Carbon*, vol. 36, n° 10, p. 1539-1554, oct. 1998.
[32] M. M. Maroto-Valer, Z. Tang, et Y. Zhang, « CO2 capture by activated and impregnated anthracites », *Fuel Process. Technol.*, vol. 86, n° 14, p. 1487-1502, oct. 2005.
[33] S. K. Smart, A. I. Cassady, G. Q. Lu, et D. J. Martin, « The biocompatibility of carbon nanotubes », *Carbon*, vol. 44, n° 6, p. 1034-1047, mai 2006.
[34] Y. Lin *et al.*, « Advances toward bioapplications of carbon nanotubes », *J. Mater. Chem.*, vol. 14, n° 4, p. 527-541, 2004.
[35] P. M. Ajayan, « Nanotubes from Carbon », *Chem. Rev.*, vol. 99, n° 7, p. 1787-1800, juill. 1999.
[36] M. Cinke, J. Li, C. W. Bauschlicher, A. Ricca, et M. Meyyappan, « CO2 adsorption in single-walled carbon nanotubes », *Chem. Phys. Lett.*, vol. 376, n° 5, p. 761-766, juill. 2003.
[37] C. Lu, H. Bai, B. Wu, F. Su, et J. F. Hwang, « Comparative Study of CO2 Capture by Carbon Nanotubes, Activated Carbons, and Zeolites », *Energy Fuels*, vol. 22, n° 5, p. 3050-3056, sept. 2008.
[38] S. S. Razavi, S. M. Hashemianzadeh, et H. Karimi, « Modeling the adsorptive selectivity of carbon nanotubes for effective separation of CO2/N2 mixtures », *J. Mol. Model.*, vol. 17, n° 5, p. 1163-1172, mai 2011.
[39] L. Huang *et al.*, « Simulations of Binary Mixture Adsorption of Carbon Dioxide and Methane in Carbon Nanotubes: Temperature, Pressure, and Pore Size Effects », *J. Phys. Chem. C*, vol. 111, n° 32, p. 11912-11920, août 2007.

[40] C. N. R. Rao, K. Biswas, K. S. Subrahmanyam, et A. Govindaraj, « Graphene, the new nanocarbon », *J. Mater. Chem.*, vol. 19, n° 17, p. 2457-2469, avr. 2009.
[41] C. N. R. Rao, K. Gopalakrishnan, et A. Govindaraj, « Synthesis, properties and applications of graphene doped with boron, nitrogen and other elements », *Nano Today*, vol. 9, n° 3, p. 324-343, juin 2014.
[42] A. Ghosh *et al.*, « Uptake of H2 and CO2 by Graphene », *J. Phys. Chem. C*, vol. 112, n° 40, p. 15704-15707, oct. 2008.
[43] J. S. Beck *et al.*, « A new family of mesoporous molecular sieves prepared with liquid crystal templates », *J. Am. Chem. Soc.*, vol. 114, n° 27, p. 10834-10843, déc. 1992.
[44] C. T. Kresge et W. J. Roth, « The discovery of mesoporous molecular sieves from the twenty year perspective », *Chem. Soc. Rev.*, vol. 42, n° 9, p. 3663-3670, avr. 2013.
[45] R. T. Yang, *Adsorbents: Fundamentals and Applications*. John Wiley & Sons, 2003.
[46] S. Bourrelly, P. L. Llewellyn, C. Serre, F. Millange, T. Loiseau, et G. Férey, « Different Adsorption Behaviors of Methane and Carbon Dioxide in the Isotypic Nanoporous Metal Terephthalates MIL-53 and MIL-47 », *J. Am. Chem. Soc.*, vol. 127, n° 39, p. 13519-13521, oct. 2005.
[47] P. D. C. Dietzel, V. Besikiotis, et R. Blom, « Application of metal–organic frameworks with coordinatively unsaturated metal sites in storage and separation of methane and carbon dioxide », *J. Mater. Chem.*, vol. 19, n° 39, p. 7362-7370, oct. 2009.
[48] K. S. Walton *et al.*, « Understanding Inflections and Steps in Carbon Dioxide Adsorption Isotherms in Metal-Organic Frameworks », *J. Am. Chem. Soc.*, vol. 130, n° 2, p. 406-407, janv. 2008.
[49] V. Guillerm *et al.*, « A Series of Isoreticular, Highly Stable, Porous Zirconium Oxide Based Metal–Organic Frameworks », *Angew. Chem. Int. Ed.*, vol. 51, n° 37, p. 9267-9271, sept. 2012.
[50] Q. Yang, A. D. Wiersum, P. L. Llewellyn, V. Guillerm, C. Serre, et G. Maurin, « Functionalizing porous zirconium terephthalate UiO-66(Zr) for natural gas upgrading: a computational exploration », *Chem. Commun.*, vol. 47, n° 34, p. 9603-9605, août 2011.
[51] P. D. C. Dietzel *et al.*, « Adsorption properties and structure of CO2 adsorbed on open coordination sites of metal–organic framework Ni2(dhtp) from gas adsorption, IR spectroscopy and X-ray diffraction », *Chem. Commun.*, vol. 0, n° 41, p. 5125-5127, oct. 2008.
[52] A. D. Wiersum, J.-S. Chang, C. Serre, et P. L. Llewellyn, « An Adsorbent Performance Indicator as a First Step Evaluation of Novel Sorbents for Gas Separations: Application to Metal–Organic Frameworks », *Langmuir*, vol. 29, n° 10, p. 3301-3309, mars 2013.
[53] F. Millange, C. Serre, et G. Férey, « Synthesis, structure determination and properties of MIL-53as and MIL-53ht: the first CrIII hybrid inorganic–organic microporous solids: CrIII(OH)·{O2C–C6H4–CO2}·{HO2C–C6H4–CO2H}x », *Chem. Commun.*, vol. 0, n° 8, p. 822-823, avr. 2002.
[54] G. Férey, M. Latroche, C. Serre, F. Millange, T. Loiseau, et A. Percheron-Guégan, « Hydrogen adsorption in the nanoporous metal-benzenedicarboxylate M(OH)(O2C–C6H4–CO2)(M = Al3+, Cr3+), MIL-53 », *Chem. Commun.*, vol. 0, n° 24, p. 2976-2977, déc. 2003.
[55] E. V. Anokhina, M. Vougo-Zanda, X. Wang, et A. J. Jacobson, « In(OH)BDC·0.75BDCH2 (BDC = Benzenedicarboxylate), a Hybrid Inorganic−Organic Vernier Structure », *J. Am. Chem. Soc.*, vol. 127, n° 43, p. 15000-15001, nov. 2005.
[56] M. Vougo-Zanda, J. Huang, E. Anokhina, X. Wang, et A. J. Jacobson, « Tossing and Turning: Guests in the Flexible Frameworks of Metal(III) Dicarboxylates », *Inorg. Chem.*, vol. 47, n° 24, p. 11535-11542, déc. 2008.
[57] J. P. S. Mowat, S. R. Miller, A. M. Z. Slawin, V. R. Seymour, S. E. Ashbrook, et P. A. Wright, « Synthesis, characterisation and adsorption properties of microporous scandium carboxylates with rigid and flexible frameworks », *Microporous Mesoporous Mater.*, vol. 142, n° 1, p. 322-333, juin 2011.
[58] F. Nouar *et al.*, « Tuning the breathing behaviour of MIL-53 by cation mixing », *Chem. Commun.*, vol. 48, n° 82, p. 10237-10239, sept. 2012.

[59] C. Serre *et al.*, « Very Large Breathing Effect in the First Nanoporous Chromium(III)-Based Solids: MIL-53 or CrIII(OH)·{O2C−C6H4−CO2}·{HO2C−C6H4−CO2H}x·H2Oy », *J. Am. Chem. Soc.*, vol. 124, n° 45, p. 13519-13526, nov. 2002.
[60] S. S.-Y. Chui, S. M.-F. Lo, J. P. H. Charmant, A. G. Orpen, et I. D. Williams, « A Chemically Functionalizable Nanoporous Material [Cu3(TMA)2(H2O)3]n », *Science*, vol. 283, n° 5405, p. 1148-1150, févr. 1999.
[61] C. R. Wade et M. Dincă, « Investigation of the synthesis, activation, and isosteric heats of CO_2 adsorption of the isostructural series of metal-organic frameworks $M_3(BTC)_2$ (M = Cr, Fe, Ni, Cu, Mo, Ru) », *Prof Dinca Erja Kajosalo*, avr. 2012.
[62] J. H. Cavka *et al.*, « A New Zirconium Inorganic Building Brick Forming Metal Organic Frameworks with Exceptional Stability », *J. Am. Chem. Soc.*, vol. 130, n° 42, p. 13850-13851, oct. 2008.
[63] M. Kandiah *et al.*, « Synthesis and Stability of Tagged UiO-66 Zr-MOFs », *Chem. Mater.*, vol. 22, n° 24, p. 6632-6640, déc. 2010.
[64] A. Phan, C. J. Doonan, F. J. Uribe-Romo, C. B. Knobler, M. O'Keeffe, et O. M. Yaghi, « Synthesis, Structure, and Carbon Dioxide Capture Properties of Zeolitic Imidazolate Frameworks », *Acc. Chem. Res.*, vol. 43, n° 1, p. 58-67, janv. 2010.
[65] S. R. Venna et M. A. Carreon, « Highly Permeable Zeolite Imidazolate Framework-8 Membranes for CO2/CH4 Separation », *J. Am. Chem. Soc.*, vol. 132, n° 1, p. 76-78, janv. 2010.
[66] N. C. Burtch, H. Jasuja, et K. S. Walton, « Water Stability and Adsorption in Metal–Organic Frameworks », *Chem. Rev.*, vol. 114, n° 20, p. 10575-10612, oct. 2014.
[67] F. Brandani et D. M. Ruthven, « The Effect of Water on the Adsorption of CO2 and C3H8 on Type X Zeolites », *Ind. Eng. Chem. Res.*, vol. 43, n° 26, p. 8339-8344, déc. 2004.
[68] L. B. Adams, C. R. Hall, R. J. Holmes, et R. A. Newton, « An examination of how exposure to humid air can result in changes in the adsorption properties of activated carbons », *Carbon*, vol. 26, n° 4, p. 451-459, janv. 1988.
[69] N. Chanut *et al.*, « Screening the Effect of Water Vapour on Gas Adsorption Performance: Application to CO2 Capture from Flue Gas in Metal–Organic Frameworks », *ChemSusChem*, vol. 10, n° 7, p. 1543-1553, avr. 2017.
[70] A. Ö. Yazaydın *et al.*, « Enhanced CO2 Adsorption in Metal-Organic Frameworks via Occupation of Open-Metal Sites by Coordinated Water Molecules », *Chem. Mater.*, vol. 21, n° 8, p. 1425-1430, avr. 2009.
[71] J. Liu, J. Tian, P. K. Thallapally, et B. P. McGrail, « Selective CO2 Capture from Flue Gas Using Metal–Organic Frameworks—A Fixed Bed Study », *J. Phys. Chem. C*, vol. 116, n° 17, p. 9575-9581, mai 2012.
[72] B. Liu et B. Smit, « Molecular Simulation Studies of Separation of CO2/N2, CO2/CH4, and CH4/N2 by ZIFs », *J. Phys. Chem. C*, vol. 114, n° 18, p. 8515-8522, mai 2010.
[73] K. T. Chue, J. N. Kim, Y. J. Yoo, S. H. Cho, et R. T. Yang, « Comparison of Activated Carbon and Zeolite 13X for CO2 Recovery from Flue Gas by Pressure Swing Adsorption », *Ind. Eng. Chem. Res.*, vol. 34, n° 2, p. 591-598, févr. 1995.
[74] R. W. Baker, « Future Directions of Membrane Gas Separation Technology », *Ind. Eng. Chem. Res.*, vol. 41, n° 6, p. 1393-1411, mars 2002.
[75] L. M. Robeson, « The upper bound revisited », *J. Membr. Sci.*, vol. 320, n° 1, p. 390-400, juill. 2008.
[76] T.-S. Chung, L. Y. Jiang, Y. Li, et S. Kulprathipanja, « Mixed matrix membranes (MMMs) comprising organic polymers with dispersed inorganic fillers for gas separation », *Prog. Polym. Sci.*, vol. 32, n° 4, p. 483-507, avr. 2007.
[77] H. Yang *et al.*, « Progress in carbon dioxide separation and capture: A review », *J. Environ. Sci.*, vol. 20, n° 1, p. 14-27, janv. 2008.

[78] M. Benzaqui *et al.*, « Revisiting the Aluminum Trimesate-Based MOF (MIL-96): From Structure Determination to the Processing of Mixed Matrix Membranes for CO2 Capture », *Chem. Mater.*, vol. 29, n° 24, p. 10326-10338, déc. 2017.
[79] T. Loiseau *et al.*, « MIL-96, a Porous Aluminum Trimesate 3D Structure Constructed from a Hexagonal Network of 18-Membered Rings and µ3-Oxo-Centered Trinuclear Units », *J. Am. Chem. Soc.*, vol. 128, n° 31, p. 10223-10230, août 2006.
[80] R. S. Pillai, V. Benoit, A. Orsi, P. L. Llewellyn, P. A. Wright, et G. Maurin, « Highly Selective CO2 Capture by Small Pore Scandium-Based Metal–Organic Frameworks », *J. Phys. Chem. C*, vol. 119, n° 41, p. 23592-23598, oct. 2015.
[81] T. Loiseau, C. Mellot-Draznieks, H. Muguerra, G. Férey, M. Haouas, et F. Taulelle, « Hydrothermal synthesis and crystal structure of a new three-dimensional aluminum-organic framework MIL-69 with 2,6-naphthalenedicarboxylate (ndc), Al(OH)(ndc)·H2O », *Comptes Rendus Chim.*, vol. 8, n° 3–4, p. 765-772, mars 2005.
[82] S. Bourrelly, P. L. Llewellyn, C. Serre, F. Millange, T. Loiseau, et G. Férey, « Different Adsorption Behaviors of Methane and Carbon Dioxide in the Isotypic Nanoporous Metal Terephthalates MIL-53 and MIL-47 », *J. Am. Chem. Soc.*, vol. 127, n° 39, p. 13519-13521, oct. 2005.
[83] J. Gascon, U. Aktay, M. D. Hernandez-Alonso, G. P. M. van Klink, et F. Kapteijn, « Amino-based metal-organic frameworks as stable, highly active basic catalysts », *J. Catal.*, vol. 261, n° 1, p. 75-87, janv. 2009.
[84] E. Stavitski *et al.*, « Complexity behind CO2 Capture on NH2-MIL-53(Al) », *Langmuir*, vol. 27, n° 7, p. 3970-3976, avr. 2011.
[85] C. Serre *et al.*, « Synthesis, Structure and Properties of Related Microporous N,N'-Piperazinebismethylenephosphonates of Aluminum and Titanium », *Chem. Mater.*, vol. 18, n° 6, p. 1451-1457, mars 2006.
[86] V. Benoit *et al.*, « MIL-91(Ti), a small pore metal–organic framework which fulfils several criteria: an upscaled green synthesis, excellent water stability, high CO2 selectivity and fast CO2 transport », *J. Mater. Chem. A*, vol. 4, n° 4, p. 1383-1389, janv. 2016.

Chapter 2 – Adsorption, experimental techniques and derived data

Table of contents

Chapter 2 - Adsorption, experimental techniques and derived data

First of all, this chapter aims to describe and explain the adsorption phenomenon which occurs when a solid material surface is enriched in contact with a liquid or gas phase. The adsorption phenomenon is quantified thanks to the determination of adsorption isotherm plotting amount adsorbed as function of pressure. The second part of this chapter is devoted to the experimental set up to get adsorption isotherms below atmospheric pressure and at pressure higher than 1 bar. From adsorption isotherm, several characteristics of material can be determined: textural parameters, adsorption capacity, adsorption enthalpy and the prediction of selectivity which are exposed in last part. The knowledge of these parameters allows to select suitable adsorbents for a given gas separation application.

A. Preambule

Some definitions related to adsorption phenomenon are provided below [1]:

- Adsorption: surface phenomenon that appears when a solid material is in contact with a liquid or gas phase at the equilibrium. It corresponds to the enrichment of one or more components or the density increase of fluid at the vicinity of a solid/ gas or solid/liquid interface.
- Absorption: penetration of fluid molecules into the solid material governed by diffusion, unlike adsorption.
- Sorption: this term is used when adsorption and absorption phenomena occur.
- Physisorption: phenomenon that appears whenever a gas is at the vicinity of gas/ solid interface. This is governed by low Van der Waals interactions. Physisorption differs from chemisorption where chemical bounds are created between gas or liquid phase and solid material.
- Adsorbent: this designates solid materials which can be porous. A pore is defined as a cavity or channel deeper than large. Porous materials for which pores size do not exceed 100 nm can be classified as function of pore size as follows in Figure 2.1 [2]:

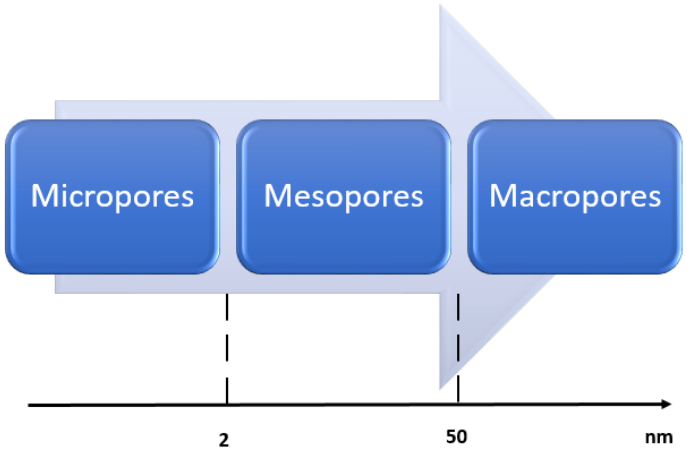

Figure 2.1 – Scheme highlighting various pore width: micropores (< 2nm), mesopores (between 2 and 50 nm), macropores (> 50 nm)

Note that, micropores can be divided into two categories the ‘narrow pores’ or ‘ultramicropores’ and the ‘wide micropores’ or ‘supermicropores’.

- Adsorptive: this designates a vapor or a gas which can be potentially adsorbed at the adsorbent surface. This is also named the bulk phase.
- Adsorbate: this refers to the adsorbed state of the adsorptive at the vicinity of gas/ solid interface.
- Desorption: this concerns the transition of adsorbed state toward bulk phase (gas or liquid), meaning the release of fluid retained by adsorption on the solid surface.

B. Description of adsorption phenomenon

Adsorption is a surface phenomenon for which Van der Waals-type forces can be involved, characteristic of physisorption. At the microscopic scale, the forces involved in physisorption can be described by means of mathematical function with the aim to reproduce as far as possible the potential energy of the adsorbate/ adsorbent interactions. While at the macroscopic level, adsorption phenomenon can be quantified thanks to Gibbs representation based on the concept of 'surface excess'.

1. Intermolecular potential function of adsorption

Adsorption phenomenon is governed by interactions of low energy including the Van der Waals dispersion forces and repulsion forces at short distances. An equilibrium is established between these forces when the adsorbent surface and adsorbate molecules are in contact each other. The potential energy of the adsorbate-adsorbent interactions can be modelled by a mathematical function whereby interactions are additive and expressed by [1]:

$$\varphi = \varphi_D + \varphi_R + \varphi_P + \varphi_E \tag{2.1}$$

The terms $\varphi_D, \varphi_R, \varphi_P$ refer respectively to forces of dispersion, repulsion and polarization interactions. For each adsorbate-adsorbent systems, these forces and interactions are implied and can be considered as 'non-specific' interactions. While the electrostatic term φ_E is considered as 'specific' interactions because it appears for certain adsorbate-adsorbent systems.

The expression of dispersion forces is:

$$\varphi_D(r) = -\frac{A}{r^6} \tag{2.2}$$

In the relation 2.2, A and r stand for respectively a dispersion force constant which is characteristic of the atoms pair and the distance between the adsorbate and adsorbent atoms. This relation expressed only the dipole-dipole interactions and can be modified to take into account other interactions:

$$\varphi_D(r) = -\frac{A_6}{r^6} - \frac{A_8}{r^8} - \frac{A_{10}}{r^{10}} \tag{2.3}$$

The terms r^{-6}, r^{-8}, r^{-10}, define respectively the interactions dipole-dipole, dipole-quadrupole and quadrupole-quadrupole or dipole-octupole.

The repulsion forces occur when the atoms approach each other and their electronic clouds are overlapped. The exponential Born-Mayer function defines these forces as follows:

$$\varphi_R(r) = \frac{B}{r^{12}} \tag{2.4}$$

B represents constant of the adsorbate-adsorbent pair.

The association of dispersion and repulsion terms led to a Lennard-Jones potential energy providing a global picture of physisorption and expressed as [3]:

$$\varphi(r) = \frac{B}{r^{12}} - \frac{A}{r^6} \tag{2.5}$$

The proximity between adsorbent electric field and the adsorbate induces polarization interactions whose relation is:

$$\varphi_P = -\frac{\alpha.E^2}{2} \tag{2.6}$$

α is the dipole polarizability of the adsorbate while E matches to the electric field generated by the adsorbent.

The electrostatic term expresses the monopole-monopole interaction as follows:

$$\varphi_E = \frac{q.q'}{4\pi\epsilon_0 r} \tag{2.7}$$

In this relation, q and q' are the charges of atoms of the adsorbate and adsorbent while ϵ_0 is the vacuum permeability.

Note that, certain molecules as carbon dioxide and nitrogen have a quadrupolar moment while water possesses a permanent dipole. Thus, the 'polar' molecules will induce specific interactions with a surface which may also be generated with surface groups as hydroxyl groups, cations or other functionalization at the adsorbent surface.

2. Gibbs representation

Adsorption phenomenon gives an accumulation of adsorptive molecules at the vicinity of adsorbent surface, called 'adsorbed layer'. This assumes a variation of local concentration ($c = dn/dV$) of adsorptive components. When the distance z increases from adsorbent surface, the local concentration of adsorptive molecules decreases progressively. When the distance z reaches the value of thickness t of adsorbed layer, the local concentration is equal to this of gas or bulk phase, c_F^g. This is shown schematically in Figure 2.2.

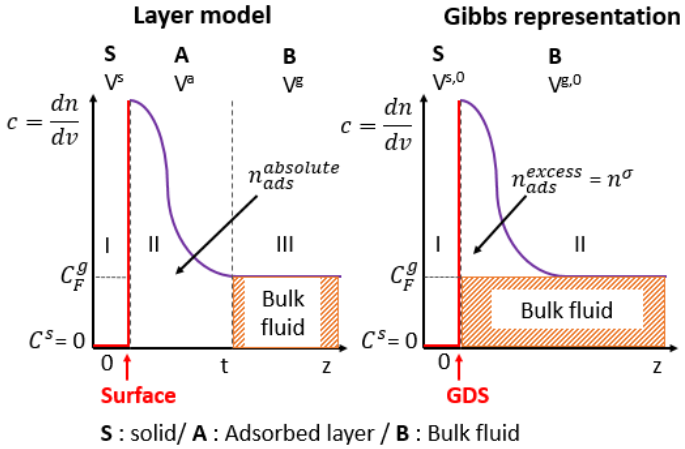

Figure 2.2 – Representation of the layer model (left) and Gibbs dividing surface (GDS) of the surface excess amount

The layer model constitutes the hypothetical variation of adsorptive local concentration (i.e, $c = dn/dV$) that is divided in three zones: I, II and III. The first one or 'zone I' represents the solid adsorbent where the adsorptive concentration is zero, c^s= 0. This assumes that gas molecules do not penetrate in the adsorbent (i.e, absorption). At a distance z>t, the third zone or 'zone III' is the bulk phase where the adsorptive concentration is homogeneous and only dependent to pressure and temperature equilibriums. The second one or 'zone II' is defined as the area comprised between z = 0 and z = t corresponding to the 'adsorbed layer' for which the local concentration is dependent on distance z and is higher than this in the bulk phase. The absolute amount adsorbed, $n_{ads}^{absolute}$, of adsorptive in the adsorbed layer is expressed as follows:

$$n_{ads}^{absolute} = A \int_0^t c dz \tag{2.8}$$

The total amount of adsorptive, n , is the amount adsorbed ('zone II') and the remaining gas amount in the bulk phase $c_F^g V^g$ ('zone III') defined as:

$$n = A \int_0^t c dz + c_F^g V^g \tag{2.9}$$

In the equation 2.9, V^g represents the volume occupied by the bulk phase where the concentration c^g is uniform. The expression of absolute amount adsorbed is:

$$n_{ads}^{absolute} = n - c_F^g V^g \tag{2.10}$$

The determination of the amount adsorbed needs to know the exact values of the bulk phase volume V^g and the local concentration as function of distance z. However, it is not possible to obtain these data. A new approach has been proposed by Gibbs to overcome these barriers in the calculation of the amount adsorbed [1]. Gibbs has introduced the concept of 'surface excess' to assess the amount adsorbed. He has suggested to divide the adsorption phenomena into two areas: gas and solid phases separated by an imaginary surface parallel and close to the adsorbent surface called 'Gibbs Dividing Surface (GDS)'.

From Gibbs, the surface excess amount, n^σ, is defined by the difference between the total amount, n, and the amount of gaseous adsorptive which would be present in the volume $V^{g,0}$ at the final equilibrium if the concentration remains constant up to GDS. The expression is:

$$n^\sigma = n - c_F^g V^{g,0} \tag{2.11}$$

For the physical interpretation of adsorption data, it is evident to coincide the GDS with the adsorbent surface available for adsorptive. From this assumption V_g^0 is the sum of V^a and V^g and the surface excess amount n^σ is:

$$n^\sigma = n - c_F^g (V^a + V^g) \tag{2.12}$$

The volume $V^{g,0}$ that corresponds to 'dead-space volume' can be determined in two ways: from the knowledge of adsorption cell volume and the adsorbent volume or from adsorption of inert gas as helium assumed not adsorbed (see section C.1).

From the combination of the equations 2.10 and 2.12, the expression of amount adsorbed is:

$$n_{ads}^{absolute} = n^\sigma + c_F^g V^a \tag{2.13}$$

The excess gas amount adsorbed,n^{σ}, by a solid of mass m^{s}, depends on the equilibrium pressure, the temperature and the nature of adsorbent/ adsorptive (interface). The adsorption experiments are carried out for temperature and volume fixed, only the gas amount introduced into the adsorption system varies. Thus, the excess amount adsorbed is measured for each equilibrium states established between the adsorbed phase and the bulk phase which are represented by means of adsorption isotherm. This allows to quantify the adsorption phenomenon which occurs for an adsorbent/ adsorptive given. Therefore, an adsorption isotherm represents equilibrium states which corresponds to amount adsorbed as function of pressure in gas phase at constant temperature: $n^{\sigma} = f(p)T$, an example is provided in Figure 2.3.

In the case where the adsorption experiments are performed up to 1 bar, the amount $c_F^g V^a$ is much lower than the adsorbed phase and the amount adsorbed $n_{ads}^{absolute}$ is considered as equivalent to the surface excess amount n^{σ} (i.e, $n_{ads}^{absolute} \sim n^{\sigma}$). This is especially applicable for nitrogen gas adsorption at 77K or gas adsorption at room temperature up to atmospheric pressure.

However for pressures above 1 bar, the adsorptive concentration in the bulk phase is no longer negligible (i.e, the term $c_F^g V^a$) compared to its concentration in the adsorbed phase. Consequently, there is a divergence between absolute and excess amounts adsorbed. It is necessary to assess the volume of adsorbed phase. For highly porous adsorbents, this volume can be considered as the total porous volume of the solid assuming the amount adsorbed on external surface is negligible compared to this into the porosity. Thus, the equation 2.13 becomes:

$$n_{ads}^{absolute} = n^{\sigma} + c_F^g V_{pore} \tag{2.14}$$

This divergence has been evidenced for microporous MOFs by A. Wiersum in 2012 [4] for which an example is provided in Figure 2.3.

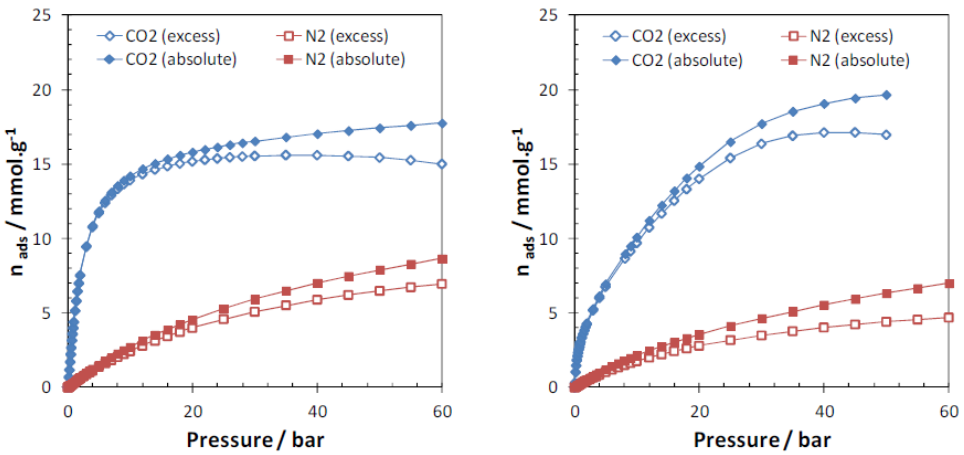

Figure 2.3 – Representation of excess and absolute amounts adsorbed for CO_2 and N_2 at 303K on CuBTC (left) and MIL-100(Fe) from A.Wiersum (2012) [4]

During this thesis, excess amounts adsorbed were measured experimentally and represented in adsorption isotherms.

C. Determination and interpretation of adsorption isotherm

The two most widely used techniques to get adsorption data and to build adsorption isotherm are the manometric and gravimetric methods. During this thesis, adsorption isotherms were mainly determined via manometry device. Adsorption isotherms have been classified in various categories as function of the adsorbent nature (i.e, microporosity, mesoporosity, non-porous solids) from IUPAC recommendation [5].

1. Manometry adsorption device

To collect adsorption data, there are many commercial and homemade apparatus based on the same experimental principle that is detailed in Figure 2.4.

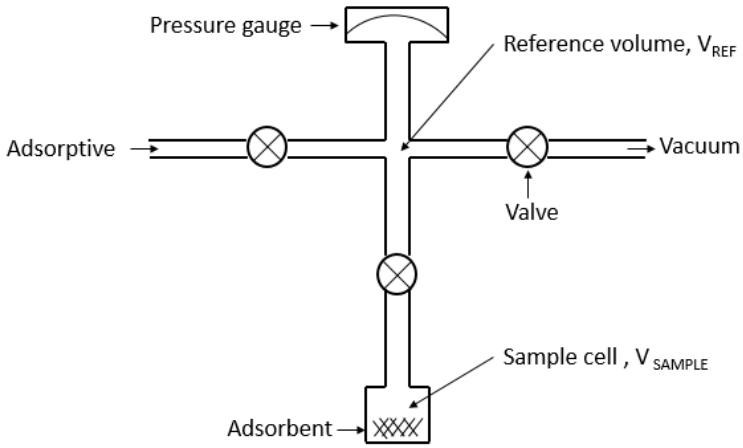

Figure 2.4 – Scheme of adsorption manometry device adapted from Rouquerol *et al.* [1]

In the literature, the term 'volumetric' is still widely used to make reference to 'manometric' methods. The term 'volumetric' references to former experiments in which mercury was used to measure gas phase volume variations. Currently, commercial devices are equipped of sensitive pressure gauges.

Prior to gas adsorption, the measurement of 'dead space' or 'void volume' ($V^{g,0}$) is carried out using helium as probe molecule. The 'dead space' represents the measuring cell as well as the part of device up to pressure gauge that should be determined for each adsorption experiments owing to the variation of samples density. Helium is considered as a gas that does not adsorb that is why this is used as probe molecule.

The adsorption measurement consists of introducing a gas dose of known amount into the reference volume (V_{REF}). The valve of reference volume is then open on sample volume (V_{SAMPLE}) where the gas is in contact with the sample until the equilibrium is reached. One can consider that the equilibrium is established when the pressure change is below a certain limit for a given time or when time is fixed. Note that the equilibrium should be well established to prevent the distortion of adsorption data. Gas desorption is mainly carried out by the decrease of pressure thanks to vacuum pump.

Note that, a second way widely used to get adsorption data is the 'gravimetric method' where the principle is based on the measure of the adsorbent mass during adsorption by means of a balance. Indeed, the adsorbent is weighed before and after gas adsorption and amounts adsorbed are determined from the mass variation. This type of device has been mainly developed by the company Rubotherm with a magnetic suspension balance taking into accounts buoyancy effects [6].

2. Interpretation of adsorption isotherm: adsorption mechanism

When adsorption occurs, the pore filling mechanisms are different as function of pore size: micro- meso- or macropores. A typical example of an adsorption isotherm is provided in Figure 2.5.

The area A matches to the filling of micropores divided into narrow and wider micropores for which adsorption occurs on specific adsorption sites on the adsorbent surface. Specific adsorption sites can be cations or defects of crystalline structure [3]. The narrow micropores filling is governed by enhanced fluid-solid interactions while for wider micropores it is both fluid-solid and fluid-fluid interactions. Narrow micropores are filled for relative pressures $p/p^0 < 0.01$ against $p/p^0 = 0.01$-0.15 for wider micropores. The relative pressures for which micropores filling occurs are dependent on pore shape, effective pore width and the nature and size of adsorbate molecules. Molecular size of available adsorbate and experimental conditions governs the capacity of pore filling.

The zone B-C matches to the coverage of adsorbent surface by adsorptive molecules to form a monolayer adsorbed. The thickness of adsorbed layer increases with relative pressures to get multilayer adsorbed (zone D). In the case of microporous adsorbent, the amounts adsorbed achieve a plateau indicating a low external surface area.

The zone D-E coincides to pores condensation which represents a gas-liquid transition and takes place in mesopores often accompanied by a pore condensation.

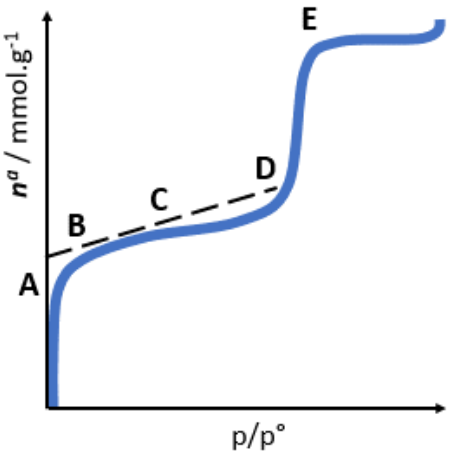

Figure 2.5 – Representation of an adsorption isotherm plotting amount adsorbed as function of relative pressure

3. Adsorption isotherm: IUPAC classification

In the literature, different adsorption isotherms are encountered for many gas-solid systems showing various shapes. These shapes give informations about pores structure of the adsorbent.

Initially, the first classification of physical adsorption isotherms has been suggested by Brunauer, Deming, and Teller in 1940 [4]. The original classification has been extended by the IUPAC recommendation in 1985 by Sing et al, in 1999 by Rouquerol et al, and more recently in 2015 by Thommes et al [1], [5], [7]. The classification of adsorption isotherms, $n = f(p/p^0)$, is presented in Figure 2.6.

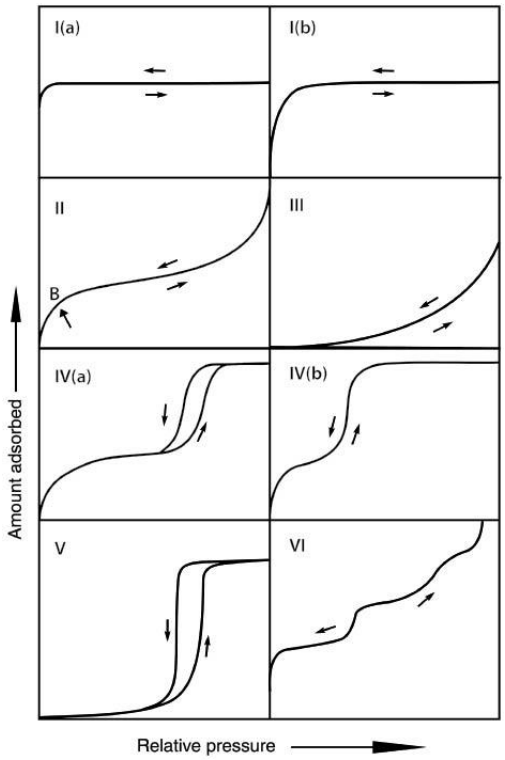

Figure 2.6 – Classification of physical adsorption isotherms from IUPAC report in 2015 [7]

Adsorption isotherms of type I(a) and I(b) are reversible and characteristic of microporous adsorbents (d_p < 20 Å) such as some of activated carbons, molecular sieve zeolites. Types I(a) and I(b) are concave to the relative pressure p/p^0 axis. These adsorption isotherms show a steep slope for a low range of relative pressure p/p^0 which matches to micropores-filling and suggests strong adsorbent-adsorbate interactions and adsorption energy. The types I(a) and I(b) are distinguished by micropores width narrow and wider respectively for type I(a) and I(b). For type I(b), the presence of narrow mesopores (d_p< 25 Å) within adsorbent can be possible. For higher relative pressures, the amounts adsorbed reach a nearly horizontal plateau indicating a low external surface area.

The adsorption isotherm of type II is reversible and characteristic of nonporous or macroporous adsorbents. The shape of this adsorption isotherm indicates the formation of multilayer adsorption for high relative pressures p/p^0. Point B on adsorption isotherm until the middle of quasi-linear section (Figure 2.6) represents the completion of monolayer. Beyond this area, the curve increases progressively and matches to the multilayer coverage formation with a thickness 't' only limited by the relative pressure $p/p^0 = 1$.

The shape of type III adsorption isotherm is found for non-porous or macroporous adsorbents and indicates relatively weak adsorbent-adsorbate interactions. In contrast to a type II, the absence of point B shows that the formation of monolayer adsorption is no identifiable. Adsorption isotherm of type III is unusual.

Adsorption isotherm of type IV is obtained for mesoporous adsorbents (20 < d_p < 50 Å) basically many oxide gels, industrial adsorbents and mesoporous molecular sieves. Physisorption in mesoporous adsorbents is governed by adsorbent-adsorbate interactions and the interactions between adsorptive molecules in the condensed state. The shape of this adsorption isotherm, especially the area of monolayer-multilayer adsorption, looks like a type II. Beyond this area, the pore condensation occurs followed by a saturation plateau which can be also an inflexion point.

The pore condensation occurs in the pore network when gas condenses to a liquid-like phase for a relative pressure near to saturation pressure of the bulk liquid. Types IV(a) and IV(b) are distinguished by the presence of hysteresis loop for type IV(a) which matches to filling mesopores 'adsorption branch (right)' and their emptying 'desorption branch (left)'. Both width and shape of mesopores governs the hysteresis loop. Adsorption isotherm of type IV(a) is more common and its shape of hysteresis loop depends on gas-solid system studied. Adsorption isotherm of type IV(b) is reversible and an example is the mesoporous oxide MCM-41 having a hexagonal pore arrangement [8] .

The shape of type V adsorption isotherms is near to a type III and illustrates weak adsorbent-adsorbate interactions. A hysteresis loop is found for high relative pressures and matches with the filling and emptying of pores. This kind of adsorption isotherms can be found for hydrophobic microporous and mesoporous adsorbents.

The type VI or stepwise isotherm is associated to an adsorption layer-by-layer on highly uniform nonporous surface.

However, this classification is idealized because experimentally a combination of different types of adsorption isotherms is often observed. During this project, the porous materials studied are microporous and present usually adsorption isotherms of type I.

D. Thermodynamic aspect of adsorption

Adsorption isotherms provide adsorbent capacities for gas separation or storage applications while adsorption enthalpies characterize adsorbent surface to highlight adsorbent-adsorbate interactions [1] or deformation of an adsorbent under pressure [6]. In addition, the knowledge of adsorption enthalpy is an important factor to the development of industrial process. Indeed, a high adsorption enthalpy suggests strong adsorbent-adsorbate interactions which can involve any difficulties for regeneration steps. There are two most common methods to determine adsorption energies: the isosteric method based on the calculation of isosteric heats of adsorption using the Clausius-Clapeyron equation and the direct measure of adsorption enthalpies by means of microcalorimeter.

1. Isosteric method

The isosteric heats of adsorption are determined from the measure of adsorption isotherms obtained at various temperatures using the Clausius-Clapeyron following equation:

$$\Delta \dot{h}_{ads} = -\frac{RT_1T_2}{T_1-T_2} ln \frac{p_2}{p_1} \quad (2.15)$$

The isosteric heat of adsorption is calculated for each values of excess surface amount to equilibrium pressures and temperatures matching to (p_1, p_2, T_1, T_2).

However, this method presents any disadvantages such as:

- Adsorption process should be reversible
- Adsorption isotherms should be measured in small temperature intervals (5-10K) to maintain the same adsorption mechanisms. Nevertheless, using small temperature intervals can contribute to increase experimental errors.
- The isosteric method is sensitive to errors related to the measure of equilibrium pressures. Therefore, equilibrium pressures should be measured with high accuracy, especially at low pressures.

In order to overcome the limitations of isosteric method as well as to carry out many adsorption experiments, the adsorption enthalpies were measured directly by microcalorimetry.

2. Direct measurement of adsorption enthalpy

Micro-calorimeters are the devices the most suited to get the adsorption enthalpies. There are two kinds of procedures which can be used: discontinuous and continuous. In this paragraph, the determination of adsorption enthalpies is explained for the most common method: the discontinuous procedure that was used during this thesis.

The discontinuous procedure assumes that:

- The calorimetric cell containing adsorbent and gas is considered as an open system
- The gas is introduced reversibly into the adsorption system (step by step)
- The amount of gas introduced and the increase of pressure are small enough to be infinitesimal: dn^{σ} and dp

Under these conditions, the differential internal energy is written:

$$dU = dQ_{rev} + dW_{rev} + u_T^g dn \tag{2.16}$$

In the relation 2.16, dQ_{rev} represents the heat reversibly exchanged with the surrounding at the fixed temperature T ; dW_{rev} is the reversible work of the gas in response to external pressure; u_T^g is the molar internal energy of the adsorptive at the constant temperature T; dn is the amount of adsorptive introduced for each step.

The work received by the calorimetric cell can be written:

$$dW_{rev} = RTdn^{\sigma} + Vdp \tag{2.17}$$

In the equation 2.17, V represents the dead volume of the calorimetric cell.

The combination of the equations 2.16 and 2.17 allows to get the expression of the differential enthalpy adsorption:

$$\Delta_{ads}\dot{h} = \left(\frac{dQ_{rev}}{dn^{\sigma}}\right)_{T,A} + V_c\left(\frac{dp}{dn^{\sigma}}\right)_{T,A} \tag{2.18}$$

The terms of the equation 2.18 represent:

- dQ_{rev}, is the heat measured by the calorimeter which is reversibly exchanged with outside at the temperature T.
- dn^{σ}, is the amount adsorbed.
- dp, is the increase in equilibrium pressure.
- V_c, is the dead volume of the cell immersed in the heat-flowmeter of the microcalorimeter. The term $V_c dp$ can be determined by means of inert gas adsorption, usually helium.

Experimentally, gas doses introduced (basically reversible) are not quite small to consider them infinitesimal and to calculate a differential adsorption enthalpy. Thus, 'pseudo-differential' enthalpy of adsorption are obtained.

3. Thermodynamic profile of pore filling

Micro-calorimetric experiments allow plotting the adsorption enthalpy as function of gas amount adsorbed or surface coverage. The curves of adsorption enthalpy result of three types of interactions [9]: specific, non-specific as well as lateral interactions. When each type of interactions is considered separately, one can define:

- Surface energetically heterogeneous: it can be induced by pore size distribution and/or surface chemistry (presence of defects in crystalline structure, cations…). Firstly, adsorbate molecules occupy specific adsorption sites of high energy. At zero (extrapolation) or low coverage, this led to strong differential adsorption enthalpy. At highest coverage, adsorbate molecules occupy less specific adsorption sites of lower energy and the differential adsorption enthalpy decreases gradually.
- Surface energetically homogeneous: the energies of adsorption sites are closed to each other. This implies adsorption enthalpy relatively constant.
- Lateral interactions: they contribute to increase differential adsorption enthalpy at high surface coverage.

Experimentally, each interaction contributes to the curves of adsorption enthalpy which can be distinguished as function of surface: heterogeneous or homogeneous with respect to nature of adsorptive (Figure 2.7)

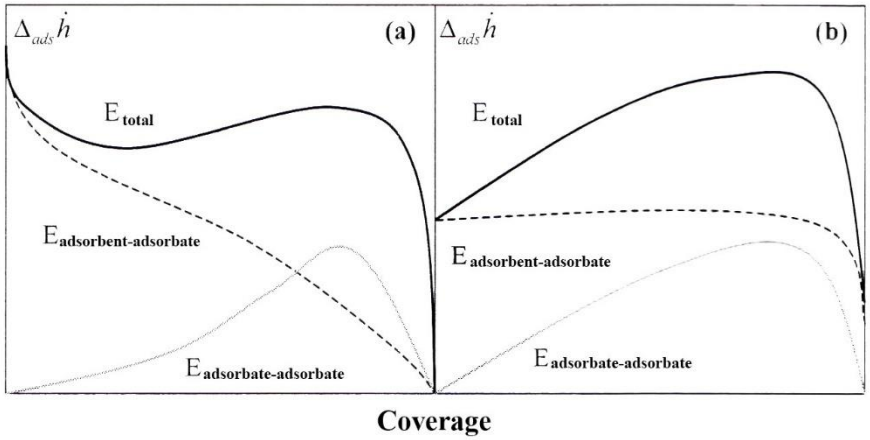

Figure 2.7 - Schematic representation of adsorption enthalpy respectively for a heterogeneous (a) and homogeneous (b) surface as function of coverage

In the case of heterogeneous surface, the decrease of adsorption enthalpy with pore filling can be compensated by the increase of lateral interactions. While, for a homogeneous surface the increase of adsorption enthalpy as function of coverage can be attributed to the gradual increase of lateral interactions between adsorbed molecules.

The extrapolation of adsorption enthalpy at zero coverage (i.e, at the y-intercept) allows quantifying the strength of adsorption sites on which gas molecules are first adsorbed. Usually adsorption enthalpies are near or slightly higher than these of gas liquefaction, except for microporous adsorbents where they are significantly higher. One can suppose that adsorbents having small pore size (< 20 Å) contribute to increase adsorption enthalpy by means of higher confinement effect.

Experimentally, the difference of adsorption enthalpy between a 'polar' molecule (CO_2, moment quadrupolar) and an 'apolar' molecule (CH_4) gives an information on the adsorbent surface polarizability.

E. Experimental techniques

This part is devoted to the different experimental techniques used to get adsorption data based on manometry method. Prior to gas adsorption, a preliminary analysis consists of the determination of activation temperature to remove physisorbed molecules and avoid adsorbent degradation before gas adsorption experiments. Adsorption data were determined below atmospheric pressure, especially for nitrogen gas adsorption at 77K using a commercial device. While, adsorption data for pressures above atmospheric pressure were obtained for CO_2, N_2 and CH_4 at 303K using a home-made device. Simultaneously, adsorption enthalpies were determined thanks to a Tian-Calvet microcalorimeter coupled with a manometry system.

1. Thermogravimetric analysis (TGA)

Thermogravimetric analysis (TGA) is a thermal analysis method to measure mass change when the material is exposed to a temperature ramp under a controlled atmosphere. Thermogravimetric analyzer used is the 'TGA Q500' from TA instruments.

The thermogravimetric analyzer 'TGA Q500' is constituted of various pieces:

- A sample holder that allows to analyze 16 samples one by one. For analyze, the sample is contained into platinum crucible due to the chemical inertness of platinum and its ease to be clean.
- A vertical thermobalance highly sensitive (0,1 µg) that is able to contain a sample maximum amount of 1g with an uncertainty on initial mass around 0,01%. In practice for analyze, a low sample amount is needed around 10-25 mg.
- A vertical furnace that works in a temperature range from 25 up to 1000°C.

During thermal analysis, the sample contained in platinum crucible is introduced in suspension into furnace. A sweep or purge gas (Ar, He, N_2, Air…) passes horizontally through the sample into vertical thermobalance/ furnace system. The use of sweep gas aims to remove physisorbed weakly molecules at the surface and those from heating which were trapped in the porosity of the adsorbent in order to prevent their re-adsorption. Usually, it is an inert gas to avoid the formation of oxidant species in the controlled atmosphere because they can react with the adsorbent. Purge gas is directly in contact with the sample that reduces buoyancy effects. Thermocouple close to the sample allows to measure environment temperature.

Prior to analysis, the tare is performed. Among modes included in this device, the ramp mode was chosen (5°C/ min up to 700°C) under inert gas (argon) to study thermal behavior. Prior to the ramp temperature, the first stage is an isotherm step for 30 minutes at room temperature to eliminate physisorbed weakly molecules (water, solvent, by-products from synthesis) at the surface of the adsorbent.

An example of thermogravimetric curve as well as its derivative obtained on the microporous MIL-96(Al) MOF with the 'TGA-Q500' is provided in Figure 2.8.

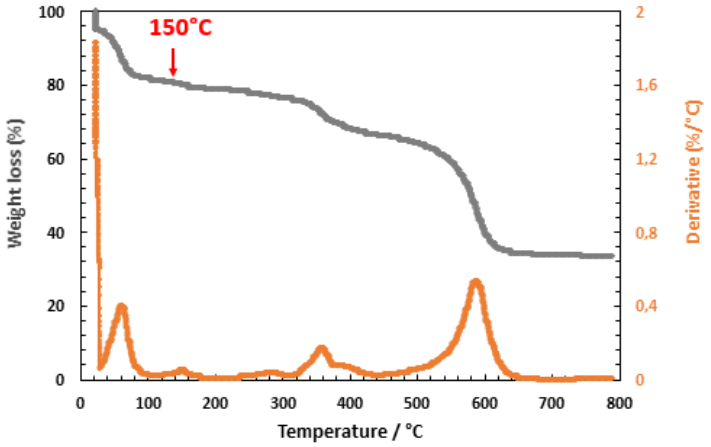

Figure 2.8 – Representation of thermogravimetric curve (grey) for the MIL-96(Al) microporous MOF plotting weight loss as function of temperature and its derivative (orange)

Up to 150°C, there is a weight loss approximatively of 20% which can be attributed to the release of molecules weakly physisorbed on the surface (i.e, impurity, water). For a range temperature of 150°C until 300°C, the weight loss seems to achieve stabilization before the adsorbent degradation marked by a collapse of weight loss. Thus, it allows to fixing the activation temperature at 150°C for which physisorbed molecules are removed not blocking the porosity for gas adsorption without any adsorbent degradations.

2. Gas adsorption up to 1 bar: Nitrogen at 77K

Gas adsorption experiments up to 1 bar were carried out using a full automatic gas adsorption-desorption device, the BELSORP-max, from BEL Japan. Adsorption isotherms are obtained in the range of relative pressure from $p/p^0 = 10^{-8}$ to 0.997.

Samples pre-treatment are performed by means of turbo molecular pump (TMP) and a furnace for which maximum vacuum value and temperature range are respectively of $6.7.10^{-7}$ Pa and 50-550°C with a stability of ± 0.5°C. The pre-treatment time is basically fixed to 900 minutes.

The BELSORP-max can treat three samples simultaneously having similar pre-treatment conditions. The volume of a measuring cell is approximatively 1.8 cm^3. However, one measuring cell is the reference cell (empty) to get the dead volume. Prior to each gas adsorption, the dead volume was assessed using helium as probe molecule. The BELSORP-max apparatus allows to use various non-corrosive gas adsorptive as N_2, Ar, CO_2, H_2, etc. or vapor adsorptive as H_2O, MeOH, etc. After gas adsorption-desorption experiments, sample cells should be weighed to overcome the possibility that some adsorptive molecules are blocked in the porosity.

During this thesis, the BELSORP-max was used to perform mainly nitrogen gas adsorption at the nitrogen liquefaction temperature, 77K, or water adsorption at 25°C. In both cases, the sample masses introduced in measuring cells were approximatively 60 mg. The software allows getting nitrogen and water adsorption isotherms as well as textural parameters as the specific surface area, the external surface (t-method), the pore volume.

An example of nitrogen adsorption isotherm obtained from for the microporous MIL-96(Al) MOF is provided in Figure 2.9:

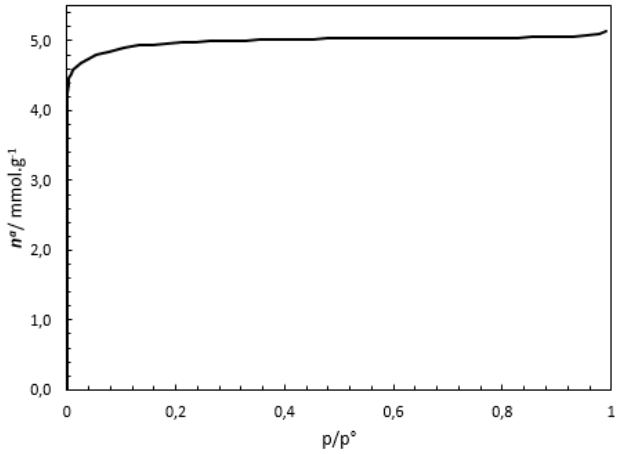

Figure 2.9 – Nitrogen gas adsorption isotherm at 77K for the MIL-96(Al) microporous MOF plotting amount adsorbed as function of relative pressure

Figure 2.9 suggests a type I isotherm from IUPAC classification highlighting the microporous character of the MIL-96(Al).

3. Gas adsorption above 1 bar at 303K

a) High-throughput system

In order to get quickly adsorption isotherms at high pressures (i.e, maximum pressure of 40 bar) and to assess CO_2 adsorption capacities of adsorbent batches, a home-made manometry apparatus was used [10]. The schematic diagram of the apparatus is provided in Figure 2.10.

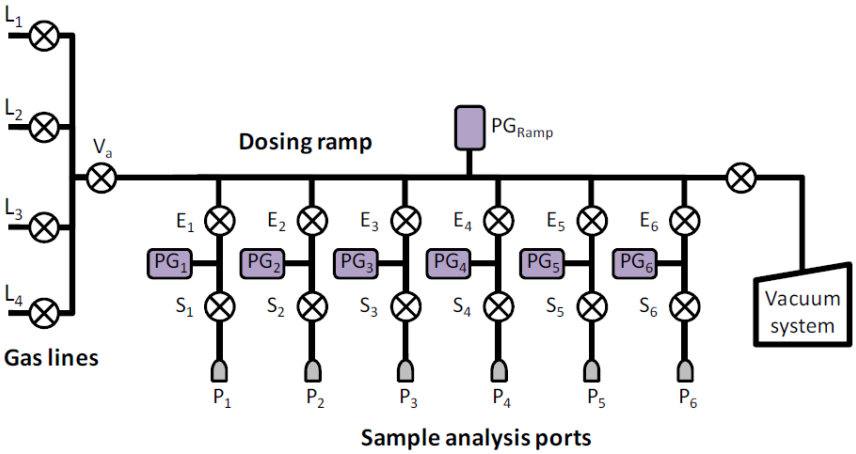

Figure 2.10 – Schematic representation of high-throughput adsorption apparatus [4]

This apparatus is composed of four gas lines, six measuring cells as well as a vacuum system involving a rapid screening of six samples in parallel.

The sample mass introduced in a measuring cell is around 80 mg depending on the sample density. This apparatus was designed to be able to carry on reliable measurements on an adsorbent mass limit that does not exceed 100 mg. In order to increase the accuracy of manometric measurements, the ratio amount of gas adsorbed to amount of gas in the system should be maximized. This can be done

by increasing the adsorbent amount, nevertheless for this apparatus the aim is to use the smallest adsorbent amount as possible. Instead of the gas amount was reduced by minimizing the dead-space volumes in the system, including the size of the reference volumes and sample cells. The volume of measuring cells is approximatively 5-6 cm^3.

Prior to each gas adsorption experiments, samples are activated thanks to heating muffle for which the activation temperature is fixed individually by means of an electronic unit. Samples are generally activated for 16 hours under a primary vacuum. After the activation step, each measuring sample cell is placed in individual sand baths connected to a liquid thermostat maintaining the temperature at 30°C. The thermostat used is a Julabo F25 ME where the temperature range extends from -15 to 200°C (± 0.01 °C). Add to that, the overall system is placed into a cage thermally regulated at 30°C.

During adsorption experiments, the gas is transmitted from gas bottle to the ramp by means of pneumovalves. For each samples, a gas dose is introduced into the reference volume which is defined as the volume between E_i and S_i valves. When the pressure is stabilized into the reference volume (controlled by a pressure gauge (PG_i)), the sample valve (S_i) is opened allowing the gas expansion and the contact with adsorbent until equilibrium occurs. The equilibrium time into the reference volume is fixed to 15 minutes while in the sample volume this depends on the adsorptive nature (i.e, CO_2 = 60 minutes, N_2 and CH_4 = 40 minutes, He (calibration) = 30 minutes). After gas adsorption, the gas is exhausted from measuring sample cells by means of valves, however, the vacuum system constituted of a primary vacuum can be used. The amounts adsorbed were calculated using an equation state [4].

With this home-made apparatus several gas adsorption cycles can be performed to assess the regeneration of each sample under mild conditions. Indeed, between each gas adsorption cycle there is a step under a primary vacuum at 30°C for 1 hour.

This home-made apparatus is very useful :

- To get rapidly adsorption isotherms at high pressures at 30°C as well as the samples adsorption capacities.
- To assess the adsorbent regeneration under mild conditions (i.e, for 1 hour at 30°C under a primary vacuum).

b) Adsorption manometry device coupled with a Tian-Calvet microcalorimeter

The apparatus used is a manometry system coupled with a Tian-Calvet type microcalorimeter, the experimental scheme is given in Figure 2.11.

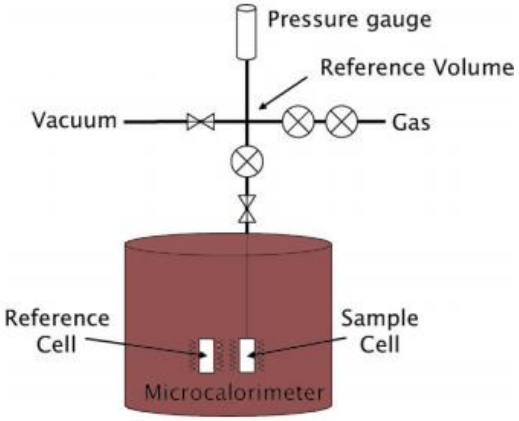

Figure 2.11 – Home-made device consisting of a manometry device coupled with a Tian-Calvet microcalorimeter

Prior to gas adsorption experiments, adsorbent included into calorimetric cell is activated ex-situ under a secondary vacuum.

The Tian-Calvet microcalorimeter is constituted by two thermopiles mounted in electrical opposition. Each thermopile possesses around 500 chromel-alumel thermocouples. Temperature of the system is controlled and can be fixed in the temperature range of 25 up to 150°C. In this work, the adsorption capacities as well as the adsorption enthalpies were measured at a temperature fixed at 30°C. Manometry system withstands to pressures up to 100 bar, however adsorption isotherms can be achieve up to 50 bar owing to the limit of pressure gauge. The gas introduction in the system is done point by point. In practice, the gas is introduced by means of pneumovalves into the reference volume. Usually, the equilibrium time into the reference volume is fixed to 15 minutes. When pressure is stabilized into the reference volume, a pneumovalve is opened allowing the contact between the gas and the adsorbent until the equilibrium is reached. Usually, equilibrium time was fixed at 90 mins for CO_2, N_2 or CH_4, however a longer equilibrium time can be setup when diffusion occurs in adsorbent.

4. Adsorptive features

The properties of various adsorptives used are summarized in table below.

Adsorptive	Nitrogen N_2	Carbon dioxide CO_2	Methane CH_4
Molecular weight/ $g.mol^{-1}$	28.01	44.01	16.04
Kinetic diameter/ nm	0.364	0.330	0.380
Polarisability $\alpha/ 10^{-3}.nm^3$	1.74	2.91	2.59
Quadrupolar moment $Q/ 10^{-40} C.m^2$	-5.0	-14.0	-
$-\Delta_{vap}H/$ $kJ.mol^{-1}$	5.57	17.2	8.19

Table 2.1 – Properties of adsorptives [11]

F. Derived data from adsorption isotherm

From nitrogen gas adsorption isotherm at 77K below atmospheric pressure, some textural parameters can be determined: specific surface area and pore volume. While for pressures higher than 1 bar, adsorption capacity as well as adsorption enthalpy can be obtained which are key parameters to select adsorbent for a given gas separation. From single-gas adsorption isotherms, the selectivity of adsorbent can be predicted based on IAST model.

1. Determination of specific surface area with Brunauer, Emett and Teller (BET) method

The assessment of specific surface area of an adsorbent uses widely the BET equation for which the model has been proposed in 1938 by Brunauer, Emett and Teller [12].

The model proposed by Brunauer, Emett and Teller stipulates that there is the growth of supplementary layers after the formation of a statistical monolayer. The monolayer is considered as adsorption sites for the next layers formed. As for the Langmuir theory, Brunauer, Emett and Teller assume that there is one kind of adsorption sites as well as no lateral interactions between adsorbed layers. However, they added one assumption which is that the second and others layers have the same characteristics as the bulk fluid phase. Therefore, they consider that the adsorption energy of monolayer is different from second and next layers which are equal to the liquefaction enthalpy.

From these assumptions, they have established a relation linking the amount adsorbed and relative pressures p/p^0.

$$\frac{1}{n^a(1-p/p^0)} = \frac{1}{n_m^a C} + \left[\frac{C-1}{n_m^a C}\right](p/p^0) \tag{2.19}$$

The terms of equation 2.19 are:

- n^a, the amount adsorbed
- p/p^0, the relative pressure
- n_m^a, the adsorbate amount needed to cover entirely the adsorbent surface to form a monolayer
- C, the constant that takes into account the adsorption molar energy of monolayer(E_1) as well as liquefaction energy (E_l) of adsorbate at the adsorption temperature fixed and R the constant of ideal gas. C takes the expression:

$$C \sim exp\left[\frac{E_1 - E_l}{RT}\right] \tag{2.20}$$

From equation 2.19 which is the transformed BET equation, the parameters n_m^a and C are obtained by plotting $\frac{1}{n^a(1-p/p^0)}$ as function of (p/p^0). The knowledge of monolayer capacity,n_m^a, allows to get the specific surface area of a solid from the following relation:

$$a_{BET} = \left[\frac{n_m^a}{m^s}\right].N_A.\sigma_m \tag{2.21}$$

The terms of equation 2.21 represent:

- a_{BET}, specific surface area, m²/g
- m^s, mass of adsorbent solid, g
- n_m^a, monolayer capacity/mol
- N_A, the Avogadro constant (= 6,023.10^{23} mol^{-1})
- σ_m, average area occupied by each molecule adsorbed at the adsorbent surface into the monolayer/m^2

The BET equation is applied for a range of relative pressures p/p^0 from 0.05 up to 0.35 which matches to the linear region of the BET plot. It is in this region that the BET equation is verified and usually applicable for non-porous and mesoporous adsorbents. For microporous solids, the BET equation is often applied for lower relative pressures, $p/p^0 < 0.05$. The relative pressures range is reduced due to limited linearity of the BET plots. This assumes that a monolayer is formed inside micropores as flat surface. In the particular case of microporous adsorbents, the specific surface area can be over- or under-estimated owing to the presence of ultra- or super-micropores. The ultra-micropores are defined as the ratio w/d below 3 while for super-micropores this ratio is above 3, where w represents the opening of pore and d the diameter of the probe molecule. Therefore, the term 'equivalent BET surface area' is basically used for microporous material [1], [13].

The specific surface area determination using the BET method can be validated through the calculation of three criteria [13]. Firstly, the value of C parameter should be positive. A negative value indicates that the BET equation is not applied in the good range of relative pressures. Secondly, the term $n^a(1 - p/p^0)$ should increase gradually with p/p^0 in the pressure range chosen for the BET equation application. Last the value of relative pressure p/p^0, whose the expression is $1/\sqrt{C}$ +1, which matches to n_m^a, should be included in the calculation range of BET equation.

2. Determination of external surface area and pore volume

The external surface area of a solid, $a(t)$, is defined as the surface outside the pores (i.e, non-microporous surface) as well as pores large enough to allow the adsorbed multilayer formation. The external surface area determined for non-porous and mesoporous materials coincides with this calculated from BET equation. In the case of microporous adsorbents the difference between the equivalent BET surface area and the external surface area gives assess to the microporosity.

To assess the external surface area of an adsorbent, the t-[8] and α_s- [14]methods can be used. In this work, the t-method was used and is detailed below.

The t-method has been proposed by de Boer and is based on the comparison of the thickness of adsorbed layer of the adsorbent studied against this of a non-porous solid taken as reference, for each relative pressures [15].

In this method, the thickness 't ' of adsorbed multilayer is calculated from the number N of adsorbed layers and the thickness 'e' of one layer, for each value of relative pressures.

$$t = N.e \tag{2.22}$$

De Boer assumes that the adsorbed layer is in liquid state and each molecular layer has the same thickness:

$$e = (M/\rho_l)/(N_A.\sigma) \tag{2.23}$$

The number 'N' of adsorbed layer is given by: $N = n^a/n_m^a$

Therefore in the case of nitrogen adsorption at 77K, the thickness of a monomolecular layer is of 0.354 nm. The parameters used are M = 28 g.mol^{-1}, ρ_l = 0,809 g.cm^3 and σ = 0,162 nm² [13].

Thanks to the knowledge of the number ($= n^a/n_m^a$) of monomolecular layers, the expression of the thickness becomes:

$$t/nm = 0{,}354(n^a/n_m^a) \tag{2.24}$$

From adsorption isotherms obtained on non-porous adsorbent, the thickness 't' can be plotted as function of relative pressure p/p^0. From nitrogen adsorption at 77K performed on non-porous oxides, De Boer evidenced that the plots $f(t) = p/p^0$ are similar suggesting a 'universal' plot.

Some relations have been established to fit this universal plot and the most widely used is the one proposed by Harkins and Jura [16]:

$$\frac{t}{nm} = \left(\frac{0{,}1399}{0{,}034 - log\left(\frac{p}{p^0}\right)}\right)^{0{,}5} \tag{2.25}$$

For a given adsorbent, the t-plot is built by plotting n^a measured as function of t. The slope, S_t, of the t-plot allows to calculate external surface area $a(t)$ with the following equation:

$$a(t) = \frac{M}{\rho^l} * S_t \tag{2.26}$$

When adsorptive is N_2, equation 2.26 becomes:

$$a(t) = 34.6 * S_t \tag{2.27}$$

Typically, the t-plot for a microporous material shows a steep slope at low thicknesses follows by a plateau that suggests an adsorbent saturation. Therefore, the amount adsorbed at this plateau is used to obtain both the external surface area and the micropore volume. In most cases for microporous adsorbents, the t-plot does not intercept the origin, it can be related to the strong adsorbent-adsorbate interactions at low pressures. Usually for microporous adsorbents, the external surface area is negligible and adsorption occurs mainly in micropores (i.e, pores filling). Thus, the difference between BET and external surface area can be attributed to the area of the micropores.

3. Determination of Henry's constant

For low enough pressures, the amounts adsorbed are small and governed by interactions between superficial atoms at the adsorbent surface and adsorbate molecules. In this region, the surface excess amount increases linearly with pressure and then Henry's law can be applied:

$$n^\sigma = k_H p \tag{2.28}$$

In equation 2.28, n^σ is the surface excess amount obtained from adsorption isotherms, p is the equilibrium pressure and k_H the Henry's constant [1].

Therefore, the determination of Henry's law constant allows assessing the affinity of adsorbent-adsorbate system.

In practice, for a given solid material the Henry's law constant is obtained by plotting $ln(n^\sigma/p)$ as function of n^σ:

$$k_H = \lim_{p \to 0}\left(\frac{n^{\sigma}}{p}\right) \tag{2.29}$$

4. Determination of Working Capacity (WC)

The working capacity (WC) is determined from single gas adsorption isotherms and an example is provided in Figure 2.12 for two gases. The working capacity represents the difference of amounts adsorbed between two pressures, an upper and a lower ones. These pressures are fixed with respect to pressure conditions of process. For example for conditions near to post-combustion we fixed the upper and lower pressures respectively at 0.15-0.2 and 0 bar against 15 and 1 bar for conditions close to pre-combustion.

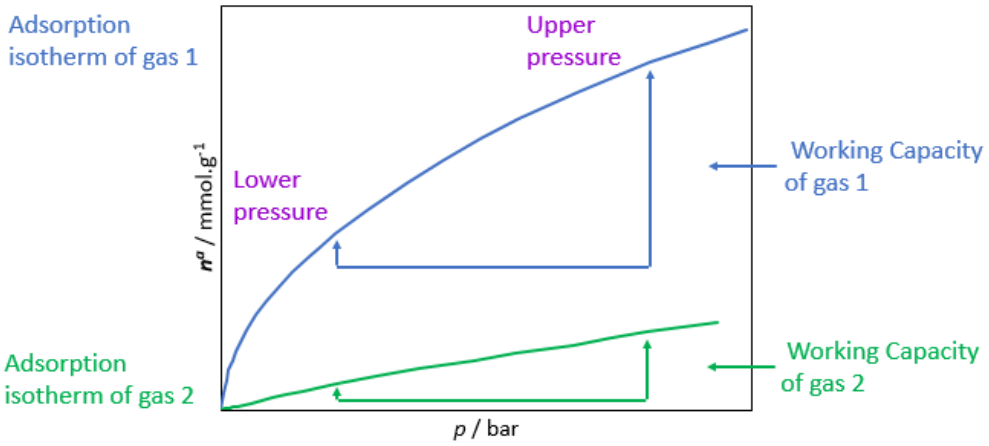

Figure 2.12 – Adsorption isotherms of gas 1 (blue) and gas 2 (green) plotting amount adsorbed against pressure

The unit of working capacity is expressed in $cm^3.cm^{-3}$ to be in agreement with those used in industrial processes. For this, crystallographic density ($g.cm^{-3}$) of an adsorbent determined experimentally or from literature is used to calculate the working capacity.

5. Determination of adsorption enthalpy

The experimental measurements of adsorption enthalpy were performed via a manometry device coupled with a Tian-Calvet microcalorimeter (section E.3.b). Adsorption is an exothermic process in which each gas doses adsorbed leads to an exothermic effect. Thus, during adsorption experiments the heat flow and pressure signals were recorded as function of time. An example of these recorded signals is provided in Figure 2.13.

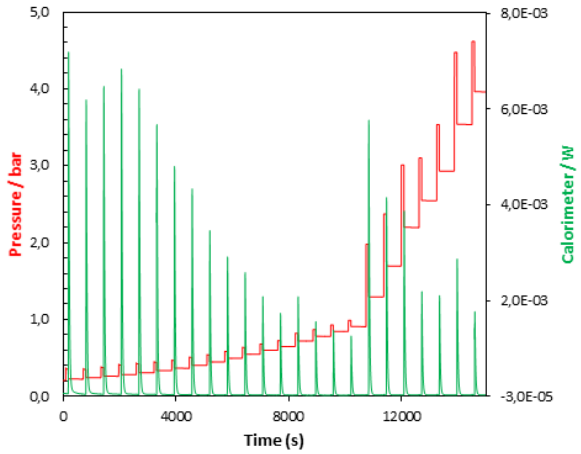

Figure 2.13 –Recorded signals obtained from a microcalorimetry experiment at 303K: pressure (red) and heat flow (green)

Note that, the return of the heat flow to baseline highlights that equilibrium between the gas and the adsorbent is well established. The area under the heat flow curve against time is integrated to get the 'pseudo-differential' adsorption enthalpy for each gas doses.

6. Determination of selectivity

A high CO_2 selectivity over other components of the gas mixture is an essential factor for CO_2 capture applications. For gas separation processes, the selectivity assessment is used as an indicator of separation ability of porous materials. For a given pressure, the expression of selectivity (α) between two species 1 and 2 is:

$$\alpha_{1/2} = (x_1/x_2)/(y_1/y_2) \tag{2.30}$$

In this equation, x_1 and x_2 are the mole fractions of species 1 and 2 in the adsorbed phase while y_1 and y_2 are the mole fractions in the bulk phase.

The selectivity can originate from two mechanisms: based on size molecules and the difference in affinity of various components present in gas mixture to be adsorbed on pore surface [11]. In practice, it is not easy to measure directly the selectivity of an adsorbent for gas mixtures. Thus, the most common method is to predict the selectivity based on experimental single-gas adsorption although gas molecules competition on adsorption sites is not taken into account.

In this work, the selectivities were calculated using the 'Ideal Adsorbed Solution Theory (IAST)' model developed by Myers and Prausnitz [17]. This model allows to predict co-adsorption isotherms based on the use of only pure gas adsorption data and considers that the equilibrium between the adsorbed phase and gas phase is similar to this between a liquid solution and a vapour phase. The IAST model has been already used to study gas mixtures related to post-combustion [18]–[20] and pre-combustion [21], [22] for CO_2 capture. Some works highlighted that the IAST model can be applied to flexible MOFs as [Cu(dhbc)2(4,4'-bipy)] for hydrocarbons mixture [23], Cu-MOF equally for hydrocarbons mixture [24] or for the MIL-53(Al) for CO_2/CH_4 mixture [25].

However to apply IAST model, the pure adsorption isotherms are fitted with empirical models: Freundlich equation, Langmuir-Freundlich equation, Toth equation, Langmuir Multisite equation [26], Jensen-Seaton equation [27]. Potential empirical models used in this work are described below.

a) Freundlich equation

One of the first empirical equations has been proposed by Freundlich in 1926 and takes the following form [1]:

$$n_{ads} = K_H(T)P^{1/t} \quad (2.31)$$

K_H and t are constant parameters which are temperature dependent. In the Freundlich equation, the t parameter takes into account the non-ideality. When $t = 1$, this reduces the Freundlich equation to the Henry's law equation. However, in most cases t is higher than 1 and there is an isotherm deviation from linearity.

Usually, the Freundlich equation is used to describe organics adsorption on activated carbons from aqueous streams[28], [29]. Nevertheless, this can be applied to gas adsorption systems in small pressure ranges. Indeed, at low pressures it does not match with Henry's law under dilute conditions while at high pressures there is not limit values of amount adsorbed as function of pressure.

b) Langmuir-Freundlich equation

The Sips equation (1948) is the combination of the Freundlich and Langmuir equations in order to improve the fit of adsorption isotherms at high pressures [30]. The expression of Sips equation is:

$$n_{ads} = n_{ads}^{m} \frac{(bp)^{1/t}}{1+(bp)^{1/t}} \quad (2.32)$$

In this equation, the term n_{ads}^{m}, represents the limiting adsorption capacity.

c) Toth equation

The Toth equation is a popular empirical equation (1971), initially proposed for monolayer adsorption (1962), which has the advantage to satisfy the limits for both low and high pressure ranges. The Toth equation expression is:

$$n_{ads} = n_{ads}^{m} \frac{bP}{(1+(bp)^{t})^{\frac{1}{t}}} \quad (2.33)$$

In this expression, the t parameter describes the system heterogeneity as for the Langmuir-Freundlich equation. Nevertheless, when t = 1, the Toth equation is reduced to the Langmuir equation.

The Toth equation describes accurately many adsorbate/ adsorbent systems and is widely used to fit experimental adsorption isotherms.

d) Jensen-Seaton equation

Both the Langmuir and Toth equations deals with two conditions to have a thermodynamic and experimental consistency of adsorption isotherm models: in the low pressure range, the models should be reduced to the Henry's equation while for higher pressure range, finite values of the amount adsorbed should be reached with respect to adsorbent saturation capacity highlighting the compressibility of adsorbate.

The expression of the Jensen-Seaton equation is:

$$n^{a} = K_H P \left[1 + \left({K_H P}/{a(1+\kappa P)}\right)^{t}\right]^{-1/t} \quad (2.34)$$

In this equation, K_H represents the Henry's constant and κ refers to the compressibility of adsorbate. The Jensen-Seaton takes the form of the Toth equation when κ = 1 and if t = 1 this becomes the empirical Langmuir equation. Usually, the Jensen-Seaton equation provides good fit for microporous adsorbents up to high pressure.

e) Langmuir Multisite equation

Amongst the variety of empirical model, the Langmuir equation is the simplest [4]. However in many cases, the fit of experimental adsorption isotherm is not optimal. An approach was to consider the experimental adsorption isotherm as the sum of several Langmuir-type isotherms having various monolayer capacities and affinities. Thus, it is envisaged that the adsorbent possesses several distinct types of homogeneous adsorption where Langmuir equation is applied to each. The expression of Langmuir multisite equation is:

$$n_{ads} = \sum_i n_{ads,i}^m \frac{b_i P}{1+b_i P} \tag{2.35}$$

In this relation, i represents the number of different types of adsorption sites, usually this does not exceed three. In the literature, both dual-site (i =2) and triple-site (i =3) are commonly used to fit accurately gas adsorption isotherm on zeolites and MOFs at room temperature[31], [32].

7. Determination of an Adsorbent Performance Indicator (API)

Owing to industrial processes as for gas separation applications, the development of new porous materials grows as: MOFs, ZIFs, in addition to the improvement of traditional adsorbents as activated carbons, zeolites and organo-silicas. These materials have a large variety of features such as pore size, specific surface area and surface chemistry involving various isotherm shapes, adsorption capacities, adsorption enthalpies and selectivities. Thus, it can be difficult to compare these adsorbents for a given application. The ideal adsorbent deals with a high selectivity, a high adsorption capacity and a low adsorption enthalpy. Therefore, an indicator of adsorbent performance was defined including these parameters [33].

The aim of the 'Adsorbent Performance Indicator (API)' is to propose a parameter allowing an easy comparison of adsorbents as well as the identification of the most promising materials for a given separation. The API takes into account three parameters which are:

- The selectivity: this is the most important parameter because if porous materials are non-selective, the separation will not be possible
- The working capacity: this determines the size of unit separation and the cost of the installation. However this is dependent on the adsorbent volume, consequently, it is more suitable to compare volumetric adsorption capacity of the adsorbents. To achieve volumetric uptakes, the crystallographic density can be used
- The adsorption enthalpy: as the adsorption is an exothermic process, the knowledge of adsorption enthalpy gives an information about the heat required for adsorbent regeneration

The expression of the adsorbent performance indicator is:

$$API = \frac{(\alpha_{12}-1)^A * wc_1^B}{\left|\Delta H_{ads,1}\right|^C} \tag{2.36}$$

In the equation 2.36, α_{12}, WC_1, $\Delta H_{ads,1}$, represent respectively the selectivity, the working capacity and the adsorption enthalpy directly measured. While, A, B, C are exponents related to the nature of process.

Summary

Firstly, this chapter defined adsorption phenomenon at the microscopic (i.e, intermolecular potential function) and macroscopic levels (i.e, Gibbs Dividing Surface). The adsorption is a surface phenomenon which occurs when a gas or a liquid is at the vicinity of a solid surface. During adsorption, interactions of low energy can be involved as Van der Waals-type forces.

Experimentally, home-made and commercial apparatus were used to get adsorption isotherms below atmospheric pressure and for higher pressures. From adsorption isotherms obtained below atmospheric pressure, usually N_2 adsorption at 77K, textural parameters as BET surface area and pore volume were calculated. While from adsorption isotherms obtained above atmospheric pressure, data like adsorbents adsorption capacities, working capacities were determined as well as initial or average adsorption enthalpies. The knowledge of adsorption enthalpy is an essential parameter for CO_2 capture to assess ability of the adsorbent regeneration.

The prediction of selectivities can be carried out using experimental single gas adsorption isotherms and IAST model, they may be compared to those obtained from type 'Grand Canonical Monte Carlo' modeling methods. The selectivity is a crucial factor for CO_2 gas separation applications which can be governed by various mechanisms as: pore size involving molecular sieve effect, the affinity of components with the surface and chemical interactions related to the adsorbent functionalization. For microporous adsorbents, one can suppose that there is a combination of molecular sieve effect as function of pore size as well as a high confinement effect owing to small pore size (chapter 3).

References

[1] J. Rouquerol, F. Rouquerol, P. Llewellyn, G. Maurin, et K. S. W. Sing, *Adsorption by Powders and Porous Solids: Principles, Methodology and Applications*. Academic Press, 2013.

[2] D. W. Bruce, D. O'Hare, et R. I. Walton, *Multi Length-Scale Characterisation: Inorganic Materials Series*. John Wiley & Sons, 2013.

[3] H. C. Hamaker, « The London—van der Waals attraction between spherical particles », *Physica*, vol. 4, n° 10, p. 1058-1072, oct. 1937.

[4] A. Wiersum, *Developing a strategy to evaluate the potential of new porous materials for the separation of gases by adsorption*. Aix-Marseille, 2012.

[5] M. Thommes, « Physical Adsorption Characterization of Nanoporous Materials », *Chem. Ing. Tech.*, vol. 82, n° 7, p. 1059-1073, juill. 2010.

[6] « Magnetic Suspension Balances - Rubotherm ». [En ligne]. Disponible sur: http://www.rubotherm.com/magnetic-suspension-balances.html. [Consulté le: 02-nov-2017].

[7] « Physisorption of gases, with special reference to the evaluation of surface area and pore size distribution (IUPAC Technical Report) : Pure and Applied Chemistry », 01-oct-2015. [En ligne]. Disponible sur: https://www.degruyter.com/view/j/pac.2015.87.issue-9-10/pac-2014-1117/pac-2014-1117.xml.

[8] J. S. Beck *et al.*, « A new family of mesoporous molecular sieves prepared with liquid crystal templates », *J. Am. Chem. Soc.*, vol. 114, n° 27, p. 10834-10843, déc. 1992.

[9] P. L. Llewellyn et G. Maurin, « Gas adsorption microcalorimetry and modelling to characterise zeolites and related materials », *Comptes Rendus Chim.*, vol. 8, n° 3, p. 283-302, mars 2005.

[10] A. D. Wiersum *et al.*, « Experimental Screening of Porous Materials for High Pressure Gas Adsorption and Evaluation in Gas Separations: Application to MOFs (MIL-100 and CAU-10) », *ACS Comb. Sci.*, vol. 15, n° 2, p. 111-119, févr. 2013.

[11] K. Sumida *et al.*, « Carbon Dioxide Capture in Metal–Organic Frameworks », *Chem. Rev.*, vol. 112, n° 2, p. 724-781, févr. 2012.

[12] S. Brunauer, P. H. Emmett, et E. Teller, « Adsorption of Gases in Multimolecular Layers », *J. Am. Chem. Soc.*, vol. 60, n° 2, p. 309-319, févr. 1938.

[13] « Texture des matériaux divisés - Aire spécifique des matériaux pulvérulents ou nanoporeux ». [En ligne]. Disponible sur: https://www-techniques-ingenieur-fr.lama.univ-amu.fr/base-documentaire/materiaux-th11/surfaces-et-structures-fonctionnelles-42534210/texture-des-materiaux-divises-p1050/. [Consulté le: 04-août-2017].

[14] D. H. Everett et R. H. Ottewill, *Surface Area Determination: Proceedings of the International Symposium on Surface Area Determination Held at the School of Chemistry, University of Bristol, U.K., 16—18 July, 1969*. Elsevier, 2013.

[15] B. C. Lippens et J. H. de Boer, « Studies on pore systems in catalysts », *J. Catal.*, vol. 4, n° 3, p. 319-323, juin 1965.

[16] W. D. Harkins et G. Jura, « Surfaces of Solids. XII. An Absolute Method for the Determination of the Area of a Finely Divided Crystalline Solid », *J. Am. Chem. Soc.*, vol. 66, n° 8, p. 1362-1366, août 1944.

[17] A. L. Myers et J. M. Prausnitz, « Prediction of the adsorption isotherm by the principle of corresponding states », *Chem. Eng. Sci.*, vol. 20, n° 6, p. 549-556, juin 1965.

[18] J. M. Simmons, H. Wu, W. Zhou, et T. Yildirim, « Carbon capture in metal–organic frameworks—a comparative study », *Energy Environ. Sci.*, vol. 4, n° 6, p. 2177-2185, juin 2011.

[19] Y.-S. Bae, O. K. Farha, J. T. Hupp, et R. Q. Snurr, « Enhancement of CO2/N2 selectivity in a metal-organic framework by cavity modification », *J. Mater. Chem.*, vol. 19, n° 15, p. 2131-2134, mars 2009.

[20] S. Keskin, « High CO2 Selectivity of A Microporous Metal–Imidazolate Framework: A Molecular Simulation Study », *Ind. Eng. Chem. Res.*, vol. 50, n° 13, p. 8230-8236, juill. 2011.

[21] S. Keskin et D. S. Sholl, « Assessment of a Metal−Organic Framework Membrane for Gas Separations Using Atomically Detailed Calculations: CO2, CH4, N2, H2 Mixtures in MOF-5 », *Ind. Eng. Chem. Res.*, vol. 48, n° 2, p. 914-922, janv. 2009.
[22] Y. Liu, D. Liu, Q. Yang, C. Zhong, et J. Mi, « Comparative Study of Separation Performance of COFs and MOFs for CH4/CO2/H2 Mixtures », *Ind. Eng. Chem. Res.*, vol. 49, n° 6, p. 2902-2906, mars 2010.
[23] L. Li, R. Krishna, Y. Wang, J. Yang, X. Wang, et J. Li, « Exploiting the gate opening effect in a flexible MOF for selective adsorption of propyne from C1/C2/C3 hydrocarbons », *J. Mater. Chem. A*, vol. 4, n° 3, p. 751-755, janv. 2016.
[24] T. Hähnel *et al.*, « Adsorptive separation of C2/C3/C4-hydrocarbons on a flexible Cu-MOF: The influence of temperature, chain length and bonding character », *Microporous Mesoporous Mater.*, vol. 224, p. 392-399, avr. 2016.
[25] F.-X. Coudert, C. Mellot-Draznieks, A. H. Fuchs, et A. Boutin, « Prediction of Breathing and Gate-Opening Transitions Upon Binary Mixture Adsorption in Metal−Organic Frameworks », *J. Am. Chem. Soc.*, vol. 131, n° 32, p. 11329-11331, août 2009.
[26] I. Langmuir, « THE ADSORPTION OF GASES ON PLANE SURFACES OF GLASS, MICA AND PLATINUM. », *J. Am. Chem. Soc.*, vol. 40, n° 9, p. 1361-1403, sept. 1918.
[27] C. R. C. Jensen et N. A. Seaton, « An Isotherm Equation for Adsorption to High Pressures in Microporous Adsorbents », *Langmuir*, vol. 12, n° 11, p. 2866-2867, janv. 1996.
[28] D. D. D, *Adsorption Analysis: Equilibria And Kinetics (With Cd Containing Computer Matlab Programs)*. World Scientific, 1998.
[29] D. Kim, Z. Cai, et G. A. Sorial, « Determination of gas phase adsorption isotherms—a simple constant volume method », *Chemosphere*, vol. 64, n° 8, p. 1362-1368, août 2006.
[30] R. Sips, « On the Structure of a Catalyst Surface », *J. Chem. Phys.*, vol. 16, n° 5, p. 490-495, mai 1948.
[31] P. Chowdhury, S. Mekala, F. Dreisbach, et S. Gumma, « Adsorption of CO, CO2 and CH4 on Cu-BTC and MIL-101 metal organic frameworks: Effect of open metal sites and adsorbate polarity », *Microporous Mesoporous Mater.*, vol. 152, n° Supplement C, p. 246-252, avr. 2012.
[32] L. Hamon *et al.*, « Separation of CO2–CH4 mixtures in the mesoporous MIL-100(Cr) MOF: experimental and modelling approaches », *Dalton Trans.*, vol. 41, n° 14, p. 4052-4059, mars 2012.
[33] A. D. Wiersum, J.-S. Chang, C. Serre, et P. L. Llewellyn, « An Adsorbent Performance Indicator as a First Step Evaluation of Novel Sorbents for Gas Separations: Application to Metal–Organic Frameworks », *Langmuir*, vol. 29, n° 10, p. 3301-3309, mars 2013.

Chapter 3 – Complete gas adsorption study of various MOFs

Table of contents

Chapter 3 – Complete gas adsorption study of various MOFs

Metal-Organic Frameworks (MOFs) are three-dimensional (3D) crystalline porous structures built up from metal clusters linked together through organic moieties [1] (see scheme in Figure 1.6, chapter 1). Based on the diversity both of metal clusters and organic linkers, many thousands of MOFs can be synthesized. In recent years, MOFs have received a considerable attention due to their high specific surface area and pore volume that can exceed those of some traditional adsorbents as zeolites used in industrial processes as 'Pressure Swing Adsorption' [2] or activated carbons [3]. For example, both specific surface area and pore volume of MOF-5, a typical MOF that is a crystalline microporous coordination polymer, are higher than those of NaX and Takeda 5A (defined as reference materials in chapter 1). Indeed, specific surface area ($m^2.g^{-1}$) and pore volume ($cm^3.g^{-1}$) are respectively: 2800/1.2 (MOF-5) [4]; 710/0.25 (NaX) and 1180/0.46 (Takeda 5A) [5].

Microporous MOFs can be used for various gas separations (CO_2/N_2; H_2/CO_2; CO_2/CH_4; acetylene/ethylene; xenon/krypton; propylene/propane etc.). They are attractive, especially for CO_2 capture from binary mixtures with, for example, N_2 (flue gas treatment) and CH_4 (natural gas or biogas purification) due to their potential confinement and molecular sieving effects [6].

During this thesis, we received 38 microporous MOFs from different partners of M^4CO_2 project. The preliminary study consisted of analyzing their thermal stabilities and textural properties thanks to thermogravimetric analysis (TGA) and nitrogen gas adsorption at 77K. Thus, textural parameters as: BET surface area, pore volume and external surface area were experimentally determined (listed in Annex A). Following the textural characterization, a screening step of gas adsorption properties (i.e, CO_2, N_2, CH_4) of MOFs was carried out using an home-made high-throughput system detailed in chapter 2 (section E.3)a)) to get quickly adsorption isotherms at 303K. Those analyzes allowed to identify ten MOFs that combine a high thermal stability, a certain degree of porosity as well as interesting CO_2 adsorption properties. Moreover, pore size of some MOFs suggest confinement or/ molecular sieving effects in favor of CO_2 over N_2 and CH_4. Therefore, we performed a study in-depth of gas adsorption properties of those ten MOFs using a manometry system coupled to a Tian-Calvet microcalorimeter (chapter 2, section E.3)b)). With this kind of apparatus, accuracy gas adsorption isotherms and adsorption enthalpies were determined at 303K.

Those ten MOFs can be classified as function of organic linker nature:

- Carboxylate: NH_2-MIL-53(Al), MIL-69(Al), MIL-91(Ti), MIL-96(Al) and $Sc_2(BDC\text{-}NO_2)_3$
- Imidazolate: ZIF-8, ZIF-94, ZIF-93, ZIF-11 and $Zn[2\text{-nIm}]_2$

In this chapter, CO_2 adsorption properties of carboxylate-based MOFs are discussed through five aspects in view of post-combustion application (i.e, CO_2/N_2 gas separation). Note that, CO_2 adsorption properties of imidazolate family are detailed in chapter 4. Those five important aspects to select adsorbents are:

- Working capacity (WC/ $cm^3.cm^{-3}$)
- Adsorption enthalpy at zero coverage ($-\Delta_{ads0}\dot{h}$/ $kJ.mol^{-1}$)
- Selectivity (α)
- Moisture conditions
- An Adsorbent Performance Indicator (API)

A. Working capacity (WC)

The working capacity was defined in chapter 2 (section F.4) as the difference of gas amount adsorbed between two pressures (upper and lower) fixed by the targeted process conditions. In our study, the upper and lower pressures were fixed respectively around 0.15-0.2 and 0 bar, near to post-combustion conditions. The working capacities were calculated in volume unit ($cm^3.cm^{-3}$) by means of MOFs crystallographic densities to be consistent with units used in industrial processes.

CO_2 working capacities around 0.15-0.2 bar at 303K were determined for the ten MOFs selected amongst 38 MOFs of M^4CO_2 project. They were compared to those of MOFs previously studied within the laboratory as well as to reference materials NaX and Takeda 5A (Figure 3.1).

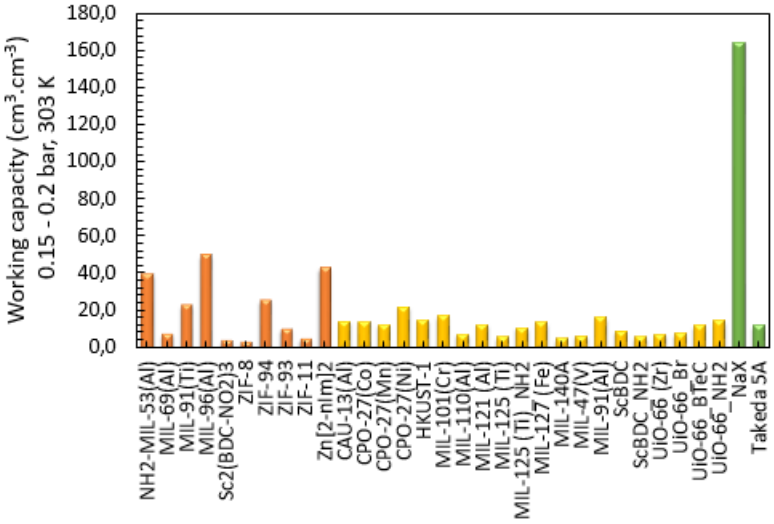

Figure 3.1 – CO_2 working capacities ($cm^3.cm^{-3}$) calculated for a low pressure range (0.15-0.2 bar) at 303K for MOFs of M^4CO_2 project (orange), MOFs previously studied within the laboratory (yellow) as well as NaX and Takeda 5A (green)

The CO_2 working capacities of MOFs are considerably lower than this of NaX that is known to have an excellent CO_2 adsorption capacity especially at low pressures [7]. Nevertheless, CO_2 working capacities of MOFs are equal or outperform this of Takeda 5A. Amongst MOFs of the M^4CO_2 project, the CO_2 working capacities of some of them stand out such as: NH_2-MIL-53(Al) (38.4 $cm^3.cm^{-3}$), MIL-91(Ti) (21.8 $cm^3.cm^{-3}$), MIL-96(Al) (48.8 $cm^3.cm^{-3}$), ZIF-94 (24.8 $cm^3.cm^{-3}$) and Zn[2-nIm]$_2$ (42.5 $cm^3.cm^{-3}$). The CO_2 working capacities that have been reported in literature for some MOFs are equal or higher: MIL-100(Fe) (136.2 $cm^3.cm^{-3}$) [8], MIL-68(Ga) (75 $cm^3.cm^{-3}$) [9], MIL-91(Al) (31.5 $cm^3.cm^{-3}$) [10], STA-12(Ni) (242 $cm^3.cm^{-3}$) [11] for CO_2/N_2 gas separation in the pressure range of 0-1 bar at 303K.

From Figure 3.1, one can observe that the microporous aluminum trimesate MIL-96(Al) stands out with the best CO_2 working capacity in those specific conditions (i.e, 0.15-0.2 bar, at 303K). In the revisited structure of the MIL-96(Al) by Marvin *et al*., they showed that this material possesses some specific adsorption sites that are: aluminum acid sites, hydroxyl groups as well as coordinating water, potentially attractive for quadrupolar CO_2 over N_2 [12]. In literature, some MOFs with specific adsorption sites have already been reported for CO_2 adsorption, typically: HKUST-1 [13], MOF-74 [14] or MIL-100 [15] having 'coordinative unsaturated site' (CUS).

1. CO_2 working capacity versus 'BET' surface area

Adsorption is a surface phenomenon at ambient temperature, thus, the CO_2 working capacities of MOFs calculated in the pressure range 0.15-0.2 bar at 303K were reported against the BET surface area (Figure 3.2) determined from nitrogen gas adsorption at 77K.

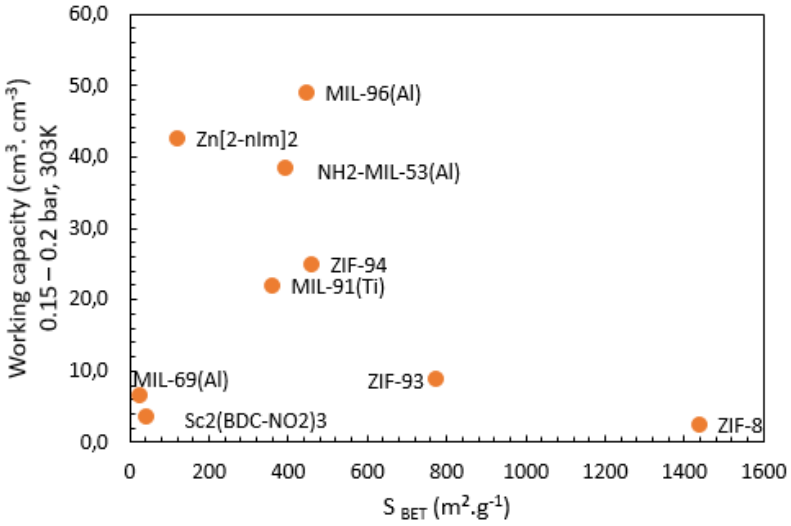

Figure 3.2 – CO_2 working capacities calculated for a low pressure range (i.e, 0.15-0.2 bar) at 303K as function of BET surface area

One can observe that there is no obvious correlation between the CO_2 working capacities in these specific conditions (i.e, 0.15-0.2 bar at 303K) and the BET surface area of the different MOFs studied. However based on the study conducted by Marvin *et al.* on the MIL-96(Al) in which we have contributed (publication and supporting information in Annex B, [12]), the BET surface area can be correlated to crystals size. Indeed, they reported various crystals sizes of the MIL-96(Al) from micrometric down to nanometric scale owing to requirement of pure nanoparticles for MMM application. Amongst various synthesis routes investigated to yield the MIL-96(Al) nanoparticles (experimental section [12]), water reflux conditions were retained for which no nanoparticle aggregation were detected (Figure 5, [12]), while in the work conducted by Knebel *et al.* [16] MIL-96(Al) nanoparticles aggregates were formed using solvothermal synthesis in a mixture of H_2O/DMF solvents. However, the presence of nanoparticle aggregates can affect negatively the working capacity and selectivity of MMM.

During this thesis, I worked on two crystal sizes of the MIL-96(Al): microcrystals of dimensions 20 µm long, 5 µm wide and nanocrystals with diameter of 200 nm ± 30 nm denoted respectively 'MIL-96(Al)-HR' as well as 'MIL-96(Al)-NP2' (Figure 3.3).

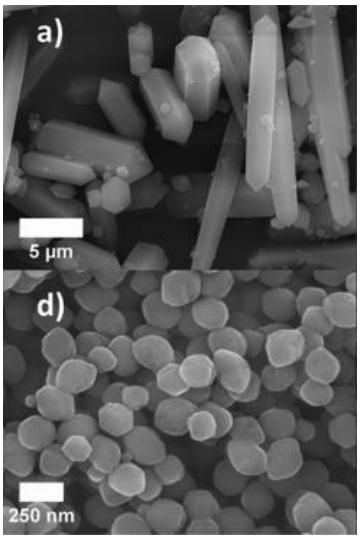

Figure 3.3 – SEM images of the MIL-96(Al) particles: micro ('MIL-96(Al)-HR, top) and nano ('MIL-96(Al)-NP2, bottom) (Figure 1, [12])

When crystal sizes decrease, one can expect an increasing of external surface area of adsorbents. It has been verified for the MIL-96(Al) where the decrease of crystals size led to an increase of external surface area accompanied by an increase of the BET surface area (table 3.1). Note that, external surface areas were estimated via t-plot method.

Lots	BET surface area ($m^2.g^{-1}$)	External surface area ($m^2.g^{-1}$)
MIL-96(Al)-HR	597	6
MIL-96(Al)-NP2	691	40

Table 3.1 – BET surface area and external surface area of the MIL-96(Al) for two crystals sizes (i.e, micro and nano) deduced from nitrogen gas adsorption at 77K

In addition, the trend is confirmed by the external surface area estimated to 100 $m^2.g^{-1}$ for third batch of the MIL-96(Al) nanocrystals (i.e, denoted MIL-96(Al)-NP3) with an average diameter of 70 nm.

Both the BET surface area and external surface area increased between micro- and nano-crystals respectively of 13.6% and 85%. CO_2 adsorption properties were investigated on the MIL-96(Al) particles of micrometric and nanometric size and their matching CO_2 adsorption isotherms at 303K plotting amounts adsorbed against pressure were represented in Figure 3.4.

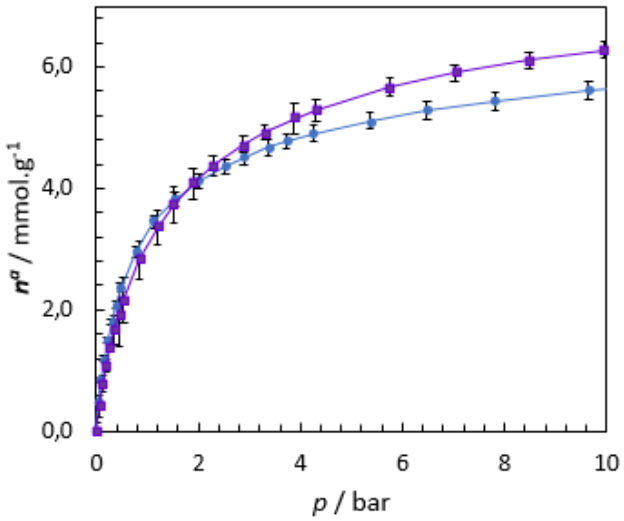

Figure 3.4 – Adsorption isotherms plotting CO_2 amounts adsorbed as function of pressure at 303K for the MIL-96(Al)-HR (blue circle) and the MIL-96(Al)-NP2 (purple square). Error bars were determined from the repetition of CO_2 adsorption at 303K (two times) on the MIL-96(Al)-HR and MIL-96(Al)-NP2

For pressures up to 3 bar, the CO_2 amounts adsorbed are similar for the MIL-96(Al)-HR and the MIL-96(Al)-NP2 suggesting almost zero effects of crystals size (i.e, micro- or nano-) in this pressure range. For pressures above 3 bar, the CO_2 amount adsorbed is slightly higher for the MIL-96(Al)-NP2 than for the MIL-96(Al)-HR and the difference was estimated around 11%. This seems to be in agreement with the decrease of the specific surface area generated when crystals size decrease from micrometric down to nanometric scale. Thus, one can suppose that there is a link between morphology and specific surface area for the MIL-96(Al) particles.

2. CO_2 working capacity versus 'pore size '

From Figure 3.2, it has been observed that there is no precise correlations between CO_2 working capacities and specific surface area as might be expected. This suggests that the adsorption phenomenon at ambient temperature is governed by other textural parameters. Thus, the CO_2 working capacities of MOFs were reported as function of pores size (Figure 3.5).

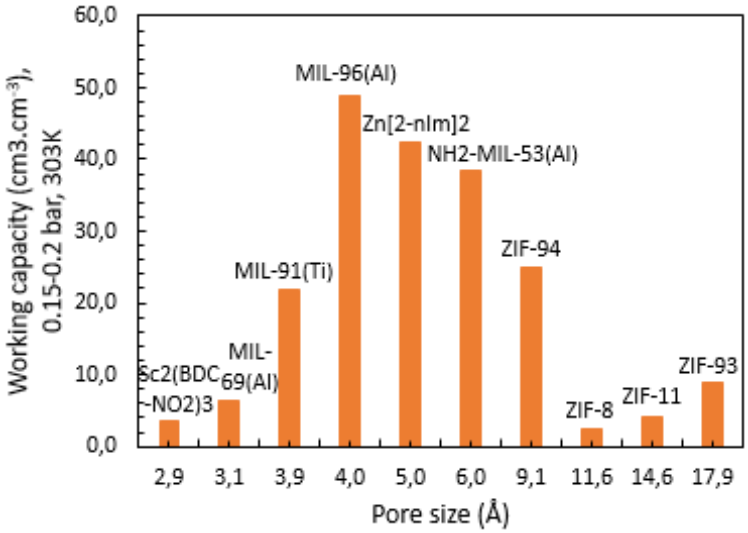

Figure 3.5 – CO_2 working capacities of MOFs determined for a low pressure range around 0.15-0.2 bar at 303K against pores size (Å)

From Figure 3.5, in those specific conditions near to post-combustion two aspects are noticeable:

- There are no precise correlations between the CO_2 working capacities and the pores size of the ten MOFs selected.
- There is a kind of threshold for a pore size of 4 Å matching to the highest CO_2 working capacity, approximatively of 48 $cm^3.cm^{-3}$. This corresponds to the microporous aluminum trimesate MIL-96(Al).

In the case of MIL-96(Al), an average pore size of 4 Å was fixed by modelling method (group of G.Maurin) due to its complex structure composed of three cavities whose general view with the three types of cages are presented in Figure 3.6.

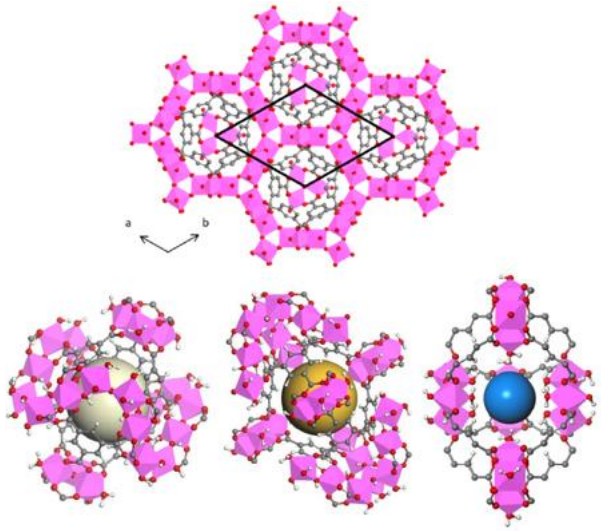

Figure 3.6 – General view of the MIL-96(Al) framework along the c axis (top) and scheme showing its three cages A (white), B (yellow) and C (blue) (bottom) (Figure 2a and Figure S2, [12])

Initially, the MIL-96(Al) structure was described by Loiseau *et al.* as containing four non-equivalent aluminum sites [17]. Nevertheless, the Al-O distances of the fourth aluminum (denoted Al4) were suspected as unrealistic because very short suggesting a crystallographic disorder of the MIL-96(Al) initial structure. So, Marvin *et al.* revisited the MIL-96(Al) structure using synchrotron-based single X-ray diffraction (XRD), solid state Nuclear Magnetic Resonance (NMR) and Density Functional Theory (DFT).

As described by Loiseau *et al.* the MIL-96(Al) structure results from the assembly of two building units. The first one is an oxo-centered trimer octahedra (called Al(1)) coordinated to bridging trimesate and μ_3-O ligands. While the second building unit is composed of a 2D hexagonal network containing 18-membered rings built by sinusoidal chains of aluminum octahedra. These chains contain two non-equivalent types of aluminum, respectively called Al(2) and Al(3). The Al(2) octahedra is coordinated to four trimesate oxygen and two bridging μ_2-hydroxo moieties while the Al(3) octahedra is coordinated to two and three trimesate oxygen and bridging μ_2-hydroxo moieties. The hexagonal 18-membered rings are interconnected each other by another type of trimer that is an 'unusual' Al(3) composed of three Al(3) octahedral that are corner-linked by μ_2-OH groups. Various aluminum trimers present in the microporous MIL-96(Al) are exposed in Figure 2 (i.e, c), d) and e)) of publication [12]. The connection of Al(1) octahedral with 2D hexagonal network (i.e, Al(2) and Al(3)) through the trimesate ligands lead to a 3D framework with a complex arrangement of three types of cavities denoted A, B and C (Figure 3.6).

Morphology and dimensions of three types of cavities were estimated as follows (Figure S2, Table S1 [12]):

- Cage A: sphere with a free diameter of 11 Å and a volume cell of 520 $Å^3$
- Cage B: ellipsoid with dimensions 9.5*12.6*11.3 Å and a volume cell of 700 $Å^3$
- Cage C: bipyramid with dimensions of 3.6*4.5 Å and a cell of volume of 10 $Å^3$

Nevertheless, all cages of the MIL-96(Al) framework are not connected each other as one would expect:

- The cages of same type (i.e, A-A, B-B or C-C) are not connected.
- The cage A is assumed as no connected to the cages B and C due to the narrow windows size below 2 Å. Windows dimensions between two cavities were estimated from the Van der Waals radius from oxygen atoms (for more details see Figure S4 [12]).

However, the cages B and C are connected and dimensions of windows size are of 3.6 Å horizontally (distance between two oxygen atoms of μ_2-OH trimer) and 4.5 Å vertically (distance between two oxygen atoms of μ_3-oxo trimer) (Figure S4, [12]). Therefore, based on those estimations of windows size an average of pore size of 4 Å has been fixed for the MIL-96(Al) framework.

Due to the fact that the cavity A is isolated within the structure, the MIL-96(Al) presents a two-dimensional (2D) porous network that consists of 'zig-zag' channels between cages B and C (Figure S3, [12]). Consequently, this will be probably the diffusion path during gas adsorption. In view of windows size and kinetic diameter of CO_2 and N_2, one can suppose that the CO_2 adsorption will be favored within the MIL-96(Al).

B. Adsorption enthalpy

The adsorption enthalpy was defined in chapter 2 (section D.2) characterizing adsorbent surface to highlight state changes of adsorbed layer or deformation of an adsorbent under pressure [1]. As a reminder, the adsorption enthalpies were measured experimentally at 303 K by means of manometry device coupled to Tian-Calvet microcalorimeter (chapter 2, section E.3.b)) [18]. The adsorption enthalpy profiles plot a 'pseudo-differential' enthalpy of adsorption as function of amount adsorbed (chapter 2, section D.3). From the extrapolation of adsorption enthalpy profile at y-intercept, one can get an adsorption enthalpy at low surface coverage ($-\Delta_{ads0}\dot{h}$, $kJ.mol^{-1}$).

In this section, the difference of adsorption enthalpies between CO_2 and N_2 at low surface coverage will be discussed considering CO_2 and N_2 are predominant gas of post-combustion. Adsorption enthalpies were taken at zero coverage due to the low CO_2 partial pressure in the post-combustion process (i.e, around 0.15-0.2 bar), this allows to assess the strength of adsorbent-adsorbate initial interactions. Thus, those differences were reported for the MOFs selected and compared to MOFs already studied within the laboratory as well as reference materials NaX and Takeda 5A (Figure 3.7).

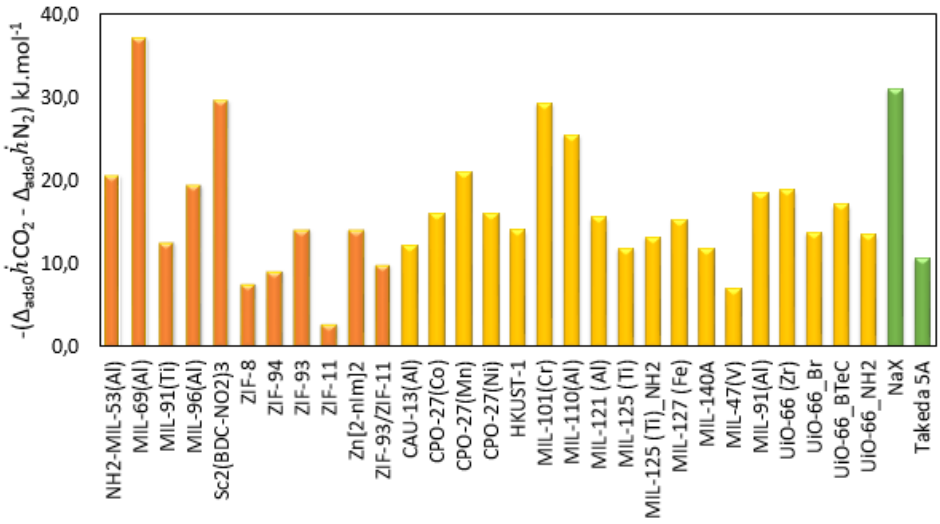

Figure 3.7 - Difference of adsorption enthalpies between CO_2 and N_2 extrapolated at zero coverage for various MOFs: M^4CO_2 project (orange), previously studied within the laboratory (yellow) as well as NaX and Takeda 5A (green)

Amongst MOFs, the greatest difference of adsorption enthalpies between CO_2 and N_2 extrapolated at zero coverage is attributed to the MIL-69(Al) (-37 kJ.mol^{-1}) outperforming those of NaX (-31 kJ.mol^{-1}) and Takeda 5A (-10.6 kJ.mol^{-1}). This is followed by those of the $Sc_2(BDC\text{-}NO_2)_3$ and NH_2-MIL-53(Al), respectively of -29.7 and -20.6 kJ.mol^{-1}. One can observe that the difference of adsorption enthalpies between CO_2 and N_2 at zero coverage for the MIL-69(Al), the $Sc_2(BDC\text{-}NO_2)_3$ and the NH_2-MIL-53(Al) are close or higher of those of adsorbents containing specific CO_2 adsorption sites as CPO-27, HKUST-1, MIL-101(Cr) with coordinative unsaturated sites 'CUS' or NaX with counter cation Na^+. The comparison of initial adsorption enthalpies with those of others adsorbents reported in literature show that they are lower: MIL-100(Fe) (-16.7 kJ.mol^{-1}) [8], MIL-140A(Zr) (-11.7 kJ.mol^{-1}) [19], STA-12 (-19 kJ.mol^{-1}) [11] or NaY (-14.7 kJ.mol^{-1}) [20]. This can suggest the presence of strong CO_2 interactions at low coverage for the MIL-69(Al), the $Sc_2(BDC\text{-}NO_2)_3$ and the NH_2-MIL-53(Al).

One can suppose that there are some textural parameters that play a role during CO_2 adsorption. Therefore as for working capacity, the difference of initial adsorption enthalpies between CO_2 and N_2 were reported as function of pore size (Figure 3.8).

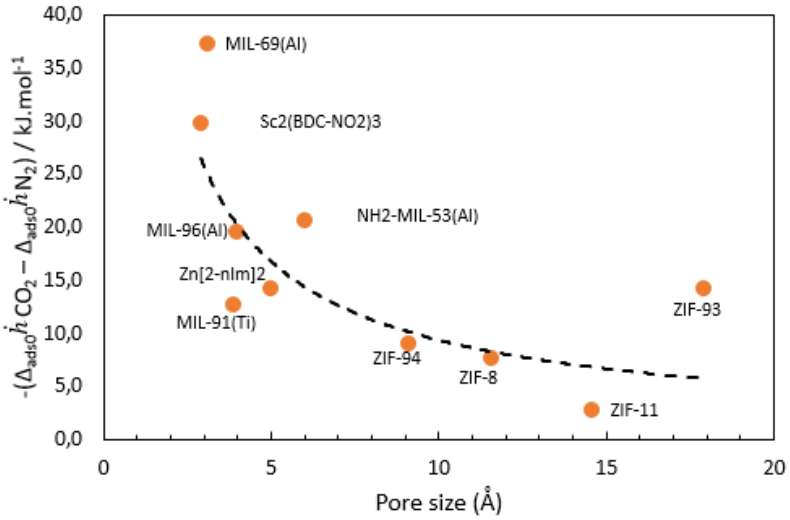

Figure 3.8 - Difference of adsorption enthalpies between CO_2 and N_2 extrapolated at low coverage as function of pore size

One can observe that the difference between CO_2 and N_2 adsorption enthalpies extrapolated at low surface coverage increase when pore sizes decrease. The greatest differences of initial adsorption enthalpies between CO_2 and N_2 are attributed to MOFs having small pore sizes around 4.0-6.0 Å: the MIL-69(Al), the $Sc_2(BDC\text{-}NO_2)_3$ and the NH_2-MIL-53(Al). This suggests that there are a combination of confinement and molecular sieving effects. Note that, the MIL-69(Al) and the MIL-53(Al) are isostructural MOFs, however in our case linker of the MIL-53(Al) was functionalized by amino ($-NH_2$) groups.

Thus, the MIL-69(Al) and NH_2-MIL-53(Al) which have analogues structures as well as $Sc_2(BDC\text{-}NO_2)_2$ are detailed.

1. Scandium-based MOFs family: Sc_2BDC_3 and functionalized counterpart $Sc_2(BDC\text{-}NO_2)_3$

Initially the scandium-based terephthalate adsorbent, of chemical formula $Sc_2(O_2CC_6H_4CO_2)_3$, was synthesized by Miller *et al.* in 2005 [21]. The scandium terephthalate is built up of isolated ScO_6 octahedra interconnected by BDC (1,4-benzenedicarboxylate) linkers to give three-dimensional (3D) small pore structure with openings about 3Å in free diameter. Miller *et al.* demonstrated that the scandium terephthalate possesses a high thermal stability up to 400°C as well as a significant pore volume of 0.26 $cm^3.g^{-1}$ making it very attractive for gas separation of small molecules as CO_2. Thereafter, the adsorption behavior of the scandium terephthalate was investigated by Miller *et al.* for small fuel-related molecules: CO_2, N_2, H_2, O_2, CH_4, C_2H_6, C_3H_8 [22]. Amongst those gas molecules, they showed that the scandium terephthalate adsorbs more strongly CO_2 than light carbons and others gas (H_2, N_2, O_2). In addition during CO_2 adsorption, they also identified a symmetry change from monoclinic to orthorhombic. Then, Mowat *et al.* [23] have demonstrated that crystal form of the scandium terephthalate can be stabilized by functional groups (amino and nitro).

Based on those data, the structures of scandium terephthalate and its amino- and nitro- derivative were optimized by Density Functional Theory (DFT) calculations from single-crystal X-ray diffraction data. Their adsorption properties, especially initial CO_2 adsorption enthalpies at 303K, were investigated during the M^4CO_2 project. The results have been published by Pillai *et al.* [20] in 2015 in which our contribution concerns the experimental measurements of adsorption enthalpies on the scandium terephthalate functionalized by nitro groups (publication and supporting information in Annex C).

Our study was focused on the $Sc_2(BDC\text{-}NO_2)_3$. As it has been demonstrated by Cmarik *et al.* [24] on functionalized UiO-66, the polarizing groups as nitro contribute to enhance CO_2 isosteric heat of adsorption. Indeed, values of isosteric heats of adsorption are -25.5 against -32 $kJ.mol^{-1}$ respectively for UiO-66 and UiO-66-NO_2. One can expect a similar effect for the $Sc_2(BDC\text{-}NO_2)_3$.

Firstly, the structures of Sc_2BDC_3 and $Sc_2(BDC\text{-}NO_2)_3$ optimized by DFT calculations are presented in Figure 3.9 when structures are CO_2-loaded (Figure S3, [20]).

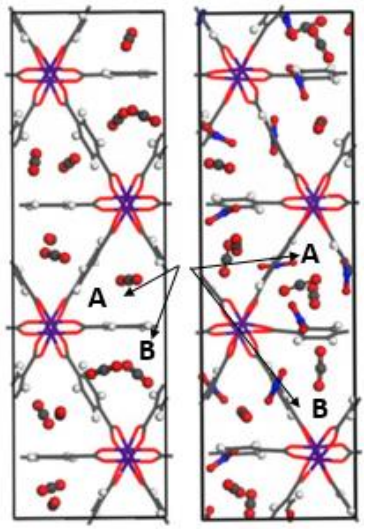

Figure 3.9 – Unit cell crystals structures of the CO_2 loaded Sc_2BDC_3 (left) and $Sc_2(BDC\text{-}NO_2)_3$ (right) (Figure S3 [20]) resolved by DFT geometry optimization from experimental unit cell parameters obtained from X-ray diffraction measurements[21], [23]

The optimization of the Sc_2BDC_3 and $Sc_2(BDC\text{-}NO_2)_3$ structures by DFT allowed to identify two kind of channels denoted A and B as well as two suspect CO_2 adsorption mechanisms. In the case of Sc_2BDC_3, CO_2 is aligned in channel A in such way that oxygen atoms of CO_2 interact with hydrogen atoms of the phenyl rings. While in channel B, CO_2 adsorption involves a tilting of organic linker. This is in agreement with the symmetry change (i.e, monoclinic to orthorhombic) identified by Miller *et al.* induced by CO_2 adsorption and leading to two kinds of channels A and B [25]. While for the $Sc_2(BDC\text{-}NO_2)_3$, Mowat *et al.* [23] suspected a reorientation of nitro groups when CO_2 adsorption occurs. This is supported by the good agreement between experimental and simulated adsorption isotherms obtained when the oxygen atoms of the nitro groups are considered as not pointing anymore toward the center of the channel (Figure 3, [20]).

For the Sc_2BDC_3 and $Sc_2(BDC\text{-}NO_2)_3$, CO_2 adsorption enthalpies extrapolated at low surface coverage were determined from modeling methods. However, initial CO_2 adsorption enthalpy for the $Sc_2(BDC\text{-}NO_2)_3$ was equally determined from experiment (complete CO_2 adsorption enthalpy profile in Figure S27 [20]). Thus, values of initial CO_2 adsorption enthalpies were reported as function of pore size (Figure 3.10).

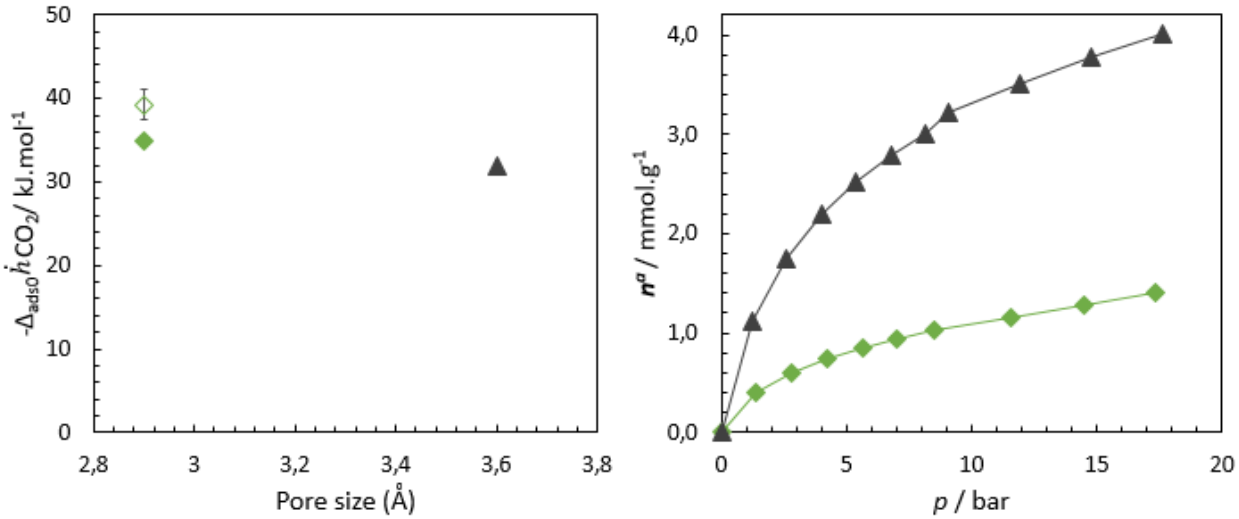

Figure 3.10 – CO_2 adsorption enthalpy extrapolated at low coverage against pore size (left) for the Sc_2BDC_3 (full grey triangle) and the $Sc_2(BDC\text{-}NO_2)_3$ (full green lozenge) determined by simulation methods. The empty green lozenge represents the initial CO_2 adsorption enthalpy determined experimentally using a manometry device coupled with a Tian-Calvet microcalorimeter on which error bars were calculated from CO_2 adsorption cycles repeated at 303K (Figure 5, [20]). On right figure were plotted CO_2 adsorption isotherms at 303K showing CO_2 uptakes against pressure respectively for Sc_2BDC_3 (full grey triangle) and $Sc_2(BDC\text{-}NO_2)_3$ (full green lozenge)

From Figure 3.10, one can observe that simulated CO_2 adsorption enthalpy at zero coverage of the $Sc_2(BDC\text{-}NO_2)_3$ is slightly higher than for the unfunctionalized scandium terephthalate. Indeed, simulated initial CO_2 adsorption enthalpies are of -32 and -35 kJ.mol^{-1} respectively for the Sc_2BDC_3 and the $Sc_2(BDC\text{-}NO_2)_3$. However, the comparison between simulated and experimental initial CO_2 adsorption enthalpies for the $Sc_2(BDC\text{-}NO_2)_3$ shows a slightly difference. The experimental value of CO_2 adsorption enthalpy at zero coverage is -39.2 kJ.mol^{-1} with an error bar of ± 1.8 kJ.mol^{-1}. Note that, the error bar was calculated from the repetition of three CO_2 adsorption cycles at 303K (Figure 5, [20]) that have equally emphasized a full regeneration of the $Sc_2(BDC\text{-}NO_2)_3$ under mild conditions (i.e, primary vacuum at 303K for 1h between each cycle).

The functionalization of scandium terephthalate by nitro groups contributed to a slight increase of initial CO_2 adsorption enthalpy, this is not as high as expected as for UiO-66 adsorbent [24]. This suggests that confinement effects are predominant within the $Sc_2(BDC\text{-}NO_2)_3$ due to its small pore size, 2.9 Å, hindering stronger CO_2 adsorption enthalpy. Although the presence of nitro groups contributed in a slightly increase of CO_2 adsorption enthalpy this led to a decrease of CO_2 uptakes (Figure 3.10).

2. Aluminum-based MOFs: the NH_2-MIL-53(Al)/ MIL-69(Al) system

Some MOFs such as the MIL-53(Al, Cr) have the characteristic of being flexible in response to external stimuli as temperature change [26], mechanical pressure [27] as well as probe molecule [28]. The MIL-53(Al) possesses interesting CO_2 adsorption properties over N_2 and CH_4 with an initial adsorption enthalpy of -35 kJ.mol^{-1} as well as a breathing phenomenon (i.e, narrow to open form) around 6 bar at 304K [28]. However in our study, MOFs with a rigid rather than flexible frameworks are explored to ensure a good cohesion between MOFs and polymers to avoid potential collapses of mixed matrix membranes (MMMs) in the studied pressure range. In order to maintain the MIL-53(Al) structure in narrow pore form, two strategies were setup:

- Functionalization of linker (i.e, 1,4 benzenzdicarboxylate) by amino (-NH_2) groups leading to the NH_2-MIL-53(Al) (Figure 3.11)
- Linker exchange by 2,6 naphtalenedicarboxylate leading to the MIL-69(Al) (Figure 3.11)

Consequently, this involved a decrease of pores sizes: respectively 6 and 3 Å for the NH_2-MIL-53(Al) and the MIL-69(Al) against 8 Å for the MIL-53(Al).

In the context of this thesis, we characterized adsorption properties of 'narrow form' of the MIL-69(Al) (provided by the Lavoisier institute). Note that Senkovska *et al.* [29] demonstrated that the MIL-69(Al) phase possesses an 'open form' when DMF is used instead of water as solvent during synthesis.

Various types of interaction that can play a role when CO_2 adsorption occurs within the NH_2-MIL-53(Al) and the MIL-69(Al) are shown in Figure 3.11.

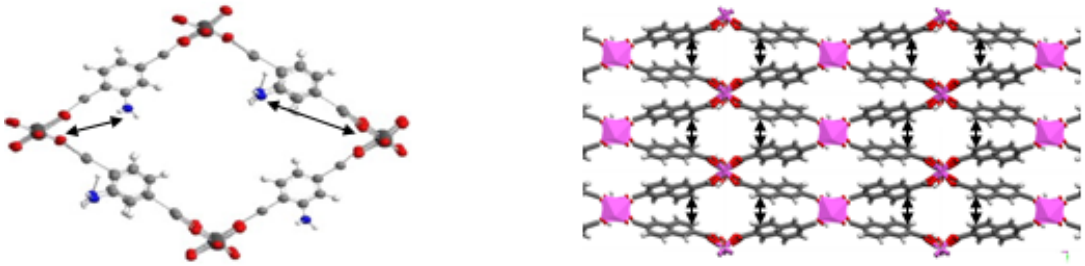

Figure 3.11 – The MIL-53(Al) structure where organic linkers: 1,4 benzenedicarboxylate (BDC) are functionalized by amino (-NH_2) groups (left) [30] and MIL-69(Al) structure modeled by G. Maurin group (ICGM). Black arrows represent various interactions: hydrogen bonds between NH_2 groups and [AlO_6] for the NH_2-MIL-53(Al) as well as π-π interactions between 2,6 naphtalenedicarboxylate (NDC) for the MIL-69(Al)

Regarding the NH_2-MIL-53(Al), its surface acidity was characterized by means of spectroscopic methods by the Bulgarian Academy of Sciences (BAS) group (Sofia) of the M^4CO_2 project. They evidenced that relatively strong hydrogen bonds are created between a part of hydroxyl and amino groups and then do not interact with weak bases as CO_2. One can assume that amino groups play an indirect role on CO_2 adsorption. Those results are in agreement with these of Stavitski *et al.* [31] regarding adsorption mechanisms identification involved when CO_2 adsorption occurs on MIL-53(Al) and NH_2-MIL-53(Al). According to the authors, the contracted state (i.e, narrow pore form) of NH_2-MIL-53(Al) is the most stable form, mainly assigned to efficient hydrogen bonds between NH_2 moities and $[AlO_6]_\infty$ rather than Van der Waals (VdW) interactions. While the open form (i.e, large pore) of MIL-53(Al) is more stable than its narrow pore state due to low strength of additional VdW interactions between terephtalate joints.

In the case of the MIL-69(Al), the BAS group characterized CO_2 adsorption sites as one type of isolated bridging hydroxyl groups (μ_2-OH) which are main CO_2 adsorption sites.

Therefore, narrow pore form of the MIL-53(Al) was maintained via hydrogen bonds or π-π interactions, respectively the NH_2-MIL-53(Al) and the MIL-69(Al) on which we performed measurements of CO_2 adsorption enthalpy at 303K (Figure 3.12).

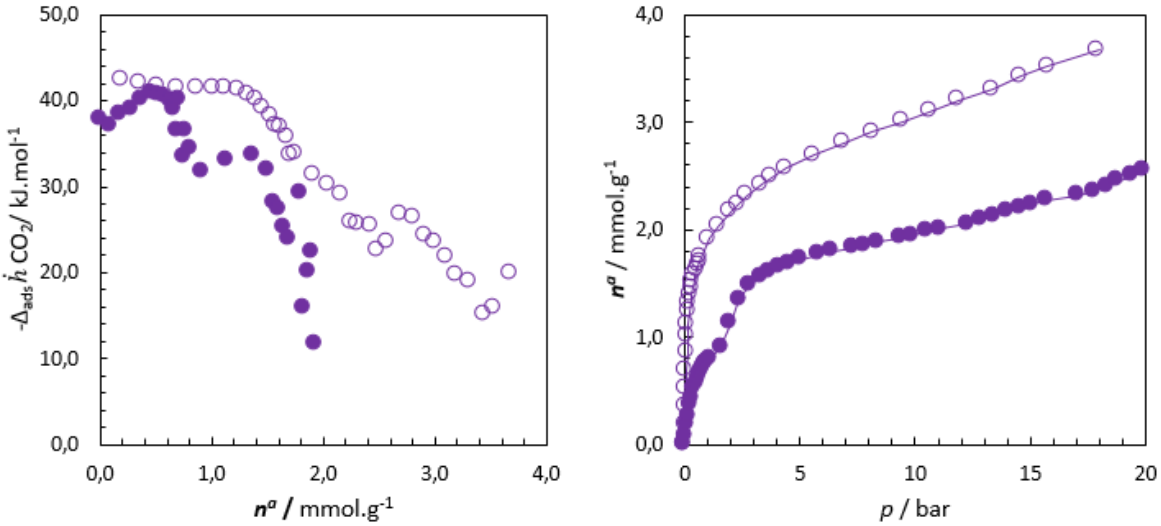

Figure 3.12 – CO_2 adsorption enthalpy profiles plotting differential adsorption enthalpies against uptakes (left) and matching adsorption isotherms representing amounts adsorbed as function of pressure (right) at 303K for the NH_2-MIL-53(Al) (empty circles) as well as for the MIL-69(Al) (full circles)

Regarding adsorption enthalpy profile of the MIL-69(Al), there is a slight increase of CO_2 adsorption enthalpies up to -41 kJ.mol^{-1} for a range of CO_2 amounts adsorbed 0-0.5 mmol.g^{-1}. While, at low pressures, the average CO_2 adsorption enthalpy is approximatively -38.9 kJ.mol^{-1} which is higher than UiO-66 (Zr)-BTEC (-34.8 kJ.mol^{-1}) [32] and lower than NaX (-49.0 kJ.mol^{-1}) [5]. This suggests that there are strong CO_2 adsorption sites within MIL-69(Al) which is probably coupled to a high degree of confinement. Between 0.8 and 1.5 mmol.g^{-1}, CO_2 adsorption enthalpies show a horizontal plateau which can be explained by a MIL-69(Al) structure expansion. Beyond 1.5 mmol.g^{-1}, there is a strong decrease of CO_2 differential adsorption enthalpies which matches to adsorbent saturation. For pressures above 1 bar, CO_2 adsorption isotherm of the MIL-69(Al) describes a step around 1.6 bar which seems to be analogous to the inflection observed for the MIL-53(Al) that appears around 4 bar.

While in the case of the NH_2-MIL-53(Al), CO_2 adsorption enthalpies are relatively homogeneous around -40 kJ.mol^{-1} in the uptake range 0-1.5 mmol.g^{-1}. In this area, this suggests there are no CO_2 specific adsorption sites and probably a filling of the micropores. For uptakes higher than 1.5 mmol.g^{-1}, CO_2 adsorption enthalpy decrease until -25 kJ.mol^{-1}. This might indicate that adsorption occurs at a certain distance of adsorption sites on external surface as well as adsorbate-adsorbate interactions. CO_2 adsorption enthalpy of NH_2-MIL-53(Al) is amongst the highest of microporous MOFs related so far: MIL-91(Ti) (-47.1 kJ.mol^{-1}) [33]; $Sc_2(BDC\text{-}NH_2)_3$ (-45.3 kJ.mol^{-1}) [20] lower than NaX (-49 kJ.mol^{-1}) [5] and higher than Takeda 5A activated carbon (-33.8 kJ.mol^{-1}) [5].

C. Selectivity

The selectivity (α) was defined as the ratio of mole fractions between the adsorbed (x) and bulk (y) phases (see chapter 2, section F.6.)). As a reminder, the prediction of selectivities arises from 'IAST' model that uses the best fit of pure gas adsorption isotherms to predict co-adsorption isotherms. Note that, only pure gas adsorption isotherms obtained from manometry device coupled to Tian-Calvet microcalorimeter were used to predict selectivities.

The predicted selectivities were determined for a low pressure range, around 0.15-0.2 bar at 303K, for CO_2/N_2 gas separation near to post-combustion conditions, as mentioned in the introduction. Those CO_2/N_2 predicted selectivities for the ten MOFs selected were compared to those of others MOFs already studied within the laboratory and equally to the NaX and Takeda 5A (Figure 3.13).

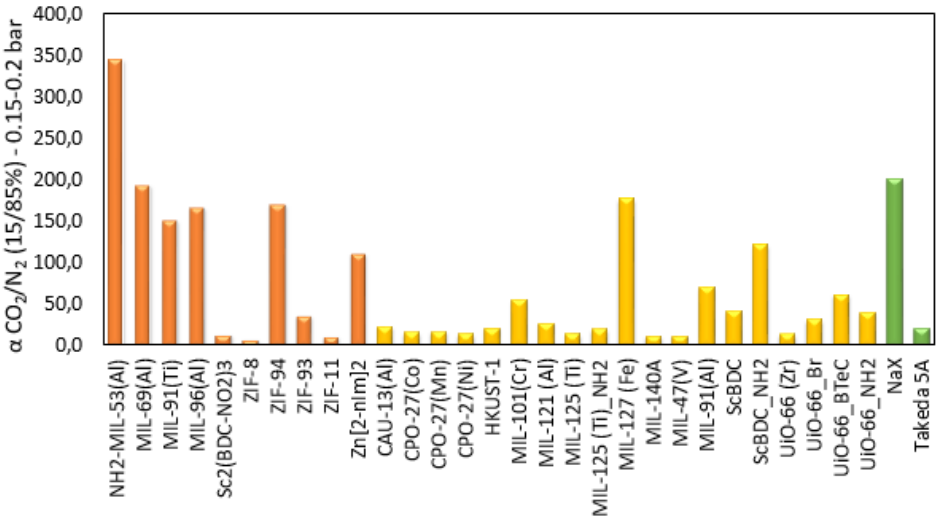

Figure 3.13 - Predicted CO_2/N_2 selectivities around 0.15-0.2 bar at 303K for various MOFs: M^4CO_2 (orange), previously studied within the laboratory (yellow) and NaX and Takeda 5A (green)

One can observe that the predicted CO_2/N_2 selectivities of MOFs that we have studied so far are equal or higher than those of others MOFs or NaX and Takeda 5A, except for the $Sc_2(BDC\text{-}NO_2)_3$. Indeed for the $Sc_2(BDC\text{-}NO_2)_3$, the predicted value of CO_2/N_2 selectivity based on experimental adsorption isotherms does not match with this obtained from simulation that predicted an infinite value. This suggests the presence of defects inside the $Sc_2(BDC\text{-}NO_2)_3$ MOF. Amongst the M^4CO_2 MOFs, one can note that the MIL-91(Ti) and the ZIF-94 have good predicted CO_2/N_2 selectivities respectively of 150 and 170. They are comparable to those of the MIL-127(Fe) and NaX respectively of 176 and 200. However, those predicted CO_2/N_2 selectivies are lower than those reported for others MOFs in literature as (15% CO_2, 0-1 bar, 303K [33]): MIL-100(Fe) (47), MIL-102(Cr) (41), MIL-68(Ga) (12) and MIL-91(Al) (68).

As for the working capacity and the adsorption enthalpy, the predicted CO_2/N_2 selectivities were reported as function of pores size (Figure 3.14).

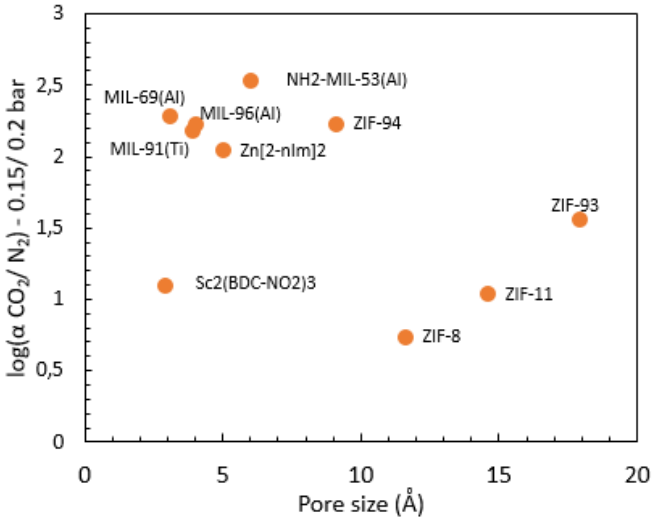

Figure 3.14 – Logarithm of predicted CO_2/N_2 selectivities (around 0.15-0.2 bar, at 303K) as function of pore size (Å)

From Figure 3.14, one can observe that there are no significant correlations between CO_2/N_2 selectivities at 0.15-0.2 bar and pore size of various MOFs characterized. However, the highest CO_2/N_2 selectivities are obtained for MOFs with small pore size around 5-10 Å (i.e: NH_2-MIL-53(Al), MIL-69(Al), MIL-96(Al), MIL-91(Ti), Zn[2-nIm]$_2$, ZIF-94) with the exception of the $Sc_2(BDC\text{-}NO_2)_3$ MOF. This suggests that various factors play a role: MOFs chemistry at low pressure as well as confinement and molecular sieving effects.

Amongst MOFs having the highest CO_2/N_2 selectivities, the MIL-91(Ti) seems to be promising for CO_2 capture with a pore size of 4 Å.

1. The small pore bis-phosphonate MIL-91(Ti)

The CO_2 adsorption properties of the small pore bis-phosphonate MIL-91(Ti) were investigated and published in 2016 [33] (publication and supporting information are in Annex D). Therefore, in this section will be discussed only adsorption mechanisms leading to a good predicted CO_2/N_2 selectivity.

The MIL-91(Ti) of chemical formula, $TiO(O_3PCH_2NHC_4H_8NHCH_2PO_3)$, is built up of TiO_6 octahedral chains connected through bis-phosphonate linkers (N,N'-piperazine bismethylenephosphonic acid) to get a three-dimensional (3D) structure (Figure 1, [33]). Pore size dimension of the MIL-91(Ti) were estimated approximatively to 0.35*0.40 nm² from crystallographic data.

To attempt to elucidate adsorption mechanisms involved in the good CO_2/N_2 selectivity of the MIL-91(Ti), several tests were performed: single gas adsorption, molecular simulation and co-adsorption experiments [33]. CO_2 and N_2 interactions with the MIL-91(Ti) framework from binary mixture are illustrated by means of GCMC simulation (Figure 3.15).

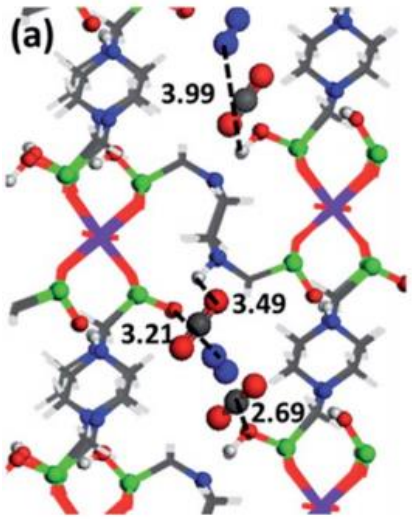

Figure 3.15 – Snapshot obtained during GCMC simulated arrangements of CO_2 and N_2 molecules from binary mixture on the MIL-91(Ti) for a molar composition of 0.05/0.95 at 303K (Figure 5, [33])

Both *in situ* PXRD and GCMC data suggested that the CO_2 adsorption mechanism is the following: during adsorption CO_2 molecules are aligned in such a way that carbon atoms of C=O groups (CCO_2) interact with oxygen atoms present in the environment of the P=O group and the N atom (PO···H···N). However, analysis of the CO_2/N_2 co-adsorption mechanism showed that the CO_2 behavior is similar to this of single gas adsorption scenario. Indeed, CO_2 molecules are mainly located in the vicinity of the PO···H···N sites with distance between CCO_2 and OPO···H···N of 2.69 Å similar to this of 2.7 Å for pure

CO_2 adsorption. Moreover, N_2 molecules are located in the center of pore with characteristic host/guest distances exceeding 3.2 Å (N_2 - PO···H···N, Figure S23 [33]). The co-adsorption mechanism proposed was validated by the good agreement between experimental and simulated CO_2/N_2 selectivities.

Within the MIL-91(Ti), the CO_2/N_2 separation is driven by preferential CO_2 adsorption sites around P-OH and NH groups of the phosphonate linkers. This is combined with a high degree of confinement of the MIL-91(Ti) due to its small pore size (i.e, 4 Å) and low pore volume which favor the CO_2 adsorption with smaller kinetic diameter compared to N_2. Therefore, the good CO_2/N_2 selectivity of the MIL-91(Ti) is explained by the combination of those several parameters.

D. Moisture conditions

As mentioned in chapter 1 (section B.1), flue gases contain traces or small amounts of water (i.e, around 10%) which affects usually negatively CO_2 adsorption capacity of adsorbents as zeolites and some MOFs. Therefore, one important factor to take into account is the CO_2 adsorption behavior of an adsorbent under moisture conditions, especially when post-combustion conditions are targeted.

A work of screening was carried out within the laboratory on 43 MOFs and 4 reference materials using a laboratory-scale protocol to assess the percentage loss in CO_2 uptake between 'wet' and 'dry' samples (Figure 3.16) [34].

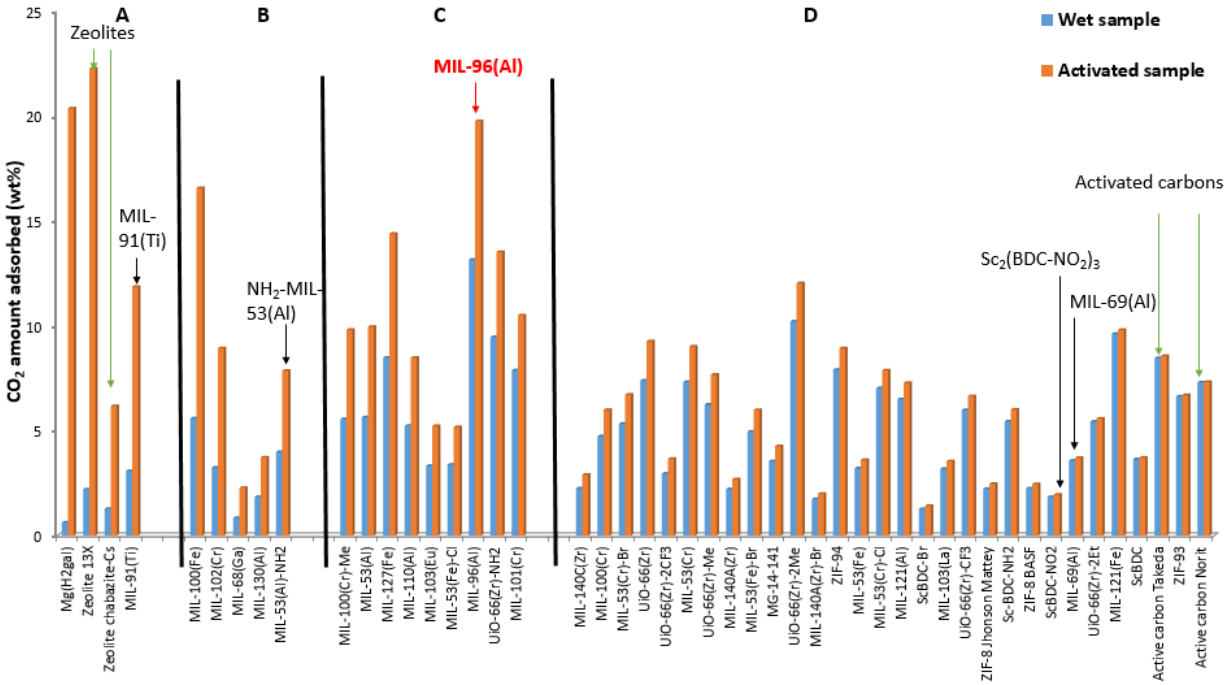

Figure 3.16 – Histogram showing CO_2 amounts adsorbed (wt%) for the 43 MOFs and 4 reference materials (i.e, zeolites and activated carbons). Orange bars correspond to the CO_2 amounts adsorbed determined in the activated state while blue bars correspond to the CO_2 uptakes obtained under moisture conditions (water pre-adsorbed). CO_2 uptakes were ranked as function of CO_2 percentage loss between 'activated' and 'wet' states: zone A corresponds to a decrease of CO_2 adsorption capacity by less than 25%, zone B between 25 and 50%, zone C between 50 and 75% and zone D by more than 75%.

One can observe that some of CO_2 adsorption capacities of MOFs are strongly affected under moisture conditions, especially for the MIL-91(Ti) and the NH_2-MIL-53(Al) where CO_2 adsorption capacities are reduced respectively of 75% and 49%. In the case of MIL-91(Ti), its CO_2 adsorption behavior under moisture conditions appears to be close to those of zeolites for which CO_2 adsorption capacities are

negatively affected in presence of water. While CO_2 adsorption behaviors of some of MOFs in presence of water as the $Sc_2(BDC\text{-}NO_2)_3$ and the MIL-69(Al) are slightly affected as activated carbons. However in the zone C, one can observe that the MIL-96(Al) stands out with the best CO_2 adsorption capacities under moisture conditions. In terms of percentage loss between 'dry' and 'wet' states for the MIL-96(Al), this represents 33%.

To assess the competition between CO_2 and H_2O adsorption sites, we reported CO_2 capacity loss against Henry's constant of water (Figure 3.17) for various MOFs.

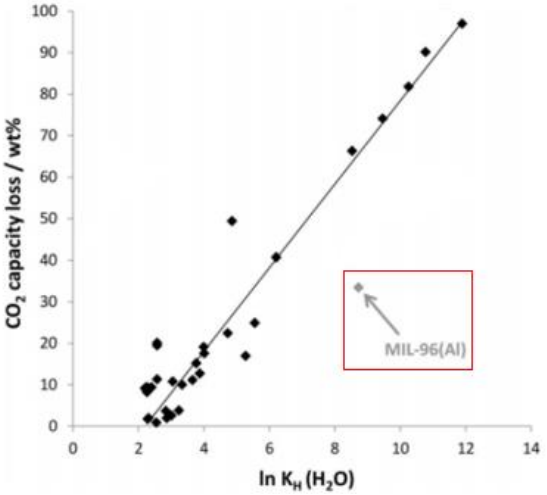

Figure 3.17 – CO_2 capacity loss (wt%) that represents the difference of CO_2 uptakes between 'dry' and 'wet' states of MOFs as function of logarithm of Henry constant (K_H) of water determined from water adsorption isotherms at 298K [34]

Firstly, one can observe on figure 3.17, that there is a linear trend between CO_2 capacity loss and logarithm of Henry constants suggesting that CO_2 and H_2O adsorption sites are similar for the MOFs studied. The upper part of graph corresponds to the MOFs for which CO_2 adsorption capacities are strongly affected under moisture conditions. However, one can observe that the MIL-96(Al) derives from the linear trend assuming adsorption mechanisms of CO_2 and H_2O more complex, probably a competition between those adsorption sites.

Therefore, we have performed a study on CO_2 adsorption properties of the MIL-96(Al) in presence of water under static and dynamic conditions near to post-combustion conditions this work was published [35] (publication and supporting information in Annex E). In this context, we used the MIL-96(Al) microparticles synthesized within Lavoisier institute by M.Benzaqui and called 'MIL-96(Al)-HR' [12].

A preliminary study was conducted on CO_2 adsorption properties of the MIL-96(Al) in the presence of water under static conditions. Prior to gas adsorption, the MIL-96(Al) is placed within a desiccator for 48h to be pre-equilibrated and one considers that the MIL-96(Al) is fully hydrated. Then, the calorimetric cell containing the pre-equilibrated MIL-96(Al) is placed inside the Tian-Calvet microcalorimeter where CO_2 gas adsorption is measured at 303K. Therefore, static conditions mean that both ~~of~~ CO_2 partial pressure and the rate of relative humidity cannot be controlled for those specific conditions. More experimental details are provided in the experimental section of article [12]. The comparison of CO_2 adsorption isotherms between the activated and pre-equilibrated states of the MIL-96(Al) (Figure 5, [35]) showed a loss of adsorption capacity of 80% at 8 bar (i.e, 5.7 against 1.2 $mmol.g^{-1}$ respectively. This is emphasized by the Henry's constant calculation leading to 16 and 5

mmol.g^{-1}.bar^{-1} respectively for the outgassed and pre-humidified states. Although CO_2 adsorption capacity is affected by water, CO_2 adsorption enthalpy increases up to -40 kJ.mol^{-1} showing a positive effect of H_2O pre-adsorbed on CO_2 interactions during pore filling. The higher CO_2 adsorption enthalpy can be attributed to a higher confinement effect and/or an increase of hydrophilicity surface owing to pre-adsorbed water.

With the home-made apparatus, CO_2 cycling adsorption measurements were performed on the pre-equilibrated MIL-96(Al) at 303K under static conditions. Cycling (Figure 6, [35]) showed that CO_2 uptakes increase with cycles suggesting that CO_2 adsorption gives a water displacement involving a porosity release. However, CO_2 uptakes remain lower than those of the activated MIL-96(Al). Regarding CO_2 adsorption enthalpies during cycling, they remain above that of the activated MIL-96(Al).

The study of CO_2 adsorption properties on the pre-equilibrated MIL-96(Al) has been pursued under dynamic conditions at 303K to tend towards post-combustion conditions. Results are presented in the next section.

Unlike static conditions, in the case of dynamic conditions the CO_2 partial pressure as well as the rate of relative humidity can be fixed. Experimentally, the MIL-96(Al) was pre-equilibrated at a fixed relative humidity in a nitrogen flow prior to blending in CO_2 for a partial pressure of 0.2 bar, at 303K. Details about the full experimental home-made apparatus used are provided in supporting information (Figure S18, [35]). Thus, CO_2 amounts adsorbed at 0.2 bar and adsorption enthalpies were measured on the MIL-96(Al) for various rates of relative humidity that are: 3, 10, 20 and 40 % (Figure 3.18). Note that for 3% relative humidity, the MIL-96(Al) is CO_2-loaded around 1.6 mmol.g^{-1} at 0.2 bar-matching to this determined under static conditions.

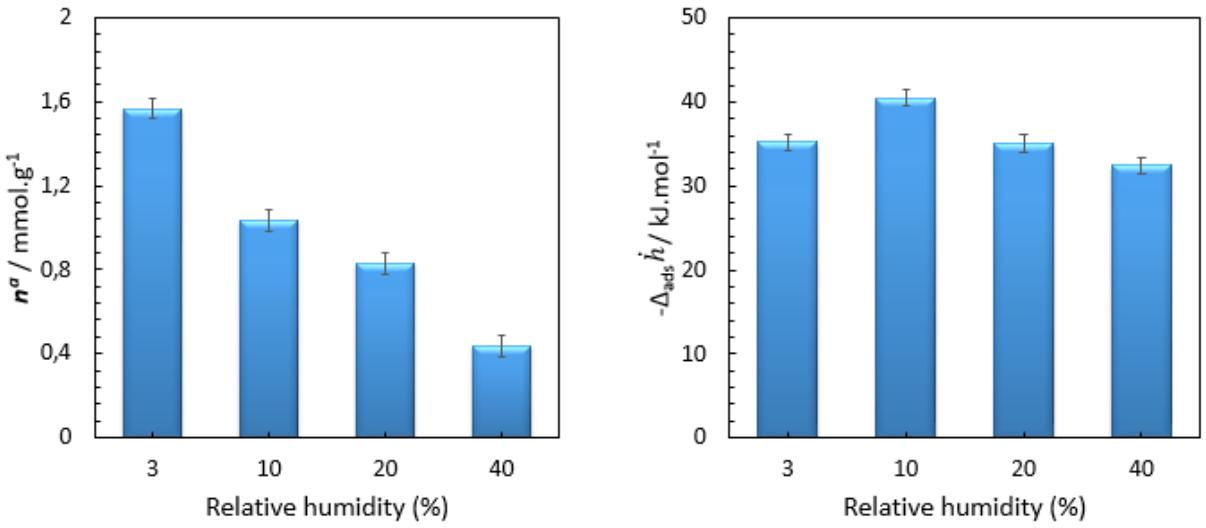

Figure 3.18 – CO_2 amounts adsorbed at 0.2 bar and matching adsorption enthalpies obtained under dynamic conditions at 303K for various rate of relative humidity (%): 3 (considered as 'outgassed state'), 10, 20 and 40 for which errors were estimated and represented (black)

One can observe a decrease of CO_2 amounts adsorbed when the percentage of relative humidity increases. The losses of CO_2 adsorption capacities were established at 33%, 49% and 72% respectively for relative humidities of 10%, 20% and 40% and match with water uptakes from water adsorption isotherm (Figure 2 top, [35]). Then, this suggests that the CO_2 entirely fill the remaining pore volume that the water leaves after pre-adsorption at each relative pressure.

At a fixed relative humidity of 10% there is an increase of CO_2 adsorption enthalpy that is of -40 kJ.mol^{-1} against -35 kJ.mol.$^{-1}$ for a relative humidity of 3% that corresponds to the outgassed state. One can observe that above 10%, when relative humidities increase this led to a decrease of CO_2 adsorption enthalpies measured. Due to dynamic conditions, one can assume that a part of water pre-adsorbed is partially displaced during CO_2 adsorption, consuming energy, and leading to lower adsorption enthalpy than would be expected for CO_2 adsorption alone. Moreover, a closer examination of the measured enthalpy signal showed an unusual signal which seems to be the resultant of initial rapid exothermic CO_2 uptake followed by a more gradual endothermic H_2O desorption (Figure S20, supporting information).

Therefore, a relative humidity of 10% seems to be a trade-off between a decrease of CO_2 uptake and a maximum of CO_2 adsorption enthalpy. Thus, the analysis of water adsorption isotherm allowed identifying water adsorption sites within the MIL-96(A), especially at 10% of relative humidity (Figure 3.19).

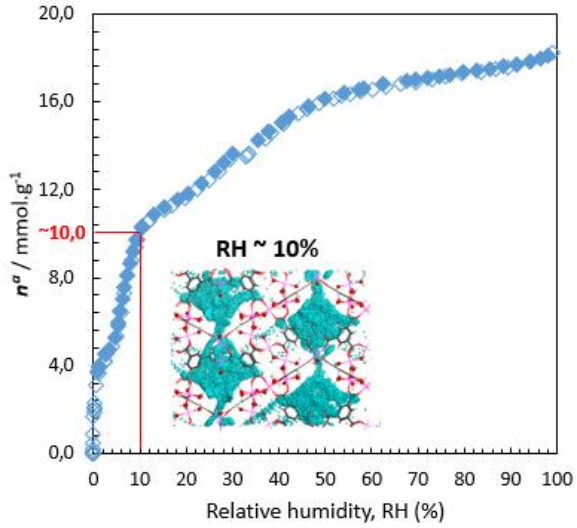

Figure 3.19 – Adsorption (empty symbol) and desorption (full symbol) isotherms of water at 298K. Map of the H_2O occupied positions in 1000 equilibrated frames extracted from the GCMC simulations at 298K at $p/p^0 = 0.1$ (Figure S4)

To assess the hydrophilicity/ hydrophobicity of the MIL-96(Al), water adsorption was performed at 298K on adsorbent beforehand outgassed (i.e, at 423K for 16 hours under primary vacuum). From Figure 3.19, one can observe an overlaying of the adsorption and desorption isotherms of the MIL-96(Al) suggesting that water adsorption is a reversible phenomenon without pore blocking effects or chemisorption. There is a fairly good agreement between experimental and simulated water adsorption isotherms at 298K although the MIL-96(Al) saturation is reached at lower relative pressure for the simulated isotherm (Figure 2 bottom, [35]).

Water adsorption isotherm of the MIL-96(Al) shows several steps:

- An initial uptake up to p/p° = 0.03, this step can be related to specific water adsorption sites (Figure 3a and 3b).
- A first relatively sharp adsorption step between p/p° = 0.03 and 0.12 that is linked to the formation of water clusters within the most hydrophilic cages of the MIL-96(Al)
- A second more gradual uptake between p/p° = 0.12 and 0.2-0.5
- A final plateau-like region

Thus, a relative humidity of 10% corresponds to the filling of the most hydrophilic cages within the MIL-96(Al). We performed CO_2 adsorption cycling under flow conditions at 10% of relative humidity (Figure 3.20).

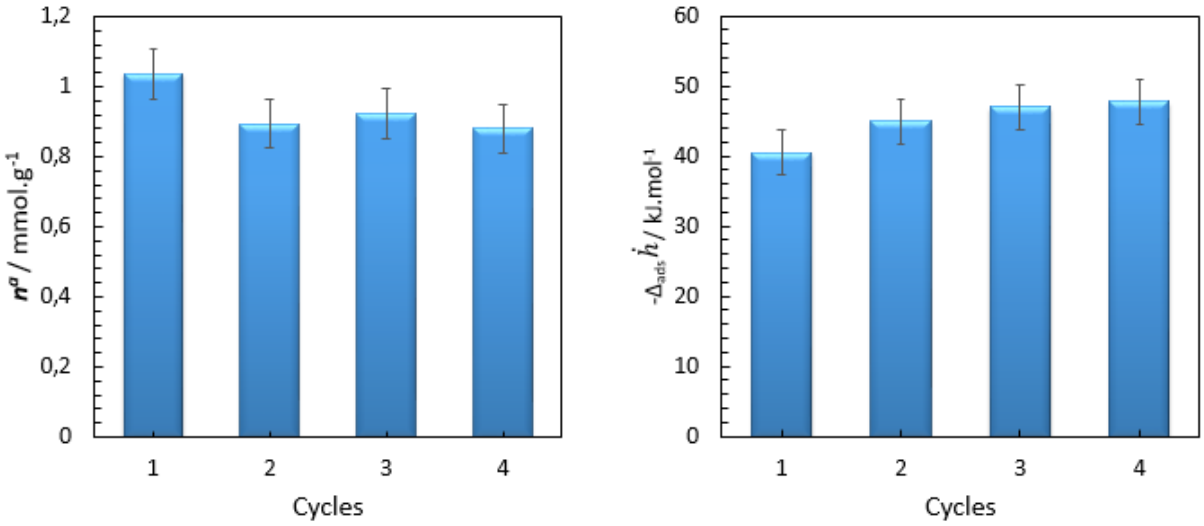

Figure 3.20 – CO_2 amounts adsorbed at 0.2 bar (left) and matching adsorption enthalpies (right) measured during cycling at 303K

Figure 3.20 shows a slight decrease of CO_2 amount adsorbed between the first and second cycle (1.03 and 0.89 mmol.g^{-1}). This suggests that there are some CO_2 molecules irreversibly adsorbed within the MIL-96(Al). However after the second cycle, the CO_2 uptakes remain relatively constant until fourth cycle. There is also an increase of CO_2 adsorption enthalpies to achieve a constant value after the second cycle. This can be attributed to some CO_2 irreversibly adsorbed under those dynamic conditions during the first step. This may be accompanied by a water displacement, which may be not involved in the following cycles, leading to a relative endothermic contribution for the first cycle. However, a quasi-steady state seems to be reached beyond the second cycle.

In order to place the performances of the MIL-96(Al) for post-combustion type conditions, it has been compared with those of others MOFs from literature (Figure 3.21).

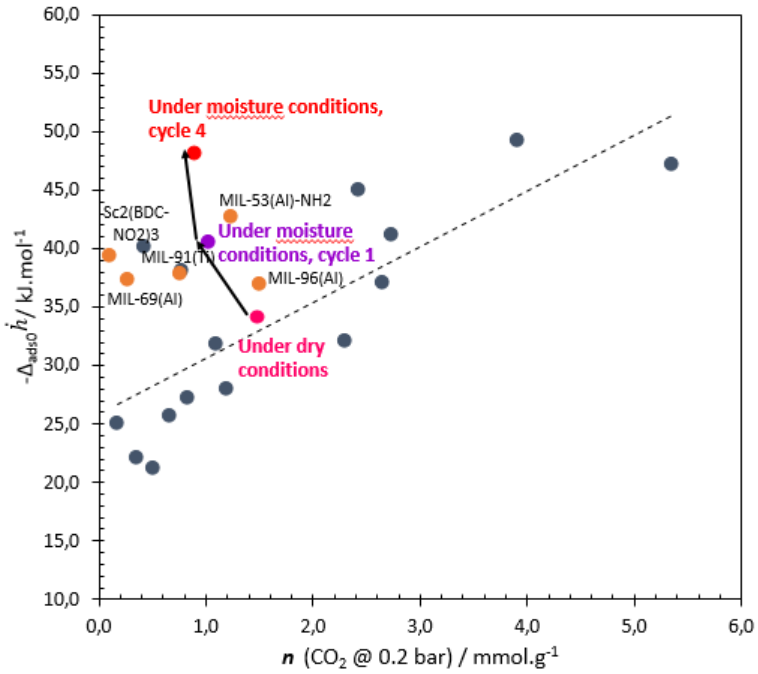

Figure 3.21 – Relationship between CO_2 adsorption enthalpies extrapolated at zero coverage and matching uptakes at 0.2 bar for: several MOFs of literature (grey circles, see Table S7 for values, [35]) and carboxylate MOFs of M^{4}CO$_2$ project (orange circles). For the MIL-96(Al): pink circle represents the outgassed state while purple and red circles show respectively the first and fourth cycles after pre-equilibration with 10% of relative humidity during cycling under flow conditions

For MOFs reported from literature and carboxylate-based MOFs of M^{4}CO$_2$ project, one can observe an overall linear trend with a certain degree of scattering. The CO_2 adsorption enthalpy at zero coverage as well as uptake at 0.2 bar for the outgassed state of the MIL-96(Al) falls into this trend. However, the slight loss of CO_2 adsorption capacity accompanied by a significant increase of CO_2 adsorption enthalpy when the MIL-96(Al) was pre-equilibrated at 10% of relative humidity led to an upward deviation from this trend. Figure 3.21 emphasizes that the CO_2 adsorption capacity of the MIL-96(Al) is affected moderately with an increase of adsorption enthalpy placing it above many other, non CUS containing, MOFs in terms of interaction strength. Thus, such relationship may help to identify adsorbents of potential interest for this kind of study.

GCMC simulations allowed ~~to~~ investigating co-adsorption mechanism for the ternary $CO_2/N_2/H_2O$ mixtures. This showed that CO_2 molecules are initially distributed in the same region of the pores than in the pure components, meaning that pore containing μ_2-OH (Figure S13 and Figure S14, [35]). GCMC simulations of the ternary mixture were performed at a relative humidity of 8.5% (Figure 3.22).

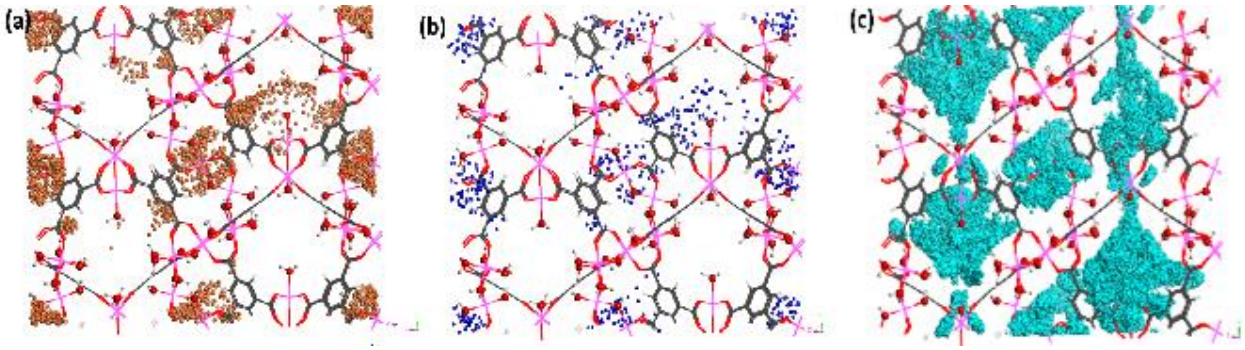

Figure 3.22 – Maps of the occupied positions of CO_2 (orange), N_2 (blue), and H_2O (cyan) in 1000 equilibrated frames extracted from GCMC simulations for co-adsorption of CO_2/N_2 (20/80) in the MIL-96(Al) at 303K and 1.0 bar in presence of humidity, RH = 8.5% (Figure 9, [35])

Figure 3.22 evidences that CO_2 and N_2 molecules are adsorbed inside cavities containing similar adsorption sites that are μ_2-OH. While, H_2O molecules are preferentially adsorbed inside cavities made by terminal sites that are Al1-$H_2O_{terminal}$, Al(3')-$OH_{terminal}$ and Al(3)-$H_2O_{terminal}$. This suggests that at the initial stage of adsorption, CO_2 and H_2O molecules have distinct adsorption sites. When relative humidity increases, H_2O molecules interact with all the available porosity due to its higher interaction energy compared to CO_2. Thus, H_2O molecules can occupy all adsorption sites explaining the decrease of CO_2 adsorption capacity with the increase of relative humidity (see Figure 3.18).

E. An Adsorbent Indicator Performance (API)

Within the laboratory, an Adsorbent Performance Indicator (API) was developed taking into account the selectivity(α), the working capacity $(WC, cm^3.cm^{-3})$ and the average of adsorption enthalpy $\left(-\Delta_{ads0}\dot{h}, kJ.mol^{-1}\right)$ (chapter 2) weighted by coefficients as function of targeted process [5]. In view of post-combustion application, we fixed the coefficients A, B and C (chapter 2, section F.7) to 2, 1 and 1 respectively for the selectivity, the working capacity and the adsorption enthalpy. The stronger coefficient was attributed to the selectivity because CO_2 selective adsorbents over N_2 are researched. Thus, the APIs of MOFs were calculated and compared to those of NaX and Takeda 5A (Figure 3.23).

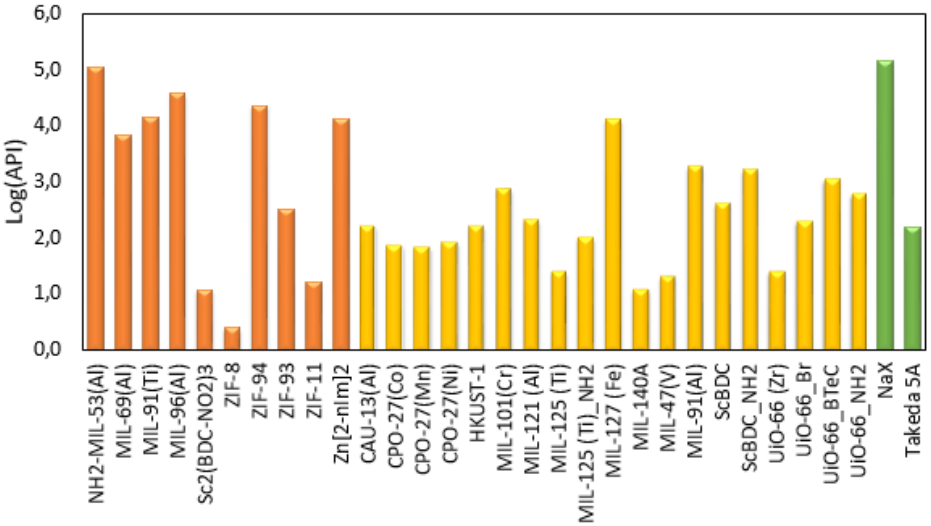

Figure 3.23 – Logarithm of Adsorbent Performance Indicator (API) for various MOFs: M^4CO_2 (orange), previously studied witihin the laboratory (yellow) and NaX and Takeda 5A (green)

Amongst various MOFs presented in Figure 3.23, one can observe that MOFs with small pore size between 3.0 and 6.0 Å, have the highest APIs apart from $Sc_2(BDC\text{-}NO_2)_3$. As indicated for selectivity (section III, Figure 3.13), crystals defects are suspected for the $Sc_2(BDC\text{-}NO_2)_3$ explaining the difference between experimental and simulated values of selectivity and therefore APIs. However, the highest APIs determined for the NH_2-MIL-53(Al), the MIL-69(Al), the MIL-91(Ti) and the MIL-96(Al)) are similar to this of NaX that is very high selective towards carbon dioxide. Thus, this highlights the characteristic of those MOFs to be CO_2 selective. One can observe that those APIs are higher to this of Takeda 5A and others MOFs previously studied within the laboratory, apart from the MIL-127(Fe) for wich it is comparable. From Figure 3.23, one can observe that some of 'Zeolitic Imidazolate Frameworks (ZIFs)' seems to be CO_2 selective for which their CO_2 adsorption are discussed in chapter 4.

Summary

As mentioned at the beginning of the chapter, a first experimental screening (i.e, home-made high-throughput system) allowed us to identify some carboxylate-based MOFs potentially interesting for CO_2 capture. In this chapter, CO_2 adsorption properties of those MOFs were explained with respect to several parameters that are crucial for the choice of an adsorbent, especially in view of post-combustion application. Those parameters are: Working capacity (WC, $cm^3.cm^{-3}$), Adsorption enthalpy extrapolated at zero coverage ($-\Delta_{ads0}\dot{h}$, $kJ.mol^{-1}$); CO_2/N_2 selectivity (α) and moisture conditions. They are summarized in Figure 3.24.

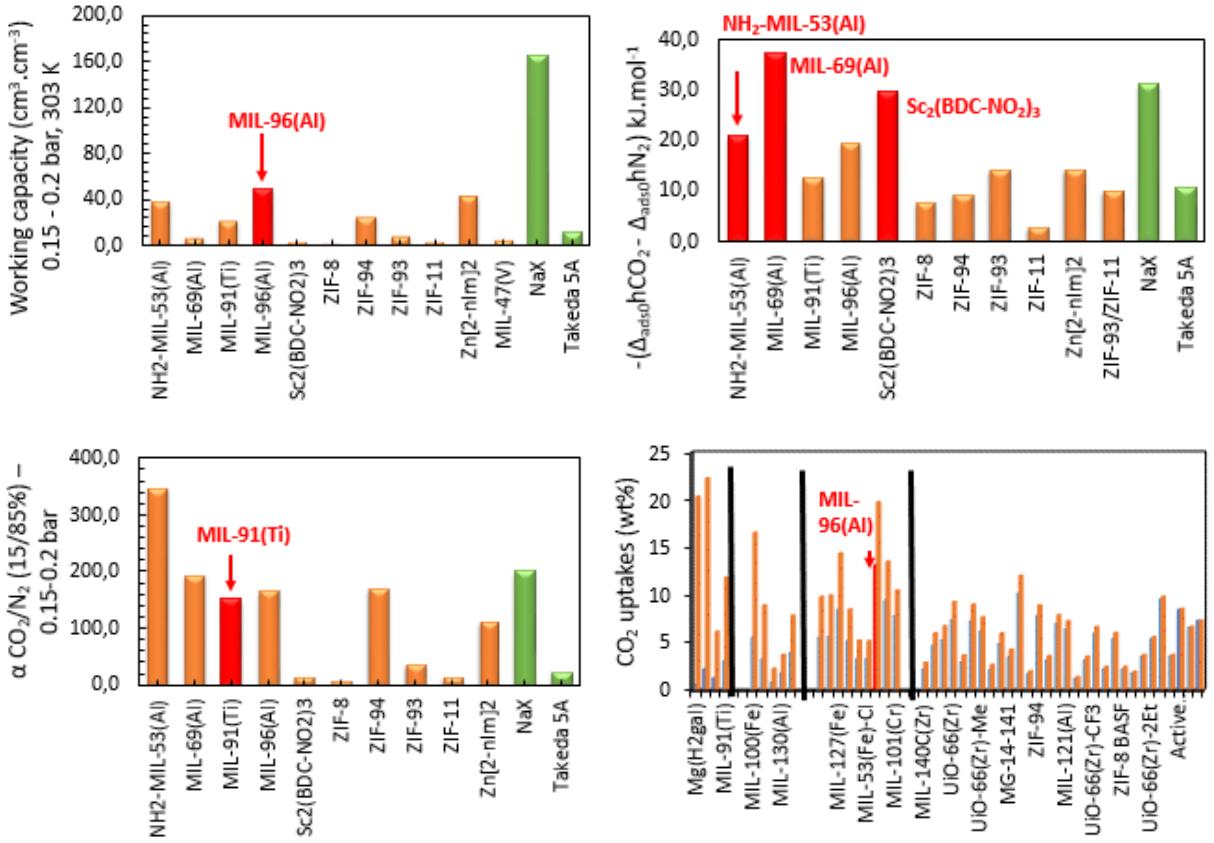

Figure 3.24 – CO_2 adsorption properties of carboxylate-based MOFs were ranked as function of several parameters: Working capacity; Adsorption enthalpy, selectivity and moisture conditions

In the case of working capacity, the MIL-96(Al) has the best CO_2 adsorption capacity in those specific conditions (i.e, a range pressure of 0.15-0.2 bar, at 303K) although it does not outperform this of NaX. We have performed CO_2 adsorption on two different crystal sizes of the MIL-96(Al): micro- and nano-particles (denoted respectively 'MIL-96(Al)-HR' and 'MIL-96(Al)-NP2'). This allowed to correlate particles morphology with external surface area and BET surface area. We have observed that the decrease of crystals size involved both of external surface area and BET surface area. Note that, an increase of 85% of external surface area was not expected.

Regarding the difference of adsorption enthalpies between CO_2 and N_2 extrapolated at zero coverage, three MOFs stand out: the NH_2-MIL-53(Al), the MIL-69(Al) and the $Sc_2(BDC\text{-}NO_2)_3$. We have measured experimentally CO_2 adsorption enthalpy at 303K on the $Sc_2(BDC\text{-}NO_2)_3$ whose the value is -39.2 $kJ.mol^{-1}$. When we compare to CO_2 adsorption enthalpy of the $Sc_2(BDC)_3$ of -32 $kJ.mol^{-1}$ (determined from modelling), we can deduce that nitro groups have a low contribution to increase CO_2 adsorption

enthalpy unlike one would expect. One can assume that it is attributed to a strong confinement effect related to small pore size (i.e, 2.9 Å).
In the literature CO_2 adsorption properties of the MIL-53(Al) were investigated. Unlike the MIL-53(Al), the NH_2-MIL-53(Al) and the MIL-69(Al) are not flexible in the pressure range studied. We have measured CO_2 adsorption enthalpies at 303K. This emphasized high initial CO_2 adsorption enthalpies of -42 and -37 kJ.mol^{-1} respectively for the NH_2-MIL-53(Al) and the MIL-69(Al). This suggests high confinement effects and molecular sieve especially for the MIL-69(Al) in view of pore size of 3 Å.

Amongst predicted selectivities reported for various MOFs, the small pore bis-phosphonate MIL-91(Ti) shows a comparable CO_2/N_2 selectivity. The good CO_2/N_2 selectivity of MIL-91(Ti) results of various parameters that are: preferential CO_2 adsorption sites (i.e, P-OH and NH groups of phosphonate linkers), a high degree of confinement related to its small pore size of 4 Å and consequently molecular sieve that favors the adsorption of molecules with small kinetic diameters.

Flue gas contains some traces or amounts of water that can affect negatively CO_2 adsorption properties of adsorbents. A screening was performed within the laboratory and allowed us to compare CO_2 adsorption capacities of 43 MOFs under 'dry' and 'wet' states. From this screening, we have identified the MIL-96(Al) as a good compromise with a noticeable loss of CO_2 adsorption capacity approximatively of 33%. On the MIL-96(Al), CO_2 uptakes at 0.2 bar and adsorption enthalpies were measured at 303K under flow conditions in the presence of water for various relative humidities (i.e, 10%, 20%, 40%). Maximum of CO_2 uptake and adsorption enthalpy are observed for a relative humidity of 10% that corresponds well with water percentage in post-combustion application. High CO_2 adsorption enthalpy suggests strong host/guest interactions. CO_2 adsorption cycling was performed at 10% of relative humidity and shown constant adsorption properties.

For each parameters reported, we have identified one or several MOFs that stand out. That is why we have used an additional parameter developed within the laboratory, an Adsorbent Performance Indicator (API) to identify best MOFs for targeted application. In the context of post-combustion application, we have fixed the stronger coefficient to the selectivity because selective MOFs are required. This showed that MOFs with smallest pore sizes have highest APIs. Nevertheless, the API is a parameter at the lab scale that gives an overall information on gas separation performances. Moreover, the API does not take into account specific conditions as the presence of water. This does not allow also to correlate textural parameters with CO_2 adsorption properties as well as to predict adsorption properties.

During this chapter, some correlations were envisaged between textural parameters and CO_2 adsorption properties as:

- Working capacity vs BET surface area
- CO_2 uptake vs pore size
- Difference of initial adsorption enthalpies between CO_2 and N_2 vs pore size
- Logarithm (CO_2/N_2 selectivity) vs pore size
- CO_2 capacity loss vs logarithm of Henry's constant of water
- CO_2 initial adsorption enthalpy vs uptake at 0.2 bar

While adsorption is surface phenomenon, we do not have observed correlation between CO_2 working capacity and BET surface area. However for correlations with pores size, one can observe the highest CO_2 adsorption capacity is obtained for an average of pore size of 4.0 Å (i.e, the MIL-96(Al)). Both ~~of~~ the initial CO_2 adsorption enthalpies and predicted CO_2/N_2 selectivities are obtained for a range of pore size between 3.0-6.0 Å.

Such relationships may help to identify materials of potential interest for gas separation applications. This provides data base to the establishment of 'Quantitative Structure-Property Relationship (QSPR)' to predict adsorption properties and/or new structures. In this context, new correlations are developed in the chapter 4 for another kind of separation, CO_2/CH_4, with imidazolate-based MOFs ('Zeolitic Imidazolate Frameworks').

References

[1] J. Rouquerol, F. Rouquerol, P. Llewellyn, G. Maurin, et K. S. W. Sing, *Adsorption by Powders and Porous Solids: Principles, Methodology and Applications*. Academic Press, 2013.

[2] K. T. Chue, J. N. Kim, Y. J. Yoo, S. H. Cho, et R. T. Yang, « Comparison of Activated Carbon and Zeolite 13X for CO2 Recovery from Flue Gas by Pressure Swing Adsorption », *Ind. Eng. Chem. Res.*, vol. 34, n° 2, p. 591-598, févr. 1995.

[3] J. L. C. Rowsell et O. M. Yaghi, « Metal–organic frameworks: a new class of porous materials », *Microporous Mesoporous Mater.*, vol. 73, n° 1, p. 3-14, août 2004.

[4] M. Sabo, A. Henschel, H. Fröde, E. Klemm, et S. Kaskel, « Solution infiltration of palladium into MOF-5: synthesis, physisorption and catalytic properties », *J. Mater. Chem.*, vol. 17, n° 36, p. 3827-3832, sept. 2007.

[5] A. D. Wiersum, J.-S. Chang, C. Serre, et P. L. Llewellyn, « An Adsorbent Performance Indicator as a First Step Evaluation of Novel Sorbents for Gas Separations: Application to Metal–Organic Frameworks », *Langmuir*, vol. 29, n° 10, p. 3301-3309, mars 2013.

[6] K. Adil *et al.*, « Gas/vapour separation using ultra-microporous metal–organic frameworks: insights into the structure/separation relationship », *Chem. Soc. Rev.*, vol. 46, n° 11, p. 3402-3430, juin 2017.

[7] A. Sayari, Y. Belmabkhout, et R. Serna-Guerrero, « Flue gas treatment via CO2 adsorption », *Chem. Eng. J.*, vol. 171, n° 3, p. 760-774, juill. 2011.

[8] P. L. Llewellyn *et al.*, « High Uptakes of CO2 and CH4 in Mesoporous Metal—Organic Frameworks MIL-100 and MIL-101 », *Langmuir*, vol. 24, n° 14, p. 7245-7250, juill. 2008.

[9] Q. Yang *et al.*, « Probing the adsorption performance of the hybrid porous MIL-68(Al): a synergic combination of experimental and modelling tools », *J. Mater. Chem.*, vol. 22, n° 20, p. 10210-10220, mai 2012.

[10] P. L. Llewellyn *et al.*, « Structural Origin of Unusual CO2 Adsorption Behavior of a Small-Pore Aluminum Bisphosphonate MOF », *J. Phys. Chem. C*, vol. 119, n° 8, p. 4208-4216, févr. 2015.

[11] S. R. Miller *et al.*, « Structural Transformations and Adsorption of Fuel-Related Gases of a Structurally Responsive Nickel Phosphonate Metal−Organic Framework, Ni-STA-12 », *J. Am. Chem. Soc.*, vol. 130, n° 47, p. 15967-15981, nov. 2008.

[12] M. Benzaqui *et al.*, « Revisiting the Aluminum Trimesate-Based MOF (MIL-96): From Structure Determination to the Processing of Mixed Matrix Membranes for CO2 Capture », *Chem. Mater.*, vol. 29, n° 24, p. 10326-10338, déc. 2017.

[13] S. S.-Y. Chui, S. M.-F. Lo, J. P. H. Charmant, A. G. Orpen, et I. D. Williams, « A Chemically Functionalizable Nanoporous Material [Cu3(TMA)2(H2O)3]n », *Science*, vol. 283, n° 5405, p. 1148-1150, févr. 1999.

[14] P. D. C. Dietzel, R. E. Johnsen, R. Blom, et H. Fjellvåg, « Structural Changes and Coordinatively Unsaturated Metal Atoms on Dehydration of Honeycomb Analogous Microporous Metal–Organic Frameworks », *Chem. – Eur. J.*, vol. 14, n° 8, p. 2389-2397, mars 2008.

[15] G. Férey *et al.*, « A Chromium Terephthalate-Based Solid with Unusually Large Pore Volumes and Surface Area », *Science*, vol. 309, n° 5743, p. 2040-2042, sept. 2005.

[16] A. Knebel, S. Friebe, N. C. Bigall, M. Benzaqui, C. Serre, et J. Caro, « Comparative Study of MIL-96(Al) as Continuous Metal–Organic Frameworks Layer and Mixed-Matrix Membrane », *ACS Appl. Mater. Interfaces*, vol. 8, n° 11, p. 7536-7544, mars 2016.

[17] T. Loiseau *et al.*, « MIL-96, a Porous Aluminum Trimesate 3D Structure Constructed from a Hexagonal Network of 18-Membered Rings and µ3-Oxo-Centered Trinuclear Units », *J. Am. Chem. Soc.*, vol. 128, n° 31, p. 10223-10230, août 2006.

[18] P. L. Llewellyn et G. Maurin, « Gas adsorption microcalorimetry and modelling to characterise zeolites and related materials », *Comptes Rendus Chim.*, vol. 8, n° 3, p. 283-302, mars 2005.

[19] G. D. Pirngruber *et al.*, « A Method for Screening the Potential of MOFs as CO2 Adsorbents in Pressure Swing Adsorption Processes », *ChemSusChem*, vol. 5, n° 4, p. 762-776, avr. 2012.

[20] R. S. Pillai, V. Benoit, A. Orsi, P. L. Llewellyn, P. A. Wright, et G. Maurin, « Highly Selective CO2 Capture by Small Pore Scandium-Based Metal–Organic Frameworks », *J. Phys. Chem. C*, vol. 119, n° 41, p. 23592-23598, oct. 2015.

[21] S. R. Miller, P. A. Wright, C. Serre, T. Loiseau, J. Marrot, et G. Férey, « A microporous scandium terephthalate, Sc2(O2CC6H4CO2)3, with high thermal stability », *Chem. Commun.*, vol. 0, n° 30, p. 3850-3852, juill. 2005.

[22] S. R. Miller *et al.*, « Single Crystal X-ray Diffraction Studies of Carbon Dioxide and Fuel-Related Gases Adsorbed on the Small Pore Scandium Terephthalate Metal Organic Framework, Sc2(O2CC6H4CO2)3 », *Langmuir*, vol. 25, n° 6, p. 3618-3626, mars 2009.

[23] J. P. S. Mowat *et al.*, « Structural Chemistry, Monoclinic-to-Orthorhombic Phase Transition, and CO2 Adsorption Behavior of the Small Pore Scandium Terephthalate, Sc2(O2CC6H4CO2)3, and Its Nitro- And Amino-Functionalized Derivatives », *Inorg. Chem.*, vol. 50, n° 21, p. 10844-10858, nov. 2011.

[24] G. E. Cmarik, M. Kim, S. M. Cohen, et K. S. Walton, « Tuning the Adsorption Properties of UiO-66 via Ligand Functionalization », *Langmuir*, vol. 28, n° 44, p. 15606-15613, nov. 2012.

[25] « Single Crystal X-ray Diffraction Studies of Carbon Dioxide and Fuel-Related Gases Adsorbed on the Small Pore Scandium Terephthalate Metal Organic Framework, Sc2(O2CC6H4CO2)3 - Langmuir (ACS Publications) », 20-août-2017. [En ligne]. Disponible sur: http://pubs.acs.org/doi/abs/10.1021/la803788u. [Consulté le: 20-août-2017].

[26] Y. Liu, J.-H. Her, A. Dailly, A. J. Ramirez-Cuesta, D. A. Neumann, et C. M. Brown, « Reversible Structural Transition in MIL-53 with Large Temperature Hysteresis », *J. Am. Chem. Soc.*, vol. 130, n° 35, p. 11813-11818, sept. 2008.

[27] I. Beurroies *et al.*, « Using Pressure to Provoke the Structural Transition of Metal–Organic Frameworks », *Angew. Chem. Int. Ed.*, vol. 49, n° 41, p. 7526-7529, oct. 2010.

[28] S. Bourrelly, P. L. Llewellyn, C. Serre, F. Millange, T. Loiseau, et G. Férey, « Different Adsorption Behaviors of Methane and Carbon Dioxide in the Isotypic Nanoporous Metal Terephthalates MIL-53 and MIL-47 », *J. Am. Chem. Soc.*, vol. 127, n° 39, p. 13519-13521, oct. 2005.

[29] I. Senkovska, F. Hoffmann, M. Fröba, J. Getzschmann, W. Böhlmann, et S. Kaskel, « New highly porous aluminium based metal-organic frameworks: Al(OH)(ndc) (ndc = 2,6-naphthalene dicarboxylate) and Al(OH)(bpdc) (bpdc = 4,4'-biphenyl dicarboxylate) », *Microporous Mesoporous Mater.*, vol. 122, n° 1–3, p. 93-98, juin 2009.

[30] J. Gascon, U. Aktay, M. D. Hernandez-Alonso, G. P. M. van Klink, et F. Kapteijn, « Amino-based metal-organic frameworks as stable, highly active basic catalysts », *J. Catal.*, vol. 261, n° 1, p. 75-87, janv. 2009.

[31] E. Stavitski *et al.*, « Complexity behind CO2 Capture on NH2-MIL-53(Al) », *Langmuir*, vol. 27, n° 7, p. 3970-3976, avr. 2011.

[32] Q. Yang *et al.*, « A Water Stable Metal–Organic Framework with Optimal Features for CO2 Capture », *Angew. Chem.*, vol. 125, n° 39, p. 10506-10510, sept. 2013.

[33] V. Benoit *et al.*, « MIL-91(Ti), a small pore metal–organic framework which fulfils several criteria: an upscaled green synthesis, excellent water stability, high CO2 selectivity and fast CO2 transport », *J. Mater. Chem. A*, vol. 4, n° 4, p. 1383-1389, janv. 2016.

[34] N. Chanut *et al.*, « Screening the Effect of Water Vapour on Gas Adsorption Performance: Application to CO2 Capture from Flue Gas in Metal–Organic Frameworks », *ChemSusChem*, vol. 10, n° 7, p. 1543-1553, avr. 2017.

[35] V. Benoit *et al.*, « A promising metal–organic framework (MOF), MIL-96(Al), for CO2 separation under humid conditions », *J. Mater. Chem. A*, vol. 6, n° 5, p. 2081-2090, janv. 2018.

Chapter 4 – Correlations establishment to assess MOFs CO_2 performances

Table of contents

Chapter 4 - Correlations establishment to assess MOFs CO_2 performances

I. Introduction

In the same way as for low pressure conditions, each parameters: working capacity, adsorption enthalpy, selectivity and an adsorbent performance indicator (API) were calculated for high pressure conditions (between 1 and 15 bar) approaching to pre-combustion process (i.e, reforming of methane from natural gas) for the ten selected MOFs from screening (chapter 3). The Figures corresponding to each parameters with a comparison to others MOFs and reference materials are provided in Annex F. Although the API is more useful at the laboratory scale, it gives an indication on CO_2 separation performances of adsorbents [1]. Thus, the APIs for the ten MOFs selected were calculated for CO_2/CH_4 gas separation and equally compared to those of others MOFs whose CO_2 adsorption properties have been already characterized within the laboratory as well as to those of reference materials NaX and Takeda 5A (Figure 4.1). To determine APIs, we fixed coefficients as follows: 0.5, 1 and 1 respectively for the selectivity, the working capacity and the adsorption enthalpy (details provided in chapter 2, section F). For CO_2/CH_4 separation at high pressures, adsorbents with good CO_2 adsorption capacities are favored and that is why a high coefficient was not fixed for selectivity unlike to CO_2/N_2 separation as noted in chapter 3.

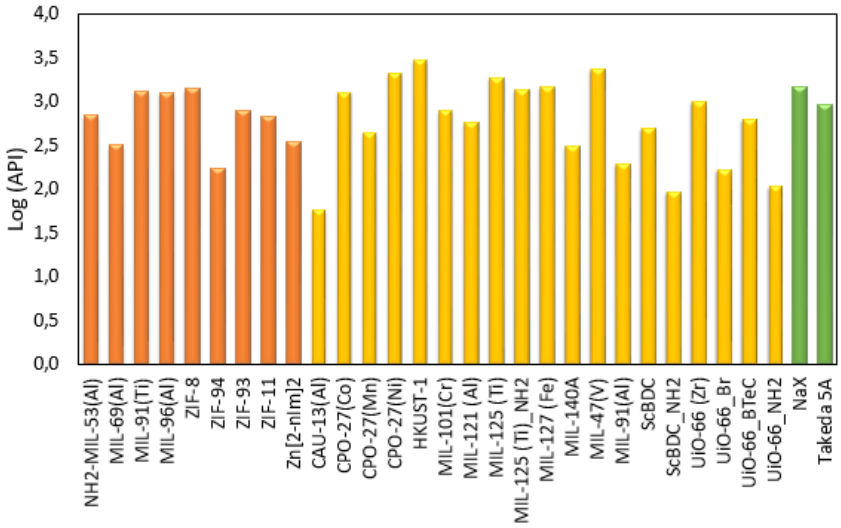

Figure 4.1 – Logarithm of adsorbent performance indicator (API) against various adsorbents: M^4CO_2 MOFs (orange), MOFs previously characterized within the laboratory (yellow) as well as NaX and Takeda 5A (green)

From Figure 4.1, one can observe that the APIs of carboxylate-based MOFs and Zeolitic Imidazolate Frameworks (ZIFs) are in the same order of magnitude and comparable to those of MOFs already characterized within the laboratory and those of NaX and Takeda 5A. Note that, the characterization of CO_2 adsorption properties of some MOFs (yellow) was performed earlier the M^4CO_2 project within the laboratory with the aim to assess best MOFs for CO_2/CH_4 separation [2].

As mentioned in chapter 3, lots of data were collected experimentally during this thesis both on textural properties and on adsorption properties of MOFs: BET surface area, pore volume, CO_2 uptakes, and adsorption enthalpies for which some of them are used to determine selectivity that is a major factor in the choice of an adsorbent for a gas separation. However such amount of experimental data, requires tools based on models, usually mathematical, allowing to predict separation performances of

adsorbents (i.e, for gas separation applications) against structural or/ and physicochemical features. In recent years, those types of models were developed and called quantitative structure-properties relationship (QSPR).

Firstly in this chapter, we provided principles and interests of QSPR models to various fields. Thereafter those QSPR models were explained for a specific application: CO_2 capture by Metal-Organic Frameworks as adsorbents.

Secondly, we attempted to correlate textural properties with adsorption features of MOFs towards a 'QSPR' or a 'descriptor-property' approach that did not require specific models. Indeed, microscopic features as: pore size, surface polarity and pore volume were correlated with a macroscopic property: CO_2 maximum excess uptake (i.e, CO_2 amount adsorbed at adsorbent saturation) to highlight some linear trends. Owing to the variety of MOFs (pore shape, pore size, chemistry …) studied in this thesis, those correlations were restricted to a sub-class of microporous MOFs: Zeolitic Imidazolate Frameworks (ZIFs) due to their well-defined porosity as well as their chemical and thermal stability. Amongst the variety of ZIFs based on zeolite topologies, we have focused this work on two kinds of topologies: Sodalite (ZIF-8, ZIF-94) and Rhomboedral (ZIF-93, ZIF-11).

II. Quantitative structure-property relationship (QSPR) models

1. History of QSPR models

Quantitative structure-activity relationships (QSAR) and quantitative structure-property relationships (QSPR) are based on correlation developments between the structure and targeted properties of compounds. The strategy of QSAR and QSPR models is to obtain the optimum quantitative relationship which can be used to predict compound properties including those which are unknown. This approach would allow to adjust and to select compounds with desirable properties for given applications.

The development of quantitative structure-property relationships dates back more than one century with some pioneering works. Indeed, Crum-Brown and Fraser provided the first formulation of a quantitative relationship between 'physiological activity' and 'chemical structure' in 1868 [3]. Later, Mills developed structure-property relationships to predict both melting and boiling points of a homologous series of organic molecules in 1884 [4]. In 1935, Hammett highlighted the existence of a relationship between the rate of reaction and equilibrium constants of organic compounds [5].

In this field, a breakthrough was made with the works of Hansch and Fujita [6] and Free and Wilson [7] in 1963 and 1964 where mathematical models were developed to describe structure-activity relationship in biological systems. Hansch and Fujita used regression analyses to correlate the hydrophobic, electronic and steric properties on biological activity. While, Free and Wilson employed mathematical models to describe the effect of series of chemical analogs on biological activity.

Structure-activity relationship have been widely developed in the pharmaceutical field drug design [8], [9]. However, QSPR models are currently being extended to of single molecules, polymers, surfactants properties, interaction between various species, gas adsorption [10].

The principle of QSPR and QSAR analysis is to correlate macroscopic properties against microscopic quantitative molecular properties denominated descriptors by means of mathematical models:

$$Properties = f(Descriptors) \quad (4.1)$$

2. QSPR models applied to porous materials

In the field of gas separation, some studies have been reported so far which set up quantitative structure-property relationship (QSPR) models for various porous materials [11]–[16].

A study has been conducted by Gogotsi *et al.* on microporous carbide-derived carbons (CDCs) comparing their H_2 adsorption capacities (at 77K, 1 atm) for different materials with tunable pore size and specific surface area varying respectively from 0.5 to 1.5 Å and 500 to 2000 $m^2.g^{-1}$ [17].

They observed a linear trend when H_2 adsorption capacities are normalized with respect to specific surface area and plotted as function of the pore size. This evidenced that highest H_2 adsorption capacities are obtained for smallest pores (< 20Å) rather than larger pores (> 20Å). Thus, H_2 adsorption which occurs on CDCs seems to be governed mainly by small pores and indirectly to specific surface area.
In another study performed by Gogotsi *et al.*on CDCs for H_2 storage, they also observed a linear trend when H_2 excess uptakes are plotted against specific surface area [18]. However, when H_2 uptakes at 1 bar are plotted there is no linear trend suggesting that pore size or pore shape can play an important role. From the plot of H_2 excess uptakes normalized to specific surface area against pore sizes, they identified that a pore size range centered on 7 Å are more efficient for H_2 adsorption. Indeed, they suggest that H_2 adsorption is governed by smallest pores in which strong carbon-hydrogen interactions (pore wall) occur. For larger pores, H_2-H_2 interactions have a low contribution to H_2 adsorption.

Hydrogen adsorption at 77K on various MOFs has been performed by Noguera-Diaz *et al.* [19]. They demonstrated relatively linear relationships when H_2 maximum excess uptakes are plotted as a function of specific surface area and pore volume. Indeed, maximum H_2 amounts adsorbed are obtained for MOFs having highest specific surface area and pore volume with a certain degree of scattering. These linear trends show a higher degree of scattering for lower surface specific areas which can be explained by small pore size and the difference of pore volume. When H_2 maximum excess uptakes are plotted against specific surface area, the UiO-66 and UiO-67 materials outperform trend line highlighting the effect of topology compared to other MOFs as: MOF-74, HKUST-1, ZIF-11 etc. While, the linker functionalization effect is evidenced with the IRMOF-1 and IRMOF-3 materials, where H_2 maximum excess uptake is slightly higher for IRMOF-1. However, no relationships have been found which correlate H_2 maximum excess uptakes with pore size, probably due to the diversity of pore sizes or pore shapes of the MOFs under consideration.

Some works have reported QSPR models based on computational tools devoted to methane storage in a huge database of theoretical Metal-Organic Frameworks. Fernandez *et al.* conducted a quantitative structure-property relationship (QSPR) analysis on 130 000 hypothetical MOFs for which geometric descriptors are: volumetric surface area, pore diameter and void fraction against methane adsorption capacity as property at 1, 35 and 100 bar at 298K [20]. They used various mathematical tools including multilinear regression (MLR), decision trees (DTs) and nonlinear support vector machines (SVMs).

They performed a univariate analysis that correlates individually geometric descriptors: volumetric surface area, pore diameter and void fraction against methane adsorption capacity at 35 and 100 bar at 298K. This showed that maximum methane uptake are obtained for MOFs having pore diameter ranges of 4-9 Å and 8 Å respectively at 35 and 100 bar. Methane uptakes increase linearly as a function of volumetric surface area at 35 and 100 bar with regression coefficient of R^2 = 0.789 and 0.837 respectively.

Regarding void fraction, no relationship was found because methane uptakes increase for void fractions up to 0.8 and then decrease. However, the main drawback of a univariate analysis is that this does not allow to identify the interactions between properties which play a role on methane uptakes. Thus, MLR analysis provided two models to predict methane uptakes at 35 and 100 bar combining the dominant pore diameter, the void fraction and the gravimetric surface area as geometrical descriptors. In view of regression coefficients, MLR models predicts more accurate methane uptakes than the univariate analysis. The void fraction seems to have a strong contribution in the MLR models determined.

Some trends emerged from the construction of decision tree models: high methane uptakes are obtained at 35 bar for MOFs having densities and void fractions above 0.43 and 0.52 $g.cm^{-1}$ respectively against 0.33 $g.cm^{-1}$ and 0.62 at 100 bar.

Thus, the choice of MOFs should be based on predicted performance and experimental constraints (i.e, synthesis conditions, equipment, cost …).

In the context of CO_2 capture, the study conducted by Wu *et al.* established a QSPR model for a large series of MOFs (105) to predict selectivity of a binary mixture CO_2/N_2 (15/ 85%, 1 bar, 298K) near to post-combustion conditions by means of computational tools [21].

Several descriptors have been considered: the difference in isosteric heats between CO_2 and N_2 at infinite dilution (ΔQ_{st}^0), the specific accessible surface area (S_{acc}), the free volume (V_{free}) and the porosity (φ) against the CO_2/N_2 selectivity (S) at 1 bar, 298K as predicted property. Among these descriptors, only ΔQ_{st}^0 and φ were chosen to build a QSPR model which are more representative of industrial pressure conditions. The optimal QSPR model is an exponential relation connecting (S) and the ratio $\Delta Q_{st}^0/\varphi$. There is a good agreement of predicted CO_2/N_2 selectivities obtained from this exponential relation, those simulated and those found in literature validating this QSPR model. From a careful analysis of this QSPR model, some trends emerged: a decrease of porosity involves an increase of CO_2/ N_2 selectivity; a ΔQ_{st}^0 minimal value of 8 $kJ.mol^{-1}$ is needed to get CO_2/ N_2 selectivity above 40, an increase of ΔQ_{st}^0 and a decrease of φ can contribute to improve CO_2/ N_2 selectivity. They validated these conclusions by applying this model to UiO-66(Zr) and its functionalized analogues UiO-66(Zr)-NH_2 and UiO-66(Zr)-$(CF_3)_2$. Indeed, the ΔQ_{st}^0 increase, the φ decrease or the combination of both (ΔQ_{st}^0 increase and φ decrease) contribute to enhance CO_2/ N_2 selectivity.

Figure 4.2 is a scheme summarizing microscopic and macroscopic descriptors which can be considered in QSPR models for gas separation applications of MOFs.

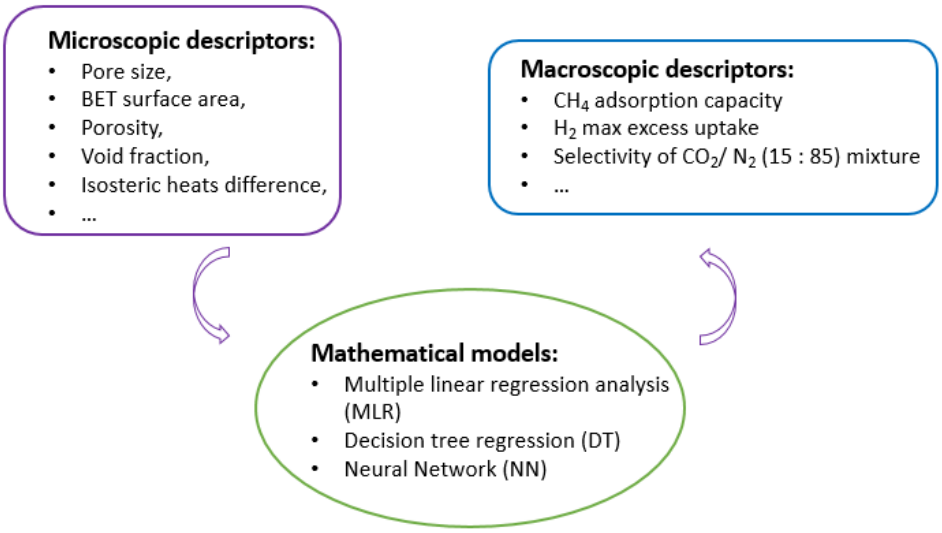

Figure 4.2 - Illustration of microscopic descriptors, macroscopic properties as well as mathematical models which can be used in QSPR models applied to MOFs

III. Strategy set up to get correlations towards 'descriptor-property'

During this thesis, we attempted to correlate various parameters of adsorption to get type 'descriptor-property' trends. Note that in this context, only correlations and no mathematical models specific to QSPR field were investigated, that is why we mention a 'QSPR' or a 'descriptor-property' approach.

The first descriptor selected was pore size often used to describe adsorbents in the field of adsorption. Indeed, one can suppose that size and shape of pores contribute to various effects as: confinement and molecular sieve that are determining for gas separation of small molecules. We investigated various types of 'property' that determine the choice of an adsorbent as: CO_2 uptakes at 0.15-0.2 bar (see chapter 3), difference of initial CO_2 and N_2 adsorption enthalpies (see chapter 3) for which no linear trends were observed against MOFs pore size although MOFs with pore size around 4.0-5.0 Å stand out.

However, we reported initial CO_2 adsorption enthalpies against pore size for specific MOFs (Figure 4.3) to investigate various effects: functionalization, change of linker and metal to get trends. The MOFs corresponding to various effects studied are respectively: NH_2-MIL-53(Al), MIL-69(Al), MIL-47(V) compared to the reference MIL-53(Al). Initial CO_2 adsorption enthalpy was selected as the property because it gives an information on adsorbent-adsorbate interactions strength within pores during adsorption.

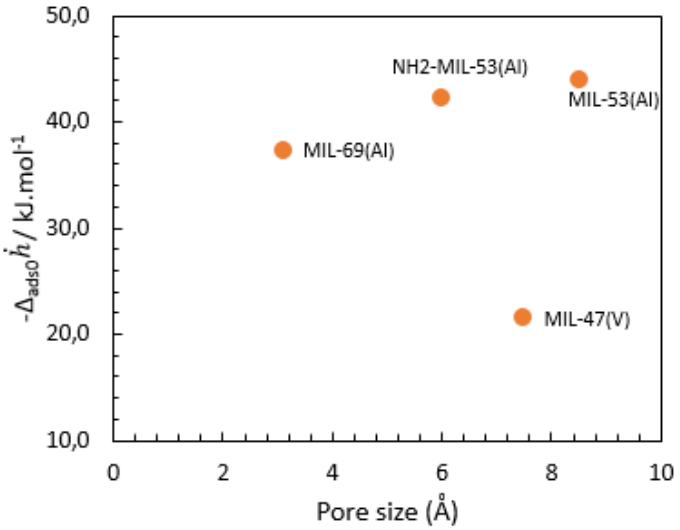

Figure 4.3 – Initial CO_2 adsorption enthalpies against pore size for four MOFs: MIL-69(Al), NH_2-MIL-MIL-53(Al), MIL-47(V) and MIL-53(Al)

Figure 4.3 shows that there is no linear trend between initial CO_2 adsorption enthalpies and pores size for the NH_2-MIL-53(Al), the MIL-69(Al), the MIL-47(V) and the MIL-53(Al). Pores size of the MIL-69(Al) and the NH_2-MIL-53(Al) are smaller via linker change (NDC against BDC) as well as linker functionalization (amino groups grafted). However, one can observe that this does not contribute to outperform initial CO_2 adsorption enthalpy of the MIL-53(Al). As mentioned in chapter 3, amino groups of the MIL-53(Al) have a low interaction with CO_2 molecules due to their role to maintain the structure in narrow pore [22]. One can suppose that the small pore size of the MIL-69(Al) prevents stronger CO_2 interactions against this of MIL-53(Al). While the metal change, aluminum against vanadium, contributed significantly to improve initial CO_2 adsorption enthalpy from 23.2 kJ.mol^{-1} up to 43.9 kJ.mol^{-1} respectively for the MIL-47(V) and the MIL-53(Al).

There is no clear correlation that can be deduced from Figure 4.3 regarding linker change, linker functionalization or metal change for those MOFs. However, it would be interesting to extend this type of 'pore size-initial CO_2 adsorption enthalpy' correlation to others MOFs systems to emerge trends.

Amongst various parameters to select an adsorbent, selectivity is a determining factor highlighting affinity of an adsorbent for a gas in a mixture. Thus, we reported CO_2/CH_4 predicted selectivities (50/50%) calculated at 15 bar as the property against pores size (Figure 4.4).

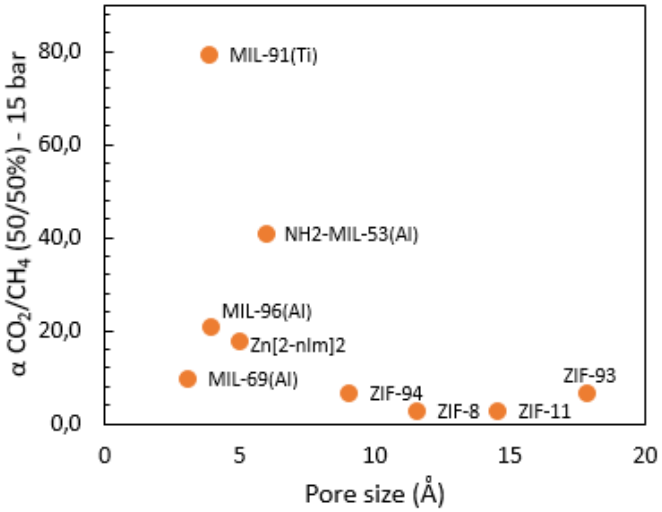

Figure 4.4 – CO_2/CH_4 predicted selectivities (50/50%) at 15 bar as function of pore size for various MOFs

From Figure 4.4, one can observe that there is no trend between CO_2/CH_4 predicted selectivities and pores size as for CO_2/N_2 predicted selectivities for low pressure conditions (chapter 3). This suggests that MOFs pores size do not govern their performances in terms of selectivity.

Based on the work of Gogotsi *et al.* [23], we have reported CO_2 maximum uptakes normalized to specific surface area as function of pore size (Figure 4.5).

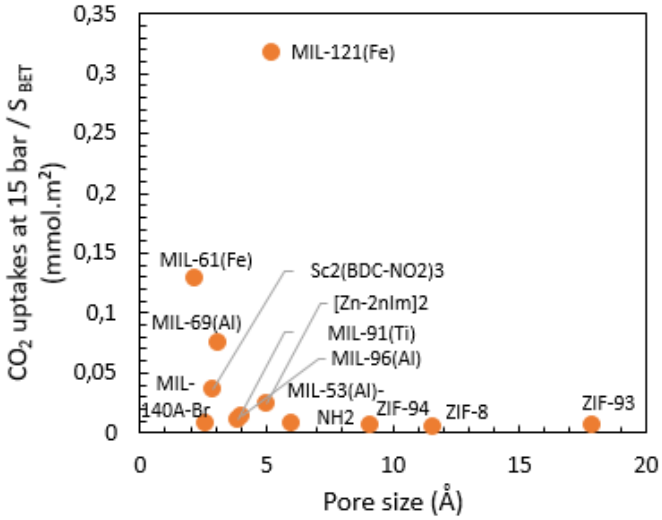

Figure 4.5 – A type of 'descriptor-property' trend illustrating CO_2 uptakes at the isotherm plateau (maximum) normalized-to BET surface area against pore size for various MOFs

From Figure 4.5, there is no linear trend between CO_2 maximum uptakes normalized to BET surface area and pores size for MOFs. One can suppose that it is related to the diversity of pore shape and pore size distribution of those MOFs. Moreover this is in agreement with some works highlighting equally no correlation with pore size as descriptors due to the diversity of pore shape and pore size of MOFs [18], [20], [21].

Those three correlations of type 'descriptor-property' with pores size as descriptor showed no trends probably due to the diversity of pore sizes and pore shapes of these MOFs. However amongst these MOFs, four zeolitic imidazolate frameworks (ZIFs) were identified as potential adsorbents to establish 'descriptor-property' trends due to their well-defined porosity and to their topologies [24]. Indeed as mentioned in chapter 1, these ZIFs (i.e, ZIF-8, ZIF-94, ZIF-93 and ZIF-11) possess the same metal ion (i.e, Zn^{2+}), various linkers and two types of topologies that are sodalite (SOD) and rhomboedral (RHO) yielding to well-defined windows and cages.

Since MOFs pores size do not appear to have an influence on their performances for high pressure conditions, we selected two others descriptors that are surface polarity and pore volume. Based on literature we chose CO_2 maximum uptake as property due to the possibility of various isotherm shapes as already observed for MIL-53 [29], ZIF-7 discovered in 2003 [30] that undergo a gate-opening effect upon variation of CO_2 partial pressure or temperature. Moreover as mentioned earlier for high pressure conditions, adsorbents with a good CO_2 adsorption capacity are favored, then 'descriptor-property' correlations are presented in the following section.

IV. Investigation of correlation based on 'descriptor-property'

1. First factor: surface polarity

The surface polarity of an adsorbent was defined as the difference of initial adsorption enthalpies between a quadrupolar (CO_2) and an apolar (CH_4) molecule. Therefore, CO_2 maximum uptakes against the differences of initial adsorption enthalpy between CO_2 and CH_4 were plotted in Figure 4.6 for selected ZIFs and other porous materials. The aim is to probe the effect of adsorbent surface polarity on CO_2 adsorbed amounts at saturation (i.e, uptakes taken at 15 bar).

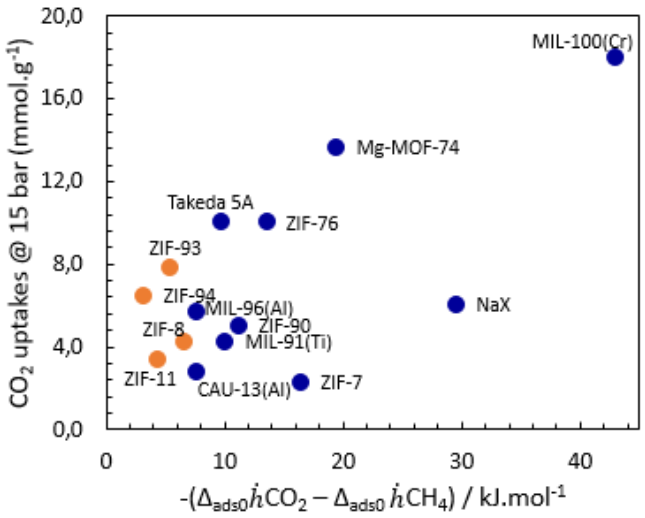

Figure 4.6 - CO_2 maximum uptake as function of differences of initial CO_2 and CH_4 adsorption enthalpies or surface polarity effect for ZIFs materials characterized and others materials

From Figure 4.6, a linear trend seems to emerge with a certain degree of scattering, indeed the regression coefficient is not optimal. One can observe that ZIFs possess low surface polarities that are in the same order of magnitude with others adsorbents apart from the Mg-MOF-74, the MIL-100(Cr) or the NaX. These latest contain specific adsorption sites: some CUS for the Mg-MOF-74 and the MIL-100(Cr) while Na^+ counter cation for NaX. This suggests that CO_2 uptakes at adsorbent saturation increases as the adsorbent surface becomes polarizable.

The analysis of interactions of those ZIFs with CO_2 is provided in Figure 4.7 via CO_2 adsorption enthalpy profiles at 303K.

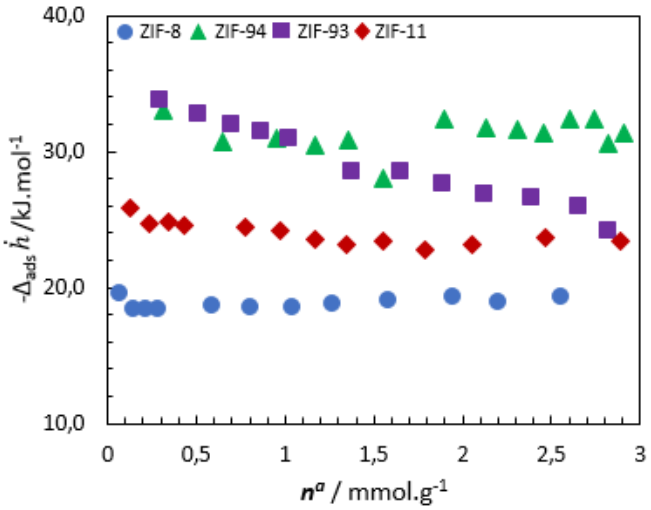

Figure 4.7 – CO_2 adsorption enthalpy profiles at 303K plotting differential adsorption enthalpies against amounts adsorbed for the ZIF-8 (blue circle), the ZIF-94 (green triangle), the ZIF-93 (purple square) and the ZIF-11 (red lozenge)

From Figure 4.7, the CO_2 adsorption enthalpy profile of ZIF-93 seems to be relatively heterogeneous; shown by a decreasing enthalpy of adsorption with coverage. The CO_2 adsorption enthalpy extrapolated to zero coverage is around -35 kJ.mol^{-1} against -27.5 kJ.mol^{-1} at high surface coverage respectively for the ZIF-93 and ZIF-11, whereas the CH_4 adsorption enthalpies are comparable (see Annex F). This can suggest that ZIF-93 possesses some specific CO_2 adsorption sites at low coverage. Unlike to the ZIF-93, CO_2 adsorption enthalpy profile of ZIF-11 is relatively homogeneous, i.e. with a relatively horizontal profile, highlighting adsorption sites of same magnitude. The average value of CO_2 adsorption enthalpy for ZIF-11 is approximatively of -23.5 kJ.mol^{-1}.

As observed in Figure 4.6, in both cases with the ZIF-11 and the ZIF-93, CO_2 amounts adsorbed at saturation increase proportionally with the surface polarity. These two compounds differ mainly by the functionalization on the imidazole unit, a benzene ring and a carbonyl group respectively for the ZIF-11 and the ZIF-93. This suggests that carbonyl groups contribute to the increase of the surface polarity and consequently to the adsorbent affinity for a quadrupolar molecule such as CO_2. Moreover, this is consistent with water adsorption isotherm profiles suggesting a more hydrophilic surface for the ZIF-93 (see Annex F).

From Figure 4.7, CO_2 adsorption enthalpy profiles of the ZIF-8 and ZIF-94 seem to be relatively homogeneous. This highlights that there are no CO_2 specific adsorption sites especially at low pressures. This is confirmed by the negligible difference between the values of CO_2 adsorption enthalpy extrapolated to zero and higher coverage which are -33 and -32.2 kJ.mol^{-1} for the ZIF-94 as well as -20 and -19.3 kJ.mol^{-1} for the ZIF-8 (larger than the liquefaction adsorption enthalpy of CO_2, -17.2 kJ.mol^{-1}). The higher CO_2 adsorption enthalpy for the ZIF-94 could be explained by the influence of organic ligand chemistry as well as the lower cage size. CO_2 adsorption enthalpies of the ZIF-94 and especially of the ZIF-8 are lower than some other microporous MOFs and zeolites such as: MIL-91(Ti) (-47 kJ.mol^{-1}) [25], $Sc_2(BDC\text{-}NH_2)_3$ (-45.3 kJ.mol^{-1}) [26], NaX (-49 kJ.mol^{-1} [27]. The CO_2 adsorption enthalpy of the ZIF-94 is however comparable to that of UiO-66(Zr)-BTEC (-34.8 kJ.mol^{-1}) [28]. Regarding CH_4 adsorption enthalpies, the average for the ZIF-8 and the ZIF-94 are respectively -15.0 kJ.mol^{-1} and -25.8 kJ.mol^{-1} (see Annex F).

Regarding the ZIF-8, a low surface polarity is observed that is in agreement with its hydrophobic surface deduced from water adsorption isotherm (see Annex 7) and results found in literature. Higher CO_2 maximum excess uptakes of the ZIF-8 (compared to these of the ZIF-11, the ZIF-93 and the ZIF-94) can be explained by its higher pore volume rather than its surface polarity.

However, for comparable surface polarities (ZIF-93/ ZIF-94 and ZIF-76/ ZIF-7), CO_2 amounts adsorbed at saturation seem to be governed by another parameter rather than the surface ability to be polarizable. One assumes that it is related to pore volume, this is the second descriptor that we selected and detailed in the following section.

2. Second parameter: pore volume

The pore volume was selected as a descriptor and were determined from the exploitation of the nitrogen adsorption isotherm at 77K using Brunauer Emett and Teller (BET) method. CO_2 maximum uptakes measured at 303K were plotted as a function of pore volume for the ZIF-8, -93, -94 as well as other materials found in literature (Figure 4.8) (references in Annex F).

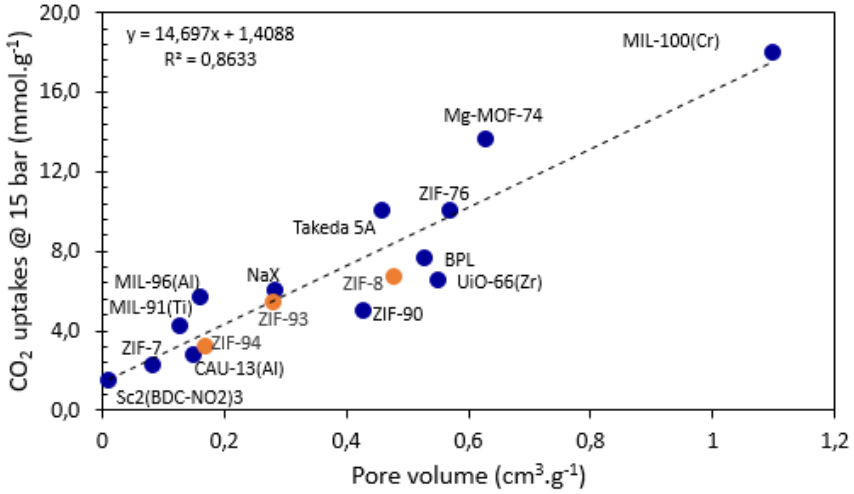

Figure 4.8 – Linear trend towards a 'descriptor-property' approach plotting CO_2 maximum uptake as function of pore volume

From Figure 4.8, one can observe a relatively linear correlation with a certain degree of scattering between CO_2 maximum uptakes and pore volume. Similar correlations were observed for hydrogen adsorption in the case of microporous MOFs [19]. CO_2 maximum uptakes increase proportionally to pore volume suggesting that there are no specific CO_2 interactions which predominate at high pressure unlike to low surface coverage. Therefore, CO_2 adsorbent saturation does not seem to be governed by the materials chemistry.

Regarding ZIF's materials characterized and reported from literature of this work, CO_2 uptake of ZIF-76 outperform those of others ZIF's. The cage size of ZIF-76 (12.2 Å) is lower than those of ZIF-93 (17.9 Å) and ZIF-11 (14.6 Å) but comparable to those of ZIF-8 (11.4 Å), ZIF-90 (10.8 Å) as well as pore volume. This highlights that 'LTA (Linde Type A)' topology outperforms 'SOD' and 'RHO' topologies for CO_2 adsorption.

CO_2 maximum uptakes of the ZIF-93, ZIF-8 and ZIF-90 are comparable to this of zeolite NaX and lower than those of activated carbon such as Takeda 5A. While CO_2 uptake of the ZIF-94 is in the range of

other microporous MOFs having small pore sizes such as ZIF-7, CAU-13(Al) or MIL-91(Ti) and is consistent with its pore volume.

CO_2 adsorption capacities of the ZIF-8, the ZIF-94, the ZIF-93 and the ZIF-11 were analyzed via adsorption isotherms in Figure 4.9.

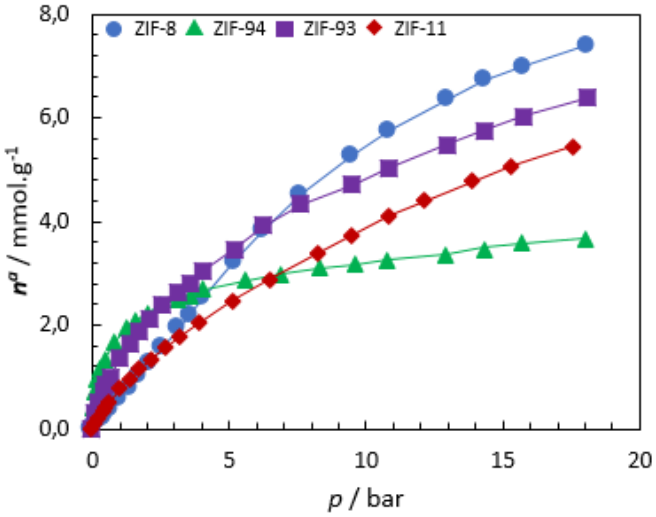

Figure 4.9 – CO_2 adsorption isotherms at 303K plotting amounts adsorbed against pressure for the ZIF-8 (blue circle), the ZIF-94 (green triangle), the ZIF-93 (purple square) and the ZIF-11 (red lozenge)

For pressures below 4 bar, CO_2 adsorbed amounts are higher for the ZIF-94 than for the ZIF-8. For instance at 1 bar, CO_2 uptakes are approximatively of 0.6 and 1.8 mmol.g^{-1} respectively for the ZIF-8 and the ZIF-94. Indeed, for pressures below 1 bar, the ZIF-94 adsorption isotherm shows a steep slope compared to this of the ZIF-8 suggesting stronger adsorbent-adsorbate interactions for ZIF-94/CO_2 than for ZIF-8/CO_2. To conclude, in the 0-4 bar pressure range, there is a stronger affinity of the ZIF-94/CO_2 system than for the ZIF-8/CO_2.

For pressures above 4 bar, CO_2 adsorbed amounts are higher for the ZIF-8 than for the ZIF-94. CO_2 maximum excess uptakes are of 6.7 and 3.2 mmol.g^{-1} respectively for ZIF-8 and ZIF-94. In the case of the ZIF-94, CO_2 uptakes seem to reach a plateau suggesting adsorbent saturation. This can be explained by the pore volume which is lower for ZIF-94 (0.17 cm^3/g) than for ZIF-8 (0.48 cm^3/g) (see table, Annex F). These Pore volumes experimentally measured are in the same magnitude as those found in literature, respectively of 0.22 cm^3.g^{-1} and 0.50 cm^3.g^{-1} for the ZIF-94 and the ZIF- 8 [33], [34].

In the pressure range studied 0-20 bar, CO_2 adsorption isotherms obtained for ZIF-93 and ZIF-11 show CO_2 uptakes higher for ZIF-93 over ZIF-11. For instance at 1 bar, CO_2 uptakes are 1.5 and 0.77 for ZIF-93 and ZIF-11. The pore volume measured on ZIF-93 from nitrogen adsorption at 77K is approximatively 0.27 cm^3.g^{-1}. Oppositely nitrogen adsorption showed that ZIF-11 is nonporous due to its pore aperture (3.0 Å) smaller than nitrogen kinetic diameter (3.6Å) in agreement with literature [35], [36]. However CO_2 adsorption carried out at 273K on ZIF-11 allowed to obtain a pore volume of 0.16 cm^3/g [36]. This suggests that smaller CO_2 adsorbed amounts are related to a lower pore volume.

Summary

Over the past century, quantitative structure-property relationship (QSPR) models have been widely developed in various fields (pharmaceutical, gas separation etc.) by means of mathematical analysis. These models aim to get some correlations between microscopic features of materials and studied macroscopic properties. Therefore, QSPR models are useful tools: to identify best materials with targeted properties, to predict materials performances and to design unknown compounds.

Metal-Organic Frameworks (MOFs) are very promising crystalline porous materials especially for gas separation applications. There is a great diversity of MOFs due to metal nodes and organic linkers available, thus there is a need to be able to predict their separation performances to improve MOF design in view of CO_2 capture from CO_2/ N_2 or CO_2/ CH_4 gas mixtures.

Recently, some studies set up QSPR models to assess and to predict MOF separation performances for hydrogen, methane and carbon dioxide adsorption.

In this work, we demonstrated that there is no correlation with pore size as descriptor due to the diversity of pore shape and pore size distribution of MOFs. Therefore, a 'descriptor-property' approach has been performed on ZIF materials, a sub-class of MOFs, which possess: a well-defined porosity, high specific surface area and pore volume, thermal and chemical stability. Some linear trends have been observed when CO_2 maximum uptakes are correlated to pore volume. Thus, the highest CO_2 uptakes at saturation are obtained for highest pore volume. CO_2 uptakes at saturation seem to be governed by pore volume rather than surface polarity.

The ZIF-8, known for its molecular sieving property, has been widely studied as nano-fillers into mixed matrix membranes (MMMs) in various separations: propylene/ propane [35]; dehydration of alcohols [36]; dehydration of isopropanol [37]; CO_2/N_2 [38]; CO_2/CH_4 [39]–[42].

Indeed, Vankelecom *et al.* conducted a study on the ZIF-8 as nano fillers and Matrimid® as polymer for dense and asymmetric MMM for binary gas mixture separation [43]. The ZIF-8 was included into Matrimid® polymer with 30% of loading. They reported a selectivity around 22 for CO_2/CH_4 binary gas mixture separation at 35°C and 10 bar. This selectivity is in the same magnitude of these obtained for the $[Cu_3(BTC)_2]$ and the MIL-53(Al) used as nano fillers in the same conditions which are approximatively of 24. While for CO_2/N_2 gas separation, the selectivities obtained are 20, 24 and 23 respectively for the ZIF-8, the $[Cu_3(BTC)_2]$ and the MIL-53(Al). This slightly difference can be attributed to the strong CO_2 interactions: (1) with unsaturated sites into the $[Cu_3(BTC)_2]$ and (2) with hydroxyl groups of MIL-53(Al). This leads to higher CO_2 adsorption enthalpies of 25 and 26.4 $kJ.mol^{-1}$ respectively for the $[Cu_3(BTC)_2]$ and the MIL-53(Al) [44] compared to the ZIF-8 where it is of 16 $kJ.mol^{-1}$. Beyond adsorption properties of nano fillers, separation performances of MMMs depend on the polymer/ filler interaction and the presence of voids at the interface which can decrease the membrane efficiency.

The ZIF-8 has been considered with others types of commercial polymers especially for CO_2/N_2 gas separation: Ultem®[38], Pebax® [45]. Indeed, CO_2/N_2 selectivities obtained are 36 (17% of ZIF-8 loading) et 32.3 (35% of ZIF-8 loading) respectively for Ultem® and Pebax® commercial polymers.

As for the ZIF-8, the ZIF-11 has been shaped with various polymers: PBI with a ZIF-11 loading of 55 wt% with a selectivity of 7 at 150°C for H_2/CO_2 separation [46]; Pebax® with the ZIF-11 loading of 77% with a selectivity is of 12.64 at 20°C for CO_2/CH_4 separation [47].

Up to now, there is no meaningful work regarding the ZIF-93 and the ZIF-94 for gas separation using mixed matrix membrane applications and the present work suggests that these materials are indeed worth further study in this area due to their good CO_2 adsorption capacities and adsorption enthalpies.

References

[1] A. D. Wiersum, J.-S. Chang, C. Serre, et P. L. Llewellyn, « An Adsorbent Performance Indicator as a First Step Evaluation of Novel Sorbents for Gas Separations: Application to Metal–Organic Frameworks », *Langmuir*, vol. 29, n° 10, p. 3301-3309, mars 2013.

[2] A. Wiersum, *Developing a strategy to evaluate the potential of new porous materials for the separation of gases by adsorption*. Aix-Marseille, 2012.

[3] A. C. Brown et T. R. Fraser, « On the Connection between Chemical Constitution and Physiological Action; with special reference to the Physiological Action of the Salts of the Ammonium Bases derived from Strychnia, Brucia, Thebaia, Codeia, Morphia, and Nicotia », *J. Anat. Physiol.*, vol. 2, n° 2, p. 224-242, 1868.

[4] E. J. M. D. S. F.R.S, « XXIII. On melting-point and boiling-point as related to chemical composition », *Philos. Mag.*, vol. 17, n° 105, p. 173-187, mars 1884.

[5] L. P. Hammett, « Some Relations between Reaction Rates and Equilibrium Constants. », *Chem. Rev.*, vol. 17, n° 1, p. 125-136, août 1935.

[6] C. Hansch et T. Fujita, « p-σ-π Analysis. A Method for the Correlation of Biological Activity and Chemical Structure », *J. Am. Chem. Soc.*, vol. 86, n° 8, p. 1616-1626, avr. 1964.

[7] S. M. Free et J. W. Wilson, « A Mathematical Contribution to Structure-Activity Studies », *J. Med. Chem.*, vol. 7, n° 4, p. 395-399, juill. 1964.

[8] M. Grover, B. Singh, M. Bakshi, et S. Singh, « Quantitative structure–property relationships in pharmaceutical research – Part 1 », *Pharm. Sci. Technol. Today*, vol. 3, n° 1, p. 28-35, janv. 2000.

[9] M. Grover, B. Singh, M. Bakshi, et S. Singh, « Quantitative structure–property relationships in pharmaceutical research – Part 2 », *Pharm. Sci. Technol. Today*, vol. 3, n° 2, p. 50-57, févr. 2000.

[10] A. R. Katritzky *et al.*, « The Present Utility and Future Potential for Medicinal Chemistry of QSAR / QSPR with Whole Molecule Descriptors », *Curr. Top. Med. Chem.*, vol. 2, n° 12, p. 1333-1356, déc. 2002.

[11] Y. Gogotsi *et al.*, « Importance of pore size in high-pressure hydrogen storage by porous carbons », *Int. J. Hydrog. Energy*, vol. 34, n° 15, p. 6314-6319, août 2009.

[12] M. Fernandez, T. K. Woo, C. E. Wilmer, et R. Q. Snurr, « Large-Scale Quantitative Structure–Property Relationship (QSPR) Analysis of Methane Storage in Metal–Organic Frameworks », *J. Phys. Chem. C*, vol. 117, n° 15, p. 7681-7689, avr. 2013.

[13] H. Amrouche, B. Creton, F. Siperstein, et C. Nieto-Draghi, « Prediction of thermodynamic properties of adsorbed gases in zeolitic imidazolate frameworks », *RSC Adv.*, vol. 2, n° 14, p. 6028-6035, 2012.

[14] D. Wu *et al.*, « Revealing the Structure–Property Relationships of Metal–Organic Frameworks for CO2 Capture from Flue Gas », *Langmuir*, vol. 28, n° 33, p. 12094-12099, août 2012.

[15] D. Kim *et al.*, « Quantitative structure–uptake relationship of metal-organic frameworks as hydrogen storage material », *Catal. Today*, vol. 120, n° 3, p. 317-323, févr. 2007.

[16] A. Noguera-Díaz, N. Bimbo, L. T. Holyfield, I. Y. Ahmet, V. P. Ting, et T. J. Mays, « Structure–property relationships in metal-organic frameworks for hydrogen storage », *Colloids Surf. Physicochem. Eng. Asp.*, vol. 496, p. 77-85, mai 2016.

[17] Y. Gogotsi, R. K. Dash, G. Yushin, T. Yildirim, G. Laudisio, et J. E. Fischer, « Tailoring of Nanoscale Porosity in Carbide-Derived Carbons for Hydrogen Storage », *J. Am. Chem. Soc.*, vol. 127, n° 46, p. 16006-16007, nov. 2005.

[18] Y. Gogotsi *et al.*, « Importance of pore size in high-pressure hydrogen storage by porous carbons », *Int. J. Hydrog. Energy*, vol. 34, n° 15, p. 6314-6319, août 2009.

[19] A. Noguera-Díaz, N. Bimbo, L. T. Holyfield, I. Y. Ahmet, V. P. Ting, et T. J. Mays, « Structure–property relationships in metal-organic frameworks for hydrogen storage », *Colloids Surf. Physicochem. Eng. Asp.*, vol. 496, p. 77-85, mai 2016.

[20] M. Fernandez, T. K. Woo, C. E. Wilmer, et R. Q. Snurr, « Large-Scale Quantitative Structure–Property Relationship (QSPR) Analysis of Methane Storage in Metal–Organic Frameworks », *J. Phys. Chem. C*, vol. 117, n° 15, p. 7681-7689, avr. 2013.
[21] D. Wu *et al.*, « Revealing the Structure–Property Relationships of Metal–Organic Frameworks for CO2 Capture from Flue Gas », *Langmuir*, vol. 28, n° 33, p. 12094-12099, août 2012.
[22] E. Stavitski *et al.*, « Complexity behind CO2 Capture on NH2-MIL-53(Al) », *Langmuir*, vol. 27, n° 7, p. 3970-3976, avr. 2011.
[23] Y. Gogotsi, R. K. Dash, G. Yushin, T. Yildirim, G. Laudisio, et J. E. Fischer, « Tailoring of Nanoscale Porosity in Carbide-Derived Carbons for Hydrogen Storage », *J. Am. Chem. Soc.*, vol. 127, n° 46, p. 16006-16007, nov. 2005.
[24] A. Phan, C. J. Doonan, F. J. Uribe-Romo, C. B. Knobler, M. O'Keeffe, et O. M. Yaghi, « Synthesis, Structure, and Carbon Dioxide Capture Properties of Zeolitic Imidazolate Frameworks », *Acc. Chem. Res.*, vol. 43, n° 1, p. 58-67, janv. 2010.
[25] V. Benoit *et al.*, « MIL-91(Ti), a small pore metal–organic framework which fulfils several criteria: an upscaled green synthesis, excellent water stability, high CO2 selectivity and fast CO2 transport », *J. Mater. Chem. A*, vol. 4, n° 4, p. 1383-1389, janv. 2016.
[26] R. S. Pillai, V. Benoit, A. Orsi, P. L. Llewellyn, P. A. Wright, et G. Maurin, « Highly Selective CO2 Capture by Small Pore Scandium-Based Metal–Organic Frameworks », *J. Phys. Chem. C*, vol. 119, n° 41, p. 23592-23598, oct. 2015.
[27] A. D. Wiersum, J.-S. Chang, C. Serre, et P. L. Llewellyn, « An Adsorbent Performance Indicator as a First Step Evaluation of Novel Sorbents for Gas Separations: Application to Metal–Organic Frameworks », *Langmuir*, vol. 29, n° 10, p. 3301-3309, mars 2013.
[28] Q. Yang *et al.*, « A Water Stable Metal–Organic Framework with Optimal Features for CO2 Capture », *Angew. Chem.*, vol. 125, n° 39, p. 10506-10510, sept. 2013.
[29] S. Bourrelly, P. L. Llewellyn, C. Serre, F. Millange, T. Loiseau, et G. Férey, « Different Adsorption Behaviors of Methane and Carbon Dioxide in the Isotypic Nanoporous Metal Terephthalates MIL-53 and MIL-47 », *J. Am. Chem. Soc.*, vol. 127, n° 39, p. 13519-13521, oct. 2005.
[30] X. Huang, J. Zhang, et X. Chen, « [Zn(bim)2] · (H2O)1.67: A metal-organic open-framework with sodalite topology », *Chin. Sci. Bull.*, vol. 48, n° 15, p. 1531-1534, août 2003.
[31] S. Aguado *et al.*, « Guest-induced gate-opening of a zeolite imidazolate framework », *New J. Chem.*, vol. 35, n° 3, p. 546-550, mars 2011.
[32] W. Morris *et al.*, « A Combined Experimental-Computational Study on the Effect of Topology on Carbon Dioxide Adsorption in Zeolitic Imidazolate Frameworks », *J. Phys. Chem. C*, vol. 116, n° 45, p. 24084-24090, nov. 2012.
[33] H. Amrouche *et al.*, « Experimental and Computational Study of Functionality Impact on Sodalite–Zeolitic Imidazolate Frameworks for CO2 Separation », *J. Phys. Chem. C*, vol. 115, n° 33, p. 16425-16432, août 2011.
[34] K. S. Park *et al.*, « Exceptional chemical and thermal stability of zeolitic imidazolate frameworks », *Proc. Natl. Acad. Sci.*, vol. 103, n° 27, p. 10186-10191, mai 2006.
[35] J. Sánchez-Laínez *et al.*, « Beyond the H2/CO2 upper bound: one-step crystallization and separation of nano-sized ZIF-11 by centrifugation and its application in mixed matrix membranes », *J. Mater. Chem. A*, vol. 3, n° 12, p. 6549-6556, mars 2015.
[36] C. Zhang, Y. Dai, J. R. Johnson, O. Karvan, et W. J. Koros, « High performance ZIF-8/6FDA-DAM mixed matrix membrane for propylene/propane separations », *J. Membr. Sci.*, vol. 389, n° Supplement C, p. 34-42, févr. 2012.
[37] G. M. Shi, T. Yang, et T. S. Chung, « Polybenzimidazole (PBI)/zeolitic imidazolate frameworks (ZIF-8) mixed matrix membranes for pervaporation dehydration of alcohols », *J. Membr. Sci.*, vol. 415, n° Supplement C, p. 577-586, oct. 2012.
[38] S. Fazlifard, T. Mohammadi, et O. Bakhtiari, « Chitosan/ZIF-8 Mixed-Matrix Membranes for Pervaporation Dehydration of Isopropanol », *Chem. Eng. Technol.*, vol. 40, n° 4, p. 648-655, avr. 2017.

[39] Y. Dai, J. R. Johnson, O. Karvan, D. S. Sholl, et W. J. Koros, « Ultem®/ZIF-8 mixed matrix hollow fiber membranes for CO2/N2 separations », *J. Membr. Sci.*, vol. 401, nº Supplement C, p. 76-82, mai 2012.
[40] N. Azizi et M. M. Zarei, « CO2/CH4 separation using prepared and characterized poly (ether-block-amide)/ZIF-8 mixed matrix membranes », *Pet. Sci. Technol.*, vol. 35, nº 9, p. 869-874, 2017.
[41] S. R. Venna et M. A. Carreon, « Highly Permeable Zeolite Imidazolate Framework-8 Membranes for CO2/CH4 Separation », *J. Am. Chem. Soc.*, vol. 132, nº 1, p. 76-78, janv. 2010.
[42] N. A. H. M. Nordin, A. F. Ismail, et N. Yahya, « Zeolitic Imidazole Framework 8 Decorated Graphene Oxide (zif-8/Go) Mixed Matrix Membrane (mmm) for Co2/Ch4 Separation », *J. Teknol.*, vol. 79, nº 1-2, p. 59-63, 2017.
[43] H. B. T. Jeazet, C. Staudt, et C. Janiak, « Metal–organic frameworks in mixed- matrix membranes for gas separation », *Dalton Trans.*, vol. 41, nº 46, p. 14003-14027, 2012.
[44] S. Basu, A. Cano-Odena, et I. F. J. Vankelecom, « MOF-containing mixed-matrix membranes for CO2/CH4 and CO2/N2 binary gas mixture separations », *Sep. Purif. Technol.*, vol. 81, nº 1, p. 31-40, sept. 2011.
[45] P. Rallapalli, K. P. Prasanth, D. Patil, R. S. Somani, R. V. Jasra, et H. C. Bajaj, « Sorption studies of CO2, CH4, N2, CO, O2 and Ar on nanoporous aluminum terephthalate [MIL-53(Al)] », *J. Porous Mater.*, vol. 18, nº 2, p. 205-210, avr. 2011.
[46] V. Nafisi et M.-B. Hägg, « Development of dual layer of ZIF-8/PEBAX-2533 mixed matrix membrane for CO2 capture », *J. Membr. Sci.*, vol. 459, nº Supplement C, p. 244-255, juin 2014.
[47] J. Sanchez-Lainez, B. Zornoza, C. Tellez, et J. Coronas, « On the chemical filler-polymer interaction of nano- and micro-sized ZIF-11 in PBI mixed matrix membranes and their application for H-2/CO2 separation », *J. Mater. Chem. A*, vol. 4, nº 37, p. 14334-14341, 2016.
[48] A. Ehsani et M. Pakizeh, « Synthesis, characterization and gas permeation study of ZIF-11/Pebax (R) 2533 mixed matrix membranes », *J. Taiwan Inst. Chem. Eng.*, vol. 66, p. 414-423, sept. 2016.

Conclusion

Conclusion

Carbon dioxide (CO_2) capture based on amine scrubbing technology is the current recognized standard method. Nevertheless, several disadvantages are associated to this approach including the regeneration cost due to the heating of a solution, amine degradation leading to corrosion and health issues. This therefore adds a significant energy cost to the separation cost, a considerable carbon footprint and installation problems. In recent years, gas separation based on membrane processes were developed due to their potential benefits over conventional technologies: smaller units involving both a lower mechanical complexity and carbon footprint.

Currently, only polymeric membranes are implemented to the industrial scale for gas separation application. Nevertheless, in terms of separation performance there is a trade-off between permeability and selectivity that does not allow to exceed the Robeson upper bound. In order to outperform this limit, mixed matrix membranes (MMMs) were designed to combine advantages in separation performances both polymeric and inorganic membranes: easy processing and mechanical strength as well as high selectivity. As a reminder, a MMM is a composite of filler particles in a polymeric matrix. In recent years, various types of inorganic particles are considered as fillers: carbon nanotubes, activated carbons, mesoporous silicas, and metal-organic frameworks (MOFs).

The main objective of M^4CO_2 project is to design MMMs based on Metal-Organic Frameworks (MOFs) the most sophisticated family of nanostructured materials as fillers for CO_2 capture. A large variety of MOFs exists thanks to the diversity of metal centers and ligands to build tri-dimensional structure (3D). MOFs were chosen owing to their good stability (i.e, thermal and chemical) as well as their high surface area and pore volume often above those of zeolites. Moreover, pore sizes of MOFs can be fine-tuned to gas selective adsorption by the incorporation of the appropriate building blocks, post-synthetic modification as well as ligand functionalization. This allows equally an optimization of MOF-polymer compatibilities, interesting for MMMs applications.

During this thesis, we have been involved in characterization of textural properties and CO_2 separation performances assessment (i.e, working capacity, adsorption enthalpy, selectivity and moisture conditions) of microporous MOFs for which pore size does not exceed 20 Å, that can potentially be used as fillers. The strategy developed and experimental techniques used during this project are described in the following Figure C.1:

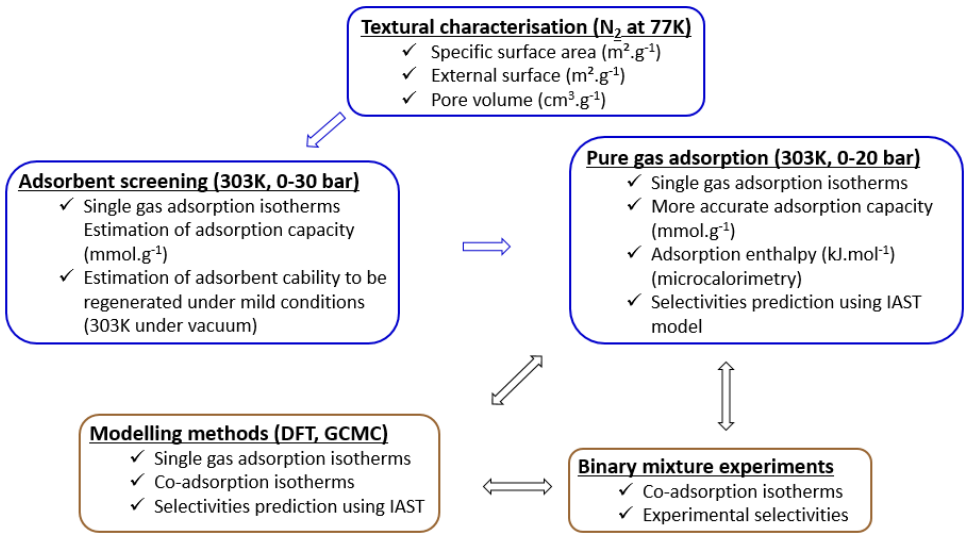

Figure C1– Strategy set up during M^4CO_2 project to characterize CO_2 adsorption properties of MOFs with the approaches carried out in MADIREL in the blue boxes. The modeling was carried out in Montpellier (collaboration with G. Maurin group) and the mixture adsorption was carried out in Mons (G. De Weireld).

Prior to each gas adsorption, the porosity of MOFs were probed via nitrogen gas adsorption at 77K allowing to determine textural parameters such as surface area and pore volume. The next step consists of a rapid screening of MOFs allowing to determine approximate adsorption isotherms (CO_2, N_2 and CH_4) at 303K using a home-made device. That can analyze up to six samples simultaneously. From this step, MOFs having promising CO_2 adsorption capacities were selected to be further analyzed using a manometry device coupled with a Tian-Calvet microcalorimeter. With this set-up, adsorption enthalpies as well as more accurate single gas adsorption isotherms were determined. Indeed, the adsorption enthalpies determination give an information on the heterogeneous or homogeneous surface energetic nature. Further, the high or small difference between CO_2 and N_2 or CH_4 adsorption enthalpies provide an indication on CO_2 selective adsorption of MOFs.

For the screening, 38 MOFs were analyzed using the high-throughput system to get their adsorption properties at 303K. Amongst them, ten MOFs stand out with good CO_2 adsorption capacities and were ranked in two families according to the nature of the linker: carboxylate or imidazolate. During this project, CO_2 adsorption properties of those ten MOFs were investigated for two types of conditions at 303K: for low (i.e, 0.15-0.2 bar) and high (i.e, 15 bar) pressure conditions approaching respectively the post-combustion and pre-combustion conditions.

At this stage of the project and based on literature, we attempted to correlate microscopic features of MOFs as pores size with a macroscopic property as CO_2 adsorption capacity at saturation to tend towards a type of 'QSPR' or 'descriptor-property' approach. Nevertheless, there is no correlation between pores size and maximum of CO_2 uptakes, probably due to the diversity of pores shape and pores size distribution of the MOFs considered. Consequently we focused our study on Zeolitic Imidazolate Frameworks (ZIFs), a sub-class of MOFs that possess a well-defined porosity. Moreover, the analysis of an Adsorbent Indicator Performance (API) for high pressures conditions evidenced that ZIFs adsorbents have CO_2 adsorption capacities similar to those of carboxylate-based MOFs. This 'descriptor-property' approach highlighted that for high pressure conditions, CO_2 uptakes seem to be governed by the pore volume of materials while surface polarity has a moderate effect.

While for low pressure conditions, around 0.15-0.2 bar, and each macroscopic features: working capacity, adsorption enthalpy and selectivity that support the choice of an adsorbent, various MOFs stand out. In this work, no linear correlations were noted between each of those macroscopic features and pores size as descriptor. However, we identified a range of pore size around 4.0 Å that stands out for CO_2 adsorption at low pressure. Towards post-combustion conditions, we investigated CO_2 adsorption under moisture conditions whose screening highlighted promising CO_2 performances of the MIL-96(Al) despite a loss of adsorption capacity. Moreover, the MIL-96(Al) has a pore size around 4.0 Å.

The MIL-96(Al) nanocrystals were selected to prepare mixed matrix membrane (MMM) due to their good CO_2 adsorption capacity under dry and moisture conditions, especially for 10% of relative humidity, corresponding to relative humidity of flue gas. In addition, they show an excellent colloidal stability (for the two batches: 'MIL-96(Al)-NP2' and 'MIL-96(Al)-NP3').

MMMs based on the MIL-96(Al) nanocrystals were prepared with the 6FDA-DAM as polymer matrix by the group of Delft. For each MMM, 25 wt % of the MIL-96(Al) nanocrystals –NP2 or –NP3 were incorporated into the 6FDA-DAM and for which CO_2/N_2 (15/85 (vol%)) gas separation properties were investigated at 298K at 2 bar (Figure C2) [1].

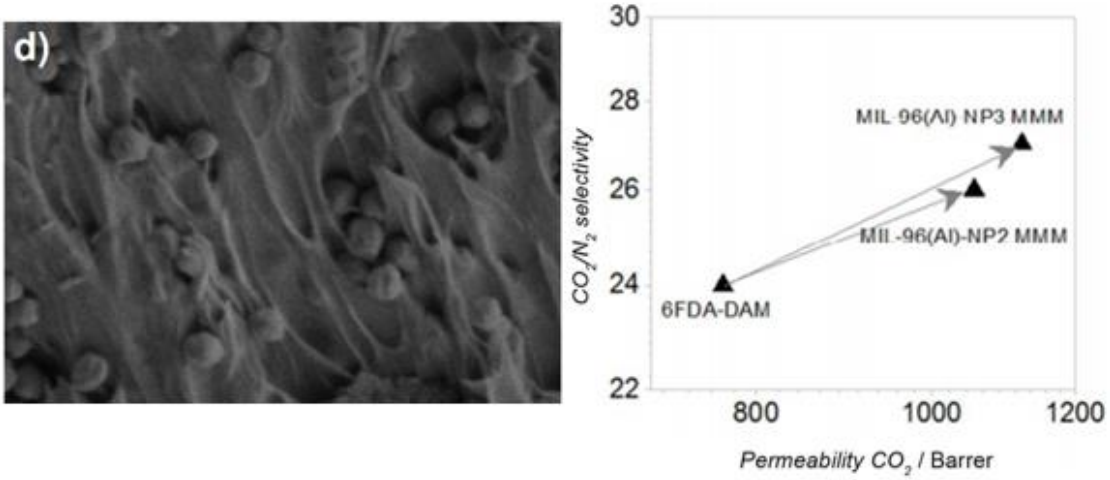

Figure C2 – SEM image of the 'MIL-96(Al)-NP2'/6FDA-DAM membrane showing a homogeneous distribution (left) as well as Robeson 2008 upper bound and the gas separation performance of 6FDA-DAM with 25 wt.% loading of 'MIL-96(Al)-NP2 and –NP3' [1]

The cross sectional SEM image evidences a homogeneous distribution for the MIL-96(Al) nanocrystals (-NP2) in the volume of the membrane, similar results are determined for the 'MIL-96(Al)-NP3'. This shows that there are no defects or voids at the MIL-96(Al) nanocrystals/ polymer interface that could affect CO_2/N_2 gas separation. Performances of the composite membranes based on the MIL-96(Al) nanocrystals, in terms of permeability and CO_2/N_2 selectivities, do not exceed the Robeson upper bound (Figure C.2). Although the Robeson limit is not outperformed, it has been demonstrated that addition of the MIL-96(Al) nanocrystals as fillers contributes to enhance the overall CO_2/N_2 separation performances compared to the neat polymeric membrane (Figure C2). Such results pave the way for the processing of composite membranes with a higher MOF loading.

Regarding M^4CO_2 project, the MOFs ZIF-94 as well as the MIL-140A(Zr)-Br and ZIF-8 were selected as filler for mixed matrix membrane respectively for post- and pre-combustion. These choices are based on the MOF/ polymer interaction, the formation of aggregates, the stability of the system. Nevertheless, one of the main issues found during this project was the problem of the interface between the polymer and the MOF filler with the formation of gaps due to poor compatibility or even polymer chain penetration into the MOF pores for overly compatible systems.[1]

For future research activities, it can be interesting to investigate: various 'green synthesis' of MOFs for upscale and use at the pilot scale. The humidity on CO_2 adsorption capacity is another parameter to investigate due to that an indicator as API does not take into account this effect. In addition, modeling methods are critical to identify adsorption mechanisms as the competition between CO_2 and H_2O molecules on adsorption sites.

Another aspect that can be pursued is the development of quantitative structure-property relationship (QSPR) using mathematical models in order to extend the understanding and prediction of the interactions between various parameters such as specific surface area, surface polarizability on CO_2 adsorption capacity and selectivity.

[1] Multiscale Modeling of the HKUST-1/Poly(vinyl alcohol) Interface: From an Atomistic to a Coarse Graining Approach, R. Semino, J.P. Durholt, R. Schmid, G. Maurin, J. Phys. Chem. C, 2017, 121(39), 21491-21496
Toward an Understanding of the Microstructure and Interfacial Properties of PIMs/ZIF-8 Mixed Matrix Membranes, M. Benzaqui, R. Semino, N. Menguy, F. Carn, T. Kundu, J.-M. Guigner, N. B. McKeown, K. J. Msayib, M. Carta, R. Malpass-Evans, C. Le Gnillouzer, G. Clet, N. A. Ramsahye, C. Serre, G. Maurin, N. Steunou, Appl. Mater. & Interf., 2016, 8(40) 27311-27321
Microscopic Model of the Metal Organic Framework/Polymer Interface: A First Step toward Understanding the Compatibility in Mixed Matrix Membranes, R. Semino, N. A. Ramsahye, A. Ghoufi, G. Maurin, Appl. Mater. & Interf., 2016, 8(1) 809-819
[1] M. Benzaqui *et al.*, « Revisiting the Aluminum Trimesate-Based MOF (MIL-96): From Structure Determination to the Processing of Mixed Matrix Membranes for CO2 Capture », *Chem. Mater.*, vol. 29, nº 24, p. 10326-10338, déc. 2017.

Dissemination during this thesis:

This work has been exposed in various conferences:

- Association Française de l'adsorption (AFA), « Adsorption de CO_2 : effet de confinement dans les micropores », 3 - 5 Février 2016, Paris
- Groupe Français des Zéolites (GFZ), « Quels MOFs en vue de la séparation CO_2/N_2 ? » 29 Mars au 1 Avril 2016, Montagnac
- Journées de calorimétrie et d'analyse thermique (JCAT), « Microcalorimetry contribution in order to predict relationships between structure-CO_2 adsorption properties of microporous MOFs », 17 au 20 Mai 2016, Anglet
- 5th International Conference on Metal-Organic Frameworks & Open Framework Compounds (MOF): "Searching for MOFs for the uptake of CO_2 under wet conditions", 11 -15 Septembre 2016, Long Beach
- M^4CO_2 project meetings

Regarding various publications:

- 'MIL-91(Ti), a small pore metal–organic framework which fulfils several criteria: an upscaled green synthesis, excellent water stability, high CO_2 selectivity and fast CO_2 transport'. Virginie Benoit, Renjith S. Pillai, Angelica Orsi,c Perine Normand, Herve Jobic, Farid Nouar, Pierre Billemont, Emily Bloch, Sandrine Bourrelly, Thomas Devic, Paul A. Wright, Guy de Weireld, Christian Serre, Guillaume Maurin and Philip L. Llewellyn, J. Mater. Chem. A, 2016, 4, 1383–1389-1383, DOI: 10.1039/c5ta09349j
- 'Highly Selective CO_2 Capture by Small Pore Scandium-Based Metal−Organic Frameworks' Renjith S. Pillai, Virginie Benoit, Angelica Orsi, Philip L. Llewellyn, Paul A. Wright, and Guillaume Maurin, J. Phys. Chem. C 2015, 119, 23592−23598, DOI: 10.1021/acs.jpcc.5b07903
- 'Porous zinc and cobalt 2-nitroimidazolate frameworks with six-membered ring windows and a layered cobalt 2-nitroimidazolate polymorph', Angelica Orsi, David J. Price, Jürgen Kahr, Renjith S. Pillai, Scott Sneddon, Shuai Cao, Virginie Benoit, Magdalena M. Łozińska, David B. Cordes, Alexandra M. Z. Slawin, Philip L. Llewellyn, Ian Casely, Sharon E. Ashbrook, Guillaume Maurin, and Paul A. Wright, CrystEngComm, DOI: 10.1039/C6CE02476A
- 'Revisiting the Microporous Aluminum Trimesate-based MOF (MIL-96): from the Structure Determination, Synthesis of Nanoparticles to the Processing of Mixed Matrix Membranes for CO_2 Capture', Marvin Benzaqui, Renjith S Pillai, Anahid Sabetghadam, Virginie Benoit, Perine Normand, Jérôme Marrot, Nicolas Menguy, David Montero, Antoine Tissot, Charlotte Martineau, Clémence Sicard, Mihail Mihaylov, Florent Carn, Isabelle Beurroies, Philip L. Llewellyn, Guy De Weireld, Konstantin Hadjiivanov, Jorge Gascon, Freek Kapteijn, Guillaume Maurin, Nathalie Steunou, Christian Serre, Chemistry of Materials, DOI: 10.1021/acs.chemmater.7b03203
- 'A promising metal-organic framework (MOF), MIL-96(Al) for CO_2 separation under humid conditions', Virginie Benoit, Nicolas Chanut, Renjith S. Pillai, Marvin Benzaqui, Isabelle Beurroies, Sabine Devautour-Vinot, Christian Serre, Nathalie Steunou, Guillaume Maurin, Philip L. Llewellyn , Journal of Materials Chemistry A, DOI: 10.1039/C7TA09696H

Appendices

Annex A – Experiments and textural properties

Sample	Origin (reference)	Thermogravimetric Analysis (TGA)	N_2 at 77K (Belsorp-max)	H_2O at 298K (Belsorp-max)	Gas adsorption at 303K (home-made high throughput system)			Gas adsorption coupled to Tian-Calvet microcalorimeter at 303K (home-made system)				Magnetic suspension balance (Rubotherm)		
					CO_2	N_2	CH_4	CO_2	N_2	CH_4	H_2	CO_2	N_2	CH_4
MIL-69(Al)	ILV (FA554)	×	×		×	×	×	×	×	×				
MIL-69(Al)	ILV (NK8)	×	×		×	×	×							
NH_2-MIL-53(Al)	Delft	×	×					×	×	×				
MIL-69(Fe)	ILV	×	×											
MIL-121(Fe)	ILV	×	×					×	×	×				
MIL-130(Al)	ILV	×	×											
MIL-68(Ga)	ILV	×	×											
MIL-102(Cr)	ILV (FM463)	×	×											
MIL-103	ILV (td889)	×	×											
MIL-160	ILV (NPC-M-3)	×	×											
MIL-88	ILV (b-2CF3)	×	×											
MIL-91(Ti)	STA	×	×					×	×	×				
MIL-91(Ti) - DMSO	STA (AO-1-88B)	×	×		×	×	×							
MIL-91(Ti) – reflux 2-propanol	STA (AO-1-88C)	×	×		×	×	×							
MIL-91(Ti)	STA (AO-1-67B)	×	×		×	×	×	×	×	×				
MIL-91(Ti) – 20% N,N-2-methyl	STA (AO-1-102)	×	×		×	×	×							

MIL-91(Ti) – 30% N,N-2-methyl	STA (AO-1-55A)	×	×		×	×	×							
MIL-91(Ti) – 50% N,N-2-methyl	STA (AO-1-55C)	×	×		×	×	×							
MIL-91(Ti) – 100% N,N-2-methyl	STA (AO-1-60A)	×	×		×	×	×							
MIL-91(Ti) – 4x linker	STA (AO-1-62C)	×	×		×	×	×							
MIL-91(Ti) – 4x linker	STA (AO-1-72A)	×	×		×	×	×							
MIL-96(Al)	ILV	×	×	×				×	×	×		×	×	×
MIL-96(Al)-NP2	ILV	×	×					×	×	×				
MIL-140A	ILV	×	×											
MIL-140A-Br	ILV	×	×					×	×	×				
MIL-61(Fe)	ILV	×	×					×		×				
Al-pda	ILV	×	×		×	×	×							
Sc_2BDC_3	STA (AO-1-103 (A+B))	×	×		×	×	×							
$Sc_2(BDC\text{-}Br)_3$	STA (AO-1-66D)	×	×		×	×	×							
$Sc_2(BDC\text{-}Br)_3$	STA (AO-1-81A)	×	×		×	×	×							
$Sc_2(BDC\text{-}Br)_3$	STA (AO-1-111E)	×	×		×	×	×							
$Sc_2(BDC\text{-}NH_2)_3$	STA (AO-1-68A)	×	×		×	×	×	×	×	×				
$Sc_2(BDC\text{-}NO_2)_3$	STA (AO-1-96B)	×	×		×	×	×	×	×	×				
ZIF-8	JM	×	×		×	×	×	×	×	×		×	×	×
ZIF-93	JM	×	×		×	×	×	×	×	×		×	×	×

ZIF-94	JM	×	×		×	×	×	×	×	×		×	×	×
ZIF-11	USTAN	×						×	×	×				
Zn[2-nIm]$_2$ - MeOH	STA	×	×		×	×	×							
Zn[2-nIm]$_2$ – Solvothermal synthesis	STA (AO-1-108A)	×	×		×	×	×	×	×	×				
ZIF-300	STA (MMLM114)	×	×		×	×	×							

Table A.1 – List of samples studied during this thesis project as well as various analysis performed and symbolized by crosses. ILV: Lavoisier Institute; STA: University of S^t Andrews; JM: Johnson Matthey Institute; Delft: University of Delft; USTAN: the University court of the University of S^t Andrews

Name	Origin	Activation Temperature (°C)	S_{BET} ($m^2.g^{-1}$)	Pore Volume ($cm^3.g^{-1}$)
MIL-69 (Al)	ILV	250	26	0.01
MIL-53 (Al)-NH_2	ILV	150	394	0.154
MIL-91 (Ti)	STA	200	362	0.129
MIL-96 (Al)	ILV	150	448	0.162
MIL-140A-Br	ILV	150	141	0.05
MIL-121 (Fe)	ILV	200	14	0.005
MIL-61 (Fe)	ILV	120	0.91	0.0003
Sc_2 (BDC-NO_2)$_3$	STA	200	42	0.012
ZIF-8	JM	110	1439	0.48
ZIF-93	JM	125	773	0.28
ZIF-94	JM	180	462	0.17
ZIF-11	JM	200	-	-
Zn[2-nIm]$_2$	STA	200	123	0.04

Table A.2- Origin, activation temperature, specific surface area and pore volume for MOFs studied during this thesis

Annex B

CHEMISTRY OF MATERIALS

Article

pubs.acs.org/cm

Revisiting the Aluminum Trimesate-Based MOF (MIL-96): From Structure Determination to the Processing of Mixed Matrix Membranes for CO_2 Capture

Marvin Benzaqui,[†,‡] Renjith S Pillai,[§] Anahid Sabetghadam,[∥] Virginie Benoit,[⊥] Perine Normand,[#] Jérôme Marrot,[†] Nicolas Menguy,[▽] David Montero,[○] William Shepard,[◆] Antoine Tissot,[†,‡] Charlotte Martineau-Corcos,[†,¶] Clémence Sicard,[†] Mihail Mihaylov,[◇] Florent Carn,[▼] Isabelle Beurroies,[⊥] Philip L. Llewellyn,[⊥] Guy De Weireld,[#] Konstantin Hadjiivanov,[◇] Jorge Gascon,[∥,■] Freek Kapteijn,[∥] Guillaume Maurin,[§] Nathalie Steunou,[*,†] and Christian Serre[†,‡]

[†]Institut Lavoisier de Versailles, UMR CNRS 8180, Université de Versailles Saint Quentin en Yvelines, Université Paris Saclay, 45 avenue des Etats-Unis, 78035 Cedex Versailles, France

[‡]Institut des Matériaux Poreux de Paris, FRE 2000 CNRS, Ecole Normale Supérieure, Ecole Supérieure de Physique et de Chimie Industrielle de Paris, PSL Research University, 75005 Paris, France

[§]Institut Charles Gerhardt Montpellier, UMR 5253 CNRS, Université; de Montpellier, Place E. Bataillon, 34095 Cedex 05 Montpellier, France

[∥]Catalysis Engineering−Chemical Engineering Department, Delft University of Technology, Van der Maasweg 9, 2629 HZ Delft, The Netherlands

[⊥]CNRS, MADIREL, UMR 7246, Aix Marseille University, 13397 Marseille, France

[#]Service de Thermodynamique et de Physique mathématique, Faculté Polytechnique, Université de Mons, 20 Place du Parc, 7000 Mons, Belgium

[▽]Institut de Minéralogie de Physique des Matériaux et de Cosmochimie, UMR 7590 CNRS, MNHN IRD, UPMC Université Paris 06—Sorbonne Universités, 4 place Jussieu, 75005 Paris, France

[○]Institut des Matériaux de Paris Centre (IMPC), FR 2482 CNRS, UPMC Université Paris 06—Sorbonne Universités, 4 place Jussieu, 75252 Cedex 05 Paris, France

[◆]Synchrotron Soleil, L'Orme des Merisiers, Saint Aubin, BP 48, 91192 Gif-sur-Yvette, France

[¶]CNRS, CEMHTI UPR3079, Université d'Orléans, F-45071 Orléans, France

[◇]Institute of General and Inorganic Chemistry, Bulgarian Academy of Sciences, Sofia 1113, Bulgaria

[▼]Laboratoire Matière et Systèmes Complexes (MSC), UMR CNRS 7057, Université Paris Diderot, Bâtiment Condorcet, 10 rue A. Domon et L. Duquet, 75013 Paris, France

[■]King Abdullah University of Science and Technology, KAUST Catalysis Center, Advanced Catalytic Materials, Thuwal 23955, Saudi Arabia

Supporting Information

ABSTRACT: A microporous Al trimesate-based metal−organic framework (MOF), denoted MIL-96-(Al), was selected as a porous hybrid filler for the processing of mixed matrix membranes (MMMs) for CO_2/N_2 postcombustion separation. First, the structural model of MIL-96-(Al) initially reported was revisited using a combination of synchrotron-based single-crystal X-ray diffraction, solid-state nuclear magnetic resonance spectroscopy, and density functional theory (DFT) calculations. In a second step, pure MIL-96-(Al) crystals differing by their size and aspect ratio, including anisotropic hexagonal platelets and nanoparticles of about 70 nm in diameter, were prepared. Then, a combination of *in situ* IR spectroscopy, single-gas, and CO_2/N_2 coadsorption experiments, calorimetry, and molecular simulations revealed that MIL-96-(Al) nanoparticles show a relatively high

continued...

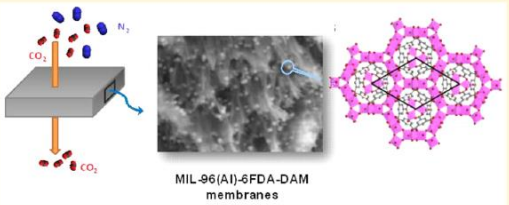

Received: July 29, 2017
Revised: November 5, 2017
Published: November 8, 2017

DOI: 10.1021/acs.chemmater.7b03203
Chem. Mater. 2017, 29, 10326−10338

CO_2 affinity over N_2 owing to strong interactions between CO_2 molecules and several adsorption sites such as Al^{3+} Lewis centers, coordinated water, and hydroxyl groups. Finally, the high compatibility between MIL-96-(Al) nanoparticles and the 6FDA-DAM polymer allowed the processing of homogeneous and defect-free MMMs with a high MOF loading (up to 25 wt %) that outperform pure polymer membranes for CO_2/N_2 separation.

INTRODUCTION

Metal−organic frameworks (MOFs) have developed rapidly due to their outstanding properties and myriad of potential applications such as gas storage, separations, catalysis, biomedicine, electronic devices, and information storage among others.[1,2] These hybrid porous crystalline materials consist of periodic coordination networks composed of inorganic building blocks and organic multifunctional ligands and can be rationally designed through crystal engineering. The explosion of interest in this class of materials stems from their endless chemical variability and unprecedented diversity of pore structure (shape and diameter of pores) and topology (two to three periodic extended frameworks), enabling the fine-tuning of their physicochemical features for a targeted application.[1−4] As a result of their crystallinity, these materials are well suited to in-depth characterization of their structure as well as establishing clear structure−property relationships.[5,6] However, the synthesis and/or structure determination of numerous MOFs remains a hurdle, particularly due to the high reactivity of their precursors and thus their low crystallinity.[7] In addition, the complexity of their architecture associated with a possible structural disorder (water molecules, guest molecules, free ions, and defects, *etc.*) and, more importantly, the existence of crystals with large unit cells and low symmetry have led to the development of methodologies that combine X-ray or neutron diffraction to advanced complementary experimental (solid-state NMR, EXAFS, and transmission electron microscopy, *etc.*) and computational tools.[8] For instance, solid-state NMR experiments integrating high magnetic field, specific pulse sequences, multiple-resonance decoupling and ultrafast magic-angle spinning (MAS) have become a powerful tool to provide information on the local environment of atoms (symmetry, coordination shell, and so on) and probe their spatial proximity and connectivity, thereby constraining the possible structural solutions.[9,10] Moreover, modeling tools involving energy minimization techniques at the force field (interatomic potential) and/or electronic (quantum) levels were combined with experimental information for the structure resolution of numerous MOFs with low symmetry and/or poor crystallinity.[8,11−14]

Here, this work intends to reinvestigate the crystallographic structure of the microporous aluminum trimesate MIL-96-(Al),[15] with a subtle combination of advanced experimental (X-ray diffraction, solid-state NMR, and infrared spectroscopy) techniques and density functional theory calculations. The periodic aluminum−oxo framework including the coordination sphere of Al centers was carefully determined. Moreover, the location of water molecules and hydroxo groups has allowed the description of the hydrogen-bond network in the porosity of the material. Narrow pore MOFs are a subclass of porous materials of special interest owing to their pore aperture sizes below 4−7 Å that can potentially address key challenges such as carbon capture and separation of olefin/paraffin, acetylene/ethylene, linear/branched alkanes, and xenon/krypton.[16] The separation ability of MIL-96-(Al) was previously demonstrated for several relevant applications of interest.[17−21] Moreover, its rigid framework with relative small pores incorporating diverse potential adsorption sites (Al acid sites, hydroxyl groups, and coordinating water) makes this MOF attractive for the selective capture of CO_2 over N_2. This has been here further confirmed by a subtle combination of single-component CO_2 and N_2 and their binary mixture adsorption measurements and grand canonical Monte Carlo simulations.

Due to its high thermal and hydrothermal stability, MIL-96-(Al) was further envisaged for the processing of mixed matrix membrane (MMM) for postcombustion CO_2 capture. These composite membranes which consist of filler particles dispersed into an organic polymer phase potentially combine the gas transport and separation properties of the incorporated particles with the good processability and mechanical properties of the polymers. Indeed, MOFs were recently proposed as fillers due to their outstanding gas separation properties.[5] However, MOF-based MMMs suffer from several limitations mainly related to a possible physicochemical mismatch between MOFs and polymers.[22−26] Such a lack of chemical compatibility between both components limits the MOF loading of numerous MMMs and thus their performance.[22−26] Indeed, for numerous MOF-based MMMs, the transport properties and thus the selectivity of the membrane are driven by the polymer matrix which is the dominant component. In addition, a poor dispersion of MOF fillers in the polymer matrix may take place, thereby creating interphase defects (macro- or nanovoids).[27,28] Such voids provide bypasses through the MMMs that reduce the separation efficiency and compromise performance.[29] In the present study, the shaping of MMMs requires the synthesis of MIL-96-(Al) particles at the nanoscale. Therefore, the synthesis of MIL-96-(Al) crystals of different morphology and diameter was achieved in water or water/DMF solvents. Two sets of nanoparticles of MIL-96-(Al) with a monodisperse size distribution (200 and 70 nm in diameter) were then selected as inorganic fillers for the processing of MMMs. The glassy and high free-volume polyimide 6FDA-DAM was selected owing to its high CO_2 permeability, good mechanical properties, and easy processability. Defect-free membranes were prepared that consisted of homogeneously distributed MIL-96-(Al) particles in the polymer matrix with adequate interfacial properties. Their gas sorption properties were fully characterized, showing very encouraging performances for postcombustion CO_2/N_2 separation. Such results are very promising in the field of MMMs for CO_2 capture.

EXPERIMENTAL SECTION

Microwave Synthesis of MIL-96-(Al) Hexagonal Platelets. MIL-96-(Al) hexagonal platelets (MIL-96-(Al)-HPs) were synthesized by microwave-assisted hydrothermal synthesis. Aluminum nitrate nonahydrate (191.7 mg, 0.511 mmol) and trimesic acid (70.4 mg, 0.335 mmol) were dissolved in distilled water (45 mL) under vigorous stirring. Acetic acid (14 μL, 0.25 mmol) was added, and the reaction mixture was stirred for 10 min at room temperature (RT) and then introduced into the microwave oven. After hydrothermal treatment at 200 °C (1600 W) for 2 min, the resulting mixture was cooled with an ice bath and centrifuged at 14500 rpm for 15 min. The liquid fraction was discarded, and the white product was washed twice with deionized water (30 mL) and twice with EtOH (30 mL). After a final centrifugation, the powder was dried in air at RT.

DOI: 10.1021/acs.chemmater.7b03203
Chem. Mater. 2017, 29, 10326−10338

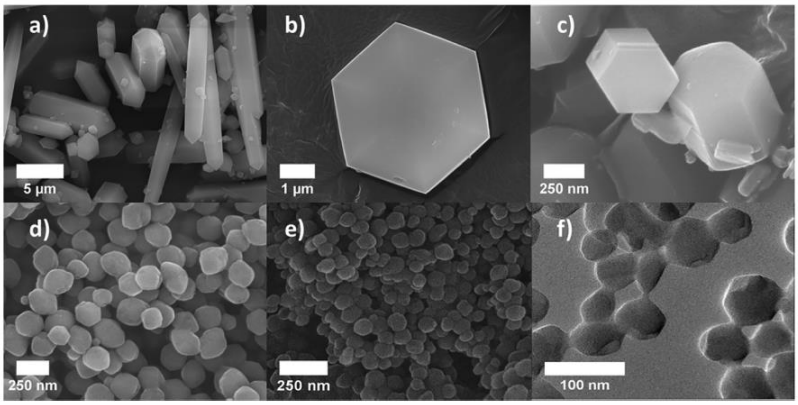

Figure 1. SEM images of the different MIL-96-(Al) particles: (a) hexagonal rods (HR); (b) hexagonal platelets (HP); (c) nanoparticles from reflux in water (NP1); (d) nanoparticles from reflux in H_2O/DMF (NP2); (e) SEM image of NP3; (f) TEM-bright field image of NP3.

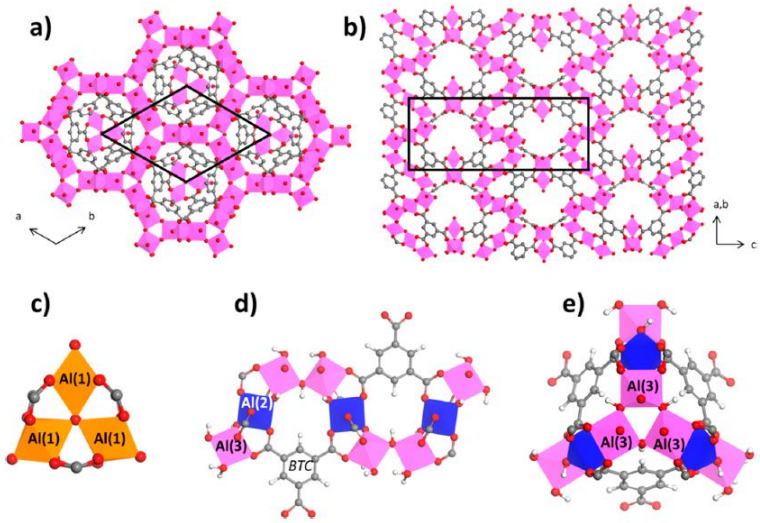

Figure 2. (a) Framework of MIL-96-(Al) along the *c* axis; (b) framework of MIL-96-(Al) along the *a* axis; (c–e) structural description of the different inorganic subunits of MIL-96-(Al) [(c) {Al(1)}-trimer; (d) sinusoidal chain composed of two Al(3) bridged by Al(2); (e) {Al(3)} trimer].

Synthesis of MIL-96-(Al) Nanoparticles in Water. A first solution was prepared by dissolving trimesic acid (210 mg, 1 mmol) in 70 mL of deionized water under reflux conditions. A second solution was obtained by dissolving aluminum nitrate nonahydrate (570 mg, 1.5 mmol) in 65 mL of deionized water. Both solutions were heated separately under reflux, and then the Al solution was poured into the ligand solution. Reflux was kept for about 3 h, and the white powder was cooled in an ice bath before centrifugation at 14500 rpm for 15 min. The solid was washed twice with deionized water (30 mL) and twice with EtOH (30 mL). Pure MIL-96-(Al) nanoparticles (MIL-96-(Al)-NP1s) were finally obtained and dried in air at RT.

Synthesis of MIL-96-(Al) Nanoparticles in Water/DMF. Aluminum nitrate nonahydrate (4.5 g, 12 mmol) and trimesic acid (2.52 g, 12 mmol) were dissolved in 300 mL of a H_2O/DMF (1/1 (v:v)) mixture. Acetic acid (1.68 mL, 30 mmol) was added, and the mixture was heated under reflux for 16 h. The resulting white mixture was centrifuged at 14500 rpm for 15 min and then washed once with deionized water (30 mL) and one more time with a H_2O/EtOH (1/1) mixture (30 mL) and finally with EtOH (30 mL). The obtained white powder was dried at RT, and pure MIL-96-(Al) NPs (*i.e.*, MIL-96-(Al)-NP2s) of 200 nm in diameter were obtained, with no traces of trimesic acid, nitrates, or DMF. MIL-96-(Al) NPs of 70 nm in diameter (*i.e.*, MIL-96-(Al)-NP3s) were also prepared at the gram scale by using the same reactants but with concentrations two times lower.

Preparation of MIL-96-(Al)-6FDA-DAM MMMs. A high free-volume 6FDA-DAM copolymer supplied by Akron was used. 6FDA-DAM was degassed at 453 K under vacuum overnight. A polymer solution was prepared by dissolving 0.4 g of polymer in 3 mL of tetrahydrofuran (THF). MIL-96-(Al) crystals (NP2 and NP3) were dispersed in 1.5 mL of THF by ultrasonication and stirring for 30 min. Then, 10% of the volume of the polymer solution was added to the MOF suspension followed by further stirring for 2 h (priming). The remaining volume of polymer solution was added to the MOF suspension and stirred overnight. This slurry solution was poured on the glass plate and cast by Doctor Blade technique tuning the thickness to about 80 μm. The solvent/(filler + polymer) weight ratio was kept constant (90/10) for all MMMs. MMMs were prepared with a MOF loading of 25 wt %. Then, membranes were covered with a top-drilled box and dried

DOI: 10.1021/acs.chemmater.7b03203
Chem. Mater. 2017, 29, 10326−10338

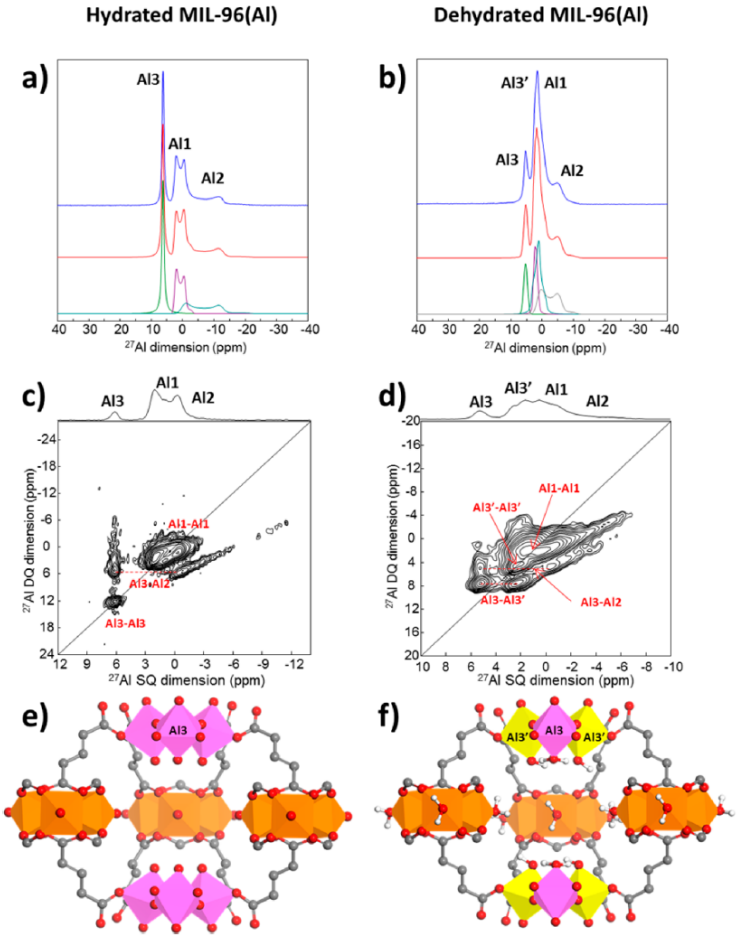

Figure 3. Experimental (Exp., top) and deconvoluted (Dec., middle) ^{27}Al MAS NMR spectra of (a) hydrated MIL-96-(Al) and (b) dehydrated MIL-96-(Al) (*i.e.*, previously dried overnight at 423 K) and (bottom) individual contributions. ^{27}Al−^{27}Al DQ-SQ correlation NMR spectra of (c) hydrated MIL-96-(Al) and (d) dehydrated MIL-96-(Al) (slop of diagonals, 2). For panel c the autocorrelations Al(3)−Al(3) and Al(1)−Al(1) are the diagonal peaks while the cross-correlation Al(3)−Al(2) is indicated by the dashed line. For panel d the autocorrelations Al(3′)−Al(3′) and Al(1)−Al(1) are the diagonal peaks while the cross-correlations Al(3)−Al(3′) and Al(3)−Al(2) are indicated by the dashed lines. Views of the {Al(1)} and {Al(3)} trimers subunits of (e) hydrated MIL-96-(Al) and (f) dehydrated MIL-96-(Al).

overnight under THF-saturated atmosphere. Finally, they were peeled off and heat treated at 433 K for 24 h under vacuum.

■ RESULTS AND DISCUSSION

Synthesis of MIL-96-(Al) and Structure Resolution by Combining Single-Crystal X-ray Diffraction Analysis, Solid-State NMR Spectra, and DFT Calculations. The microporous MIL-96-(Al) (see Figures 1 and 2) was first reported using hydrothermal conditions from a mixture of trimesic acid (BTC) and aluminum nitrate.[15] However, these conditions have to be strictly controlled since two larger pore Al trimesates, MIL-100-(Al) and MIL-110-(Al), among others, can be produced in the same reaction system.[19,30−33] Indeed, it was reported that MIL-100-(Al) is the kinetic phase of this system and forms at short reaction times and low pH, whereas MIL-96-(Al) is mainly obtained for longer reaction times following a crystallization−hydrolysis−recrystallization process.[31] In addition, this route involves the use of HF and tetraethoxysilane.[15] We also failed to reproduce single crystals of MIL-96-(Al) of a suitable size following this method. Thus, we developed first an alternative easier and friendlier hydrothermal route by using a mixture of trimesic acid and aluminum nitrate in water at 180 °C (rather than 210 °C), which led to hexagonal rods (MIL-96-(Al)-HR) up to 20 μm long and 5 μm wide (see Figure 1a and Figure S1 of the Supporting Information (SI)).

The structure of MIL-96 (Al), initially described by Loiseau *et al.*,[15] presents four non-equivalent aluminum sites. The fourth aluminum, labeled as Al4, exhibits very short and unrealistic Al−O distances which suggest a crystallographic disorder of the initial structure. Therefore, in the present article, this structure has been reinvestigated using first microfocused beam synchrotron-based single-crystal X-ray diffraction (see the SI for details).

DOI: 10.1021/acs.chemmater.7b03203
Chem. Mater. 2017, 29, 10326−10338

As previously described, the structure results from the assembly of two distinct building units (see Figure 2a,b). The first one is an oxo-centered trimer {Al(1)} of crystallographically equivalent Al(1) octahedra which are coordinated to bridging trimesate and μ_3-O ligands (see Figure 2c). The second building unit consists of a 2D hexagonal network containing 18-membered rings built by sinusoidal chains of aluminum octahedra. These chains contain two non-equivalent types of aluminum, Al(2) and Al(3), which are coordinated to four and two trimesate oxygen atoms and two and three bridging μ_2-hydroxo moieties (Figures 2d, e) respectively. The hexagonal 18-membered rings are interconnected with each other by another type of trimer. This "unusual" {Al(3)} trimer, seldom observed so far in the field of MOFs, is composed of three Al(3) octahedra that are corner-linked by μ_2-OH groups. The connection of the {Al(1)} trimer with the 2D network of Al(2) and Al(3) octahedra through the trimesate ligands results in a 3D framework with a complex arrangement of three types of cavities (see Figure S2 and Table S1 of the SI).

The microporosity of MIL-96-(Al) consists of one spherical cage A with a cavity-free diameter of about 11 Å, an elongated cavity B with dimensions of 9.5 × 12.6 × 11.3 Å, and a narrow cavity C with dimensions of 3.6 × 4.5 Å. The complex packing and connectivity between cavities as described in Figure S3 show that cavities of the same type (A-A, B-B, or C-C) are not connected. According to the size of the windows between two cavities that could be estimated from the van der Waals radius of oxygen atoms, windows between cavity B and cavity C are relatively narrow (≈4.5 Å × 3.6 Å) and hence accessible to H_2, CO_2, and, to a lesser extent, N_2 (Figure S4), which is crucial for high CO_2/N_2 selectivity. On the other hand, no connection between cavity A and cavities B/C is possible, which means that cavity A is isolated in the structure. Consequently, MIL-96-(Al) presents a two-dimensional (2D) pore structure that consists of "zig−zag" channels between cavities B and C (Figure S3). The nitrogen adsorption isotherm of MIL-96-(Al) at 77 K (Figure S5a) is of type I-(a) from the IUPAC classification which is characteristic of a microporous adsorbent. A BET area of ∼600 ± 10 $m^2 \cdot g^{-1}$ and a pore volume of 0.23 $cm^3 \cdot g^{-1}$ are obtained. In addition, the semilogarithmic plot of the N_2 isotherm is consistent with a narrow pore size distribution (Figure S5b).

In contrast to the previously reported structure,[15] no electronic residue could be attributed to a fourth octahedral aluminum site. This observation contradicts the initial set of ^{27}Al MAS NMR spectroscopy data which evidenced the presence of four ^{27}Al NMR signals in MIL-96-(Al).[15] In order to explain such a deviation, this phase was thoroughly investigated by combining solid-state NMR and thermogravimetric analysis (TGA) and density functional theory (DFT) calculations. First, the ^{27}Al MQMAS NMR spectrum (see Figure S6a of the SI) of the hydrated MIL-96-(Al) shows only three ^{27}Al signals at δ_{iso} of 3.2, 3.4, and 6.2 ppm, which, according to the deconvolution of the ^{27}Al MAS NMR spectrum (Figure 3a), have respective relative intensity close to 1:1:2 (see Table S2 for the NMR parameters). This is consistent with the presence in the crystal structure of three Al sites with different multiplicities (the multiplicity of Al(1) and Al(2) is 6 while that of Al(3) is 12) and indicates that Al(3) corresponds to the line at 6.2 ppm. Al(1) and Al(2) can be distinguished based on the ^{27}Al−^{27}Al double-quantum−single-quantum (DQ-SQ) NMR spectrum, in which close spatial proximities between ^{27}Al nuclei are observed. This spectrum (Figure 3c) shows a pair of cross-peaks between Al(3) and the line at 3.4 ppm, which is thus assigned to the connected Al(2) center. A strong diagonal peak for the Al(3) resonance is observed, in agreement with the presence of connected Al(3) octahedra. For Al(1), only a diagonal peak is detected in agreement with the presence of isolated Al(1) sites. Upon dehydration of the MIL-96-(Al) at 423 K, removal of water molecules entrapped in the porosity of MIL-96-(Al) takes place without altering the crystallographic structure of MIL-96-(Al) as shown both by TGA and temperature-dependent powder X-ray diffraction (PXRD; see Figures S7 and S8). However, the dehydration provokes a modification of the local environment of Al^{3+} cations since a fourth ^{27}Al resonance (labeled Al(3′)) is detected in the ^{27}Al 1D MAS (Figure 3b), MQMAS (Figure S6b of the SI), and ^{27}Al−^{27}Al DQ-SQ NMR spectra (Figure 3d).

Moreover, deconvolution of the ^{27}Al MAS NMR spectrum indicates that the four signals at δ_{iso} = 3.0, 3.1, 3.4, and 5.3 ppm have respective relative intensity of 1.3:1:1:0.66 (Figure 3b and Table S2) and thus are assigned to Al(3′), Al(2), Al(1), and Al(3), respectively. Note that the ^{27}Al NMR spectrum reported previously by Loiseau *et al.*[15] was similar to our spectrum with the presence of four signals (one was assigned to the fourth aluminum site not present in our new model). However, the relative intensity of the signals is different, suggesting that the corresponding NMR spectrum was initially collected on a partially hydrated sample. This observation points out the importance of accurately controlling the hydration state of hydrophilic MOFs prior to NMR measurements. In the ^{27}Al−^{27}Al DQ-SQ NMR spectrum, the Al(3) resonance is no longer associated with a diagonal peak but strongly correlates with the signal of Al(3′). All these results are consistent with the presence of one Al(3) and two equivalent Al(3)' sites in each {Al(3)} trimer of the dehydrated MIL-96-(Al).

According to the single-crystal X-ray structure and TGA analysis (Figure S7), MIL-96-(Al) with the chemical formula $Al_{12}O\text{-}(OH)_{16}(H_2O)_5[BTC]_6 \cdot nH_2O$ (n = 29) contains one {Al(1)} trimer for two {Al(3)}-trimers. The oxo core of this formula unit is composed of one μ_3-O, 12 μ_2-OH, and nine terminal oxygen ligands (OH or H_2O). For electroneutrality purposes, these terminal groups correspond to four hydroxyl groups and five water molecules that are linked either to Al(1) or Al(3)/Al(3′) sites. Indeed, Al(2) cations are not coordinated to any terminal oxygen ligands. Since Al(1) centers are chemically equivalent in the dehydrated MIL-96-(Al), they are coordinated to one type of terminal oxygen ligand (OH or H_2O) while the non-equivalent Al(3) and Al(3′) centers are presumably not linked to the same terminal oxygen groups. Taking into account the total number of terminal OH and H_2O and the symmetry of the Al(1)} and {Al(3)} trimers, the only possible configuration is that both Al(1) and Al(3) centers are coordinated to terminal water molecules while Al(3)' is covalently attached to a hydroxyl group. However, a statistical distribution of hydroxyl groups and water molecules over the terminal oxygen ligands of Al(3)/Al(3′) cannot be ruled out.

The structural model of the anhydrous MIL-96-(Al) thus proposed was geometry optimized at the DFT-level (Figure S29). These calculations included the relaxation of the atomic positions of the MOF framework while the unit cell (u.c.) parameters were fixed at the values determined experimentally. The same procedure was applied to the hydrated form of MIL-96-(Al) starting with the experimental structural model containing a concentration of free water present in the pores as determined by TGA (58 H_2O/u.c.; Figure S7). In this case, the positions of both the atoms of the MOF framework and the free water molecules were relaxed. The so-obtained structural models were further validated by a good agreement between the

DOI: 10.1021/acs.chemmater.7b03203
Chem. Mater. 2017, 29, 10326−10338

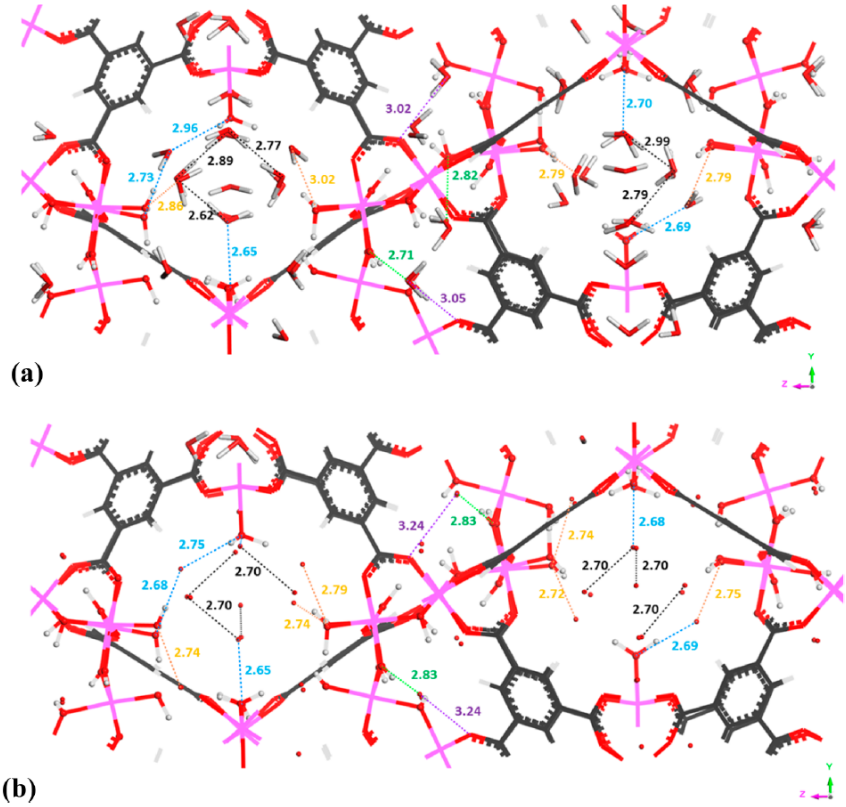

Figure 4. Crystal structure of MIL-96-(Al) in its hydrated form (gray, carbon; white, hydrogen; red, oxygen; pink, aluminum): (a) DFT optimized model; (b) refined experimental model. Interatomic distances are in angstroms. The dashed lines represent a selection of representative interactions between the water molecules themselves (black), between water and water coordinated to the framework (blue), between water and hydroxyl group coordinated to the framework (orange), between water and the μ_2-OH functions (green), and between the water and the carboxylate group Oc (purple). Hydrogen bonds are involved between free water molecules and coordinative water molecules at the Al(1) sites (blue). Water molecules located near the Al(2) sites are arranged in such a way that they form hydrogen bonds with the framework between (1) their oxygen atoms Ow and the proton of the μ_2-(OH) functions (orange) and (2) their protons Hw and the oxygen atoms of the carboxylate group (purple). In addition, the water molecules located near Al(3) sites make hydrogen bonds with framework between (1) their protons Hw and the oxygen atoms of either the hydroxyl group (orange) or water coordinated to Al(3′) and/or Al(3) sites (blue) and (2) their oxygen atoms Ow and the proton of the nearby water molecules (black).

first-principle-calculated ^{27}Al NMR parameters including isotropic chemical shifts as well as quadrupolar coupling constants/asymmetric constants and the corresponding experimental data (see Table S2). The DFT predicted structure for the hydrated form reveals that the free water molecules make strong hydrogen bonds with the framework (Al centers or hydroxy groups, trimesate ligands, or coordinating water molecules; see Figure 4a).

The characteristic distances between two water/host oxygen atoms range from 2.6 and 3.05 Å, which fit well with those evidenced from the experimentally refined structure. The confined water molecules form a relatively strong hydrogen-bond network with corresponding Ow−Ow distances (2.77 Å) as short as those usually observed for water in the bulk state. This H_2O network is extended throughout the porosity by hydrogen-bonded water molecules between cavities B and C as shown in Figure S9. Finally, a theoretically accessible surface area of 700 $m^2 \cdot g^{-1}$ was evaluated, in fair agreement with the BET area of 600 $m^2 \cdot g^{-1}$ (see *vide supra*), thereby providing additional evidence of the reliability of the so-built structural models.

Control of the Particle Size and Morphology: Synthesis of Nanoparticles of MIL-96-(Al). The characteristic morphology of MIL-96-(Al) crystals, as initially described, is that of a truncated hexagonal bipyramid.[15] Several solvo- and hydrothermal routes led to MIL-96-(Al) crystals with such a morphology but with different diameters (ranging from 0.8 to 40 μm) using Me_3BTC or trimesic acid.[19,31,34,35] Finally, nanoparticles of MIL-96-(Al) (from 160 to 55 nm) were recently reported by Knebel *et al.*[18] following a solvothermal synthesis in a mixture of H_2O/DMF solvents. We report here several synthesis routes yielding pure MIL-96-(Al) with various morphologies and sizes, down to the nanoscale as required for further MMM preparation. Microwave (MW)-assisted synthesis is known to reduce the size and the polydispersity of the particles due to fast and homogeneous heating favoring the nucleation process.[36] In contrast to the synthesis conditions of MIL-96-(Al)-HR, the initial aqueous solution of both aluminum and ligand precursors was diluted and an amount of acetic acid was added. A 2 min microwave-assisted hydrothermal synthesis performed at 473 K led to pure

DOI: 10.1021/acs.chemmater.7b03203
Chem. Mater. 2017, 29, 10326−10338

MIL-96-(Al) hexagonal platelets (*i.e.*, MIL-96-(Al)-HP), with a diameter of a few micrometers and an average thickness of a few 100 nm as determined by SEM (see Figure 1b). This process shows that MIL-96-(Al) can be isolated even at short reaction times as a pure phase without the presence of MIL-100-(Al) or MIL-110-(Al). Noteworthy, PXRD of both MIL-96-(Al)-HR and -HP (Figure 5a) show changes in the relative intensity of several Bragg peaks indicating a preferential orientation of such crystals with a shape anisotropy. This phenomenon is noticeable by comparing PXRD recorded with reflection (Bragg−Brentano method) and transmission (Debye−Sherrer method) geometry for HR (Figure S10) and HP (Figure S11). Hexagonal rods present a strong (010) reflection, while the intensity of (00l) peaks is reduced and (002) almost extinct. On the other hand, (00l) and (0*k*l) reflections are much more intense in crystals with hexagonal platelet morphologies. Therefore, (0*k*0) (and thus (*h*00)) reflections can be assigned to the long facets of hexagonal rods while (0*k*l) (and by symmetry (*h*0l)) reflections correspond to the trigonal facets present on top of the hexagonal platelets (see Figure 5b,c), in agreement with that previously reported for MIL-96-(Al) crystals of similar morphology.[18] Since acetic acid may act as a modulator as reported for several polycarboxylate-based MOFs,[37,38] it can be suggested that the presence of acetic acid impacts the nucleation and growth of MIL-96-(Al) crystals and thus its morphology. However, even without this modulator, MIL-96-(Al)-HP was also obtained along with MIL-100-(Al) as a byproduct. Such results emphasize that the formation of trimesate Al-based MOFs strongly depends on the speciation of molecular Al complexes in solution. The MW synthesis conditions were transferred to reflux synthesis in water. An aqueous diluted solution of Al salt, trimesic acid, and acetic acid was heated at reflux (~100 °C) for a variable period of time. After only 3 h at reflux, the colorless solution becomes cloudy indicating the formation of MIL-96-(Al) nanoparticles (*i.e.*, MIL-96-(Al)-NP1s) as shown by PXRD (Figure 5a). As observed by SEM (Figure 1c), hexagonal nanorods with a dimension up to 500 nm are formed by this route. This is, to our knowledge, the first synthesis producing pure MIL-96-(Al) nanoparticles in water under reflux conditions, with however a quite low yield (150 mg, Y = 45% based on Al). Increasing the concentration of the reactants failed to produce MIL-96-(Al). The formation of MIL-96-(Al)-NP1 under reflux in water is certainly mainly limited by the poor solubility of trimesic acid in pure water. Therefore, half of the volume of water was replaced by DMF to dissolve the entire 12 mmol of trimesic acid. After 16 h of reflux, nanoscale MIL-96-(Al) crystals were obtained as indicated by the presence of broad Bragg peaks on the XRD pattern (*i.e.*, MIL-96-(Al) NP2; see Figure 5a). As shown by the structureless refinement (Figure S12) and SEM images (Figure 1d and Figure S13), MIL-96-(Al) NP2 consists of pure nanocrystals with a diameter of 200 ± 30 nm. It is worth noting that synthesis conditions without acetic acid led to MIL-96-(Al) nanocrystals with a similar size and shape, however with a larger polydispersity in diameter (*i.e.*, diameter of particles of 190 ± 100 nm; see Figure S14). Such results are consistent with those previously reported by Sindoro *et al.*[34]

Following this synthetic route, a large amount of MIL-96-(Al)-NP2 (*e.g.*, 13 g in one batch with Y = 96% based on Al) was obtained. By decreasing by 2-fold the concentration of the reactants, smaller MIL-96-(Al) NP were synthesized at the gram scale (yield similar to that for NP2) as shown by PXRD (*i.e.*, MIL-96-(Al)-NP3; see Figure 5a). The structureless refinement (Figure S15) indicates MIL-96-(Al) nanocrystals with an average diameter of 70 nm, in agreement with the size distribution of 67 ± 40 nm given by SEM and TEM images (Figure 1e,f and Figure S16 of the SI). Nitrogen adsorption/desorption measurements (77 K) can be used to extract an "external surface area" (*i.e.*, without the porosity), and it would be expected that the smaller the particles are, the higher the external surface area is. The *t*-plot analysis was used which leads to values of 6, 40, and 100 $m^2 \cdot g^{-1}$ for the -HR, -NP2, and -NP3 samples highlighting the increasing nanoparticular size of this series (Figure S17). Dilute solutions of MIL-96-(Al)-NP2 and MIL-96-(Al)-NP3 in water were then studied by small angle X-ray scattering (SAXS). The SAXS curves (Figure 5d) are fairly well fitted on the whole *q*-range by the form factor of ellipsoids with rather low index of polydispersity. The dimensions extracted from fit (R_1 = 55 nm (PD = 0.1) and R_2 = 48 nm (PD = 0.2) for MIL-96-(Al)-NP3; R_1 = 100 nm (PD = 0.01) and R_2 = 80 nm (PD = 0.15) for MIL-96-(Al)-NP2) are in fair agreement with SEM observations. Noteworthy, no nanoparticle aggregation could be detected in

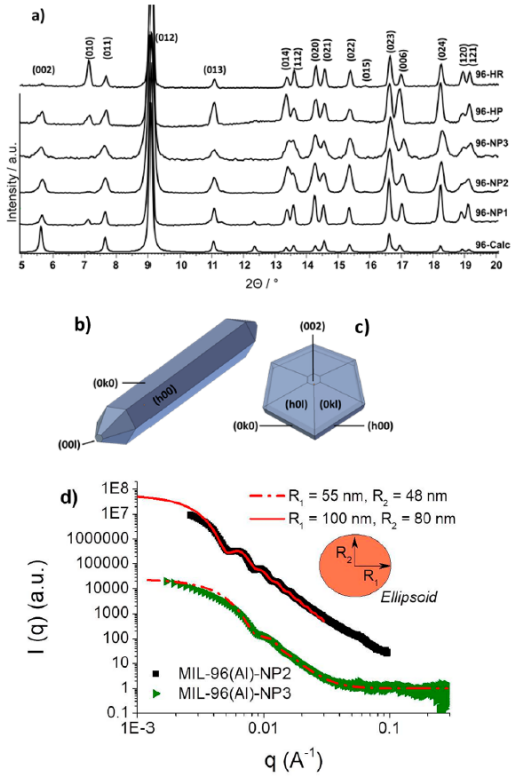

Figure 5. (a) PXRD of the different MIL-96-(Al) particles [all patterns normalized using the (012) reflection]; (b, c) 3D representations of the crystal morphology and the (*hkl*) planes of MIL-96-(Al) [(b) hexagonal rods and (c) hexagonal platelets]; (d) SAXS curves of MIL-96-(Al)NP2 (black squares) and MIL-96-(Al)-NP3 (green triangles) solutions at 0.1 g/L in water obtained at Alba and Soleil synchrotrons, respectively. The red lines correspond to the best fit with the ellipsoid form factor with radius indicated in the inset and log-normal polydispersity. For the continuous line the polydispersity indices (PDs) are PD R_1 = 0.01 and PD R_2 = 0.15, while for the dashed−dotted line PD R_1 = 0.1 and PD R_2 = 0.2.

DOI: 10.1021/acs.chemmater.7b03203
Chem. Mater. 2017, 29, 10326−10338

the available q-range. Finally, dynamic light scattering (DLS) experiments with 1.25 wt % MIL-96-(Al)-NP2 and -NP3 dispersed in pure tetrahydrofuran (THF) were performed to better characterize the colloidal stability. This solvent is currently used for dissolving 6FDA-DAM. DLS measurements (Figure S18) have shown only one population centered at 220 and 70 nm in diameter for MIL-96-(Al)-NP2 and -NP3, respectively, indicating the absence of any aggregation even at such high concentrations (1.25 wt % ≈ 10 g·L^{-1}) that are used for MMMs preparation. The colloidal solution is stable for at least 6 h, which is of high interest for the preparation of MMMs since the drying process takes generally a few hours.

***In Situ* IR Spectroscopy: Characterization of Adsorbed Water, Hydroxyl Groups, and Al^{3+} Sites.** FTIR spectra were recorded to study the stability and location of adsorbed water, characterize both the hydroxyl groups and Al sites of the MOF, and finally probe the interactions between the MOF and different guest molecules. Detailed interpretations of the IR spectra are provided in the SI. The IR spectrum of the as-prepared hydrated MIL-96-(Al)-HR sample (see Figure 6A, spectrum a) shows (i) the lack of free trimesic acid (evidenced by the absence of bands in the 1740−1710 cm^{-1} region),[39,40] (ii) a significant amount of adsorbed water (OH stretching band at 3388 cm^{-1} and combination band at 5215 cm^{-1}, as well as a δ-(D_2O) band at *ca.* 1205 cm^{-1} recorded with the deuterated sample),[41] and (iii) the existence of some amount of "free" -OH groups that are not involved in H-bonding with adsorbed water (combination band around 4690 cm^{-1} and deformation band at 1071 cm^{-1}).[41] The position of the latter IR bands indicates a very low acidity of (at least part of) the OH groups. Since the activation procedure for MOFs strongly impacts their sorption capacity, FTIR spectra of the MIL-96-(Al)-HR sample were recorded after outgassing at increasing temperature. Water trapped in the MOF is mostly removed by outgassing at RT as evidenced by the strong decrease in intensity of the bands at 5215 and 3388 cm^{-1} (Figure 6A, spectrum b). Only H_2O coordinated to Al sites remains in the pores after evacuation at 323 K, as shown by a weak ν-(OH) band at 3415 cm^{-1}, two weak combination bands at 5364 and 5288 cm^{-1}, and, for the deuterated sample, two δ-(D_2O) components at 1218 and 1209 cm^{-1} (Figure 6B, right inset).

Further, the remaining water is removed after evacuation at 423−448 K, in agreement with TGA results. The removal of the water leads to the appearance of free OH groups, as shown by two characteristic combination bands at 4688 and 4640 cm^{-1}. In addition, a set of bands appears in the ν-(OH) region (Table 1),

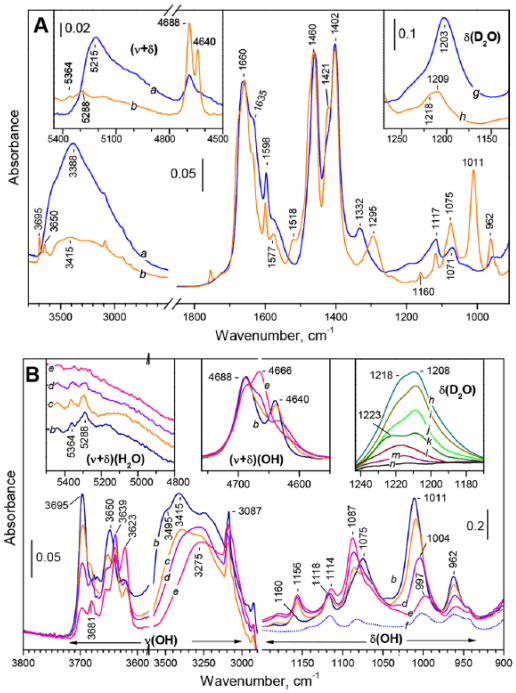

Figure 6. (A) IR spectra of MIL-96-(Al)-HR [(a) as-prepared sample and (b) after activation at RT; (left inset) spectrum in the ($\nu + \delta$) region; (right inset) δ(D_2O) mode with a deuterated sample (g) under D_2O vapor and (h) after activation at RT]; (B) IR spectra of MIL-96-(Al)-HR in the ν-(OH) and δ-(OH) regions [sample activated at (b) RT, (c) 373 K, (d) 423 K, and (e) 473 K; (f) deuterated sample activated at 473 K; (left and middle insets) spectra in the ($\nu + \delta$) region of H_2O and OH groups, respectively; (right inset) δ-(D_2O) mode with a deuterated sample after activation at (h) RT, (i) 323 K, (j) 348 K, (k) 373 K, (l) 398 K, (m) 423 K, and (n) 448 K].

Table 1. Vibrational Bands of the Hydroxyl Groups of MIL-96-(Al)

type of OH group	notation	ν(OH)	ν(OD)	δ(OH)	(ν+δ)(OH)
terminal	T1	3695	2724	962	4640
terminal	T2	3681	2714	997	
bridging	B1	3650	2692	1011	4640
bridging	B2	3639	2683	1075	4690
bridging	B3	3623	2672	1087	4665
H-bonded in C cages	C	3275	2448	1160	

the assignment of which is more complicated due to the possible overlapping between OH vibrations of adsorbed water and free hydroxyl groups.[41] For a correct assignment, partly deuterated samples were also investigated, thereby showing that all bands above 3600 cm^{-1} are due to -OH groups (see details in Figure S19 of the SI). Therefore, the water OH modes appear below 3600 cm^{-1}, which suggests that the two protons of residual adsorbed water are involved in H-bonding with basic sites (presumably oxygen atoms of carboxylates) from the MOF structure.

The T-type species (3695 and 3681 cm^{-1}) are assigned to structural terminal Al−OH hydroxyl while the B-type species (3650, 3639, and 3623 cm^{-1}) can be attributed to bridging μ_2-OH-type groups (see Table 1).[41] In addition, stable H-bonded OH groups (C-type) were also detected by a band at 3275 cm^{-1}. (Figure 6B, spectrum d). The low ν-(OH) frequency and the large bandwidth indicate that these hydroxyls are also involved in strong H-bonding with basic sites from the walls and are likely confined in small pores (presumably cages C). The bands of the terminal hydroxy develop after evacuation at RT as a result of the breaking of OH···(H_2O) bonds , which confirms the very weak acidity of these hydroxyls. Upon evacuation, the intensity of these bands decreases above 323 K pointing out some possible dehydroxylation process (for details see Figure S20). Bridging and C-type hydroxy groups are thermally stable (see Figures S19 and S20 and the SI for more details). As shown by ^{27}Al NMR spectroscopy, a modification of the Al environment takes place at temperatures higher than 473 K: a ^{27}Al resonance centered

DOI: 10.1021/acs.chemmater.7b03203
Chem. Mater. 2017, 29, 10326−10338

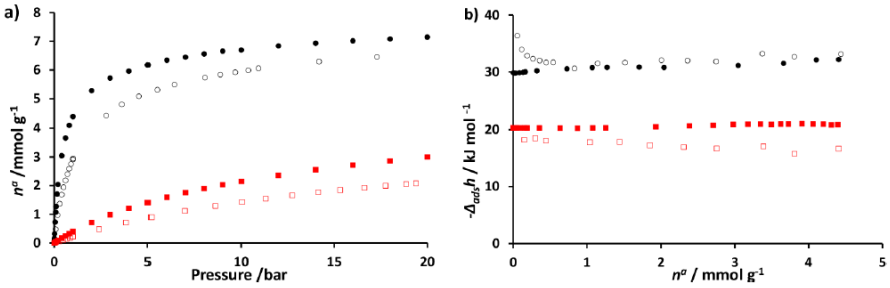

Figure 7. Experimental (empty symbols) and simulated (full symbols) CO_2 (black circle) and N_2 (red square) single-gas adsorption at 303 K on MIL-96-(Al)-NP2 activated at 423 K: (a) adsorption isotherm (*i.e.*, amount adsorbed as a function of pressure) and (b) adsorption enthalpies as a function of the coverage collected by microcalorimetry.

around 35 ppm, corresponding to five-coordinated Al sites, appears (Figure S21). Finally, we studied samples activated at different temperatures and then subjected to water vapor and evacuated again at ambient temperature (Figure S22). Noteworthy, the reversibility of water adsorption/desorption and the excellent stability of MIL-96-(Al) under water atmosphere or after thermal evacuation treatments was confirmed as the final spectra are essentially the same for samples evacuated up to 473 K.

In order to probe the accessibility of the cavities of MIL-96-(Al)-HR for gas sorption and to assess the Brønsted and Lewis acidity, adsorption of different probe molecules (CO, $^{15}N_2$, and CO_2) was monitored by *in situ* FTIR spectroscopy. Before such experiments, MIL-96-(Al)-HR was evacuated at different temperatures. Details are described in the SI (Figures S23–S26). While the pores of MIL-96-(Al)-HR evacuated at RT are not accessible to CO or $^{15}N_2$ at T = 100 K, a slight accessibility of the pores is observed after activation at 423 K that increases with the activation temperature (up to 573 K). Upon CO adsorption, OH groups are detected through a carbonyl band at 2155–2152 cm^{-1}[142] which develops with the pre-evacuation temperature up to 473 K (due to an increase in accessibility) and then decreases as a result of a possible dehydroxylation. Since two kinds of terminal OH groups (T1 and T2) differ only in the extent of H-bonding to the framework, the formation of OH···CO adducts leads to a red shift of the two OH modes to one band at 3669 cm^{-1}. This phenomenon indicates breaking of the pre-existing H-bond and the shift value is consistent with the very weak acidity of the hydroxyls. The same phenomena are observed with the bridging hydroxyls. Some Al^{3+} coordinatively unsaturated sites (CUS) are also detected by CO or $^{15}N_2$ (adsorbed at 100 K) with a sample evacuated at temperatures as high as 423 K. In contrast to the low-temperature experiments, adsorption of CO_2 on a sample evacuated at RT leads to the formation of Al^{3+}···OCO ($\nu_3(CO_2)$ at 2345 cm^{-1}) and OH···OCO adducts (2338 cm^{-1}).[43,44] The amount of the former species increases with the pre-evacuation temperature up to 473 K due to the removal of coordinated water while that of OH···OCO decreases.

CO_2/N_2 Gas Sorption Properties of MIL-96-(Al)-NP2: Single-Gas Adsorption, CO_2/N_2 Coadsorption, and Molecular Simulations. According to IR spectroscopy, MIL-96-(Al) needs to be activated by outgassing the sample to around 423 K in order to remove all the free water or residual free trimesic acid. Single-gas adsorption experiments were first performed on MIL-96-(Al)-NP2 samples. Figure 7a shows the excess adsorption isotherms of pure single-gas components CO_2 and N_2 obtained at 303 K for MIL-96-(Al)-NP2 activated at 423 K (see Figure S27 for comparison with isotherms on MIL-96-(Al)-HR). At 1 bar, the adsorption capacities are 3.2 mmol·g^{-1} for CO_2, while a much lower capacity of about 0.2 mmol·g^{-1} for N_2 is obtained. Grand canonical Monte Carlo (GCMC) simulations were carried out at 303 K to predict the single-component adsorption of CO_2 and N_2 (see the SI for details). The experimental findings are qualitatively reproduced by the GCMC simulations (see Figure 7a), even though the calculated amounts adsorbed slightly overestimate the experimental data for the two gases. This discrepancy is likely due to the fact that GCMC simulations consider that both gases can adsorb in the entire porosity available in the solid. As explained above, the adsorption of gas in MIL-96-(Al) might be restricted to cavities B and C since cavities A seem to be isolated in the framework. Interestingly, the experimental adsorption uptakes of CO_2 at 1 bar (~3.2 mmol·g^{-1} at 303 K) and 10 bar (~6.3 mmol·g^{-1}) are among the best performances for small pore MOFs previously reported for CO_2 separation such as MIL-91-(Ti) (~3.0 mmol·g^{-1} at 1 bar and 303 K and ~4.5 mmol·g^{-1} at 10 bar and 303 K),[45] MIL-53-(Al)-NH_2 (1.6 mmol·g^{-1} at 283 K and 1 bar),[46] $Sc_2(BDC\text{-}NO_2)_3$ (1.1 mmol·g^{-1} at 303 K and 1 bar),[47] UiO-66-(Zr)-2COOH (1.0 mmol·g^{-1} at 303 K and 1 bar),[48] and SIFSIX-3-Zn (2.3 mmol·g^{-1} at 308 K and 1 bar).[49] However, this CO_2 adsorption capacity value is lower than both that of a benchmark zeolite 13X (5.0 mmol·g^{-1} at 1 bar and 298 K)[50] and Mg-MOF-74 (8.0 mmol·g^{-1} at 1 bar and 298 K), although the latter is not water stable.[51] The initial slope of the CO_2 adsorption isotherm is significantly higher than that of N_2, and this emphasizes a much stronger affinity of MIL-96-(Al) for CO_2. Such results are fully consistent with FTIR, showing a strong adsorption of CO_2 at both the Lewis acid Al^{3+} sites (2345 cm^{-1}) and terminal/bridging hydroxyl groups (2338 cm^{-1}) of MIL-96-(Al)-HR (see Figure S26). The enthalpy of adsorption for CO_2 in MIL-96-(Al)-NP2 as a function of loading is given in Figure 7b. The high experimental enthalpy values at low coverage are certainly due to the interaction of CO_2 molecules with Al^{3+} CUS. Experimental and simulated enthalpy values of CO_2 adsorption remain between −35 and −30 kJ·mol^{-1} throughout the CO_2 uptake except at lower coverage. This relatively flat energetic profile indicates a homogeneous energetic interaction with the adsorption sites. Interestingly, this adsorption enthalpy for CO_2 is substantially higher or comparable to other MOFs (*i.e.*, UiO-66(Zr), ~−26 kJ·mol^{-1};[52] UiO-66-(Hf)-$(OH)_2$, −28.4 kJ·mol^{-1};[53] and UiO-66-(Hf), ~−22.8 kJ·mol^{-1}),[53] however lower than other highly efficient CO_2 adsorbents such as zeolite 13X

DOI: 10.1021/acs.chemmater.7b03203
Chem. Mater. 2017, 29, 10326−10338

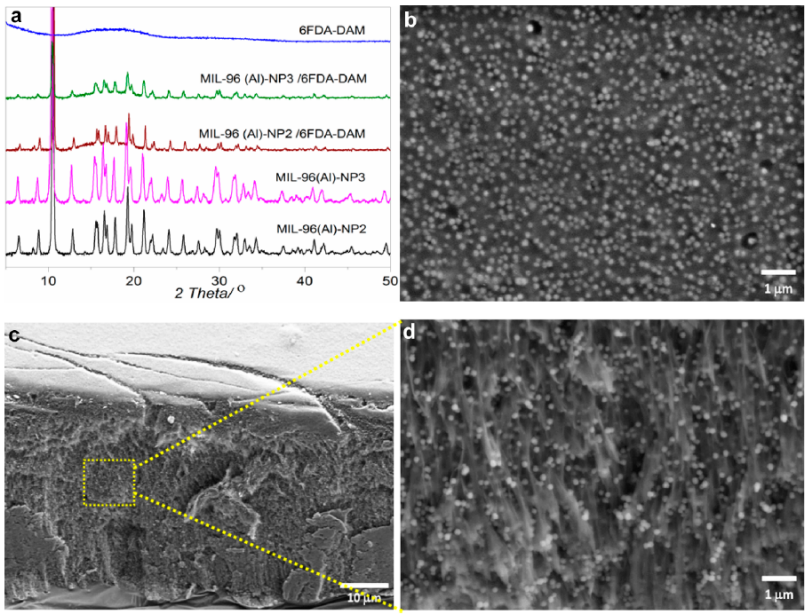

Figure 8. (a) PXRD of MIL-96-(Al)-NP2/6FDA-DAM and MIL-96-(Al)-NP3/6FDA-DAM MMMs in comparison with the pure polymer and MIL-96-(Al) NP; (b) SEM image of the top surface of MIL-96-(Al)-NP2/6FDA-DAM; (c) cross-section SEM image of MIL-96-(Al)-NP2/6FDA-DAM; (d) higher magnification SEM image confirming high dispersion of MIL-96-(Al)-NP2 in the volume of the membrane.

(−38 kJ·mol^{-1}),[50] and MIL-91-(Ti) (∼−43 kJ·mol^{-1}),[45] MIL-53-(Al)-NH_2 (∼−40 kJ·mol^{-1}),[46,54] Mg-MOF-74 (∼ −50 kJ·mol^{-1}),[51,55] SIFSIX-3-Zn (−45 kJ·mol^{-1}),[49] and SIFSIX-3-Co (−47 kJ·mol^{-1}).[56] Such a moderate adsorption enthalpy suggests an easy reversibility of adsorption−desorption cycles, which is highly desirable for the adsorbent regeneration process as a balance between separation performance and energy cost is required in real industrial operations.

Experimental and simulated enthalpy values of N_2 adsorption are lower than that of CO_2, confirming the much lower affinity of MIL-96-(Al) for this guest molecule. However, this value is higher than many medium to large pore MOFs but less than those containing CUS sites, suggesting that the small amount of nitrogen adsorbed is relatively confined, as reported for other MOFs with small pores size (3.0−4.0 Å).[16,45]

The sorption-based binary gas separation performance of MIL-96-(Al)-NP2 was evaluated by considering postcombustion CO_2 capture, in which 10−15% of CO_2 needs to be removed from flue gas mixtures containing N_2. Coadsorption measurements were performed on about 10 g of MIL-96-(Al)-NP2. Such real coadsorption data, rarely reported in the literature, were collected by using an advanced homemade device that combines a volumetric apparatus and gas chromatography analysis (see the SI for more details). The measurements were performed at 303 K for a gas mixture CO_2/N_2 = 10/90 and 15/85 at 1.0 and 3.0 bar, *i.e.*, the typical industrial concentration and pressure conditions for the membrane separation of flue gas emitted from power plants or cement plants. Each mixture point was repeated several times, and an average selectivity value was given. The coadsorption selectivity of ∼36 was obtained at 1 bar and 303 K for the case of CO_2/N_2 = 10/90 and remains nearly constant on increasing the CO_2 concentration (CO_2/N_2 = 15/85). The selectivity values are slightly modified by increasing the pressure to 3 bar (*i.e.*, S_{EXP} = 29 for CO_2/N_2 = 15/85). Such results are in excellent agreement with data obtained by GCMC simulations (*i.e.*, S_{GCMC} = 34 for CO_2/N_2 = 15/85 at 1 bar and 303 K) (see Figure S31 of the SI).

Processing of Mixed Matrix Membrane and Post-combusion CO_2/N_2 Separation. Due to the excellent colloidal stability of MIL-96-(Al)-NP2 and -NP3 in THF, MMMs with a high MOF content (25 wt %) could be prepared by dispersing both MIL-96-(Al)-NPs in a solution of 6FDA-DAM in THF. PXRD of both MIL-96-(Al)-NP2/6FDA-DAM and MIL-96-(Al)-NP3/6FDA-DAM MMMs (Figure 8a) superimpose well with the one of MIL-96-(Al)-NP, confirming that the crystalline structure of MIL-96-(Al) is preserved upon its association with 6FDA-DAM. SEM images (Figure 8b and Figure S32) of the top surface of MMMs show the excellent dispersion of MIL-96-(Al)-NP2s in the polymer matrix with the absence of any significant aggregation. Such results are confirmed by cross-sectional SEM images (Figure 8c,d and Figure S32), showing a homogeneous distribution of MIL-96-(Al) nanocrystals in the volume of the membranes. The thickness of the supported membranes lies between 60 and 65 μm. Similar results were obtained with MMMs based on MIL-96-(Al)-NP3. According to SEM images, no defects or voids of about a few nanometers in size could be observed at the interface between the MIL-96-(Al) NP and polymer.

The CO_2 adsorption isotherms of membranes with 25 wt % loading of MIL-96-(Al)-NP2 and -NP3 in 6FDA-DAM are illustrated in Figure 9a. To illustrate the possible effect of filler on adsorption properties of MMMs, theoretical isotherms were calculated assuming the additive CO_2 adsorption in 25 wt % MOF and 75 wt % polymer (see Figure 9a) corresponding to the

DOI: 10.1021/acs.chemmater.7b03203
Chem. Mater. 2017, 29, 10326−10338

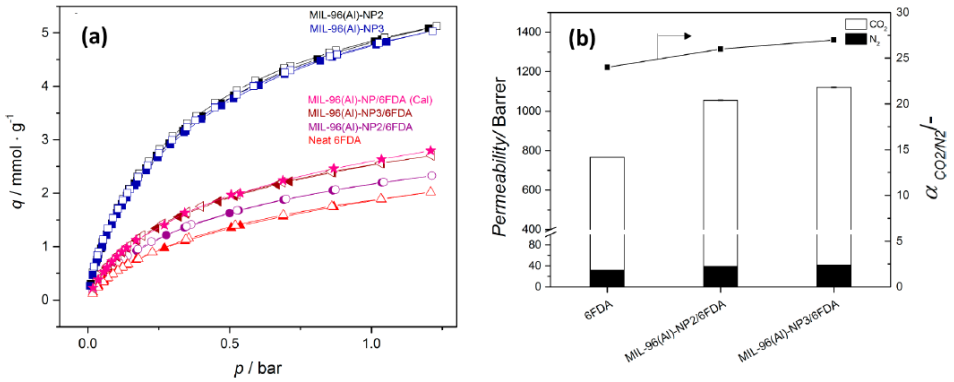

Figure 9. (a) CO_2 adsorption isotherms at 273 K of MIL-96-(Al)-NP2 and -NP3, neat 6FDA-DAM, experimental and calculated isotherms of MMMs with 25 wt % MIL-96-(Al)-NP2 and -NP3 loading; (b) permeation properties for a CO_2 and N_2 mixture (15/85) of MMMs comprising 25 wt % MIL-96-(Al)-NP2 and -NP3 as filler and 6FDA-DAM as polymer matrix at 298 K and 2 bar feed pressure. Permeate side atmospheric with helium as sweep gas.

composition of the MMM. Noteworthy, the experimental CO_2 adsorption capacity of MMMs based on MIL-96-(Al)-NP2 is lower than the theoretical one, whereas experimental and calculated CO_2 adsorptions are almost similar for MMMs based on MIL-96-(Al)-NP3. This is tentatively attributed to a better dispersion of the smaller NP3 particles in the polymer and thus a higher accessibility to gas molecules.

The CO_2 and N_2 separation (15/85 (vol %)) at 298 K, 2 bar (abs) feed pressure and helium sweep gas was carried out to study the permeation performance of the MMMs. Remarkably, the addition of MIL-96-(Al)-NP2 and -NP3 to the high free-volume polymer led to an ~37% enhancement of the CO_2 permeability in 6FDA-DAM, attributed to the high CO_2 uptake by MIL-96-(Al) (see above). The selectivity improved somewhat as well, slightly more for the smaller particles (Figure 9). Moreover, to further examine the performance of MMMs in different feed concentrations, the MIL-96-(Al)-NP3/6FDA-DAM MMM was tested under 15/85, 50/50, and 85/15 ratios of CO_2/N_2 in the feed (Table S6). The almost unchanged CO_2/N_2 selectivity of MIL-96-(Al)-NP2/6FDA-DAM MMM for increased CO_2 concentration is in line with the nearly constant selectivity for the CO_2/N_2 coadsorption of pure MOF (see *vide supra*). Although the permeability of the membrane decreased (~27%) with increased CO_2 concentration, ascribed to saturation of adsorption sites in the membrane matrix,[57] the CO_2 flux through the membrane nevertheless increases with concentration. The influence of the humidity on the CO_2/N_2 separation properties of the neat 6FDA-DAM and MIL-96-(Al)-NP3/6FDA-DAM membranes was further evaluated (see details in the SI). As shown in Table S7, similar results of CO_2/N_2 permeability and selectivity were obtained for MIL-96-(Al)-NP3/6FDA-DAM membranes exposed to air humidity after two cycles of adsorption/desorption of water. The impact of humidity on the permeation of neat 6FDA-DAM membrane is almost negligible.

Finally, the performance in terms of permeability and selectivity of the MIL-96-(Al)-based MMMs regarding the Robeson 2008 limit is illustrated in Figure S33.[58,59] A comparison of their performance with membranes prepared with 6FDA-based polymer is also shown (see Figure S33 and Table S8). Although the Robeson upper bound is not exceeded, the addition of the filler significantly improved the overall performance of the neat polymeric membrane. Moreover, in comparison to MMMs previously reported, the composite membranes based on MIL-96-(Al) present promising performances for postcombustion application with enhanced CO_2/N_2 selectivity.

■ CONCLUSION

In the present study, by using a wide variety of advanced complementary experimental and computational tools, the crystalline structure of the microporous Al trimesate MIL-96-(Al) (anhydrous or hydrated) was reinvestigated allowing a clear description of the local environment of Al sites (symmetry, nature of oxygen ligands). This refinement was required in order to fill gaps in the original structural model reported for MIL-96-(Al),[15] which remained questionable due to inconsistencies between solid-state NMR and single-crystal XRD experiments. The complex hydrogen-bond network formed by the adsorbed water molecules within the MOF framework and its hydroxyl groups was fully described. Several synthesis routes were reported leading to pure MIL-96-(Al) crystals with various morphologies and sizes, down to the nanoscale as required for MMM preparation. Monodisperse MIL-96-(Al) nanoparticles were obtained at high yield under reflux conditions, and the colloidal solutions present an excellent stability in different solvents (water and THF). The complete characterization of the CO_2/N_2 gas sorption properties of MIL-96-(Al) including *in situ* FTIR, CO_2/N_2 adsorption/coadsorption experiments, calorimetry, and GCMC simulations has shown that MIL-96-(Al) presents a high CO_2 uptake at low concentration due to the high affinity of CO_2 molecules to Al^{3+} CUS and OH ligands of MIL-96-(Al). Finally, MMMs based on MIL-96-(Al)-NP and 6FDA-DAM with a high MOF loading (~25 wt %) were cast, showing an excellent dispersion of the MOF fillers in the polymer matrix and very promising CO_2/N_2 performance (permeability and selectivity). Such properties are likely to be due to the excellent chemical compatibility between MIL-96-(Al) and 6FDA-DAM and the absence of any defects or voids at the MOF/polymer interface. Such results pave the way for the processing of composite membranes with a higher MOF content (>30 wt %).

■ ASSOCIATED CONTENT

Supporting Information

The Supporting Information is available free of charge on the ACS Publications website at DOI: 10.1021/acs.chemmater.7b03203.

DOI: 10.1021/acs.chemmater.7b03203
Chem. Mater. 2017, 29, 10326−10338

^{27}Al MQMAS NMR and FTIR spectra; TGA; PXRD pattern and structureless refinement of MIL-96-(Al) samples; size distributions of MIL-96-(Al)-NPs; single-adsorption isotherms; simulated CO_2/N_2 selectivity; SEM images and CO_2/N_2 separation experiments of membranes(PDF)
Crystal structure of MIL-96-(Al) (CIF)
CIF structure report (PDF)

AUTHOR INFORMATION

Corresponding Author

*Tel.: 33 1 39 25 43 73. E-mail: nathalie.steunou@uvsq.fr.

ORCID

Renjith S Pillai: 0000-0003-0165-3305
Philip L. Llewellyn: 0000-0001-5124-7052
Konstantin Hadjiivanov: 0000-0002-7622-4620
Jorge Gascon: 0000-0001-7558-7123
Freek Kapteijn: 0000-0003-0575-7953
Guillaume Maurin: 0000-0002-2096-0450
Nathalie Steunou: 0000-0002-7049-7388

Notes

The authors declare no competing financial interest.

ACKNOWLEDGMENTS

We acknowledge the European Community Seventh Framework Program (FP7/2007-2013) for funding the research presented in this article under Grant Agreement No. 608490 (Project M4CO2). We thank IMPC FR2482 for SEM-FEG instrumentation funded by CNRS, UPMC, and C'Nano projects of Région Ile-de-France. We also acknowledge synchrotrons SOLEIL (Saint-Aubin, France) and ALBA (Barcelona, Spain) for SAXS beam time allocation. We additionally thank Thomas Bizien (SWING, SOLEIL) for his help during SAXS experiments and the staff of the PROXIMA 2A at SOLEIL for technical assistance. G.M. thanks Institut Universitaire de France for its support.

REFERENCES

(1) Metal−Organic Frameworks (MOFs). Kitagawa, S., Zhou, H.-C. J., Guest Eds. *Chem. Soc. Rev.* **2014**, *43*, 5415−6176 (Themed Collection).
(2) Metal-Organic Frameworks and Porous Polymers—Current and Future Challenges. Maurin, G., Serre, C., Cooper, A., Férey, G., Guest Eds. *Chem. Soc. Rev.*. **2017**,*46*, 3104−3481 (Themed Collection).
(3) Almeida Paz, F. A.; Klinowski, J.; Vilela, S. M. F.; Tomé, J. P. C.; Cavaleiro, J. A. S.; Rocha, J. Ligand Design for Functional Metal−Organic Frameworks. *Chem. Soc. Rev.* **2012**, *41*, 1088−1110.
(4) Padial, N. M.; Quartapelle Procopio, E.; Montoro, C.; Lopez, E.; Oltra, J. E.; Colombo, V.; Maspero, A.; Masciocchi, N.; Galli, S.; Senkovska, I.; Kaskel, S.; Barea, E.; Navarro, J. A. R. Highly Hydrophobic Isoreticular Porous Metal−Organic Frameworks for the Capture of Harmful Volatile Organic Compounds. *Angew. Chem., Int. Ed.* **2013**, *52*, 8290−8294.
(5) Trickett, C. A.; Helal, A.; Al-Maythalony, B. A.; Yamani, Z. H.; Cordova, K. E.; Yaghi, O. M. The Chemistry of Metal−Organic Frameworks for CO_2 Capture, Regeneration and Conversion. *Nature Rev. Mater.* **2017**, *2*, 17045.
(6) Cadiau, A.; Belmabkhout, Y.; Adil, K.; Bhatt, P. M.; Pillai, R. S.; Shkurenko, A.; Martineau-Corcos, C.; Maurin, G.; Eddaoudi, M. Hydrolytically Stable Fluorinated Metal-Organic Frameworks for Energy-Efficient Dehydration. *Science* **2017**, *356*, 731−735.
(7) Assi, H.; Mouchaham, G.; Steunou, N.; Devic, T.; Serre, C. Titanium Coordination Compounds: from Discrete Metal Complexes to Metal−Organic Frameworks. *Chem. Soc. Rev.* **2017**, *46*, 3431−3452.
(8) Maurin, G. Role of Molecular Simulations in the Structure Exploration of Metal-Organic Frameworks: Illustrations through recent advances in the field. *C. R. Chim.* **2016**, *19*, 207−215.
(9) Martineau, C. NMR Crystallography: Applications to Inorganic Materials. *Solid State Nucl. Magn. Reson.* **2014**, *63*−*64*, 1−12.
(10) Bonhomme, C.; Gervais, C.; Babonneau, F.; Coelho, C.; Pourpoint, F.; Azaïs, T.; Ashbrook, S. E.; Griffin, J. M.; Yates, J. R.; Mauri, F.; Pickard, C. J. First-Principles Calculation of NMR Parameters Using the Gauge Including Projector Augmented Wave Method: A Chemist's Point of View. *Chem. Rev.* **2012**, *112*, 5733−5779.
(11) Férey, G.; Mellot-Draznieks, C.; Serre, C.; Millange, F.; Dutour, J.; Surblé, S.; Margilolaki, I. A Chromium Terephthalate−Based Solid with Unusually Large Pore Volumes and Surface Area. *Science* **2005**, *309*, 2040−2042.
(12) Alvarez, E.; Guillou, N.; Martineau, C.; Bueken, B.; Van de Voorde, B.; Le Guillouzer, C.; Fabry, P.; Nouar, F.; Taulelle, F.; de Vos, D.; Chang, J.-S.; Cho, K. H.; Ramsahye, N.; Devic, T.; Daturi, M.; Maurin, G.; Serre, S. The Structure of the Aluminum Fumarate Metal−Organic Framework A520. *Angew. Chem., Int. Ed.* **2015**, *54*, 3664−3668.
(13) Rouquerol, F.; Rouquerol, J.; Sing, K. S. W.; Llewellyn, P. L.; Maurin, G. In *Adsorption by Powders and Porous Solids*, 2nd ed.; Elsevier: Oxford, U.K., 2014; Chapter 6, pp 191−235, DOI: 10.1016/B978-0-08-097035-6.00006-1.
(14) Maurin, G. In *The Chemistry of Metal Organic Frameworks: Synthesis, Characterization and Applications*; Kaskel, S., Ed.; Wiley-VCH Verlag: Weinheim, Germany, 2016; Vol. 2.
(15) Loiseau, T.; Lecroq, L.; Volkringer, C.; Marrot, J.; Férey, G.; Haouas, M.; Taulelle, F.; Bourrelly, S.; Llewellyn, P. L.; Latroche, M. MIL-96, a Porous Aluminum Trimesate 3D Structure Constructed from a Hexagonal Network of 18-Membered Rings and μ_3-Oxo-Centered Trinuclear Units. *J. Am. Chem. Soc.* **2006**, *128*, 10223−10230.
(16) Adil, K.; Belmabkhout, Y.; Pillai, R. S.; Cadiau, A.; Bhatt, P. M.; Assen, A. H.; Maurin, G.; Eddaoudi, M. Gas/vapour Separation using Ultra-microporous Metal−Organic Frameworks: Insights into the Structure/Separation Relationship. *Chem. Soc. Rev.* **2017**, *46*, 3402−3430.
(17) Maes, M.; Alaerts, L.; Vermoortele, F.; Ameloot, R.; Couck, S.; Finsy, V.; Denayer, J. F. M.; De Vos, D. E. Separation of C5-Hydrocarbons on Microporous Materials: Complementary Performance of MOFs and Zeolites. *J. Am. Chem. Soc.* **2010**, *132*, 2284−2292.
(18) Knebel, A.; Friebe, S.; Bigall, N. C.; Benzaqui, M.; Serre, C.; Caro, J. Comparative Study of MIL-96-(Al) as Continuous Metal-Organic Frameworks Layer and Mixed-Matrix Membrane. *ACS Appl. Mater. Interfaces* **2016**, *8*, 7536−7544.
(19) Qiu, M.; Chen, C.; Li, W. Rapid Controllable Synthesis of Al-MIL-96 and Its Adsorption of Nitrogenous VOCs. *Catal. Today* **2015**, *258*, 132−138.
(20) Lan, X.; Zhang, H.; Bai, P.; Guo, X. Investigation of Metal Organic Frameworks for the Adsorptive Removal of Hydrochloride from Dilute Aqueous Solution. *Microporous Mesoporous Mater.* **2016**, *231*, 40−46.
(21) Zhang, N.; Yang, X.; Yu, X.; Jia, Y.; Wang, J.; Kong, L.; Jin, Z.; Sun, B.; Luo, T.; Liu, J. Al-1,3,5-benzenetricarboxylic Metal-Organic Frameworks: A Promising Adsorbent for Defluoridation of Water with pH Insensitivity and Low Aluminum Residual. *Chem. Eng. J.* **2014**, *252*, 220−229.
(22) Zornoza, B.; Tellez, C.; Coronas, J.; Gascon, J.; Kapteijn, F. Metal Organic Framework based Mixed Matrix Membranes: An Increasingly Important Field of Research with a Large Application Potential. *Microporous Mesoporous Mater.* **2013**, *166*, 67−78.
(23) Seoane, B.; Coronas, J.; Gascon, I.; Benavides, M. E.; Karvan, O.; Caro, J.; Kapteijn, F.; Gascon, J. Metal−Organic Framework based Mixed Matrix Membranes: a Solution for Highly Efficient CO_2 Capture? *Chem. Soc. Rev.* **2015**, *44*, 2421−2454.
(24) Qiu, S.; Xue, M.; Zhu, G. Metal−Organic Framework Membranes: from Synthesis to Separation Application. *Chem. Soc. Rev.* **2014**, *43*, 6116−6140.
(25) Zhang, Y.; Feng, X.; Yuan, S.; Zhou, J.; Wang, B. Challenges and Recent Advances in MOF-polymer Composite Membranes for Gas Separation. *Inorg. Chem. Front.* **2016**, *3*, 896−909.
(26) Denny, M. S., Jr.; Moreton, J. C.; Benz, L.; Cohen, S. M. Metal-organic Frameworks for Membrane-based Separations. *Nature Rev. Mater.* **2016**, *1*, 16078.

DOI: 10.1021/acs.chemmater.7b03203
Chem. Mater. 2017, 29, 10326−10338

(27) Perez, E. V.; Balkus, K. J., Jr.; Ferraris, J. P.; Musselman, I. H. Mixed-Matrix Membranes Containing MOF-5 for Gas Separations. *J. Membr. Sci.* **2009**, *328*, 165−173.
(28) Ordonez, M. J. C.; Balkus, K. J., Jr; Ferraris, J. P.; Musselman, I. H. Molecular Sieving Realized with ZIF-8/Matrimid-(R) Mixed-Matrix Membranes. *J. Membr. Sci.* **2010**, *361*, 28−37.
(29) Benzaqui, M.; Semino, R.; Menguy, N.; Carn, F.; Kundu, T.; Guigner, J.−M.; McKeown, N. B.; Msayib, K. J.; Carta, M.; Malpass-Evans, R.; Le Guillouzer, C.; Clet, G.; Ramsahye, N. A.; Serre, C.; Maurin, G.; Steunou, N. Toward an Understanding of the Microstructure and Interfacial Properties of PIMs/ZIF-8 Mixed Matrix Membranes. *ACS Appl. Mater. Interfaces* **2016**, *8*, 27311−27321.
(30) Khan, N. A.; Lee, J. S.; Jeon, J.; Jun, C.-H.; Jhung, S. H. Phase-Selective Synthesis and Phase-Conversion of Porous Aluminum-Benzenetricarboxylates with Microwave Irradiation. *Microporous Mesoporous Mater.* **2012**, *152*, 235−239.
(31) Haouas, M.; Volkringer, C.; Loiseau, T.; Férey, G.; Taulelle, F. In Situ NMR, Ex Situ XRD and SEM Study of the Hydrothermal Crystallization of Nanoporous Aluminum Trimesates MIL-96, MIL-100, and MIL-110. *Chem. Mater.* **2012**, *24*, 2462−2471.
(32) Seoane, B.; Dikhtiarenko, A.; Mayoral, A.; Tellez, C.; Coronas, J.; Kapteijn, F.; Gascon, J. Metal Organic Framework Synthesis in the Presence of Surfactants: Toward Hierarchical MOFs? *CrystEngComm* **2015**, *17*, 1693−1700.
(33) Qiu, M.; Guan, Q.; Li, W. Controllable Assembly of Al-MIL-100 via an Inducing Occupied effect and Its Selective Adsorption Activity. *Cryst. Growth Des.* **2016**, *16*, 3639−3646.
(34) Sindoro, M.; Jee, A.-Y.; Granick, S. Shape-Selected Colloidal MOF Crystals for Aqueous Use. *Chem. Commun.* **2013**, *49*, 9576−9578.
(35) Liu, D.; Liu, Y.; Dai, F.; Zhao, J.; Yang, K.; Liu, C. Size- and Morphology-Controllable Synthesis of MIL-96-(Al) by Hydrolysis and Coordination Modulation of Dual Aluminum Source and Ligand Systems. *Dalton Trans.* **2015**, *44*, 16421−16429.
(36) Reinsch, H.; Stock, N. High-throughput Studies of Highly Porous Al-based MOFs. *Microporous Mesoporous Mater.* **2013**, *171*, 156−165.
(37) Zahn, G.; Zerner, P.; Lippke, J.; Kempf, F. L.; Lilienthal, S.; Schröder, C. A.; Schneider, A. M.; Behrens, P. Insight into the Mechanism of Modulated Syntheses: in situ Synchrotron Diffraction Studies on the Formation of Zr-fumarate MOF. *CrystEngComm* **2014**, *16*, 9198−9207.
(38) Schaate, A.; Roy, P.; Godt, A.; Lippke, J.; Waltz, F.; Wiebcke, M.; Behrens, P. Modulated Synthesis of Zr-Based Metal−Organic Frameworks: From Nano to Single Crystals. *Chem. - Eur. J.* **2011**, *17* (24), 6643−6651.
(39) Leclerc, H.; Vimont, A.; Lavalley, J.-C.; Daturi, M.; Wiersum, A. D.; Llewellyn, P. L.; Horcajada, P.; Férey, G.; Serre, C. Infrared Study of the Influence of Reducible Iron-(III) Metal Sites on the Adsorption of CO, CO_2, Propane, Propene and Propyne in the Mesoporous Metal−Organic Framework MIL-100. *Phys. Chem. Chem. Phys.* **2011**, *13*, 11748−11756.
(40) Lieb, A.; Leclerc, H.; Devic, T.; Serre, C.; Margiolaki, I.; Mahjoubi, F.; Lee, J. S.; Vimont, A.; Daturi, M.; Chang, J.-S. MIL-100-(V) − A Mesoporous Vanadium Metal Organic Framework with Accessible Metal Sites. *Microporous Mesoporous Mater.* **2012**, *157*, 18−23.
(41) Hadjiivanov, K. Identification and Characterization of Surface Hydroxyl Groups by Infrared Spectroscopy. *Adv. Catal.* **2014**, *57*, 99−318.
(42) Hadjiivanov, K.; Vayssilov, G. Characterization of Oxide Surfaces and Zeolites by Carbon Monoxide as an IR Probe Molecule. *Adv. Catal.* **2002**, *47*, 307−511.
(43) Mihaylov, M.; Chakarova, K.; Andonova, S.; Drenchev, N.; Ivanova, E.; Pidko, E. A.; Sabetghadam, A.; Seoane, B.; Gascon, J.; Kapteijn, F.; Hadjiivanov, K. Adsorption of CO_2 on MIL-53-(Al): FTIR Evidence of the Formation of Dimeric CO_2 Species. *Chem. Commun.* **2016**, *52*, 1494−1497.
(44) Serre, C.; Bourrelly, S.; Vimont, A.; Ramsahye, N. A.; Maurin, G.; Llewellyn, P. L.; Daturi, M.; Filinchuk, Y.; Leynaud, O.; Barnes, P.; Férey, G. An Explanation for the Very Large Breathing Effect of a Metal−Organic Framework during CO_2 Adsorption. *Adv. Mater.* **2007**, *19*, 2246−2251.
(45) Benoit, V.; Pillai, R. S.; Orsi, A.; Normand, P.; Jobic, H.; Nouar, F.; Billemont, P.; Bloch, E.; Bourrelly, S.; Devic, T.; Wright, P. A.; de Weireld, G.; Serre, C.; Maurin, G.; Llewellyn, P. L. MIL-91-(Ti), a Small Pore Metal−organic Framework Which Fulfils Several Criteria: An Upscaled Green Synthesis, Excellent Water Stability, High CO_2 Selectivity and Fast CO_2 Transport. *J. Mater. Chem. A* **2016**, *4*, 1383−1389.
(46) Stavitski, E.; Pidko, E. A.; Couck, S.; Remy, T.; Hensen, E. J. M.; Weckhuysen, B. M.; Denayer, J.; Gascon, J.; Kapteijn, F. Complexity behind CO_2 Capture on NH_2-MIL-53-(Al). *Langmuir* **2011**, *27*, 3970−3976.
(47) Pillai, R. S.; Benoit, V.; Orsi, A.; Llewellyn, P. L.; Wright, P. A.; Maurin, G. Highly Selective CO_2 Capture by Small Pore Scandium-Based Metal−Organic Frameworks. *J. Phys. Chem. C* **2015**, *119*, 23592−23598.
(48) Yang, Q.; Vaesen, S.; Ragon, F.; Wiersum, A. D.; Wu, D.; Lago, A.; Devic, T.; Martineau, C.; Taulelle, F.; Llewellyn, P. L.; Jobic, H.; Zhong, C.; Serre, C.; De Weireld, G.; Maurin, G. A Water Stable Metal−Organic Framework with Optimal Features for CO_2 Capture. *Angew. Chem., Int. Ed.* **2013**, *52*, 10316−10320.
(49) Nugent, P.; Belmabkhout, Y.; Burd, S. D.; Cairns, A. J.; Luebke, R.; Forrest, K.; Pham, T.; Ma, S.; Space, B.; Wojtas, L.; Eddaoudi, M.; Zaworotko, M. J. Porous Materials with Optimal Adsorption Thermodynamics and Kinetics for CO_2 Separation. *Nature* **2013**, *495*, 80−84.
(50) Cavenati, S.; Grande, C. A.; Rodrigues, A. E. Adsorption Equilibrium of Methane, Carbon Dioxide, and Nitrogen on Zeolite 13X at High Pressures. *J. Chem. Eng. Data* **2004**, *49*, 1095−1101.
(51) Caskey, S. R.; Wong-Foy, A. G.; Matzger, A. J. Dramatic Tuning of Carbon Dioxide Uptake via Metal Substitution in a Coordination Polymer with Cylindrical Pores. *J. Am. Chem. Soc.* **2008**, *130*, 10870−10871.
(52) Yang, Q.; Wiersum, A. D.; Llewellyn, P. L.; Guillerm, V.; Serre, C.; Maurin, G. Functionalizing Porous Zirconium Terephthalate UiO-66-(Zr) for Natural Gas Upgrading: a Computational Exploration. *Chem. Commun.* **2011**, *47*, 9603−9605.
(53) Hu, Z.; Nalaparaju, A.; Peng, Y.; Jiang, J.; Zhao, D. Modulated Hydrothermal Synthesis of UiO-66-(Hf)-Type Metal−Organic Frameworks for Optimal Carbon Dioxide Separation. *Inorg. Chem.* **2016**, *55*, 1134−1141.
(54) Serra-Crespo, P.; Berger, R.; Yang, W.; Gascon, J.; Kapteijn, F. Separation of CO_2/CH_4 Mixtures over NH_2-MIL-53-An Experimental and Modelling Study. *Chem. Eng. Sci.* **2015**, *124*, 96−108.
(55) Britt, D.; Furukawa, H.; Wang, B.; Glover, T. G.; Yaghi, O. M. Highly Efficient Separation of Carbon Dioxide by a Metal-Organic Framework Replete with Open Metal Sites. *Proc. Natl. Acad. Sci. U. S. A.* **2009**, *106*, 20637−20640.
(56) Elsaidi, S. K.; Mohamed, M. H.; Schaef, H. T.; Kumar, A.; Lusi, M.; Pham, T.; Forrest, K. A.; Space, B.; Xu, W.; Halder, G. J.; Liu, J.; Zaworotko, M. J.; Thallapally, P. K. Hydrophobic Pillared Square Grids for Selective Removal of CO_2 from Simulated Flue Gas. *Chem. Commun.* **2015**, *51*, 15530−15533.
(57) Paul, D. R. Gas Sorption and Transport in Glassy Polymers. *Ber. Bunsen.-Ges. Phys. Chem.* **1979**, *83*, 294−302.
(58) Robeson, L. M. Correlation of Separation Factor Versus Permeability for Polymeric Membranes. *J. Membr. Sci.* **1991**, *62*, 165−185.
(59) Robeson, L. M. The Upper Bound Revisited. *J. Membr. Sci.* **2008**, *320*, 390−400.

DOI: 10.1021/acs.chemmater.7b03203
Chem. Mater. 2017, 29, 10326−10338

Annex B

Revisiting the Aluminum Trimesate-based MOF (MIL-96): from Structure Determination to the Processing of Mixed Matrix Membranes for CO_2 Capture.

Marvin Benzaqui,[†,‖] Renjith S Pillai,[‡] Anahid Sabetghadam,[§] Virginie Benoit,[⊥] Perine Normand,[∂] Jérôme Marrot,[†] Nicolas Menguy,[δ] David Montero,[φ] William Shepard,[ζ] Antoine Tissot,[†,‖] Charlotte Martineau-Corcos,[†,#] Clémence Sicard,[†] Mihail Mihaylov,[Δ] Florent Carn,[ϒ] Isabelle Beurroies,[⊥] Philip L. Llewellyn,[⊥] Guy De Weireld,[∂] Konstantin Hadjiivanov,[Δ] Jorge Gascon,[§,Φ] Freek Kapteijn,[§] Guillaume Maurin,[‡] Nathalie Steunou,[†*] Christian Serre[†,‖]

[†] Institut Lavoisier de Versailles, UMR CNRS 8180, Université de Versailles St Quentin en Yvelines, Université Paris Saclay, 45 avenue des Etats-Unis 78035 Versailles Cedex. France.

[‖]Institut des Matériaux Poreux de Paris, FRE 2000 CNRS, Ecole Normale Supérieure, Ecole Supérieure de Physique et des Chimie Industrielles de Paris, PSL Research University, 75005 Paris, France.

[‡] Institut Charles Gerhardt Montpellier, UMR 5253 CNRS, Université de Montpellier, Place E. Bataillon, 34095 Montpellier Cedex 05, France.

[§] Catalysis Engineering-Chemical Engineering Department, Delft University of Technology, Van der Maasweg 9, 2629 HZ Delft, The Netherlands.

[⊥]Aix Marseille University, CNRS, MADIREL, UMR 7246, 13397 Marseille, France.

[∂]Service de Thermodynamique et de Physique mathématique, Faculté Polytechnique, Université de Mons, 20 Place du Parc , 7000 Mons, Belgique.

[δ] Institut de Minéralogie de Physique des Matériaux et de Cosmochimie, UMR 7590 CNRS UPMC Université Paris 06 MNHN IRD – Sorbonne Universités, 4 place Jussieu, 75005 Paris, France.

[φ] Institut des Matériaux de Paris Centre (IMPC), FR 2482 CNRS UPMC-Sorbonne Universités, 4 place Jussieu, 75252 Paris cedex 05, France.

[ζ] Synchrotron Soleil, L'Orme des Merisiers, Saint Aubin, BP 48, 91192 Gif-sur-Yvette, France.

[#]CNRS, CEMHTI UPR3079, Université d'Orléans, F-45071 Orléans, France.

[Δ] Institute of General and Inorganic Chemistry, Bulgarian Academy of Sciences, Sofia 1113, Bulgaria.

[ϒ]Laboratoire Matière et Systèmes Complexes (MSC), UMR CNRS 7057, Université Paris Diderot, Bât. Condorcet, 10 rue A. Domon et L. Duquet, 75013 Paris, France.

[Φ] King Abdullah University of Science and Technology, KAUST Catalysis Center, Advanced Catalytic Materials. Thuwal 23955, Saudi Arabia.

Table of Contents

I-Synthesis of MIL-96(Al) and Structure Resolution by combining Single-crystal X-ray Diffraction, Solid-State NMR and DFT calculations.

1-Materials. The chemicals in this work were obtained commercially and used without further purification. The chemicals in this work were $Al(NO_3)_3.9H_2O$ (Merck, 98.5%), benzene tricarboxylic acid (H_3BTC) (Sigma Aldrich, 95 %), acetic acid (Sigma Aldrich, 99.7%), dimethylformamide (DMF) (Sigma Aldrich, 99.8 %).

2-Hydrothermal synthesis of MIL-96(Al) hexagonal rods (MIL-96(Al)-HR). MIL-96(Al) microcrystals were synthesized via a hydrothermal route. Trimesic acid (2.100 g, 10 mmol) was poured into a 125 mL Teflon-lined steel autoclave with 40 mL of deionized water under vigorous stirring. Aluminum nitrate nonahydrate (18.760 g, 50 mmol) was dissolved in 30 mL of deionized water and poured into the ligand solution. The mixture was stirred for 10 min and heated to 180°C for 24 hours under autogenous pressure. A yellowish powder (m = 2.98 g) was obtained after filtration, washed with deionized water and dried in air at room temperature. Traces of remaining trimesic acid and nitrates were removed by washing the product with 500 mL of $EtOH/H_2O$ mixture (1/1). White powder (m = 2.77 g) was obtained by filtration and dried in air at room temperature.

3-Characterization of MIL-96(Al) crystals. X-ray powder diffraction patterns (XRPD) were collected using Bruker D8 diffractometer mounted with a rotating capillary (θ–2θ) with Cu radiation ($\lambda K_{\alpha 1}$ = 1.54059 Å). Surface area of the materials was determined by N_2 adsorption in a BELSORP-Max porosimeter at 77 K. Thermogravimetric analyses (TGA) were performed on a Perkins Elmer SDA 6000 apparatus. Solids were heated up to 800°C with a heating rate of 3 $°C.min^{-1}$ in an oxygen atmosphere. SEM images of MIL-96(Al) crystals have been recorded on a JEOL JSM-7001F microscope using gold-coated samples equipped with an X-ray energy-dispersive spectrometry (XEDS) detector with a X-Max SDD (Silicon Drift Detector) by Oxford. Dynamic light scattering (DLS) measurements were performed on a Zetasizer from Malvern Instruments. High angle annular dark field in the scanning transmission electron microscopy mode (i. e. STEM-HAADF) and HRTEM experiments were recorded on a JEOL 2100F microscope operating at 200kV using a JEOL annular detector.

4- X-ray crystallography

The single crystal data of MIL-96(Al)-HR were collected on Proxima-2A microfocus beamline at the SOLEIL Synchrotron (λ = 0.8266 Å) at 100 K. The crystallographic data of MIL-96(Al)-HR have been deposited at the Cambridge Crystallographic Data Centre as supplementary publication no. CCDC 1558833.

3

5-Crystallographic structure and characterization of MIL-96(Al)-HR

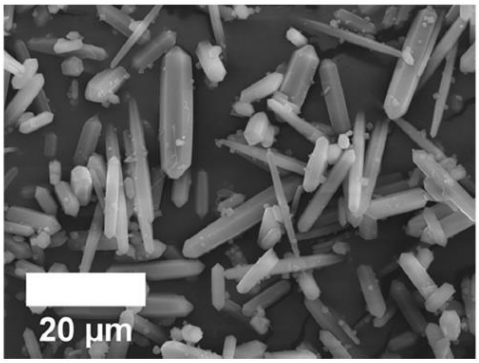

Figure S1. SEM images of MIL-96(Al)-HR crystals obtained by hydrothermal synthesis and used for single-crystal X-Ray diffraction.

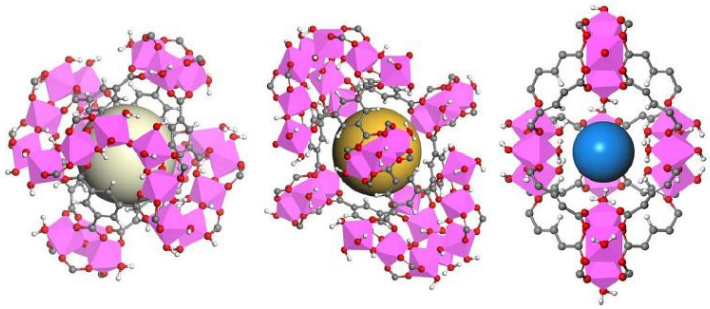

Figure S2. Scheme representing the three cavities of MIL-96(Al); cavity A (left, white sphere), B (middle, yellow sphere) and C (right, blue sphere). Aluminum octahedra are represented in pink, carbon atoms in grey, oxygen atoms in red and hydrogen atoms in white.

The first cavity (noted A) is centered on the special position 0 0 0 (2a), the second one (noted B), is located at the special position 2/3 1/3 1/4 (2d) and the third one is centered on the position 1/3 2/3 1/4 (2c).

Table S1. Structural description of the three cavities located in MIL-96(Al)

	A	**B**	**C**
Morphology	Sphere	Ellipsoid	Bipyramid
Dimensions (Å)	11	9.5 * 12.6 * 11.3	3.6 * 4.46
Volume	520 $Å^3$	700 $Å^3$	10 $Å^3$

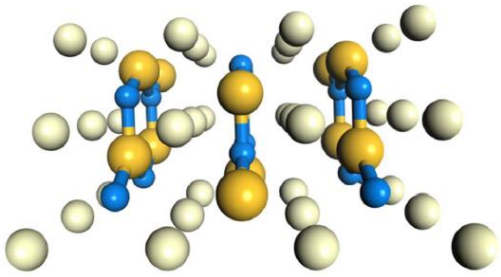

Figure S3. Blueprint of MIL-96(Al) with connections between cavities; White = cavity A, Yellow = cavity B and Blue = cavity C

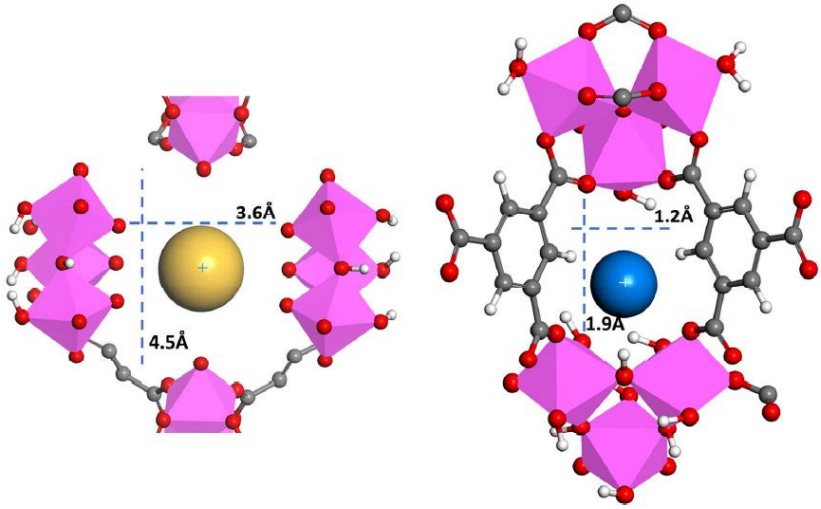

Figure S4. Scheme representing windows between two different cavities; left: view from cavity C (blue cross) to cavity B (yellow sphere), right: view from cavity A (white cross) to cavity C (blue sphere).

Windows dimensions are estimated based on the distances between two atoms minus their respective van der Waals radius. For window between C and B, horizontal distance between two O of the μ_2-OH trimer is 6.7 – 2*1,52 = 3.6Å and vertical distance between two O from the μ_3-oxo trimer is 7.6 – 2*1.52 = 4.5Å.

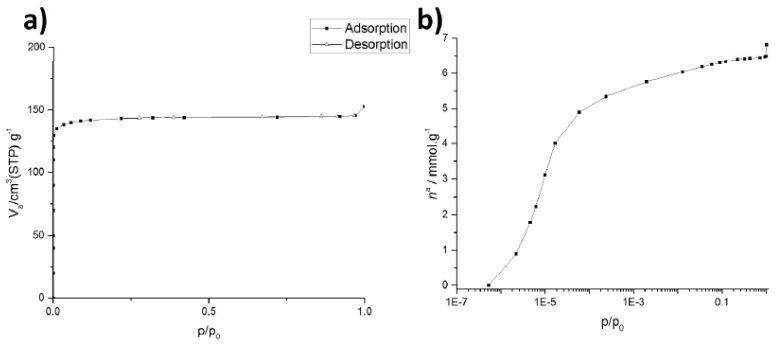

Figure S5. (a) Nitrogen adsorption isotherm at 77K of MIL-96(Al) (HR); (b) Semi-loogarithmic plot.

Solid State NMR of MIL-96(Al)-HR The ^{1}H and ^{27}Al MAS NMR spectra were recorded on an Avance III 850 MHz spectrometer (CEMHTI, Orléans) using a 3.2 mm double resonance probehead at spinning frequency of 20 kHz. The spectra were recorded on a hydrated sample (*i.e.*, a sample stored in air after the synthesis) and on a sample previously heated at 150°C overnight. The ^{1}H MAS NMR spectrum was recorded using a rotor-synchronized Hahn-echo sequence with a 3.0 µs 90° pulse length. 16 transients with 1 s recycle delay were accumulated. The ^{27}Al Hahn-echo NMR spectra were recorded using a 4.0 µs 90° pulse length. 128 transients with 0.5 s recycle delay were accumulated for each sample. The ^{27}Al multiple-quantum (MQMAS) NMR spectrum was acquired using the *z*-filter sequence.[1] The durations of the first two pulses are 2.8 and 0.6 µs, while the last pulse is selective on the central transition. For each sample, 64 t_1 slices with 192 transients each were co added (recycle delay of 0.5 s). The ^{27}Al-^{27}Al double-quantum single-quantum (DQ-SQ) spectrum used the supercycled symmetry-based $R2_2^1R2_2^{-1}$ sequence[2] with a recoupling radio-frequency that matches a rotary resonance condition (n = 2). The duration of the recoupling period is 1.2 ms. A 180° pulse during the t_1 evolution filters out the single-spin double quantum transitions connected to satellite transitions.[3] For each sample, 90 t_1 slices with about 900 transients each were co added (recycle delay of 0.5 s). For all 2D experiments, the States procedure[4] was applied to obtain phase sensitive NMR spectra. Further ^{27}Al MAS NMR spectra were recorded on an Avance 500 Bruker NMR spectrometer (11.7 T) where solids were packed in 4 mm rotors and put in an oven at temperature ranging between 100 and 300°C under 5 mbar vacuum. The rotors were then rapidly closed to prevent rehydration and the measurements were performed at room temperature. Finally, the sample heated at 300°C was let in air to rehydrate for a week and a ^{27}Al MAS NMR spectrum was recorded. The ^{1}H chemical shifts are referenced to TMS, while those of ^{27}Al are referenced to a 0.1 M solution of aluminum nitrate. The NMR spectra were analyzed using the DMfit software.[5]

Table S2. ^{27}Al NMR isotropic chemical shift (δ_{iso}, ppm), quadrupolar coupling constant (C_Q, MHz) and asymmetry parameter (η_Q) of MIL-96(Al) determined from the reconstruction of the ^{27}Al MAS NMR spectra. In italic are given the DFT-calculated values.

Site	δ_{iso} (± 0.1)	C_Q (± 0.1)	η_Q (± 0.1)	Relative Intensity
	Hydrated MIL-96(Al)			
Al1	3.2	4.6 *(5.2)*	0 *(0.3)*	1
Al2	3.4	9.1 *(11.3)*	0 *(0.1)*	1
Al3	6.2	0.2 *(3.7)*	*/(0.6)*	2
	Dried MIL-96(Al)			
Al1	3.4	3.4 *(1.1)*	0.7 *(0.7)*	1
Al2	3.1	6.8 *(9.5)*	0 *(0.2)*	1
Al3	5.3	0.2 *(2.6)*	*/(0.8)*	0.66
Al3'	3.0	2.7 *(7.1)*	0.5 *(0.4)*	1.34

7

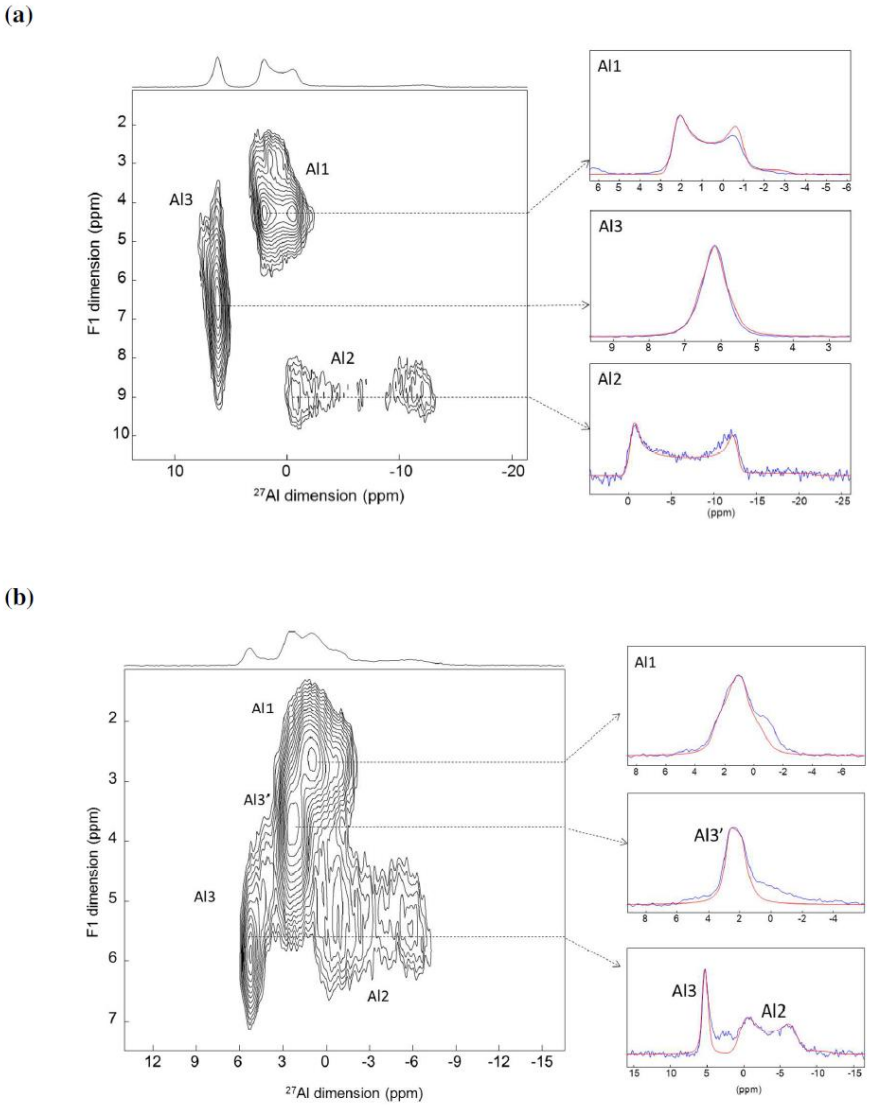

Figure S6. ^{27}Al MQMAS NMR spectrum of (a) MIL-96(Al) hydrated and (b) MIL-96(Al) previously dried at 150°C overnight under 5 mbar vacuum. The individual components (blue) along with their reconstruction (red) are shown on the right part of each spectrum. The lines are assigned.

8

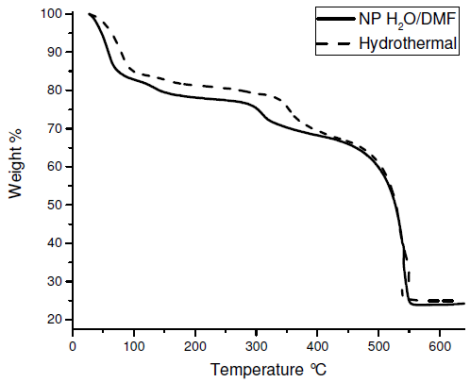

Figure S7. Thermogravimetric Analysis of MIL-96(Al) particles; hexagonal rods (dashed line), MIL-96(Al)-NP2 from H_2O/DMF reflux (full line).

Thermogravimetric analysis was performed to validate the new structural model as well as the number of free H_2O molecules. TGA (under pure O_2 at 3°C/min) indicates a first weight loss from 25°C to 150°C corresponding to the removal of free water trapped in the porosity. The second weight loss follows a two steps process and corresponds to the degradation of the framework starting from 330°C. 25% of Aluminum oxide (Al_2O_3) is obtained at temperatures above 550°C which is consistent with the proposed formula. From the first weight loss, we estimate the number of free H_2O molecules as 58 per unit cell (n=29).

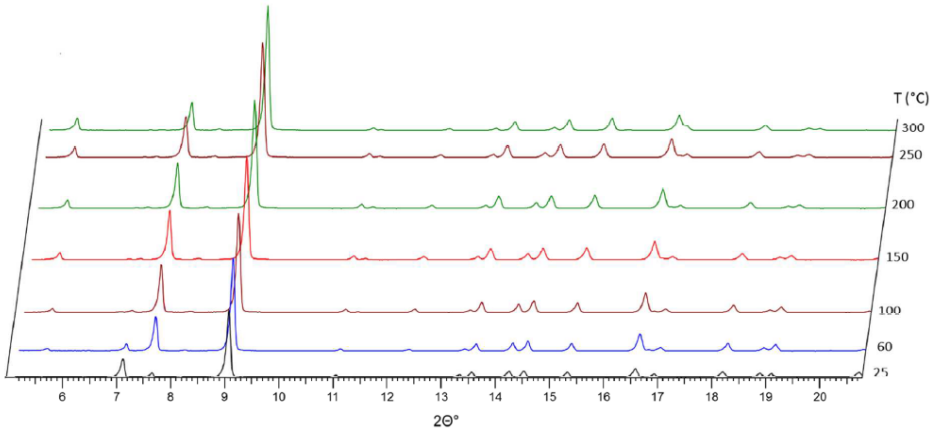

Figure S8. Temperature dependent XRPD collected at ambient pressure on hexagonal rods (hydrothermal) showing the rigid framework of MIL-96(Al).

9

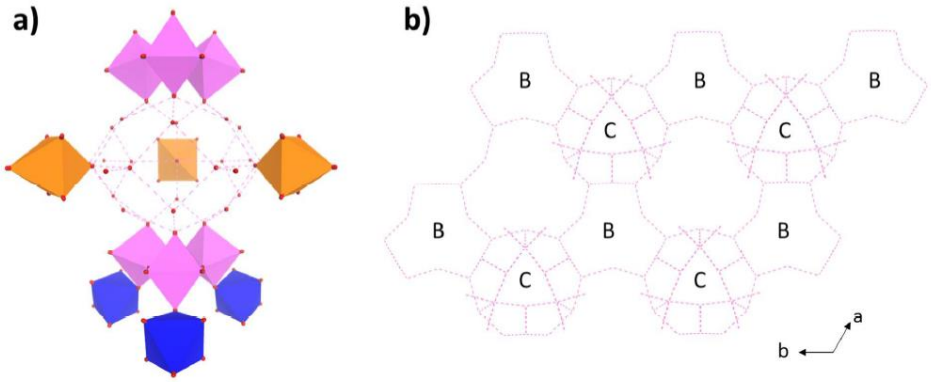

Figure S9. Scheme showing a) close contacts (< 2.9 Å) between oxygen atoms from framework and free water molecules forming a H-bond cluster in cavity C; b) H-bond network throughout the porosity by connection between cavity B and C.

II- Control of the particle size and morphology: synthesis of nanoparticles of MIL-96(Al).

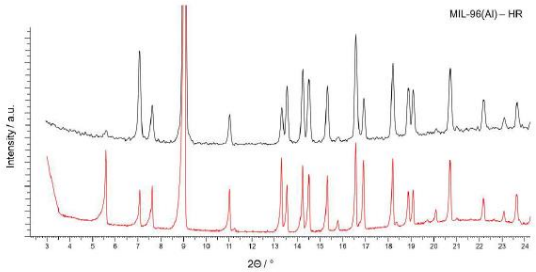

Figure S10. PXRD of MIL-96(Al)–HR recorded using reflection (black line) and transmission (red line) geometry.

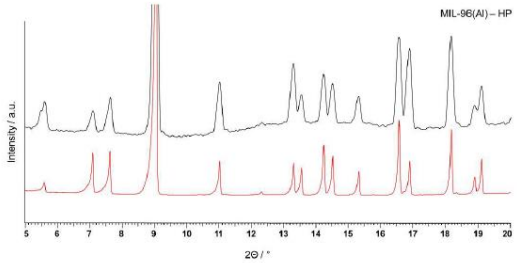

Figure S11. PXRD of MIL-96(Al)–HP recorded using reflection (black line) and transmission (red line) geometry.

.

10

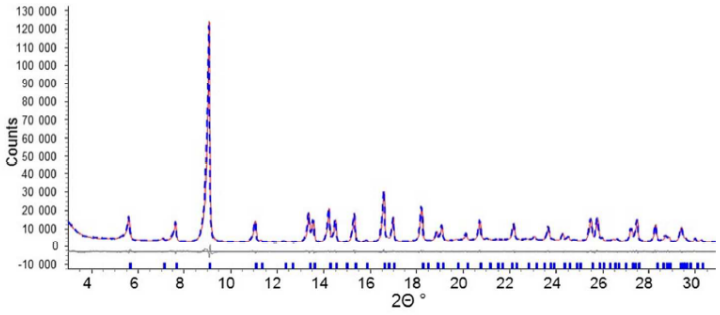

Figure S12. Structureless refinement of MIL-96(Al)-NP2 (H_2O/DMF); a = 14.3094 Å, c = 31.1728 Å, V = 5527.8 $Å^3$, space group: $P6_3/mmc$; experimental data in blue and calculated pattern in red. Particle size: 212 nm (calculated by the TOPAS software fitting the XRD line by a Lorentzian).

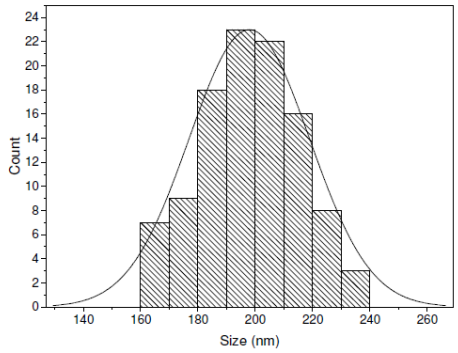

Figure S13. Size distribution of MIL-96(Al)-NP2 as determined by STEM images

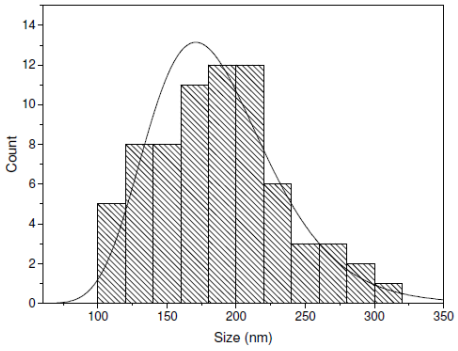

Figure S14. Size distribution of MIL-96(Al)-NP without acetic acid as determined by STEM images.

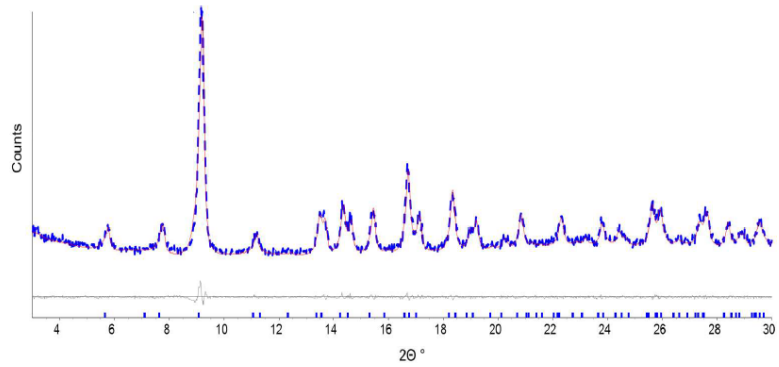

Figure S15. Structureless refinement of MIL-96(Al)-NP3; a = 14.3613 Å, c = 31.2697 Å, V = 5585.2 $Å^3$, space group: $P6_3/mmc$; experimental data in blue and calculated pattern in red. Particle size: 70 nm (calculated by the TOPAS software fitting the XRD line by a Lorentzian).

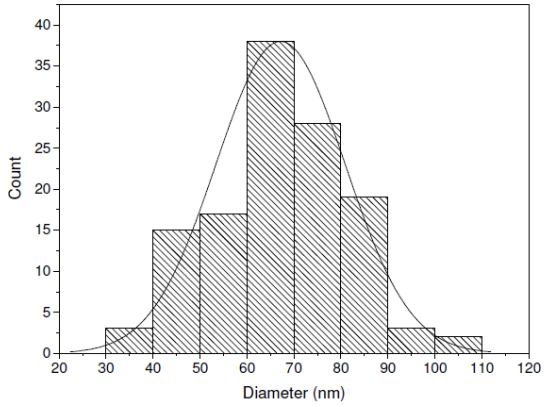

Figure S16. Size distribution of MIL-96(Al)-NP3 as determined by TEM images. Mean diameter = 67±40 nm

12

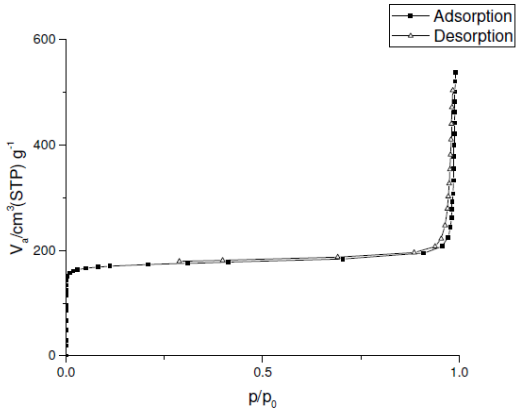

Figure S17. N_2 adsorption/desorption isotherm performed at 77 K on MIL-96(Al)-NP2 (H_2O/DMF)

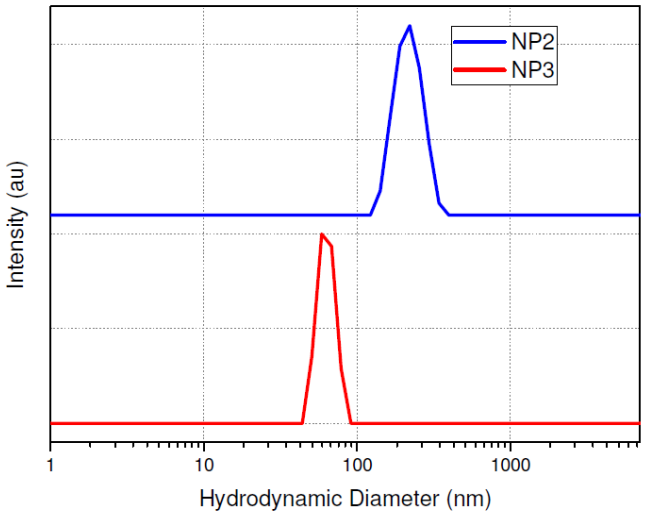

Figure S18. Size Distribution (diameter in nm) of 1.25 wt% MIL-96(Al)-NP3 (red line) and 1.25 wt% MIL-96(Al)-NP2 (blue line) in pure THF by DLS.

13

III- In situ IR spectroscopy analysis: characterization of sorbed water, hydroxyl groups and Al^{3+} sites.

Two techniques were used to record the IR spectra. For most of the experiments the MIL-96(Al)-HR sample was spread onto a KBr pellet. In these cases, due to the low amount of MOF in the IR beam path, the maxima of the most intense bands are well detected. For some experiments, the sample was supported on a tungsten grid. In this case the bands were ca. 5 times more intense and some bands of the functional group/fingerprint regions were out of scale. However, high quality spectra were obtained in the overtone/combination modes region (> 4000 cm^{-1}). The IR measurements were performed with Nicolet Avatar 360 and Nicolet 6700 FTIR spectrometers. A purpose made IR cell, allowing measurements at low and ambient temperature, was used for the experiments. The cell was connected to vacuum-adsorption apparatus with a residual pressure lower than 10^{-3} Pa.
Carbon monoxide (>99.5% purity) was supplied by Merck. Labeled dinitrogen ($^{15}N_2$, isotopic purity of 99.7%) was provided by Isotec Inc. (a Matheson USA company). D_2O was purchased from Cambridge Isotope Laboratories, Inc. and had an isotopic purity of 99.9%.

1- Interpretation of the IR spectra in the 1800 – 900 cm^{-1} region (Fig. 6A)

The IR spectrum of MIL-96(Al)-HR, recorded after evacuation at ambient temperature is presented in Fig. 6A from the main text. The two strong bands at 1660-1598 and 1460-1402 cm^{-1} are assigned to coordinated carboxylates. Contribution of the C=C aromatic bond is expected at ca. 1630 cm^{-1}. The band at 1117 cm^{-1} is attributed to C–H in-plane bending modes. Finally, the bands at 1160, 1075, 1011 and 962 cm^{-1} arise from OH deformation modes.

2- Spectra of partly deuterated samples

Partially deuterated samples were prepared in order to determine whether vibrations of adsorbed water molecules are observed in the 3700-3600 cm^{-1} region (Fig. S19). If some of the bands in the region were due to asymmetric H_2O modes they should have decreased in intensity and OH modes originating from DOH molecules should have appeared. However, such phenomenon was not observed. Therefore, all bands in the 3700 – 3600 cm^{-1} region are associated with hydroxyl groups. This leads to an important conclusion about the residual adsorbed water: the two protons of each molecule are involved in H-bonding with basic sites from the MOF structure. Indeed, if one of the water OH groups remains free, a stretching mode above 3600 cm^{-1} should be observed.[6] Noteworthy that the ν_{as}(OH) mode of water with the absence of H bonding should also be observed at high frequencies .[7] This conclusion is consistent with the crystal structure of the hydrated phase revealing that protons of water molecules are involved in H bonding with oxygen atoms of carboxylates.

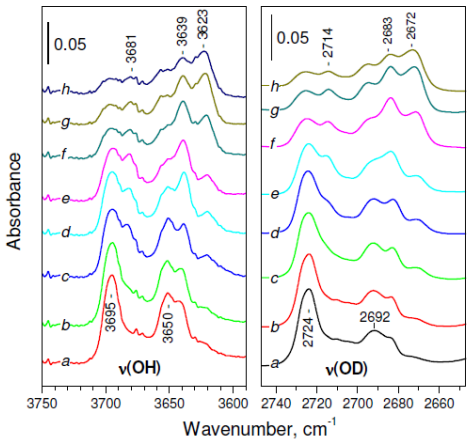

Figure S19. IR spectra in ν(OH) and ν(OD) regions of partially deuterated MIL-96(Al) (50 % degree of deuteration) evacuated at different temperatures: (a) RT, (b) 323 K, (c) 348 K, (d) 373 K, (e) 398 K, (f) 423 K, (g) 448 K and (h) 473 K.

For sample evacuated at RT the principal band of terminal hydroxyls is T1, although a T2 band can be distinguished as a weak shoulder. With increasing the evacuation temperature up to 473 K (Fig. 6 from the main text, spectra b-e and Figs. S19 and S20, spectra b-h), the T1 band progressively decreases in intensity while the intensity of the T2 band passes through a maximum. These results suggest that, in parallel with sample dehydration/dehydroxylation, the "free" OH groups (T1) become involved in weak H-bonding being thus converted to T2 groups. To the best of our knowledge, such a behavior can be explained by the following assumption: upon desorption of water molecules (or removal of OH groups), basic oxygen sites from the carboxylate anions are formed and can be further involved in H-bonding with OH groups:

$$\text{Al-OH} + {}^{-}\text{OOC-C}_6\text{H}_5\text{-COO}^{-}\cdots\text{HOH} \rightarrow \text{Al-OH}\cdots{}^{-}\text{OOC-C}_6\text{H}_5\text{-COO}^{-}\ldots + \text{H}_2\text{O}. \qquad (1)$$

This scheme explains the initial increase of the population of the T2 groups with rising the evacuation temperature. Consider now the bridging hydroxyls. In this case again a tendency of forming H-bonds is detected by increasing the evacuation temperature. The observation indicates that the reaction (1) occurs also with the bridging hydroxyls. However, these species are thermally stable and the overall intensity of their bands even slightly increases with the evacuation temperature (Fig. S20). Although the band of the C-type hydroxyls is overlapped with those of adsorbed water, it seems that the respective species are also stable by evacuation up to 473 K (Fig. 6B).

3- Spectra of fully deuterated samples

The changes in intensities of different OD groups as a function of the evacuation temperature are shown on Fig. S20.

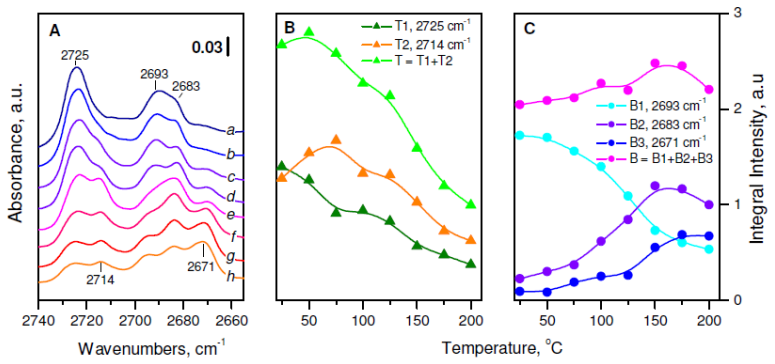

Figure S20. (A) IR spectra in ν(OD) region of completely deuterated MIL-96(Al)-HR evacuated at different temperatures: (a) RT, (b) 323 K, (c) 348 K, (d) 373 K, (e) 398 K, (f) 423 K, (g) 448 K and (h) 473 K. (B) Dependence of the integral intensities of T type hydroxyl bands on the evacuation temperature. (C) Dependence of the integral intensities of B type hydroxyl bands on the evacuation temperature.

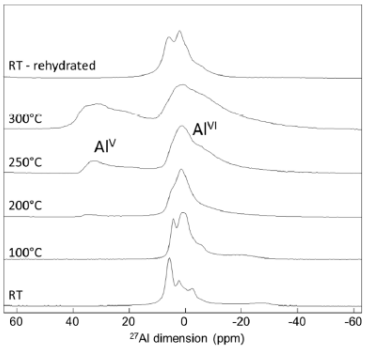

Figure S21. ^{27}Al MAS NMR spectra of MIL-96(Al)-HR recorded on the sample previously heated in the range RT-573 K. After heating at 573 K, the sample was let in air for days to allow spontaneous rehydration (top spectrum).

As shown by ^{27}Al NMR spectroscopy, a modification of the Al environment takes place at temperatures higher than 473 K: a ^{27}Al resonance centered around 35 ppm, corresponding to five-coordinated Al sites, appears (Figure S21). This observation is fully consistent with the IR results, although the experimental conditions for the two sets of experiments are not identical.

4- Water adsorption/desorption cycles

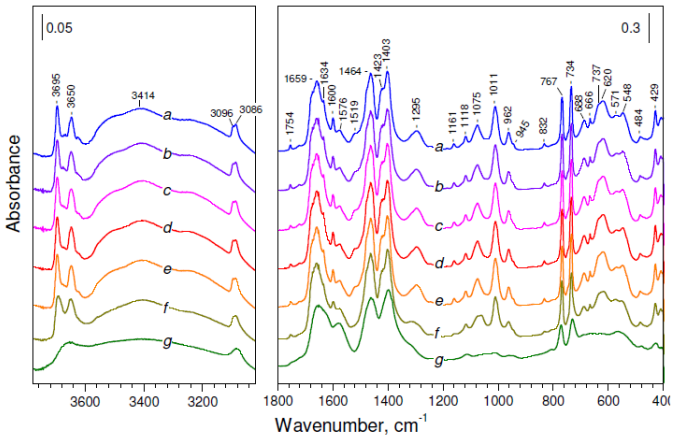

Figure S22. IR spectra of MIL-96(Al)-HR after adsorption-desorption of H_2O at RT. Before water adsorption the sample was evacuated at different temperatures: RT (a), 323 K (b), 373 K (c), 423 K (d), 473 K (e), 523 K (f) and 523 K (g).

5- Low-temperature adsorption of CO

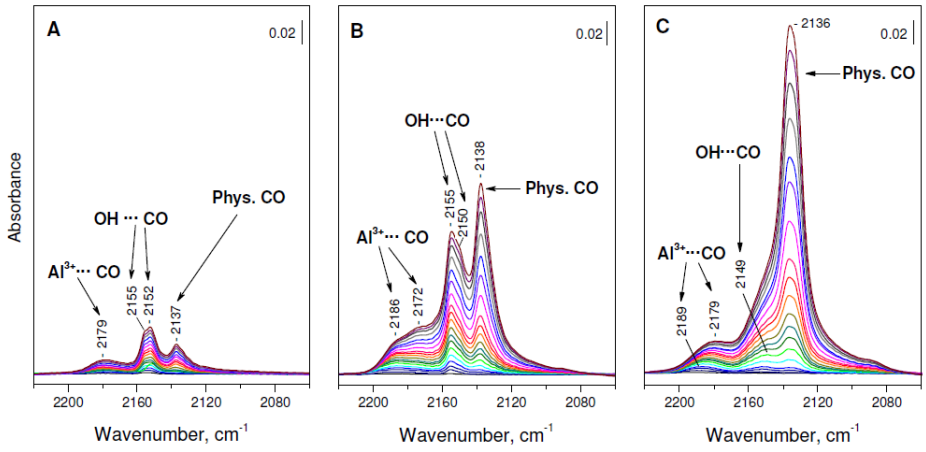

Figure S23. IR spectra of CO adsorbed on MIL-96(Al)-HR by addition of small doses of CO up to equilibrium pressure of 5 mbar at 100 K. Before adsorption the sample was evacuated at (A) 423 K, (B) 473 K and (C) 573 K.

No carbonyl bands were detected after low temperature CO adsorption on a sample evacuated at temperatures up to 373 K (spectra not shown). The results indicate that the pores of the sample are inaccessible at these conditions (note the absence of any physically adsorbed CO). With sample

17

evacuated at 423 K several carbonyl bands of low intensity were recorded (Fig. S23A): on open Al^{3+} sites (ca. 2180 cm^{-1}); on OH groups (2155 - 2152 cm^{-1}) and physically adsorbed CO (2137 cm^{-1}).

With a sample evacuated at 473 K all of the carbonyl bands appeared with enhanced intensity. The heterogeneity of the Al^{3+} sites is evidenced by the appearance of two maxima at 2186 and 2172 cm^{-1}. The most pronounced increase in intensity is that of the band associated with physically adsorbed CO (2138 cm^{-1}) in agreement with an enhanced pore accessibility.
Further increase of the evacuation temperature up to at 573 K (Fig. S23C) is accompanied by a decrease in the amount of CO attached to Lewis acid sites and to OH groups while the band due to physically adsorbed CO further develops. These results are consistent with TGA showing a partial degradation of the sample under vacuum treatment at 500- 523 K.

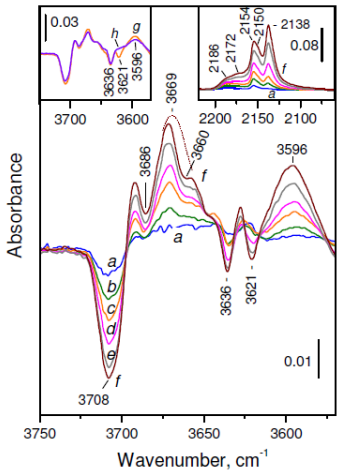

Figure S24. Spectral changes in the ν(OH) region of MIL-96(Al) activated at 473 K upon CO adsorption at 100 K by addition of small doses of CO up to equilibrium pressure of 5 mbar (a-f). The right inset shows the spectra in the ν(CO) region. The left inset shows the ν(OH) region but upon CO desorption by short evacuations (g, h).

Consider the CO-induced changes in the ν(OH) region (Fig. S24). We discuss the spectra obtained with the 473 K evacuated sample since the observed bands are of high intensity (Fig. S23). Because the experiments were performed at 100 K it is also important to note that the ν(OH) bands were slightly shifted at this temperature and detected at 3708, 3686, 3660, 3636 and 3621 cm^{-1}. The two T-hydroxyl bands are shifted to one band at ca. 3670 cm^{-1} and the B-type bands, to another band at 3596 cm^{-1}. The results can explained by the fact that the two T-type hydroxyls are of the same structural type but involved in H-bonding of different strength with the MOF framework. Adsorption of CO leads to breaking (or considerable weakening) of the preexisting H-bond and, as a result, the final ν(OH) position for the OH···CO species coincides in both cases. The same considerations are valuable for the B-type bands.

6- Low-temperature adsorption of $^{15}N_2$

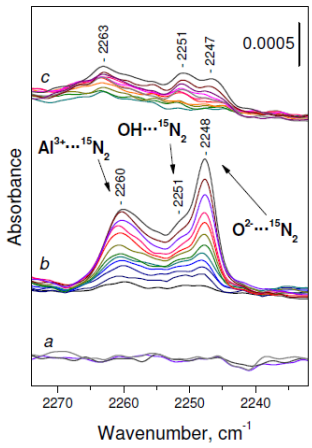

Figure S25. IR spectra of $^{15}N_2$ adsorbed on MIL-96(Al) by addition of small doses of $^{15}N_2$ up to equilibrium pressure of 50 mbar at 100 K. Before adsorption the sample was evacuated at (a) RT, (b) 473 K and (c) 573 K.

As in the case of CO, no adsorbed $^{15}N_2$ was observed after evacuation of the sample at ambient temperature. The results on $^{15}N_2$ adsorption on a sample evacuated at 473 K are consistent with the CO adsorption results: $^{15}N_2$ on open Lewis acid sites was detected at 2263-2260 cm^{-1} (corresponding to $^{14}N_2$ at 2341-2338 cm^{-1}), while $^{15}N_2$ on Brønsted acid sites, at 2255-2251 cm^{-1} ($^{14}N_2$ at 2332-2328 cm^{-1}). In addition, a $\nu(^{15}N\text{-}^{15}N)$ band at 2248 cm^{-1} (2325 cm^{-1} for $^{14}N_2$) is observed that may be assigned to $^{15}N_2$ on coordinatively unsaturated O^{2-} sites.

7-Adsorption of CO_2

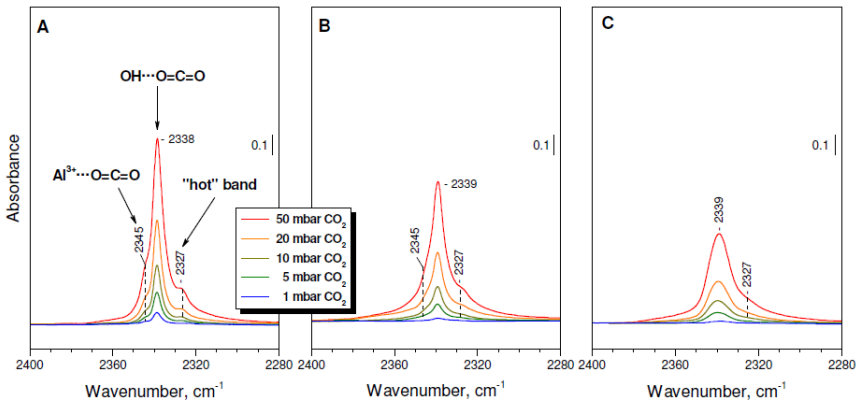

Figure S26. IR spectra of CO_2 adsorbed on MIL-96(Al) at different equilibrium pressures at RT. Before adsorption the sample was evacuated at (A) RT, (B) 473 K and (C) 573 K

19

The formation of Al^{3+}···OCO complexes on RT evacuated sample is associated with displacement of coordinated water by CO_2 molecules. This is supported also by the decrease in intensity of the water combination band at 5295-88 cm^{-1} and development of a band at ~5180 cm^{-1}.

IV- CO_2/N_2 gas sorption properties of MIL-96(Al) nanoparticles

1- Pure gas adsorption measurements.

Pure component adsorption equilibrium measurements have been performed using a homemade apparatus around a high-pressure magnetic suspension balance provided by Rubotherm GmbH which allows measurements in a pressure range of 0–150 bar and in a temperature range of 233.15–403.15 K.[9,10]

The excess adsorbed masses are determined by correcting the buoyancy effect of the gas phase on the adsorbent sample volume.[11] The buoyancy effect on the adsorbed phase is not considered.

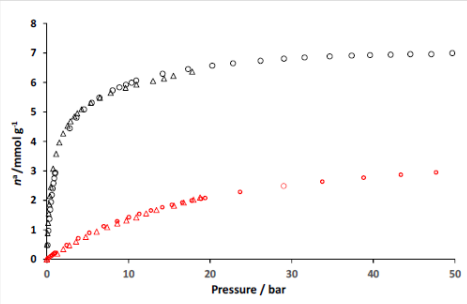

Figure S27. CO_2 (back) and N_2 (red) single adsorption isotherms at 303 K on both MIL-96(Al)-NP2 (circle) and on MIL-96(Al)-HR (triangle) activated at 423 K

Calorimetric measurements

The device used for microcalorimetry experiments is able to measure both adsorption isotherms and experimental adsorption enthalpies in the temperature range from 298 to 423 K.[8] The Tian-Calvet microcalorimeter is coupled with a manometric device built to withstand pressures up to 100 bar with a pressure gauge suitable for pressure measurements up to 50 bar. A point-by-point introduction of gas is most adapted to this system. In this procedure, it is important to consider that the gas is introduced reversibly. Each introduction of adsorbate to the sample is accompanied by an exothermic thermal effect, until equilibrium is reached. The heat flow peak with time has to be integrated to provide an integral (or pseudodifferential) molar adsorption enthalpy for each dose. Errors in this calculation can be estimated at ± 1 kJ $mol.^{-1}$. The calorimetric cell (including the relevant amounts of adsorbent and gas) is considered as an open system. Under these conditions it is possible to determine the differential enthalpy of adsorption $\Delta_{ads}\dot{h}$, via the following expression:

$$\Delta_{ads}\boldsymbol{h} = \left(\frac{dQ_{rev}}{dn^a}\right)_T + V_c\left(\frac{dp}{dn^a}\right)_T, \textbf{ eq.1}$$

20

Here dQ_{rev} is the heat reversibly exchanged with the surrounding environment at temperature T, as measured by the calorimeter, dn^a is the amount adsorbed after introduction of the gas dose, dp is the pressure increase and V_c is the dead space volume of the sample cell within the calorimeter itself (thermopile). The term $V_c dp$ can be obtained via blank experiments. For this kind of experiment the amount of MIL-96(Al) introduced into calorimetric cell is around 0.250 g. Prior to each experiment, the MIL-96(Al) was outgassed ex-situ at 423K or 483K for 16h under a vacuum of 10^{-3} mbar. The carbon dioxide (99.998% purity) and nitrogen (99.9995% purity) were provided from Air Liquide (Alphagaz, France).

2- Co-adsorption measurements

In order to acquire mixture adsorption equilibrium data, we used a homemade volumetric apparatus as shown in Figure S28.

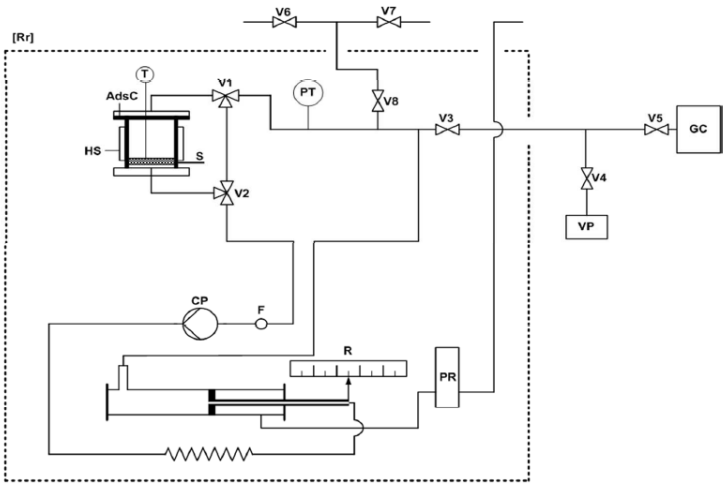

Figure S28. Mixture adsorption volumetric apparatus: (AdsC) adsorption cell; (PT) pressure transmitter; (V1 and V2) three way manual valves; (V3 to V8) manual valves; (T) Pt-100 temperature probe; (F) filter; (HS) in-situ heating system; (VP) vacuum pump; (CP) circulation pump; (R) ruler; (PR) pressure regulator; (GC) gas chromatograph; (Rr) refrigerated room.

The principle of volumetric co-adsorption measurements[12,13] is based on the same principle as "classic pure compound manometric apparatus".[14–16] The homemade installation allows the measurement of isobaric-isothermal mixture adsorption equilibria in a pressure range from 1 to 10 bar and in a temperature range from 298 K to 353 K. The cylinder piston provides a variable volume in order to keep constant the pressure on a set point value during the adsorption. A circulation pump allows to homogenize the mixture and a gas chromatograph coupled with a thermal conductivity detector, provided by Agilent (GC 6850), allows the determination of the gas mole fraction of each component in the mixture. The pressure transmitter is provided by Endress-Hauser (0 – 10 bar Cerabar PMP 731) with an uncertainty of 0.1% of the full scale. The adsorbent

was outgassed by maintaining it under primary vacuum at ambient temperature for one hour and then by heating the adsorption cell up to 423 K for 12 hours. The latter operation was still performed under secondary vacuum to ensure the regeneration of the adsorbent without destructing its structure. After that, the gas mixture was introduced in the installation without going through the adsorption cell. When both equilibrium and homogenization were reached (checked by constant values of both pressure and composition obtained using a chromatography device), the gas composition was determined after ten chromatographic analyses and the pressure and temperature values were recorded. With these measurements and the knowledge of the installation volume, the adsorption amounts of both the components in each mixture are determined thanks to a mixture equation of state.[17] In the second phase, the adsorption cell was controlled to be accessible via two three-way valves. During the adsorption, the pressure was kept constant on a set point value by adapting the installation volume using the cylinder piston. When the equilibrium was reached, same operations were performed as in the first phase. The pressure, temperature and volume of the system were recorded and the gas composition was determined by ten chromatographic analyses. The total installation volume knowing, the amount of each component in the gas phase after adsorption can be calculated using the same mixture equation of state. The adsorbed amounts were determined by difference between the number of moles in the gas phase before and after adsorption. Finally, the adsorbent was outgassed to repeat the above procedures with another composition of the initial mixture. The relative uncertainties associated to the adsorbed amounts are lower than 3% for CO_2 and 28% for N_2.

V-Molecular simulations

1-Density Functional Theory calculations on the structure.

The structural model of the anhydrous MIL-96(Al) form proposed experimentally was saturated by the missing hydrogen atoms using Materials Studio software package (Figure S29). Indeed, the hydrogen atoms were added to the carbon atoms of the organic linkers and to the μ_2-oxygen atoms connecting Al sites Al2. Further, all Al sites both Al1 and Al3 were terminated by coordinative water while Al sites Al3' were saturated by hydroxyl groups. The resulting structure model of MIL-96(Al) was then geometry optimized at the Density Functional Theory (DFT) level using the CP2K package.[18–21] These calculations included the relaxation of the positions of the atoms of the MOF framework while the unit cell parameters were fixed at the values determined experimentally (see CIF file, Table S1). The PBE[22] functional was combined with the use of Gaussian basis set and pseudopotential. For Carbon, Oxygen, and Hydrogen, a triple zeta (TZVP-MOLOPT) basis set was considered, while a double zeta (DZVP-MOLOPT) was applied for Aluminum.[23] The pseudopotentials used for all of the atoms were those derived by Goedecker, Teter and Hutter.[24] The van der Waals effects interactions were taken into account via the use of semi-empirical dispersion corrections as implemented in the DFT-D3 method.[25] The same methodology was applied to the hydrated MIL-96(Al). The first-principles calculations of the NMR parameters were performed from the structural models for both the dry and hydrated forms of MIL-96(Al) with CASTEP[26,27]

22

using the PBE functional and ultra-soft pseudo-potentials generated 'on the fly'.[28] The wave functions were expanded on a plane wave basis set with a kinetic energy cut-off of 610 eV. The projector augmented waves (PAW)[29] and gauge included projector augmented waves (GIPAW)[30] algorithms were used for the EFGs and NMR chemical shifts, respectively.

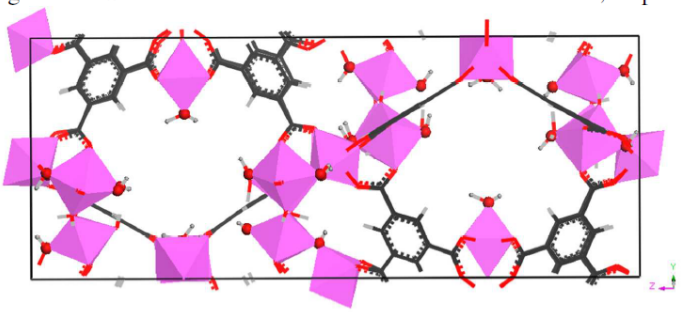

Figure S29. The simulation box considered for the DFT calculations (1×1×1 unit cells) viewed along the *a* direction for MIL-96(Al) (Gray, carbon; white, hydrogen; red, oxygen; pink, Aluminum)

2-Force-field based molecular simulations

2.1 Microscopic models for the host framework.

The DFT-optimized structure for the anhydrous form of MIL-96(Al) was considered for the prediction of the single component adsorption and binary co-adsorption behaviors of MIL-96(Al). The atomic partial charges for all atoms of the MIL-96(Al) framework were further obtained by fitting the electrostatic potential from a single point energy calculation with Dmol^3 on cluster model appropriately cut from the periodic structure to fairly describe the inorganic and organic regions of the MOF framework (see Table S3, Figure 4(a)). These calculations were also based on the PBE functional and the double numerical basis set containing polarization functions (DNP).[31]

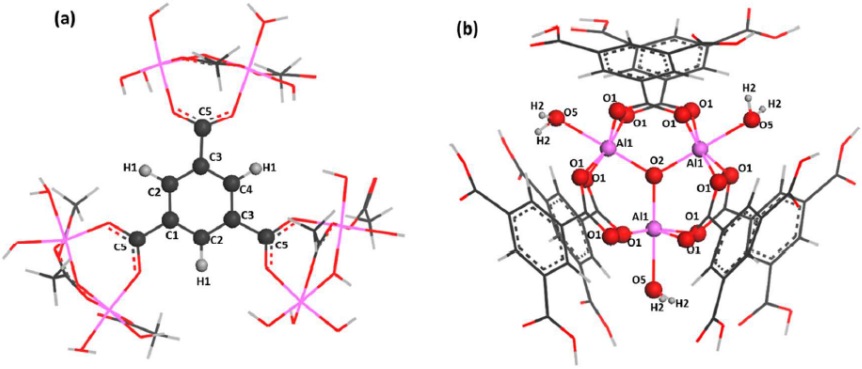

Figure S30. Labels of the atoms for the organic (a) and the inorganic (b, c) parts of the MOF structure. The color code is the same as the one reported in Figure 4.

Table S3. Atomic partial charges for the MIL-96(Al) structure derived at the DFT/PBE Level.

Atomic types	**Al1**	**Al2**	**Al3**	**C1**	**C2**	**C3**	**C4**	**C5**
Charge (e)	1.582	1.394	1.825	0.006	-0.197	0.098	-0.327	0.644
Atomic types	**H1**	**H2**	**H3**	**H4**	**H5**	**H6**	**O1**	**O2**
Charge (e)	0.176	0.441	0.433	0.445	0.444	0.421	-0.545	-1.173
Atomic types	**O3**	**O4**	**O5**	**O6**	**O7**	**O8**	**O9**	
	-0.581	-0.606	-0.782	-1.063	-0.964	-0.870	-0.841	

2.2 Force fields

The interactions between MIL-96(Al) and the guest species (CO_2 and N_2) were modeled using the sum of a 12-6 Lennard-Jones (LJ) contribution and a coulombic term. The Universal force field (UFF) was adopted to describe the LJ parameters for the atoms of the MOF framework (see Figure 4 and Table S4).[32] For the adsorbate molecules, CO_2 was described by a 3-sites charged LJ model as defined by Harris and Yung[35] and N_2 was represented by a 3-sites charged model with two LJ sites located at the N atoms while a third site present at its center of mass (COM) only involves electrostatic interactions as previously described in the TraPPE potential model (Table S5).

Table S4. LJ potential parameters for the atoms of the MIL-96(Al).

Atomic type	**UFF**	
	σ (Å)	**ε /k_B (K)**
Al	4.399	0.000
C	3.431	52.841
H	2.571	22.143
O	3.118	30.195

Table S5. Potential parameters and partial charges for the adsorbates

Atomic type	**σ (Å)**	**ε /k_B (K)**	***q* (*e*)**
N2_N	3.310	36.000	-0.4820
N2_COM	0.00	0.000	0.9640
CO2_C	2.757	28.129	0.6512
CO2_O	3.033	80.507	-0.3256

2.3 GCMC Simulations

Grand Canonical Monte Carlo (GCMC) simulations were carried out at 303 K to predict the single component adsorption of CO_2 and N_2, and the co-adsorption of CO_2/N_2 by employing the Complex Adsorption and Diffusion Simulation Suite (CADSS) code.[36] The simulation box was made of 4 (2×2×1) unit cells of MIL-96(Al) and the short-range dispersion forces described by LJ potentials were truncated at a cut-off radius of 12 Å while the long-range electrostatic interactions were handled using the Ewald summation technique. The fugacities for each adsorbed species at a given thermodynamic condition were computed with the Peng-Robinson equation of state (EoS).[37] For each state point, 5×10^7 Monte Carlo steps have been used for both equilibration and production runs. Three types of trials were considered for the molecules: (i) translation or rotation, (ii) creation/deletion and (iii) exchange of molecular identity. The adsorption enthalpy at low coverage (Δh) for each gas was calculated through configurational-bias Monte Carlo simulations performed in the NVT ensemble using the revised Widom's test particle insertion method.[38]

2.4 Computational predictions

Separation of CO_2/N_2 mixture

In separation processes, a good indication of the separation ability consists of estimating the selectivity of a porous material. The selectivity (S) for CO_2 over N_2 is defined by the following expression: $S(CO_2/N_2) = (x_{CO_2} / x_{N_2})(y_{N_2} / y_{CO_2})$ where x_{CO_2} and x_{N_2} are the mole fractions of CO_2 and N_2, in the adsorbed phase, respectively, while y_{CO_2} and y_{N_2} are the mole fractions of CO_2 and N_2 in the bulk phase, respectively. The calculated selectivity for CO_2/N_2 (molar ratio =15/85) is shown in Figure S31 as a function of the bulk pressure.

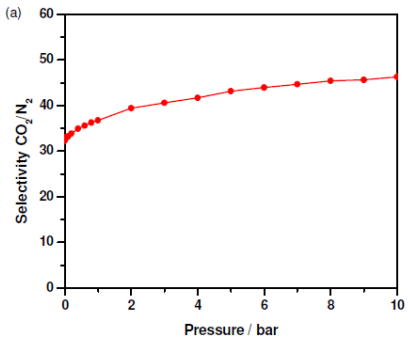

Figure S31. Simulated selectivities for CO_2/N_2 from its 15/85 molar ratio gas mixture, in MIL-96(Al) as a function of the bulk pressure at 303 K.

VI- Characterization of MIL-96(Al) based Mixed Matrix Membranes.

1- Microstructural characterization

Scanning electron microscopy (SEM): MIL-96(Al)-6FDA-DAM MMMs were simply scissors cut, stuck to stubs using carbon tape and subsequently carbon evaporated. A layer of 20 nm of carbon was deposited. No deformation of the membrane was reported caused by evaporation treatment. As a control, membrane without evaporation treatment was also observed at low accelerating voltage. Imaging was performed at 1 and 5 kV in a Hitachi SU-70 FEGSEM, lower detector was used. Magnification in article is 10.000x. The section of MMMs was observed with a 40° tilt.
Cross-sectional SEM images were also recorded with Dual Beam Strata 235 (FEI) and AURIGA Compact (Zeiss) microscopes with a secondary electron detector operated at 5 kV. Membrane samples were cryo-cracked to record the cross-sectional structure of the membranes. XRPD of the MMMs were recorded in a Bruker-D8 Advance diffractometer using Co-$K\alpha$ radiation (λ = 1.78897Å).

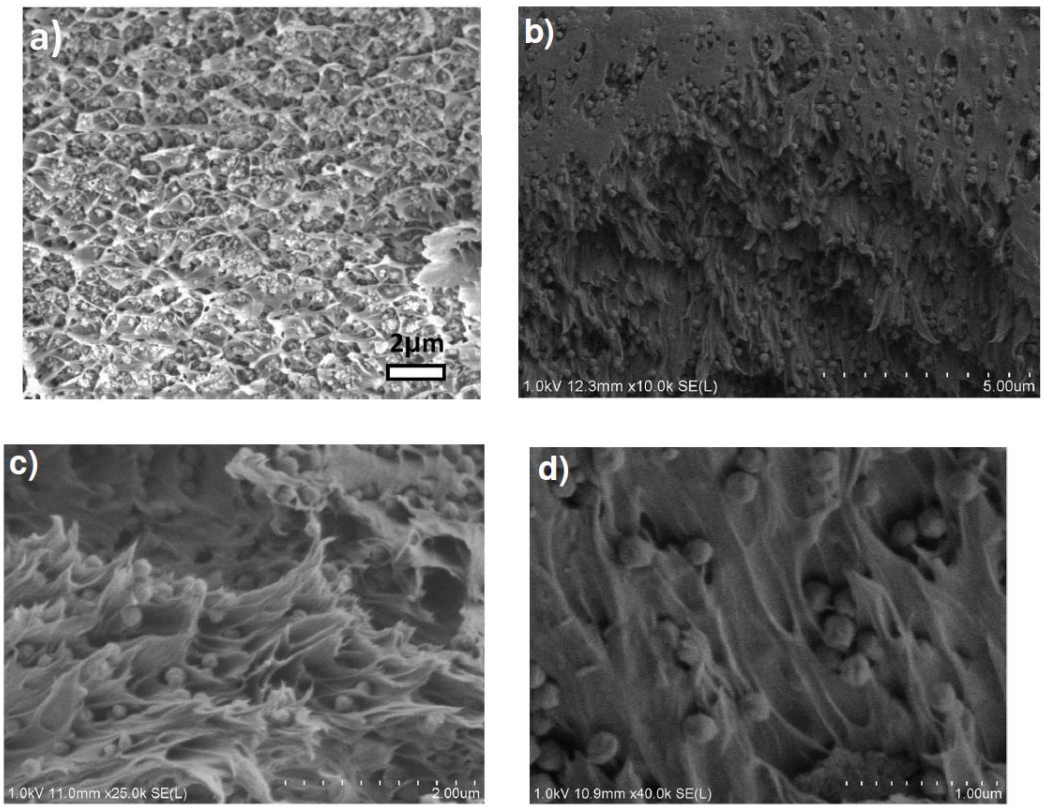

Figure S32. SEM images of MIL-96(Al)-NP2/6FDA-DAM membranes. a) cross-sectional image recorded on a cryo-cracked sample; b-d) section of the membrane showing the homogeneous distribution of MIL-96(Al)-NP2.

26

2- N_2 and CO_2 separation measurements.

CO_2 adsorption isotherms of MOFs and MMMs were recorded in a Tristar II 3020 (Micromeritics) setup at 273 K. Prior to the measurements, the samples were degassed at 423 K under N_2 flow for 16 h. The N_2 and CO_2 separation measurements were carried out in a home-made set-up employing an 15/85 mixture of CO_2/N_2 (20/113 cm^3 (STP)/min) as feed at 25 °C. He (5 cm^3 (STP) /min) was used as sweep gas for the permeate stream (atmospheric), while the trans-membrane pressure was adjusted using a back-pressure controller at the retentate side. An online gas chromatograph (Interscience Compact GC) equipped with a packed Carboxen 1010 PLOT (30 m x 0.32 mm) column and TCD and FID detectors was used to analyze the permeate stream.

Table S6. Permeation properties of MMMs MIL-96(Al)-NP3/6FDA-DAM (MOF content of 25 wt.%) under different CO_2 concentration of feed at 298 K and 2 bars feed pressure.

Feed Composition CO_2/N_2	P_{CO2} (Barrer)	P_{N2} (Barrer)	α
15/85	1122 ± 4	43 ± 0	26.4 ± 0.0
50/50	922 ± 1	36 ± 0	25.6 ± 0.1
85/15	810 ± 1	31 ± 0	26.1 ± 0.2

To study the influence of humidity on CO_2/N_2 separation, the MIL-96(Al)-NP3/6FDA-DAM (MOF content of 25 wt.%) MMM was exposed to air humidity (relative humidity (RH) ~100%) at 323 K for 72h. The CO_2/N_2 separation of these MMMs was performed by using a CO_2/N_2 15/85 vol% mixture at 298 K and 2 bar. The membrane was then heat treated in vacuum at 393 K and their separation properties were evaluated. Finally, the MMMs were exposed to another treatment under humid conditions, followed by the N_2 and CO_2 separation measurements. The permeation results of MMMs are presented in Table S7 in comparison to that of the initial MIL-96(Al)-NP3/6FDA-DAM MMM which was dried at room temperature (298 K). The impact of humidity on the permeation of neat 6FDA-DAM membrane was also studied. The 6FDA-DAM membrane was exposed to air humidity and then was heat treated, following the same treatment as MIL-96(Al)-NP3/6FDA-DAM MMM.

Table S7. Separation performance of dried and humidity-treated MIL-96(Al)-NP3-6FDA-DAM membranes (MOF content of 25 wt.%) under 15/85 vol.% of CO_2/N_2 mixture at 2 bar feed pressure and 298 K. The permeation performance of the neat 6FDA-DAM membrane is also given for comparison.

Membranes	**P_{CO2} (Barrer)**	**P_{N2} (Barrer)**	**$\alpha_{CO2/N2}$**
Initial MIL-96(Al)-NP3/6FDA-DAM dried at 298 K	811 ± 4	31± 0.0	26± 1
MIL-96(Al)-NP3/6FDA-DAM exposed to air humidity (RH~100 %)	842 ± 3	30 ± 0	28 ± 0
Heat-treated MIL-96(Al)-NP3/6FDA-DAM	981 ± 3	37± 0	26 ± 0
MIL-96(Al)-NP3/6FDA-DAM exposed to air humidity (2^{nd} cycle)	851 ± 3	31 ± 0	27 ± 0
Neat 6FDA-DAM membrane dried at 298 K	790 ± 7	29± 0	27± 1
Neat 6FDA-DAM membrane exposed to air humidity (RH~100 %)	794 ± 9	29 ± 0	28 ± 1
Heat-treated neat 6FDA-DAM membrane	734 ± 2	27± 0	27 ± 0

27

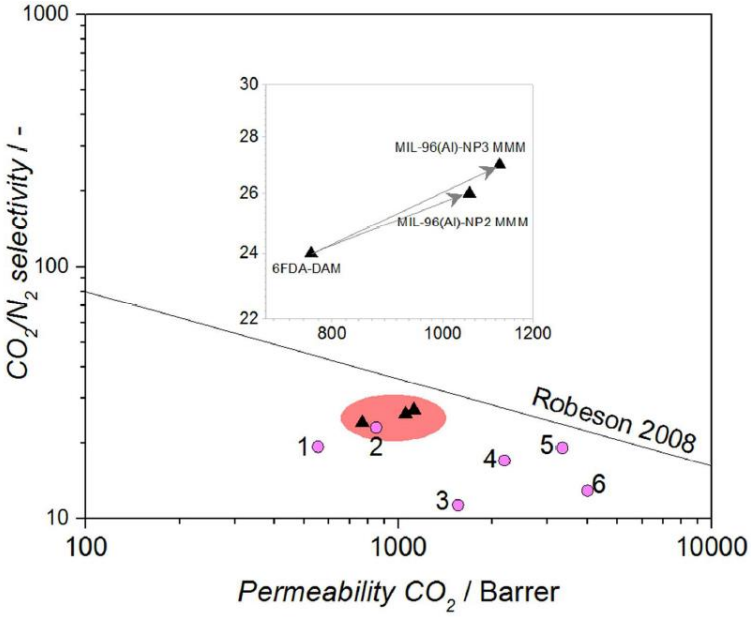

Figure S33. Robeson 2008 upper bound and the gas separation performance of 6FDA-DAM with 25 wt.% loading of MIL-96(Al)-NP2 and -NP3 (▲). The performance of previously reported MMMs with 6FDA-based polyimide for CO_2 / N_2 is also shown for comparison (●). (CO_2 and N_2 (15/85 vol.%) mixture was used as feed at 298 K and 2 bars).

Table S8. Comparison of the gas separation properties of MMMs prepared by using 6FDA based polymer for CO_2 / N_2 separation.

Polymer	MOF	Maximum wt% MOF loading	P CO_2 (Barrer)	α (CO_2/N_2) selectivity	Graph Code	reference
6-FDA-DAM:DABA[a]	ZIF-8	20	553	19	1	39
6-FDA-TMPDA[b]	CPO-27(Mg)	10	850	23	2	40
6-FDA-durene	ZIF-8	33	1553	11	3	41
6-FDA-durene	ZIF-8	30	2185	17	4	42
6-FDA-4MPD[c]	$[Zn_2(1,4\text{-bdc})_2(dabco)]$[d]	30	3330	19	5	43
6-FDA-durene	ZIF-71	20	4006	13	6	44
6-FDA-DAM	MIL-96(Al)-NP3	25	1121	27		This study
6-FDA-DAM	MIL-96(Al)-NP2	25	1055	26		This study

[a] DABA: 3,5-diaminobenzoic acid; [b] TMPDA: 2,4,6-trimethyl-m-phenylenediamine;[c] 4MPD (or durene): 2,3,5,6-tetramethyl-1,4 phenylenediamine;[d] DABCO: 1,4-diazabicyclo[2.2.2]octane;

28

VII. Small Angle X-Ray Scattering (SAXS)

Small angle X-ray scattering (SAXS) experiments were performed at 25 ° C with samples placed in sealed quartz capillaries on two different synchrotrons:
- SWING beamline (SOLEIL, Saint-Aubin, France) with a configuration D = 2 m and λ = 1 Å to get a q-range from 1.7×10^{-3} Å^{-1} to 0.28 Å^{-1}.
- NCD beamline (ALBA, Barcelona, Spain) with: D = 6 m and λ = 1 Å to get a q-range from 2.6×10^{-3} Å^{-1} to 9.6×10^{-2} Å^{-1}.

The 2D scattering intensity function for oriented ellipsoids of revolution with uniform scattering length density is given by (39).

$$P(q,\alpha) = \frac{scale}{V} f^2(q) + G$$

Where

$$f(q) = \frac{3(\Delta\rho)V(sin[qr(R_1,R_2,\alpha)] - qrcos[qr(R_1,R_2,\alpha)])}{[qr(R_1,R_2,\alpha)]^3}$$

And

$$r(R_1,R_2,\alpha) = [R_2^2 sin^2\alpha + R_1^2 cos^2\alpha]^{1/2}$$

α is the angle between the axis of the ellipsoid and the q-vector, V is the volume of the ellipsoid, R_2 is the radius along the rotational axis of the ellipsoid, R_1 is the radius perpendicular to the rotational axis of the ellipsoid, G is the background scattering and Δρ (contrast) is the scattering length density difference between the scatterer and the solvent.

References:

(1) Amoureux, J.; Fernandez, C.; Steuernagel, S. Z Filtering in MQMAS NMR. *J. Magn. Reson. A* **1996**, *123* (1), 116–118.

(2) Edén, M.; Zhou, D.; Yu, J. Improved Double-Quantum NMR Correlation Spectroscopy of Dipolar-Coupled Quadrupolar Spins. *Chem. Phys. Lett.* **2006**, *431* (4–6), 397–403.

(3) Mali, G.; Fink, G.; Taulelle, F. Double-Quantum Homonuclear Correlation Magic Angle Sample Spinning Nuclear Magnetic Resonance Spectroscopy of Dipolar-Coupled Quadrupolar Nuclei. *J. Chem. Phys.* **2004**, *120* (6), 2835–2845.

(4) States, D. J.; Haberkorn, R. A.; Ruben, D. J. A Two-Dimensional Nuclear Overhauser Experiment with Pure Absorption Phase in Four Quadrants. *J. Magn. Reson. 1969* **1982**, *48* (2), 286–292.

(5) Massiot, D.; Fayon, F.; Capron, M.; King, I.; Le Calvé, S.; Alonso, B.; Durand, J.-O.; Bujoli, B.; Gan, Z.; Hoatson, G. Modelling One- and Two-Dimensional Solid-State NMR Spectra. *Magn. Reson. Chem.* **2002**, *40* (1), 70–76.

(6) Pazé, C.; Bordiga, S.; Lamberti, C.; Salvalaggio, M.; Zecchina, A.; Bellussi, G. Acidic Properties of H–β Zeolite As Probed by Bases with Proton Affinity in the 118–204 Kcal Mol-1 Range: A FTIR Investigation. *J. Phys. Chem. B* **1997**, *101* (24), 4740–4751.

(7) Hadjiivanov, K. Chapter Two - Identification and Characterization of Surface Hydroxyl Groups by Infrared Spectroscopy. In *Advances in Catalysis*; Jentoft, F. C., Ed.; Academic Press, 2014; Vol. 57, pp 99–318.

(8) Llewellyn, P. L.; Maurin, G. Gas Adsorption Microcalorimetry and Modelling to Characterise Zeolites and Related Materials. *Comptes Rendus Chim.* **2005**, *8* (3–4), 283–302.

(9) Weireld, G. D.; Frère, M.; Jadot, R. Automated Determination of High-Temperature and High-Pressure Gas Adsorption Isotherms Using a Magnetic Suspension Balance. *Meas. Sci. Technol.* **1999**, *10* (2), 117.

(10) Heymans, N.; Vaesen, S.; De Weireld, G. A Complete Procedure for Acidic Gas Separation by Adsorption on MIL-53 (Al). *Microporous Mesoporous Mater.* **2012**, *154*, 93–99.

(11) Billemont, P.; Coasne, B.; De Weireld, G. Adsorption of Carbon Dioxide, Methane, and Their Mixtures in Porous Carbons: Effect of Surface Chemistry, Water Content, and Pore Disorder. *Langmuir* **2013**, *29* (10), 3328–3338.

(12) Lewis, W. K.; Gilliland, E. R.; Chertow, B.; Cadogan, W. P. Adsorption Equilibria Hydrocarbon Gas Mixtures. *Ind. Eng. Chem.* **1950**, *42* (7), 1319–1326.

(13) Kaul, B. K. A Modern Version of Volumetric Apparatus for Measuring Gas-Solid Equilibrium Data. *Ind. Eng. Chem. Res.* **1987**, *26* (5), 928–933.

(14) Joy, A. S. Methods and Techniques for the Determination of Specific Surface by Gas Adsorption. *Vacuum* **1953**, *3* (3), 254–278.

(15) Berlier, K.; Bougard, J.; Olivier, M.-G. Automatic Measurement of Isotherms of Adsorption on Microporous Media in Large Ranges of Pressure and Temperature. *Meas. Sci. Technol.* **1995**, *6* (1), 107.

(16) Belmabkhout, Y.; Frère, M.; Weireld, G. D. High-Pressure Adsorption Measurements. A Comparative Study of the Volumetric and Gravimetric Methods. *Meas. Sci. Technol.* **2004**, *15* (5), 848.

(17) Kunz, O.; Wagner, W. The GERG-2008 Wide-Range Equation of State for Natural Gases and Other Mixtures: An Expansion of GERG-2004. *J. Chem. Eng. Data* **2012**, *57* (11), 3032–3091.

(18) VandeVondele, J.; Krack, M.; Mohamed, F.; Parrinello, M.; Chassaing, T.; Hutter, J. Quickstep: Fast and Accurate Density Functional Calculations Using a Mixed Gaussian and Plane Waves Approach. *Comput. Phys. Commun.* **2005**, *167* (2), 103–128.

(19) VandeVondele, J.; Hutter, J. An Efficient Orbital Transformation Method for Electronic Structure Calculations. *J. Chem. Phys.* **2003**, *118* (10), 4365–4369.

(20) Lippert, G.; Hutter, J.; Parrinello, M. The Gaussian and Augmented-Plane-Wave Density Functional Method for Ab Initio Molecular Dynamics Simulations. *Theor. Chem. Acc.* **1999**, *103* (2), 124–140.

(21) Lippert, G.; Hutter, J.; Parrinello, M. A Hybrid Gaussian and Plane Wave Density Functional Scheme. *Mol. Phys.* **1997**, *92* (3), 477–488.
(22) Perdew, J. P. Density-Functional Approximation for the Correlation Energy of the Inhomogeneous Electron Gas. *Phys. Rev. B* **1986**, *33* (12), 8822–8824.
(23) VandeVondele, J.; Hutter, J. Gaussian Basis Sets for Accurate Calculations on Molecular Systems in Gas and Condensed Phases. *J. Chem. Phys.* **2007**, *127* (11), 114105.
(24) Goedecker, S.; Teter, M.; Hutter, J. Separable Dual-Space Gaussian Pseudopotentials. *Phys. Rev. B* **1996**, *54* (3), 1703–1710.
(25) Grimme, S.; Antony, J.; Ehrlich, S.; Krieg, H. A Consistent and Accurate Ab Initio Parametrization of Density Functional Dispersion Correction (DFT-D) for the 94 Elements H-Pu. *J. Chem. Phys.* **2010**, *132* (15), 154104.
(26) Segall, M. D.; Lindan, P. J. D.; Probert, M. J.; Pickard, C. J.; Hasnip, P. J.; Clark, S. J.; Payne, M. C. First-Principles Simulation: Ideas, Illustrations and the CASTEP Code. *J. Phys. Condens. Matter* **2002**, *14* (11), 2717.
(27) Clark, S. J.; Segall, M. D.; Pickard, C. J.; Hasnip, P. J.; Probert, M. I. J.; Refson, K.; Payne, M. C. First Principles Methods Using CASTEP. *Z. Für Krist. - Cryst. Mater.* **2009**, *220* (5/6), 567–570.
(28) Yates, J. R.; Pickard, C. J.; Mauri, F. Calculation of NMR Chemical Shifts for Extended Systems Using Ultrasoft Pseudopotentials. *Phys. Rev. B* **2007**, *76* (2), 024401.
(29) Profeta, M.; Mauri, F.; Pickard, C. J. Accurate First Principles Prediction of 17O NMR Parameters in SiO2: Assignment of the Zeolite Ferrierite Spectrum. *J. Am. Chem. Soc.* **2003**, *125* (2), 541–548.
(30) Pickard, C. J.; Mauri, F. All-Electron Magnetic Response with Pseudopotentials: NMR Chemical Shifts. *Phys. Rev. B* **2001**, *63* (24), 245101.
(31) Hehre, W. J.; Lathan, W. A. Self□Consistent Molecular Orbital Methods. XIV. An Extended Gaussian□Type Basis for Molecular Orbital Studies of Organic Molecules. Inclusion of Second Row Elements. *J. Chem. Phys.* **1972**, *56* (11), 5255–5257.
(32) Rappe, A. K.; Casewit, C. J.; Colwell, K. S.; Goddard, W. A.; Skiff, W. M. UFF, a Full Periodic Table Force Field for Molecular Mechanics and Molecular Dynamics Simulations. *J. Am. Chem. Soc.* **1992**, *114* (25), 10024–10035.
(33) Martin, M. G.; Siepmann, J. I. Transferable Potentials for Phase Equilibria. 1. United-Atom Description of N-Alkanes. *J. Phys. Chem. B* **1998**, *102* (14), 2569–2577.
(34) Reid, R. C.; Sherwood, T. K. *The Properties of Gases and Liquids*; New York; McGraw-Hill, 1958.
(35) Harris, J. G.; Yung, K. H. Carbon Dioxide's Liquid-Vapor Coexistence Curve And Critical Properties as Predicted by a Simple Molecular Model. *J. Phys. Chem.* **1995**, *99* (31), 12021–12024.
(36) Yang, Q.; Zhong, C. Molecular Simulation of Carbon Dioxide/Methane/Hydrogen Mixture Adsorption in Metal–Organic Frameworks. *J. Phys. Chem. B* **2006**, *110* (36), 17776–17783.
(37) Peng, D.-Y.; Robinson, D. B. A New Two-Constant Equation of State. *Ind. Eng. Chem. Fundam.* **1976**, *15* (1), 59–64.
(38) Vlugt, T. J. H.; García-Pérez, E.; Dubbeldam, D.; Ban, S.; Calero, S. Computing the Heat of Adsorption Using Molecular Simulations: The Effect of Strong Coulombic Interactions. *J. Chem. Theory Comput.* **2008**, *4* (7), 1107–1118.
(39) Lively, R. P.; Dose, M. E.; Xu, L.; Vaughn, J. T.; Johnson, J. R.; Thompson, J. A.; Zhang, K.; Lydon, M. E.; Lee, J. S.; Liu, L.; Hu, Z.; Karvan, O.; Realff M. J.; Koros, W. J. A high-Flux Polyimide Hollow Fiber Membrane to Minimize footprint and Energy Penalty for CO_2 Recovery from flue Gas *J. Membr.Sci.***2012**, *423–424*, 302–313.
(40) Bae, T. H.; Long, J. R. CO_2/N_2 Separations with Mixed-Matrix Membranes Containing Mg_2(dobdc) Nanocrystals. *Energy Environ. Sci.* **2013**, *6*, 3565–3569.
(41) Wijenayake, S. N.; Panapitiya, N. P.; Versteeg, S. H.; Nguyen, C. N.; Goel, S.; Balkus, K. J.; Musselman, I. H.; Ferraris, J. P. Surface Cross-Linking of ZIF-8/Polyimide Mixed Matrix Membranes (MMMs) for Gas Separation.*Ind. Eng. Chem. Res.* **2013**, *52*, 6991–7001.
(42) Nafisi, V.; Hagg, M. B. Gas Separation Properties of ZIF-8/6FDA-durene Diamine Mixed

Matrix Membrane. *Sep. Purif. Technol.* **2014**, *128*, 31–38.
(43) Fritsch, D.; Peinemann, K.-V.; Gomes, and D. D. F. US Pat., 7,658,784. 9, 2010.
(44) Japip, S.; Wang, H.; Xiao, Y. C.; Chung, T. S. Highly Permeable Zeolitic Imidazolate Framework (ZIF)-71 Nano-particles Enhanced Polyimide Membranes for Gas separation. *J. Membr.Sci.***2014**, *467*, 162–174.

Annex C

THE JOURNAL OF PHYSICAL CHEMISTRY C

Article

pubs.acs.org/JPCC

Highly Selective CO_2 Capture by Small Pore Scandium-Based Metal–Organic Frameworks

Renjith S. Pillai,[†] Virginie Benoit,[¥] Angelica Orsi,[‡] Philip L. Llewellyn,[¥] Paul A. Wright,[‡] and Guillaume Maurin*[,†]

[†]Institut Charles Gerhardt Montpellier, UMR-5253, Université de Montpellier, CNRS, ENSCM, Place E. Bataillon, 34095 Montpellier cedex 05, France

[¥]Aix Marseille University, CNRS, Madirel, UMR 7246, 13397 Marseille, France

[‡]Eastchem School of Chemistry, University of St. Andrews, St. Andrews, Fife KY16 9ST, United Kingdom

Supporting Information

ABSTRACT: The selective CO_2 adsorption performance of a series of functionalized small pore scandium terephthalate MOFs was explored by quantum and force-field-based molecular simulations. The NO_2 derivative was predicted to be highly selective for CO_2 over N_2 and CH_4, outperforming most of the MOFs as well as other classes of porous solids reported so far. The potential of this solid for physisorption based-applications was further confirmed by (i) an adsorbent performance indicator (API) which exceeds that previously evaluated for many MOFs, (ii) an easy regeneration under mild condition as revealed by high-throughput manometric adsorption experiments although a relatively high CO_2 adsorption enthalpy was confirmed by microcalorimetry, and (iii) a good stability under moisture.

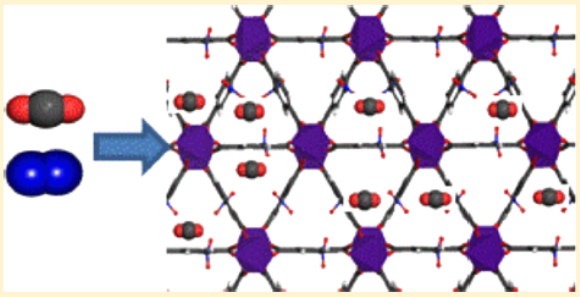

1. INTRODUCTION

Porous coordination polymers (PCPs) or metal−organic frameworks (MOFs) have attracted great attention over the past decade for their potential uses in societally relevant applications.[1,2] The combinatorial chemistry has covered only a small fraction of synthetic variables which prevented so far a full scan of all the possible MOF structures.[3] This is particularly true for the small pore MOFs with openings of about 3−3.5 Å which have been only rarely synthesized and later characterized for their separation properties.[4−6] This subclass of MOFs is expected to exhibit optimal structural features for a selective adsorption of CO_2 over other molecules of larger kinetic diameters such as CH_4 and N_2. This makes these materials of potential interest in the areas of natural gas purification and flue gas treatment, respectively.

Scandium terephthalate $Sc_2(O_2CC_6H_4CO_2)_3$ (hereafter Sc_2BDC_3, BDC = 1,4-benzenedicarboxylate) is constructed of rows of isolated ScO_6 octahedra interconnected by BDC linkers, giving small pore triangular channels[7] that are potentially attractive for the selective capture of CO_2. This solid shows several advantages including (i) a very high thermal stability, (ii) an environmentally friendly synthesis route with only use of water and scandium salts, (iii) a pronounced hydrophobicity, and (iv) an availability of a range of analogues where the terephthalate group is functionalized with different groups. This last feature offers a priori the opportunity to finely tune its pore size openings, the degree of confinement for guests and/or the strength of the host/guest interactions, for the design of an optimal adsorbent. In this context, the separation performances of Sc_2BDC_3 and its NH_2 and NO_2 derivatives for CO_2/CH_4 and CO_2/N_2 mixtures have been explored by a computational strategy integrating force-field and quantum-based calculations that accounts for the complex structural behavior of the small pore MOFs upon adsorption, e.g., the ligand reorientation and cell volume changes. This is beyond the conventional molecular simulations generally applied to scrutinize the adsorption properties of MOFs which assume the absence of guest-assisted structural change of their frameworks.[8,9] In complement to this, an in-depth analysis of the adsorption mechanisms at the microscopic level is delivered to reveal the role of the functionalization on the separation. This global modelling approach is validated first by comparison with single-component adsorption data and in situ diffraction data. The selectivity of this series of solids was further predicted for the two mixtures of interest since direct coadsorption measurements are complex for small pore solids due very small amounts adsorbed and long time equilibration that lead to large error bars.[10]

The adsorbent performance indicator (API) of the most promising material, i.e., $Sc_2(BDC\text{-}NO_2)_3$ for the gas separations

Received: August 13, 2015
Revised: September 22, 2015
Published: September 23, 2015

DOI: 10.1021/acs.jpcc.5b07903
J. Phys. Chem. C 2015, 119, 23592−23598

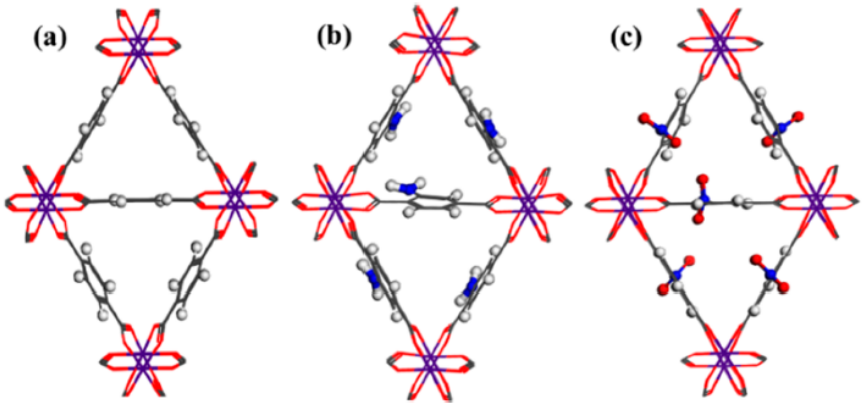

Figure 1. Local views of the DFT-optimized structures along the triangular channel: Sc_2BDC_3 (a), $Sc_2(BDC\text{-}NH_2)_3$ (b), and $Sc_2(BDC\text{-}NO_2)_3$ (c). The atoms are represented as follows: Sc, purple; C, gray; O, red; N, blue; H, white.

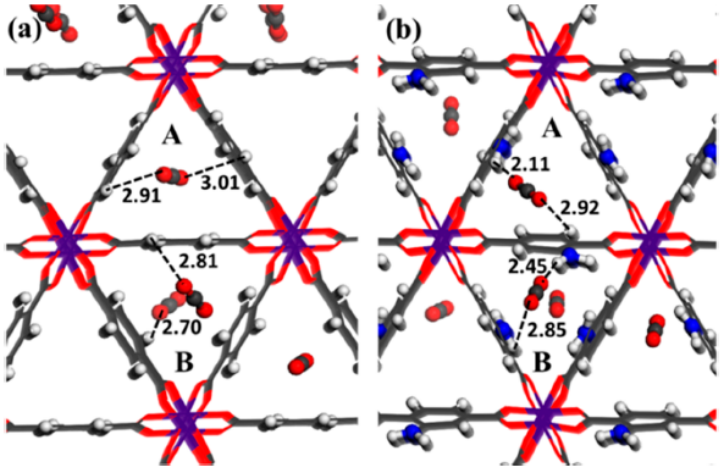

Figure 2. Local views of the snapshots extracted from the GCMC simulations at 1 bar and 303 K: Sc_2BDC_3 (a) and $Sc_2(BDC\text{-}NH_2)_3$ (b). The interacting distances are reported in angstroms, and the color code is the same as in Figure 1.

of interest, is further compared with that previously reported for other porous solids. The regeneration and the water stability of this solid are finally assessed by means of high-throughput manometric and powder X-ray diffraction experiments.

2. MATERIALS AND METHODS

Modeling. The crystal structures of the empty and CO_2-loaded Sc_2BDC_3 and its NH_2 and NO_2 derivatives were geometry optimized at the density functional theory (DFT) level. These calculations were performed with the QUICKSTEP module, available as part of the CP2K code.[11−14] The PBE functional[15] and the triple-ζ basis set (TZVP-MOLOPT) were used for all atoms, except for the Al centers where double-ζ functions (DZVP-MOLOPT) were employed.[16] Semi-empirical dispersion corrections as implemented in the DFT-D3 method were considered.[17] The influence of these dispersion corrections on the structural features of the Sc_2BDC_3/CO_2 system is discussed in the Supporting Information. These DFT calculations were performed for all MOFs using a P1 symmetry. Grand Canonical Monte Carlo (GCMC) simulations were further carried out at 273 and 303 K to predict the adsorption of CO_2, CH_4, and N_2, and the coadsorption of CO_2/CH_4 and CO_2/N_2 (molar composition of 50/50 and 15/85, respectively) in the DFT-optimized structures using the Complex Adsorption and Diffusion Simulation Suite (CADSS) code.[18] The simulation boxes were made of 64 (8 × 2 × 4) unit cells for both Sc_2BDC_3 and $Sc_2(BDC\text{-}NO_2)_3$ and 48 (8 × 3 × 2) unit cells for $Sc_2(BDC\text{-}NH_2)_3$. Each atom of the MOF frameworks was treated as a charged Lennard−Jones (LJ) interacting site with LJ parameters taken from the universal force field (UFF)[19] and partial charges extracted from our DFT calculations. While CH_4 was described by the TraPPE single LJ interacting site model.[20] CO_2 and N_2 were represented by the three-site LJ charged EMP2[21] and TraPPE[20] models, respectively. For each state point, 5×10^7 Monte Carlo steps have been used for both equilibration and production runs, and the adsorption enthalpy at low coverage (Δh) for each gas was calculated through configurational-bias Monte Carlo simulations performed in the NVT ensemble using the revised Widom's test particle insertion method.[22] The radial distribution functions (RDF) reported in Supporting Information for the guest/MOF pairs were obtained by averaging over the 5×10^7 Monte Carlo production steps. All details of both DFT and GCMC

DOI: 10.1021/acs.jpcc.5b07903
J. Phys. Chem. C 2015, 119, 23592−23598

calculations are provided in Supporting Information. In complement to this, the adsorbent performance indicators (API) of this series of solids were further calculated using the strategy previously reported,[23] and the resulting values are compared with that obtained for other porous solids of interest for CO_2 capture.

Materials. The synthesis of the most promising solid $Sc_2(BDC\text{-}NO_2)_3$ has undergone development from the original hydrothermal method[24](190 °C, 3 days, $Sc(NO_3)_3{\cdot}H_2O$ metal source). This study employed microwave-assisted heating of the reaction mixture in a sealed glass vessel within a CEM Discover SP microwave. The synthesis protocol is described in more details in Supporting Information. Laboratory PXRD patterns were obtained from a Stoe STAD i/P diffractometer in capillary mode (transmission) with primary monochromation (Cu $K_{\alpha 1}$, λ = 1.54051 Å) at room temperature. Phase identification of samples was accomplished by direct comparison of the observed patterns with those from the literature.[24] For moisture sensitivity testing, the white MOF material (0.17 g) was placed in an alumina crucible within a tube furnace (60 °C), and a wet nitrogen gas stream (20 °C, water vapor pressure 2310 Pa) was passed over the sample (18 h).

Adsorption Measurements. Several adsorption cycles of carbon dioxide with a simple primary vacuum outgassing at 303 K were collected by manometric gas adsorption experiments on $Sc_2(BDC\text{-}NO_2)_3$ with the use of a high-throughput adsorption apparatus developed in-house (see Supporting Information for more details).[25] The microcalorimetry experiments were performed using a home-built manometric adsorption apparatus coupled with a Tian−Calvet-type microcalorimeter.[26] This experimental device allows the simultaneous determination of the adsorption isotherm and the adsorption enthalpy using a point by point introduction of gas to the sample (see Supporting Information for more details).

3. RESULTS AND DISCUSSION

The structure of Sc_2BDC_3 was first DFT-geometry optimized starting from single-crystal X-ray diffraction data[7,27] (see details of the calculations in Supporting Information, Figure 1a). This model was further loaded with 6.5 mmol·g^{-1} of CO_2, i.e., the

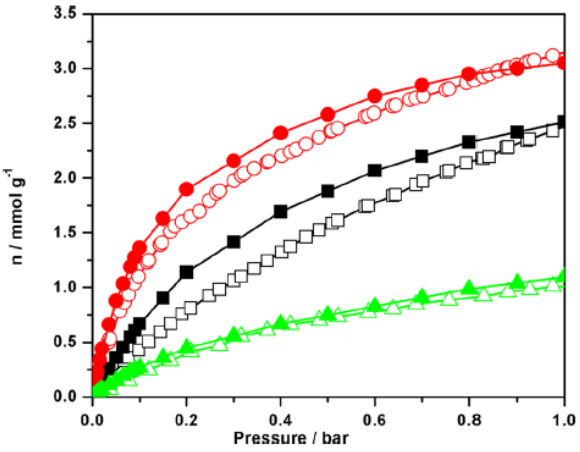

Figure 3. Comparison between the GCMC simulated (full symbols) and experimental adsorption isotherms (empty symbols) for CO_2 in Sc_2BDC_3 (squares), $Sc_2(BDC\text{-}NH_2)_3$ (circles), and $Sc_2(BDC\text{-}NO_2)_3$ (triangles) at 273 K.

Table 1. Pore Diameter (Å), BET Area ($m^2{\cdot}g^{-1}$), and Pore Volume ($cm^3{\cdot}g^{-1}$) Calculated from the DFT-Optimized Crystal Structures (see Supporting Information for details)[a]

MOF	d_{pore}	S_{BET}	V_{pore}	$S(CO_2/N_2)$	$S(CO_2/CH_4)$
Sc_2BDC_3	3.60	596	0.251	65	17
$Sc_2(BDC\text{-}NH_2)_3$	3.60	340	0.124	151	56
$Sc_2(BDC\text{-}NO_2)_3$	2.90	0	0.000	1050	~4000

[a]Predicted selectivities at 303 K and 1.0 bar by GCMC simulations.

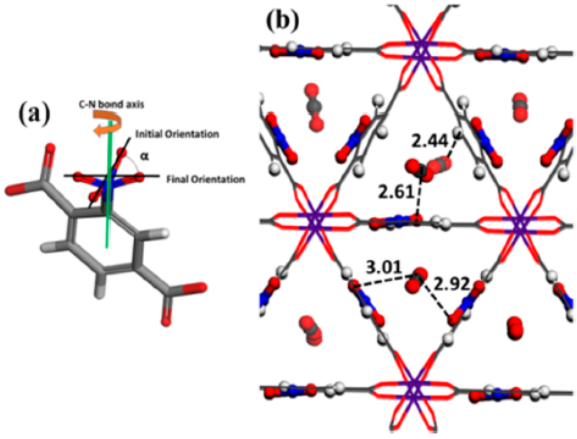

Figure 4. (a) Schematic representation of the NO_2 rotation in the BDC-NO_2 linker of $Sc_2(BDC\text{-}NO_2)_3$. (b) Local views of snapshots extracted from the GCMC simulations at 1.0 bar and 303 K. The distances are reported in angstroms, and the color code is the same as in Figure 1.

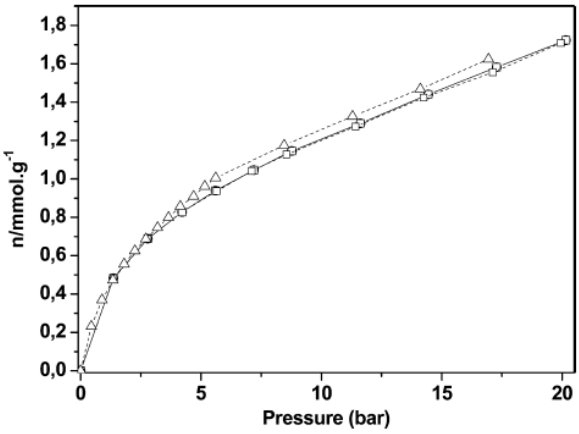

Figure 5. Three CO_2 adsorption cycles measured on $Sc_2(BDC\text{-}NO_2)_3$ at 303 K (with distinct circle, square, and triangle symbols) using a simple primary vacuum outgassing at room temperature between each cycle for 1 h.

experimental saturation capacity measured at 196 K and 1 bar,[24] using Monte Carlo simulations and subsequently fully relaxed at the DFT-level, allowing both atomic positions and unit cell parameters of the system to be changed. The predicted cell dimensions (V = 3145.3 Å^3) and space group ($C2/c$) are in very good agreement with the in situ X-ray diffraction data (V = 3122.7 Å^3, $C2/c$) collected in the presence of CO_2[27] (Table S2). These calculations reproduce also well the guest-assisted

DOI: 10.1021/acs.jpcc.5b07903
J. Phys. Chem. C 2015, 119, 23592−23598

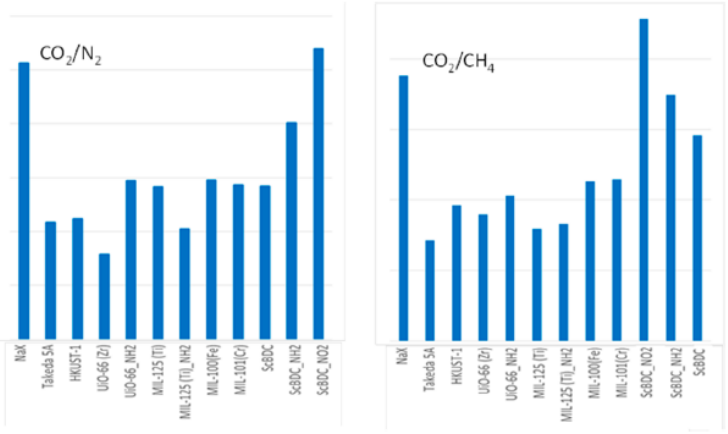

Figure 6. Adsorbent performance indicators (API) for the series of Sc_2BDC_3 compared to those obtained for other porous solids.[23]

rotation of the terephthalate linkers resulting in two different types of triangular channels denoted A and B, as revealed experimentally (Figure 2a). This validated CO_2-loaded structure model was further used to predict the single-component adsorption behavior of CO_2 in Sc_2BDC_3 at different temperatures by means of GCMC simulations. Figure 3 shows that the simulated CO_2 adsorbed amount at 273 K reproduces well the gravimetric data at 1 bar while there is an overestimation of the experimental adsorption isotherm collected in the low pressure domain [0−1 bar].

Analysis of the adsorption mechanism additionally shows that the two types of channels adsorb CO_2 in a different manner. Channel A allows CO_2 to be aligned in such a way that its oxygen atom interacts with the hydrogen atoms of the phenyl ring with characteristic distances ranging from 2.5 to 3.9 Å (see radial distribution functions in Figure S14). In contrast, the CO_2 molecules are not aligned anymore in channel B due to the tilting of the organic linker. This spatial guest distribution illustrated in Figure 2a is fully consistent with the one elucidated from in situ X-ray diffraction and suggests the absence of strong adsorption sites for CO_2. This is confirmed by the moderate adsorption enthalpy simulated at low coverage ∼−32 kJ/mol. To emphasize the nature of the host/guest interactions, we switched off the electrostatic interactions between the CO_2 and the adsorbents by setting the partial charges of the MOF framework to zero. The resulting adsorption enthalpy of −29.4 kJ/mol (vs −32 kJ/mol for the electrostatic and LJ contributions) supports that the adsorption of CO_2 in this parent solid is mainly driven by van der Waals interactions.

This relative agreement between experiments and simulations on the CO_2/Sc_2BDC_3 system validated the computational strategy, and this motivated the exploration of the adsorption of other gases of interest in the series of functionalized Sc_2BDC_3 solids. The adsorption isotherms simulated at 303 K for N_2 and CH_4 in Sc_2BDC_3 are indeed favorably compared with the corresponding experimental data[27] (Figure S10) and show that the corresponding amounts adsorbed are much smaller than the CO_2 uptake. Further, the simulated adsorption enthalpies obtained for N_2 and CH_4 in Sc_2BDC_3 of −18.5 and −22.4 kJ mol^{-1}, respectively (Figure S13a), are similar to the values reported for other small pore MOFs[4−6,28] (Supporting Information). These resulting moderate energy values are consistent with a distribution of these molecules in the center of the triangular channels with host/guest interacting distances over 3.0 Å (Figures S16, S17).

The next consisted of predicting the separation performances of Sc_2BDC_3 for the two mixtures of interest, i.e., CO_2/N_2 and CO_2/CH_4, with a molar concentration of 15/85 and 50/50, respectively (Figure S21). The simulated selectivities obtained at 1 bar and 303 K for both gas mixtures are $S(CO_2/N_2) = 65$ and $S(CO_2/CH_4) = 17$ (Table 1). The corresponding gas separation is mainly driven by the high degree of confinement of this solid due to its restricted pore size (3.6 Å) conjugated to a small pore volume (0.251 cm^3/g).

$Sc_2(BDC\text{-}NH_2)_3$ is expected to surpass the performance of the unfunctionalized material by maintaining the advantage of the confinement while enhancing the affinity of the MOF surfaces to CO_2 by the incorporation of the amino function. Characterization of the DFT-optimized $Sc_2(BDC\text{-}NH_2)_3$ structure reveals that the pore opening remains unchanged because the hydrogen atom of the amino group is predicted to not be pointing toward the center of the pore (Figure 1b) as also evidenced on the structure resolved by single-crystal X-ray diffraction. This latter observation suggests that all three gases are still able to penetrate the channel. In addition, the pore volume significantly decreases (0.124 cm^3/g), i.e., the degree of confinement is even higher.

The CO_2 loaded structure model for $Sc_2(BDC\text{-}NH_2)_3$ was then built using the same DFT strategy detailed above with the consideration of a CO_2 loading of 5.5 mmol/g corresponding to the saturation capacity measured experimentally at 196 K and 1 bar.[27] Table S2 shows that the cell dimensions of this simulated structure (V = 6306.6 $Å^3$) are in agreement with the in situ X-ray diffraction data (V = 6247.0 $Å^3$) collected upon CO_2 adsorption.[29] Figure 2b reveals that the guest-assisted structure response of the framework is similar to the one shown by Sc_2BDC_3 with the presence of two types of channels. This structure model is further validated by a good agreement between the GCMC simulated adsorption isotherm and the corresponding gravimetric data at 273 K (Figure 3). Figure 2b also illustrates that the amino function strongly influences the adsorption mechanism, the CO_2 molecules interacting with either single or two nearby amino groups with a mean characteristic $O(CO_2)$−$H(NH_2)$ distance of 2.58 Å (Figure S17). This leads to a drastic increase of the simulated CO_2 adsorption enthalpy at low coverage (−40.0 kJ/mol) mainly due to the additional electrostatic interactions between the

DOI: 10.1021/acs.jpcc.5b07903
J. Phys. Chem. C 2015, 119, 23592−23598

amino groups and CO_2. Further, this value is among the highest one reported so far for functionalized MOFs.[6,25] In contrast, the grafting does not modify the interaction between the two other gases and the pore wall as revealed by (i) the same spatial distributions of CH_4 and N_2 in the center of the pore (Figures S11, S18, S19) and (ii) the almost unchanged adsorption enthalpies at low coverage, i.e., −19.5 kJ/mol (N_2) and −22.6 kJ/mol (CH_4) (Figure S13b) compared to the unfunctionalized solid. The high predicted adsorption enthalpy differences $\Delta(\Delta H(CO_2) - \Delta H(CH_4)) \sim -17.4$ kJ/mol and $\Delta(\Delta H(CO_2) - \Delta H(N_2)) \sim -20.5$ kJ/mol suggest that the functionalization should drastically improve the performances of this Sc-based MOF for the selective capture of CO_2 (Table S9). This is confirmed by the GCMC simulations which predict selectivity values at 303 K and 1 bar, i.e., $S(CO_2/N_2) = 151$ and $S(CO_2/CH_4) = 56$, much higher than that of Sc_2BDC_3 (Table 1 and Figure S22).

As a further step, the functionalization of Sc_2BDC_3 by nitro groups was considered. The DFT-optimized structure shows that the oxygen atoms of the grafted functions project into the channel[24] (Figure 1c), leading to a significant decrease of the pore size (Table 1). Such a tuning of the pore dimension is expected to strongly favor the selective adsorption of CO_2 over CH_4 and N_2 via a size exclusion effect. To confirm this, the adsorption/separation properties of $Sc_2(BDC\text{-}NO_2)_3$ was explored computationally. The DFT calculations predicted that the adsorption of CO_2 induces a cell expansion of ∼3.6%, slightly larger than the one evidenced for the amino derivative (1.2%), and this is associated with a more pronounced tilting of the BDC-NO_2 linker while the orientation of the oxygen atoms of the NO_2 groups remains the same as in the empty structure. The GCMC simulations performed on this structure were however not able to reproduce the single-component CO_2 uptake experimentally evidenced at 196 K and 1 bar (see Supporting Information). Mowat et al.[24] previously suspected that a significant reorientation of the NO_2 groups might be at the origin of the relatively large CO_2 uptake (3 mmol/g) measured for this solid. Such a structural rearrangement of the bulky polar group is not captured by the DFT calculations performed at 0 K because it would require overcoming a relatively high energy barrier. To circumvent this limitation, a few configurations were built by rotating the $-NO_2$ groups along the C−N bond axis, where both N−O bond distances and C−N−O bond angles were kept intact (Figure 4a). It was found that all the structures generated with a rotation angle α below 90° failed to reproduce the experimental uptake (Figure S12).

Indeed, Figure 3 shows a very good agreement between the simulated and experimental CO_2 adsorption isotherms when one considers the case where the O atoms of the nitro groups are not pointing anymore toward the center of the channel. This observation supports that such a large magnitude of flexibility of the functionalized group is expected to occur for accommodating CO_2 in the pore. Figure 4b clearly emphasizes that despite the high degree of confinement of this channel, this solid also allows an optimal role of the grafting functions by authorizing a direct interaction between the $-NO_2$ groups and the CO_2 molecules with a mean characteristic $C(CO_2)$−$O(NO_2)$ distance of 2.75 Å (Figure S20). The GCMC simulations performed for the gas mixtures evidenced that $Sc_2(BDC\text{-}NO_2)_3$ adsorbs only negligible amounts of N_2 and CH_4, leading to very high separation performances, i.e., $S(CO_2/N_2) \sim 1050$ and $S(CO_2/CH_4) \sim 4000$ at 303 K and 1 bar (Table 1 and Figure S23).

It is generally desirable for the strongly adsorbed species to have a relatively low adsorption enthalpy for an easy regeneration of the adsorbent. The resulting simulated adsorption enthalpy for CO_2 in $Sc_2(BDC\text{-}NO_2)_3$ (∼−35.0 kJ/mol) is very similar to the values previously reported in other small pore MOFs, such as UiO-66 (Zr)-BTEC (−34.8 kJ/mol)[30] and SIFSIX-2-Cu-i (−31.9 kJ/mol),[4] while it remains significantly lower than that of the zeolite 13X (−45.0 kJ/mol)[31] currently used in pressure swing adsorption processes for such a gas separation at the industrial level. This predicted adsorption enthalpy was confirmed experimentally by microcalorimetry measurements performed at low coverage (∼−34.0 kJ/mol) (see Supporting Information). To assess the regeneration of this material, complementary manometric experiments were performed to record several adsorption cycles of CO_2 using a simple primary vacuum outgassing at 303 K for 1 h between each cycle. Figure 5 reports the CO_2 adsorption isotherms measured for three cycles. It can be observed that the three curves overlap in the entire range of pressure up to 20 bar. This emphasizes that, like many MOFs, a full regeneration of the sample is obtained under mild conditions, i.e., primary vacuum at room temperature. In addition, PXRD data comparison of before and after water stability testing indicated that no structural degradation of the MOF had occurred (see Supporting Information), a prerequisite for potential application at the industrial level.

A way to rank the separation ability of this material with respect to those reported so far for other porous solids is to determine their adsorbent performance indicators (API)[23] which integrates the CO_2 working capacity, the selectivity, and the differences in adsorption enthalpies between CO_2 and either CH_4 or N_2. Figure 6 suggests that $Sc_2(BDC\text{-}NO_2)_3$ outperforms most of the MOFs and the active carbon considered in the original API paper.[23] It would equally suggest that $Sc_2(BDC\text{-}NO_2)_3$ even compares favorably with the reference zeolite 13X. This outcome is due to the high selectivities calculated for these materials even though the working capacities are not optimal, although similar to that of 13X.

4. CONCLUSIONS

In summary, a computational strategy combining advanced quantum and force-field-based tools has been devised to rigorously assess the separation performances of small pore MOFs for CO_2 capture. These calculations revealed that $Sc_2(BDC\text{-}NO_2)_3$ is among the best MOF reported so far for CO_2 capture. The promises of this solid were further supported by the determination of the API while complementary experiments evidenced an easy regeneration of the sample under vacuum at room temperature and a very good water stability. This study suggests that this solid is potentially of interest for membrane-type separations where the selectivity, and size exclusion, can be of great importance, although diffusion aspects need to be considered in future work. We will also pay attention to the effect of entropy on the adsorption process in this narrow pore solid by considering further free energy calculations.

DOI: 10.1021/acs.jpcc.5b07903
J. Phys. Chem. C 2015, 119, 23592−23598

■ ASSOCIATED CONTENT

Supporting Information

The Supporting Information is available free of charge on the ACS Publications website at DOI: 10.1021/acs.jpcc.5b07903.

DFT and GCMC simulations details, API results and comparisons, microcalorimetry/manometry measurements, and water stability testing (PDF)

■ AUTHOR INFORMATION

Corresponding Author

*E-mail: guillaume.maurin@um2.fr.

Notes

The authors declare no competing financial interest.

■ ACKNOWLEDGMENTS

The research leading to these results has received funding from the European Community Seventh Framework Program (FP7/2007-2013) under grant agreement no. 608490 (project M^4CO_2) and the ANR Chesdens. A.O. thanks the Society of Chemical Industry (SCI) for a scholarship. G.M. thanks the Institut Universitaire de France for its support.

■ REFERENCES

(1) Zhou, H.-C.; Long, J. R.; Yaghi, O. M. Themed Collection of Metal−Organic Frameworks. *Chem. Rev.* **2012**, *112*, 673.

(2) Zhou, H.-C.; Kitagawa, S. Metal Organic Frameworks. *Chem. Soc. Rev.* **2014**, *43*, 5415.

(3) Stock, N.; Biswas, S. Synthesis of Metal-Organic Frameworks (MOFs): Routes to Various MOF Topologies, Morphologies, and Composites. *Chem. Rev.* **2012**, *112*, 933−969.

(4) Nugent, P.; Belmabkhout, Y.; Burd, S. D.; Cairns, A. J.; Luebke, R.; Forrest, K.; Pham, T.; Ma, S.; Space, B.; Wojtas, L.; et al. Porous Materials with Optimal Adsorption Thermodynamics and Kinetics for CO_2 Separation. *Nature* **2013**, *495*, 80−84.

(5) Park, K. S.; Ni, Z.; Cote, A. P.; Choi, J. Y.; Huang, R. D.; Uribe-Romo, F. J.; Chae, H. K.; O'Keeffe, M.; Yaghi, O. M. Exceptional Chemical and Thermal Stability of Zeolitic Imidazolate Frameworks. *Proc. Natl. Acad. Sci. U. S. A.* **2006**, *103*, 10186−10191.

(6) Llewellyn, P. L.; Garcia-Rates, M.; Gaberova, L.; Miller, S. R.; Devic, T.; Lavalley, J. C.; Bourrelly, S.; Bloch, E.; Filinchuk, Y.; Wright, P. A.; et al. Structural Origin of Unusual CO_2 Adsorption Behavior of a Small-Pore Aluminum Bisphosphonate MOF. *J. Phys. Chem. C* **2015**, *119*, 4208−4216.

(7) Miller, S. R.; Wright, P. A.; Serre, C.; Loiseau, T.; Marrot, J.; Férey, G. A Microporous Scandium Terephthalate, $Sc_2(O_2CC_6H_4CO_2)_3$, with High Thermal Stability. *Chem. Commun.* **2005**, 3850−3852.

(8) Yang, Q.; Liu, D.; Zhong, C.; Li, J. R. Development of Computational Methodologies for Metal−Organic Frameworks and Their Application in Gas Separations. *Chem. Rev.* **2013**, *113*, 8261−8323.

(9) Colon, Y. J.; Snurr, R. Q. High-Throughput Computational Screening of Metal-Organic Frameworks. *Chem. Soc. Rev.* **2014**, *43*, 5735−5749.

(10) Mason, J. A.; McDonald, T. M.; Bae, T.-H.; Bachman, J. E.; Sumida, K.; Dutton, J. J.; Kaye, S. S.; Long, J. R. Application of a High-Throughput Analyzer in Evaluating Solid Adsorbents for Post-Combustion Carbon Capture via Multicomponent Adsorption of CO_2, N_2, and H_2O. *J. Am. Chem. Soc.* **2015**, *137*, 4787−4803.

(11) VandeVondele, J.; Krack, M.; Mohamed, F.; Parrinello, M.; Chassaing, T.; Hutter, J. QUICKSTEP: Fast and Accurate Density Functional Calculations Using a Mixed Gaussian and Plane Waves Approach. *Comput. Phys. Commun.* **2005**, *167*, 103−128.

(12) VandeVondele, J.; Hutter, J. An Efficient Orbital Transformation Method for Electronic Structure Calculations. *J. Chem. Phys.* **2003**, *118*, 4365−4369.

(13) Lippert, G.; Hutter, J.; Parrinello, M. The Gaussian and Augmented-Plane-Wave Density Functional Method for Ab Initio Molecular Dynamics Simulations. *Theor. Chem. Acc.* **1999**, *103*, 124−140.

(14) Lippert, G.; Parrinello, M.; Hutter, J. A Hybrid Gaussian and Plane Wave Density Functional Scheme. *Mol. Phys.* **1997**, *92*, 477−488.

(15) Perdew, J. P. Density-Functional Approximation for the Correlation-Energy of the Inhomogeneous Electron-Gas. *Phys. Rev. B* **1986**, *33*, 8822−8824.

(16) VandeVondele, J.; Hutter, J. Gaussian Basis Sets for Accurate Calculations on Molecular Systems in Gas and Condensed Phases. *J. Chem. Phys.* **2007**, *127*, 114105.

(17) Grimme, S.; Antony, J.; Ehrlich, S.; Krieg, H. A Consistent and Accurate Ab Initio Parametrization of Density Functional Dispersion Correction (DFT-D) for the 94 Elements H-Pu. *J. Chem. Phys.* **2010**, *132*, 154104.

(18) Yang, Q.; Zhong, C. Molecular Simulation of Carbon Dioxide/Methane/Hydrogen Mixture Adsorption in Metal−Organic Frameworks. *J. Phys. Chem. B* **2006**, *110*, 17776−17783.

(19) Rappe, A. K.; Casewit, C. J.; Colwell, K. S.; Goddard, W. A.; Skiff, W. M. UFF, a Full Periodic-Table Force-Field for Molecular Mechanics and Molecular-Dynamics Simulations. *J. Am. Chem. Soc.* **1992**, *114*, 10024−10035.

(20) Martin, M. G.; Siepmann, J. I. Transferable Potentials for Phase Equilibria. 1. United-Atom Description of n-Alkanes. *J. Phys. Chem. B* **1998**, *102*, 2569−2577.

(21) Harris, J. G.; Yung, K. Carbon Dioxide's Liquid-Vapor Coexistence Curve and Critical Properties as Predicted by a Simple Molecular Model. *J. Phys. Chem.* **1995**, *99*, 12021−12024.

(22) Vlugt, T. J. H.; Garcia-Perez, E.; Dubbeldam, D.; Ban, S.; Calero, S. Computing the Heat of Adsorption Using Molecular Simulations: The Effect of Strong Coulombic Interactions. *J. Chem. Theory Comput.* **2008**, *4*, 1107−1118.

(23) Wiersum, A. D.; Chang, J. S.; Serre, C.; Llewellyn, P. L. An Adsorbent Performance Indicator as a First Step Evaluation of Novel Sorbents for Gas Separations: Application to Metal−Organic Frameworks. *Langmuir* **2013**, *29*, 3301−3309.

(24) Mowat, J. P. S.; Miller, S. R.; Griffin, J. M.; Seymour, V. R.; Ashbrook, S. E.; Thompson, S. P.; Fairen-Jimenez, D.; Banu, A. M.; Duren, T.; Wright, P. A. Structural Chemistry, Monoclinic-to-Orthorhombic Phase Transition, and CO_2 Adsorption Behavior of the Small Pore Scandium Terephthalate, $Sc_2(O_2CC_6H_4CO_2)_3$, and Its Nitro- and Amino-Functionalized Derivatives. *Inorg. Chem.* **2011**, *50*, 10844−10858.

(25) Wiersum, A. D.; Giovannangeli, C.; Vincent, D.; Bloch, E.; Reinsch, H.; Stock, N.; Lee, J. S.; Chang, J. S.; Llewellyn, P. L. Experimental Screening of Porous Materials for High Pressure Gas Adsorption and Evaluation in Gas Separations: Application to MOFs (MIL-100 and CAU-10). *ACS Comb. Sci.* **2013**, *15*, 111−119.

(26) Llewellyn, P. L.; Maurin, G. Gas Adsorption Microcalorimetry and Modelling to Characterise Zeolites and Related Materials. *C. R. Chim.* **2005**, *8*, 283−302.

(27) Miller, S. R.; Wright, P. A.; Devic, T.; Serre, C.; Férey, G.; Llewellyn, P. L.; Denoyel, R.; Gaberova, L.; Filinchuk, Y. Single Crystal X-ray Diffraction Studies of Carbon Dioxide and Fuel-Related Gases Adsorbed on the Small Pore Scandium Terephthalate Metal Organic Framework, $Sc_2(O_2CC_6H_4CO_2)_3$. *Langmuir* **2009**, *25*, 3618−3626.

(28) Miller, S. R.; Pearce, G. M.; Wright, P. A.; Bonino, F.; Chavan, S.; Bordiga, S.; Margiolaki, I.; Guillou, N.; Férey, G.; Bourrelly, S.; et al. Structural Transformations and Adsorption of Fuel-Related Gases of a Structurally Responsive Nickel Phosphonate Metal−Organic Framework, Ni-STA-12. *J. Am. Chem. Soc.* **2008**, *130*, 15967−15981.

(29) Greenaway, A.; Gonzalez-Santiago, B.; Donaldson, P. M.; Frogley, M. D.; Cinque, G.; Sotelo, J.; Moggach, S.; Shiko, E.; Brandani, S.; Howe, R. F.; et al. In situ Synchrotron IR Micro-

DOI: 10.1021/acs.jpcc.5b07903
J. Phys. Chem. C 2015, 119, 23592−23598

spectroscopy of CO2 Adsorption on Single Crystals of the Functionalized MOF $Sc_2(BDC\text{-}NH_2)(3)$. *Angew. Chem., Int. Ed.* **2014**, *53*, 13483−13487.
(30) Yang, Q. Y.; Vaesen, S.; Ragon, F.; Wiersum, A. D.; Wu, D.; Lago, A.; Devic, T.; Martineau, C.; Taulelle, F.; Llewellyn, P. L.; et al. A Water Stable Metal-Organic Framework with Optimal Features for CO_2 Capture. *Angew. Chem., Int. Ed.* **2013**, *52*, 10316−10320.
(31) Yang, Q. Y.; Wiersum, A. D.; Llewellyn, P. L.; Guillerm, V.; Serre, C.; Maurin, G. Functionalizing Porous Zirconium Terephthalate UIO-66(Zr) for Natural Gas Upgrading: A Computational Exploration. *Chem. Commun.* **2011**, *47*, 9603−9605.

DOI: 10.1021/acs.jpcc.5b07903
J. Phys. Chem. C 2015, 119, 23592−23598

Annex C

A. Scandium family ($Sc_2(BDC)_3$, $Sc_2(BDC\text{-}NH_2)_3$, $Sc_2(BDC\text{-}NO_2)_3$)

Supporting Information

1. Crystalline Structures of Scandium terephthalate and its two functionalized crystal structures studied in this Work

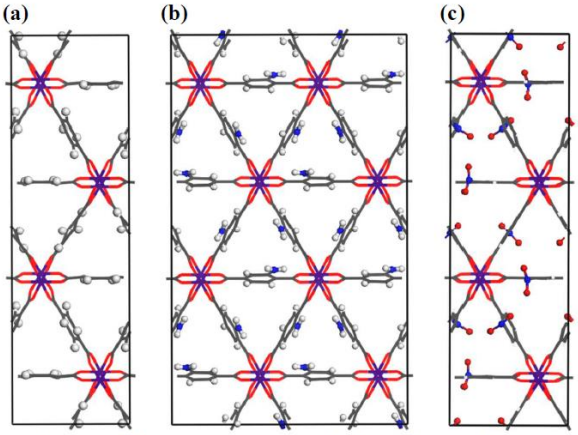

Figure S1. Experimental unit cell structures extracted from X-ray diffraction measurements[1, 2] for Sc_2BDC_3 (a), $Sc_2(BDC\text{-}NH_2)_3$ (b), and $Sc_2(BDC\text{-}NO_2)_3$ (c) viewed along the *a* vector direction, where (a) and (c) are slightly twisted for better views of its triangular channels. (Colour code: Sc, purple; C, gray; O, red; N, blue; H, white).

2. Density Functional Theory (DFT) Calculations

2.1. Optimization of Empty Scandium terephthalate and its two functionalized crystal structures

The experimentally refined Scandium terephthalate[1, 2] and its two functionalized[2] crystal structures, i.e. $Sc_2(O_2CC_6H_3XCO_2)_3$ where X= H, -NH_2, or –NO_2 (hereafter Sc_2BDC_3, BDC = 1,4-benzenedicarboxylate, $Sc_2(BDC\text{-}NH_2)_3$, BDC-NH_2 = 2-amino-1,4-benzenedicarboxylate, $Sc_2(BDC\text{-}NO_2)_3$, BDC-NO_2 = 2-nitro-1,4-benzenedicarboxylate), were saturated with the missing hydrogen atoms using Materials Studio software package, Figure S1, that is H atoms were added to the carbon atoms of the organic linker and amino groups. As consistent with the experimental assessment for the structural symmetry of these three solids, the initial symmetry of these materials were preferred as monoclinic for both Sc_2BDC_3 and $Sc_2(BDC\text{-}NO_2)_3$, and orthorhombic for $Sc_2(BDC\text{-}NH_2)_3$. All the structural optimizations were done using PBE[3] functional along with a combined Gaussian basis set and pseudopotential in Density Functional Theory (DFT) by employing the CP2K package[4-7]. In case of Carbon, Oxygen, Nitrogen and Hydrogen, a triple zeta (TZVP-MOLOPT)[8] basis set was considered, but a double zeta (DZVP-MOLOPT)[8] was applied for Scandium. The pseudopotentials used for all of the atoms were those derived by Goedecker, Teter and Hutter.[9] The van der Waals effects interactions were taken into account via the use of semi-empirical dispersion corrections as implemented in the DFT-D3 method.[10] In these simulations, the positions of atoms of the framework were relaxed. Figure S2 shows the optimized single crystal structures for Sc_2BDC_3, $Sc_2(BDC\text{-}NH_2)_3$ and $Sc_2(BDC\text{-}NO_2)_3$, and Table S1 reports the cell details used for the geometry optimization of these scandium terephthalate structures.

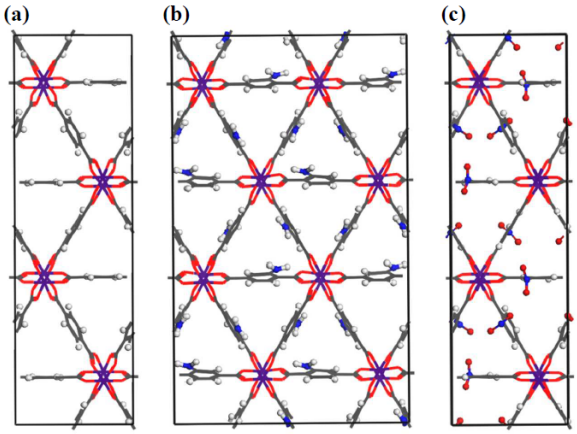

Figure S2. Single crystal structures of the Sc_2BDC_3 (a), $Sc_2(BDC\text{-}NH_2)_3$ (b), and $Sc_2(BDC\text{-}NO_2)_3$ (c) determined by density functional theory (DFT) geometry optimization based on the experimental unit cell parameters extracted from X-ray diffraction measurements[1, 2] viewed along the *a* vector direction, where (a) and (c) are slightly twisted for better views of its triangular channels. (Colour code is same as in Figure S1).

Table S1. Cell parameters used for the geometrical optimization of empty Sc_2BDC_3, $Sc_2(BDC\text{-}NH_2)_3$ and $Sc_2(BDC\text{-}NO_2)_3$.

Materials	Lattice sizes (Å)			Angles (°)			Cell Volume ($Å^3$)
	a	B	C	A	β	γ	
Sc_2BDC_3	8.754	34.385	11.145	90.000	111.479	90.000	3122.00
$Sc_2(BDC\text{-}NH_2)_3$	8.714	20.820	34.363	90.000	90.000	90.000	6234.35
$Sc_2(BDC\text{-}NO_2)_3$	8.677	34.418	11.061	90.000	110.476	90.000	3094.41

2.2. Optimization of CO_2-loaded Crystalline Structures of Sc_2BDC_3, $Sc_2(BDC\text{-}NH_2)_3$ and $Sc_2(BDC\text{-}NO_2)_3$.

The experimentally determined CO_2 saturation capacities[2, 11, 12] of 6.5, 5.5, and 3.0 mmol g^{-1} were loaded into the optimized empty Sc_2BDC_3, $Sc_2(BDC\text{-}NH_2)_3$ and $Sc_2(BDC\text{-}NO_2)_3$ structures using Monte Carlo method, respectively, further these CO_2-loaded structures were considered for geometry optimization. These simulations were performed using CP2K package[4-7] at the DFT-level keeping the same functional and basis set used for the empty structure, where (i) the positions of both the atoms of the Sc-MOFs

framework and the CO_2 molecules, and (ii) its cell parameters were fully relaxed. The optimized unit cell parameters for these structures are reported in Table S2.

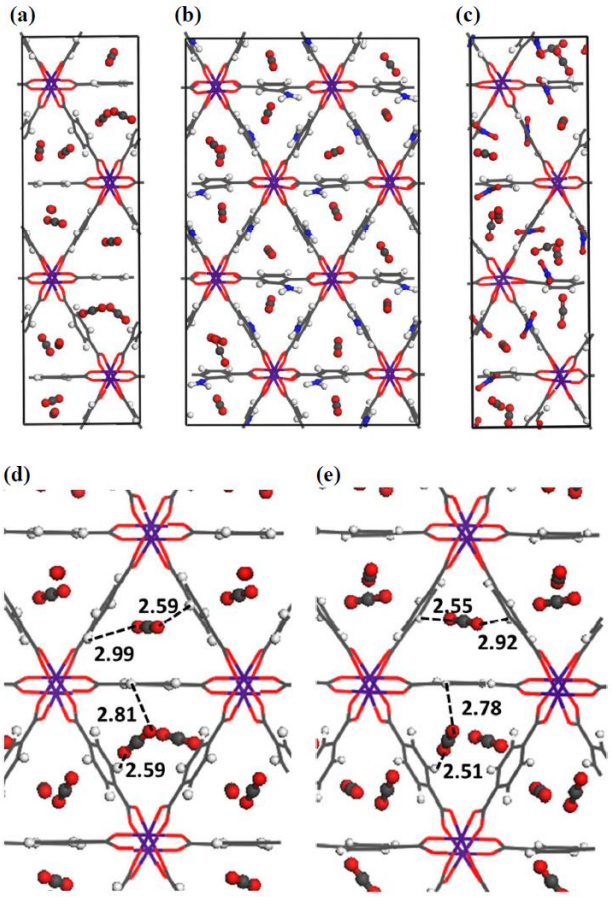

Figure S3. Unit cell Crystal structures of the CO_2 loaded Sc_2BDC_3(a), $Sc_2(BDC\text{-}NH_2)_3$ (b), $Sc_2(BDC\text{-}NO_2)_3$ (c) determined by density functional theory (DFT) geometry optimization based on the experimental unit cell parameters extracted from X-ray diffraction measurements[1, 2] viewed along the *a* vector direction, where (a) and (c) are slightly twisted for better views of triangular channels. Local views of the snapshots extracted from the DFT optimized CO_2 loaded Sc_2BDC_3 with (d) and without (e) dispersion correction. (The interacting distances are reported in Å and the colour code is same as in Figure S1).

Table S2. Unit cell parameters of CO_2 loaded Sc_2BDC_3, $Sc_2(BDC\text{-}NH_2)_3$ and $Sc_2(BDC\text{-}NO_2)_3$ obtained by DFT calculations. The data in parentheses are obtained without the dispersion correction.

Materials	Lattice sizes (Å)			Angles (°)			Cell Volume (Å^3)	Cell Volume Change (%)
	a	B	c	α	B	γ		
Sc_2BDC_3								
Simulation	8.788 (8.747)	34.506 (34.464)	11.127 (11.092)	89.949 (90.000)	111.222 (110.950)	90.051 (90.000)	3145.32 (3122.17)	0.75 (0.00)
Experimental[11]	8.747	34.464	11.092	90.000	110.950	90.000	3122.71	0.00
$Sc_2(BDC\text{-}NH_2)_3$								
Simulation	8.738	20.935	34.474	90.002	90.001	90.019	6306.63	1.16
Experimental[12]	8.720	20.815	34.420	90.000	90.000	90.000	6247.00	0.21
$Sc_2(BDC\text{-}NO_2)_3$								
Simulation	8.927	34.425	11.161	89.962	110.994	90.005	3206.25	3.61

3. Pore size distribution, pore volume, specific surface area calculations

The pore size distributions (PSD) of optimized empty Sc_2BDC_3, $Sc_2(BDC\text{-}NH_2)_3$ and $Sc_2(BDC\text{-}NO_2)_3$ were calculated by Gelb and Gubbins methodology [13], as shown in Figure S4. In these calculations the van der Waals parameter for the framework atoms were adopted from UFF forcefield.[14]

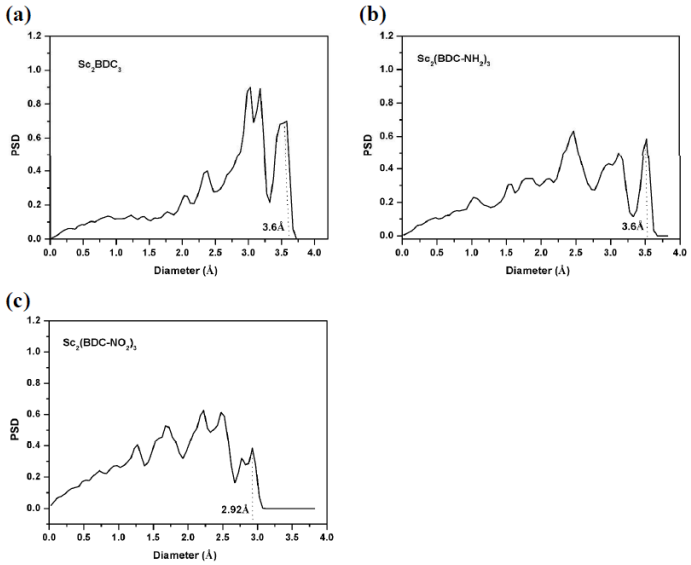

Figure S4. Pore size distributions for optimized empty structure: (a) Sc_2BDC_3, (b) $Sc_2(BDC\text{-}NH_2)_3$, and (c) $Sc_2(BDC\text{-}NO_2)_3$.

As shown by Bae et al.,[15] the general BET equation can be expressed as

$$\frac{x}{V_{excess}(1-x)} = \frac{c-1}{V_m c}x + \frac{1}{V_m c} \qquad (2)$$

In this equation, V_{excess} in unit of cm^3(STP)/g is the excess adsorbed amount of N_2 under a given equilibrium pressure P and 77 K; x is the relative pressure P/P_0, where P_0 (=1.0 atm) is the saturation vapor pressure of N_2 at 77 K; V_m is the monolayer adsorbed amount in unit of cm^3(STP)/g and c is the BET constant. With such microporous materials (see PSD in Figure S4), the BET surface areas of the Sc_2BDC_3 series were calculated with two consistency criteria suggested by Rouquerol et al.[16] and promoted by Snurr and co-workers:[15, 17] (i) within the pressure range chosen for S_{BET} calculation, $\nu_{excess}(1 - x)$ should always increase with x increasing, (ii) the straight line fitted to the BET plot must have a positive intercept to yield a meaning value for the c parameter (c>0). The so-obtained value of ν_m is used to calculate the surface area in unit of m^2/g from Equation 2,

$$S_{BET} = \frac{V_m s_0 N_a}{V_{STP}} \qquad (3)$$

where N_a is Avogadro's number, s_0 is the cross section area (16.2 Å^2) of one nitrogen molecule at the liquid state.[Error! Bookmark not defined.] V_{STP} is the molar volume of N_2 at standard temperature and pressure (273 K, 1 atm), its value being 2.24 ×10^4 cm^3(STP)/mol. The details of the analysis of BET are given in Figure S5 and S6 and the corresponding results are given in Table *S*3.

The pore volumes (V_{pore}) of the adsorbents presented in Table S3 were obtained based on the capillary condensation, which occurs within the pore structure of the material such as smaller pores are filled more quickly and large pores are filled as the pressure is increased. When the saturation point is reached the internal pores of the materials contains condensed nitrogen. Then the pore volume can be calculated by assuming that the density of condensed nitrogen is the same as that of bulk nitrogen (see equation 4).

$$V_{Pore} = \frac{V_{\max} M_{N_2}}{V_{STP} \rho_{N_2}} \qquad (4)$$

Where V_{max} (cm^3/g) is the maximum loading at P/Po = 0.9, M_{N2} and ρ_{N2} are molecular weight and density of the probe being used, which for N_2 adsorbed at 77 K have values of 28.01 g/mol and 0.807 g/cm^3, respectively. V_{STP} is the molar volume of N_2 at standard temperature and pressure (273 K, 1 atm), its value being 2.24 ×10^4 cm^3(STP)/mol.

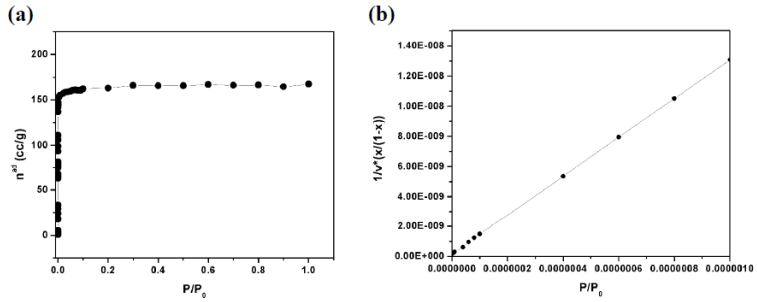

Figure S5. BET surface area calculation for Sc_2BDC_3 using the simulated isotherm of N_2 at 77 K. (a) plot of V_{excess} (1 - P/P_0) vs P/P_0 for the determination using the first consistency criterion, (b) the selected linear plot that satisfies the second consistency criterion and the corresponding BET surface area from the linear fit.

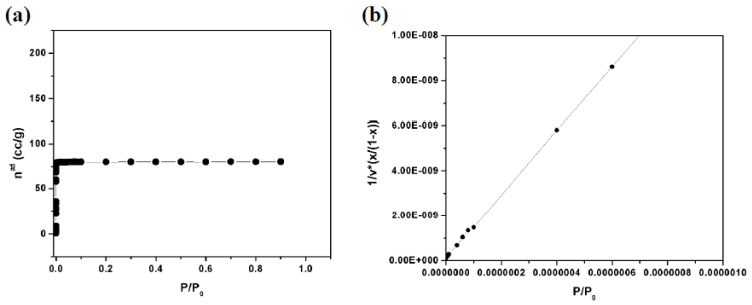

Figure S6. BET surface area calculation for $Sc_2(BDC\text{-}NH_2)_3$ using the simulated isotherm of N_2 at 77 K. (a) plot of V_{excess} (1 - P/P_0) vs P/P_0 for the determination using the first consistency criterion, (b) the selected linear plot that satisfies the second consistency criterion and the corresponding BET surface area from the linear fit.

Table S3. Properties of the Scandium Terephthalate and its functionalized solids (Pore diameter: $\mathbf{d_{pore}}$, Surface areas: $\mathbf{S_{BET}}$, pore volume: $\mathbf{V_{pore}}$)

Materials	d_{pore} (Å)	S_{BET} ($m^2\ g^{-1}$)	V_{pore} ($cm^3.g^{-1}$)
Sc_2BDC_3			
Simulation	3.60	596	0.251
Experimental[11]		558	0.215
$Sc_2(BDC\text{-}NH_2)_3$			
Simulation	3.57	340	0.124
Experimental[12]		315	0.128
$Sc_2(BDC\text{-}NO_2)_3$			
Simulation	2.92	0	0
Experimental[2]		0	0

4. Microscopic models for the host framework.

Due to the large quadruple moment of CO_2 molecule, many studies have demonstrated that it is very important to take the CO_2-MOF electrostatic interactions into account, especially for the functionalized MOF materials with polar groups.[18, 19] The partial charges used for atoms in all structural models used for single component and multi-component adsorption are reported in Table S4-S6, for that a single point energy calculations were performed for the optimized Sc_2BDC_3, $Sc_2(BDC\text{-}NH_2)_3$ and $Sc_2(BDC\text{-}NO_2)_3$, structure at the Density Functional Theory level using Dmol[3] to extract the partial charges using a Mulliken partitioning method[20] for each atom of the all the structures (see Tables S4-S6, Figure S7-S9). These calculations were also based on the PBE generalized gradient approximation (GGA) functional and the double numerical basis set containing polarization functions (DNP).[21]

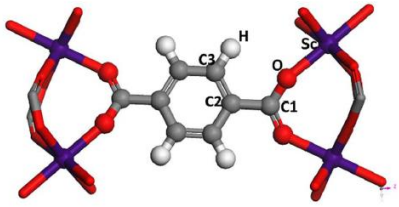

Figure S7. Labels of the atoms for the organic and the inorganic parts of the Sc_2BDC_3. Colour code is same as in Figure S1.

Table S4. **Atomic partial charges for the Sc_2BDC_3 structure derived on DFT/PBE Level.**

Atomic types	C1	C2	C3	H	O	Sc
Charge (e)	0.5998	-0.0773	-0.0513	0.1168	-0.5821	1.5321

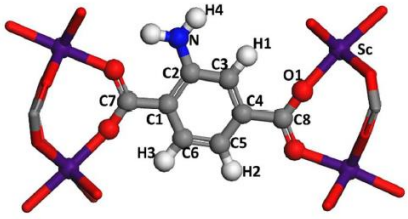

Figure S8. Labels of the atoms for the organic and the inorganic parts of the $Sc_2(BDC\text{-}NH_2)_3$. Colour code is same as in Figure S1.

Table S5. **Atomic partial charges for the $Sc_2(BDC\text{-}NH_2)_3$ structure derived on DFT/PBE Level.**

Atomic types	C1	C2	C3	C4	C5	C6	C7	C8
Charge (e)	-0.1159	0.1517	-0.0525	-0.0898	-0.0589	-0.0223	0.5245	0.5176
Atomic types	H1	H2	H3	H4	N	O1	Sc	
Charge (e)	0.1171	0.0735	0.0907	0.195	-0.2491	-0.5929	1.6425	

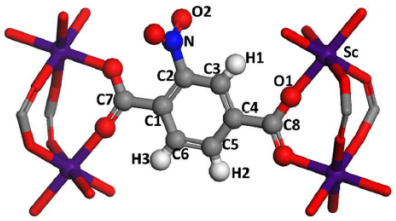

Figure S9. Labels of the atoms for the organic and the inorganic parts of the $Sc_2(BDC\text{-}NO_2)_3$. Colour code is same as in Figure S1.

Table S6. **Atomic partial charges for the $Sc_2(BDC\text{-}NO_2)_3$ structure derived on DFT/PBE Level.**

Atomic types	C1	C2	C3	C4	C5	C6	C7	C8
Charge (e)	-0.0412	0.0985	-0.0102	-0.0532	-0.0781	-0.0215	0.5371	0.5385
Atomic types	H1	H2	H3	N	O1	O2	Sc	
Charge (e)	0.1377	0.1548	0.1398	0.3228	-0.5685	-0.2747	1.6476	

5. Interatomic Potentials

The interaction between the MOF framework and the guest species (CO_2, CH_4 and N_2) was derived from the intermolecular potential U_{ab} which is a sum of dispersive terms and coulombic interactions.

$$U_{ab} = \underbrace{4\varepsilon_{ab}\left[\left(\frac{\sigma_{ab}}{r_{ab}}\right)^{12} - \left(\frac{\sigma_{ab}}{r_{ab}}\right)^{6}\right]}_{\text{Lennard-Jones term}} + \underbrace{\sum_{a<b}{}_{a,b} \frac{1}{4\pi\varepsilon_0}\frac{q_a q_b}{r_{ab}}}_{\text{Electrostatic term}} \quad (1)$$

Here, $r_{ab} = |r_b - r_a|$ accounts for the distance between centers a and b, ε_{ab} and σ_{ab} are the Lennard-Jones (LJ) parameters between such sites and q_a is the electrostatic partial charge of center a (being ε_0 the permittivity of the vacuum in SI units).

Short-range dispersion forces were described by Lennard-Jones (LJ) potentials truncated at a cutoff radius of 12 Å. Interactions between unlike force field centers a and b were treated by means of the Lorentz-Berthelot (LB) combination rules; $\varepsilon_{ab} = \sqrt{\varepsilon_a \varepsilon_b}$, $\sigma_{ab} = (\sigma_a + \sigma_b)/2$, where ε_a and σ_a are the LJ parameters for the species a. The Universal force field (UFF) has been adopted to describe LJ interactions between the atoms in the framework (see Figure S7 – S9 and Table S7). In this work, a single LJ interaction site model was used to describe a CH_4 molecule with potential parameters taken from the TraPPE forcefield[22] (Table S8). For adsorbate molecules, CO_2 has been modeled as a rigid molecule through the EPM2 intermolecular potential,[23] and N_2 molecule was represented by a three-site charged model with two LJ sites located at the N atoms while a third site present at its center of mass (COM) only involves electrostatic interactions as previously described in the TraPPE potential model[22] (Table S8).

Table S7. LJ potential parameters for the atoms of the Scandium Terephthalate series.

Atomic type	UFF	
	σ (Å)	ε /k_B (K)
C	3.431	52.841
H	2.571	22.143
N	3.261	34.724
O	3.118	30.195
Sc	3.295	9.561

[a] The attractive van der Waals force exerted by the hydrogen atoms in amino groups is not considered following the same criteria explained in a previous study.[24, 25]

Table S8. Potential parameters and partial charges for the adsorbates

Atomic type	σ **(Å)**	ε/k_B **(K)**	q **(*e*)**
CH_4	3.730	148.000	0.0000
N2_N	3.310	36. 000	-0.4820
N2_COM	0.00	0.00	0.9640
CO2_C	2.757	28.129	0.6512
CO2_O	3.033	80.507	-0.3256

6. GCMC Simulations

Grand Canonical Monte Carlo (GCMC) simulations were carried out at 273 and 303 K to predict the single component adsorption of gases, CO_2, CH_4 and N_2, and co-adsorption of CO_2/N_2 and CO_2/CH_4 at 303K by employing the Complex Adsorption and Diffusion Simulation Suite (CADSS) code.[26] The structural models representing each adsorbate and the MOF framework, the set of the Lennard-Jones (LJ) potential parameters used for both the MOF and the adsorbates, and the DFT calculations used to find the partial charges centred on each atom of the MOF framework. The simulation boxes were made of 64 (8×2×4) unit cells for both Sc_2BDC_3 and $Sc_2(BDC\text{-}NO_2)_3$ structures and 48 (8×3×2) unit cells for $Sc_2(BDC\text{-}NH_2)_3$ structure previously DFT optimized in CO_2 loaded states. Short-range dispersion forces described by LJ potentials were truncated at a cut-off radius of 12 Å while the long-range electrostatic interactions were handled using the Ewald summation technique. The fugacities for each adsorbed species at a given thermodynamic condition were computed with the Peng-Robinson equation of state (EoS).[27] For each state point, 5×10^7 Monte Carlo steps have been used for both equilibration and production runs. Three types of trials were considered for the molecules: (i) translation or rotation, (ii) creation/deletion and (iii) exchange of molecular identity. The adsorption enthalpy at low coverage (Δh) for each gas was calculated through configurational-bias Monte Carlo simulations performed in the NVT ensemble using the revised Widom's test particle insertion method.[28] In order to gain insight into the configurational distribution of the adsorbed species in Scandium Terephthalate series, some additional data were calculated at different pressures including the radial distribution functions between the guests and the host.

7. Comparison of the single component isotherms

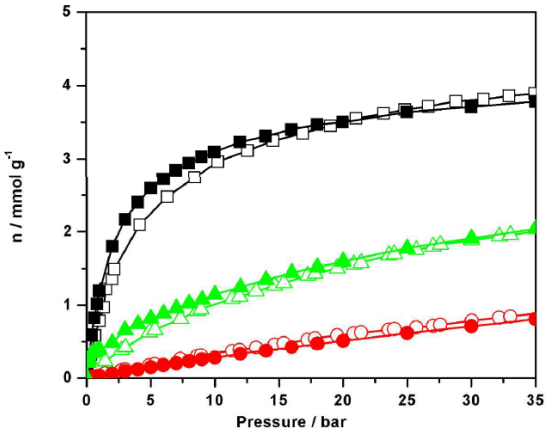

Figure S10. Comparison of the pure component simulated isotherms (full symbols) for CO_2 (squares), N_2 (circles) and CH_4 (triangles) with the experimental data[11] (empty symbols) in Sc_2BDC_3 at and 304 K.

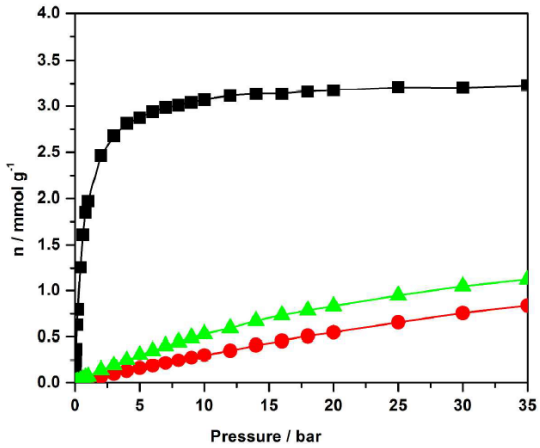

Figure S11. Simulated single component adsorption isotherm for CO_2 (squares), N_2 (circles) and CH_4 (triangles) in $Sc_2(BDC\text{-}NH_2)_3$ at 303 K.

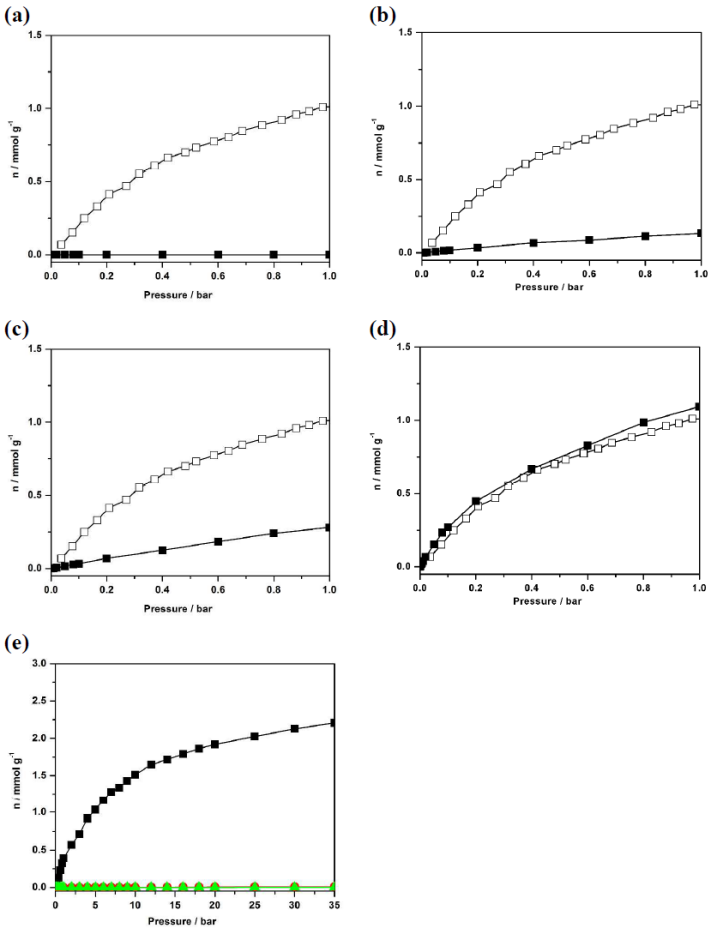

Figure S12. Comparison of the single component simulated isotherms (full symbols) for CO_2 (squares) with the experimental data[2] (empty symbols) in the nitro-functionalized Scandium Terephthalate with re-aligned orientation of $-NO_2$ group by rotating in its terephthalate linker with an angle of α=0° (a), α=30° (b), α=60° (c) and α=90° (d) at 273 K. Simulated single component adsorption isotherm for CO_2 (squares), N_2 (circles) and CH_4 (triangles) in $Sc_2(BDC\text{-}NO_2)_3$ at 303 K (e).

8. Comparison of the Enthalpy of adsorption

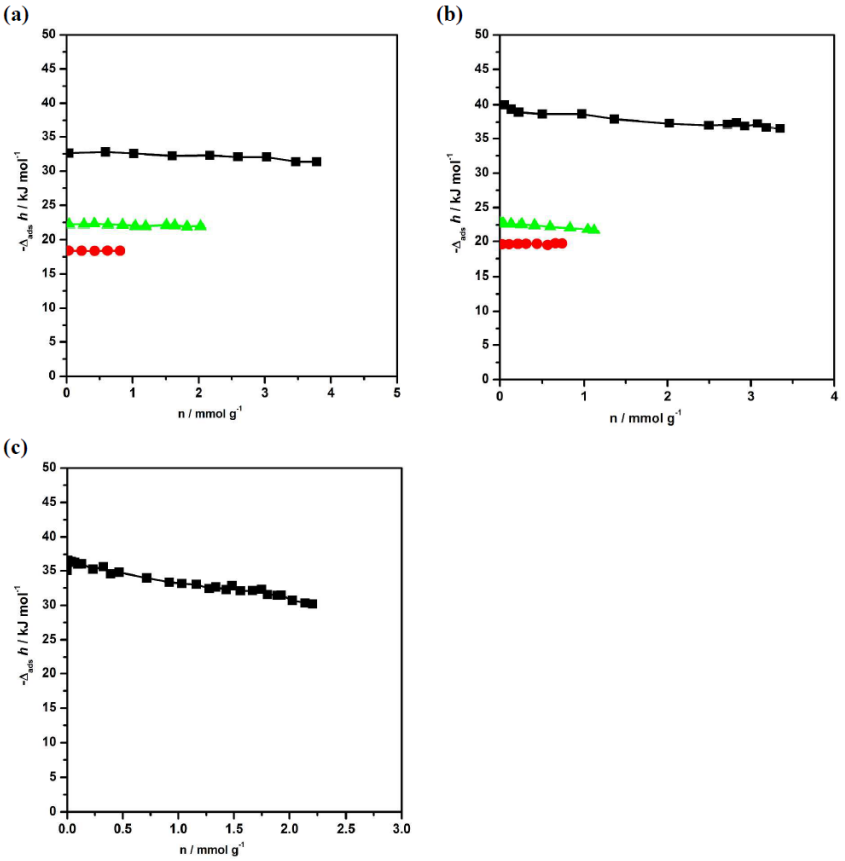

Figure S13. Enthalpy of adsorption for CO_2 (squares), N_2 (circles) and CH_4 (triangles) in optimized structure of Sc_2BDC_3 (a), $Sc_2(BDC\text{-}NH_2)_3$ (b), $Sc_2(BDC\text{-}NO_2)_3$ (c) at 303 K.

Table S9: Differences in enthalpy values at zero coverage for various MOFs and zeolites.

Material	$\lvert\Delta_{ads}\dot{h}_{\theta=0}(CO_2) - \Delta_{ads}\dot{h}_{\theta=0}(CH_4)\rvert$ / **kJ mol^{-1}**	$\lvert\Delta_{ads}\dot{h}_{\theta=0}(CO_2) - \Delta_{ads}\dot{h}_{\theta=0}(N_2)\rvert$ / **kJ mol^{-1}**
Sc_2BDC_3	9.6	13.5
$Sc_2(BDC\text{-}NH_2)_3$	17.4	20.5
$Sc_2(BDC\text{-}NO_2)_3$	-	-
NaY	15.0	14.7
KCHA	-	19.2
NaCHA	21.9	23.5
LiCHA	-	29.0
CHA	22.7	23.4
Linde 4A	10.1	18.5
H+MOR	5.8	7.1
CPO-27(Ni)	20.0	22.5
HKUST-1	8.3	13.7
UiO-66	8.5	12.6
MIL47	10.0	11.0
STA-12	19.0	19.0
MIL-91(Al)	15.0	19.0

9. Radial Distribution Functions calculated in the Scandium Terephthalate series

9.1. CO_2, N_2, and CH_4 gases in the Sc_2BDC_3

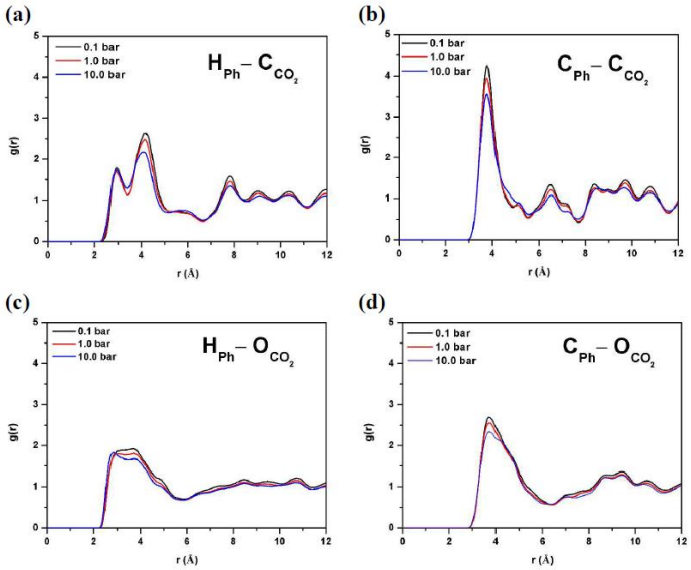

Figure S14. Radial distribution functions of the CO_2 molecules around the Phenyl hydrogen (H_{ph}) and Phenyl carbon (Cph) atoms of the Terephthalate groups in the Sc_2BDC_3 at three pressures: (a, b) and (c, d) for the C and O atom in the CO_2 molecule, respectively.

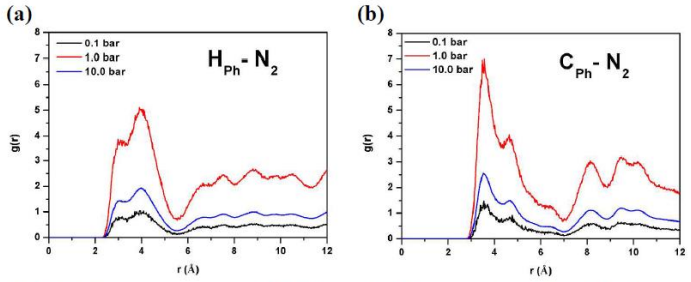

Figure S15. Radial distribution functions of the N_2 molecules around the Phenyl hydrogen, H_{Ph}, (a) and Phenyl carbon, C_{Ph}, (b) atoms of the Terephthalate groups in the Sc_2BDC_3 at three pressures.

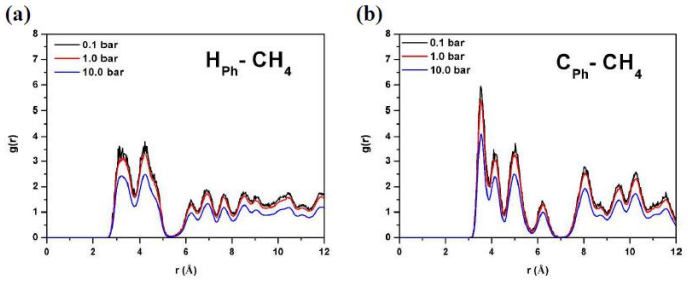

Figure S16. Radial distribution functions of the CH_4 molecules around the Phenyl hydrogen, H_{ph}, (a) and Phenyl carbon, C_{ph}, (b) atoms of the Terephthalate groups in the Sc_2BDC_3 at three pressures.

9.2. CO_2, N_2 and CH_4 gases in the $Sc_2(BDC\text{-}NH_2)_3$

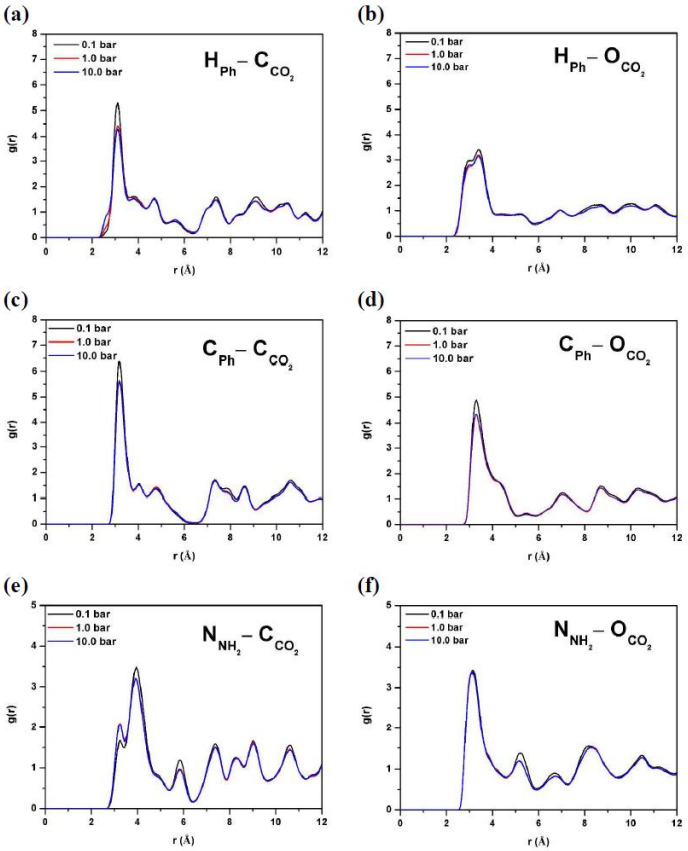

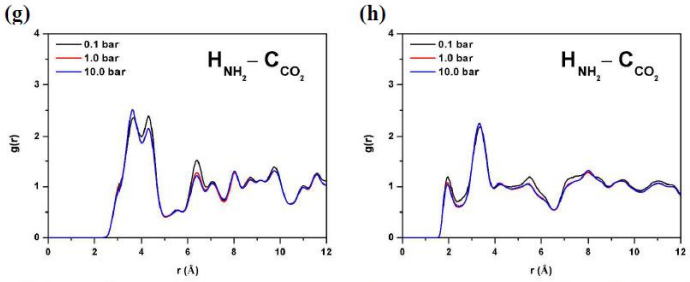

Figure S17. Radial distribution functions of the CO_2 molecules around the Phenyl hydrogen (H_{ph}), Phenyl carbon (Cph), Amino nitrogen (N_{NH2}), and Amino hydrogen (H_{NH2}) atoms of the Terephthalate groups in the functionalized material $Sc_2(BDC\text{-}NH_2)_3$ at three pressures: (a, c, e, g) and (b, d, f, i) for the C and O atom in the CO_2 molecule, respectively.

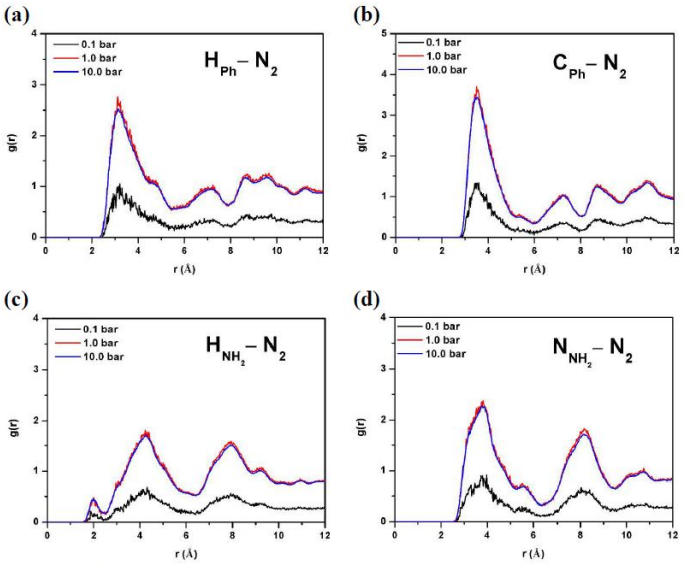

Figure S18. Radial distribution functions of the N_2 molecules around the Phenyl hydrogen (H_{ph}), (a) Phenyl carbon , Cph, (b), Amino hydrogen, H_{NH2}, (c) and Amino nitrogen, N_{NH2}, (d) atoms of the Terephthalate groups in the functionalized material $Sc_2(BDC\text{-}NH_2)_3$ at three pressures.

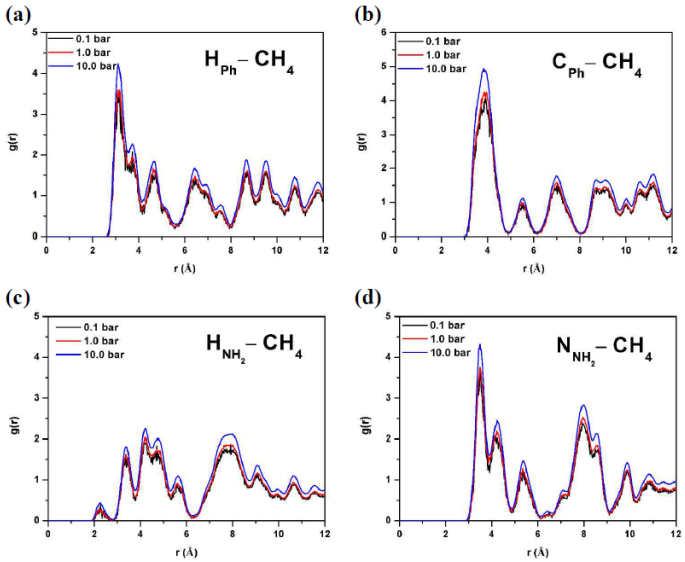

Figure S19. Radial distribution functions of the CH_4 molecules around the Phenyl hydrogen, H_{ph}, (a) Phenyl carbon (Cph), (b), Amino hydrogen, H_{NH2}, (c), and Amino nitrogen, N_{NH2}, (d) atoms of the Terephthalate groups in the functionalized material $Sc_2(BDC\text{-}NH_2)_3$ at three pressures.

9.3. CO_2 gases in the $Sc_2(BDC\text{-}NO_2)_3$

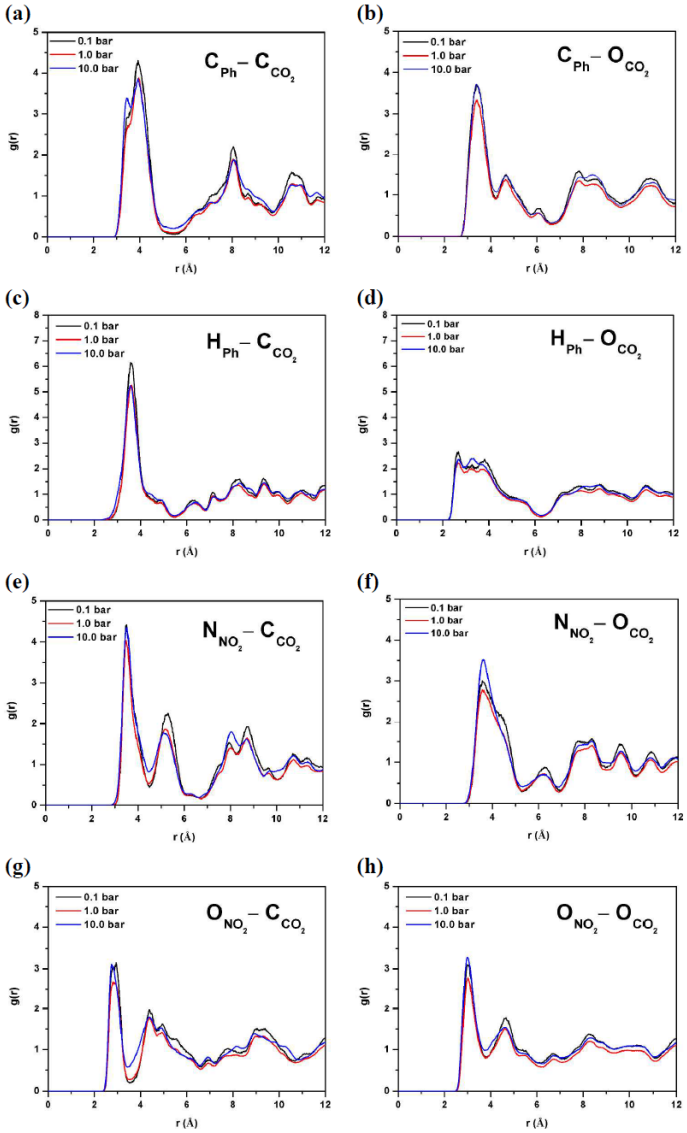

Figure S20. Radial distribution functions of the CO_2 molecules around the Phenyl hydrogen (H_{ph}), Phenyl carbon (Cph), Nitro nitrogen (N_{NO2}), and Nitro oxygen (H_{NO2}) atoms of the Terephthalate groups in the functionalized material $Sc_2(BDC\text{-}NO_2)_3$ at three pressures: (a, c, e, g) and (b, d, f, i) for the C and O atom in the CO_2 molecule, respectively.

10. Separation of CO_2/N_2 and CO_2/CH_4 mixtures

In separation processes, a good indication of the separation ability consists of estimating the selectivity of a porous material. The selectivity (S) for CO_2 over N_2 and CH_4 is defined by the following expression: $S(CO_2/N_2) = (x_{CO_2} / x_{N_2})(y_{N_2} / y_{CO_2})$, and $S(CO_2/CH_4) = (x_{CO_2} / x_{CH_4})(y_{CH_4} / y_{CO_2})$, where x_{CO_2}, x_{N_2} and x_{CH_4} are the mole fractions of CO_2, N_2, and CH_4 in the adsorbed phase, respectively, while y_{CO_2}, y_{N_2} and y_{CH_4} are the mole fractions of CO_2, N_2 and CH_4 in the bulk phase, respectively. The calculated selectivities for both CO_2/N_2 (molar ratio =15/85) and CO_2/CH_4 (molar ratio = 50/50) mixture in Sc_2BDC_3, $Sc_2(BDC\text{-}NH_2)_3$ and $Sc_2(BDC\text{-}NO_2)$ are shown in Figure S21, S22 and S23, respectively as a function of the bulk pressure. Furthermore, the simulated co-adsorption isotherms for gases in CO_2/N_2 and CO_2/CH_4 from their 15/85 and 50/50 molar ratio gas mixture in Sc_2BDC_3, $Sc_2(BDC\text{-}NH_2)_3$ and $Sc_2(BDC\text{-}NO_2)$ are shown in Figure S24 and S25 respectively. In addition, Adsorbent Performance Indicators (API) for CO_2/N_2 and CO_2/CH_4 system in all Sc-MOFs were calculated and then compared with other porous solids as shown in Figure 6 of the manuscript, this API integrates the CO_2 working capacity, the selectivity and the differences in adsorption enthalpies between CO_2 and either CH_4 or N_2.[22]

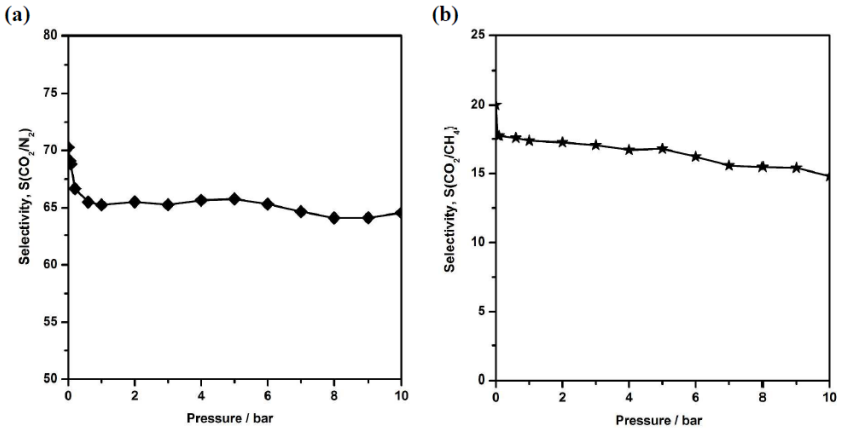

Figure S21. Simulated selectivities for CO_2/N_2 (a) and CO_2/CH_4 (b) from their 15/85 and 50/50 molar ratio gas mixture, respectively, in $Sc_2(BDC)_3$ as a function of the bulk pressure at 303 K.

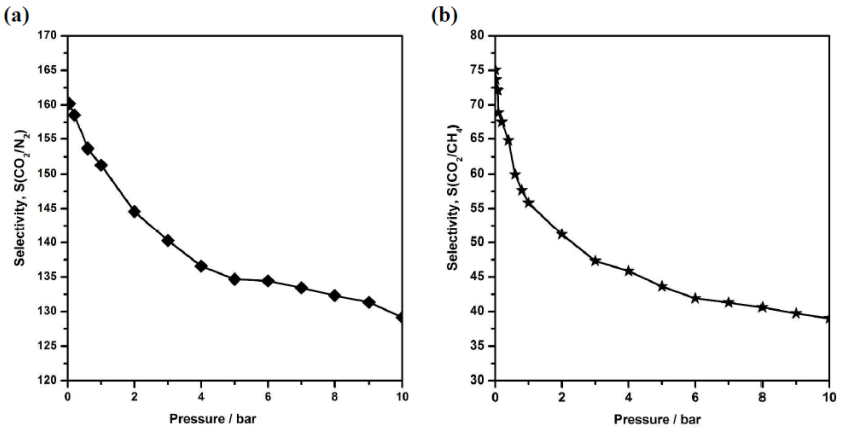

Figure S22. Simulated selectivities for CO_2/N_2 (a) and CO_2/CH_4 (b) from their 15/85 and 50/50 molar ratio gas mixture, respectively, in $Sc_2(BDC\text{-}NH_2)_3$ as a function of the bulk pressure at 303 K.

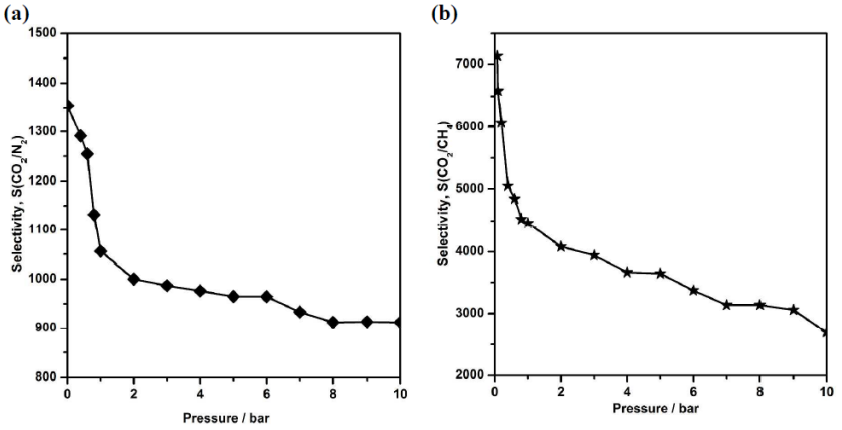

Figure S23. Simulated selectivities for CO_2/N_2 (a) and CO_2/CH_4 (b) from their 15/85 and 50/50 molar ratio gas mixture, respectively, in $Sc_2(BDC\text{-}NO_2)_3$ as a function of the bulk pressure at 303 K.

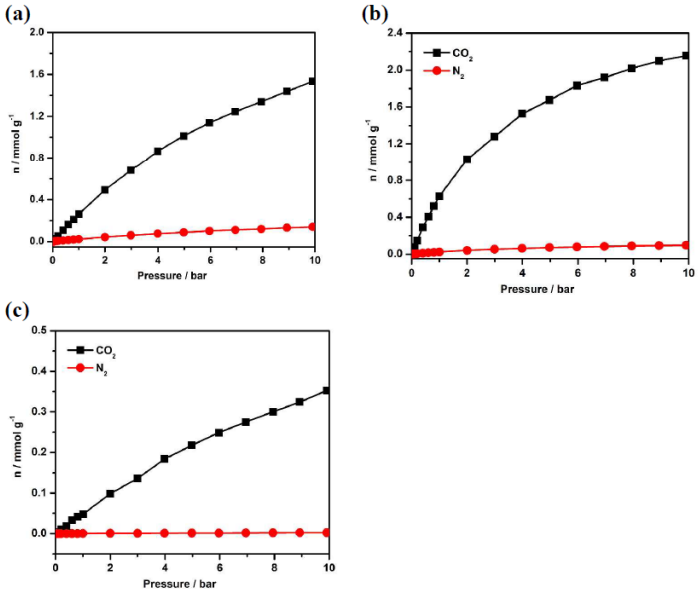

Figure S24. Simulated co-adsorption isotherm for CO_2 (squares) and N_2 (circles) from their 15/85 molar ratio of binary gas mixture in Sc_2BDC_3 (a), $Sc_2(BDC\text{-}NH_2)_3$ (b), and $Sc_2(BDC\text{-}NO_2)_3$ (c) as a function of the bulk pressure at 303 K.

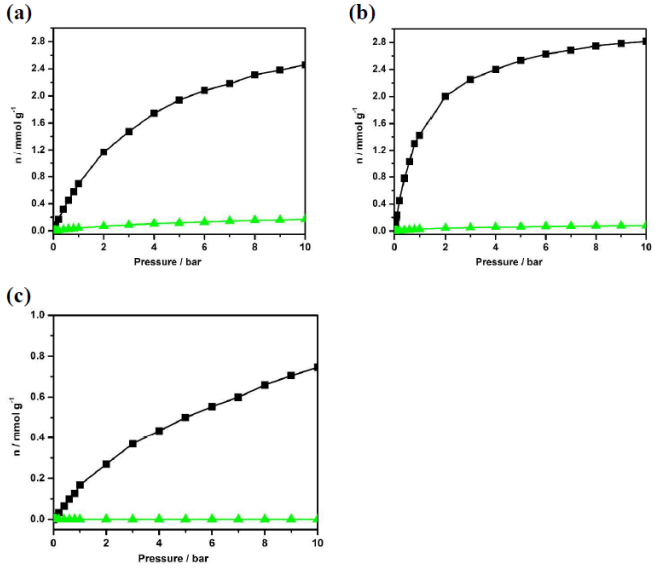

Figure S25. Simulated co-adsorption isotherm for CO_2 (squares) and CH_4 (triangles) from their 50/50 molar ratio of binary gas mixtures in Sc_2BDC_3 (a), $Sc_2(BDC\text{-}NH_2)_3$ (b), and $Sc_2(BDC\text{-}NO_2)_3$ (c) as a function of the bulk pressure at 303 K.

11. Regeneration of $Sc_2(BDC\text{-}NO_2)_3$

In order to assess the regeneration of $Sc_2(BDC\text{-}NO_2)_3$ with respect to CO_2, manometric gas adsorption measurements were carried out by using high-throughpout adsorption apparatus developed in house [29] The equation of state used to take into account gas non-ideality was obtained from the Reference Fluid Thermodynamic and Transport Properties (REFPROP) software package 8.0 of the National Institute of Standards and Technology (NIST). The regeneration of $Sc_2(BDC\text{-}NO_2)_3$ was assessed via several adsorption cycles of carbon dioxide with a simple primary vacuum at 30°C between each cycle. About 100 mg of $Sc_2(BDC\text{-}NO_2)_3$ was outgassed at 200 °C under primary vacuum for 16 hours. At this temperature, the weight loss was estimated about 1.3 percent. The CO_2 adsorption cycles were explored up to 20 bar. Between two carbon dioxide adsorption cycles, a primary vacuum stage was performed for 1 hour and 3 cycles were carried out. It is important to note that during the measurement, the temperatures of both the cage and the device containing $Sc_2(BDC\text{-}NO_2)_3$ were controlled at 303 K.

11. Materials synthesis, characterization and water stability testing.

Synthesis

The synthesis of the MOF, $Sc_2(BDC\text{-}NO_2)_3$, has undergone development from the original hydrothermal method [2](190 °C, 3 days, $Sc(NO_3)_3.H_2O$ metal source). This study employed microwave assisted heating of the reaction mixture in a sealed glass vessel within a CEM Discover SP microwave. $Sc_2(BDC\text{-}NO_2)_3$ was synthesized from the microwave heating (190 °C, 2 minutes, 300 W, high stirring) of a pre-stirred (10 minutes) mixture of 1.5 M scandium chloride solution (1.92 mL, 2.88 mmol) and 2-nitroterephthalic acid (0.88 g, 4.18 mmol) in water (25 mL). Post-heating, the sample was placed in an ice bath (20 minutes) and cold water (10 mL) was added to the solution. The white powder (0.39 g, 39 % yield with respect to the organic ligand) was filtered under gravity, washed with distilled water (3 x 20 mL) and dried in air (room temperature) overnight.

Characterisation

Laboratory Powder X-ray diffraction (PXRD) patterns were obtained from a Stoe STAD i/P diffractometer in capillary mode (transmission) with primary monochromation (Cu $K_{\alpha 1}$, λ = 1.54051 Å) at room temperature. Prior to analysis, samples were ground to a fine powder and introduced to a 0.7 mm glass capillary. Phase identification of samples was accomplished by direct comparison of the observed patterns with those from literature. [2]

Water stability test

For moisture sensitivity testing the white MOF material (0.17 g) was placed in an alumina crucible within a tube furnace (60 °C) and a wet nitrogen gas stream (20 °C), water vapour pressure 2310 Pa [2.3%]) was passed over the sample (18 hours). PXRD data comparison (Figure S26) of before and after water stability testing indicated that no structural degradation of the MOF had occurred.

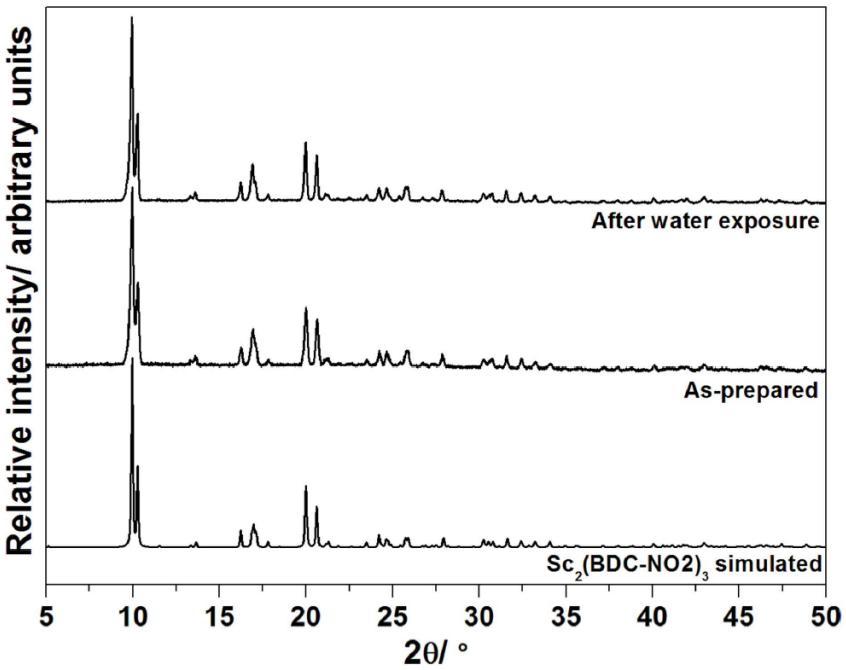

Figure S26. Offset PXRD data (room temperature) of as-prepared $Sc_2(BDC\text{-}NO_2)_3$ and after heating (18 hours, 60 °C) with exposure to a wet N_2 gas flow.

12. Adsorption calorimetry of CO_2 on $Sc_2(BDC\text{-}NO_2)_3$

Around 0.2 g of sample was used for adsorption experiments. Prior to each experiment, samples were outgassed ex situ at 423 K for 16 h under a secondary vacuum of 10^{-3} mbar.

The microcalorimetry experiments were performed using a home built manometric adsorption apparatus coupled with a Tian–Calvet type microcalorimeter.[30] This experimental device allows the simultaneous determination of the adsorption isotherm and the adsorption enthalpy using a point by point introduction of gas to the sample. A multi-pneumovalve system allows the introduction of the adsorbate to the sample. An exothermic thermal effect accompanied each introduction which is due to both the adsorption process and gas compression. This peak in the energy curve with time is thus integrated in order to calculate a pseudo-differential enthalpy of adsorption for each dose. Errors in this calculation can be estimated at ± 1 kJ mol^{-1}. Experiments were carried out at 303 K and up to 5 bars with CO_2 of a purity of above 99.998%. The enthalpies of adsorption, as a function of coverage are shown in Figure S27. They show an average enthalpy of -34 kJ mol^{-1}, in agreement with that calculated by molecular simulation.

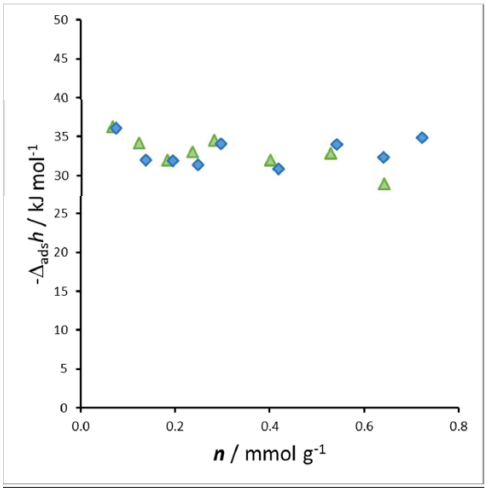

Figure S27. Adsorption enthalpies of CO_2 on $Sc_2(BDC\text{-}NO_2)_3$ obtained by microcalorimetry at 303 K

References:

1. Miller, S. R.; Wright, P. A.; Serre, C.; Loiseau, T.; Marrot, J.; Férey, G., A Microporous Scandium Terephthalate, $Sc_2(O_2CC_6H_4CO_2)_3$, with High Thermal Stability. *Chem. Commun.* **2005**, 3850-3852.
2. Mowat, J. P.; Miller, S. R.; Griffin, J. M.; Seymour, V. R.; Ashbrook, S. E.; Thompson, S. P.; Fairen-Jimenez, D.; Banu, A. M.; Düren, T.; Wright, P. A., Structural Chemistry, Monoclinic-to-Orthorhombic Phase Transition, and CO2 Adsorption Behavior of the Small Pore Scandium Terephthalate, $Sc_2(O_2CC_6H_4)CO_2)_3$, and its Nitro- and Amino-Functionalized Derivatives. *Inorg. Chem.* **2011,** *50,* 10844-10858.
3. Perdew, J. P., Density-Functional Approximation for the Correlation-Energy of the Inhomogeneous Electron-Gas. *Phys.Rev.B* **1986,** *33,* 8822-8824.
4. VandeVondele, J.; Krack, M.; Mohamed, F.; Parrinello, M.; Chassaing, T.; Hutter, J., QUICKSTEP: Fast and Accurate Density Functional Calculations Using a Mixed Gaussian and Plane Waves Approach. *Comput. Phys. Commun.* **2005,** *167,* 103-128.
5. VandeVondele, J.; Hutter, J., An Efficient Orbital Transformation Method for Electronic Structure Calculations. *J. Chem. Phys.* **2003,** *118,* 4365-4369.
6. Lippert, G.; Hutter, J.; Parrinello, M., The Gaussian and Augmented-Plane-Wave Density Functional Method for Ab Initio Molecular Dynamics Simulations. *Theor. Chem. Acc.* **1999,** *103,* 124-140.
7. Lippert, B. G.; Parrinello, J. H.; Michele, A Hybrid Gaussian and Plane Wave Density Functional Scheme. *Mol. Phys.* **1997,** *92,* 477-488.
8. VandeVondele, J.; Hutter, J., Gaussian Basis Sets for Accurate Calculations on Molecular Systems in Gas and Condensed Phases. *J. Chem. Phys.* **2007,** *127,* 114105.
9. Goedecker, S.; Teter, M.; Hutter, J., Separable Dual-Space Gaussian Pseudopotentials. *Phys.Rev. B* **1996,** *54,* 1703-1710.
10. Grimme, S.; Antony, J.; Ehrlich, S.; Krieg, H., A Consistent and Accurate Ab Initio Parametrization of Density Functional Dispersion Correction (DFT-D) for the 94 Elements H-Pu. *J. Chem. Phys.* **2010,** *132,* 154104.
11. Miller, S. R.; Wright, P. A.; Devic, T.; Serre, C.; Férey, G.; Llewellyn, P. L.; Denoyel, R.; Gaberova, L.; Filinchuk, Y., Single Crystal X-Ray Diffraction Studies of Carbon Dioxide and Fuel-Related Gases Adsorbed on the Small Pore Scandium Terephthalate Metal Organic Framework, $Sc_2(O_2CC_6H_4CO_2)_3$. *Langmuir* **2009,** *25,* 3618-3626.
12. Greenaway, A.; Gonzalez-Santiago, B.; Donaldson, P. M.; Frogley, M. D.; Cinque, G.; Sotelo, J.; Moggach, S.; Shiko, E.; Brandani, S.; Howe, R. F.; et al., In Situ Synchrotron IR Microspectroscopy of CO_2 Adsorption on Single Crystals of the Functionalized MOF Sc2(BDC-NH2)3. *Angew. Chem. Int. Ed.* **2014,** *53,* 13483-13487.
13. Gelb, L. D.; Gubbins, K. E., Pore Size Distributions in Porous Glasses: A Computer Simulation Study. *Langmuir* **1998,** *15,* 305-308.

14. Rappe, A. K.; Casewit, C. J.; Colwell, K. S.; Goddard, W. A.; Skiff, W. M., UFF, a Full Periodic-Table Force-Field for Molecular Mechanics and Molecular-Dynamics Simulations. *J. Am. Chem. Soc.* **1992,** *114,* 10024-10035.

15. Bae, Y. S.; Yazaydin, A. O.; Snurr, R. Q., Evaluation of the BET Method for Determining Surface Areas of MOFs and Zeolites that Contain Ultra-Micropores. *Langmuir* **2010,** *26,* 5475-5483.

16. Rouquerol, F.; Rouquerol, J.; Sing, K., *Adsorption by Powders and Porous Solids: Principles, Methodology and Applications*. Academic Press: 1999.

17. Duren, T.; Millange, F.; Ferey, G.; Walton, K. S.; Snurr, R. Q., Calculating Geometric Surface Areas As a Characterization Tool for Metal-Organic Frameworks. *J. Phys. Chem. C* **2007,** *111,* 15350-15356.

18. Bae, Y. S.; Mulfort, K. L.; Frost, H.; Ryan, P.; Punnathanam, S.; Broadbelt, L. J.; Hupp, J. T.; Snurr, R. Q., Separation of CO_2 from CH_4 Using Mixed-Ligand Metal-Organic Frameworks. *Langmuir* **2008,** *24,* 8592-8598.

19. Yang, Q. Y.; Zhong, C. L., Electrostatic-field-induced enhancement of gas mixture separation in metal-organic frameworks: A computational study. *Chem. Phys. Chem.* **2006,** 7, 1417-1421.

20. Mulliken, R. S., Electronic Population Analysis on Lcao-Mo Molecular Wave Functions .1. *J. Chem. Phys.* **1955,** *23,* 1833-1840.

21. Hehre, W. J.; Ditchfie.R; Pople, J. A., Self-Consistent Molecular-Orbital Methods .12. Further Extensions of Gaussian-Type Basis Sets for Use in Molecular-Orbital Studies of Organic-Molecules. *J. Chem. Phys.* **1972,** *56,* 2257.

22. Martin, M. G.; Siepmann, J. I., Transferable Potentials for Phase Equilibria. 1. United-Atom Description of n-Alkanes. *J. Phys. Chem. B* **1998,** *102,* 2569-2577.

23. Harris, J. G.; Yung, K., Carbon Dioxide's Liquid-Vapor Coexistence Curve And Critical Properties as Predicted by a Simple Molecular Model. *J. Phys. Chem.* **1995,** *99,* 12021-12024.

24. Yang, Q. Y.; Vaesen, S.; Vishnuvarthan, M.; Ragon, F.; Serre, C.; Vimont, A.; Daturi, M.; De Weireld, G.; Maurin, G., Probing the Adsorption Performance of the Hybrid Porous MIL-68(Al): A Synergic Combination of Experimental and Modelling Tools. *J. Mater. Chem.* **2012,** *22,* 10210-10220.

25. Llewellyn, P. L.; Garcia-Rates, M.; Gaberova, L.; Miller, S. R.; Devic, T.; Lavalley, J. C.; Bourrelly, S.; Bloch, E.; Filinchuk, Y.; Wright, P. A.; et al., Structural Origin of Unusual CO_2 Adsorption Behavior of a Small-Pore Aluminum Bisphosphonate MOF. *J. Phys. Chem. C* **2015,** *119,* 4208-4216.

26. Yang, Q. Y.; Zhong, C. L., Molecular Simulation of Carbon Dioxide/Methane/Hydrogen Mixture Adsorption in Metal-Organic Frameworks. *J. Phys. Chem. B* **2006,** *110,* 17776-17783.

27. Peng, D.-Y.; Robinson, D. B., A New Two-Constant Equation of State. *Ind. Eng. Chem. Fundam.* **1976,** *15,* 59-64.

28. Vlugt, T. J. H.; Garcia-Perez, E.; Dubbeldam, D.; Ban, S.; Calero, S., Computing the Heat of Adsorption Using Molecular Simulations: The Effect of Strong Coulombic Interactions. *J. Chem. Theory. Comput.* **2008,** *4,* 1107-1118.

29. Wiersum, A. D.; Gioyannangeli, C.; Vincent, D.; Bloch, E.; Reinsch, H.; Stock, N.; Lee, J. S.; Chang, J. S.; Llewellyn, P. L., Experimental Screening of Porous Materials for High Pressure Gas Adsorption and Evaluation in Gas Separations: Application to MOFs (MIL-100 and CAU-10). *ACS Comb. Sci.* **2013,** *15,* 111-119.

30. Llewellyn, P. L.; Maurin, G., Gas Adsorption Microcalorimetry and Modelling to Characterise Zeolites and Related Materials. *C. R. Chimie* **2005,** *8,* 283-302.

B. NH_2-MIL-53(Al)/ MIL-69(Al)

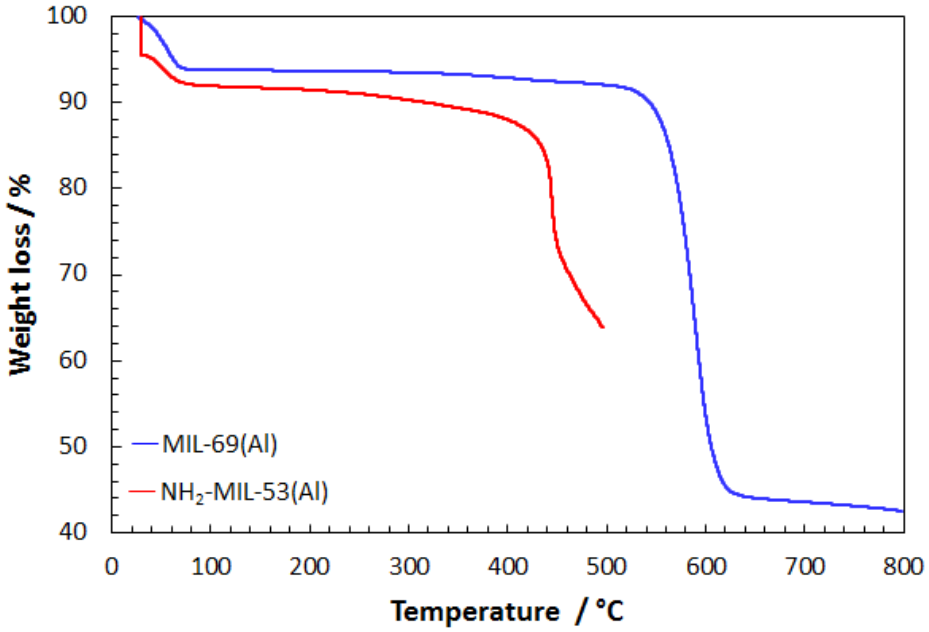

Figure B.1 – Thermogravimetric curves of the MIL-69(Al) (blue) and the NH_2-MIL-53(Al) (red)

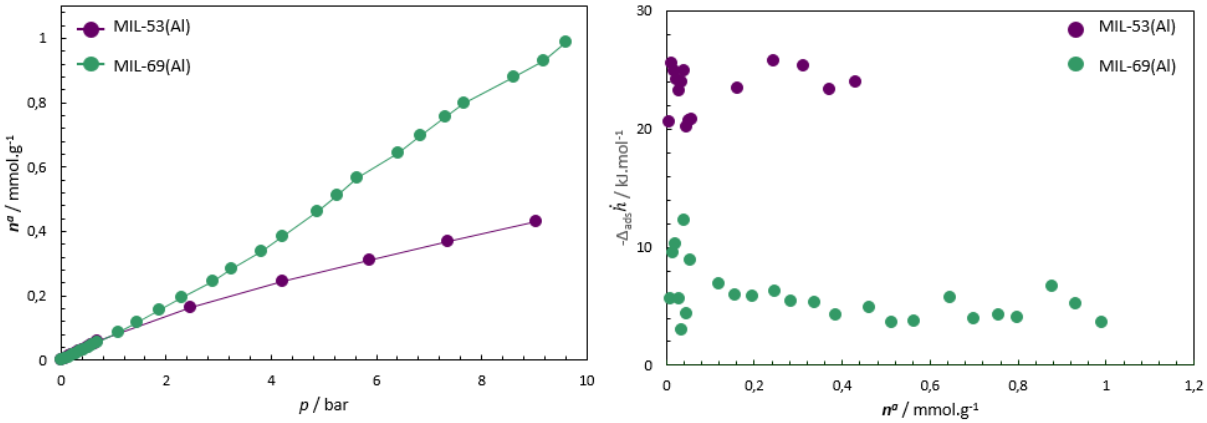

Figure B.2 – N_2 adsorption isotherms (left) and matching adsorption enthalpy profiles (right) at 303K for the MIL-69(Al) (green circles) and the NH_2-MIL-53(Al) (purple circles)

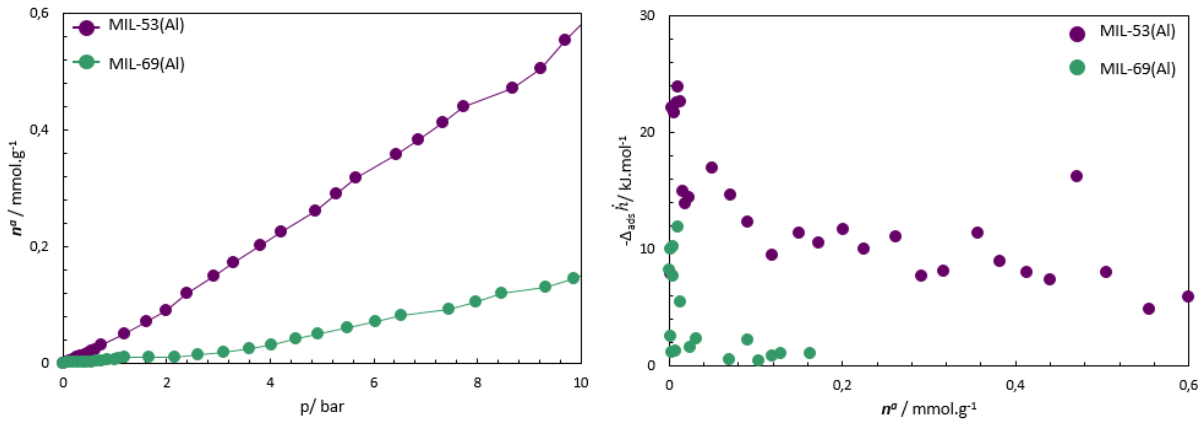

Figure B.3 – CH_4 adsorption isotherms (left) and matching adsorption enthalpy profiles (right) at 303K for the MIL-69(Al) (green circles) and the NH_2-MIL-53(Al) (purple circles)

Annex D

Journal of Materials Chemistry A

PAPER

View Article Online
View Journal | View Issue

Cite this: J. Mater. Chem. A, 2016, 4, 1383

MIL-91(Ti), a small pore metal–organic framework which fulfils several criteria: an upscaled green synthesis, excellent water stability, high CO_2 selectivity and fast CO_2 transport†

Virginie Benoit,[a] Renjith S. Pillai,[b] Angelica Orsi,[c] Périne Normand,[d] Hervé Jobic,[e] Farid Nouar,[f] Pierre Billemont,[d] Emily Bloch,[a] Sandrine Bourrelly,[a] Thomas Devic,[f] Paul A. Wright,[c] Guy de Weireld,[d] Christian Serre,[f] Guillaume Maurin*[b] and Philip L. Llewellyn*[a]

Received 18th November 2015
Accepted 17th December 2015

DOI: 10.1039/c5ta09349j

www.rsc.org/MaterialsA

A multidisciplinary approach combining advanced experimental and modelling tools was undertaken to characterize the promises of a small-pore type Ti-based metal–organic framework, MIL-91(Ti) for CO_2 capture. This material was prepared using two synthesis strategies, *i.e.* under hydrothermal conditions and under reflux, and its single component adsorption behaviour with respect to CO_2, CH_4 and N_2 was first revealed by gravimetry measurements. This hydrophilic and highly water stable MOF is characterized by a relatively high CO_2 adsorption enthalpy. Molecular simulations combined with *in situ* powder X-ray diffraction evidenced that this is due to the combined interaction of this probe with N–H and P–O groups in the phosphonate linker. High CO_2 selectivities in the presence of either N_2 or CH_4 were also predicted and confirmed by co-adsorption measurements. The possibility to prepare this sample under reflux represents an environmentally friendly route which can easily be upscaled. This green synthesis route, excellent water stability, high selectivities and relatively fast transport kinetics of CO_2 are significant points rendering this sample of utmost interest for CO_2 capture.

Introduction

Metal–Organic Frameworks (MOFs) are porous coordination polymers which combine the diverse architectures of coordination chemistry with porous properties relevant to materials science, leading to novel solids targeted for societally relevant applications.[1,2] These crystalline hybrid materials, where inorganic nodes are linked through polytopic organic moieties to give porous frameworks, show promise for applications such as catalysis, biomedicine, adsorption and separation, among others.[3–7] In spite of their attractive properties, some of these materials have received criticism in light of their poor chemical stability,[8,9] the extensive use of organic solvents during their synthesis and the high cost of certain reactants required for scale up of their synthesis to a commercial level.[10] Whilst such points would limit the use of any material for many applications, these disadvantages do not apply universally to MOFs. Indeed, the wide spectrum of possible inorganic and organic building blocks permits the design of water-stable MOFs and 'green' synthesis routes can be devised.[11–13] Amongst the water-stable MOFs reported so far, there is the potential to find promising candidates for a targeted application. For instance, it has been reported that small pore MOFs[14–23] with openings of 3.0–4.0 Å, could be of interest for diverse gas separations. More particularly, most of these promising MOFs can be used for CO_2 capture from binary gas mixtures with molecules of larger kinetic diameters such as N_2 (flue gas treatment) and/or CH_4 (natural gas or biogas purification) *via* molecular sieving.

The small pore bis-phosphonate MIL-91(Al),[24] one of the relatively few porous phosphonate MOF reported so far,[24–29] was shown to interact strongly with CO_2 due to the presence of accessible phosphonate P–OH groups and the high degree of confinement afforded by its narrow pores.[18] However, it displays an S-shaped CO_2 adsorption isotherm below 1 bar, as a result of guest-induced rearrangement of the MOF framework. Previous

[a]Aix-Marseille University, CNRS, MADIREL UMR 7246, 13397 Marseille, France
[b]Institut Charles Gerhardt Montpellier, UMR-5253, Université Montpellier, CNRS, ENSCM, Place E. Bataillon, 34095 Montpellier Cedex 05, France
[c]Eastchem School of Chemistry, University of St. Andrews, Purdie Building, North Haugh, St Andrews, Fife KY16 9ST, United Kingdom
[d]Service de Thermodynamique, Faculté Polytechnique, Université de Mons, Place du Parc 20, 7000 Mons, Belgium
[e]Institut de Recherches sur la Catalyse et l'Environnement de Lyon, CNRS, Université de Lyon, 2. Av. A. Einstein, 69626 Villeurbanne, France
[f]Institut Lavoisier, UMR CNRS 8180, Université de Versailles St Quentin en Yvelines, Université Paris-Saclay, 45 avenue des Etats-Unis, Versailles, 78035, France

† Electronic supplementary information (ESI) available: These include the experimental details and complementary figures and tables. See DOI: 10.1039/c5ta09349j

work has suggested that such a structural flexibility is not ideal in mixture separation.[30,31] By analogy with the flexible MIL-53(Al, Cr, Fe)/MIL-47(V) systems,[30–32] a possible way to modulate the structural behaviour of a MOF solid upon adsorption is to change the metal centre. Hence, here we focus on the Ti-version of MIL-91 (Fig. 1). This differs structurally from the Al analogue by the absence of bridging hydroxyl groups between adjacent metal centres (Ti_{IV}–O–Ti_{IV} *vs.* Al_{III}–OH–Al_{III}). A combination of advanced experimental and modelling tools reveals that this solid exhibits a standard Type I CO_2 adsorption isotherm, with no S-shape, while maintaining a significantly higher affinity for CO_2 compared to other gases (N_2, CH_4). This results in MIL-91 being highly favourable in comparison with other MOFs in terms of CO_2 uptake and separation ability.

We also report a new preparative aqueous HF free reflux route to this water-stable MOF,[24] suitable for its easy and green upscaled preparation. Co-adsorption measurements which have been only very rarely reported for small pore solids due to slow adsorption kinetics and large error bars as a result of the very small amounts adsorbed were further performed on this material. They confirm the predicted promise of MIL-91(Ti) for CO_2/CH_4 and CO_2/N_2 separation. Moreover, this solid shows adsorption performance indicators ranking above most of the MOFs reported so far. Finally, quasi-elastic neutron scattering (QENS) experiments evidence that although this solid has quite small pore channels, the diffusivity of CO_2 is relatively high, a requirement for its further application in physisorption-based processes for CO_2 recovery.

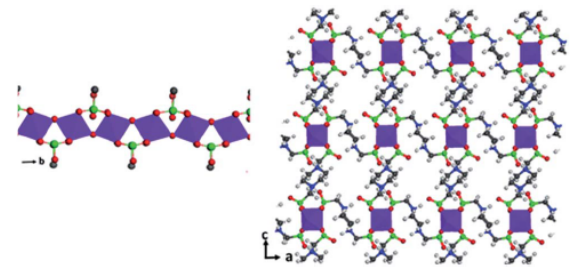

Fig. 1 Structure of MIL-91(Ti) ($TiO(O_3PCH_2NHC_4H_8NHCH_2PO_3)$), showing the chain of corner-sharing TiO_6 octahedra along the *b*-axis (left) and the view down the *b* axis (right). The atoms are represented as follows: Ti, violet; P, green; C, grey; O, red; N, blue; H, white.

MIL-91(Ti) prepared by hydrothermal synthesis

Textural characterization and water stability. The synthesis for MIL-91(Ti) reported previously[24] employs hydrothermal conditions and hydrofluoric acid (HF) as a mineralizing agent. This leads to a material with zeolite-like textural properties in terms of pore size and pore volume, a hydrophilic character although stable to humidity. The free pore size of MIL-91(Ti) can be estimated at around 0.35 × 0.40 nm^2 from crystallographic data which can be considered in the small range for many porous materials. Further, the porosity of this material, measured using nitrogen physisorption at 77 K, shows a BET area of ~380 $m^2\ g^{-1}$ and a pore volume of 0.141 $cm^3\ g^{-1}$ (at $p/p_0 = 0.1$, Table S1, Fig. S7†) in good agreement with the theoretically accessible N_2-surface area (~403 $m^2\ g^{-1}$) and pore volume (0.160 $cm^3\ g^{-1}$) calculated from the crystal structure of MIL-91(Ti) (Table S2†). The increase in uptake in the N_2 isotherm at high p/p_0 can be attributed to intra-particular adsorption.

The water adsorption isotherm obtained at 25 °C after outgassing to 150 °C is of Type I, (Fig. 2). A second water adsorption cycle recorded after identical outgassing led to an overlapping isotherm suggesting that no structural degradation occurs during water adsorption–desorption. However, placing the sample under secondary vacuum for 1 hour between cycles is not sufficient to completely liberate the porosity, as a 16% decrease in uptake was observed (Fig. S8†). In a separate series of experiments after outgassing to 80 °C under nitrogen flow, the sample showed reversible behaviour for three water cycles, which indicates this MOF's stability under these conditions and within the 3 week experimental period (Fig. S8†). The water stability was finally confirmed by powder X-ray diffraction

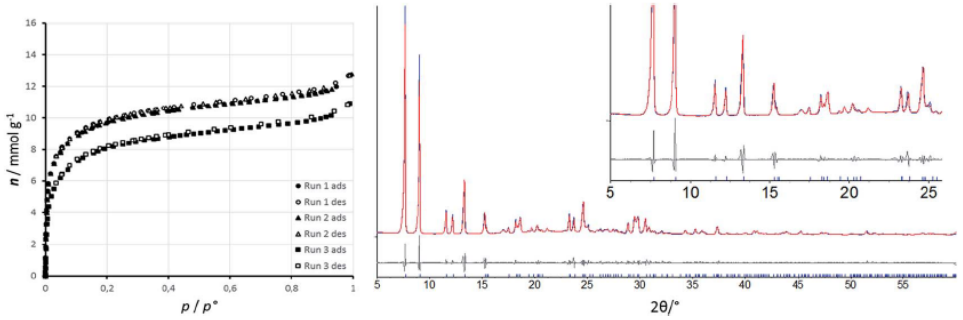

Fig. 2 Water adsorption cycles at 25 °C (left) and pattern matching (right) for MIL-91(Ti) synthesised under hydrothermal conditions after water adsorption/desorption cycling at 25 °C for 3 weeks. Capillary data was collected on a Bruker D8 Advance diffractometer (λ_{Cu} ~ 1.5406 Å), pattern matching was performed using Topas software.[33] a = 19.448(8) Å, b = 7.044(4) Å, c = 11.465(6) Å, β = 93.20(3)°, V = 1568(1) $Å^3$; rwp = 9.25. It should be noted that impurities (probably a polymorph phase) are present within the material before and after water treatments (2θ values of about 17° and 21.2°). A pattern matching of the material before the treatment was also performed (not shown here), the following cell parameters were obtained: a = 19.414(9) Å, b = 7.040(4) Å, c = 11.449(7) Å, β = 92.98(4)°, V = 1562(1) $Å^3$; rwp = 9.25.

(PXRD), which evidenced a very similar pattern for the sample dispersed in boiling water for 24 hours compared to that of the pristine solid. This valuable latter feature is not shown by most of the MOFs proposed so far for CO_2 capture.[34,35]

Single gas adsorption and comparison with molecular simulations. The adsorption isotherms of MIL-91(Ti) were initially evaluated using gravimetry and the adsorption enthalpies were measured using calorimetry at 303 K, with CO_2, CH_4 and N_2. The corresponding data are reported in Fig. 3.

The amounts adsorbed for both CH_4 and N_2 are relatively low with saturation capacities of ~1.5 mmol g^{-1} and ~1.0 mmol g^{-1} at 40 bar, respectively, while their enthalpies are slightly larger than those obtained from many other MOFs (see the comparison on Table S3†). This can be explained by the more confined pore space exhibited by this structure. Grand Canonical Monte Carlo (GCMC) simulations confirmed (i) the low amounts adsorbed of both gases and (ii) their relatively high adsorption enthalpies at zero coverage, *i.e.* around ~−19.6 kJ mol^{-1} (exp. −19.5 kJ mol^{-1}) and ~−24.6 kJ mol^{-1} (exp. −23.8 kJ mol^{-1}) for N_2 and CH_4 respectively (Fig. 3). Analysis of the adsorption mechanism for these two guest molecules indicated the absence of specific adsorption sites for these probes at the MOF surfaces, as both N_2 and CH_4 are mainly distributed in the centre of the pores (Fig. S19 and S20†).

For CO_2, the adsorption uptakes at 1 bar (~3.0 mmol g^{-1}) and 10 bar (~4.5 mmol g^{-1}) are rather high compared to other small pore MOFs previously proposed for separation purposes, such as MIL-53(Al)-NH_2 (1.6 mmol g^{-1} at 283 K and 1 bar[36]), Sc_2BDC_3-NO_2 (1.1 mmol g^{-1} at 303 K and 1 bar[20]), UiO-66(Zr)-$2CO_2H$ (1.0 mmol g^{-1} at 303 K and 1 bar[12]) and SIFSIX-3-Zn (2.3 mmol g^{-1} at 308 K and 1 bar[21]). Interestingly, the adsorption enthalpies for CO_2, ranging from −47 kJ mol^{-1} to −43 kJ mol^{-1}, are amongst the highest reported to date for MOFs and in particular these values are larger than those observed for MOFs without open metal sites (Table S3†). Furthermore, this isotherm is completely reversible and repeatable after primary vacuum treatment at 303 K, indicating that a simple regeneration process for this porous solid is possible.

Furthermore, in contrast to its Al-analogue,[18] the CO_2 adsorption isotherm for MIL-91(Ti) does not show any inflection point below 1 bar, but exhibits a standard Langmuir-type shape, also applicable to the other gases, CH_4 and N_2. *In situ* synchrotron PRXD data collected on the sample during CO_2 loading (Fig. S12†) and Density Functional Theory (DFT) calculations (see ESI†) performed on the structure in the presence of CO_2 both suggest that a volume change of only ~2% occurs (Table S9†) with respect to the pristine structure (predicted and experimental unit cell volumes of 1576.05 $Å^3$ and 1574.73 $Å^3$, respectively, *vs.* 1516.86 $Å^3$ for the unloaded solid). However, the fact that there is no particular signature in the isotherm (inflection point) or change in the enthalpy curve suggests that this structure change on CO_2 adsorption may be gradual.

The CO_2 adsorption data are well reproduced by the GCMC simulations performed on the DFT-optimized CO_2 loaded structure. Both *in situ* PXRD and GCMC data reveal that CO_2 molecules preferentially interact in a dual manner with the phosphonate linkers, the CO_2 molecules being aligned in such a way that carbon atoms of C=O groups (CCO_2) interact with O atoms present in the environment of the P=O group and the N atom (PO···H···N), giving rise to CCO_2 – OPO···H···N distances of about 2.7 Å (Fig. 4). Such a confined geometry gives rise to a very high, predicted CO_2 adsorption enthalpy at low coverage (*i.e.* −44.0 kJ mol^{-1}), which is consistent with the microcalorimetry measurements (Fig. 3).

From the combination of experimental and modelling single component adsorption data it was possible to make a preliminary comparison, using the energies of adsorption, to deliver a first evaluation of MIL-91(Ti) for gas separation. The high adsorption enthalpy differences between CO_2 and other gases, *i.e.* $\Delta(\Delta H(CO_2) - \Delta H(CH_4)) \sim -20.0$ (simulated: 19.4) kJ mol^{-1} and $\Delta(\Delta H(CO_2) - \Delta H(N_2)) \sim -25$ (simulated: −24.4) kJ mol^{-1}, suggested that MIL-91(Ti) is of interest both for the selective adsorption of CO_2 over CH_4 and/or N_2 (see Table S3†). However further comparisons and mixture adsorption data were required to validate this initial approach, as shown below.

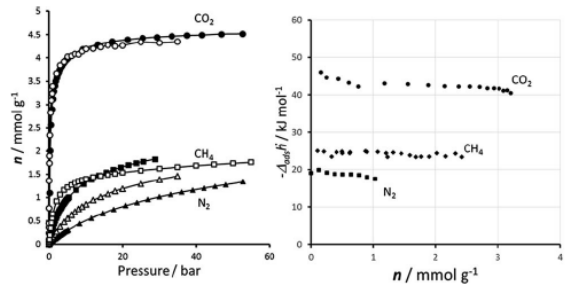

Fig. 3 Comparison of the adsorption isotherms (left) obtained by gravimetry (filled symbols) and by GCMC simulations (open symbols) at 303 K for CO_2 (circles), CH_4 (squares), N_2 (triangles) for MIL-91(Ti). The corresponding adsorption enthalpies as a function of the coverage collected by microcalorimetry (right).

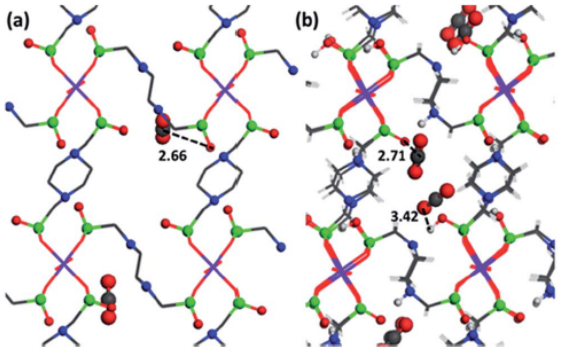

Fig. 4 (a) Crystal structure obtained from the *in situ* synchrotron XRPD data collected at P_{CO_2} = 35 bar and 230 K. (b) Local views of the snapshots extracted from the GCMC simulations of MIL-91(Ti) at 1 bar and 303 K. The interacting distances are reported in Å and the atoms are represented with the same colour code as in Fig. 1.

Green synthesis of MIL-91(Ti) under reflux conditions

Synthesis and comparison between samples. To confirm the promise of MIL-91(Ti) for CO_2 capture, a relatively large amount of sample was required to perform co-adsorption experiments. To upscale the synthesis of this material, a method is required which does not necessitate hydrothermal conditions or the use of HF. Hence, a reflux route in water was developed (see ESI† for full details) where *N*,*N*′-piperazinebis(methylenephosphonic acid) is dissolved, with the aid of NaOH, in water under reflux before the addition of titanium oxyacetylacetonate and prior to a further reflux for 68 hours. The initial characterization data of this material (PXRD, TGA, SEM) is provided in the ESI.† The BET area of the obtained solid was 360 $m^2 g^{-1}$ and the pore volume 0.138 $cm^3 g^{-1}$. Both values are similar to those obtained for the hydrothermally synthesized sample (380 $m^2 g^{-1}$ and 0.141 $cm^3 g^{-1}$), which validates this new synthetic route.

The water isotherms (Fig. S8†) shows that this solid has attractive water stability with a fully reversible water adsorption/desorption cycling under nitrogen flow. This is further confirmed by structure analysis where comparable PXRD patterns are obtained with the pristine sample and the one recorded after the 3 weeks of water adsorption/desorption cycling (Fig. S9†). Further comparison between the samples was made using single gas adsorption at 303 K (Fig. S10†). It was shown that the uptakes and adsorption enthalpies for CH_4 and N_2 were similar for the two samples. A small deviation is observed for the CO_2 adsorption with a slightly higher enthalpy for the sample prepared under hydrothermal conditions. This is equally translated in a steeper uptake at lower pressures and a sharper knee in the isotherm. However, the overall uptakes are similar at pressures above 10 bar for both samples.

Adsorption of gas mixtures: modelling and real co-adsorption measurements. GCMC simulations, which concur with experimental data from single gas adsorptions, are a convenient initial means to predict the behaviour of this MOF with respect to binary gas mixtures. Hence, an evaluation of the potential applications of MIL-91(Ti) can then be deduced. With both post-combustion and natural gas upgrading scenarios in mind, GCMC simulations were carried out with mixtures of CO_2/N_2 (gas phase composition: 0.05/0.95; 0.1/0.9 and 0.15/0.85) and CO_2/CH_4 (gas phase composition: 0.5/0.5) at 303 K and 313 K (details in ESI†). The predicted selectivities varied from 80 to 100 at 1 bar, for CO_2/N_2 with 0.05/0.95; 0.1/0.9 and 0.15/0.85 molar concentrations and in the temperature range 303–313 K (Fig. S25†).

For CO_2/CH_4, the simulated data for an equimolar concentration resulted in values from 16 to 20 for the same temperature range (Fig. S26†). These separation performances are amongst the highest reported so far for water stable MOFs (Tables S5 & S6†). Analysis of the co-adsorption mechanism revealed that the behaviour of CO_2 is similar to the single gas component scenario (Fig. 5), *i.e.* the CO_2 molecules are mainly distributed in the vicinity of the PO···H···N sites, with mean distances between CCO_2 and OPO···H···N for CO_2/N_2 and CO_2/CH_4 systems of 2.69 and 2.72 Å, respectively (Fig. 5). Both N_2 and CH_4 are distributed in the centre of the pore with characteristic host/guest distances exceeding 3.2 Å (N_2 – PO···H···N: Fig. S23;† CH_4 – PO···H···N: Fig. S24†).

This clearly emphasizes that for both mixtures, the separations are mainly driven by a preferential CO_2 adsorption around P–OH and NH groups combined with the high degree of confinement of this solid due to its restricted pore size conjugated with a small pore volume, which favours the adsorption of molecules with smaller kinetic diameters.

To investigate this MOF further, co-adsorption measurements were performed on several grams of the sample, prepared under reflux conditions. The results are given in Tables 1 and 2.

Each mixture point was repeated several times and an average separation value was obtained. The co-adsorption selectivity of ~90 was observed at 1 bar and 303 K for the case of $CO_2/N_2 = 10/90$, which then decreased to 60 at 1 bar and 303 K for the mixture $CO_2/N_2 = 15/85$. For the co-adsorption of the equimolar mixture of CO_2/CH_4, MIL-91(Ti) shows a selectivity of around 18 at 1 bar and 303 K. All of this experimental data concurs with the predicted data from GCMC simulations.

Adsorption performances of MIL-91(Ti) *vs.* other MOFs. The above discussion indicates how MIL-91(Ti) competes well with other porous materials as a CO_2 adsorbent. Indeed, the relatively high adsorption enthalpies and selectivities suggest that this material could be of interest for the recovery of CO_2 from N_2 or CH_4. A third factor to consider is the working capacity, *i.e.* the adsorption/desorption between an upper and lower working pressure as defined by a given pressure swing adsorption (PSA) process. Making a comparison between MOFs is not simple as most materials are still only available in powder form. Furthermore, one would wish to compare the uptakes per volume of material as this is what is required for process design. However, the real density of many MOFs is not always given. Thus, to make a comparison, the uptakes of available MOF powders were deduced and the individual crystallographic densities were obtained to calculate uptakes per unit volume. A comparison between MOF samples is provided in Table S4† for the two separations under investigation. For the CO_2/N_2

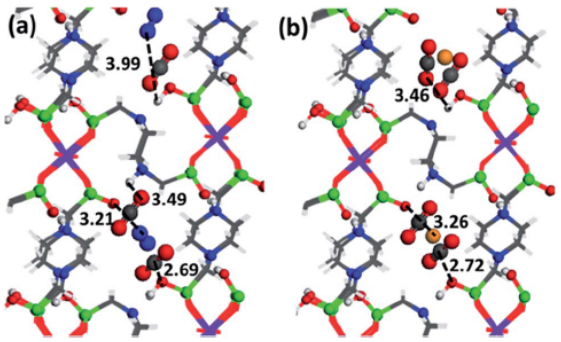

Fig. 5 Snapshots obtained during GCMC simulated arrangements of CO_2 and N_2 molecules (left) and CO_2 and CH_4 molecules (right) from binary mixture simulations on MIL-91(Ti)_CO_2, (CO_2/N_2 system at a molar composition of 0.05/0.95 and the CO_2/CH_4 system at a molar composition of 0.5/0.5, both in the gas phase at 303 K).

Table 1 CO_2/N_2 experimental selectivities measured at 303 K

Total pressure	% CO_2	Measured selectivity	Average measured selectivity
1 bar	0.108	65	86
	0.099	89	
	0.102	106	
	0.173	67	60
	0.168	53	
3 bars	0.103	89	73
	0.117	61	
	0.118	69	
	0.176	60	51
	0.169	49	
	0.168	45	

Table 2 CO_2/CH_4 experimental selectivities measured at 303 K

Total pressure	% CO_2	Measured selectivity
1 bar	50	18
5 bars	50	15
13 bars	50	13

separation at 1 bar, MIL-91(Ti) has however a working capacity which is not amongst the highest; being at around a third of that obtained with HKUST-1 for example (Table S4†). One shall nevertheless bear in mind the poor water stability of the copper MOF ruling its use for the recovery of CO_2 from flues.

Noteworthy, for the recovery of CO_2 from methane, considered at 30 bar, the working capacity of MIL-91(Ti) is amongst the highest of the MOFs considered.

These varying results thus open the question of how to make a fair but global comparison between samples, which, *inter alia*, resulted in the development of the concept of the adsorption performance indicator (API).[37] The API considers the volumetric working capacity (WC), adsorption enthalpies ($\Delta_{ads}\dot{h}$) and selectivities ($\alpha_{1/2}$), as indicated below.

$$\mathrm{API} = \frac{(\alpha_{1/2} - 1)^A \mathrm{WC}_1^B}{\Delta_{ads}\dot{h}^C}$$

Each parameter can be emphasised using power laws, defined by the process under consideration. In the present comparison, gas sweetening is considered and thus the selectivity towards was emphasized ($A = 2$). In this exercise, single gas data previously obtained in house on fully activated samples are used as the conditions of collection are identical ($T = 30$ °C) and the enthalpies have been measured directly. For MIL-91(Ti) the measured selectivities were applied, but for other MOF species the calculated IAST values were considered. Note that in this reported exercise there was fairly good agreement between experimental and IAST calculated selectivities that make the comparison with the other MOFs consistent. The API values for the two separations, CO_2/CH_4 and CO_2/N_2, obtained for MIL-91(Ti) were compared with around 20 other MOFs (Fig. 6).

For CO_2/CH_4 separation, the zeolite NaX shows the highest API value, which is due to its very high selectivity. However, for the analysed MOFs (*i.e.* where data was obtainable), MIL-91(Ti) is highly ranked, which again reflects the medium to high selectivity and relatively high working capacity. For CO_2/N_2 separation, MIL-91(Ti) is again deduced to be the most interesting material considered by our group thus far, which is also attributed to its relatively high measured selectivity. Nevertheless, one should temper this conclusion with the fact that other MOFs from other groups may also be of interest (for example, those in ref. 21–23).

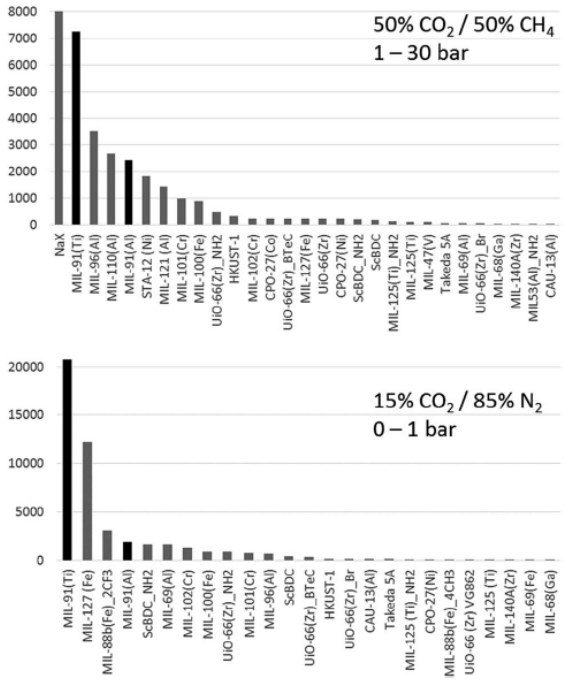

Fig. 6 API values for CO_2/CH_4 (upper) and CO_2/N_2 (lower) for several MOFs. Both MIL-91(Ti) and MIL-91(Al) are given in black. Data for an activated carbon (Takeda 5A) and a zeolite (NaX) are also given for comparison.

Kinetics of CO_2 and N_2 in MIL-91(Ti). Nevertheless, for such a small pore material with relatively large interactions, the question arises as to whether the adsorption could have some kinetic limitations. Therefore, the dynamics of CO_2 and N_2 were probed using QENS measurements (see ESI† for details). This approach has previously proven to be successful when applied to deduce the transport diffusivity (D_t) of two species (CO_2 and N_2) in a diverse range of MOFs.[38–42] It was found that in the low loading range (0.7 N_2 molecule per u.c. and 1.2 CO_2 molecule per u.c.), the D_t values for CO_2 and N_2 are respectively, 8.5×10^{-10} $m^2\ s^{-1}$ at 300 K and 1.4×10^{-9} $m^2\ s^{-1}$ at 220 K. These values for MIL-91(Ti) are as high as those previously shown for UiO-66(Zr)-$2CO_2H$[12] (CO_2: 1.0×10^{-10} $m^2\ s^{-1}$ and N_2: 4.0×10^{-9} $m_2\ s^{-1}$) and also in the reference zeolite NaX for the same region of temperature (CO_2: 1.5×10^{-10} $m^2\ s^{-1}$ and N_2: 2×10^{-9} $m^2\ s^{-1}$) measured at 230 K.[43,44] These values confirm that kinetics should not be a hindrance to the use of MIL-91(Ti) in physisorption-based processes.

Conclusions

In summary, the titanium form of MIL-91 is a promising candidate for CO_2 recovery while its "green" reflux synthesis conditions pave the way for its upscale production. This hydrophilic metal bisphosphonate material seems to be one of the relatively few MOFs that are stable towards humidity. The nature of the small pores and the chemistry of this porous framework results in significant CO_2 uptakes at low pressures, along with strong interactions towards this greenhouse gas. However the strength of this interaction and the small pore nature of this material does not hinder the transport kinetics of CO_2 in the pore system as measured by QENS. Co-adsorption measurements confirmed the performances predicted from molecular simulations, with selectivities for CO_2/CH_4 and CO_2/N_2 above 18 and 90, respectively, at 1 bar and 298 K. This makes MIL-91(Ti) attractive for the selective capture of CO_2 from both CH_4 and N_2. Evaluation of the APIs for a wide range of MOFs at our disposition further suggests that MIL-91(Ti) compares well with respect to many other materials. In addition to these separations, one can consider that good results could be obtained with hydrogen purification from CO_2 as H_2 generally does not adsorb on porous materials at ambient temperatures.

Indeed this study shows that MIL-91(Ti) seems to tick boxes concerning up-scalable environmentally favourable synthesis, water stability, high CO_2 selectivity and rapid kinetics promoting this MOF as one of the very few of real interest for CO_2 capture.

Acknowledgements

The research leading to these results has received funding from the European Community Seventh Framework Program (FP7/2007-2013) [grant agreement number 608490] (project M^4CO_2) and from the ANR 'CHESDENS' (ANR-13-SEED-0001-01). The authors would like to thank the ESRF (SNBL & Prof. Y. Filinchuk) for X-ray beamtime and ILL (IN6 & Dr M. M. Koza) for neutron beamtime. G. M. thanks the Institut Universitaire de France for their support.

Notes and references

1 H.-C. Zhou, J. R. Long and O. M. Yaghi, *Chem. Rev.*, 2012, **112**, 673.
2 H.-C. Zhou and S. Kitagawa, *Chem. Soc. Rev.*, 2014, **43**, 5415.
3 M. Zhao, S. Ou and C. D. Wu, *Acc. Chem. Res.*, 2014, **47**(4), 1199.
4 M. W. Zhang, Z. Y. Gu, M. Bosch, Z. Perry and H.-C. Zhou, *Coord. Chem. Rev.*, 2015, **293**, 327.
5 P. Horcajada, R. Gref, T. Baati, P. K. Allan, G. Maurin, P. Couvreur, G. Ferey, R. E. Morris and C. Serre, *Chem. Rev.*, 2012, **112**(2), 1232.
6 B. Seoane, J. Coronas, I. Gascon, M. E. Benavides, O. Karvan, J. Caro, F. Kapteijn and J. Gascon, *Chem. Soc. Rev.*, 2015, **44**(8), 2421.
7 E. Barea, C. Montoro and J. A. R. Navarro, *Chem. Soc. Rev.*, 2014, **43**(16), 5419.
8 J. J. Low, A. I. Benin, P. Jakubczak, J. F. Abrahamian, S. A. Faheem and R. R. Willis, *J. Am. Chem. Soc.*, 2009, **131**(43), 15834.
9 P. Guo, D. Dutta, A. G. Wong-Foy, D. W. Gidley and A. J. Matzger, *J. Am. Chem. Soc.*, 2015, **137**(7), 2651.
10 J. Liu, P. K. Thallapally, B. P. McGrail, D. R. Brown and J. Liu, *Chem. Soc. Rev.*, 2012, **41**(6), 2308.
11 A. G. Marquez, P. Horcajada, D. Grosso, G. Ferey, C. Serre, C. Sanchez and C. Boissiere, *Chem. Commun.*, 2013, **49**(37), 3848.
12 Q. Yang, S. Vaesen, F. Ragon, A. D. Wiersum, D. Wu, A. Lago, T. Devic, C. Martineau, F. Taulelle, P. L. Llewellyn, H. Jobic, C. L. Zhong, C. Serre, G. de Weireld and G. Maurin, *Angew. Chem., Int. Ed.*, 2013, **52**(39), 10316.
13 H. Reinsch, B. Bueken, F. Vermoortele, I. Stassen, A. Lieb, K.-P. Lillerud and D. de Vos, *CrystEngComm*, 2015, **17**(22), 4070.
14 K. S. Park, Z. Ni, A. P. Cote, J. Y. Choi, R. D. Huang, F. J. Uribe-Romo, H. K. Chae, M. O'Keeffe and O. M. Yaghi, *Proc. Natl. Acad. Sci. U. S. A.*, 2006, **103**, 10186.
15 S. R. Miller, P. A. Wright, C. Serre, T. Loiseau, J. Marrot and G. Férey, *Chem. Commun.*, 2005, 3850.
16 S. R. Miller, P. A. Wright, T. Devic, C. Serre, G. Ferey, P. L. Llewellyn, R. Denoyel, L. Gaberova and Y. Filinchuk, *Langmuir*, 2009, **25**(6), 3618.
17 J. P. S. Mowat, S. R. Miller, J. M. Griffin, V. R. Seymour, S. E. Ashbrook, S. P. Thompson, D. Fairen-Jimenez, A. M. Banu, T. Duren and P. A. Wright, *Inorg. Chem.*, 2011, **50**, 10844.
18 P. L. Llewellyn, M. Garcia-Rates, L. Gaberova, S. R. Miller, T. Devic, J.-C. Lavalley, S. Bourrelly, E. Bloch, Y. Filinchuk, P. A. Wright, C. Serre, A. Vimont and G. Maurin, *J. Phys. Chem. C*, 2015, **119**, 4208.
19 D. Damasceno Borges, M. Prakash, N. A. Ramsahye, P. L. Llewellyn, S. Surblé, P. Horcajada, C. Serre and G. Maurin, *Mol. Simul.*, 2015, **41**(16–17), 1357.

20 R. S. Pillai, V. Benoit, A. Orsi, P. L. Llewellyn, P. A. Wright and G. Maurin, *J. Phys. Chem. C*, 2015, **119**(41), 23592.

21 P. Nugent, Y. Belmabkhout, S. D. Burd, A. J. Cairns, R. Luebke, K. Forrest, T. Pham, S. Ma, B. Space, L. Wojtas, M. Eddaoudi and M. J. Zaworotko, *Nature*, 2013, **495**, 80.

22 D. X. Xue, Y. Belmabkhout, I. Shekhah, H. Jiang, K. Adil, A. J. Cairns and M. Eddaoudi, *J. Am. Chem. Soc.*, 2015, **137**, 5034.

23 A. H. Assen, Y. Belmabkhout, K. Adil, P. M. Bhatt, D. X. Xue, H. Jiang and M. Eddaoudi, *Angew. Chem., Int. Ed.*, 2015, **54**(48), 14353.

24 C. Serre, J. A. Groves, P. Lightfoot, A. M. Z. Slawin, P. A. Wright, N. Stock, T. Bein, M. Haouas, F. Taulelle and G. Férey, *Chem. Mater.*, 2006, **18**, 1451.

25 S. R. Miller, G. M. Pearce, P. A. Wright, F. Bonino, S. Chavan, S. Bordiga, I. Margiolaki, N. Guillou, G. Férey, S. Bourrelly and P. L. Llewellyn, *J. Am. Chem. Soc.*, 2008, **130**, 15967.

26 S. Begun, *Chem.–Eur. J.*, 2014, **20**, 8862.

27 F. P. Zhai, Q. S. Zheng, Z. X. Chen, Y. Ling, X. F. Liu, L. H. Weng and Y. M. Zhou, *CrystEngComm*, 2013, **15**, 2040.

28 P. Ramaswamy, N. E. Wong and G. K. H. Shimizu, *Chem. Soc. Rev.*, 2014, **43**, 5913.

29 M. Taddei, F. Costantino, F. Marmottini, A. Comotti, P. Sozzani and R. Vivani, *Chem. Commun.*, 2014, **50**, 14831.

30 V. Finsy, L. Ma, L. Alaerts, D. E. de Vos, G. V. Baron and J. F. M. Denayer, *Microporous Mesoporous Mater.*, 2009, **120**(3), 221.

31 L. Hamon, P. L. Llewellyn, T. Devic, A. Ghoufi, G. Clet, V. Guillerm, G. D. Pirngruber, G. Maurin, C. Serre, G. Driver, W. van Beek, E. Jolimaitre, A. Vimont, M. Daturi and G. Ferey, *J. Am. Chem. Soc.*, 2009, **131**(47), 17490.

32 P. L. Llewellyn, S. Bourrelly, C. Vagner, N. Heymans, H. Leclerc, A. Ghoufi, P. Bazin, A. Vimont, M. Daturi, T. Devic, C. Serre, G. de Weireld and G. Maurin, *J. Phys. Chem. C*, 2013, **117**(2), 962.

33 *TOPAS V4.2: General Profile and Structure Analysis Software for Powder Diffraction Data*, Bruker AXS Ltd, 2004.

34 N. C. Burtch, H. Jasuja and K. S. Walton, *Chem. Rev.*, 2014, **114**, 10575.

35 J. Canivet, A. Fateeva, Y. M. Guo, B. Coasne and D. Farrusseng, *Chem. Soc. Rev.*, 2014, **43**, 5594.

36 E. Stavitski, E. A. Pidko, S. Couck, T. Remy, E. J. M. Hensen, B. M. Weckhuysen, J. Denayer, J. Gascon and F. Kapteijn, *Langmuir*, 2011, **27**, 3970.

37 A. D. Wiersum, J.-S. Chang, C. Serre and P. L. Llewellyn, *Langmuir*, 2013, **29**(10), 3301.

38 F. Salles, H. Jobic, T. Devic, V. Guillerm, C. Serre, M. M. Koza, G. Feérey and G. Maurin, *J. Phys. Chem. C*, 2013, **117**, 11275.

39 Q. Y. Yang, A. D. Wiersum, H. Jobic, V. Guillerm, C. Serre, P. L. Llewellyn and G. Maurin, *J. Phys. Chem. C*, 2011, **115**, 13768.

40 Q. Yang, H. Jobic, F. Salles, D. Kolokolov, V. Guillerm, C. Serre and G. Maurin, *Chem.–Eur. J.*, 2011, **17**, 8882.

41 F. Salles, H. Jobic, A. Ghoufi, P. L. Llewellyn, C. Serre, S. Bourrelly, G. Ferey and G. Maurin, *Angew. Chem., Int. Ed.*, 2009, **48**, 8335.

42 D. Wu, G. Maurin, Q. Yang, C. Serre, H. Jobic and C. Zhong, *J. Mater. Chem. A*, 2014, **2**, 1657.

43 D. Plant, H. Jobic, P. L. Llewellyn and G. Maurin, *Eur. Phys. J.: Spec. Top.*, 2007, **141**, 127.

44 N.-K. Bär, P. L. Mc Daniel, C. G. Coe, G. Seiffert and J. Kärger, *Zeolites*, 1997, **18**, 71.

Annex D

Supporting information

MIL-91(Ti), a small pore Metal-Organic Framework which fulfils several criteria: an upscaled green synthesis, excellent water stability, high CO_2 selectivity and fast CO_2 transport

Virginie Benoit [a], Renjith S. Pillai [b], Angelica Orsi [c], Périne Normand [d], Hervé Jobic [e], Farid Nouar [f], Pierre Billemont [d], Emily Bloch [a], Sandrine Bourrelly [a], Thomas Devic [f], Paul A. Wright [c], Guy De Weireld [d], Christian Serre [f], Guillaume Maurin [b,†], Philip L. Llewellyn [a,†]

[a.] *Aix-Marseille Univ., CNRS, MADIREL UMR 7246, 13397 Marseille, France.*
[b.] *UMR-5253, Université Montpellier, CNRS, ENSCM, Place E. Bataillon, 34095 Montpellier cedex 05, France.*
[c.] *Eastchem School of Chemistry, University of St. Andrews, Purdie Building, North Haugh, St Andrews, Fife KY16 9ST, United Kingdom.*
[d.] *Service de Thermodynamique, Faculté Polytechnique, Université de Mons, Place du Parc 20, 7000 Mons, Belgium*
[e.] *Institut de Recherches sur la Catalyse et l'Environnement de Lyon, CNRS, Université de Lyon, 2. Av. A. Einstein, 69626 Villeurbanne, France.*
[f.] *Institut Lavoisier, UMR CNRS 8180, Université de Versailles St Quentin en Yvelines, Université Paris-Saclay, 45 avenue des Etats-Unis, Versailles, 78035, France.*
[g.]
† Corresponding authors.

.

Table of contents

1. Reflux synthesis of MIL-91(Ti) and initial characterization

1.1. Synthesis of the ligand

The ligand N,N'-piperazinebis(methylenephosphonic acid) was synthesised from a modified Mannich reaction. [1] A mixture of hydrochloric acid (10 mL, 37 wt. %) and water (10 mL) was added to piperazine (6.89 g, 0.08 mol) and phosphorous acid (17.06 g, 0.21 mol) to form a colourless solution, which was then refluxed (1 hour). Formaldehyde (20 mL, 37 wt. %) was added drop wise over a 2 hour period to form a white suspension. After refluxing for 24 hours, the reaction was cooled and the solvent volume reduced by 70% under vacuum. An ethanol-water (9:1, 40 mL) solution was added to the product and refrigerated overnight to precipitate any remaining ligand. The product was collected by filtration, washed with an ethanol-water (9:1, 2 × 30 mL) solution and dried (90 °C, overnight) to afford a white powder (19.5 g, 89 % yield based on piperazine). δ_H (500 MHz, D_2O/NaOH, Me_4Si) 3.13 (4H, broad s, C<u>H</u>$_2$) and 2.79 (8H, d, *J* 11.9 Hz, C<u>H</u>$_2$). δ_C (126 MHz, D_2O/NaOH, Me_4Si) 57.1 (C-1, <u>C</u>P, ^1J(C-P) 140.6 Hz) and 53.6 (C-2, <u>C</u>N, ^3J(C-P) 8.5 Hz). δ_P (202 MHz, D_2O/NaOH, 85% H_3PO_4) 14.4 (t, ^2J(P-H) 12.2 Hz).

1.

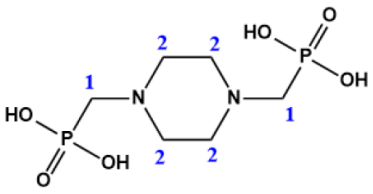

Figure S1. Numbered carbons of N,N'-piperazine(bismethylenephosphonic acid) ligand for ^{13}C-NMR analysis.

1.2. Preparation of MIL-91[Ti] from reflux heating involved mixing (60 °C, 30 minutes)

N,N'-piperazinebis(methylenephosphonic acid) (1.14 g, 4.17 mmol) in water (30 mL) to produce an opaque white suspension. 1M NaOH was added drop wise to increase the pH to 5 or 6 and to partially dissolve the organic ligand. The mixture was further stirred (**60 °C,** 30 minutes). Titanium oxyacetylacetonate (1.09 g, 4.17 mmol) was then added as a dry powder

and a little water was added to rinse the sides of the reaction vessel. The temperature was increased to reflux (68 hours), cooled, filtered under gravity and washed with water (3 x 20 mL). The white precipitate (0.97 g, 55 % yield) was dried overnight (room temperature). Selected area EDX analysis resulted in Ti : P ratio (expected 1 : 2) of 1 : 1.9. Found: C, 19.6; H, 5.4; N, 7.5. Calc. for MIL-91[Ti] ($TiO_{10.6}P_2C_6N_2H_{23.2}$): C, 17.6; H, 5.7; N, 6.9 %.

1.3. Capillary PXRD

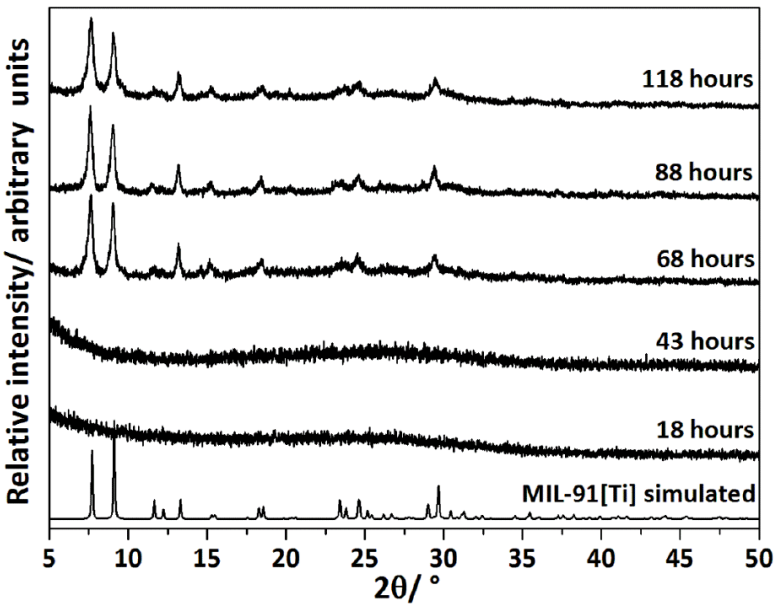

Figure S2. PXRD of samples taken periodically (after 18, 43, 68, 88, 118 hours) from an initial test run of the reflux solution.

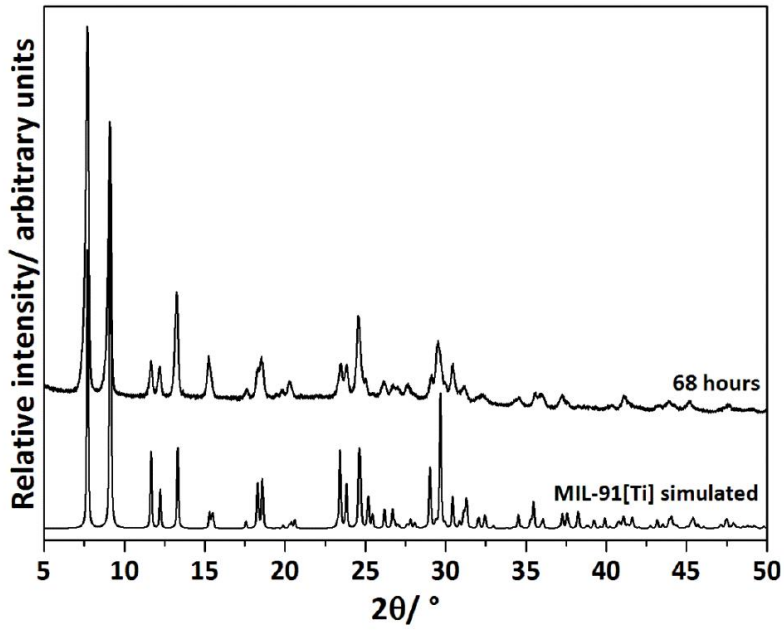

Figure S3. Overnight PXRD of MIL-91(Ti) reflux sample after 68 hours.

1.4 SEM image

Image S4 was obtained from the facility (FEGSEM Jeol JSM-6700F) at the University of St Andrews. The sample was sputter coated three times with gold in a Quorum Q150R ES (10 mA, 30 seconds and 2.3 tooling factor).

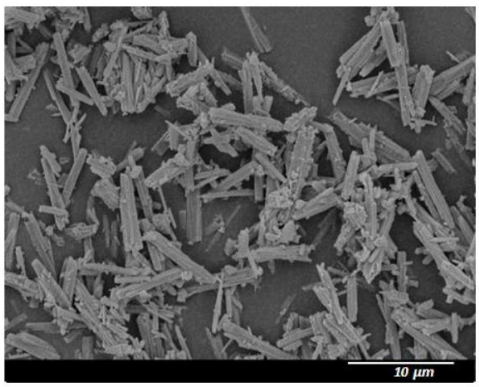

Image S4. SEM image of MIL-91[Ti] reflux sample after 68 hours.

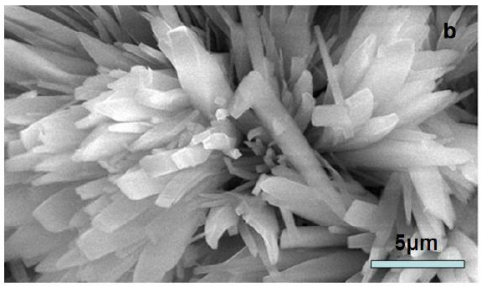

Image S5. SEM image of MIL-91[Ti] hydrothermal sample. (Courtesy of L. Gaberova, O. Schaef)

2. Characterization of MIL-91(Ti) prepared by hydrothermal and reflux synthesis methods

2.1. Thermogravimetric analysis

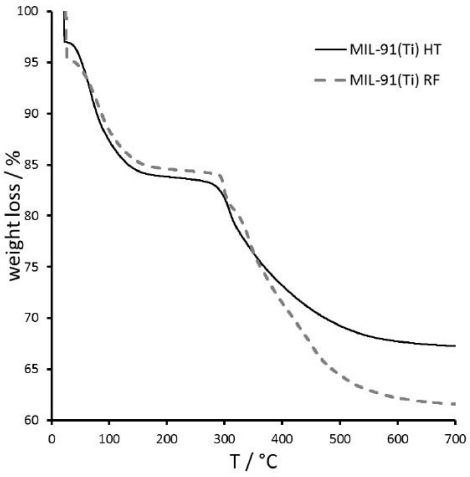

Figure S6. Thermogravimetric analysis of MIL-91(Ti) samples prepared under hydrothermal (HT) and reflux (RF) conditions.

The thermogravimetric analysis was carried out with a Q500 (TA Instruments) under air flow (100 mL/min) with a linear heating rate of 5 K / min (Figure S6).

An initial isotherm at room temperature under gas flow allows external species, such as physisorbed water, to be removed. For both samples, two main mass losses can be observed. Up to 200°C, adsorbed species within the pores are removed (probably water, and any other solvents). Under these conditions above 300°C, structure degradation occurs.

2.2. *Nitrogen physisorption at 77K*

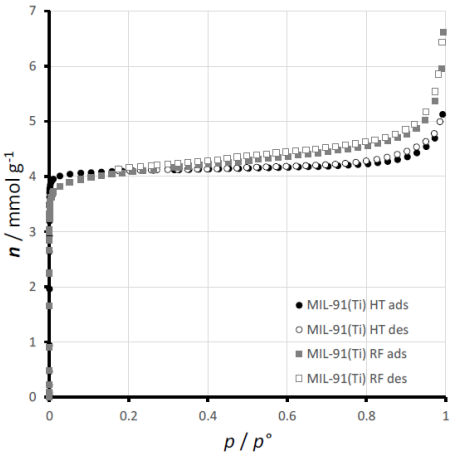

Figure S7. Nitrogen adsorption-desorption isotherms at 77 K obtained with MIL-91(Ti) samples prepared under hydrothermal (HT) and reflux (RF) conditions.

The nitrogen isotherms at 77 K (Figure S7) were obtained with a BelMAX apparatus (BEL Japan) after outgassing under secondary vacuum to 150°C. Both isotherms are of Type-I, indicative of microporosity. [2] The BET method was used to estimate an equivalent BET area [3] and the t-plot used to calculate the external surface area. This data analysis from these experiments is given in Table S1, below. It can be appreciated, in comparison with the data obtained from molecular modeling (Table S2), that maybe these samples could be improved in terms of activation to optimize the pore volume and BET area.

Table S1. Table of characteristics obtained from the nitrogen isotherms

Sample		BET area / $m^2\ g^{-1}$	BET range (p/p°)	C value	t-plot external surface area / $m^2\ g^{-1}$	pore volume at p/p°=0.1 / $cm^3\ g^{-1}$
MIL-91(Ti) (hydrothermal synthesis)	HT	382	4.10^{-6} to 0.01	68000	7	0.141
MIL-9-(Ti) (reflux synthesis)	RF	363	4.10^{-6} to 0.025	19000	23	0.138

Table S2. Pore diameter (Å), BET area ($m^2\ g^{-1}$), pore volume ($cm^3.g^{-1}$) calculated from the DFT-optimized crystal structures

MIL91(Ti)	d_{pore}	S_{BET}	V_{pore}
Simulation	3.9	403	0.16

2.3. Water adsorption at 25°C

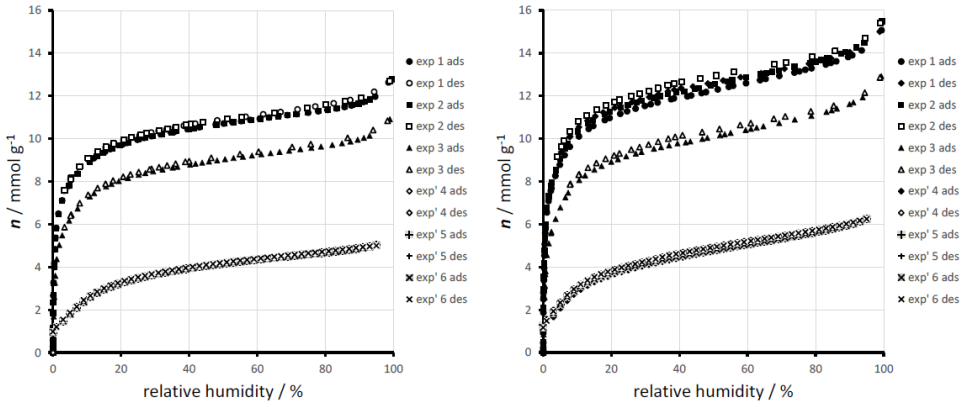

Figure S8. Water adsorption-desorption isotherms at 25°C obtained with MIL-91(Ti) samples prepared under hydrothermal (HT) (LEFT) and reflux (RF) (RIGHT) conditions.

Exp 1 was carried out after outgassing under secondary vacuum to 150+C. Exp 2 was a repeat experiment after again outgassing to 150°C. Exp 3 was carried out on the same sample after evacuation for 1 hour at 25°C. Exp' 4 was carried out on a fresh sample after outgassing to 80°C under nitrogen flow. Exp' 5 and exp'6 are repeated experiments after evacuation for 3 hours under nitrogen fglow at 25°C

Two series of water adsorption experiments were carried out on the two MIL-91(Ti) samples (Figure S8). A first series of experiments (exp 1, exp 2 & exp 3) were carried out using the BelMAX apparaus (BEL Japan) after initially outgassing under secondary vacuum to 150°C. Thse experiments are described in the main text. A second series of experiments (exp' 4, exp' 5 & exp' 6) were carried out under nitrogen flow at 25°C (Q5000, TA Instruments) after an initial outgassing under nitrogen flow to 80°C. These last three experiments took around 3 weeks to complete and the fact that a complete overlap occurs suggests a certain level of stability to water. This stability is confirmed by the unchanged XRD pattern obtained with the sample obtained under reflux after the water adsorption-desorption cycles (Figure S9).

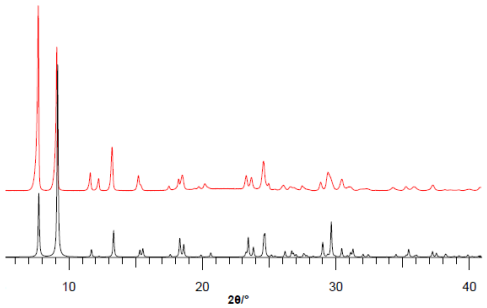

Figure S9. PXRD patterns of MIL-91(Ti) synthesised under reflux conditions (black, theoretical; red, after water adsorption cycling (over 3 weeks at 25°C) (λCu~1.5406 Å))

2.4. Adsorption calorimetry at 30°C

The microcalorimetry experiments were carried out at 303 K by means of a manometric dosing apparatus linked to the sample cell housed in a Tian-Calvet type microcalorimetrer. [4] This apparatus allows the simultaneous measurement of the isotherm and corresponding differential enthalpies of adsorption up to a maximum pressure of 40 bar in the present

study. Around 0.3 g of sample was used for these experiments. An error of ± 1 kJ mol^{-1} can be considered for these experiments. The gases used for the adsorption were obtained from Air Liquide and were of 99.998% purity or better. Prior to adsorption experiments, the samples were placed under a secondary vacuum and were heated to 150°C for 16 hours.

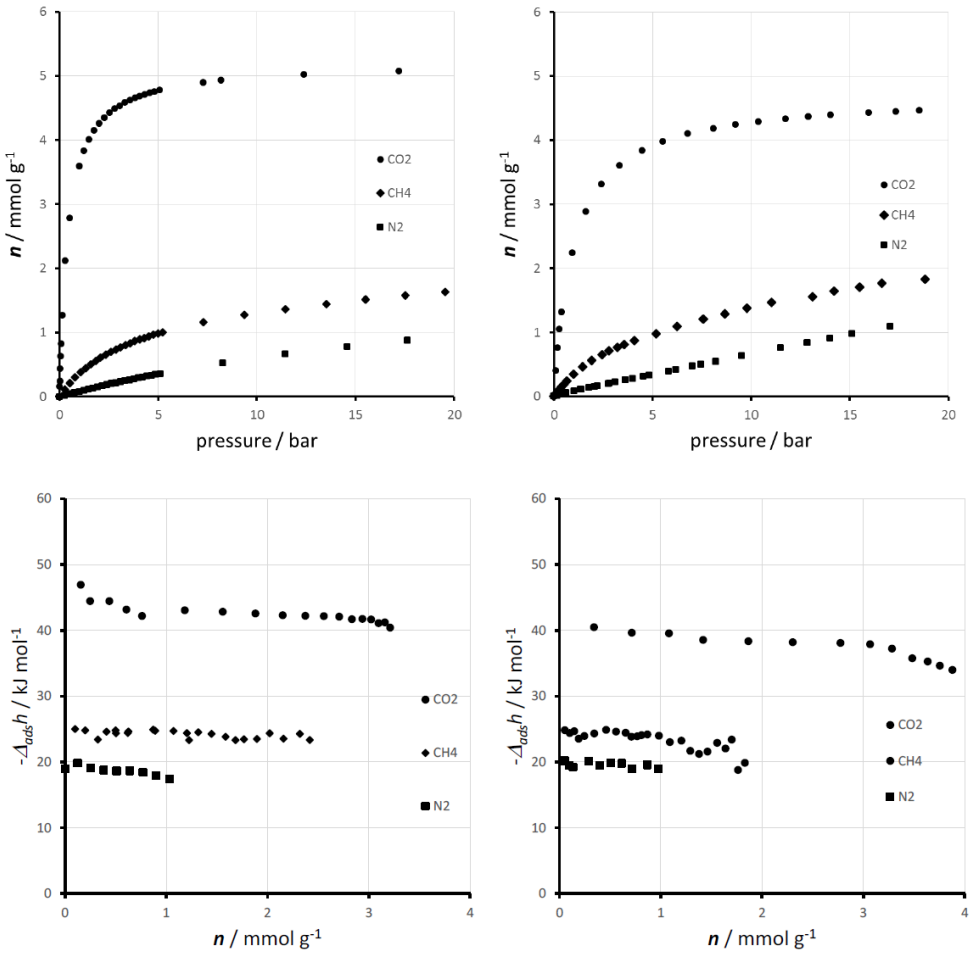

Figure S10. Comparison of the adsorption isotherms (top) and corresponding adsorption enthalpies as a function of the coverage collected by microcalorimetry (bottom) at 303 K for CO_2, CH_4, N_2 in MIL-91(Ti) prepared by hydrothermal synthesis (left) and reflux protocol (right).

3. Adsorption gravimetery at 30°C on the MIL-91(Ti) sample obtained by hydrothermal synthesis, Synchrotron PXRD during CO_2 adsorption, and comparison with molecular simulations

3.1. Adsorption gravimetry

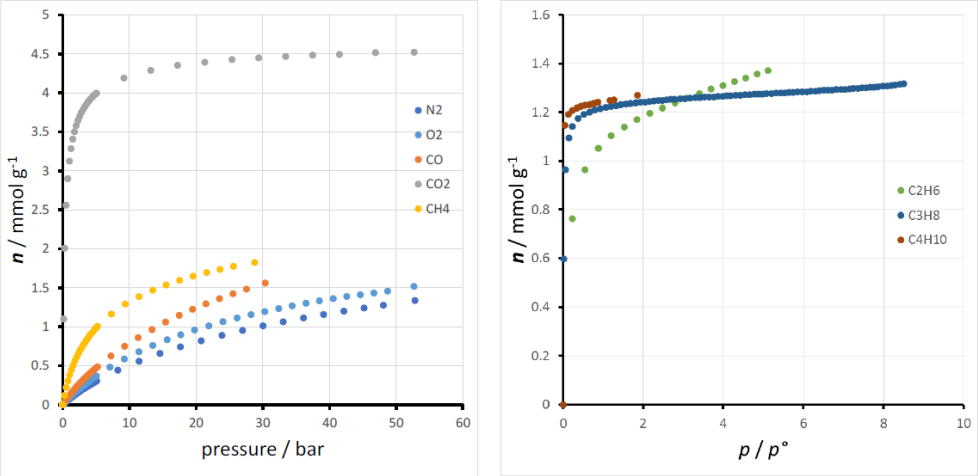

Figure S11. Gravimetric uptakes of a series of gases obtained at 30°C.

To complete the study with CO_2, CH_4 and N_2, the adsorption of other gases have equally been carried out (Figure S11). The isotherms were obtained using an adsorption gravimetric set-up constructed *in house* based on a Rubotherm balance and homemade dosing system. [5] The MIL-91(Ti) (hydrothermal synthesis) sample was outgassed to 150°C, overnight under secondary vacuum.

Several comparisons can be made. There is a slightly higher uptake of oxygen with respect to nitrogen. The adsorption of carbon monoxide is also relatively low and below that of methane. Propane and butane show very similar uptakes which are much lower than CO_2. The adsorption of ethane shows increasing uptake up to the point where the experiment is stopped (5 bars) which suggest that pore filling is not complete.

3.2. *Synchrotron PXRD during CO_2 adsorption*

In situ synchrotron power diffraction experiments were carried out at the BM01A station at the Swiss-Norwegian Beamlines at the European Synchrotron radiation facility (Grenoble, France). The data were collected on 0.5-mm quartz capillaries filled with sample and attached to a built gas manifold. [6] The sample capillary was placed at 300 mm from a MAR345 image plate detector and an X-ray wavelength of 0.694018 Å was used. The data were integrated using Fit2D program (Dr. A. Hammersley, ESRF) and a calibration measurement of a NIST LaB6 standard sample. The patterns were indexed using the Dicvol software. [7] Le Bail fits were then performed with Fullprof2k software package. [8] The carbon dioxide (Alphagaz, France, 99.9999% purity) was introduced using point by point dosing up to the desirable pressure. Equilibrium was assumed when two successively measured diffraction patterns were identical.

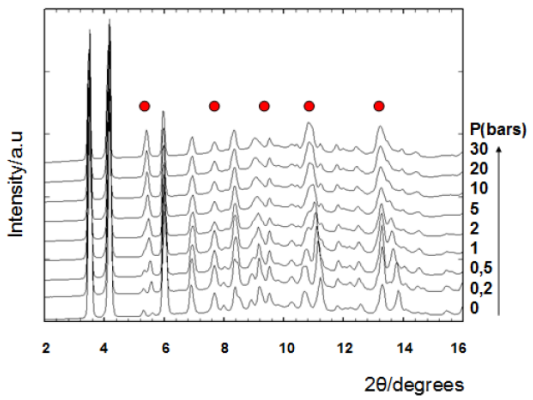

Figure S12. Diffractograms for various CO_2 pressures (303K) measured on MIL-91(Ti) (λ=0.694018Å). The first diffractogram, at p=0, corresponds to the dehydrated phase.

The diffraction patterns (Figure S12) show little change in position with loading and no large changes in the patterns is observed. Modeling the unit cell of the empty and filled structure suggest a 1.6% change in unit cell volume.

3.3. *Comparison of the adsorption properties between different MOFs*

Table S3. Comparison of initial adsorption energies of CO_2, N_2 and CH_4 obtained at 30°C by microcalorimetry with various MOFs. Differences in enthalpies, which are discussed in the main text, are equally given.

Sample	CO_2	CH_4	N_2	$\Delta[CO_2\text{-}CH_4]$	$\Delta[CO_2\text{-}N_2]$	reference
CAU-13(Al)	37.3	29.7	25.2	7.6	12.1	[9]
CPO-27(Ni)	38.0	20.0	22.0	18.0	16.0	[10]
CuBTC	29.1	20.9	15.2	8.2	13.9	[11]
MIL-100(Fe)	38.4	14.8	21.7	23.6	16.7	[13]
MIL-101(Cr)	62.8	17.0	33.6	45.8	29.3	[13]
MIL-102(Cr)	47.0	29.0	44.0	18.0	3.0	[14]
MIL-125(Ti)	26.2	17.4	14.5	8.8	11.7	[15]
MIL-125(Ti)_NH_2	29.7	19.3	16.6	10.4	13.1	[15]
MIL-140A(Zr)	29.7	17.3	18.0	12.4	11.7	[16]
MIL-47(V)	21.5	15.0	/	6.5	/	[17]
MIL53(Al)_NH_2	41.5	23.0	12.0	18.5	29.5	[18]
MIL-68(Ga)	28.3	24.5	/	3.8	/	[19]
MIL-91(Al)	38.5	24.2	/	14.3	/	[20]
MIL-91(Ti) HT	**47.1**	**23.8**	**19.5**	**23.3**	**27.6**	**This work**
MIL-91(Ti) RF	**40.4**	**23.5**	**20.1**	**16.9**	**23.5**	**This work**
NaX	49.0	19.4	18.0	29.6	31.0	[21]
ScBDC	31.8	16.7	/	15.1	/	[22]
ScBDC_NH_2	45.3	17.3	/	28.0	/	[23]
STA-12(Ni)	33.7	13.6	/	20.2	/	[24]
Takeda 5A	33.8	24.0	16.4	9.8	17.4	[21]
UiO-66(Zr)	26.4	15.9	14.8	10.5	11.7	[25]
UiO-66(Zr)_BTeC	35.0	22.8	18.0	12.2	17.1	[26]
UiO-66(Zr)_NH_2	36.0	19.7	17.7	16.3	18.2	[27]

Table S4. Comparison of working capacities for CO_2 / N_2 and CO_2 / CH_4 separations at 30°C.

Sample	WC[CO_2/N_2] / $cm^3.cm^{-3}$ (0-1 bar, 303K)	WC[CO_2/CH_4] / $cm^3.cm^{-3}$ (1-15 bar, 303K)	Ref
CAU-13(Al)	35	13.4	[9]
CPO-27(Ni)	175	21.1	[10]
CuBTC	180	14.1	[11]
MIL-100(Fe)	136.2	15.5	[13]
MIL-101(Cr)	112	16.14	[13]
MIL-102(Cr)	73	37.12	[14]
MIL-125(Ti)	153	4.9	[15]
MIL-125(Ti)_NH_2	129	9.8	[15]
MIL-140A(Zr)	69.45	4.2	[16]
MIL-47(V)	162	/	[17]
MIL53(Al)_NH_2	10.1	18.8	[18]
MIL-68(Ga)	75	1.6	[19]
MIL-91(Al)	31.5	15.5	[20]
MIL-91(Ti) HT	**50.9**	**43.5**	**This work**
NaX	70.5	/	[21]
ScBDC	73.1	8.27	[22]
ScBDC_NH_2	31.7	5.1	[23]
STA-12(Ni)	242	/	[24]
Takeda 5A	110	11.25	[21]
UiO-66(Zr)	175.2	7.1	[25]
UiO-66(Zr)_BTeC	87.06	13.68	[27]
UiO-66(Zr)_NH_2	125	22.31	[27]

Table S5. Comparison of the selectivities for CO_2 / N_2 and CO_2 / CH_4 (1) Calculated in this study.

Sample	Selectivity CO_2 / N_2 (15% CO_2, 0-1 bar, 303 K)	Selectivity CO_2 / CH_4 (1-50% CO_2, 15 bar, 303 K)
CAU-13(Al)	22 *	3 *
CPO-27(Ni)	13 *	7 *
CuBTC	19 *	7 *
MIL-100(Fe)	47 *	14 *
MIL-101(Cr)	53 *	16 *
MIL-102(Cr)	41 *	12 *
MIL-125(Ti)	12 *	5 *
MIL-125(Ti)_NH_2	18 *	6 *
MIL-140A(Zr)	10 *	4 *
MIL-47(V)	/	4 *
MIL53(Al)_NH_2	877 *	7 *
MIL-68(Ga)	12 *	4 *
MIL-69(Al)	120 *	4 *
MIL-69(Fe)	6 *	/
MIL-91(Al)	68 *	57 *
MIL-91(Ti) HT	**150 ***	**79 ***
NaX	/	212 *
ScBDC	40 *	9 *
ScBDC_NH_2	120 *	17 *
STA-12(Ni)	/	15 *
Takeda 5A	19 *	4 *
UiO-66 (Zr)	12 *	6 *
UiO-66(Zr)_Br	30 *	6 *
UiO-66(Zr)_BTeC	30 *	9 *
UiO-66(Zr)_NH_2	37 *	11 *

- * Calculated using IAST

Table S6. Comparison of the selectivities for CO_2 / N_2 and CO_2 / CH_4 (2) Obtained from the open literature

Name	Mixture	%CO_2 in mixture	Selectivity	Calculation method	Ref
MIL-68(Al)_NH_2	CO_2/CH_4	50	45	GCMC	[19]
MIL-125(Ti)	CO_2/CH_4	50	4.5	Measurement	[15]
MIL-125(Ti)_NH_2	CO_2/CH_4	50	7	VSM / GCMC	[15]
MIL-53(Al) Basolie A100	CO_2/CH_4	50	7	Measurement	[28]
MIL-100(Cr)	CO_2/CH_4	50	6-8	Measurement	[29]
eea-MOF-4	CO_2/CH_4	50	4	IAST	[30]
rtl-MOF-2	CO_2/CH_4	50	7-8	IAST	[30]
SIFSIX-2Cu-i	CO_2/CH_4	50	50	Measurement	[31]
MIL-100(V)	CO_2/CH_4	50	140	IAST	[32]
eea-MOF-4	CO_2/N_2	10	18	IAST	[30]
rtl-MOF-2	CO_2/N_2	10	38	IAST	[30]
SIFSIX-2Cu-i	CO_2/N_2	10	72	Measurement	[31]
Eu fcu-MOF	CO_2/N_2	10	82	IAST	[33]
SIFSIX-3-Cu	CO_2/N_2	10	Infinite	IAST	[34]
$Zn_4(pydc)_4(DMF)_2{\cdot}3DMF$	CO_2/N_2	15	42	IAST	[35]
MOF-508b	CO_2/CH_4	50	3.5	Measurement	[36]
MIL-53(Al)	CO_2/CH_4	50	7-8	Measurement	[37]
MIL-53(Cr)	CO_2/CH_4	50	4-14	Measurement	[38]
Cu-BTC	CO_2/CH_4	50	6-9	Measurement	[39]
IFP-5 (Imidazolate Framework Postdam)	CO_2/CH_4	50	7.5	Measurement	[40]
ZIF-176	CO_2/CH_4	50	2.5-6.5	Measurement	[41]
UiO-66 (Zr) BTEC	CO_2/N_2	15	56	Measurement	[42]
Ni/DOBDC	CO_2/N_2	15	38	Measurement	[43]
USTA-16	CO_2/CH_4	50	30	Measurement	[44]
USTA-16	CO_2/N_2	15	315	Measurement	[44]

4. Mixture adsorption

In order to acquire mixture adsorption equilibrium data, we used a home-made volumetric apparatus as shown in Figure S13.

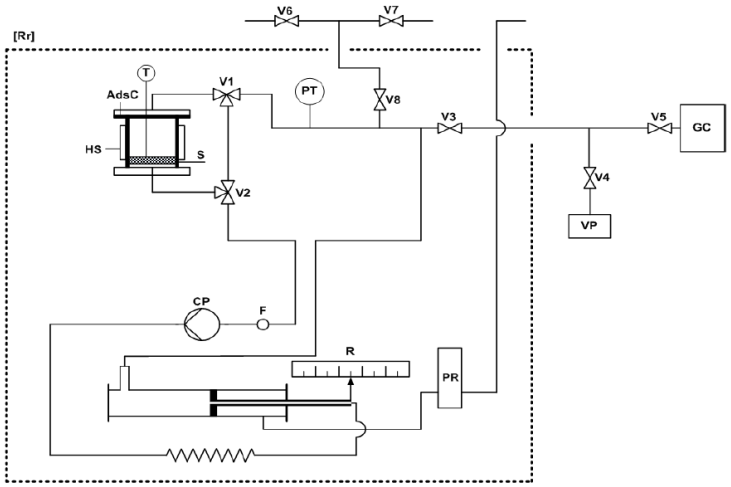

1.

Figure S13. Mixture adsorption volumetric apparatus: (AdsC) adsorption cell; (PT) pressure transmitter; (V1 and V2) three way manual valves; (V3 to V8) manual valves; (T) Pt-100 temperature probe; (F) filter; (HS) in-situ heating system; (VP) vacuum pump; (CP) circulation pump; (R) ruler; (PR) pressure regulator; (GC) gas chromatograph; (Rr) refrigerated room.

The volumetric co-adsorption measurements [45, 46] is based on the principle of pure compound manometric apparatus. [47-49]

The apparatus allows the measurement of isobaric-isothermal mixture adsorption equilibria in a pressure range from 1 to 10 bar and in a temperature range from 298 K to 353 K. In this apparatus, a cylinder piston provides a variable volume in order to fix the pressure on a set point value during the adsorption. A circulation pump was used to homogenize the mixture and a gas chromatograph coupled with a thermal conductivity detector, provided by Agilent (GC 6850), allowing the determination of the gas mole fraction of each component in the mixture. The pressure transmitter provided by Endress-Hauser (0 – 10 bar Cerabar PMP 731) with an uncertainty of 0.1% of the full scale. The adsorbent was outgassed by maintaining it under primary vacuum at ambient temperature for one hour and then by heating the

adsorption cell up to 453 K for 8 hours. After that, the gas mixture was introduced in the installation without going through the adsorption cell. When both equilibrium and homogenization were reached (checked by constant values of both pressure and composition obtained using a chromatography device), the gas composition was determined after at least six chromatographic analyses and the pressure and temperature values were recorded. With these measurements and the installation volume, we can determine the adsorption amounts of the two components in each mixture using a mixture equation of state. [50]

In the second phase, the adsorption cell was controlled to be accessible via two three-way valves. During the adsorption, the pressure was maintained on a set point value by adapting the installation volume using the cylinder piston. When the equilibrium was reached, the pressure, temperature and volume of the system were recorded and the gas composition was determined by at least six chromatographic analyses. Knowing the total installation volume, the amount of each component in the gas phase after adsorption can be calculated using the mixture equation of state adopted by Myers and Prausnitz. [51]

The adsorbed amounts were determined by the differences between the number of moles in4 the gas phase before and after adsorption. Finally, the adsorbent was outgassed to repeat the above procedures with a new composition of the initial mixture.

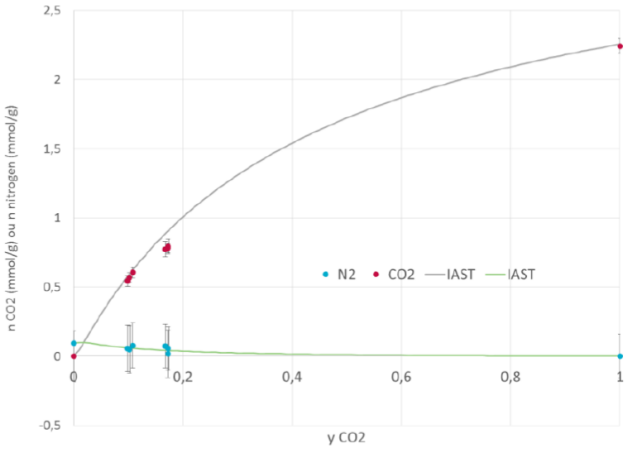

Figure S14 : Mixture adsorption results obtained with approximately 10% and 17% CO_2 in N_2 at a total pressure of 1 bar and at 30°C. Experiments at each concentration were repeated. The straight line fit corresponds to the IAST prediction from single gas data.

Table S7 : CO_2 / N_2 selectivites measured and calculated at 30°C

Total pressure	% CO_2	Measured selectivity	Average measured selectivity	Selectivity calculated by IAST
1 bar	0,108	65		
	0,099	89	86	87
	0,102	106		
	0,173	67	60	99
	0,168	53		
3 bars	0,103	89		
	0,117	61	73	130
	0,118	69		
	0,176	60		
	0,169	49	51	153
	0,168	45		

Table S8 : CO_2 / CH_4 selectivites obtained at 30°C

Total pressure	% CO_2	Measured selectivity	Selectivity calculated by IAST
1 bar	50	18	31
5 bars	50	15	74
13 bars	50	13	

5. Quasi-Elastic neutron scattering measurements

The QENS experiments were carried out with the time-of-flight spectrometer IN6, at the Institut Laue-Langevin, Grenoble, France. The incident neutron energy was set to 5.12 Å, corresponding to an incident energy of 3.12 meV. Scattered neutrons were analyzed as a function of angle and flight time. Groupings of detectors were made to avoid the Bragg peaks of MIL-91 and to obtain satisfactory counting statistics, the wave-vector transfer, *Q*, ranging from 0.29 to 1.19 $Å^{-1}$. The elastic energy resolution could be fitted by a Gaussian function, with a half-width at half-maximum varying from 39 μeV at small *Q* to 46 μeV at large *Q*.

The framework of MIL-91 was deuterated, in order to measure the signal from weak scatterers such as CO_2 and N_2. The MIL-91 sample was activated by pumping at 423 K. The powder was transferred inside a glovebox into a slab-shaped aluminum container, which was connected to a gas inlet system allowing in situ adsorption. After recording the scattering of the empty MOF, a loading of 0.7 N_2 per unit cell were measured at 220 K. After these measurements, N_2 was evacuated by pumping at 370 K. A CO_2 loading of 1.2 molecules per unit cell were then studied at 300 K.

6. Molecular simulations .

6.1. Computational Methods

6.1.1. Microscopic models for the host framework.

The experimental dry (hereafter MIL-91(Ti)_Dry) [51] and CO_2 loaded MIL-91(Ti) (hereafter MIL-91(Ti)_CO_2) crystal structures were preliminary saturated by the missing hydrogen atoms using Materials Studio software package (Figure S15). While the hydrogen atoms were added to the carbon atoms of the organic linkers, the mobile proton in the environment of the piperazine bis methylphosphonate groups, labeled as PO···H···N, was arbitrary placed on the O atoms. The MIL-91(Ti)_dry crystal structure was then geometry optimized at the Density Functional Theory (DFT) level using the CP2K package [53-55]. These calculations included only the relaxation of the positions of the atoms of the framework while the unit cell parameters were fixed at the values previously determined by PXRD analysis (Table S9) [52]. The PBE [56] functional was combined with the use of Gaussian basis

set and pseudopotential. For Carbon, Oxygen, Nitrogen, Phosphorous and Hydrogen, a triple zeta (TZVP-MOLOPT) basis set was considered, while a double zeta (DZVP-MOLOPT) was applied for Titanium. [57] The pseudopotentials used for all of the atoms were those derived by Goedecker, Teter and Hutter. [57] The van der Waals effects interactions were taken into account via the use of semi-empirical dispersion corrections as implemented in the DFT-D3 method. [59]

The crystal structure of the CO_2 loaded MIL-91(Ti) material experimentally refined at 30 bar and 235 K was first loaded with 4.5 mmol g^{-1} of CO_2 (i.e. the saturation capacity obtained experimentally at 303 K and 30 bar) and then fully relaxed (both atomic positions of the framework and the CO_2 molecules, and cell parameters) at the DFT-level keeping the same functional and basis set used for the MIL-91(Ti)_Dry structure. The optimized unit cell parameters for this structure labelled as MIL-91(Ti)_CO_2 are reported in Table S9.

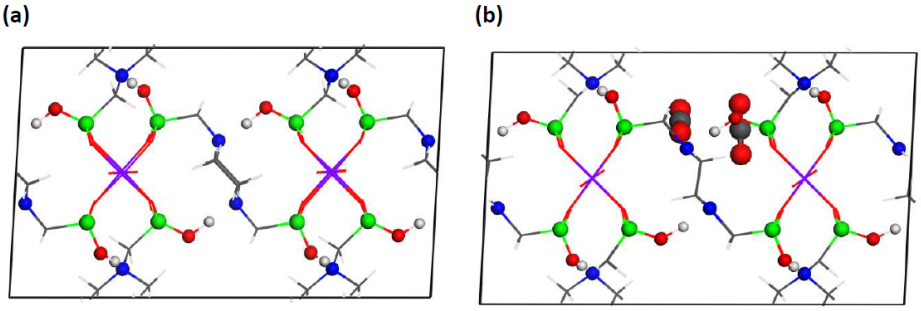

Figure S15. The simulation box considered for the DFT calculations (1×2×1 unit cells) viewed along *b* direction for MIL-91(Ti)_Dry (a) and MIL-91(Ti)_CO_2 (b), where identified interaction sites are represented by ball, and the rest of the atoms are in line representation. (Gray, carbon; white, hydrogen; blue, nitrogen; green, phosphorous; red, oxygen; violet, titanium).

Table S1_9. Comparison of the experimental and simulated unit cell parameters/symmetry obtained for the dry and the CO_2 loaded MIL-91(Ti) structures.

	Space Group	**a (Å)**	**b (Å)**	**c (Å)**	**β(°)**	**V (Å³)**
MIL-91(Ti)_CO_2						
Simulation	C2/m	18.7250	7.1760	11.8960	99.607	1576.05
Experimental	C2/m	19.4146	7.0716	11.4834	92.779	1574.73

MIL-91(Ti)_Dry						
Experimental	C2/m	19.0599	7.0499	11.3049	93.100	1516.86

The Mulliken [60] partial charges for all atoms of the MOF framework were further obtained by performing a single point energy calculation on the MIL-91(Ti)_Dry structure using Dmol^3 (see Tables S10, Figure S17). These calculations were also based on the PBE functional and the double numerical basis set containing polarization functions (DNP). [61]

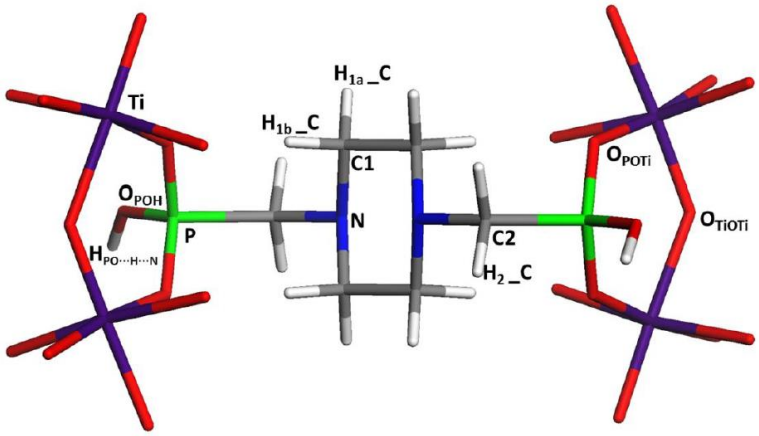

Figure S16. Labels of the atoms for the organic and the inorganic parts of the MOF structure. The color code is the same as the one reported in Figure S15.

Table S10. Mulliken partial charges for the atoms in MIL-91(Ti)

Atom types	C1	C2	H_{1a}_C	H_{1b}_C	H_2_C	$H_{PO\cdots H\cdots N}$	N	O_{TiOTi}	O_{POTi}	O_{POH}	P	Ti
Charge (e)	-0.115	-0.371	0.246	0.154	0.159	0.405	-0.432	-0.734	-0.748	-0.794	1.465	1.404

6.1.2. Force fields

The interaction between the MIL-91(Ti) framework and the guest species (CO_2, CH_4 and N_2) was modelled using the sum of a 12-6 Lennard-Jones (LJ) contribution and a Coulombic term. The Universal force field (UFF) was adopted to describe the LJ parameters for the atoms of the MOF framework (see Figure S16 and Table S11). [62] CO_2 was represented using the 3-

sites charged EPM2 model [63] while CH_4 and N_2 were treated by the uncharged united atom (UA) models.[64]

Table S11. LJ potential parameters for the framework atoms in the MIL-91(Ti) according to the notation introduced in Figure S15. The attractive van der Waals force exerted by the Ti atom is not considered as this atom is screened by its oxygen environment. The same kind of interaction is neglected for the mobile proton in the environment of the piperazine bis methylphosphonate groups to be consistent with our previous studies on MIL-91(Al) [20]

Atom type	σ (Å)	ε/k_B (K)
C1	3.431	52.838
C2	3.431	52.838
H_{1a}_C	2.571	22.141
H_{1b}_C	2.571	22.141
H_2_C	2.571	22.141
$H_{PO\cdots H\cdots N}$	2.571	0.000*
N	3.261	34.721
O_{OTiP}	3.118	30.193
O_{OTiO}	3.118	30.193
O_{PO}	3.118	30.193
P	3.695	153.482
Ti	2.829	0.000*

6.2. GCMC Simulations

Grand Canonical Monte Carlo (GCMC) simulations were carried out at 303 K for MIL-91(Ti)_CO_2 in order to predict the single component adsorption of CO_2 and their binary CO_2/N_2 and CO_2/CH_4 mixtures while the crystal structure for MIL-91(Ti)_Dry has been selected for the investigation of the single components CH_4 and N_2. These calculations were performed using the Complex Adsorption and Diffusion Simulation Suite (CADSS) code. [65] The simulation box was made of 24 (2×4×3) unit cells of MIL-91(Ti)_CO_2. Short-range dispersion forces were truncated at a cutoff radius of 12 Å while the interactions between unlike force field centers *a* and *b* were treated by means of the Lorentz-Berthelot

combination rules; $\varepsilon_{ab} = \sqrt{\varepsilon_a \varepsilon_b}$, $\sigma_{ab} = (\sigma_a + \sigma_b)/2$, where ε_a and σ_a are the LJ parameters for the species *a*. The long-range electrostatic interactions were handled using the Ewald summation technique.

The fugacities for each adsorbed species at a given thermodynamic condition were computed with the Peng-Robinson equation of state (EoS). [66] For each state point, 2×10^8 Monte Carlo steps have been used for both equilibration and production runs. Three types of trials were considered for the molecules: (i) translation or rotation, (ii) creation/deletion and (iii) exchange of molecular identity. The adsorption enthalpy at low coverage (Δh) for each gas was calculated through configurational-bias Monte Carlo simulations performed in the NVT ensemble using the revised Widom's test particle insertion method. [67] Additionally, in order to gain insight into the configurational distribution of the adsorbed species in MIL-91(Ti), some additional data were calculated at different pressure including the radial distribution functions (RDF) between the guests and the host.

6.3. Computational predictions

The cell dimension of the DFT-simulated CO_2 loaded MIL-91(Ti) structure (V = 1576.05 Å^3) is in very good agreement with the one (V = 1574.73 Å^3) determined from the *in situ* X-ray diffraction (Table S9). It can be seen from Figure S15 that the piperazine linkers are reoriented upon CO_2 adsorption resulting into a more tight packing of the adsorbate molecules. These DFT simulations also reveal that the CO_2 molecules are preferentially located in the vicinity of the phosphonate and piperazine linker (i.e. zwitterionic site of this solid), consistent with the experimental observation. The CO_2 molecule aligned in such a way that carbon atom of C═O group (C_{CO2}) interact with O atom present in the environment of the PO group and the N atom (PO···H···N), giving a C_{CO2} - $O_{PO\cdots H\cdots N}$ distance of 2.68 Å, similar to the one obtained experimentally (see Figure S17). Such a spatial distribution leads the oxygen atoms of CO_2 (O_{CO2}) to interact with the H atom in the PO···H···N environment, ($H_{PO\cdots H\cdots N}$) with a distance of 3.42 Å.

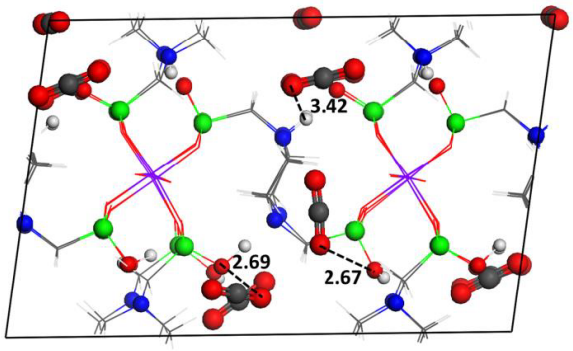

Figure S17. The CO_2 loaded MIL-91(Ti) crystal structure (MIL-91(Ti)_CO_2) determined by DFT geometry optimization. The color code is the same as the one reported in Figure S1.

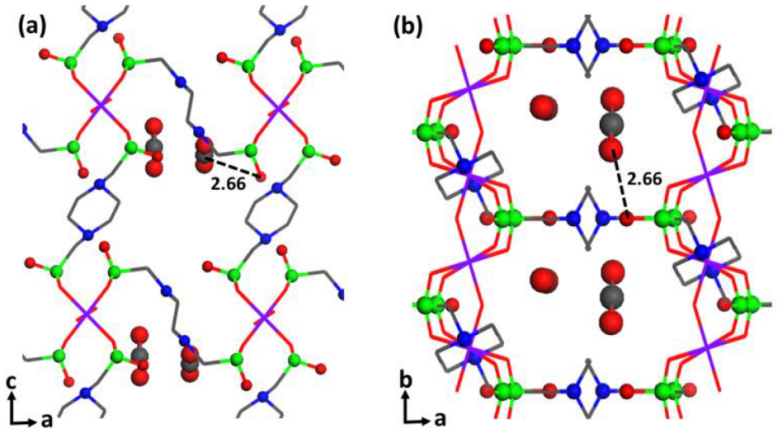

Figure S18. Illustration of the preferential ordered arrangement of CO_2 experimentally obtained from the refinement of the XRPD patterns. Views along *b* (a) and *c* (b) vector directions. The color code is the same as the one reported in Figure S15.

This validated MIL-91(Ti)_CO_2 model was further used to predict the single component adsorption isotherms at 303 K by means of GCMC simulations. We have obtained a good agreement between the simulated and the experimental adsorption isotherms at the entire pressure range [0-35 bar]. Analysis of the adsorption mechanism evidences that the simulated CO_2 distribution matches well with the one obtained by DFT calculations. The radial distribution function (RDF) analysis (Figure S19) for CO_2 in MIL-91(Ti)_CO_2 shows that

the mean distances between C_{CO2} - $O_{PO\cdots H\cdots N}$ and O_{CO2} - $H_{PO\cdots H\cdots N}$ are 2.71 and 3.48 Å, respectively. As expected, the preferential interactions occur between CO_2 and the zwitterionic sites of the solid, where H atom present in the environment of the PO group and the N atom (PO···H···N). Such a geometry (Figure S20) is consistent with has been already reported for the Al version, i.e. MIL-91(Al), [20] with the presence of a dual acid-base interaction: the O atom of CO_2 interacting with an acid site, the C atom playing the role of an electron acceptor centre towards the oxygen basic site. [67, 68]

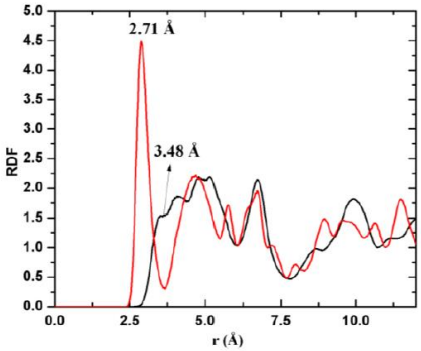

Figure S19: Radial Distribution Functions (RDF) for the pairs C_{CO2} - $O_{PO\cdots H\cdots N}$ (red) and $H_{PO\cdots H\cdots N}$ - O_{CO2} (black) extracted from the GCMC simulations at 303 K for MIL-91(Ti)_CO_2 with two CO_2 molecule per unit cell.

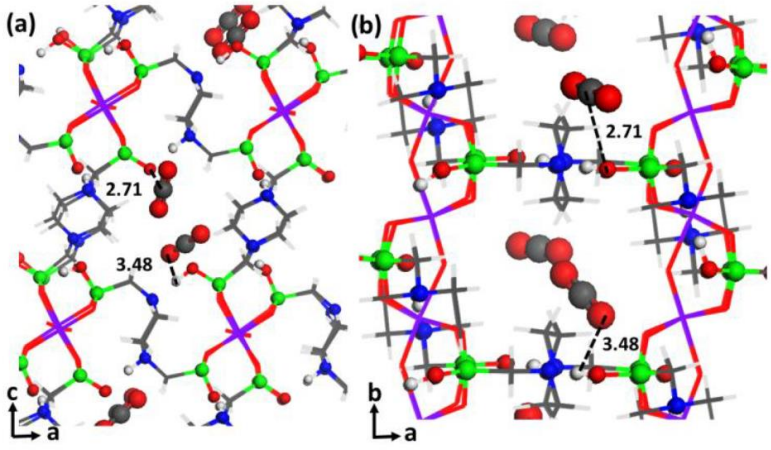

Figure S20. GCMC simulated arrangements of CO_2 molecules obtained using MIL-91(Ti)_CO_2 models at 303 K viewed along *b* (a) and *c* (b) vector. The snapshots were taken from the

simulations performed for 2 CO_2 molecules per unit cell adsorbed framework. The color code is the same as the one reported in Figure S15.

This preferential arrangement of CO_2 within the pores leads to a relatively high simulated adsorption enthalpy at low coverage (-44 kJ/mol) which is validated by microcalorimetry measurements (Figure S21).

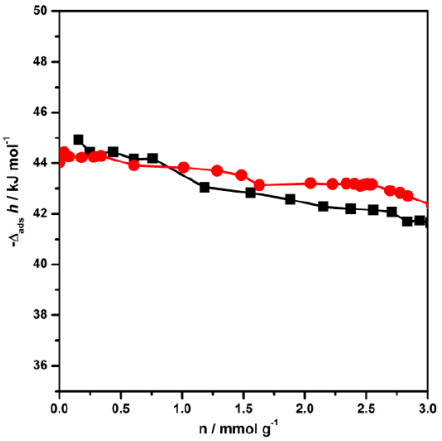

Figure S21. Experimental (black squares) and simulated (red circles) enthalpy obtained by GCMC simulation with CO_2 on MIL-91(Ti) at 303 K.

The binary mixture study was further carried out for CO_2/N_2 (gas phase composition: 0.05/0.95; 0.10/0.90 and 0.15/0.85) and CO_2/CH_4 (gas phase composition: 05/0.5) by means of GCMC simulations performed at 303 K and 313 K. Analysis of the co-adsorption mechanism for both mixtures evidenced that CO_2 molecules are mainly distributed in the same region of the pores than in the single components, i.e. in the vicinity of the PO···H···N sites, mean distances between C_{CO2} and $O_{PO\cdots H\cdots N}$ for CO_2/N_2 and CO_2/CH_4 systems at 2.69 and 2.72 Å, respectively. Similarly, the distances between O_{CO2} and $H_{PO\cdots H\cdots N}$ are 3.49 Å and 3.46 Å for co-adsorption of CO_2 in the presence of N_2 and CH_4, respectively (Figure S22). Furthermore, both N_2 and CH_4 in are distributed in the centre of the pore with very characteristic host/guest distances over 3.2 Å (N_2 - PO···H···N : Figure S23; CH_4 - PO···H···N : Figure S24). Therefore, the CO_2 molecules are interacting strongly with the PO···H···N sites, while the two other gases, N_2 and CH_4, are away from these adsorption sites and fit at the centre of pore.

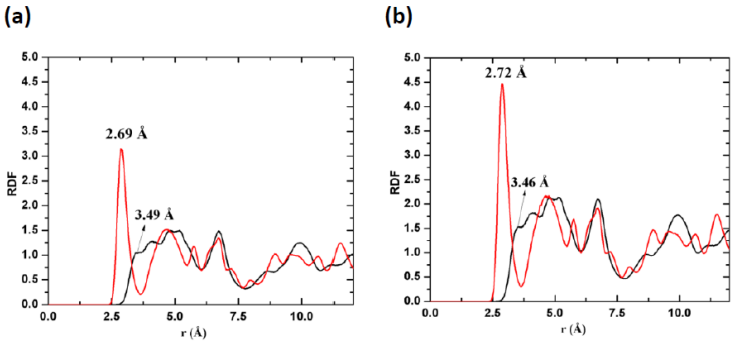

Figure S22: RDF for the pairs $\mathbf{C}_{CO2}$ - $\mathbf{O}_{PO\cdots H\cdots N}$ (red) and $\mathbf{H}_{PO\cdots H\cdots N}$ - $\mathbf{O}_{CO2}$ (black) extracted from the GCMC simulations at 303 K for the mixture with N_2 (a) and CH_4 (b).

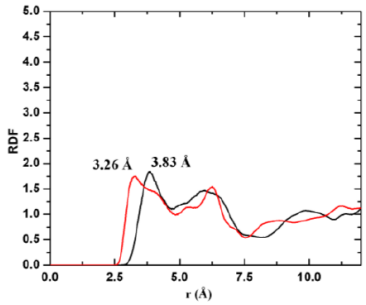

Figure S23: RDF for the pairs N_2 - $\mathbf{O}_{PO\cdots H\cdots N}$ (red) and $\mathbf{H}_{PO\cdots H\cdots N}$ - N_2 (black) extracted from the GCMC simulations at 303 K for the mixture with CO_2.

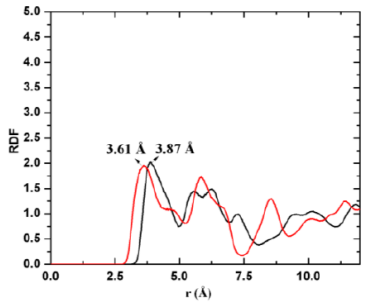

Figure S24: RDF for the pairs CH_4 - $\mathbf{O}_{PO\cdots H\cdots N}$ (red) and $\mathbf{H}_{PO\cdots H\cdots N}$ -CH_4 (black) extracted from the GCMC simulations at 303 K for the mixture with CO_2.

The separation performances of MIL-91(Ti) for the two mixtures of interest, i.e. CO_2/N_2 and CO_2/CH_4, were predicted as a function of the pressure. These data are reported in Figure S25

and Figure S26. The simulated selectivities obtained at 1 bar and 303 K for both gas mixtures is very similar to the experimental results, i.e. $S(CO_2/N_2)$ = 122.0, 122.0, and 118.5 for molar concentrations CO_2/N_2= 0.05/0.95, 0.10/0.90 and 0.15/0.85, respectively, and $S(CO_2/CH_4)$=40.9 at molar concentration of CO_2/CH_4 = 0.5/0.5.

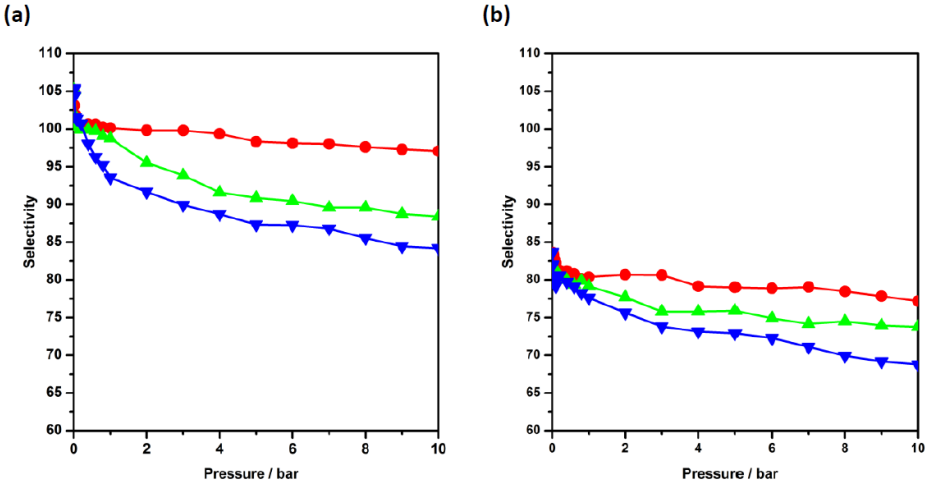

Figure S25. Simulated CO_2/N_2 selectivity at 303 K (a) and 313 K (b) for a molar composition of the gas phase: 0.05/0.95 (CO_2/N_2, red circles), 0.10/0.90 (CO_2/N_2, blue up triangles) and 0.15/0.85 (CO_2/N_2, blue down triangles).

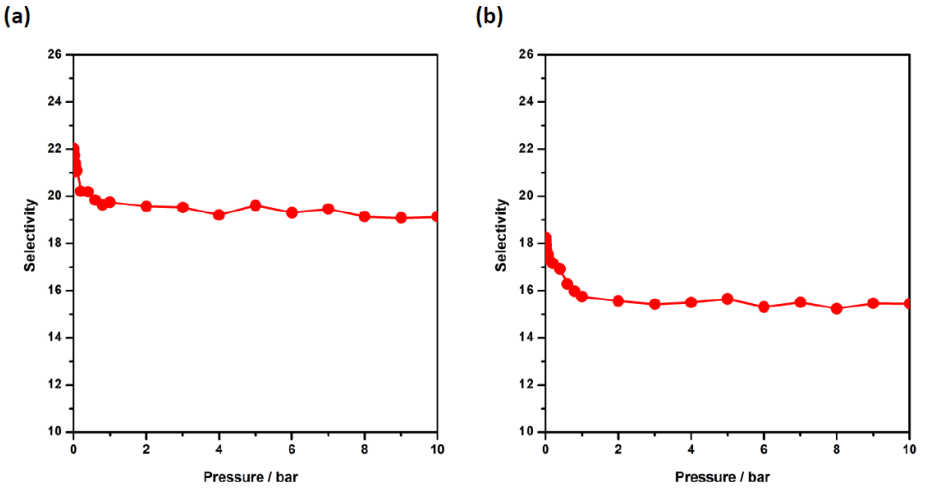

Figure S26. Simulated CO_2/CH_4 Selectivity at 303 K (a) and 313 K (b) for an equimolar composition of the gas phase.

References

[1] K. Moedritzer and R.R. Irani, *J. Org. Chem*., **1966**, 31, 1603-1607.

[2] 10.1515/pac-2014-1117 (2015) (Physisorption of gases, with special reference to the evaluation of surface area and pore size distribution (IUPAC Technical Report))

[3] J. Rouquerol, F. Rouquerol, P. Llewellyn, G. Maurin, K.S.W. Sing*, Adsorption by Powders and Porous Solids,* 2nd Edition, Academic Press, Oxford, **2014**, 646 pages. ISBN–13: 978–0080970356.

[4] P.L. Llewellyn, G. Maurin, *C. R. Chim*., **2005**, 8, 283.

[5] A. Ghoufi, L. Gaberova, J. Rouquerol, D. Vincent, P. L. Llewellyn, G. Maurin, *Micro. Meso. Mater*.**, 2009**, 119(1-3), 117-128.

[6] P. L. Llewellyn, P. Horcajada, G. Maurin, T. Devic, N. Rosenbach, S. Bourrelly, C. Serre, D. Vincent, S. Loera-Serna, Y. Filinchuk, G. Férey, *J. Amer. Chem. Soc*., **2009**, 131(36), 13002-13008.

[7] A. Boultif, D. Loüer, *J. Appl. Crystallogr*., **1991**, 24, 987–993.

[8] J. Rodriguez-Carvajal, in *Collected Abstracts of Powder Diffraction Meeting*; Toulouse, France, **1990**; 127-128.

[9] F. Niekiel, J. Lannoeye, H. Reinsch, A. S. Munn, A. Heerwig, I. Zizak, S. Kaskel, R. I. Walton, D. de Vos, P. *Llewellyn, A.* Lieb, G. Maurin, N. Stock, *Inorg. Chem*.**, 2014**, 53(9), 4610-4620.

[10] W. L. Queen, M. R. Hudson, E. D. Bloch, J. A. Mason, M. I. Gonzalez, J. S. Lee, D. Gygi, J. D. Howe, K. Lee, T. A. Darwish, M. James, V. K. Peterson, S. J. Teat, B. Smit, J. B. Neaton, J. R. Long, C. M. Brown, *Chem. Sci*., **2014**, 5, 4569.

[11] L. Grajciar, A. D. Wiersum, P. L. Llewellyn, J.-S. Chang, P. Nachtigall, *J. Phys. Chem. C***, 2011**, 115(36), 17925-17933.

[12] J. W. Yoon, Y. K. Seo, Y. K. Hwang, J.-S. Chang, H. Leclerc, S. Wuttke, P. Bazin, A. Vimont, M. Daturi, E. Bloch, P. L. Llewellyn, C. Serre, P. Horcajada, J. M. Greneche, A. E. Rodrigues, G. Férey, *Angew. Chem. Int. Ed*., **2010**, 49(34), 5949-5952.

[13] P. L. Llewellyn, S. Bourrelly, C. Serre, A. Vimont, M. Daturi, L. Hamon, G. De Weireld, J.-S. Chang, D.-Y. Hong, Y. K. Hwang, S. H. Jhung, G. Férey, G., *Langmuir*, **2008**, 24(14), 7245-7250.

[14] D. Damasceno-Borges, M. Prakash, N.A. Ramsahye, P.L. Llewellyn, S. Surblé, P. Horcajada, C. Serre, G. Maurin, *Mol. Sim*., **2015**, 41(16-17), 1357-1370.

[15] S. Vaesen, V. Guillerm, Q. Y. Yang, A. D. Wiersum, B. Marszalek, B. Gil, A. Vimont, M. Daturi, T. Devic, P. L. Llewellyn, C. Serre, G. Maurin, G. De Weireld, *Chem. Comm*., **2013**, 49(86), 10082-10084.

[16] G. D. Pirngruber, L. Hamon, S. Bourrelly, P. L. Llewellyn, E. Lenoir, V. Guillerm, C. Serre, T., *ChemSusChem*, **2012**, 5(4), 762-776.

[17] P. L. Llewellyn, S. Bourrelly, C. Vagner, N. Heymans, H. Leclerc, A. Ghoufi, P. Bazin, A Vimont, M. Daturi, T. Devic, C. Serre, G. Weireld, G. Maurin, *J. Phys. Chem. C*, **2013**, 117(2), 962-970.

[18] S. Couck, J. F. M. Denayer, G. V. Baron, T. Remy, J. Gascon, F. Kapteijn, *J. Amer. Chem. Soc*., **2009**, 131(18), 6326-6327.

[19] Q. Yang, S. Vaesen, M. Vishnuvarthan, F. Ragon, C. Serre, A. Vimont, M. Daturi, G. De Weireld, G. Maurin, *J. Mater. Chem*., **2012**, 22(20), 10210-10220

[20] P. L. Llewellyn, M. Garcia-Rates, L. Gaberova, S. R. Miller, T. Devic, J. C. Lavalley, S. Bourrelly, E. Bloch, Y. Filinchuk, P. A. Wright, C. Serre, A. Vimont, G. Maurin, *J. Phys. Chem. C*, **2015**, 119, 4208-4216.

[21] A. D. Wiersum, J.-S. Chang, C. Serre, P. L. Llewellyn, *Langmuir*, **2013**, 29(10), 3301-3309.

[22] S. R. Miller, P. A. Wright, T. Devic, C. Serre, G. Férey, P. L. Llewellyn, R. Denoyel, L. Gaberova, Y. Filinchuk, *Langmuir*, **2009**, 25(6), 3618-3626.

[23] R. S. Pillai, V. Benoit, A. Orsi, P. L. Llewellyn, P. A. Wright, G. Maurin, *J. Phys. Chem. C*, **2015**, 119 (41), 23592–23598.

[24] S. R. Miller, G. M. Pearce, P. A. Wright, F. Bonino, S. Chavan, S. Bordiga, I. Margiolaki, N. Guillou, G. Férey, S. Bourrelly, P. L. Llewellyn, *J. Amer. Chem. Soc*., **2008**, 130(47), 15967-15981.

[25] Q. Yang, A. D. Wiersum, H. Jobic, V. Guillerm, C. Serre, P. L. Llewellyn, G. Maurin, *J. Phys. Chem. C*, **2011**, 115(28), 13768-13774.

[26] F. Ragon, B. Campo, Q. Yang, C. Martineau, A. D. Wiersum, A. Lago, V. Guillerm, C. Hemsley, J. F. Eubank, M. Vishnuvarthan, F. Taulelle, P. Horcajada, A. Vimont, P. L. *Llewellyn,* M. Daturi, S. Devautour-Vinot, G. Maurin, C. Serre, T. Devic, G. Clet, *J. Mater. Chem. C*, **2015**, 3(7), 3294-3309.

[27] Q. Yang, A. D. Wiersum, P. L. Llewellyn, V. Guillerm, C. Serre, G. Maurin, *Chem. Comm.*, **2011**, 47(34), 9603-9605.

[28] N. Heymans, S. Vaesen, G. De Weireld, *Micro. Meso. Mat.*, **2012**, 154, 93–99.

[29] L. Hamon, N. Heymans, P. L. Llewellyn, V. Guillerm, A. Ghoufi, S. Vaesen, G. Maurin, C. Serre, G. De Weireld, G. D. Pirngruber, *Dalton Trans.*, **2012**, 41, 4052.

[30] Z. Chen, K. Adil, L. J. Weseliński, Y. Belmabkhouta, M. Eddaoudi, *J. Mater. Chem. A*, **2015**, 3, 6276-6281.

[31] P. Nugent, Y. Belmabkhout, S. D. Burd, A. J. Cairns, R. Luebke, K. Forrest, T. Pham, S. Ma, B. Space, L. Wojtas, M. Eddaoudi, M.J. Zaworotko, *Nature*, **2013**, 495, 80–84.

[32] J. Yang, Y. Wang, L. Li, Z. Zhang, J. Li, *J. Coll. Interf. Sci.*, **2015**, 456, 197–205.

[33] D.-X. Xue, Y. Belmabkhout, O. Shekhah, H. Jiang, K. Adil, A. J. Cairns, M. Eddaoudi, *J. Amer. Chem. Soc.*, **2015**, 137, 5034-5040.

[34] O. Shekhah, Y. Belmabkhout, Z. Chen, V. Guillerm, A. Cairns, K. Adil, M. Eddaoudi, *Nat. Comms.*, **2014**, 5, 4228.

[35] S. R. Ahrenholtz, C. Landaverde-Alvarado, M. Whiting, S. Lin, C. Slebodnick, E. Marand, A. J. Morris, *Inorg. Chem.*, **2015**, 54(9), 4328-4336.

[36] P. S. Bárcia, L. Bastin , E. J. Hurtado, J. A. C. Silva, A. E. Rodrigues, B. Chen, *Sep. Sci. Tech.*, **2008**, 43, 3494-3521

[37] V. Finsy, L. Ma, L. Alaerts, D.E. De Vos, G.V. Baron, J.F.M. Denayer, *Micro. Meso. Mater.*, **2009**, 120, 221–227

[38] L. Hamon, P. L. Llewellyn, T. Devic, A. Ghoufi, G. Clet, V. Guillerm, G. D. Pirngruber, G. Maurin, C. Serre, G. Driver, W. van Beek, E. Jolimaître, A. Vimont, M. Daturi, G. Férey, *J. Amer. Chem. Soc.*, **2009**, 131, 17490–17499

[39] Lomig Hamon, Elsa Jolimaître, and Gerhard D. Pirngruber, *Ind. Eng. Chem. Res.*, **2010**, 49(16), 7497–7503

[40] F. Debatin, J. Möllmer, S. S. Mondal, K. Behrens, A. Möller, R. Staudt, A. Thomas, H.-J. Holdt, *J. Mater. Chem.*, **2012**, 22, 10221

[41] D. Peralta, G. Chaplais, A. Simon-Masseron, K. Barthelet, G. D. Pirngruber, *Micro. Meso. Mater.*, **2012**, 153, 1–7.

[42] Q. Yang, S. Vaesen, F. Ragon, A. D. Wiersum, D. Wu, A. Lago, T. Devic, C. Martineau, F. Taulelle, P. L. Llewellyn, H. Jobic, C. Zhong, C. Serre, G. De Weireld, G. Maurin, *Angew. Chem. Int. Ed.*, **2013**, 52,

[43] J. Liu, J. Tian, P. K. Thallapally, B. P. McGrail, *J. Phys. Chem. C*, **2012**, 116(17):9575 – 9581.

[44] S. C. Xiang, Y. B. He, Z. J. Zhang, H. Wu, W. Zhou, R. Krishna and B. L. Chen, *Nat. Commun.*, **2012**, 3, 954.

[44] W. K. Lewis, E. R. Gilliland, R. Chertow, W. P. Cadogan, *Ind. Eng. Chem.*, **1950**, 42, 1319-1326.

[45] B. K. Kaul, *Ind. Eng. Chem. Res.*, **1987**, 26, 928-933.

[46] A. S. Joy, *Vacuum*, **1953**, 3, 254-278.

[47] K. Berlier, J. Bougard, M. G. Olivier, *Meas. Sci. Technol.*, **1995**, 6, 107.

[48] Y. Belmabkhout, M. Frère, G. De Weireld, *Meas. Sci. Technol.*, **2004**, 15, 848-858.

[49] O. Kunz, R. Klimeck, W. Wagner, M. Jaeschke, GERG Technical Monographie 15 Fortschr.-Ber. VDI, VDI-Verlag, Düsseldorf, **2007**.

[50] A. L. Myers, J. M. Prausnitz, *AIChE J.*, **1965**, 11, 121.

[51] Serre, C.; Groves, J.A.; Lightfoot, P.; Slawin, A.M.Z.; Wright, P.A.; Stock, N.; Bein, T.; Haouas, M.; Taulelle, F.; Férey, *Chem. Mater.*, **2006**, 18, 1451-1457.

[52] J. VandeVondele, M. Krack, F. Mohamed, M. Parrinello, T. Chassaing and J. Hutter, *Comput. Phys. Commun*, **2005**, 167, 103.

[53] J. VandeVondele and J. Hutter, *J. Chem. Phys*., **2003**, 118, 4365.

[54] G. Lippert, J. Hutter and M. Parrinello, Theor Chem Acc, 1999, 103, 124; (d) B. G. Lippert, J. H. Parrinello and Michele, *Mol. Phys*., **1997**, 92, 477.

[55] J.P. Perdew, Y. Wang, *Phys. Rev. B*, **1986**, 33, 8822.

[56] J. VandeVondele, J. J. Hutter, *Chem. Phys*., **2007**, 127, 114105.

[57] S. Goedecker, M. Teter, J. Hutter, *Phys. Rev. B*., **1996**, 54, 1703.

[58] S. Grimme, J. Antony, S. Ehrlich, H. Krieng, *J. Chem. Phys*., **2010**, 132, 154104.

[59] R.S. Mulliken, *J. Chem. Phys*., **1955**, 23, 1833.

[60] W.J. Hehre, J.A. Ditchfield, J.A. Pople, *J. Chem. Phys*., **1972**, 56, 2257.

[61] A. K. Rappé, C. J. Casewit, K. S. Colwell, W. A. Goddard III, W. M. Skiff, *J. Amer. Chem. Soc*. **1992**, 114, 10024.

[62] J. G. Harris, K. H. Yung, *J. Phys. Chem*., **1995**, 99, 12021.

[63] M. G. Martin, J. I. Siepmann, *J. Phys. Chem. B*, **1998**, 102, 2569.

[64] Q. Yang, C. Zhong, *J. Phys. Chem. B*, **2006**, 110, 17776–17783.

[65] D.-Y. Peng, D. B. Robinson, *Ind. Eng. Chem. Fundam*., **1976**, 15, 59.

[66] T. J. H. Vlugt, E. García-Pérez, D. Dubbeldam, S. Ban, S. Calero, *J. Chem. Theory Comput*., **2008**, 4, 1107-1118.

[67] G. D. Pirngruber, P. Raybaud, Y. Belmabkhout, J. Čejka, A. Zukal, *Phys. Chem. Chem. Phys*., **2010**, 12, 13534–13546.

[68] P. Nachtigall, M. R. Delgado, D. Nachtigallova, C.O. Arean, *Phys. Chem. Chem. Phys*., **2012**, 14, 1552–1569.

Annex E

Journal of Materials Chemistry A

ARTICLE

A promising metal-organic framework (MOF), MIL-96(Al) for CO_2 separation under humid conditions

Received 00th January 20xx,
Accepted 00th January 20xx

DOI: 10.1039/x0xx00000x

www.rsc.org/

Virginie Benoit,[a] Nicolas Chanut,[a] Renjith S. Pillai,[b] Marvin Benzaqui,[c,d] Isabelle Beurroies,[a] Sabine Devautour-Vinot,[b] Christian Serre,[c] Nathalie Steunou,[d] Guillaume Maurin,[b] Philip L. Llewellyn *[a]

Abstract. The CO_2 adsorption uptake and enthalpies with MIL-96(Al) were assessed in the presence of up to 40% relative humidity using via both experiment and simulation. Interestingly at 10% relative humidity, the water equilibrated in the pores of this MOF profers a significant increase in affinity for CO_2 at 0.2 bar, which is associated with a limited decrease in capacity. This study suggests that at medium RH, water and CO_2 are able to adsorb in different regions of the structure. Indeed, such behaviour is explained by the preferential adsorption of H_2O in cavities containing more hydrophilic groups including Al(1)-$H_2O_{terminal}$, Al(3')-$OH_{terminal}$ and Al(3)-$H_2O_{terminal}$ while CO_2 adsorbs in the remaining, less hydrophilic cavities containing μ_2-OH groups. This highlights the interest of using materials with this variety in pore chemistry as one way forward for CO_2 capture in the presence of contaminants such as water.

Introduction

In order to abate growing concentrations of greenhouse gases, specifically CO_2, in the atmosphere from anthropogenic sources, carbon capture and storage (CCS) processes are required with various technologies proposed for pre-combustion, post-combustion and oxy-combustion.[1] To gain an idea, in 2012 the CO_2 emissions from coal- and natural gas-fired power plants were of 11.1 Gt, representing almost 30% of total global emissions[2] Post-combustion capture is attractive to reduce CO_2 emissions from flue gas streams as it can retrofit easier than in the case of either pre-combustion or oxy-combustion.[1] Several separation methods can be used for post-combustion capture such as chemical absorption, physical adsorption, cryogenic separation or membranes.[3] Adsorption-based processes using porous materials show many advantages with respect to cost reduction, corrosion, toxicity and regeneration over conventional absorption techniques using amine solvents for example.[4] There exist a wide variety of physisorbent materials that can be used for adsorption-based gas separation: Activated Carbons, Zeolites, Alumina, Silica gels and Metal-Organic Frameworks (MOFs).[5] Over the past decade, many studies have been dedicated to this latter family of materials. Indeed, MOFs are used in several fields such as catalysis, drug delivery, gas storage and gas separation or purification.[6-9]

MOFs are composed of metal or metal cluster nodes linked to each other through organic moieties to build –one, -two or –three dimensional structures. They are well-defined crystalline porous structures and show many interesting properties such as high specific surface area and pore volume, low density, whilst some of them are flexible in response to external stimuli.[9-13] From the variety of di-valent (Cu, Zn, Mg, etc); tri-valent (Al, Cr, Ga, etc), tetra-valent (V, Zr, Ti, etc) metals and organic linkers (carboxylate, imidazolate, phosphonate, pyrazolate), the possibilities to synthesize new crystalline phases are almost infinite.

The length and functionalization of linker and the presence of coordinatively unsaturated metal sites (CUS) can be features allowing to tailor the physical and chemical properties such as pore size, pore shape and surface polarity.[9] This consequently affects adsorption capacity, adsorption kinetics and/or separation selectivity. Thus, a large spectrum of MOFs can be synthesized for a given application with the problem then of how to choose the most optimal materials. Indeed, CO_2 adsorption capacities of MOFs are comparable or higher than many reference materials. [9] For instance one can compare the current commercially used adsorbents including Zeolite NaX 7.8 mmol.g^{-1} (302K/ 30 bar)[14] and active Carbon Maxsorb 36 mmol.g^{-1} (298K/ 50 bar) [15] with MOF materials such as DUT-49 46 mmol.g^{-1} (298K/ 50 bar) [16]; MOF-210 54 mmol.g^{-1} (298K/ 50 bar)[17]; HKUST-1 14 mmol.g^{-1} (303K/ 20 bar)[18]and MIL-100(Cr) 40 mmol.g^{-1} (303K/ 50 bar).[19]

[a] *Aix-Marseille Univ, CNRS, MADIREL, Marseille, France.*
[b] *Institut Charles Gerhardt Montpellier, Université de Montpellier, CNRS, ENSCM, Place E. Bataillon, 34095 Montpellier cedex 05, France.*
[c] *PSL Res Univ, FRE CNRS 2000, Ecole Super Phys & Chim Ind Paris, Ecole Normale Super, Inst Mat Poreux Paris, 75005 Paris, France.*
[d] *Institut Lavoisier de Versailles, UMR CNRS 8180, Université de Versailles St Quentin en Yvelines, Université Paris Saclay, 45 avenue des Etats-Unis 78035 Versailles Cedex. France.*

† Electronic supplementary information (ESI) available: These include the experimental details and complementary figures and tables. See DOI: 10.1039/x0xx00000x

While MOFs have outstanding properties for CO_2 adsorption at such high pressures, this is often less the case at low pressures where CO_2 capture from post-combustion occurs. Furthermore, one critical property to consider when examining adsorbent is their stability and structural behaviour under humidity. In the case of moisture-sensitive materials, they can only be used to capture CO_2 in industrial processes with the condition that the gases are dried beforehand. However, excess drying of the gas stream is energy intensive. Thus, the search for materials able to capture significant amounts CO_2 in the presence of limited amounts of humidity is an ongoing research topic as water vapour is ubiquitous to various industrial flue gases. Considering the more traditional adsorbents, the effect of water on CO_2 adsorption capacity and selectivity does not seem to be significant for many activated carbons [22] although their CO_2 capacities at low pressures remains limited. Conversely for zeolites, where CO_2 uptake below 1 bar can be significant, the effect of humidity has a strong negative effect [23-25] leading to a significant drop of uptake and/or selectivity. Indeed, carbon dioxide and water are polar molecules which most often directly compete for the same hydrophilic adsorption sites in zeolite, with the result that they often highly favour water to the detriment of CO_2.

A wide range of behaviour can be found for MOFs. Indeed, for some of these materials, water can enhance CO_2 adsorption capacity and selectivity such as for HKUST-1 [26] or MIL-100(Fe) [27] but in the presence of specific amount of water, i.e. 4% and 40% respectively. Remarkably, the small pore MOF KAUST-8 containing coordinatively unsaturated sites and fluorine moieties has been shown to concomitantly adsorb H_2O and CO_2 on two distinct sites. [28] However, the majority of MOFs show a significant drop of their CO_2 uptake in the presence of humidity and this emphasizes again that CO_2 and H_2O compete for similar adsorption sites and that it is H_2O which is prevalent in most cases.

In order to identify optimal MOFs for CO_2 capture in the presence of humidity, a screening protocol has been developed [29] and was performed on 46 MOFs and reference materials including activated carbons and zeolites. A plot of water affinity (via ln[Henry constant]) versus CO_2 capacity loss in the presence of humidity gives an overall straightline correlation with some outliers of interest. Of these, the small pore Al trimesate based-MIL-96(Al) [30,31] (Table S3 for textural parameters) with a 3D-structure illustrated in Figure 1 stands out due to its disproportionally high CO_2 adsorption capacity in the presence of humidity. The structure of this MOF was recently refined [30] and consists of (i) a subunit with an oxo-centered trimer {Al(1)} of equivalent Al(1) octahedra which are coordinated to bridging trimesates and μ_3-O ligands, and (ii) a further building unit consisting of a 2D hexagonal network containing 18-membered rings built by sinusoidal chains of aluminum octahedra. These chains contain two non-equivalent types of aluminum, Al(2) and Al(3), which are coordinated to four and two trimesate oxygen atoms and two or three bridging μ_2-hydroxo moieties respectively. The hexagonal 18-membered rings are interconnected to each other by a further variety of trimer. This {Al(3)} trimer is composed of three Al(3) octahedra that are corner-linked by μ_2-OH groups. The connection of the {Al(1)} trimer with the 2D network of Al(2) and Al(3) octahedra through the trimesate ligands results in a 3D framework (see Figure 1). Further analysis reveals the presence of one Al(3) and two equivalent Al(3)' sites in each {Al(3)} trimer of the dehydrated MIL-96(Al). The oxo-core of this formula unit is composed of one μ_3-O, twelve μ_2-OH and nine terminal oxygen ligands (OH or H_2O). These terminal groups correspond to four hydroxyl groups and five water molecules, where both Al(1) and Al(3) centers are coordinated to terminal water molecules while Al(3)' is covalently attached to a hydroxyl group (Figure 1).

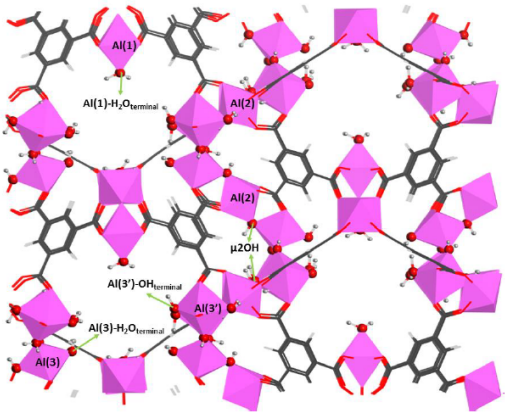

Figure 1. MIL-96(Al) structure (1×1×1 unit cells) viewed along the a direction (grey, carbon; white, hydrogen; red, oxygen; pink, aluminium). The labels of the atoms correspond to those previously reported for the revisited MIL-96(Al) structure. [31]

A previous experimental investigation highlighted that MIL-96(Al) may be of interest for low pressure CO_2 capture and suggested that CO_2 and H_2O do not compete for the same adsorption sites.[29] Further, under the conditions of this study, the CO_2 uptake of the fully activated MIL-96(Al) was above those of other MOFs and even comparable to that of Zeolite 13X.[29] Although the amount of CO_2 adsorbed on the pre-humidified MIL-96(Al) decreased compared to the uptake in the dry state, this still remains attractive for CO_2 capture unlike the majority of the other materials chosen for this study. Considering these points, MIL-96(Al) may appear as a promising candidate for CO_2 recovery in the presence of humidity. The present paper aims to take this initial screening study further and concentrate solely on the CO_2 uptake in the presence of humidity in the case of MIL-96(Al). Here, notably calorimetry experiments are exploited both under static and dynamic conditions of gas introduction. The experimental data is complemented by a computation effort based on Grand Canonical Monte Carlo (GCMC) simulations to model the adsorption behaviour of this MOF with respect to H_2O as single component and in a ternary mixture with both CO_2 and N_2.

Experimental

The MIL-96(Al) nanocrystals were synthesized following the procedure previously published.[30] Trimesic acid (2.1 g, 10 mmol) was poured into a 125 mL Teflon-lined steel autoclave with 40 mL of deionized water under vigorous stirring. @Aluminium nitrate nonohydrate (18.76 g, 50 mmol) was dissolved in 30 mL of deionized water and poured onto the ligand solution. The mixture was stirred for 10 min and heated to 180°C for 24 hours under autogenous pressure. A yellowish powder was obtained after filtration, which was washed with deionized water and dried in air at room temperature. Traces of remaining trimesic acid and nitrates were removed by washing the solid with 500 mL of an ethanol/H_2O mixture (1/1). A white powder (m=2.77 g) was finally obtained after filtration and drying in air at room temperature.

Thermogravimetric analysis (TGA). The thermal stability of MIL-96(Al) was assessed using a thermogravimetric analyzer 'TGA Q500' from TA instruments. Among modes included in this device, the ramp mode was chosen (5°C/ min up to 700°C) under inert gas (argon) with a first isotherm step for 30 minutes at room temperature.

Water vapor adsorption at 30°C. The hydrophilicity/ hydrophobicity of the adsorbent surface was probed by water vapor adsorption at 303 K (Belsorb-max, MicrotracBEL). Around 48 mg of the MIL-96(Al) was outgassed at 373 K (ramp of 1°C/min) for 16 hours under secondary vacuum (10^{-6} mbar). The water adsorption measurement was limited at a relative pressure p/p° = 0.989.

Static CO_2 adsorption manometry coupled with microcalorimetry. CO_2 adsorption isotherms and associated enthalpies at 303 K were obtained in static mode (in contrast with the dynamic mode – see below) with the MIL-96(Al) in its outgassed and pre-humidified states. Prior to each experiment, the MIL-96(Al) was outgassed *ex situ* at 423K for 16h under a secondary vacuum (10^{-3} mbar). To pre-humidify the sample, MIL-96(Al) was placed in water vapour-saturated atmosphere for two days at ambient temperature (i.e, 100 % of relative humidity) prior to transfer to the adsorption cell. Around 0.250 g of sample was used for the CO_2 adsorption / desorption experiments to a maximum pressure of 10 bar at 303 K. The manometric device introduces distinct doses of gas to the sample and a Tian-Calvet type microcalorimeter directly measures the energy change. Each dose of adsorptive to the sample is accompanied by an exothermic thermal effect, until equilibrium is reached. The heat flow with time is integrated to provide a pseudodifferential molar enthalpy of adsorption for each dose. For repeat runs, a short, 5-minute primary vacuum was carried out to remove CO_2 and H_2O from the dosing system. Carbon dioxide (99.998% purity) was provided from Air Liquide (Alphagaz, France).

For calculations, the calorimetric cell (including the relevant amounts of adsorbent and gas) is considered as an open system. In this procedure, it is important to consider that the gas is introduced reversibly. Under these conditions it is possible to determine the pseudo-differential enthalpy of adsorption $\Delta_{ads}\dot{h}$, via the following expression:

$$\Delta_{ads}\dot{\boldsymbol{h}} = \left(\frac{\boldsymbol{dQ_{rev}}}{\boldsymbol{dn^a}}\right)_{\boldsymbol{T}} + \boldsymbol{V_c}\left(\frac{\boldsymbol{dp}}{\boldsymbol{dn^a}}\right)_{\boldsymbol{T}}$$

Here dQ_{rev} is the heat reversibly exchanged with the surrounding environment at temperature T, as measured by the calorimeter, dn^a is the amount adsorbed after introduction of the gas dose, dp is the pressure increase or decrease and V_c is the dead space volume of the sample cell within the calorimeter itself (thermopile). The term $V_c dp$ can be obtained via blank experiments. Errors in this calculation can be estimated at ± 1 kJ mol^{-1}.

CO_2/N_2/H_2O flow adsorption microcalorimetry. A dynamic adsorption experiment was used as previously developed[27] to assess the impact of water vapour during CO_2 adsorption on porous solids. Here the sample can be pre-equilibrated with water at a controlled relative humidity and the CO_2 uptake can equally occur in the presence of this controlled RH. The sample is placed inside a Tian-Calvet microcalorimeter in order to directly follow the heat effects occurring during the adsorption process under flow. Details of this particular experimental set-up and protocols can be found in the SI.

Computational methods. The crystal structure of MIL-96(Al) was taken from our recently reported paper as well as the partial charges for all the atoms of the MOF framework.[30] GCMC simulations were performed on this MIL-96(Al) structure using atomistic force fields. The interaction between the MIL-96(Al) framework and the guest species (H_2O, CO_2 and N_2) was modelled using the sum of a 12-6 Lennard-Jones (LJ) contribution and a Coulombic term. The Universal force field (UFF) was adopted to describe the LJ parameters for all atoms of MIL-96(Al) (Table S1).[32] Regarding the guest molecules, (i) water was represented by using the TIP4P model, [33,34] (ii) CO_2 was represented by a conventional rigid linear triatomic model, with three charged LJ interaction sites located on each atom, previously developed by Harris and Yung (EPM2 model)[35] and (iii) N_2 was equally represented by a three-site charged model, with two LJ sites located at the N atoms, while a third site is located at its center of mass (COM), only involving electrostatic interactions as previously described in the TraPPE potential model.[36] The corresponding parameters are reported in Table S2.

The GCMC simulations were performed in order to predict the single component adsorption of H_2O and the co-adsorption of CO_2/N_2 (molar composition: 20:80 to match the experimental condition observed in the flow adsorption experiments) in the presence of different humidity rate at 298 K. The simulation boxes were made of 4 (2×2×1) unit cells of MIL-96(Al). Short-range dispersion forces were truncated at a cut-off radius of 12 Å while the cross-term interactions were treated by means of the Lorentz-Berthelot combination rules. The long-range electrostatic interactions were handled using the Ewald summation technique. The fugacities for each adsorbed species at a given thermodynamic condition were computed with the Peng-Robinson equation of state (EoS).[37] For each state point, 2×10^8 Monte Carlo steps have been used for both equilibration and production runs and the adsorption enthalpy at low coverage (Δh) for each gas was calculated through configurational-bias Monte Carlo simulations performed in the NVT ensemble using the revised Widom's test particle insertion method.[38] The Radial Distribution Functions (RDF) reported in ESI for the guest/MOF pairs as well as the density plots were obtained by averaging over the 2×10^8 Monte Carlo production steps. More details of the GCMC calculations are provided in the SI.

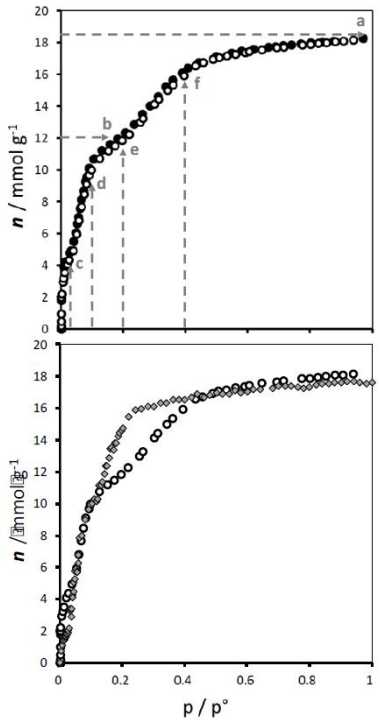

Figure 2. Experimental water isotherm at 298 K for MIL-96(Al) (top) in which the points 'a' to 'f' are discussed in the text (adsorption open symbols and desorption closed symbols). The lower figure shows a comparison between experimental (open symbols) and simulated (full symbols) water isotherms.

Results and discussion

Water adsorption and thermodesorption

Water adsorption. Water adsorption (Figure 2) was carried out on the activated sample in order to assess the hydrophilicity/ hydrophobicity as well as the pore filling. A comparison of the isotherms obtained for H_2O at 298 K by experiment and simulation (Figure 2, bottom) shows a fairly good agreement, although the saturation was observed at a lower p/p° in the case of simulated isotherm when compared to experimental one.

Indeed, one can distinguish: (i) an initial uptake up to a p/p° = 0.03, (ii) a first relatively sharp adsorption step between p/p° = 0.03 and 0.12, (iii) a second more gradual uptake between p/p° = 0.12 and 0.2-0.5, and a final plateau-like region.

The initial uptake (below p/p° = 0.001) can be linked to adsorption on specific sites and the simulated H_2O isotherm reproduces fairly well the initial hydrophilic nature of MIL-96(Al) material. At this low coverage (i.e. p/p° = 0.001), the H_2O molecules interact simultaneously with Al(1)-$H_2O_{terminal}$ site and Al(3')-$OH_{terminal}$/Al(3)-$H_2O_{terminal}$ sites. The radial

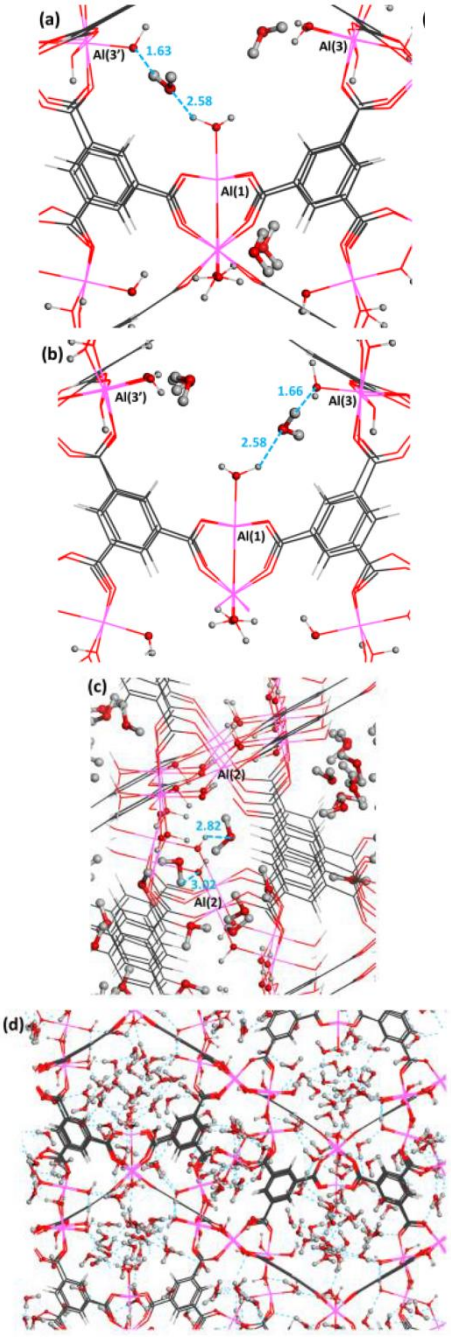

Figure 3. Local views of the GCMC simulated arrangements of H_2O molecules in MIL-96(Al) at 298 K: p/p° of 0.001 (a,b), 0.1 (c) and 0.5 (d, dashed line represents the hydrogen bond network, 1.6 -2.0 Å). (The distances are in Å).

distribution function (RDF) analysis for H_2O in MIL-96(Al) at p/p° = 0.001 shows that the mean distances between $O_{H2O} - H_{Al(1)-H2Oterminal}$, $H_{H2O} - O_{Al(3')-OHterminal}$, and $H_{H2O} - O_{Al(3)-H2Oterminal}$ are 2.58 Å, 1.64 Å and 1.66 Å, respectively (Figures S2 and S3). This emphasizes that the preferential location of H_2O molecule is mainly driven by the hydrogen bonding interactions between H_2O and both H_2O-Al(1)-$H_2O_{terminal}$ as well as Al(3')-$OH_{terminal}$ and Al(3)-$H_2O_{terminal}$ (Figure 3a and 3b). Such a geometry is associated with a high adsorption enthalpy predicted at low coverage (-67 kJ mol^{-1}) consistent with the high Henry law constant experimentally assessed (K_H = 163 mol g^{-1} bar^{-1}) that both confirm the hydrophilic nature of MIL-96(Al). Compared to other small pore MOFs (see Table S5), the MIL-96(Al) water affinity is significantly higher which is due to a high hydrophilic surface combined with a very low pore volume. At p/p° = 0.03, the small deviation between the experimental and simulated isotherms might be due to the possible presence of defects in the sample.

The first adsorption step (i.e. after p/p° = 0.03) corresponds to the formation of H_2O cluster inside the most hydrophilic cages (Figure S4c). On increasing vapour pressure, H_2O molecules occupy the channels containing Al(1)-H_2Oterminal-, Al(3')-$OH_{terminal}$/Al(3)-$H_2O_{terminal}$ (Figure S4d). When these pores are completely filled, i.e. at p/p° =0.05 - 0.1, the H_2O molecules occupy other sites and adsorb in the pores where μ_2-OH groups are present (Figure S4e) with mean characteristic distances between $O_{H2O} - H_{\mu2OH}$ and $H_{H2O} - O_{\mu2OH}$ of 2.82 and 3.02 Å, respectively (Figure 3c, S2 and S3). A steep increase in the H_2O adsorption is further observed from p/p° =0.1 to p/p° = 0.22 and this is mainly due to the filling of H_2O molecules in the pores where μ_2-OH groups are present (Figure S4f). This leads to the saturation of the pore with the formation of a very strong hydrogen bond network (Figure 3d). Beyond p/p° ~ 0.45, both experiments and simulations converge towards the same total water uptake of about 16 mmol.g^{-1}. In general, it is possible to correlate in a linear fashion the water uptake with available pore volume as is shown in Figure S23. However, deviations from this linearity are observed with small pore MOFs, but with MIL-96(Al) this upward deviation from this linear trend is quite significant suggesting that both pore confinement and pore chemistry may play significant roles in the water uptake in this material. Finally, as can be seen from Figure 2, the water isotherm is a reversible phenomenon suggesting that neither pore blocking effects nor chemisorption occur.

Estimation of the water adsorbed after pre-equilibration. Prior to the static gas adsorption experiments (see below), MIL-96(Al) was pre-equilibrated in a saturated water vapour chamber for 48 hours. It is important to ascertain the amount of water adsorbed in the sample after pre-humidification as well as the water remaining after the series of CO_2 isotherms. In order to assess the amount of water remaining on the sample at these points, thermogravimetric analysis (TGA) under argon flow was carried out on the sample taken straight after water pre-equilibration (curve A in Figure 4) and further after several CO_2 cycles on the pre-humidified sample (curve B in Figure 4). The TGA results for these samples is reported as

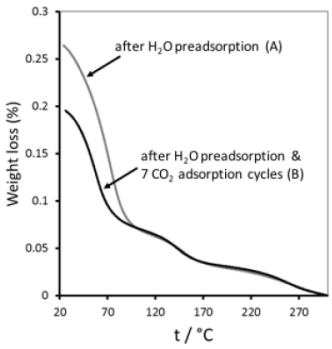

Figure 4. MIL-96(Al) thermogravimetric curves obtained with samples after pre-humidification (A) and after several CO_2 adsorption/desorption cycles (B).

weight loss with respect to the final dry mass at 300°C. After this temperature, sample degradation occurs, as shown previously. [31] Figure 4 shows similar shaped TGA curves for both samples studied. The difference in curves occurs up to around 100°C. One can consider that this weight loss observed in the temperature range from 20 to 100°C is due to water. This can be quantified at around 18.5% and 12% respectively for (A) and (B) with respect to the dry MIL-96(Al) at 300°C and these findings are consistent with the difference in sample cell weights before and after CO_2 cycling (i.e. after the results shown in Figure 6). As will be further discussed below, the difference in water content can be attributed to partial water displacement by carbon dioxide during the adsorption/desorption cycles.

Above 100°C, the TGA curves overlap confirming that water does not chemically modify the MIL-96(Al) framework [30] and further that no specific degradation occurs due to the presence of H_2O/CO_2 in the pores.

One can relate the water isotherm (Figure 2) to the TGA results in Figure 4. Indeed, the weight loss observed by TGA can be directly related to the amount of water adsorbed in the isotherm. Thus, the 18.5% weight loss observed with the sample analysed by TGA after pre-humidification corresponds to a sample which is completely filled with water (point 'a' in Figure 2). Similarly, the 12% weight loss obtained with the pre-humidified sample which had undergone several adsorption/desorption cycles with CO_2 corresponds to a sample where around 60% of the pore volume remains filled with water (point 'b' in Figure 2). This suggests that the water molecules adsorbed at specific adsorption sites and in most hydrophilic cages as discussed above are not able to be removed by the CO_2 and this has an influence in both uptakes and enthalpies as discussed below.

Experimental adsorption of CO_2 under static conditions

Adsorption of CO_2 on the MIL-96(Al) after pre-equilibration with water and comparison with the fully activated dry MIL-96(Al). Adsorption isotherms plotting CO_2 uptakes as a function of pressure and corresponding enthalpy profiles versus amount adsorbed are shown in Figure 5 for the fully

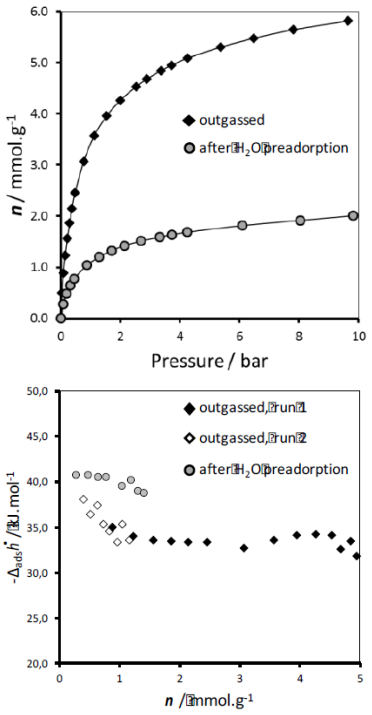

Figure 5. CO_2 adsorption isotherms (top) and enthalpy profiles (bottom) obtained at 303K on the outgassed (diamonds) and pre-humidified (circles) MIL-96(Al). Enthalpies are shown for a repeat run obtained at low pressure for the outgassed MIL-96(Al).

activated dry sample and the MIL-96(Al) sample which was pre-equilibrated with water for 48 hours.

Figure 5 (top) shows the adsorption isotherms which are both Langmuir shaped reaching quasi-plateaus before the final pressure of 10 bar. The CO_2 adsorption capacity is strongly affected by the presence of water in MIL-96(Al) with an almost 80% loss in capacity observed at 8 bar (5.7 vs. 1.2 mmol g^{-1} respectively) for the sample which was fully pre-humidified. This is consistent for a sample almost completely filled with water. The affinity of MIL-96(Al) for CO_2 was assessed through the Henry law constant calculations at low concentration with values of 16.0 and 5.0 mmol g^{-1} bar^{-1} for the activated and pre-humidified MIL-96(Al), respectively. Further evaluation of the interaction of CO_2 with the samples was obtained by calorimetry (Figure 5 bottom). The initial values obtained with the fully activated sample are around -38 kJ.mol^{-1} which are in the range of those of HKUST-1 (-35 kJ mol^{-1}) [18] with some CUS sites, small pore MOFs such as MIL-91(Ti) (-42 kJ mol^{-1}) [39] and MIL-140A (-42 kJ mol^{-1}) [40] but well above other more neutral MOFs such as UiO-66(Zr) (-26 kJ mol^{-1}). [41]

The enthalpies of adsorption of CO_2 obtained with the MIL-96(Al) pre-humidifed with water are relatively stable at a value of around -40 kJ mol^{-1} (Figure 5). It is interesting to note that this value is slightly higher than the plateau observed with the fully activated sample. These results highlight that the pre-adsorbed water shields

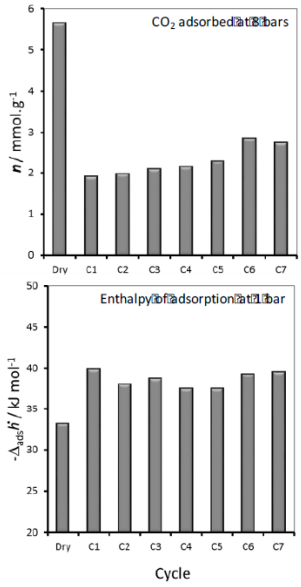

Figure 6. CO_2 uptakes at 8 bar (left) and CO_2 adsorption enthalpies at 1 bar (right), for the fully activated MIL-96(Al) (dry) for seven CO_2 adsorption/desorption cycles performed on the pre-equilibrated MIL-96(Al).

confers increased interactions with CO_2 during pore filling. This slightly increased energy might be due to higher confinement of CO_2 inside the pores or to increased surface hydrophilicity caused by the preadsorbed water. [42]

Cycling CO_2 measurements. The TGA experiments (Figure 4) suggest that the pre-humidified sample first introduced into the adsorption cell for the calorimetry experiments and the one recovered after several adsorption-desorption cycles with dry CO_2 gas, loses some of the pre-adsorbed water. Thus, cycling experiments can give an initial idea as to the effect of slightly decreasing amounts of water on both CO_2 uptake and enthalpies.

The CO_2 isotherms and enthalpies for the various cycles on the MIL-96(Al) sample pre-equilibrated with water are given in the supplementary information (Figure SI7). To follow the trends, the uptakes at 8 bar and enthalpies at 1 bar are reported in Figure 6. It is clear from this figure that the amount of CO_2 adsorbed at 8 bar increases with increased cycling suggesting the liberation of a small fraction of the pore volume. This increase corresponds to around 16% with respect to the uptake observed with the activated sample. Interestingly, the CO_2 uptake after the 7^{th} cycle is around 50% that of the activated sample which is consistent with the estimation of around 60% residual pore volume occupied by the pre-adsorbed water as calculated by TGA (Figure 4).

Turning to energetic aspects, a calculation of the Henry constants for CO_2 adsorption for each cycle suggests a significant increase in interaction strength from the initial and final adsorption run (5.05 to 10.26 mmol g^{-1} bar^{-1}, Table S4). Further estimation of the interaction of CO_2 with the samples during cycling is highlighted by

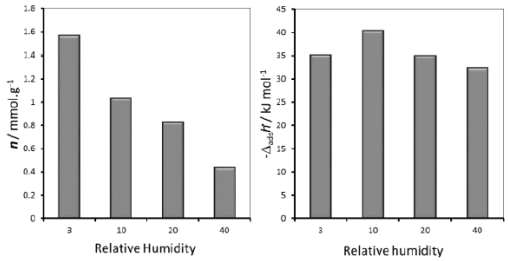

Figure 7. CO_2 uptake in flow conditions on the MIL-96(Al) at RH = 3, 10, 20 and 40% RH (left) and (right) the corresponding enthalpies of adsorption.

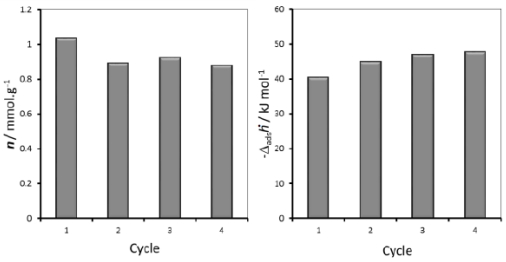

Figure 8: CO_2 uptake during cycling experiments for the flow experiments at RH = 10% (left) and (right) corresponding enthalpies of

calorimetry (Figure 6 bottom). This graph confirms the observations from Figure 5 that the CO_2 interaction with the humid sample is slightly stronger that with the fully activated MIL-96(Al). More significantly, the cycling seems to show that the CO_2 enthalpies, at 1 bar, remain relatively constant for each cycle.

Thus, whilst CO_2 adsorption cycling does liberate some porosity, due to water displacement from the MIL-96(Al) pores, this does not affect the enthalpies measured at 1 bar. Indeed, these energies remain above those of the fully activated sample.

Experimental adsorption of CO_2 under dynamic conditions

CO_2 uptake under controlled relative humidity. The static adsorption measurements described above give direct information regarding the amounts of CO_2 adsorbed and associated enthalpies as a function of pressure. Experimentally, it is not simple to know directly the amount of water pre-adsorbed for each cycle. Further, it is of interest to work under flow conditions, with N_2 as the vector gas, to approach the capture of CO_2 in any process.

Thus, pre-adsorbing water at different relative humidities is possible using a flow system developed previously.[27] Here, the sample is pre-equilibrated at a fixed relative humidity in a nitrogen flow prior to blending in CO_2 at a set of partial pressure (0.2 bar). The CO_2 uptake in a given humidity and corresponding measured enthalpy are shown in Figure 7 for four relative humidities: 3, 10, 20 and 40%.

Concerning the CO_2 uptakes at 0.2 bar, it is clear that a decrease is observed with increasing relative humidity. The 3% relative humidity (RH) corresponds to the residual value in the system under dry gas flow and a CO_2 uptake of around 1.6 mmol g^{-1} for this experiment corresponds surprisingly well to the uptake observed for the static experiment under dry conditions (Figure 5). CO_2 capacity losses with respect to the value obtained at 3% RH are estimated at 33%, 49% and 72% for relative humidities of 10%, 20% and 40% respectively. Interestingly, these capacity losses correspond to the relative water uptakes as observed in the water isotherm (points C – F, Figure 2). This suggests that the CO_2 completely fill the remaining pore volume that the water leaves after pre-adsorption at each relative pressure.

The measured enthalpy at 3% relative humidity is at around -35 kJ mol^{-1} which relates to the average enthalpy measured on the dry sample (Figure 5). Setting the relative humidity to 10% leads to an increase in enthalpy (~40 kJ mol^{-1}, result repeated) and this corresponds well to the value measured during the static measurements and with cycling (Figures 5 and 6). Increasing the relative humidity further leads to a decrease in overall enthalpy measured. Under these flow conditions, some pre-adsorbed water may be partially displaced by CO_2, consuming energy, and leading to lower overall adsorption enthalpy than would be expected for CO_2 adsorption alone. Indeed, a closer examination of the measured enthalpy signal (see Figure S20) highlights an unusual signal which would seem to be the resultant of initial rapid exothermic CO_2 uptake followed by a more gradual endothermic H_2O desorption.

CO_2 cycling under 10% relative humidity. As the CO_2 energies show a maximum at a relative humidity of 10%, then a limited series of cycling experiments were carried out under these conditions with the results shown in Figure 8.

After the first cycle, a slight decrease in CO_2 uptake is observed for the second cycle. However, the adsorption capacity remains relatively constant until the fourth cycle. This difference between the first and the second cycle may indicate that some CO_2 is irreversibly adsorbed in the material. We can also observe that the adsorption enthalpies increase to reach a plateau like region after the second cycle. An explanation could be that some CO_2 are irreversibly adsorbed under these flow conditions (corresponding to the CO_2 the most strongly adsorbed) during the first step. This may be accompanied by a water displacement, which may be not involved in the following cycles, leading to a relative endothermic contribution for this first cycle. However, a quasi-steady state seems to be attained after the second cycle.

Molecular modelling of mixture adsorption in the presence of water

The co-adsorption mechanism for CO_2 and N_2 in the dry MIL-96(Al) is very similar to their single component adsorption previously reported [30] (see also Supporting Information). At the initial stage of adsorption, both CO_2 and N_2 are preferentially located in the pores where the μ_2-OH groups are present. The CO_2 molecules interact with either single or two nearby μ_2-OH while the N_2 molecules sit towards the centre of the pore with characteristic host/guest distances of around 3.4 Å (see SI). This preferential arrangement for CO_2 in this structure leads to a simulated enthalpy for CO_2 of around -33 kJ mol^{-1} which corresponds well with that measured (see Figure S17). On increasing pressure, both CO_2 and N_2 distribute

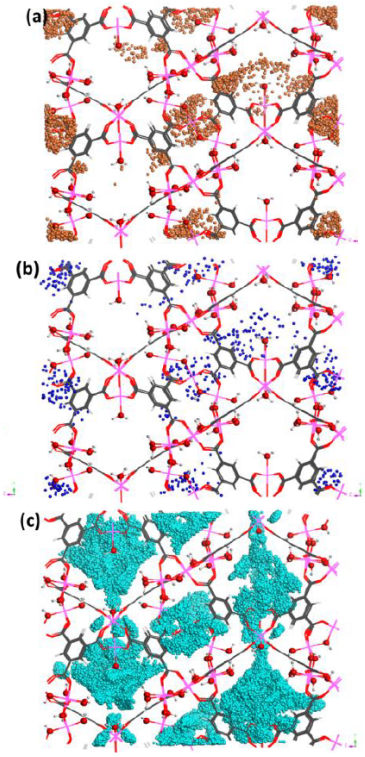

Figure 9: Maps of the occupied positions of CO_2 (orange), N_2 (blue) and H_2O (cyan) in 1000 equilibrated frames that extracted from the GCMC simulations for co-adsorption of CO_2/N_2 (20/80) in MIL-96(Al) at 303 K and 1.0 bar in presence of humidity, RH=8.5%.

in the cavities made by Al1-$H_2O_{terminal}$, Al(3')-$OH_{terminal}$ and Al(3)-$H_2O_{terminal}$.

The co-adsorption of CO_2 and N_2 was further modelled at 303 K in the presence of various humidities (RH = 8.5 %, 19.5 % and 37.5 %). Interestingly, the CO_2/N_2 (0.2/0.8) co-adsorption in the presence of RH=8.5% has largely retained CO_2 adsorption capacity, 2.0 mmol/g, when compared to the CO_2 without humidity, 4.9 mmol/g, at 10 bar (Figure S11). This behaviour confirms the experimental findings. However, the adsorption capacity for CO_2 on co-adsorption reduces significantly on increasing the relative humidity, i.e. only 0.72 and 0.2 mmol/g at RH=19.5% and 37.5%, respectively at 10 bar. However, interestingly, the CO_2/N_2 selectivity increases with increasing the relative humidity since the amount adsorbed of CO_2 drops in a lesser extent compared to N_2 (Figure S12). Indeed, the predicted selectivities are 42, 61, 76 and 85 with respect to the humidity rate RH = 0, 8.5, 19.5, and 37.5 %, respectively. Such values are compared with those previously reported for other adsorbents in the literature (see Table S6)

Analysis of the co-adsorption mechanism for the ternary $CO_2/N_2/H_2O$ mixtures evidenced that CO_2 molecules are initially distributed in the same region of the pores than in the single components, i.e. in the pore constituted by μ_2-OH with

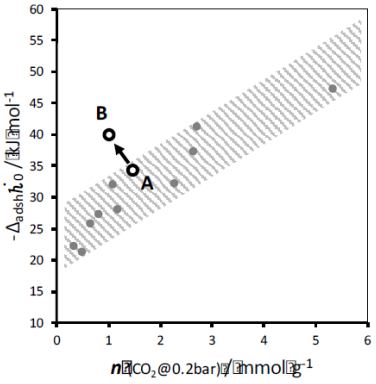

Figure 10: Relationship between initial enthalpy of adsorption and CO_2 uptake at 0.2 bars for several MOFs (see Table S7 for values). Point A corresponds to the fully outgassed MIL-96(Al) and point B to the same material after pre-equilibrium with 10% RH.

characteristic distances between C_{CO2} and $O_{\mu 2OH}$ and O_{CO2} and $H_{\mu 2OH}$ of about 2.80-2.95 Å (Figure S13 and S14).

At RH=8.5%, the water molecules preferential adsorbed in the cavities made by Al1-$H_2O_{terminal}$, Al(3')-$OH_{terminal}$ and Al(3)-$H_2O_{terminal}$, which give enough space for CO_2 and N_2 to adsorb in the other cavities containing μ_2-OH in MIL-96(Al) (Figure 9). This clearly supports the suggestion that at the initial stage of adsorption both H_2O and CO_2 have distinct interaction sites. Nevertheless, as occurs with other materials, on increasing the relative humidity, the water interacts with all the available porosity due to its higher interaction energy when compared to CO_2. Therefore, H_2O can occupy all the adsorption sites, particularly the cavity containing the μ_2-OH groups and finally end up with a decreasing profile for the CO_2 adsorption capacity on increasing the humidity.

Comparison with other materials.

In an attempt to place the performances of MIL-96(Al), under post-combustion type conditions, with those obtained with several other materials, Figure 10 shows the initial enthalpies of adsorption for CO_2 as a function of CO_2 uptake at 0.2 bar. The corresponding data can be found in Table S7. An overall linear trend (shaded area) is observed with a number of MOF samples. Indeed, the measurement observed for the fully outgassed MIL-96(Al) sample (point A, Fig. 10) falls into this trend. However, the slight loss in loading accompanied by the significant increase in enthalpy observed with the sample equilibrated with 10% RH, results in an upward deviation from this trend. Indeed, such relationships may help to identify materials of potential interest for further study. Thus, it is clear for MIL-96(Al) in the presence of 10% RH, the CO_2 recovery properties are not greatly degraded with the increase in enthalpy placing this sample above many other, non CUS containing, MOFs in terms of interaction strength.

Conclusions

MIL-96(Al) may be of interest for CO_2 recovery under flue gas conditions. Indeed, values of CO_2 uptake at 0.2 bar in the region of 1.5 mmol g^{-1} compare well to many other MOFs. Importantly, at limited relative humidity, up to 10% RH, this uptake remains of interest and is accompanied by relatively high adsorption enthalpies suggesting strong host/guest interactions. Furthermore, limited cycling experiments suggest constant adsorption properties of the material under 10% RH.

This unusual behaviour can be explained by the tendency for H_2O to preferentially adsorb in the cavities made by H_2O-Al(Trimer), Terminal-OH-Al and Terminal-H_2O-Al, which give enough space for CO_2 to adsorb at the other cavities containing μ_2-OH groups independently. For relative humidities of 20 and 40%, the CO_2 uptakes decrease significantly probably due to the competition of water and CO_2 for the remaining pore volume. Interestingly the GCMC simulations predicted that the CO_2/N_2 selectivity falls above 40 in the whole range of humidity rate.

The possibility to synthesize materials with varying specific pore chemistries may be a way forward in designing applications where contaminants may be present (e.g. water in this study) or in processes where two species of different properties (e.g. CO and CO_2) both need to be recovered.

Acknowledgements

The research leading to these results has received funding from the European Community Seventh Framework Program (FP7/2007-2013) [grant agreement number 608490] (project M^4CO_2) and from the French Ministry of National Education, Research and Technology (MENRT). G.M. thanks Institut Universitaire de France for its support.

References

1 P. Webley, "*Carbon Dioxide Capture Using Solid Sorbents*", 2018, Springer Singapore. (ISBN 978-981-10-1864-0)
2 J. A. Mason, T. M. McDonald, T.-H. Bae, J. E. Bachman, K. Sumida, J. J. Dutton, S. S. Kaye and J. R. Long, *J. Am. Chem. Soc.* 2015, **137**, 4787-4803.
3 M. Wang, A. Lawal, P. Stephenson, J. Sidders and C. Ramshaw, *Chem. Eng. Res. Des.*, 2011, **89**, 1609.
4 J. Pires, F. Martins, M. Alvim-Ferraz and M. Simões, *Chem. Eng. Res. & Des.*, 2011, **89**, 1446.
5 S. Arunkumar, Z. An, K.H, S. George, S. Partha and G. Rajender, *Ind. Eng. Chem. Res.*, 2012, **51**, 1438.
6 H.-C. Zhou and S. Kitagawa, *Chem. Soc. Rev.*, 2014, **43**, 5415.
7 H.-C. Zhou, J. R. Long and O. M. Yaghi, *Chem. Rev.*, 2012, **112**, 673.
8 G. Maurin, C. Serre, A. Cooper and G. Férey, *Chem. Soc. Rev.* 10.1039/C7CS90049J
9 F. Rouquerol, J. Rouquerol, K. Sing, P. Llewellyn and G. Maurin, *Adsorption by Powders and Porous Solids, Principles, Methodology and Applications*, 2014, Elsevier, Amsterdam..
10 S. Bourelly, P. Llewellyn, C. Serre, F. Millange, T. Loiseau and G. Férey, *J. Am. Chem. Soc.* 2005, **39**, 13519.
11 S. Kitagawa, R. Kitaura and S.-I. Noro, *Angew. Chem., Int. Ed.*, 2004, **43**, 2334
12 I. Beurroies, M. Boulhout, P. L. Llewellyn, B. Kuchta, G. Férey, C. Serre and R. Denoyel, *Angew. Chem. Int. Ed.*, 2010, **49**, 7526.
13 Y. Liu, J.-H. Her, A. Dailly, A. J. Ramirez-Cuesta, D. A. Neumann, and C. M. Brown, *J. Am. Chem. Soc.*, 2008, **130**, 11813.
14 G. Maurin, P. L. Llewellyn and R. G. Bell, *J. Phys. Chem. B*, 2005, **109**, 16084.
15 J. Silvestre-Albero, A. Wahby, A. Sepúlveda-Escribano, M. Martínez-Escandell, K. Kaneko and F. Rodríguez-Reinoso, *Chem. Commun.*, 2011, **47**, 6840.
16 U. Stoeck, S. Krause, V. Bon, I. Senkovska and S. Kaskel, *Chem. Commun.*, 2012, **48**, 10841–10843
17 H. Furukawa, N. Ko, Y. B. Go, N. Aratani, S. B. Choi, E. Choi, A. O. Yazaydin, R. Q. Snurr, M. O'Keeffe, J. Kim and O. M. Yaghi, *Science*, 2010, **329**, 424.
18 L. Grajciar, A. D. Wiersum, P. L. Llewellyn, J.-S. Chang and P. Nachtigall, *J. Phys. Chem. C*, 2011, **115**, 17925.
19 P. L. Llewellyn, S. Bourrelly, C. Serre, A. Vimont, M. Daturi, L. Hamon, G. De Weireld, J.-S. Chang, D.-Y. Hong, Y. K. Hwang, S. H. Jhung and G. Férey, *Langmuir*, 2008, **24**, 7245.
20 K. Sumida, D. L. Rogow, J. A. Mason, T. M. McDonald, E. D. Bloch, Z. R. Herm, T.-H. Bae and J. R. Long, *Chem. Rev.*, 2012, **112**, 724.
21 N. Burtch, H. Jasuja and K. Walton, *Chem. Rev*, 2014, **114**, 10575.
22 A. E. Creamer and B. Gao, *Environ. Sci. Technol*, 2016, **50**, 7276.
23 F. Brandani and D. Ruthven, *Ind. Eng. Chem. Res*, 2004, **43**, 8339.
24 S. Arunkumar, Z. An, K.H, S. George. S. Partha and G. Rajender, *Ind. Eng. Chem. Res.*, 2012, **51**, 1438.
25 G. Li, P. Xiao, P. Webley, J. Zhang, R. Singh and M. Marshall, *Adsorption*, 2008, **14**, 415.
26 A. Özgür Yazaydin, A. Benin, S. Faheem, P. Jakubczak, J. Low, R., Willis and R. Snurr, *Chem. Mater.*, 2009, **21**, 1425.
27 E. Soubeyrand-Lenoir, C. Vagner, J.-W. Yoon, P. Bazin, F. Ragon, Y.-K. Hwang, C. Serre, J.-S. Chang and P. L. Llewellyn, *J. Am. Chem. Soc.*, 2012, **134**, 10174.
28 A. Cadiau, Y. Belmabkhout, K. Adil, P. M. Bhatt, R. S. Pillai, A. Shkurenko, C. Martineau-Corcos, G. Maurin and M. Eddaoudi, *Science*, 2017, **356**, 731.
29 N. Chanut, S. Bourrelly, B. Kuchta, C. Serre, J.-S. Chang, P. A. Wright and P. L. Llewellyn, *ChemSusChem*, 2017, **10**, 1543.
30 *Revisiting the Microporous Aluminum Trimesate-based MOF (MIL-96): from the Structure Determination, Synthesis of Nanoparticles to the Processing of Mixed Matrix Membranes for CO_2 Capture*, M. Benzaqui, R.S. Pillai, A. Sabetghadam, V. Benoit, P. Normand, J. Marrot, N. Menguy, D. Montero, A. Tissot, C. Martineau, C. Sicard, M. Mihaylov, F. Carn, I. Beurroies, P.L. Llewellyn, G. De Weireld, K. Hadjiivanov, J. Gascon, F. Kapteijn, G. Maurin, N. Steunou, C. Serre, *Chem. Mater.*, 2017, id cm-2017-032039. Paper under revision.
31 T. Loiseau, L. Lecroq, C. Volkringer, J. Marrot, G. Férey, M. Haouas, F. Taulelle, S. Bourrelly, P. L. Llewellyn and M., Latroche, *J. Amer. Chem. Soc.*, 2006 **128**, 10223.
32 A. K. Rappé, C. J. Casewit, K. S. Colwell, W. A. Goddard III and W. M. Skiff, *J. Am. Chem. Soc.* 1992, **114**, 10024.
33 J. L. F. Abascal and C. Vega, *J. Chem. Phys.*, 2005, **123**, 234505.
34 H. L. Pi, J. L. Aragones, C. Vega, E. G. Noya, J. L. F. Abascal, M. A. Gonzalez and C. McBride, *Mol. Phys.*, 2009, **107**, 365.
35 J. G. Harris and K. H. Yung, *J. Phys. Chem.* 1995, **99**, 12021.
36 J. J. Potoff and J. I. Siepmann, *AIChE J.* **2001**, *47*, 1676.
37 D.-Y. Peng and D. B. Robinson, *Ind. Eng. Chem. Fundam.*, 1976, **15**, 59.
38 T. J. H. Vlugt, E. García-Pérez, D. Dubbeldam, S. Ban and S. Calero, *J. Chem. Theory Comput.* 2008, **4**, 1107.

39 V. Benoit, R. S. Pillai, A. Orsi, P. Normand, H. Jobic, F. Nouar, P. Billemont, E. Bloch, S. Bourrelly, T. Devic, P. A. Wright, G. de Weireld, C. Serre, G. Maurin and P. L. Llewellyn, *J. Mater. Chem. A.*, 2016, **4**, 1383.
40 C. Vieira Soares, D. Damasceno Borges, A. Wiersum, C. Martineau, F. Nouar, P.L Llewellyn, N.A Ramsahye, C. Serre, G. Maurin and A.A. Leitão, *J. Phys. Chem. C*, 2016, **120**, 7192.
41 A. D. Wiersum, E. Soubeyrand-Lenoir, Q. Yang, B. Moulin, V. Guillerm, M. Ben Yahia, S. Bourrelly, A. Vimont, S. Miller, C. Vagner, M. Daturi, G. Clet, C. Serre, G. Maurin and P. L. Llewellyn, *Chem.-As. J.*, 2011, **6**, 3270.
42 J. W. Yoon, Y.-K. Seo, Y. K. Hwang, J.-S. Chang, H. Leclerc, S. Wuttke, P. Bazin, A. Vimont, M. Daturi, E. Bloch, P. L. Llewellyn, C. Serre, P. Horcajada, J.-M. Greneche, A. E.Rodrigues and G. Férey, *Angew. Chem. Int. Ed.*, 2010, **49**, 5949.

Annex E

Supplementary Information

A promising Metal-Organic Framework (MOF), MIL-96(Al) for CO_2 separation under wet conditions

Virginie Benoit,[a] Nicolas Chanut,[a] Renjith S. Pillai,[b] Marvin Benzaqui,[c,d] Isabelle Beurroies,[a] Sabine Devautour-Vinot,[b] Christian Serre,[c] Nathalie Steunou,[d] Guillaume Maurin,[b] Philip L. Llewellyn [*a]

[a.] *Aix-Marseille Univ, CNRS, MADIREL, Marseille, France.*

[b.] *Institut Charles Gerhardt Montpellier, Université de Montpellier, CNRS, ENSCM, Place E. Bataillon, 34095 Montpellier cedex 05, France.*

[c.] *PSL Res Univ, FRE CNRS 2000, Ecole Super Phys & Chim Ind Paris, Ecole Normale Super, Inst Mat Poreux Paris, 75005 Paris, France.*

[d.] *Institut Lavoisier de Versailles, UMR CNRS 8180, Université de Versailles St Quentin en Yvelines, Université Paris Saclay, 45 avenue des Etats-Unis 78035 Versailles Cedex. France.*

1. Molecular simulations details.

Table S1. LJ potential parameters for all atoms of the MIL-96(Al).

Atomic type	UFF	
	σ (Å)	ε/k_B (K)
Al	4.399	0.000
C	3.431	52.841
H	2.571	22.143
N	3.261	34.724
O	3.118	30.195

Table S2. Potential parameters and partial charges for the guests

Atomic type	σ (Å)	ε/k_B (K)	*q* (*e*)
O_e	3.1589	93.200	0.0000
H_e	0.00	0.000	0.5564
M_e	0.00	0.000	-1.1128
CH_4	3.730	148.000	0.0000
N2_N	3.310	36.000	-0.4820
N2_COM	0.00	0.000	0.9640
CO2_C	2.757	28.129	0.6512
CO2_O	3.033	80.507	-0.3256

2. Computational predictions

2.1. Single component H_2O, CO_2 and N_2 adsorption

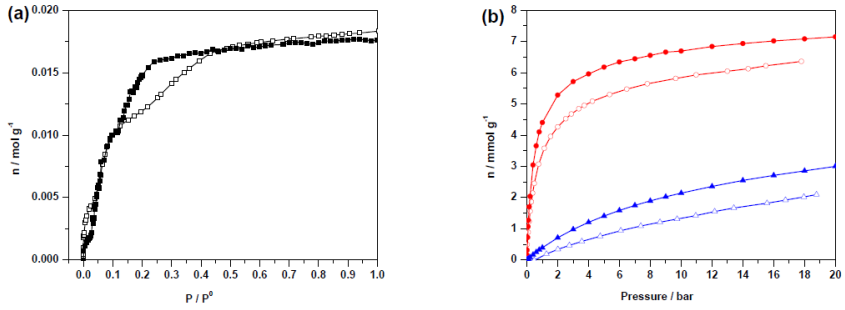

Figure S1. Comparison of the single component simulated (full symbols) and experimental (empty symbols) adsorption isotherms in MIL-96(Al) for H_2O (squares) at 298K (a) and CO_2 (squares) and N_2 (circles) at 303 K (b).

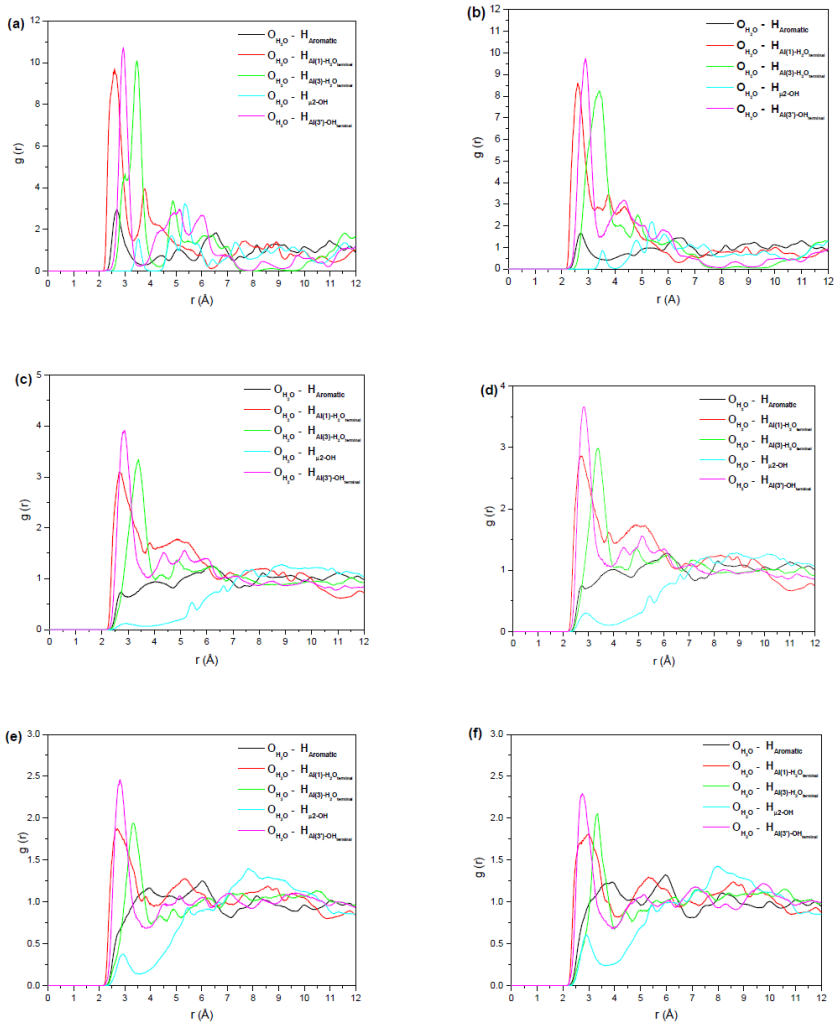

Figure S2: Radial Distribution Functions (RDF) between the oxygen atom of water (O_{H2O}) and all atoms of the MOF framework extracted from the GCMC simulations at 298 K in MIL-96(Al) at p/p°, 0.001 (a), 0.01(b), 0.05(c), 0.1 (d), 0.22 (e), and 1.0 (f).

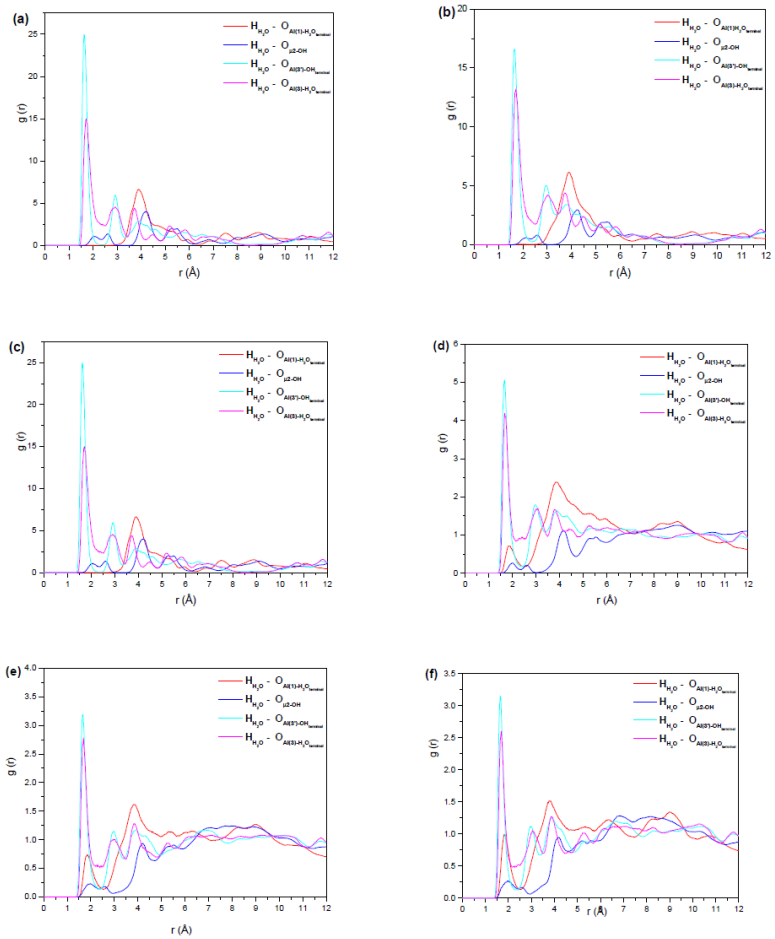

Figure S3: Radial Distribution Functions (RDF) between the hydrogen atom of water (H_{H2O}) that extracted from the GCMC simulations at 298 K in MIL-96(Al) at p/p°, 0.001 (a), 0.01(b), 0.05(c), 0.1 (d), 0.22 (e), and 1.0 (f).

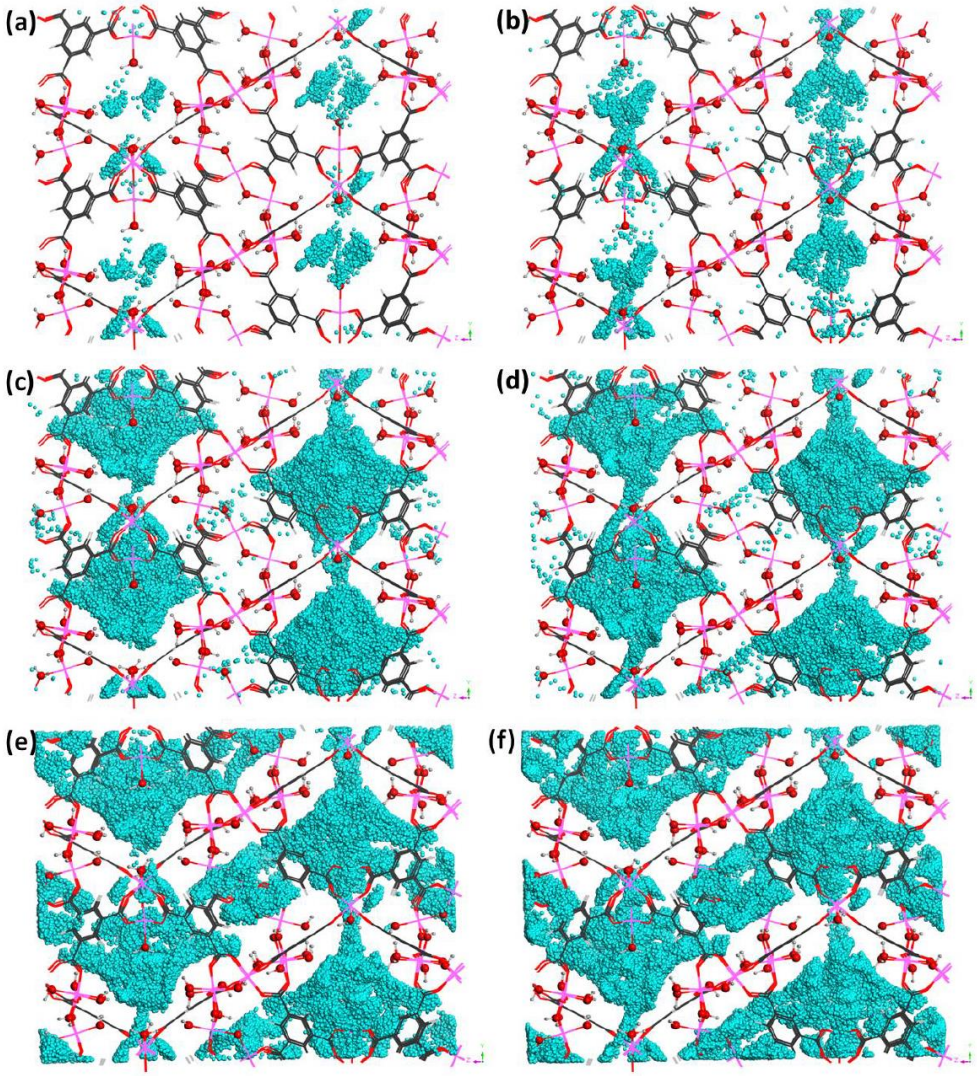

Figure S4: Maps of the occupied positions of H_2O (cyan) in 1000 equilibrated frames that extracted from the GCMC simulations at 298 K for MIL-96(Al) at p/p°, 0.001 (a), 0.01(b), 0.05(c), 0.1 (d), 0.12 (e), and 0.22 (f).

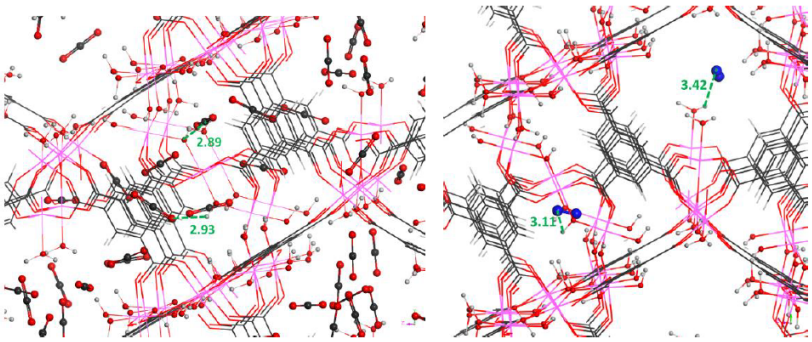

Figure S5. Local views of GCMC simulated arrangements of CO_2 (a) and N_2 (b) molecules in MIL-96(Al) at 303 K and 0.1 bar.

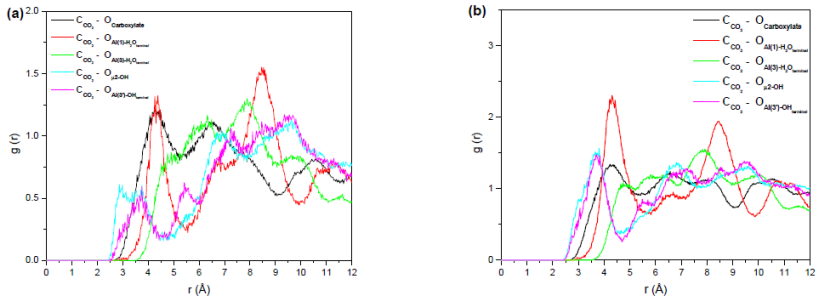

Figure S6: Radial Distribution Functions (RDF) between the Carbon of CO_2 (C_{CO2}) and all atoms of the MOF framework extracted from the GCMC simulations at 303 K in MIL-96(Al) at 0.01 bar (a) and 1.0 (b).

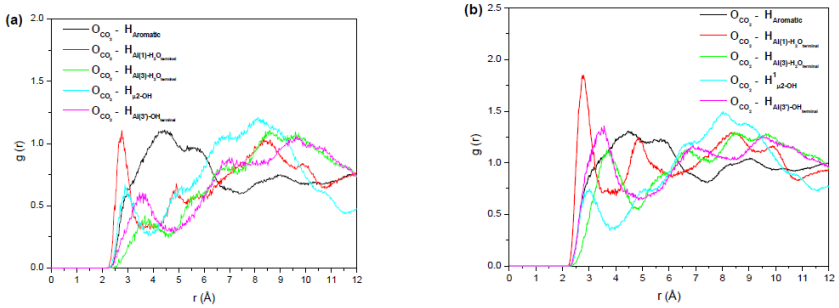

Figure S7: Radial Distribution Functions (RDF) between the oxygen in CO_2 (O_{CO2}) and all atoms of the MOF framework extracted from the GCMC simulations at 303 K in MIL-96(Al) at 0.01 bar (a) and 1.0 (b).

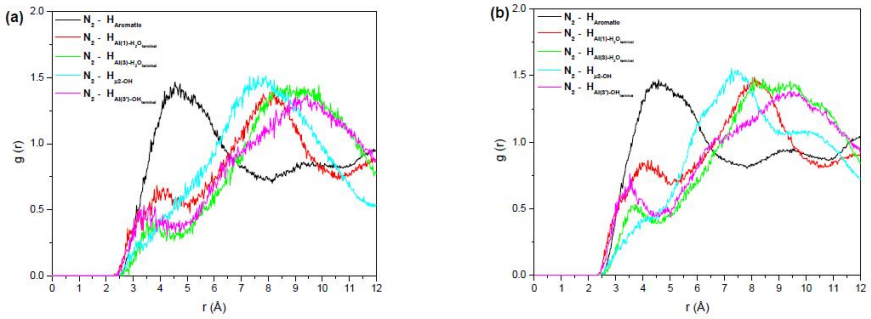

Figure S8: Radial Distribution Functions (RDF) between N_2 and all atoms of the MOF framework that extracted from the GCMC simulations at 303 K in MIL-96(Al) at 0.01 bar (a) and 1.0 (b).

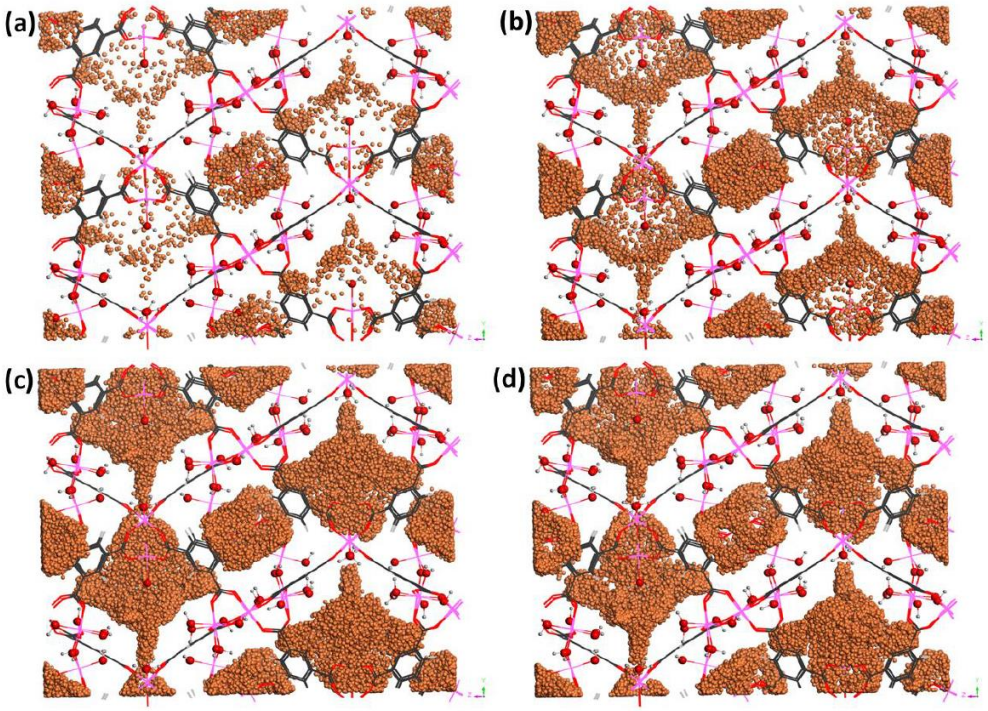

Figure S9: Maps of the occupied positions of CO_2 (orange) in 1000 equilibrated frames extracted from the GCMC simulations at 303 K for MIL-96(Al) at pressures: 0.01 bar (a), 0.1 bar (b), 1.0 bar (c), and 10.0 bar (d).

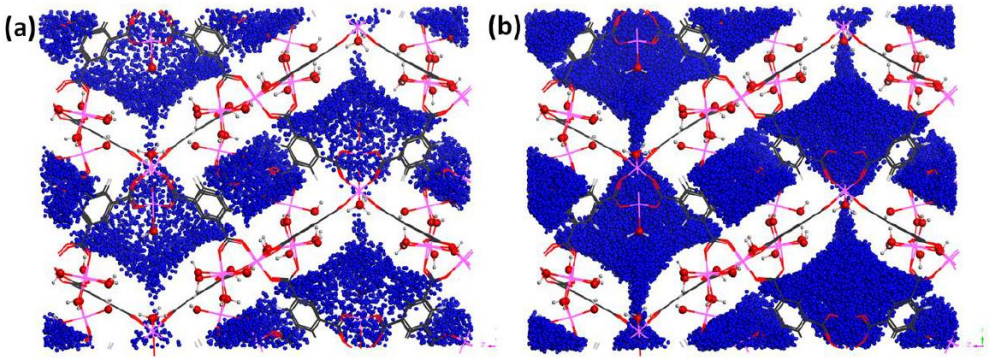

Figure S10: Maps of the occupied positions of N_2 (blue) in 1000 equilibrated frames extracted from the GCMC simulations at 303 K for MIL-96(Al) at pressures: 0.01 bar (a) and 10.0 (b).

2.2. Separation of CO_2/N_2 mixtures in presence and absence of humidity

In separation processes, a good indication of the separation ability consists of estimating the selectivity of a porous material. The selectivity (S) for CO_2 over N_2 is defined by the following expression: $S(CO_2/N_2) = \frac{(x_{CO_2} / x_{N_2})}{(y_{N_2} / y_{CO_2})}$ where x_{CO_2} and x_{N_2} are the mole fractions of CO_2 and N_2 in the adsorbed phase, respectively, while y_{CO_2} and y_{N_2} are the mole fractions of CO_2 and N_2 in the bulk gas phase, respectively. The calculated selectivities for both CO_2/N_2 (molar ratio =20/80) are shown in Figure S12 as a function of the bulk pressure.

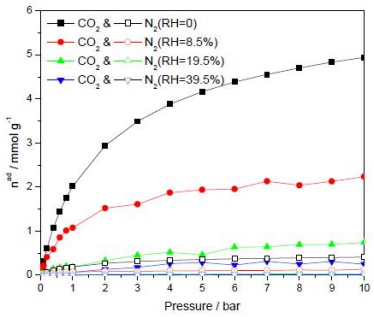

Figure S11. Simulated co-adsorption isotherm for CO_2 (closed symbols) and N_2 (open symbols) from their 20/80 molar ratio of binary gas mixture in presence of humidity, 0 % (square), 8.5% (circle), 19.5% (up-triangle) and 39.5% (down-triangle) as a function of the bulk pressure at 303 K.

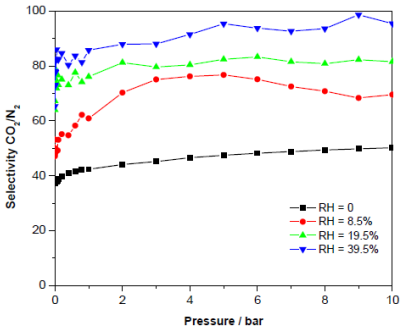

Figure S12. Simulated selectivities for CO_2/N_2 from their 20/80 molar ratio gas mixture in MIL-96(Al) as a function of the bulk pressure at 303 K and in presence of humidity (RH = 0 % (square), 8.5 % (circle), 19.5 % (up-triangle) and 39.5 % (down-triangle)).

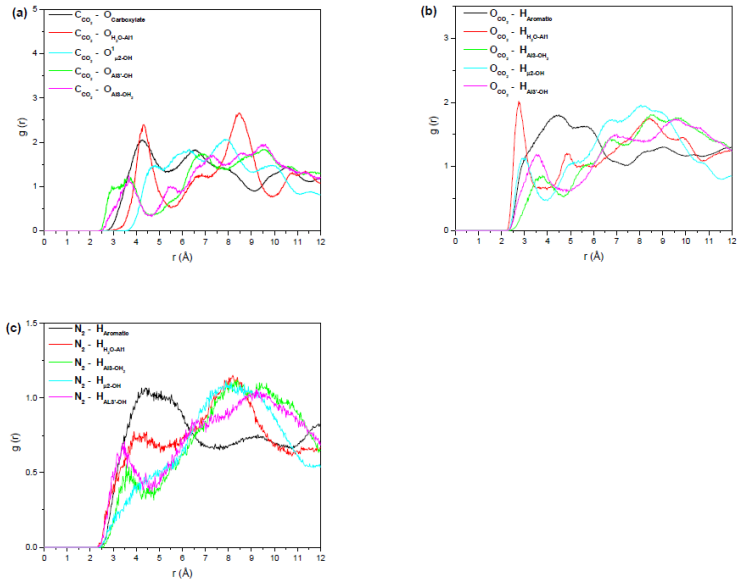

Figure S13: Radial Distribution Functions (RDF) between CO_2, C_{CO2} (a) and O_{CO2} (b), and N_2 (c) and all atoms of the MOF extracted from the GCMC simulations for co-adsorption of CO_2/N_2 = 20/80 in MIL-96(Al) at 303 K and 1.0 bar.

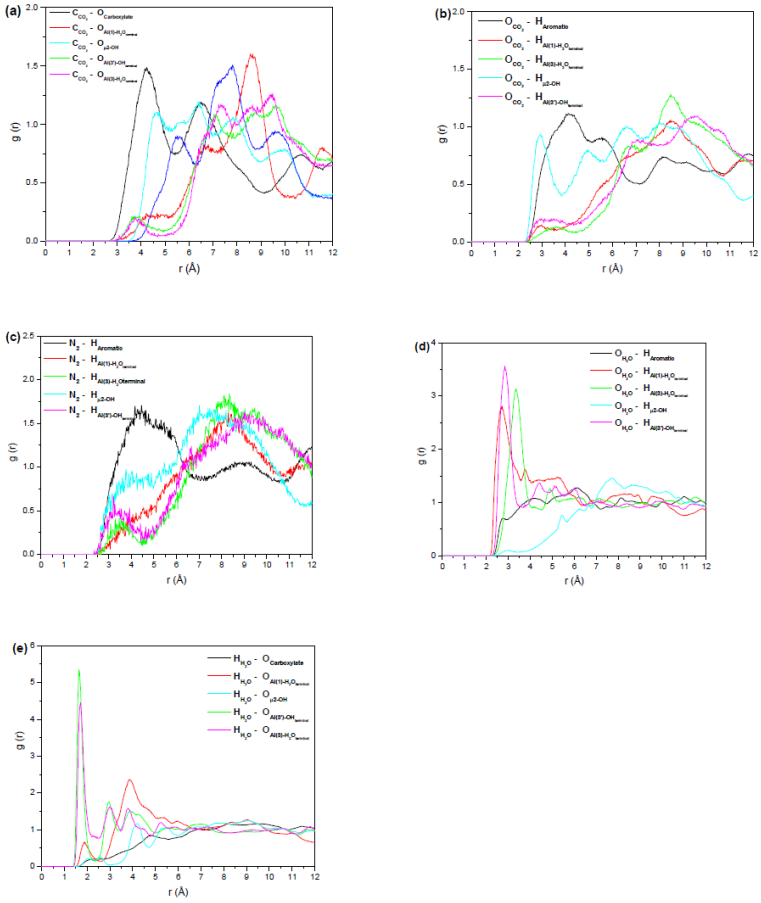

Figure S14: Radial Distribution Functions (RDF) between CO_2, C_{CO2} (a) and O_{CO2} (b), N_2 (c) and H_2O, O_{H2O} (d) and H_{H2O} (e) and all atoms of the MOF framework extracted from the GCMC simulations for co-adsorption of CO_2/N_2 = 20/80 in presence of humidity, RH=8.5%, in MIL-96(Al) at 303 K and 1.0 bar.

3. Complementary sample characterization

3.1 Textural parameters obtained from nitrogen physisorption at 77K

The accessible porosity of the MIL-96(Al) was probed by nitrogen gas adsorption at 77K using a Belsorb max apparatus. Prior to nitrogen adsorption, the MIL-96(Al) was outgassed at 150°C under secondary vacuum for 15h. From nitrogen adsorption isotherm at 77K, textural parameters were calculated such as apparent surface area, external surface and microporous volume.

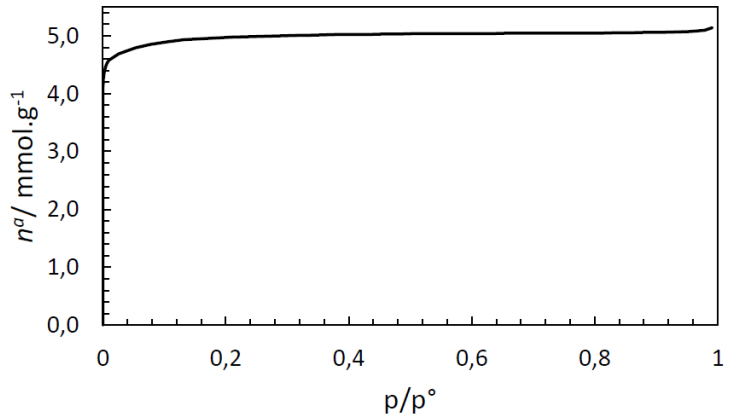

Figure S15 – Nitrogen adsorption isotherm at 77K obtained on MIL-96(Al)

Table S3. Textural parameters obtained from N_2 adsorption at 77K on the MIL-96(Al) and showing its microporous character.

	S_{BET} 'apparent' (m^2/g)	S_{EXT} (m^2/g)	$V_{MICROPOROUS}$ (cm^3/g)
MIL-96(Al)	448	1.2	0.16

3.2 Water isotherm on MIL-96(Al) at 298K

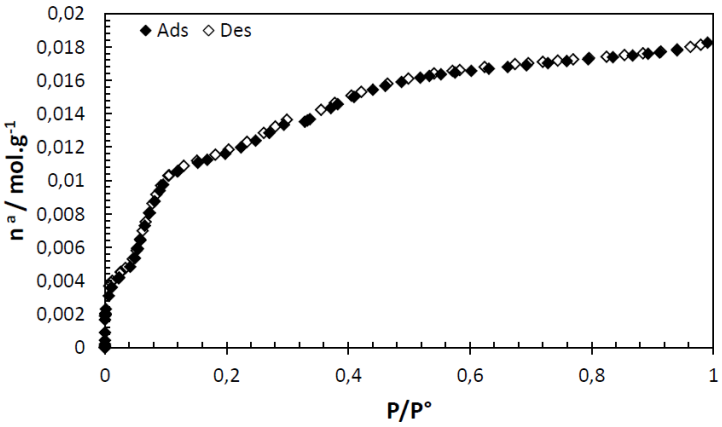

Figure S16. Water adsorption (fully lozenge) and desorption (empty lozenge) isotherms obtained at 298K on the MIL-96(Al)

4. Complementary results concerning static adsorption experiments at 303K

4.1. CO_2 adsorption isotherms and corresponding enthalpies of adsorption

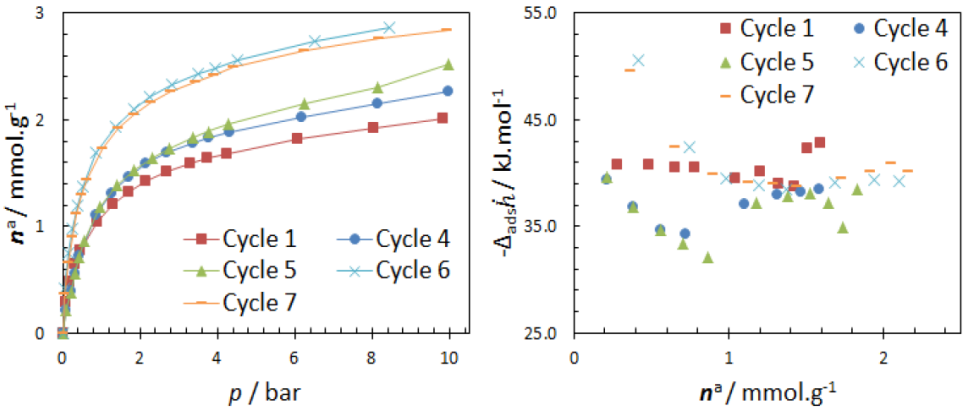

Figure S17 – CO_2 adsorption isotherms (left) and adsorption enthalpy profiles (right) obtained from cycling on the pre-humidified MIL-96(Al)

Table S4. Henry's law constant calculated at low surface coverage for CO_2 adsorption cycles: 1, 4, 6 from the MIL-96(Al) pre-humidified state and compared to these obtained on the MIL-96(Al) outgassed.

Cycle	1	4	6	Outgassed state
K_H – CO_2 / mmol.bar^{-1}.g^{-1}	5.05	6.34	10.26	17

5. Dynamic measurements to measure CO_2 uptakes in the presence of controlled relative humidity

5.1 Experimental set-up

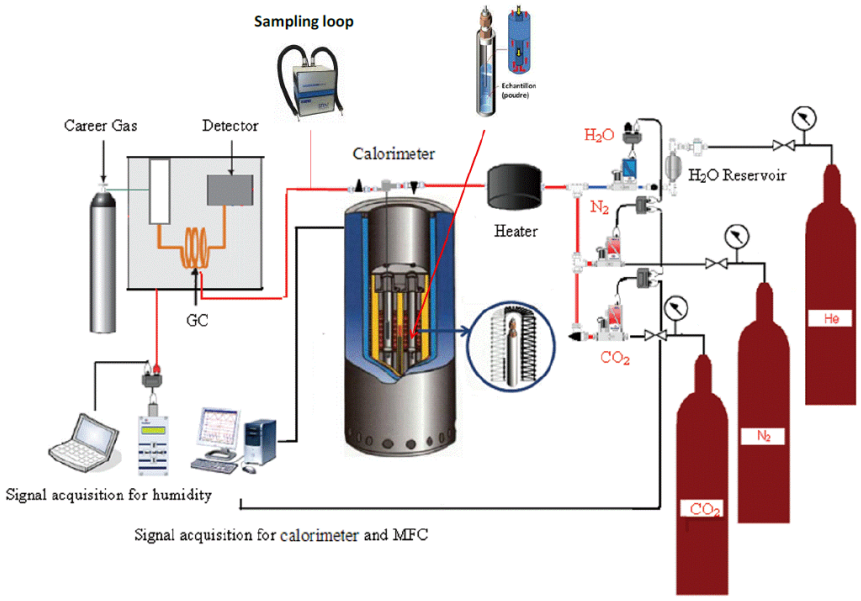

Figure S18. Schematic diagram of the flow adsorption microcalorimetry setup used to study the impact of water vapour during CO_2 adsorption on porous solids

Figure S18 shows a schematic diagram of the system used in our experiment: a Tian-Calvet type microcalorimeter and a gas chromatograph (GC6890N, Agilent) were coupled to simultaneously measure differential enthalpies of gas adsorption and CO_2 breakthrough curves. This rig was designed to operate in a dynamic mode at ambient temperature and at atmospheric pressure over a wide range of humidity. The system allowed 2 types of binary adsorption experiments (N_2/CO_2) either under dry conditions or under H_2O vapour. A central manual valve allowed a switching of the system from the dry mode to the wet mode. The sample was pre-treated directly inside the sample cell under nitrogen flow at the selected temperature. After activation, the sample was kept under continuous N_2 flow until thermal equilibrium was achieved. Then, gases (N_2, CO_2) and/or water vapour were flowed into the system, the proportion of each gas in the mixture being controlled by using mass flow controllers (MFC). In order to obtain a homogeneous mixture of gas, the flow rate of carrier gas (N_2) was 10 times larger than that of the adsorbate (CO_2). The total flow rate was maintained at a constant rate of 30 mLn/min. This part of the system is housed inside a thermostated chamber to keep the temperature constant. If an interaction between the gas mixture and the sample occurs, an energetic response is observed and recorded by the thermopiles of the microcalorimeter. The outlet gas mixture concentration from the cell is

then analyzed by the thermal conductivity detector (TCD) of the GC. In order to improve the accuracy of the measurement, a sampling loop has been added to the system in the course of this work. Indeed, when the adsorption process is fast, the time for the GC to analyze the outlet composition of the flue gas is too long which limits the number of points recorded to plot the breakthrough curve and therefore the accuracy of the measurement is lowered. The sampling loop collects and stores a sample of the flue gas (until 16 samples) at any programmed time and these collected samples are analyzed later by the GC. Thus, even if the adsorption process is fast, a large number of points can be used to plot the breakthrough curve.

5.2 Experimental protocols for the dynamic measurements

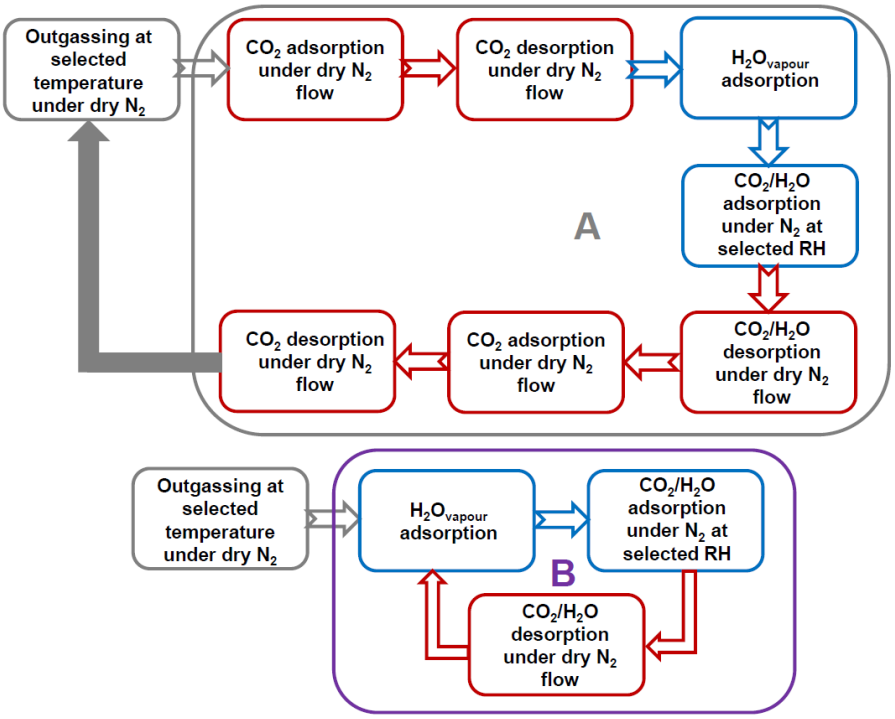

Figure S19 - Schematic representation of the different protocols used to evaluate adsorbents for post-combustion CO_2 capture in wet conditions (A) and for cycling experiments in wet conditions (B). Red frames correspond to the step performed in the dry mode of the system while blue frames correspond to the step performed in the wet mode of the system.

5.3 Complementary results from the dynamic CO_2 adsorption experiments

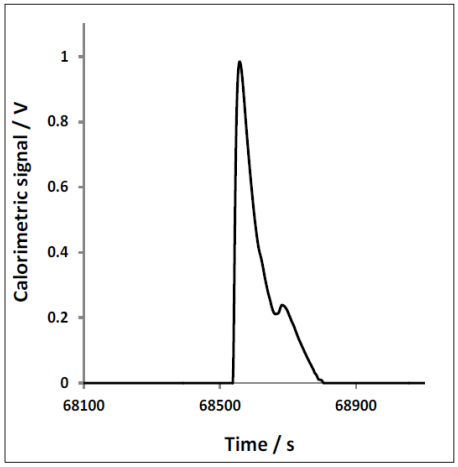

Figure S20. Unusual peak observed in the calorimetry signal which can be explained by the initial rapid (exothermic) adsorption of CO_2 followed by some H_2O desorption (endothermic) giving the trough in the overall signal.

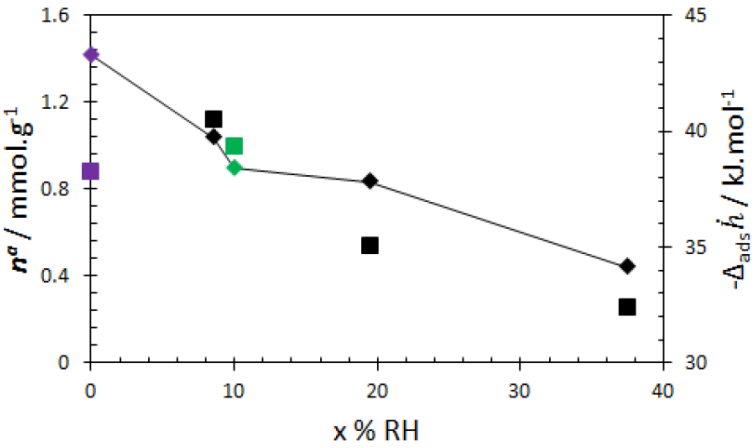

Figure S21 – CO_2 amount adsorbed (lozenge) and adsorption enthalpies (square) as function of relative humidity rate obtained from dynamic mode: 10 %, 20%, and 40% (black). After CO_2 adsorption under moisture conditions the MIL-96(Al) was dried in order to perform a new CO_2 adsorption cycle and uptake and enthalpy obtained are represented by purple points. The green points correspond to CO_2 uptake and enthalpy got from static mode after seven adsorption cycles on the pre-humidified MIL-96(Al).

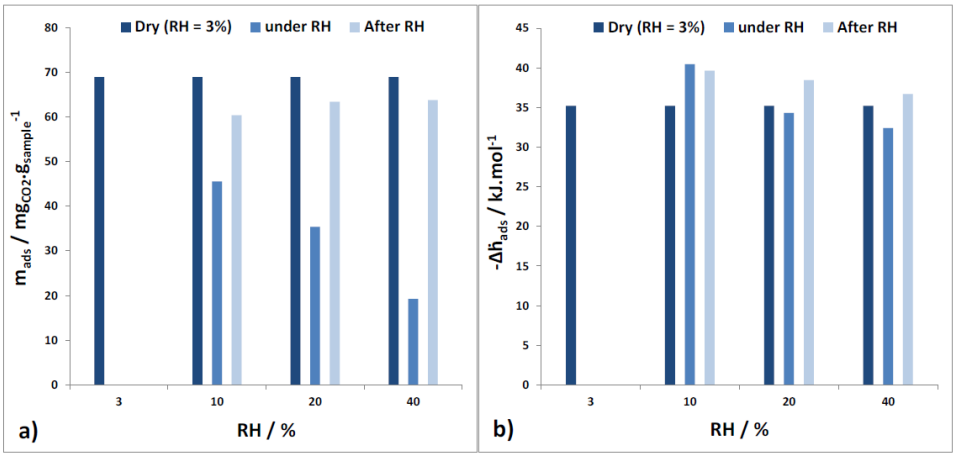

Figure S22 - CO_2 uptake on the MIL-96(Al) under dry conditions (RH = 3%), under RH = 10, 20 and 40% and after exposure to water vapour and b) the corresponding enthalpies of adsorption.

6. Further comparisons between samples

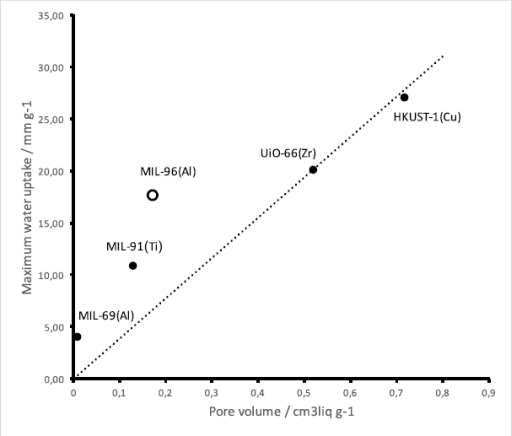

Figure S23. Correlation between maximum water uptake with respect to pore volume (calculated from N_2 physisorption at 77K) for several MOFs

Table S5. Henry's law constant calculated at low surface coverage for some MOFs having small pore size distribution.

Sample	MIL-69(Al)	MIL-91(Ti)	MIL-96(Al)	NH_2-MIL-53(Al)	MIL-53(Al)
Pore size distribution (Å)	3.1	3.9	4	6	8.5
K_H-H_2O (mol.g^{-1}.bar^{-1})	0.5	20.6	163	4.4	0.1

Table S6. Comparison of the selectivities for CO_2 / N_2 and CO_2 / CH_4 (2) Obtained from the open literature

Name	Mixture	%CO_2 in mixture	Selectivity	Calculation method	Ref
eea-MOF-4	CO_2/N_2	10	18	IAST	[1]
rtl-MOF-2	CO_2/N_2	10	38	IAST	[1]
SIFSIX-2Cu-i	CO_2/N_2	10	72	Measurement	[2]
Eu fcu-MOF	CO_2/N_2	10	82	IAST	[3]
SIFSIX-3-Cu	CO_2/N_2	10	15000	IAST	[4]
$Zn_4(pydc)_4(DMF)_2{\cdot}3DMF$	CO_2/N_2	15	42	IAST	[5]
UiO-66 (Zr) BTEC	CO_2/N_2	15	56	Measurement	[6]
Ni/DOBDC	CO_2/N_2	15	38	Measurement	[7]
USTA-16	CO_2/N_2	15	315	Measurement	[8]
MIL-91(Ti)	CO_2/N_2	15	150	IAST	[9]

Table S7. Initial enthalpies of adsorption for CO_2 as a function of CO2 uptake at low pressure, used to construct Figure 10.

Sample	Experimental conditions Temp/CO_2 partial pressure	CO_2 uptake	Enthalpy	Reference
MOF-74-Mg	296/ 0.1	5.36	47	[10]
MOF-74-Ni	296/ 0.1	2.74	41	[10]
MOF-74-Co	296/ 0.1	2.66	37	[10]
MOF-74-Zn	296/ 0.1	1.32	-	[10]
SIFSIX-3-Zn	298/ 0.15	2.43	45	[11]
SIFSIX-2-Cu-i	298/ 0.15	2.3	31.9	[11]
SIFSIX-2-Cu	298/ 0.15	0.36	22	[11]
$[Cu(bpy)_2SiF6)]$	298/ 0.2	1.1	-	[12]
$[Cu(bpy\text{-}1)_2SiF6)]$	298/ 0.15	0.84	27	[13]
$[Cu(bpy\text{-}2)_2SiF6)]$	298/ 0.15	0.52	21	[13]
UiO-66	298/ 0.1	0.67	25.5	[14]

[1] Z. Chen, K. Adil, L. J. Weseliński, Y. Belmabkhouta, M. Eddaoudi, *J. Mater. Chem. A*, **2015**, 3, 6276-6281.
[2] P. Nugent, Y. Belmabkhout, S. D. Burd, A. J. Cairns, R. Luebke, K. Forrest, T. Pham, S. Ma, B. Space, L. Wojtas, M. Eddaoudi, M.J. Zaworotko, *Nature*, **2013**, 495, 80–84.
[3] D.-X. Xue, Y. Belmabkhout, O. Shekhah, H. Jiang, K. Adil, A. J. Cairns, M. Eddaoudi, *J. Amer. Chem. Soc*., **2015**, 137, 5034-5040.
[4] O. Shekhah, Y. Belmabkhout, Z. Chen, V. Guillerm, A. Cairns, K. Adil, M. Eddaoudi, *Nat. Comms*., **2014**, 5, 4228.
[5] S. R. Ahrenholtz, C. Landaverde-Alvarado, M. Whiting, S. Lin, C. Slebodnick, E. Marand, A. J. Morris, *Inorg. Chem*., **2015**, 54(9), 4328-4336.
[6] Q. Yang, S. Vaesen, F. Ragon, A. D. Wiersum, D. Wu, A. Lago, T. Devic, C. Martineau, F. Taulelle, P. L. Llewellyn, H. Jobic, C. Zhong, C. Serre, G. De Weireld, G. Maurin, *Angew. Chem. Int. Ed*., **2013**, 52,
[7] J. Liu, J. Tian, P. K. Thallapally, B. P. McGrail, *J. Phys. Chem. C*, **2012**, 116(17):9575 – 9581.
[8] S. C. Xiang, Y. B. He, Z. J. Zhang, H. Wu, W. Zhou, R. Krishna and B. L. Chen, *Nat. Commun*., **2012**, 3, 954.
[9] V. Benoit, R. S. Pillai, A. Orsi, P. Normand, H. Jobic, F. Nouar, P. Billemont, E. Bloch, S. Bourrelly, T. Devic, P. A. Wright, G. de Weireld, C. Serre, G. Maurin and P. L. Llewellyn, *J. Mater. Chem. A*., **2016**, 4, 1383–1389
[10] S. R. Caskey, A. G. Wong-Foy, A. J. Matzger, *J. Amer. Chem. Soc.,* **2008**, 130, 33.
[11] P. Nugent, Y. Belmabkhout, S. D. Burd, A. J. Cairns,R. Luebke, K. Forrest, T. Pham, S. Ma, B.Space, L. Wojtas, M. Eddaoudi, M. J. Zaworotko, *Nature.* **2013**, 495, 80-84.
[12] K. A. Forrest, T. Pham, P. Nugent, S. D. Burd, A. Mullen, L. Wojtas, M. J. Zaworotko, B. Space, *Cryst. Growth Des.* **2013**, 13, 4542-4548.
[13] S. D. Burd, S. Ma, J. A. Perman, B. J. Sikora, R. Q. Snurr, P. K. Thallapally, J. Tian, L. Wojtas, M. J. Zaworotko, *J. Amer. Chem. Soc.* **2012**, 134, 3663-3666.
[14] Q. Wang, J. Bai , Z. Lu , Y. Pan , X. You, *Chem. Commun.* **2016**, 52, 443-452.

Annex F

A. Working capacity, adsorption enthalpy and selectivity

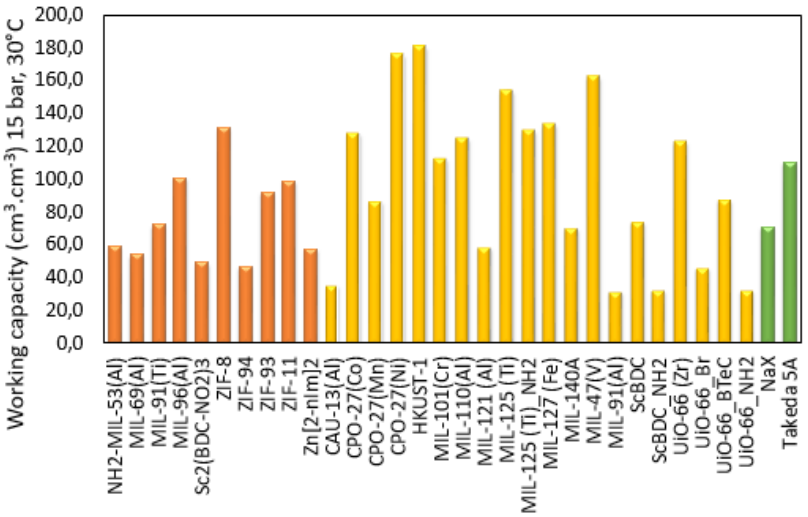

Figure F.1 - CO_2 working capacities ($cm^3.cm^{-3}$) calculated for high pressure conditions (1 and 15 bar) at 303K for MOFs of M^4CO_2 project (orange), MOFs previously studied within the laboratory (yellow) as well as NaX and Takeda 5A (green)

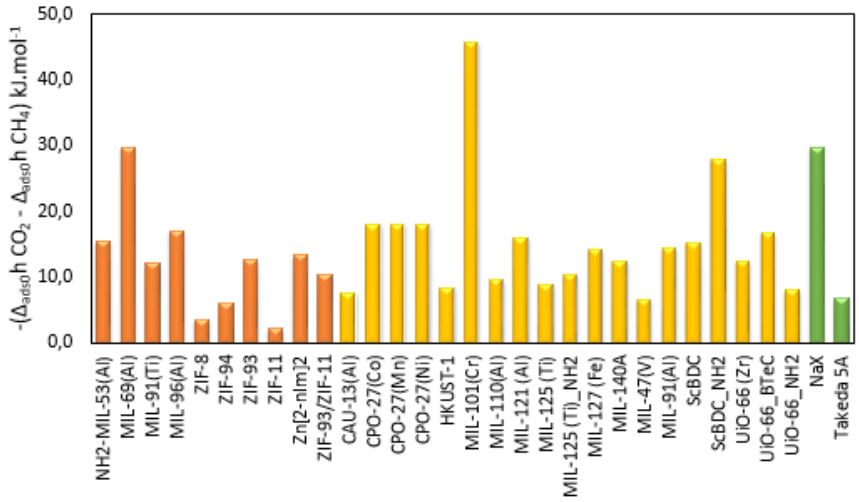

Figure F.2 - Difference of adsorption enthalpies between CO_2 and CH_4 extrapolated at zero coverage for various MOFs: M^4CO_2 project (orange), previously studied within the laboratory (yellow) as well as NaX and Takeda 5A (green)

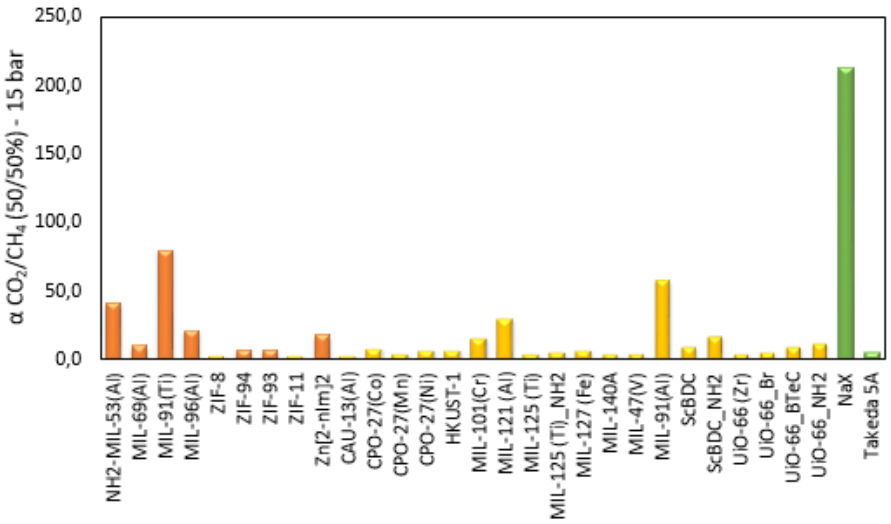

Figure F.3 - Predicted CO_2/ CH_4 selectivities between 1 and 15 bar at 303K for various MOFs: M^4CO_2 (orange), previously studied within the laboratory (yellow) and NaX and Takeda 5A (green)

B. Textural parameters from nitrogen adsorption at 77K

For the ZIF-8, ZIF-94 and ZIF-93, textural parameters as specific surface area, pore volume and external surface were obtained from nitrogen adsorption isotherm at 77K and are summarized in Table F.1.

ZIF's name	S_{BET} ($m^2.g^{-1}$)	BET range (p/p^0)	C value	V_P ($cm^3.g^{-1}$)	S_{EXT} ($m^2.g^{-1}$) (t-plot)
ZIF-8	1439	0.006-0.01	2110	0.48	102
ZIF-94	462	0.007-0.05	544	0.17	25
ZIF-93	777	0.003-0.02	1892	0.28	71

Table F.1 – Textural parameters obtained from N_2 adsorption at 77K for ZIF-8, ZIF-94 and ZIF-93

C. N_2 and CH_4 adsorption enthalpy profiles at 303K for the ZIF-8, ZIF-94, ZIF-93 and ZIF-11

N_2 and CH_4 adsorption isotherms as well as adsorption enthalpy profiles were obtained at 303K using a manometry system coupled with a Tian-Calvet microcalorimeter. The matching adsorption isotherms and enthalpy profiles are represented in Figure F.3, F.4, F.5, and F.6 respectively for the ZIF-8, ZIF-94, ZIF-93 and ZIF-11.

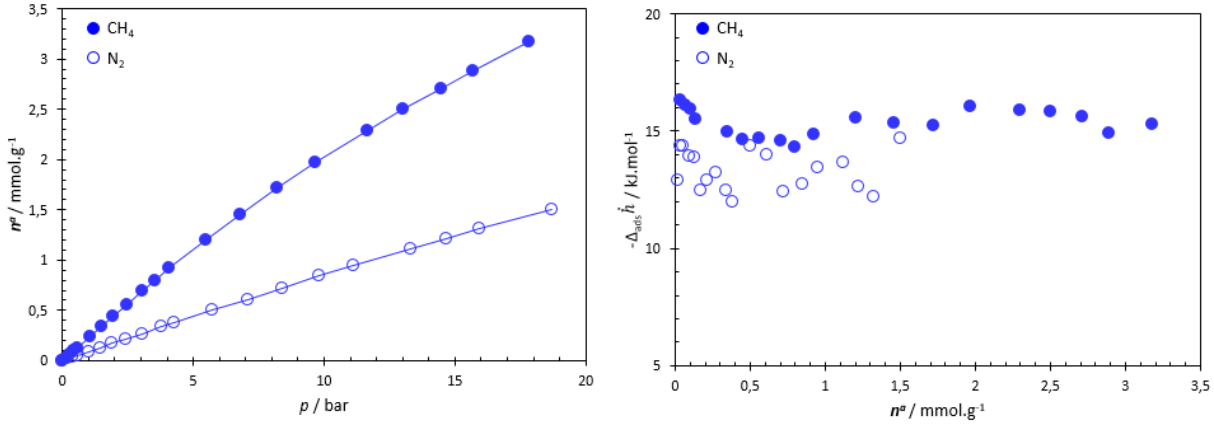

Figure F.3 – CH_4 and N_2 adsorption isotherms (left) and matching adsorption enthalpy profiles (right) at 303K on ZIF-8

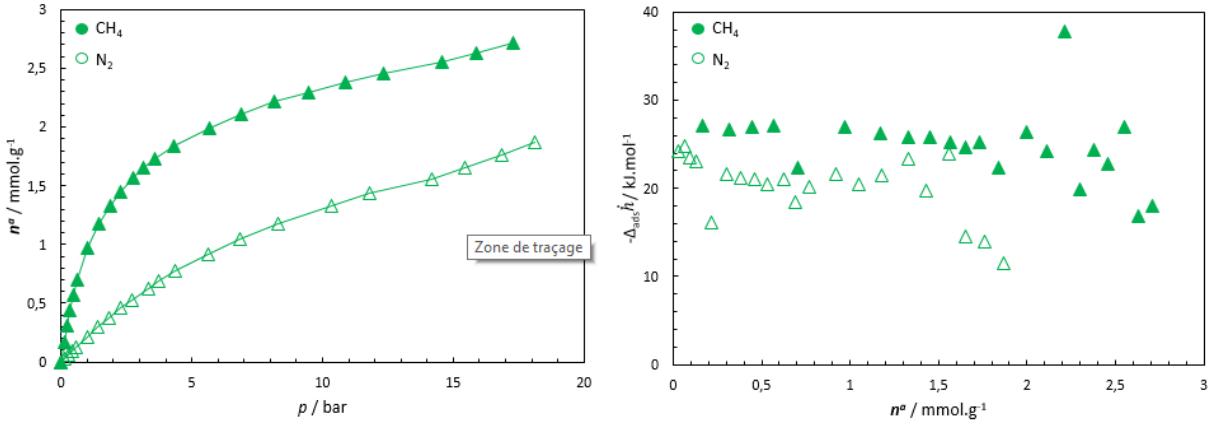

Figure F.4 – CH_4 and N_2 adsorption isotherms (left) and matching adsorption enthalpy profiles (right) at 303K on ZIF-94

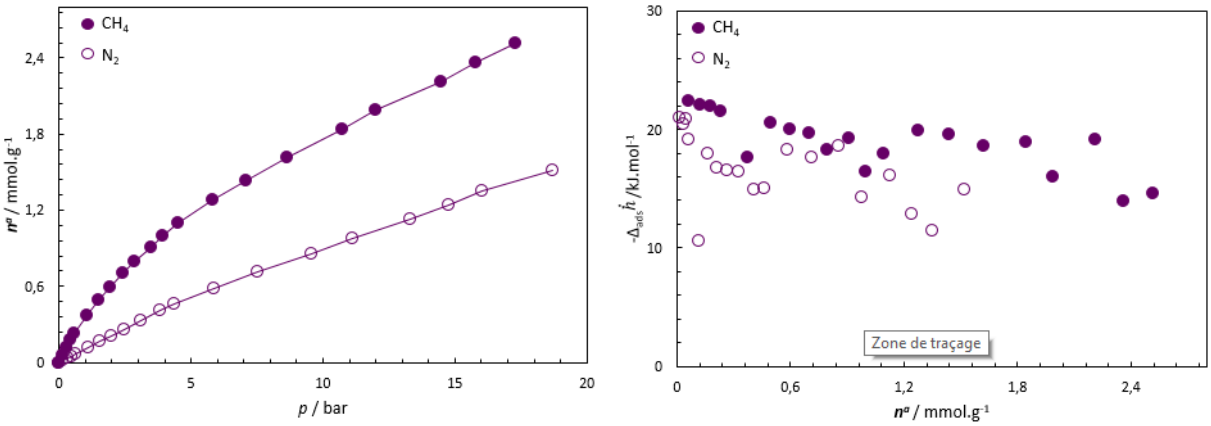

Figure F.5 – CH_4 and N_2 adsorption isotherms (left) and matching adsorption enthalpy profiles (right) at 303K on ZIF-93

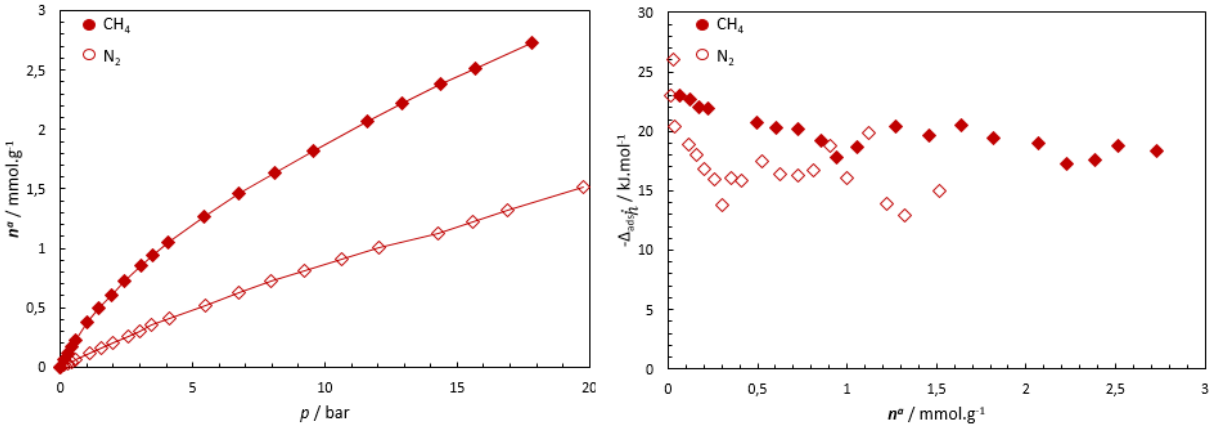

Figure F.6 – CH_4 and N_2 adsorption isotherms (left) and matching adsorption enthalpy profiles (right) at 303K on ZIF-11

D. Various parameters (pore size, specific surface area, pore volume, CO_2 amounts adsorbed at saturation, difference of adsorption enthalpies) for ZIFs materials and others MOFs

MOFs	Pore or cage size (Å)	S_{BET} ($m^2.g^{-1}$)	V_P ($cm^3.g^{-1}$)	CO_2 max excess uptake ($mmol.g^{-1}$)	$\Delta_{ads}\dot{h}[CO_2\text{-}N_2]$ ($kJ.mol^{-1}$)	$\Delta_{ads}\dot{h}[CO_2\text{-}CH_4]$ ($kJ.mol^{-1}$)	Ref
ZIF-8	11.6	1439	0.48	6.7	6.01	4.21	This work, [3]
ZIF-93	9.1	777	0.28	5.4	10.26	7.81	This work, [1]
ZIF-94	17.9	462	0.17	3.2	11.07	6.42	This work, [1]
ZIF-11	14.6	-	-	4.4	7.53	3.32	This work, [3]
ZIF-7	4.3	312	0.08	2.2	-	16.5	[4]
ZIF-90	10.8	1269	0.43	5.0	-	11.25	[5]
ZIF-76	12	1340	0.57	10.0	15.4	13.6	[6]
CAU-13(Al)	-	380	0.15	2.8	12.1	7.6	[7]
MIL-100(Cr)	25-29	1900	1.1	18.0	-	43.0	[8]
UiO-66(Zr)	11	1105	0.55	6.5	11.7	10.5	[9]
Mg-MOF-74	11-12	1542	0.63	13.6	-	19.5	[10]
MIL-91(Ti)	4.0	362	0.13	4.2	11.2	10.1	[11]
MIL-96(Al)	4.0	448	0.16	5.7	6.0	7.7	Our work
$Sc_2(BDC\text{-}NO_2)_3$	3.0-4.0	42	0.01	1.5	16.0	-	[12]
NaX	-	685	0.28	6.0	31	29.6	[13]
BPL	-	1150	0.53	7.6	-	5.9	[14]
Takeda 5A	-	1180	0.46	10.0	17.4	9.8	[13]

Table F.2 – Textural parameters as well as the difference of adsorption enthalpies CO_2 and N_2 or CO_2 and CH_4 from this work and/ or found in literature.

E. Water adsorption at 298K

The character hydrophilic/ hydrophobic of adsorbent surface can be probed by water adsorption in vapor phase. Water vapor adsorption is performed in liquid water maintained at 298K using a Belsorb-max device from BELJapan. In measuring cell, around 50-100 mg of the adsorbent is introduced and outgassed at fixed temperature (ramp of 1°C/min) for 16 hours under secondary vacuum (10^{-6} mbar).

The water adsorption measurement is limited at a relative pressure p/p° = 0.989 and equilibrium criterion was fixed at a pressure change every 300 seconds when the pressure measured corresponds to 0.5% of pressure expected.

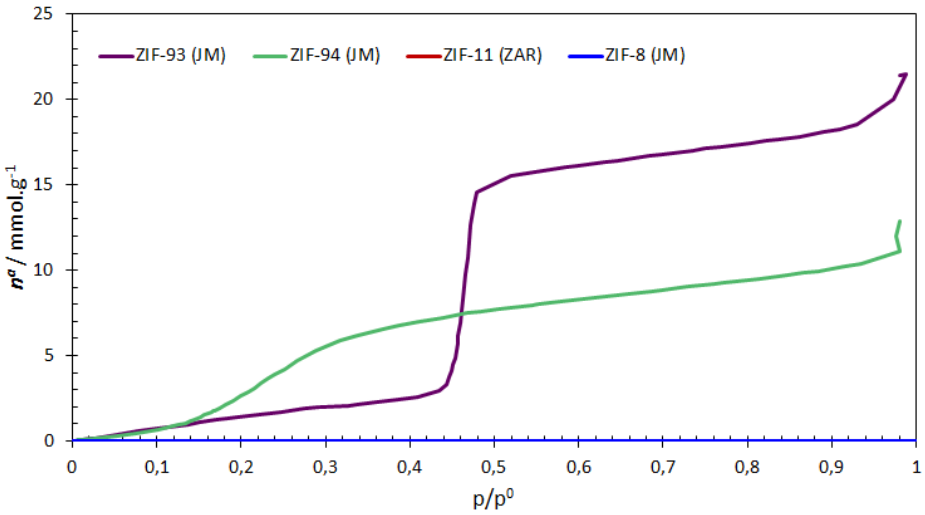

Figure F.7 – H_2O adsorption isotherms performed at 298K on ZIF-93 (purple), ZIF-94 (green), ZIF-8 (blue) and ZIF-11 (red)

From water adsorption isotherms at 298K, Henry's constants were calculated and are summarized in table 4.S3. This highlights the stronger hydrophilic surface of the ZIF-93 and the ZIF-94 compared to the ZIF-8 and the ZIF-11.

ZIF's	ZIF-93	ZIF-94	ZIF-8	ZIF-11
K_H-H_2O (mmol.g^{-1}.bar^{-1})	169	420	14	9

Table F.3 – Henry's constants of water for ZIF-93, ZIF-94, ZIF-8 and ZIF-11

[1] W. Morris *et al.*, « A Combined Experimental-Computational Study on the Effect of Topology on Carbon Dioxide Adsorption in Zeolitic Imidazolate Frameworks », *J. Phys. Chem. C*, vol. 116, n° 45, p. 24084-24090, nov. 2012.
[2] K. S. Park *et al.*, « Exceptional chemical and thermal stability of zeolitic imidazolate frameworks », *Proc. Natl. Acad. Sci.*, vol. 103, n° 27, p. 10186-10191, mai 2006.
[3] K. S. Park *et al.*, « Exceptional chemical and thermal stability of zeolitic imidazolate frameworks », *Proc. Natl. Acad. Sci.*, vol. 103, n° 27, p. 10186-10191, mai 2006.
[4] « Synthesis and characterization of zeolitic imidazolate framework ZIF-7 for CO2 and CH4 separation - ScienceDirect ». [En ligne]. Disponible sur: http://www.sciencedirect.com/science/article/pii/S1387181114000778. [Consulté le: 16-août-2017].
[5] H. Amrouche *et al.*, « Experimental and Computational Study of Functionality Impact on Sodalite–Zeolitic Imidazolate Frameworks for CO2 Separation », *J. Phys. Chem. C*, vol. 115, n° 33, p. 16425-16432, août 2011.
[6] J. Pérez-Pellitero *et al.*, « Adsorption of CO2, CH4, and N2 on Zeolitic Imidazolate Frameworks: Experiments and Simulations », *Chem. – Eur. J.*, vol. 16, n° 5, p. 1560-1571, févr. 2010.
[7] F. Niekiel *et al.*, « Conformation-Controlled Sorption Properties and Breathing of the Aliphatic Al-MOF [Al(OH)(CDC)] », *Inorg. Chem.*, vol. 53, n° 9, p. 4610-4620, mai 2014.
[8] P. L. Llewellyn *et al.*, « High Uptakes of CO2 and CH4 in Mesoporous Metal—Organic Frameworks MIL-100 and MIL-101 », *Langmuir*, vol. 24, n° 14, p. 7245-7250, juill. 2008.
[9] Q. Yang *et al.*, « Understanding the Thermodynamic and Kinetic Behavior of the CO2/CH4 Gas Mixture within the Porous Zirconium Terephthalate UiO-66(Zr): A Joint Experimental and Modeling Approach », *J. Phys. Chem. C*, vol. 115, n° 28, p. 13768-13774, juill. 2011.
[10] P. D. C. Dietzel, V. Besikiotis, et R. Blom, « Application of metal–organic frameworks with coordinatively unsaturated metal sites in storage and separation of methane and carbon dioxide », *J. Mater. Chem.*, vol. 19, n° 39, p. 7362-7370, oct. 2009.
[11] V. Benoit *et al.*, « MIL-91(Ti), a small pore metal–organic framework which fulfils several criteria: an upscaled green synthesis, excellent water stability, high CO2 selectivity and fast CO2 transport », *J. Mater. Chem. A*, vol. 4, n° 4, p. 1383-1389, janv. 2016.
[12] R. S. Pillai, V. Benoit, A. Orsi, P. L. Llewellyn, P. A. Wright, et G. Maurin, « Highly Selective CO2 Capture by Small Pore Scandium-Based Metal–Organic Frameworks », *J. Phys. Chem. C*, vol. 119, n° 41, p. 23592-23598, oct. 2015.
[13] A. D. Wiersum, J.-S. Chang, C. Serre, et P. L. Llewellyn, « An Adsorbent Performance Indicator as a First Step Evaluation of Novel Sorbents for Gas Separations: Application to Metal–Organic Frameworks », *Langmuir*, vol. 29, n° 10, p. 3301-3309, mars 2013.
[14] S. Himeno, T. Komatsu, et S. Fujita, « High-Pressure Adsorption Equilibria of Methane and Carbon Dioxide on Several Activated Carbons », *J. Chem. Eng. Data*, vol. 50, n° 2, p. 369-376, mars 2005.

Relations entre structure et texture de matériaux poreux et l'évaluation de leurs propriétés de piégeage du CO_2

Les Membranes à Matrices Mixtes (MMM's) sont des matériaux prometteurs pour la capture de CO_2 en comparaison aux technologies actuelles telles que l'absorption par solvants aminés (monoéthanolamine).
Les 'Metal-Organic Frameworks' (MOFs) sont des matériaux poreux cristallins envisagés pour être intégrés sous forme de nanoparticules aux polymères des MMM's. Ils résultent de la combinaison de nœuds métalliques et de ligands organiques pour former des structures tridimensionnelle (3D) organisées. Ils possèdent divers avantages : des aires spécifiques et des volumes poreux élevés, des tailles de pores contrôlables, et pour certains une stabilité à l'eau. Les MOFs ont une chimie adaptable aux applications souhaitées contrairement aux adsorbants classiques tels que les charbons actifs, les zéolithes.

D'une part, ce travail a eu pour objectif l'évaluation des performances de séparation du CO_2 par des MOFs microporeux en vue des séparations CO_2/N_2 et CO_2/CH_4. Les interactions 'gaz-adsorbant' sont favorisées au sein des MOFs par : (1) une réduction de la taille de pores et du volume poreux pouvant engendrer des effets de confinements, de tamis moléculaire ou (2) par la présence de groupements de surface. En conséquence, ces paramètres peuvent contribuer à l'amélioration de la sélectivité du CO_2 et ont été étudiés pour divers systèmes de MOFs microporeux.
D'autre part, les paramètres texturaux (aire spécifique, volume poreux) et thermodynamiques (enthalpies d'adsorption) ont été corrélés aux quantités maximales de CO_2 adsorbées au travers d'une approche quantitative de relation de structure-propriété pour établir des tendances linéaires.

Expérimentalement, les paramètres texturaux ont été déterminés à partir des isothermes d'adsorption de diazote à 77K. Les capacités et les enthalpies d'adsorption des gaz purs (CO_2, N_2, CH_4) ont été mesurées à 303K via un système de manométrie couplé à un microcalorimètre de type Tian-Calvet. Les sélectivités en co-adsorption ont été prédites à partir des isothermes d'adsorption de gaz pur et de la Théorie des Solutions Idéales Adsorbées ('IAST').

Mots-clés : Metal-Organic Frameworks, adsorption de gaz, microcalorimétrie, approche quantitative de relations structure-propriété

Developing relationships between the structure and texture of porous materials and their CO_2 capture properties

Mixed Matrix Membranes (MMM's) are promising materials for CO_2 capture compared to current technologies such as amine scrubbing. In the EU funded project MMM's were constricted from porous polymers with Metal-Organic Frameworks (MOFs) incorporated within the polymer matrix.
Metal-Organic Frameworks are crystalline porous materials which were integrated as nanoparticles into the polymer membrane in order to enhance their separation properties. MOFs are built from metal nodes and organic ligands to yield well-defined tridimensional structures (3D). They may possess various advantages: high specific surface area and pore volume, tunable pore size and some are stable in presence of water. The chemistry of MOFs can be finely tuned to targeted applications to a greater degree than traditional adsorbents such as activated carbons, zeolites.

This work has first aimed to assess CO_2 separation performances of microporous MOFs for CO_2/N_2 and CO_2/CH_4 gas separations. The 'gas-adsorbent' interactions are favored in MOFs by: (1) a decrease in pore size which can induce confinement effects such as molecular sieve effects or (2) the presence of surface groups. Thus, these factors can both contribute to the improvement in CO_2 selectivity and have been studied for various microporous MOFs.
In a second step, textural (specific surface area, pore volume) and thermodynamic (adsorption enthalpy) parameters have been correlated to CO_2 maximum excess uptakes through a quantitative structure-property approach to establish some linear trends.

Experimentally, textural parameters were determined from N_2 adsorption isotherm at 77K. While, adsorption capacity and enthalpy of pure gases (CO_2, N_2, CH_4) at 303K were obtained by a home-made manometry system coupled with a Tian-Calvet microcalorimeter. The selectivities for co-adsorption are calculated from single gas adsorption isotherms and the use of Ideal Adsorbed Solution Theory ('IAST').

Key words: Metal-Organic Frameworks, gas adsorption, microcalorimetry, quantitative structure-property approach